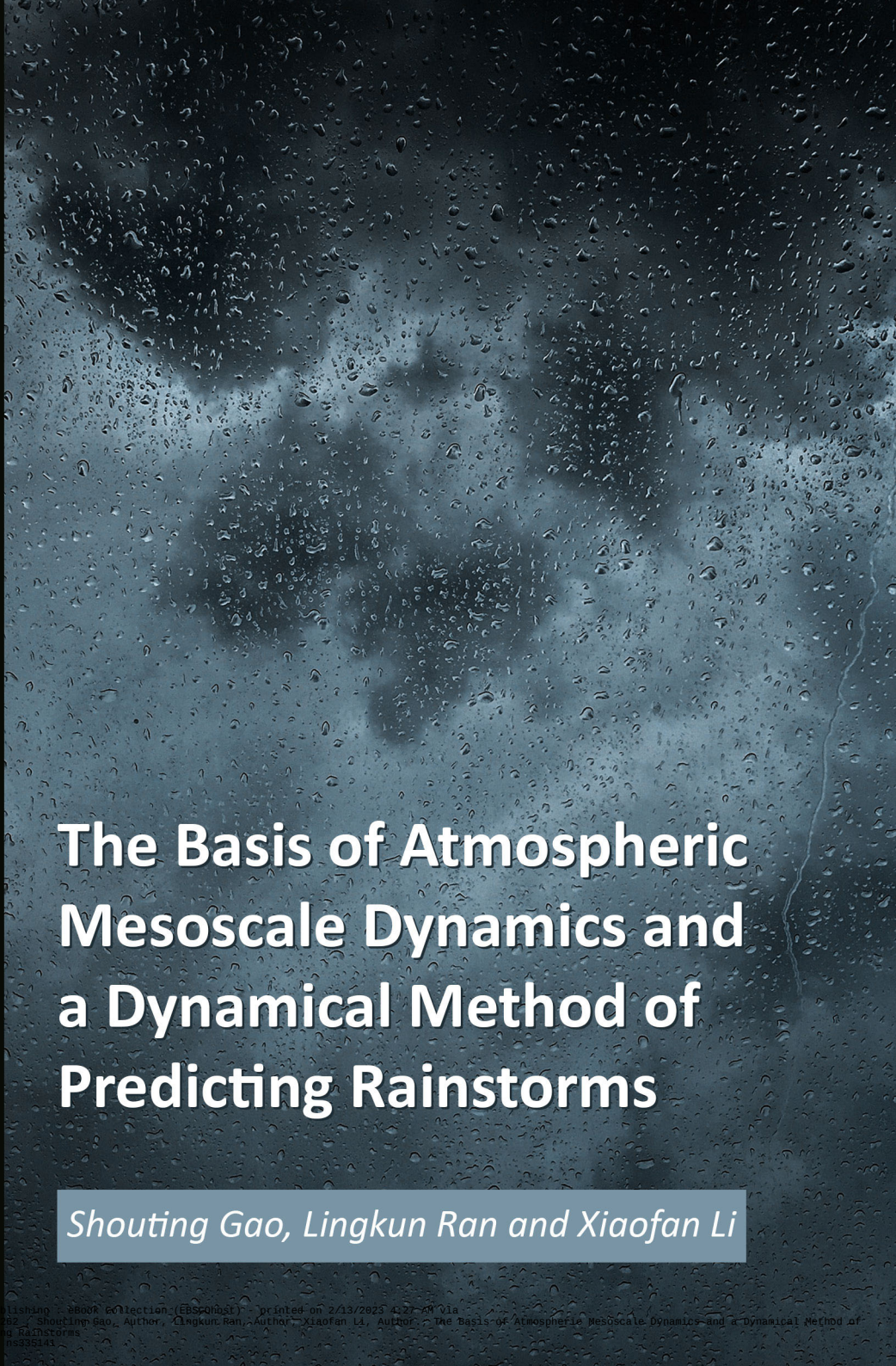

The Basis of Atmospheric Mesoscale Dynamics and a Dynamical Method of Predicting Rainstorms

Shouting Gao, Lingkun Ran and Xiaofan Li

The Basis of Atmospheric Mesoscale Dynamics and a Dynamical Method of Predicting Rainstorms

The Basis of Atmospheric Mesoscale Dynamics and a Dynamical Method of Predicting Rainstorms

By

Shouting Gao, Lingkun Ran
and Xiaofan Li

Cambridge
Scholars
Publishing

The Basis of Atmospheric Mesoscale Dynamics and a Dynamical Method of Predicting Rainstorms

By Shouting Gao, Lingkun Ran and Xiaofan Li

This book first published 2021

Cambridge Scholars Publishing

Lady Stephenson Library, Newcastle upon Tyne, NE6 2PA, UK

British Library Cataloguing in Publication Data
A catalogue record for this book is available from the British Library

ISBN (10): 1-5275-6620-X
ISBN (13): 978-1-5275-6620-0

CONTENTS

List of Tables vii

List of Figures viii

Preface xxi

Abbreviation and Meanings of the Terms used in the study xxv

Chapter One 1
Basic Atmospheric Dynamic Parameters and Their Context

Chapter Two 34
Basic Equations of Mesoscale Dynamics

Chapter Three 56
Dynamic Parameters of Inhomogeneously Saturated Air and Related Equations

Chapter Four 78
Vorticity: Introduction and Related Equations

Chapter Five 116
Divergence: Introduction and Related Equations

Chapter Six 128
Deformation: Introduction and Related Equations

Chapter Seven 148
Generalized Frontogenesis Theory

Chapter Eight 180
Atmospheric Potential Vorticity

Chapter Nine 198
Mesoscale Instability and Analysis Methods

Chapter Ten 236
Atmospheric Gravity Waves

Chapter Eleven 289
Mesoscale Balance and Unbalance

Chapter Twelve 316
Dynamic Forecasting Methods Based on Scalar Field Theory

Chapter Thirteen 394
Dynamic Forecasting Methods Based on Vector Field Theory

Chapter Fourteen 460
Methods of Forecasting Torrential Rainfall Using Dynamic Factors

Bibliography 495

Index 521

LIST OF TABLES

12.4.1. The correlation coefficient and the root-mean-square deviation between terms 1–8 and the sum of the terms in equation (12.4.1)

LIST OF FIGURES

1.1. Initial shear flow
1.2. Uniform flow after mixing enough
4.2.1. Path of typhoon Bilis
4.2.2. Horizontal distribution of winds in typhoon Bilis at 850 hPa at (a) 12:00 on 12 July 2006 and (b) 18:00 on 13 July 2006
4.2.3. Distribution of vorticity and trend in vorticity on the 850-hPa isobaric surface for 18:00 LST on 12 July 2006. The shaded area denotes positive values, the thick line marks the path of typhoon Bilis, and the typhoon symbol indicates the central position of the typhoon: (a) vorticity, (b) vorticity trend calculated using the classical vorticity equation, (c) vorticity trend calculated using the advection vorticity equation, (d) advection term, (e) pitching term, and (f) geostrophic vorticity and water advection term in the advection vorticity equation.
5.2.1. Meridional–temporal cross-section of the wave-activity density, $\langle |A| \rangle$, along the 120°E meridian (contour spacing: 10^{-5} K s^{-2}). The shadow area in the background denote the six-hour cumulative observed rainfall amount (mm).
5.2.2. Meridional–vertical cross-section of the wave-activity flux divergence, $\nabla \cdot \mathbf{F}$, along the 119°E meridian (contour spacing: 10^{-11} K m^{-1} s^{-2}) at: (a) 18:00 UTC, 7 August, (b) 18:00 UTC, 8 August, and (c) 18:00 UTC, 9 August 2009. The gray bars denote the six-hour cumulative observed rainfall amount (mm).

5.2.3. The time evolution of: (a) $\left\langle \left| \nabla \cdot \mathbf{F} \right| \right\rangle$, (b) $\left\langle \left| \nabla \cdot \mathbf{F}_1 \right| \right\rangle$, (c) $\left\langle \left| \nabla \cdot \mathbf{F}_2 \right| \right\rangle$, and (d) $\left\langle \left| \nabla \cdot \mathbf{F}_e \right| \right\rangle$. Units: 10^{-7} K s^{-2}, at the center region of the typhoon morakot.

6.3.1. Vorticity enstrophy (color-shaded area; units: 10^{-9} s^{-2}) and streamlines at 800 hPa. The black boxes enclose the whole vortex area. The red lines are the six-hour accumulated rainfall amount (mm). The triangle indicates the location of the formation of the vortex.

6.3.2. Distribution of (a) the VorE–DefE interaction term, (b) the VorE–DivE interaction term, and (c) the DivE–DefE interaction term at 800 hPa for 18:00 UTC, 16 August 2009. Units: 10^{-13} s^{-3}

6.3.3. Horizontal distributions of the two sub-terms of the VorE–DefE interaction term: (a) the term related to the Coriolis parameter and (b) the coupling of the divergence and the shear of the rotational wind (units: 10^{-13} s^{-2}). (c) The divergence at 800 hPa at 18:00 UTC, 16 August 2009.

7.1.1. The tangential velocity derived from the traditional Rankine combined vortex (solid line) and vortex (dashed line) which has a similar appearance to a smoothed version of the Rankine combined vortex.

7.1.2. Fig. 7.1.2. (a) Deformation, (b) divergence, and (c) vorticity fields (units: 10^{-5} s^{-1}) of the idealized flow shown in Fig. 7.1.1

7.1.3. A 2D relative humidity field subject to advection by an idealized deformational flow field at (a) 0 hours, (b) 12 hours, (c) 24 hours, and (d) 36 hours. The contour intervals have a spacing of 0.1, and all contours at time zero have an east–west orientation.

7.1.4. A 2D relative humidity field subject to advection by an idealized deformational flow field at (a) 0 hours, (b) 12 hours, (c) 24 hours, and (d) 36 hours. The contours have a spacing of 0.1, and all contours

at time zero have a southwest–northeast orientation.

7.2.1. Schematic illustrating right-handed Cartesian coordinate systems (*x, y*) and (*s, n*) defined locally by rotating the standard (*x, y*) Cartesian coordinates system through an angle β to give the (*s,n*) system. The *s*-axis is tangent to an isoline of θ^* and is directed such that the *n*-axis points toward colder air. The angle between $\vec{n}$ and the *x*-axis is ϕ.

7.2.2. The temporal mean frontal surface (the region of intense iso-θ^*) at 00:00 UTC, 11 August 2004 together with the values of the different terms in the frontogenesis function (equation (7.2.6)). Thick real isoline is iso-θ^* (units: K). The shading denotes the regions where the intensity of the different terms in the frontogenesis function satisfies: (a) $T_{1234} > 1$, (b) $T_1 > 1$, (c) $T_2 < -1$, (d) $T_3 > 0.2$, and (e) $T_4 > 0.2$ (units: 10^{-9} K m^{-1} s^{-1}).

8.1. The change in $\psi(rh)$ with rh (k = 9, T = 280 K, p = 1000 hPa, and $q_s = 6 \times 10^{-3}$ g g^{-1})

9.2.1. The T-lnp map: r and r_d are used to determine the atmospheric stability. (a), (b), and (c) illustrate, respectively, $r > r_d$, $r < r_d$, and $r = r_d$, which are the three types of stratified stability.

9.2.2. Illustration of types of unstable energy: (a) absolute instability, (b)

absolute stability, (c) real potential instability (the area above point c is larger than the area below point c), and (d) pseudo-potential instability (the area above point c is smaller than the area below point c)

9.3.1. Unstable symmetric unstable situation; momentum, $M = \bar{U} - fy$

9.4.1. Sketch of a vortex sheet

9.4.2. Disturbance at a discontinuous interface

9.4.3. Sketch of the vortex layer in a shear line

10.1. The phase velocity (C) and the phase-velocity components (Cy and Cz)

10.2. The relationship between the wave-number vector, $\mathbf{K} = (l, n)$, and the group-velocity, $\mathbf{C}g = (Cgy, Cgz)$.(a) $\lambda_y > 0$ and $\lambda_z > 0$; (b) $\lambda_y < 0$ and $\lambda_z < 0$

10.4.1 Schematic diagram of (a) natural light, (b) linearly polarized light, and (c) elliptically polarized light

10.4.2. Polarization diagram

10.5.1 The power spectral density of the vertical velocity. The contour represents the phase velocity $c = \omega / k$, which are 10m/s, 15m/s and 25m/s respectively.

10.5.2 Phase spectrum and condensation spectrum of vorticity and divergence.

10.5.3 Phase difference (a), cohesion spectrum (b) and amplitude spectrum (c) of vorticity and divergence with a frequency of 0.025 and cumulative precipitation (red line in a).

10.5.4 The height-zonal profile of vertical velocity of the gravity wave reconstructed by selecting the range of wavelength

40~50km and cycle 80~100 min.

12.1.1. The year-to-year change in annual mean temperature (K) and relative humidity (%) in Beijing and Tianjin from 1953 to 2003

12.1.2. Geopotential height (gpdm) and temperature (K) at 500 hPa at 00:00 UTC on 31 July 2002. The shaded area is the Tibetan Plateau.

12.1.3. Moisture transport at 850 hPa (based on the $\mathbf{v}q$ vector; gm g^{-1} s^{-1}) on 31 July 2002. The shaded area is the Tibetan Plateau.

12.1.4. Distribution of the average vertical velocity (Pa s^{-1}) from 31 July to 4 August 2002: zonal–vertical section along 39.9°N

12.1.5. Plot of *T*–ln *p* from observations made at 00:00 UTC at the Beijing station on 31 July 2002. The solid line at the left-hand side denotes the relative humidity (%), the dashed line denotes the dew-point temperature (K), and the thick and thin solid lines on the right hand side represent the state and stratification curves, respectively.

12.1.6. Generalized moist potential vorticity (GMPV: solid line with an interval of 0.2 PVU) and relative humidity (RH: dashed lines with an interval of 10%) at 925 hPa at 00:00 UTC on 31 July 31 2002. The shaded regions are regions where GMPV ≤ −0.25.

12.1.7. Vertical sections of GMPV at 00:00 UTC on 2 August 2 (units: PVU): (a) meridional–vertical section along 116.3°E; (b) zonal–vertical section along 39.9°N

12.1.8. The GMPV trend at 950 hPa (units: 10−4 PVU s−1) from (a) 18:00 UTC on 29 July to 00:00 UTC on 30 July 2002 and from (b) 18:00 UTC on 4 August to 00:00 UTC on 5 August 2002. Shaded regions have values less than −0.25.

12.2.1. Horizontal distribution of the NGMPV on the 700-hPa surface (shaded), superimposed on the geopotential height on the 1000-hPa surface (interval: 10 gpdm) for (a) 00:00 UTC, 7 April; (b) 06:00 UTC, 7 April; (c) 12:00 UTC, 7 April; (d) 18:00 UTC, 7 April; (e) 00:00 UTC, 8 April; (f) 06:00 UTC, 8 April; and (g) 18:00 UTC 8

April 2001

12.2.2. Horizontal distribution of the NGMPV on the 700-hPa surface (shaded), superimposed on the geopotential height on the 1000-hPa surface (interval: 10 gpdm) for (a) 00:00 UTC, 7 April; (b) 06:00 UTC, 7 April; (c) 12:00 UTC, 7 April; (d) 18:00 UTC, 7 April; (e) 00:00 UTC, 8 April; (f) 06:00 UTC, 8 April; (g) 12:00 UTC, 8 April; and (h) 18:00 UTC, 8 April 2001

12.2.3. Track of the low NGMPV center from 06:00 UTC on 7 April to 18:00 UTC on 8 April 2001 (dashed lined with rectangles) together with the surface track of the cyclone (solid line with circles).

12.3.1. Total precipitation from 22 June to 2 July 1999 (mm) and the distribution of the moist potential vorticity substance (shaded area)

12.3.2 (a). Distribution of moist potential vorticity substance at 700 hPa at 00:00 UTC on 23 June 1999 (units: 10^{-6} K m^{-1} s^{-1}; solid line: moist potential vorticity substance; dashed line: θ_e; the shaded area marks where the value of the moist potential vorticity substance ≤ −2.)

12.3.2 (b). 24-hour precipitation as observed at 00:00, 23 June 1999 (mm)

12.3.3 (a). As for Fig. 12.3.2 (a) but for 00:00 UTC, 24 June 1999

12.3.3 (b). As for Fig. 12.3.2 (b) but for 00:00 UTC, 24 June 1999

12.3.4 (a). As for Fig. 12.3.2 (a) but for 00:00 UTC, 25 June 1999

12.3.4 (b). As for Fig. 12.3.2 (b) but for 00:00 UTC, 25 June 1999

12.3.5 (a). As for Fig. 12.3.2 (a) but for 00:00 UTC, 26 June 1999

12.3.5 (b). As for Fig. 12.3.2 (b) but for 00:00 UTC, 26 June 1999

12.4.1. The (a) equivalent potential temperature (K) and (b) streamline fields at the 700-hPa level at 00:00 UTC, 5 July 2003

12.4.2. (a) Observed and (b) predicted 36-hour total rainfall (mm) in the middle and lower reaches of the Yangtze River from 00:00 UTC, 4 July to 12:00 UTC, 5 July 2003

12.4.3. Time–latitude cross-sections of 6-hour accumulated precipitation (mm) along 118°E from 00:00 UTC, 4 July to 12:00 UTC, 5 July 2003

12.4.4. Time–latitude cross-sections of mass divergence (10^{-5} kg m^{-3} s^{-1}) at the 4.287-km level along 118°E from 00:00 UTC, 4 July to 12:00 UTC, 5 July 2003

12.4.5. (a) The six-hour precipitation (mm) and (b) the absolute value of the six-hour mass divergence (10^{-5} kg s^{-1} m^{-3}) at the 4.287-km level at the center of the precipitation zone (119°E, 32°N)

12.4.6. Meridional–vertical section of the mass divergence along 118°E (10^{-5} kg m^{-3} s^{-1}) at 00:00 UTC, 5 July 2003. The shaded regions denote where the absolute value of the mass divergence is greater than 2.

12.4.7. Meridional–vertical sections along 118°E of (a) the horizontal component and (b) the vertical component of the mass divergence (10^{-5} kg s^{-1} m^{-3}) at 00:00 UTC, 5 July, 2003. The shaded regions denote where the absolute value of the mass divergence is greater than 2.

12.4.8. Meridional–vertical section of the vertical velocity ($m\,s^{-1}$) along 118°E at 00:00 UTC, 5 July 2003. The shaded regions denote where the absolute value of the vertical velocity is greater than 2.

12.4.9. Meridional–vertical section of R_{cm} along 118°E (10^{-6} kg m^{-3} s^{-1}) at 00:00 UTC, 5 July 2003. The shading denotes regions where the absolute value of R_{cm} is greater than 3.

12.4.10. Meridional–vertical section of q_{con} (the sum of the mixing ratios of cloud water, raindrops, ice, snow, and graupel; shown as isolines) along 118°E and q (the sum of the mixing ratio of water condensate and vapor; shown as shaded regions; units: g g^{-1} for (a) 00:00 UTC and (b) 06:00 UTC, 5 July 2003.

12.5.1. Time–latitude cross-section along 119°E for the six-hour cumulative precipitation (mm) from 06:00 UTC on 4 July to 12:00 UTC on 5 July 2003

12.5.2. Total deformation (10^{-5} s^{-1}) at 700 hPa at 00:00 UTC on 4 July 2003. The shaded areas are areas where the total deformation exceeds 5×10^{-5} s^{-1}.

12.5.3. Time–latitude cross-section of the total deformation (10^{-5} s^{-1}) along 119°E at 700 hPa from 06:00 UTC on 4 July to 12:00 UTC on 5 July 2003. The shaded areas are areas where the total deformation exceeds 6×10^{-5} s^{-1}.

12.5.4. Time–longitude cross-section along 37°N for the six-hour cumulative precipitation (mm) from 06:00 UTC, 10 October to 12:00 UTC, 11 October 2003.

12.5.5. Equivalent potential temperature (K) at (a) 00:00 UTC on 10 October and (b) 00:00 UTC on 11 October and the streamline at (c) 00:00 UTC on 10 October and (d) 00:00 UTC on 11 October 2003. The fields at 900 hPa are shown.

12.5.6. Total deformation (10^{-5} s^{-1}) at 900 hPa at 00:00 UTC, 11 August 2003. The shaded areas are areas where the value of the total deformation exceeds 5×10^{-5} s^{-1}.

12.5.7. Fig. 12.5.7. Time–latitude cross-section of the advection term (10^{-9} s^{-2}) along 119°E at 700 hPa from 00:00 UTC on 3 July to 00:00 UTC on 6 July 2003.The shaded areas are areas where the total deformation is smaller than −0.5.

12.5.8. Time–latitude cross-section of the horizontal divergence term (10^{-9} s^{-2}) along 119°E at 700 hPa from 00:00 UTC on 3 July to 00:00 UTC on 6 July 2003. The shaded areas are areas where the total deformation exceeds 1.

12.5.9. Time–latitude cross-section of the β-effect term (10^{-10} s^{-2}) along 119°E at 700 hPa from 00:00 UTC on 3 July to 00:00 UTC on

6 July 2003.The shaded areas are areas where the total deformation exceeds 0.5.

12.5.10. Time–latitude cross-section of the horizontal pressure term (10^{-9} s^{-2}) along 119°E at 700 hPa from 00:00 UTC on 3 July to 00:00 UTC on 6 July 2003.The shaded areas are areas where the total deformation exceeds 1.

12.5.11. Time–latitude cross-section of the vertical velocity term (10^{-9} s^{-2}) along 119°E at 700 hPa from 00:00 UTC on 3 July to 00:00 UTC on 6 July 2003. The shaded areas are areas where the total deformation exceeds 1.

12.5.12. Time–latitude cross-section of the sum of the terms on the right-hand side of the equation for the deformation trend (10^{-9} s^{-2}) along 119°E at 700 hPa from 00:00 UTC on 3 July to 00:00 UTC on 6 July 2003. The shaded areas are areas where the total deformation exceeds 2.

12.6.1. Path of the vapor potential vortex (in red) and the path of Typhoon Pu Gong Ying (in blue) from 27 June to 1 July 2004

12.6.2. The distribution of vapor potential vorticity advection at 00:00 UTC (shaded) and the vapor potential vorticity at 06:00 UTC (real line) at 500 hPa from 27 June to 1 July 2004

12.7.1 On July 21, 2012, (a) 24-hour cumulative precipitation, (b) TBB distribution of 1200 UTC, and (c) large-scale situation configuration of 0000 UTC superimposed on infrared cloud image

12.7.2 Horizontal distribution of the Q_{ms} absolute value by vertically integrating ($\left\langle \left| Q_{ms} \right| \right\rangle$ unit: 10^{-8} m^3 K s^{-2} kg^{-2}) of the second-order moist potential vorticity at 0000 UTC from 21 July 2012 to 22 July 2012 at 0000 UTC. The shaddow area shows 6-hour cumulative precipitation (unit: mm).

12.7.3 Time section of second-order moist potential vorticity along 40°N

0000 UTC-22 July 2012 (Unit: 10^{-8} m^3 K s^{-2} kg^{-2}). The shaddow area is 6-hour accumulated precipitation.

13.1.1. The distribution of the potential temperature

13.1.2. Horizontal distributions of (a) $[C_x]$ (10^{-2} s^{-1} K), (b) $[C_y]$ (10^{-2} s^{-1} K), (c) $[C_z]$ (10^{-4} s^{-1} K), and (d) PV (10^{-4} s^{-1} K) at 00:00 UTC on 13 August 2004. The shaded areas denote different values of CH (10^{-1} kg m^{-2}).

13.1.3. The evolution of the distribution of (a) $[C_x]$ (10^{-2} s^{-1} K), (b) $[C_y]$ (10^{-2} s^{-1} K), and (c) $[C_z]$ (10^{-4} s^{-1} K) averaged over the area from 37°N to 42°N and 112°E to 119°E for the period 00:00 UTC on 12 August to 12:00 UTC on 13 August 2004. The shaded areas denote different values of CH (10^{-1} kg m^{-2})

13.1.4. The evolution of (a) CH (10^{-1} kg m^{-2}), (b) the rainfall rate (mm h^{-1}), (c) $[C_x]$ (10^{-2} s^{-1} K), (d) $[C_y]$ (10^{-2} s^{-1} K), (e) $[C_z]$ (10^{-4} s^{-1} K), and (f) PV (10^{-4} s^{-1} K) averaged over the area from 37°N to 42°N and 112°E to 119°E for the period 00:00 UTC on 12 August to 12:00 UTC on 13 August 2004

13.2.1. The evolution of CZT (black), CZ1 (red), CZ2 (green), CZ3 (blue), CZ4 (cyan), and CZ5 (pink). The values are averaged over the area 34°N–43°N and 112°E–119°E for the period 00:00 UTC, 12 August to 12:00 UTC, 13 August 2004.

13.2.2 (a) The evolution of the distribution of the six-hour cumulative rainfall amount (left; contour spacing: 2 mm) and (b) the vertical component of the CVV (right; units: 10^{-4} s^{-1} K) along 116°E for 00:00 UTC on 12 August to 12:00 UTC on 13 August 2004.

13.5.1. Evolution of the distribution of the six-hour cumulative rainfall

amount (mm) along 118°E from 00:00 UTC on 4 July to 12:00 UTC on 5 July 2003

13.5.2. Evolution of the distribution of (a) Q_{umx} (10^{-12} hPa^{-1} s^{-3} m) and the relative humidity (%) and (b) Q_{umy} (10^{-12} hPa^{-1} s^{-3} m) and the relative humidity (%) at 750 hPa along 118°E from 00:00 UTC on 4 July to 12:00 UTC on 5 July 2003

13.5.3. Evolution of the distribution of (a) the horizontal divergence of Q_{umx} (10^{-16} hPa^{-1} s^{-3}), (b) the horizontal divergence of Q_{dry} (10^{-16} hPa^{-1} s^{-3}), and (c) the horizontal divergence of Q_m (10^{-16} hPa^{-1} s^{-3}) along 118°E at 750 hPa from 00:00 UTC, 4 July to 02:00 UTC, 5 July 2003. The shaded area denotes value of less than −2.

13.5.4. The evolution of the distribution of the vertical velocity ω (hPa s^{-1}) along 118°E at 750 hPa from 00:00 UTC, 4 July to 02:00 UTC, 5 July 2003. The shaded area denotes values of less than −0.05.

13.5.5. Time series of (a) the six-hour cumulative rainfall amount (mm) and (b) the horizontal divergence of Q_{um} (10^{-16} hPa^{-1} s^{-3}) over the rainfall center

13.6.1. Schematic diagram of the vertical circulations at the entrance and exit of high-level jets

13.6.2. Schematic diagram of the relationship between the divergence of the E vector and the development of a cyclone

13.8.1. The virtual pseudo-energy wave-action density (contours of 10^2 kg/(m·s^2)) and the observed six-hour rainfall (shaded; mm) at (a) 00:00 UTC, (b) 06:00 UTC, (c) 12:00 UTC, and (d) 18:00 UTC on 8 July 2009

13.8.2. The virtual pseudo-energy wave-action density (contours of 10^2 kg/(m·s^2) and the observed six-hour rainfall (shaded; mm) at (a) 12:00 UTC, 18 August, (b) 18:00 UTC, 18 August, (c) 00:00 UTC, 18 August, and (d) 06:00 UTC, 19 August 2009

14.1.1. Horizontal distribution of the moist thermodynamic advection parameter (10^{-8} K^2 m^{-1} s^{-13}) at 06:00 UTC, 11 July 2010. The shadow

area represent the cumulative six-hour observed rainfall amount (mm).

14.1.2. (a) The thermodynamic helicity (10^3 km^2 s^{-2}) and (b) vertical flux of the thermodynamic divergence (10^3 km^2 s^{-2}) during torrential rainfall associated with a cold vortex over northeast China at 18:00 UTC, 27 July 2010. The shadow area represent the cumulative six-hour observed rainfall amount (mm).

14.1.3. The horizontal distribution of the divergence of the Q vector with generalized potential temperature at 700 hPa on (a) 00:00 UTC 12 July and (b):00:00 UTC 13 July 2013. The shadow area represent the cumulative six-hour observed rainfall amount (mm).

14.2.1. (a) The generalized moist potential vorticity (10^{-2} K s^{-1}), (b) solenoidal vorticity (10^{-4} m s^{-3}), and (c) thermodynamic solenoidal vorticity associated with the torrential rainfall produced by a trough at 00:00 UTC, 19 July 2010. The shadow area represent the cumulative six-hour observed rainfall amount (mm).

14.2.2. Schematic diagram of horizontal wind vectors

14.2.3. Horizontal distributions of (a) potential divergence and (b) potential stretching deformation (10^{-4} K s^{-1}) for 00:00 UTC, 9 August 2009. The shadow area represent the cumulative six-hour observed rainfall amount (mm).

14.2.4. (a) The second-order potential vorticity (10^{-10} km^{-1} s^{-2}) and (b) the vertical component of the convective vorticity vector (10^{-3} K s^{-1}) associated with the torrential rainfall of Typhoon Fanapi at 06:00 UTC on 20 September 2010. The shadow area represent the cumulative six-hour observed rainfall amount (mm).

14.3.1. The wave-action densities of (a) the latent heat of condensation (10^{-7} s^{-1}), (b) potential vorticity of the latent heat of condensation (10^{-6} s^{-1}), (c) potential divergence of the latent heat of condensation (10^{-6} s^{-1}), (d) geopotential shearing deformation of the latent heat of condensation (10^{-6} s^{-1}), and (e) geopotential stretching deformation

of the latent heat of condensation (10^{-6} s^{-1}). The shadow area represent the cumulative six-hour observed rainfall amount (mm).

14.4.1. Time series of the ETS scores of the six-hour cumulative rainfall amounts forecast in 24 hour using the ensemble rainfall forecast method with dynamic factors (solid red lines) and the GFS model (dashed lines). The results shown are for forecasts of (a) over 10 mm/6 hours and (b) over 20 mm/6 hours for southern China (20°N–35°N, 105°E–125°E) for 00:00 UTC, 2 June to 1 October 2010. (c) and (d) are the same as (a) and (b), respectively, but for 2012, and (e) and (f) are the same as (a) and (b), respectively, but for 2013.

PREFACE

This book is an academic monograph that focuses on atmospheric mesoscale dynamics and the prediction of rainstorms, based on research results obtained by our team in the course of my academic career. The book includes some new research achievements made by our team in recent years.

I am grateful to my Ph.D. advisor, Professor Shiyan Tao for his constant advices in the past, and also thankful to Professor Duzheng Ye, Professor Qingcun Zeng, Professor Jifan Chou and Professor Chongyin Li for their encouragement during my career. Over a long period of time, I have also benefited greatly from the cooperation and discussions on scientific issues that I have had with my graduate classmate, Dr. Qin Xu. In recent years, Professor Qiushi Chen has helped me to advise graduate students and has also brought his ideas and methods related to the decomposition of physical processes to my research. I also benefited from discussing topics on non-uniform saturation with Professor Xingrong Wang.

The book is divided into 14 chapters. In Chapter 1, the basic dynamical parameters of the atmosphere and their physical meanings are discussed, with an emphasis on the Väisälä frequency and Richardson number. In Chapter 2, based on the governing equations of barotropic and baroclinic atmosphere, combined with a consideration of atmospheric mesoscale dynamics, the mesoscale potential vorticity equation and potential vorticity substance equation are derived. In Chapter 3, the physical quantities related to water vapor are introduced. In particular, the generalized potential temperature in a non-uniformly

saturated atmosphere is introduced and is shown to be a conserved quantity. This lays the theoretical foundation for the prediction of the area affected by a rainstorm. In Chapter 4, the vorticity equation and advection vorticity equation as well as the 'frozen-in' properties of the vorticity, streamline vorticity, and helicity are introduced. In Chapter 5, different forms of the divergence equation and potential divergence are discussed. In Chapter 6, the total deformation and deformation equation are brought in, and the interaction between the deformation, vorticity, and divergence is investigated. In Chapter 7, the generalized scalar frontogenesis function, which describes generalized scalar frontogenesis in a non-uniformly saturated atmosphere, and the trend of the frontogenesis function are described. In Chapter 8, the concept of potential vorticity and the potential vorticity equation are introduced. The concepts of second-order potential vorticity and generalized moist potential vorticity are developed. The moist potential vorticity anomaly with mass-forcing and the principle of the potential vorticity substance impermeability are demonstrated. In Chapter 9, based on a classification of the stability, several instability analysis methods, such as static instability, symmetric instability, and shear instability, are analysed. In Chapter 10, wave characteristics, wave polarization are given, and wave-action equation of three-dimensional inertial gravity waves and symmetric inertial gravity waves are discussed; a brief description of a method for identifying gravity waves from data is also presented. In Chapter 11, the mesoscale balance equation and its unbalance counterpart are investigated along with a related potential vorticity inversion technique. In Chapter 12, using a dynamic prediction method based on scalar field theory, the divergence, and deformation, as well as associated factors such as the potential vorticity, moist potential vorticity, and generalized moist potential vorticity, are used to identify and predict hot, humid weather in large cities during summer, as well as to trace and predict the movement of cyclones and to forecast torrential rainfall. In

Chapter 13, the convective vorticity vector, dynamic vorticity vector, ageostrophic Q vector, E vector, and wave-action vector are described along with related theories and dynamic prediction methods. In Chapter 14, rainstorm forecast methods with ensemble dynamic factors are discussed and demonstrated.

This book aims to deepen the understanding of mesoscale dynamics, to make the basic concepts clear, and to include new research results in the theory as far as possible. At the same time, the book also reflects the authors' own research interests and writing style, and strives to be innovative as well as being of academic value. In terms of content, the theories on which mesoscale dynamics relies are emphasized. For a long time, these concepts, including the theory of generalized potential temperature, convective vorticity vector, second-order potential vorticity, conservation of wave action, mesoscale balance equation, and generalized frontogenesis theory, have not received much attention, even though they provide the theoretical basis for the study of moist atmospheric processes. An improved method for analyzing gravity waves is also described in the book. One innovation is that some new types of vectors that can play an important role in dynamic prediction are proposed. Another feature of the book is the combination of theoretical knowledge and practical forecasting applications—this is seen in the method for forecasting rainstorms based on ensemble dynamic factors in particular. This method has been used in many operational provincial forecast centers in China. Some of the content of this book has been taught over a period of time at the University of Chinese Academy of Sciences, Zhejiang University, and Chengdu University of Information Science and Technology.

I thank Dr. Fan Ping, Dr. Xiaopeng Cui, Dr. Yushu Zhou, Dr. Shuai Yang, Dr. Feifan Zhou, Dr. Huijuan Lu, Dr. Jie Cao, Dr. Na Li, and Mrs. Shiyan Sun, as well as to Dr. Zhaoming Liang, Dr. Xiba Tang, Dr. jie Wei, Dr. Qunjie Zuo, Dr. Lu Liu, Shuping Ma, and Xiang Li for their help during the preparation of this book. I would like to thank my wife,

Rongyu Sheng, for her unselfish support. Finally, I extend my gratitude to the institutions and individuals who have helped me with the publication of the book, in particular, the Institute of Atmospheric Physics of the Chinese Academy of Sciences, the Department of Earth Science of the National Natural Science Foundation of China (NSFC).

This book is supported by NSFC (41930967 and 41875056), the National Key Research and Development (2018YFC1507104), the Chinese Academy of Sciences (XDA17010105), and the Key Scientific and Technology Research and Development Program of Jilin Province(20180201035SF).

—Shouting Gao

ABBREVIATION AND MEANINGS OF THE TERMS USED IN THE STUDY

2D	Two dimensional
ADAS	ARPS data assimilation system
ARPS	Advanced Regional Prediction System
CISK	conditional instability of the second kind
CMA	China Meteorological Administration
CRISTA	Cryogenic Infrared Spectrometers and Telescopes for the Atmosphere
CSI	Conditional symmetric instability
CVV	Convective vorticity vector
DVV	Dynamic vorticity vector
ECMWF	European Center for Medium-range Weather Forecast
ETS	Equitable threat score
GFS	Global Forecasting System
GMPV	Generalized moist potential vorticity
GPS	Global Positioning System
GRAPES	Global/Regional Assimilation and Prediction System
IPV	Isentropic potential vorticity
JMA	Japan Meteorological Agency
K-H	Kelvin-Helmholtz
LIMS	Limb Infrared Monitoring of the Stratosphere
MLS	Microwave Limb Sounder
MOS	Model output statistics
MPVS	Moist potential vorticity substance
MVV	Moist vorticity vector

NCEP	National Centers for Environmental Prediction
NGMPV	Negative generalized moist potential vorticity
PV	Potential vorticity
QPF	Quantitative precipitation forecast
UCAR	University Center for Atmospheric Research
UTC	Coordinated Universal Time
WKB	Wentzel-Kramers-Brillouin
WKBJ	Wentzel-Kramers-Brillouin-Jeffreys
WRF	Weather Research and Forecasting

CHAPTER ONE

BASIC ATMOSPHERIC DYNAMIC PARAMETERS AND THEIR CONTEXT

In order to probe into the basic principles and dynamic structures related to the generation and development of mesoscale atmospheric systems, we must first understand some basic dynamic parameters that describe the mesoscale characteristics, such as the Rossby number, which is the ratio of the advective inertial force to the Coriolis force; the internal Froude number, which measures the atmospheric stratification effect; and the Richardson number, which represents the atmospheric stability. The specific contexts related to these parameters and how the parameters can be applied to the study of mesoscale atmospheric motion are also important, and so the first chapter of this book will introduce some important universal dynamic parameters.

1.1. Parameters Related to Rotation and Stratification and Their Dynamic Similarities

The atmosphere is a rotating, stratified fluid that surrounds the Earth. (It is stratified according to temperature and humidity.) The effects of the Earth's rotation play an important role in the motion of the atmosphere. Therefore, it is important to ask at which scale the ambient rotation becomes an important factor in the atmospheric motion. To answer this question, we can begin with the ambient rotation rate, which is given by

$$\Omega = \frac{2\pi}{day} = 7.29 \times 10^{-5} / s . \tag{1.1.1}$$

If the time scale over which the atmospheric motion occurs is comparable with the time taken for one rotation of the Earth, or is longer, then this motion will be affected by the Earth's rotation. We, therefore, define the dimensionless quantity,

$$\omega_{\Omega} = \frac{2\pi/\Omega}{T} = \frac{2\pi}{T\Omega} . \tag{1.1.2}$$

If $\omega_{\Omega} \leq 1$, which corresponds to motion with a time scale of more than one day (24 hours), then it is necessary to consider the effect of the rotation. Usually, the ratio of the characteristic scale of the displacement, L, to its characteristic velocity, U, is used to represent the time scale of the atmospheric motion, T. The above dimensionless parameter is then defined as follows:

$$\tau = \frac{2\pi\Omega}{LU} = \frac{2\pi U}{\Omega L} . \tag{1.1.3}$$

If $\tau \leq 1$, consideration of the Earth's rotation is important.

Apart from the rotation, the atmospheric stratification is also very important. If the reference density of the atmosphere is ρ_0, the density change through a height H is $\Delta\rho$, and the basic velocity of the motion is U, then the corresponding potential energy change per unit volume is $(\rho_0 + \Delta\rho)gH - \rho_0 gH = \Delta\rho gH$, and the basic kinetic energy is $\frac{1}{2}\rho_0 U^2$. The following dimensionless number can then be defined:

$$\sigma = \frac{\frac{1}{2}\rho_0 U^2}{\Delta\rho g H} \quad . \tag{1.1.4}$$

If $\sigma \sim 1$, then the stratification needs to be taken into account. Given such atmospheric stratification, for a disturbance to develop fully, the amount of potential energy required will be about equal to the kinetic energy. If $\sigma << 1$, then there is not nearly enough kinetic energy available in the stratified atmosphere for the disturbance to fully develop, meaning that the stratification plays a decisive role. If $\sigma >> 1$, the changes in potential energy will have a small effect on the fundamental kinetic energy: in this case, the stratification is not important and the stratification effects can be ignored (Benoit Cushman-Roisin, 1994)[1].

In atmospheric dynamics, there are some dimensionless parameters that are often used to represent the extent of the atmospheric rotation or stratification. These dimensionless parameters are obtained by making the atmospheric equations non-dimensional using the method of scale analysis. The parameters include the Rossby number, the internal Froude number, the Burger number, and the Richardson number.

The Rossby number, R_0, is the ratio of the advective inertial force to the Coriolis force: it can be expressed as

$$R_0 = \frac{U^2 / L}{fU} = \frac{U}{fL} . \tag{1.1.5}$$

The Rossby number can be used to represent the rotation of the atmosphere.

The internal Froude number, Fri, is the ratio of the advective inertial force to the buoyancy force, or of the kinetic energy to the gravitational potential energy:

$$F_{ri} \propto [\frac{\rho_0 U^2 / L}{(\rho_2 - \rho_1)g}]^{1/2} = \frac{U}{\sqrt{g^{'} L}}, \tag{1.1.6}$$

where $g^{'} = g(\rho_2 - \rho_1)/\rho_0$ and ρ_1, ρ_2 are, respectively, the density of the upper and lower fluid layer; ρ_0 is the reference density.

$$g^{'} = g(\rho_2 - \rho_1)/\rho_0 = -g\frac{1}{\rho_0}\frac{d\rho}{dz}H = N^2 H,$$

Substituting this into (1.1.6) gives

$$F_{r_i} = \frac{U}{\sqrt{g^{'} L}} = \frac{U}{N\sqrt{HL}}. \tag{1.1.7}$$

For mesoscale systems L~H, giving $F_{ri} = U / NH$.

The internal Froude number clearly represents the atmospheric stratification effect. The definition of the Burger number is

$$B_u = \frac{f^2 L^2}{N^2 H^2}. \tag{1.1.8}$$

Furthermore, the Burger number is related to the Rossby number and the internal Froude number as follows:

$$B_u = (\frac{f^2 L^2}{N^2 H^2}) = \frac{(\frac{U}{N\sqrt{HL}})^2}{(\frac{U}{fL})^2} = (\frac{F_{ri}}{R_0})^2. \tag{1.1.9}$$

For typical deep convention systems, usually L ~ H, which gives

$$B_u = \frac{f^2}{N^2}.$$

From the above expression, it can be seen that the Burger number represents the relative sizes of the atmospheric rotation effect and the stratification effect. Broadly, there are two types of situation (Norbury et al., 2002)[2]. If $B_u << 1$, the stratification effect dominates and the viscosity of the atmosphere will cause the inertial gravity waves to break, as in low-latitude circulation or sub-synoptic scale phenomena. If $B_u >> 1$, the rotation effect dominates and the inertial gravity waves can be sustained. The geostrophic adjustment process then does not operate. Subtropical planetary-scale waves correspond to this situation. If $B_u = O(1)$, the stratification effect and rotation effect are equally important, as in the case of baroclinic instability. $B_u = 0$ corresponds to a stratified, non-rotational fluid where, if $F_{ri}<<1$, the fluid is almost horizontal and non-divergent, and the vertical velocity is very small. Finally, if $B_u = \infty$, there is rotation without any stratification; generally, this occurs only for neutral stratification and is uncommon in the real atmosphere. In addition, using the Rossby deformation radius, $\Lambda_R = NH / f$, the Burger number can also be written as $B_u = (L / \Lambda_R)^2$. From this, the relative importance of the stratification effect and the rotation effect for systems of different scales can be identified.

The Richardson number is usually divided into the bulk Richardson number, $R_i = \frac{N^2 H^2}{U^2}$, and the gradient Richardson number,

$R_i(z) = \dfrac{N^2(z)}{(\partial U / \partial z)^2}$ (the physical meaning of R_i (z) is discussed in Section 3 of this chapter). Because $R_i = \dfrac{N^2 H^2}{U^2} = \dfrac{1}{F_{ri}^2}$, the bulk Richardson number has a dynamic similarity with the reciprocal of the square of the Froude number, $\dfrac{1}{F_{ri}^2}$; thus R_i is also a way of representing the atmospheric stratification effect.

The vorticity and divergence have different magnitudes for different mesoscale systems, and so the importance of the rotation or stratification is different for different scales. For typical mesoscale systems, the vorticity and divergence have the same magnitude, which can be represented by the value of U/L. Here, we make a change to the traditional method of making the vorticity the main object of interest while neglecting the divergence effect. (Because the divergence is usually at least one order of magnitude smaller than the vorticity in the case of large-scale systems, in such situations, concentrating on the vorticity is reasonable). In the case of mesoscale systems, the divergence can be made the main object of study when considering the dimensionless parameters described above[1] (Benoit Cushman-Roisin, 1994).

Because $\Delta\rho = \left|\dfrac{d\rho}{dz}\right| \Delta z$ while, $\Delta z = WT = WL/U, \dfrac{d\rho}{dz} = \dfrac{\rho_0 N^2}{g}$,

the characteristic scale of a pressure disturbance under static equilibrium can be given by $\Delta P = gH\Delta\rho = \dfrac{\rho_0 N^2 HLW}{U}$ or as $\dfrac{\Delta P}{\rho_0} = \dfrac{N^2 HLW}{U}$.

Also, because the pressure-gradient force, the Coriolis force, and the

inertial advection force are equivalent in typical mesoscale systems, $\Delta P/L \sim \rho_0 U^2/L$, and the characteristic size of U^2 is then

$$U^2 = \frac{\Delta P}{\rho_0} = \frac{N^2 HLW}{U}. \tag{1.1.10}$$

The ratio of the characteristic vertical convergence to the characteristic horizontal divergence for mesoscale systems is

$$\frac{WH}{UL} = \frac{U^2}{N^2 H^2} = F_{ri}^2. \tag{1.1.11}$$

It is evident that, in typical mesoscale systems, the horizontal divergence has the same magnitude as the vorticity and the ratio of the vertical elongation to the horizontal divergence is completely represented by the internal Froud number, F_{ri}, which means that, in such systems, the stratification plays a more important role than the rotation.

Assuming that the divergence is still one order smaller than the vorticity in mesoscale systems, the characteristic size of the horizontal divergence can be given by $D = R_0 \frac{U}{L}$. The vertical elongation, $\frac{\partial w}{\partial z}$, can be derived from the horizontal convergence; that is $R_0 \frac{U}{L} \sim \frac{W}{H}$, and therefore

$$R_0 = \frac{WH}{UL} = \frac{WL}{UH}. \tag{1.1.12}$$

This means that, in these mesoscale systems, the rotation plays a more important role than the stratification.

When the rotation is very strong $R_0 \to 0$, thus, it can be deduced from (1.1.12) that the vertical motion basically disappears. A Taylor column usually forms in the rapidly rotating fluid because, at this time,

$D \sim R_0 \frac{U}{L}$. When $R_0 \to 0$, D$\to$0, and the fluid is then horizontally non-divergent. It can then be deduced from the continuity equation of an incompressible fluid that $\frac{\partial W}{\partial z} = 0$. If W is zero at a certain height, such as at the surface, then W = 0 at all heights and the motion becomes fully two-dimensional no matter what the terrain. This is because the air particles can neither climb nor descend along the terrain; therefore, any particles that encounter terrain must go around it. In such circumstances, for a barotropic fluid, the particle flow must maintain its rigidity in the vertical direction, which means that all the particles at all levels of the fluid must similarly go around the terrain. As the particles above the terrain cannot disperse, a Taylor column is formed.

A Taylor column is formed in a strongly rotating fluid; however, for a fluid which is strongly stratified and where the rotation is relatively weak ($F_{ri} << 1$), because of the strong stratification, the vertical displacement of the air particles is greatly restricted, which means that, when the strongly stratified air encounters obstacles, it is deflected horizontally. However, the air above the obstructions can still flow over them unimpeded. If obstacles block the entire flow, then the air cannot flow around them. In such cases, the airflow upstream of the obstacle will be obstructed. In a stratified flow, this kind of horizontal blockage is essentially similar to a Taylor column in a rotating fluid.

The above description concerns the representation and physical meaning of some dimensionless parameters related to rotation and stratification, but what is their importance? We know that in practical physics experiments (such as the rotating-table or rotating-trough experiment) and numerical experiments, setting the values of variables according to the dimensionless product is very useful. For example, for a spherical raindrop moving in sticky, moist air, the drag force can be represented by the function,

$$D_\mu = f(d, u_{rd}, \rho_l, \mu). \tag{1.1.13}$$

Here, d is the diameter of the spherical raindrop, u_{rd} is the velocity of the raindrop, the density is ρ_l, and the viscosity is μ. If dimensionless groups are not formed using the non-dimensional method, a series of experiments must be carried out to determine D_μ: this can be done, for example, by fixing the values of ρ_l, u_{rd}, and μ to find the relationship between D_μ and d and then fixing d, ρ_l, and μ to find the relationship between D_μ and u_{rd}, and so on. This is clearly a foolish approach. If we use the dimensionless process and non-dimensional analysis, the equation for the drag can be written as

$$C_D = \frac{D_\mu}{\rho_l u_{rd}^2 d^2} = f\left(\frac{\rho_l u_{rd} d}{\mu}\right) = f(\mathbf{Re}) \tag{1.1.14}$$

where Re is the Reynolds number. Thus, the five variables in equation (1.1.13) are reduced to two variables in equation (1.1.14), namely the drag coefficient, C_D, and the Reynolds number, Re. We can then draw a curve representing the relationship between C_D and Re based on this function. Thus, given any value of Re, the corresponding value of C_D can be found from the curve and, completely regardless of the density, viscosity, etc. of the raindrop, we can derive all the relevant information about C_D.

If Re is very small, this implies that the inertial force is not important, and thus ρ_l can be removed from equation (1.1.12), which becomes

$D_\mu = f(d, u_{rd}, \mu)$. There is then only one non-dimensional quantity, $D_\mu \Big/ \mu u_{rd} d$. Because this dimensionless parameter does not depend on any other parameters, then $D_\mu \propto \mu u_{rd} d$, which is equivalent to $C_D \sim 1/\mathrm{Re}$. This means that the drag force is directly proportional to the velocity, u, which is Stokes' Law of Resistance.

The concept of dynamic similarity is closely linked to the idea of a non-dimensional group. It is clear that, as the above problem concerns a raindrop moving through moist air, as long as the dimensionless number, $\mathrm{Re} = \rho_l u_{rd} d / \mu$, is the same, then the flow is dynamically similar.

Similarly, the mesoscale situation of cold air being blocked by mountains can be considered a dimensionless problem: by obtaining the relationship $L = f(F_{ri})$ between the dimensionless length, L, and the Froude number, the dependence of L on F_{ri} can be derived. Using the appropriate curve, the influence of F_{ri} on the blocked length, L, can be determined for situations in which cold air is blocked by mountains (Xu and Gao, 1995)[3].

For the situation in which a non-viscous airflow moves toward mountains, using the Boussinesq approximation with the same stability, N, and initial inflow velocity, U, the motion satisfies the Bernoulli equation (Smith, 1988)[4]:

$$u_{rd}^2 = \frac{2}{\rho_0}\left[-p - \frac{1}{2}\rho_0 N^2 h^2\right] + U^2 . \qquad (1.1.15)$$

When the airflow approaches the mountains, a stagnation point will appear near the mountains, at which point u is zero. The disturbance pressure at

the stagnation point, P, will be a function of P*, ρ_0, N, h, and U, and the local pressure coefficient can be found through non-dimensional analysis:

$$\frac{P}{\rho U^2} = f(\frac{Nh}{U}) = f(\frac{1}{F_{ri}}) . \tag{1.1.16}$$

This analysis requires the dimensionless local variables to be dynamically similar at the relevant points.

1.2 Brunt–Väisälä Frequency

If only the thermodynamic properties of the atmosphere are considered without any consideration of its motion, the Brunt–Väisälä frequency can be used to judge the stability of the stratification. However, the Brunt–Väisälä frequency is represented in different ways for dry and moist atmospheres.

1.2.1 Brunt–Väisälä Frequency for Dry Air

In a baroclinic atmosphere, the density of the air, ρ, is a function of T and P:

$$\rho = \rho(T, P) . \tag{1.2.1}$$

From the equation of state,

$$P = \rho RT , \tag{1.2.2}$$

where $R = c_p - c_v$.

Under adiabatic conditions,

$$\frac{P}{P_0} = (\frac{\rho}{\rho_0})^{\gamma} , \tag{1.2.3}$$

where $\gamma = \frac{c_p}{c_v}$. P_0 and ρ_0 are the reference pressure and density, respectively. The reference temperature is T_0, and it is also required that $T_0 = P_0 / R\rho_0$.

From this

$$\frac{P}{P_0} = (\frac{T}{T_0})^{\frac{\gamma}{(\gamma-1)}} \tag{1.2.4}$$

And $$\frac{\rho}{\rho_0} = (\frac{T}{T_0})^{\frac{1}{(\gamma-1)}} . \tag{1.2.5}$$

For mesoscale systems, the static equilibrium approximation can still be used:

$$\frac{dP}{dz} = -\rho g . \tag{1.2.6}$$

The buoyancy effect mainly relates to the vertical direction, and so when inspecting the buoyancy instability, only P, ρ, and T need to be considered as $P(z)$, $\rho(z)$, and $T(z)$. (These can also be written as $P(x, y, z)$, $\rho(x, y, z)$, and $T(x, y, z)$, although this is unnecessary.)

If an air particle at a height z moves through an upward displacement of δz, it can cause a pressure change $\delta P = -\rho g \delta z$ and

also cause a change in the density and temperature according to (1.2.3) and (1.2.4):

$$\delta\rho = {}^{-\rho g\delta z}\!\!\diagup_{\gamma RT} \quad \text{and} \quad \delta T = {}^{-(\gamma-1)g\delta z}\!\!\diagup_{\gamma RT}. \tag{1.2.7}$$

The density of the particle at the new location is

$$\rho_1 = \rho + \delta\rho = \rho - {}^{\rho g\delta z}\!\!\diagup_{\gamma RT}, \tag{1.2.8}$$

but, at the new location, the density of the environment has changed to

$$\rho_2(z+\delta z) = \rho(z) + \frac{d\rho}{dz}\delta z. \tag{1.2.9}$$

The upward buoyancy is then

$$\begin{aligned} \mathbf{F} &= g(\rho_2 - \rho_1)\mathbf{k} \\ &= g(\rho(z) + \frac{d\rho}{dz}\delta z - \rho + {}^{\rho g\delta z}\!\!\diagup_{\gamma RT})\mathbf{k}. \\ &= g(\frac{d\rho}{dz} + \frac{\rho g}{\gamma RT})\delta z\,\mathbf{k} \end{aligned} \tag{1.2.10}$$

Under isentropic motion conditions, the acoustic speed is defined as

$$C = (\frac{\partial P}{\partial \rho})^{\frac{1}{2}} \quad \text{or} \quad C^2 = \gamma RT,$$

and so $\mathbf{F} = g(\frac{d\rho}{dz} + \frac{\rho g}{C^2})\delta z\,\mathbf{k}$. (1.2.11)

The acceleration due to the buoyancy is

$$\mathbf{a} = \frac{g}{\rho}(\frac{d\rho}{dz} + \frac{\rho g}{C^2})\delta z\,\mathbf{k}. \tag{1.2.12}$$

$$N^2 = -\frac{g}{\rho}(\frac{d\rho}{dz} + \frac{\rho g}{C^2}), \tag{1.2.13}$$

where N is the Brunt–Väisälä frequency.

Substituting (1.2.13) into (1.2.12) gives

$$\mathbf{a} = -N^2 \delta z \, \mathbf{k} \, . \tag{1.2.14}$$

If the temperature is being used to represent buoyancy, the buoyancy can be written as

$$\mathbf{F} = -\frac{\rho g}{T}\left(\frac{dT}{dz} + \frac{g}{c_p}\right)\delta z \, \mathbf{k} \, , \tag{1.2.15}$$

and so the equation for N^2 is

$$N^2 = \frac{g}{T}\left(\frac{dT}{dz} + \frac{g}{c_p}\right) . \tag{1.2.16}$$

In order to avoid having to subtract g / C_P every time, usually, the potential temperature is used to replace the temperature. From the definition of potential temperature,

$$\theta = T\left(\frac{P_0}{P}\right)^{\frac{R}{c_p}} = T\left(\frac{P_0}{P}\right)^{\frac{\gamma - 1}{\gamma}} . \tag{1.2.17}$$

N^2 can then be represented as

$$N^2 = g \frac{d \ln \theta}{dz} . \tag{1.2.18}$$

Equations (1.2.18) and (1.2.16) are equivalent.

The density corresponding to the potential temperature is called the potential density; that is

$$\rho^* = \rho\left(\frac{P_0}{P}\right)^{1/\gamma} . \tag{1.2.19}$$

N^2 can thus also be defined as

$$N^2 = -\frac{g}{\rho}\frac{d\rho}{dz}, \tag{1.2.20}$$

and so the compressible fluid can be represented by an incompressible fluid.

Next, the problem of describing the stability of the atmospheric stratification using the Brunt–Väisälä frequency will be discussed. From (1.2.14), we know that if $N^2 > 0$, the atmosphere is stable and that if $N^2 < 0$, it is unstable. For $N^2 > 0$, we must have $\frac{\rho g}{C^2} > 0$; also, from (1.2.13), it can be seen that $\frac{d\rho}{dz}$ should not only be smaller than zero but also clearly negative. In other words, having $\frac{d\rho}{dz} < 0$ is not enough for stable stratification: we must also have $(\frac{d\rho}{dz} + \frac{\rho g}{C^2}) < 0$ to maintain the static stability.

1.2.2 The Brunt–Väisälä Frequency of Saturated Moist Air and Its Corrected Equivalent Potential Temperature

1.2.2.1 The Brunt–Väisälä Frequency of Saturated Moist air

For saturated moist air, the Brunt–Väisälä frequency is usually represented as

$$N_{m^2} = g\frac{d\ln\theta_e}{dz}, \tag{1.2.21}$$

where θ_e is the equivalent potential temperature:

$$\theta_e = \theta \exp(\frac{Lq_s}{c_p T}). \tag{1.2.22}$$

Here, L is the condensation latent heat for a unit mass, and q_s is the saturated specific humidity. Expression (1.2.21) looks reasonable at first glance. However, there is an implicit problem because the premise of the definition of θ_e is that all the condensed liquid water from the saturated parcel of air is removed and that only the latent heat is involved in the heating of the air parcel. However, under such circumstances, the convection will be vigorous and there will clearly be precipitation: this means that the stratification is already unstable and, therefore, the use of the Brunt-Väisälä frequency is not appropriate. Sometimes, then, the following definition is used:

$$N_m^2 = \frac{g}{T}(\frac{dT}{dz} + \Gamma_m), \tag{1.2.23}$$

where Γ_m is the saturated adiabatic lapse rate.

The definitions (1.2.22) and (1.2.23) are not equivalent (Fraser et al., 1973)[5]. Later, other researchers (Durran and Klemp, 1982; Lalas and Einaudi, 1974)[6-7] derived what they considered to be a better expression for N_m^2:

$$N_m^2 = \frac{g}{T}(\frac{dT}{dz} + \Gamma_m)(1 + \frac{Lr_s}{RT}) - (\frac{g}{1+r_w}\frac{dr_w}{dz})_e - (\frac{g}{1+r_w}\frac{dr_w}{dz})_p. \tag{1.2.24}$$

Here, r_w is the total mixing ratio of water, which is equal to the sum of the saturated mixing ratio, r_s, and the mixing ratio of liquid water, r_L, Subscripts *e* and *p* respresent environment and air parcel respectively. If an air parcel is lifted according to a reversible moist adiabatic process without any liquid water being removed from the air parcel, then:

$$\frac{dr_w}{dz}|_p = 0 . \tag{1.2.25}$$

Therefore,

$$N_m^2 = \frac{g}{T}(\frac{dT}{dz} + \Gamma_m)(1 + \frac{Lr_s}{RT}) - (\frac{g}{1 + r_w}\frac{dr_w}{dz}) . \tag{1.2.26}$$

It should be carefully noted that (1.2.26) assumes that: (1) the atmosphere is always in a saturated state and (2) the concentration of liquid water is small and the liquid water is distributed throughout the moist air in the form of very small droplets. Small droplets such as these do not fall down, and so they have no dragging effect on the motion of moist air.

Objectively speaking, if liquid water condenses in a real, saturated atmosphere, such as when a cloud cluster develops into cloud systems producing precipitation, some of this liquid water must be expelled from the moist air parcel in the process by which the saturated air increases. Therefore, for cloud systems that produce (possibly heavy) precipitation in the early stages of their development, the buoyancy effect of saturated air with weak precipitation should be considered (Liu and Gao, 2003)[8].

From (1.2.26), for an air parcel undergoing a reversible saturated adiabatic process:

$$\frac{dr_w}{dz} = \frac{d(r_s + r_L)}{dz} = \frac{dr_s}{dz} + \frac{dr_L}{dz} = 0 , \tag{1.2.27}$$

and so

$$\frac{dr_L}{dz} = -\frac{dr_s}{dz}. \tag{1.2.28}$$

If, from z_0 to z, the mixing ratio of the liquid water in the air parcel changes to $r_L(z) = r_L(z_0) + \Delta r_L$, then the partially condensed liquid water will be expelled from the air parcel but the air parcel will remain saturated during the uplift process. Then,

$$r_L(z) = r_L(z_0) + \alpha \Delta r_L. \tag{1.2.29}$$

In this case

$$\frac{d\hat{r}_w}{dz} = \frac{dr_s}{dz} + \frac{d\hat{r}_L}{dz} = \frac{dr_s}{dz} + \alpha\frac{dr_L}{dz} = \frac{dr_s}{dz} + \frac{dr_L}{dz} - (1-\alpha)\frac{dr_L}{dz} = \frac{dr_w}{dz} + (1-\alpha)\frac{dr_s}{dz} \tag{1.2.30}$$

Therefore, when the condensed water is expelled from the air parcel, N_m^2 can be written as

$$N_m^2 = \frac{g}{T}\left(\frac{dT}{dz} + \Gamma_m\right)\left(1 + \frac{Lr_s}{R_d T}\right) - \frac{g}{1+r_w}\left[\frac{dr_w}{dz}\Big|_e + (1-\alpha)\frac{dr_s}{dz}\Big|_p\right]. \tag{1.2.31}$$

It should be noted that the subscript *p* is the differential with respect to the air parcel, whereas the subscript *e* is the differential with respect to the environment; both of these can be calculated. From a theoretical viewpoint, (1.2.31) is reasonable; however, the actual calculation is quite difficult, mainly because α is not easy to determine.

1.2.2.2 The Corrected Equivalent Potential Temperature, θ_q

The potential temperature of dry air is a familiar concept. It is defined

as the temperature that is reached when dry air moves adiabatically from its initial pressure to 1000 hPa. The basic definition of the potential temperature of unsaturated moist air is the same, but the mathematical expression is a little more complex (Bolton, 1980)[9]:

$$\theta_m = T\left(\frac{1000}{p}\right)^{\left(\frac{R}{c_p(\bar{p},\bar{T})}\right)\times(1-0.28\times10^{-3}r)} . \tag{1.2.32}$$

Here, C_p is the specific heat at constant pressure of dry air, $\bar{p} = \frac{1}{2}(1000 + p)$, $\bar{T} = \frac{1}{2}(\theta + T)$, and r is the mixing ratio of water vapor and dry air, for which the units are $g \cdot kg^{-1}$.

If the change in c_p with temperature and pressure is neglected, θ_m is approximately given by

$$\theta_m = T\left(\frac{1000}{p}\right)^{0.2854(1-0.28\times10^{-3}r)} . \tag{1.2.33}$$

There is an error of about 0.2 K between (1.2.33) and (1.2.32).

The equivalent potential temperature, sometimes also called the pseudo-equivalent potential temperature, is defined as the temperature of a moist air parcel which is uplifted to the condensation altitude by a dry adiabatic process then is elevated to the free convection height by a moist adiabatic process (in which all the water vapor condenses and is expelled) and finally falls to 1000 mb under a dry adiabatic process (Holton, 1972; Betts and Dugan, 1973; Simpson, 1978; Bolton, 1980)[9-12]. The usual mathematical expression for the equivalent potential temperature is

$$\theta_e = \theta(T, p)\exp\left(\frac{Lq_s(T,p)}{c_{pd}T}\right), \tag{1.2.34}$$

where q_s is the saturated specific humidity.

(1.2.34) is similar to the expression for the equivalent potential temperature that neglects $c_w q_s (dT / T)$ during the calculation (Bolton, 1980)[9]. In some studies, θ_e is used to calculate N_m^2 and then determine the stability of a saturated atmosphere. However, doing so creates certain problems because θ_e is not an ideal quantity in the context of problems related to atmospheric stability. For this to be an ideal quality, all of the condensed water needs to be expelled from the uplifted air parcel. When the precipitation conditions in a saturated atmosphere clearly stay the same, or if the atmosphere is already unstable, using the expressions related to θ_e (such as those for N_m^2 or the wet Richardson number) to judge the stability of the atmosphere is meaningless. Furthermore, judgments about the atmospheric stability usually use the small perturbation method, in which the physical variables related to the wet atmosphere are divided into basic states and small perturbations. However, for precipitation systems that are clearly convective, it is difficult to find the basic state and only the average state can be determined. In this situation, it is very difficult to use the small perturbation method. Therefore, particular care needs to be taken when using θ_e to discuss the stability of the atmosphere; otherwise conceptual errors can be made. Some researchers (Durran et al., 1982; Green, 1999; Nielsen-Gammon et al., 2000)[7,13-14] introduced another quantity, θ_q. First, it is assumed that liquid water can condense in the saturated atmosphere—the condensed liquid water is not expelled from the air parcel but all remains within the parcel. The temperature corresponding

to the temperature when the parcel adiabatically falls to 1000 hPa is then recorded as θ_q. The details of calculation follow.

First, assume that, in the saturated air, the mass of dry air is M_c, the mass of water vapor is M_v, the mass of condensed water is M_L, and there is no mass exchange with the surroundings: namely $dM_d = 0$ and $d(M_L + M_v) = 0$. Then, $d(r_s + r_L) = dr_w = 0$, r_c is the mixing ratio of hydrometeors and dry air ($r_c = M_c / M_d$). The thermodynamic equation for this saturated air parcel is then

$$\begin{aligned} dS &= \frac{\delta Q}{T} = M_d dS_d + d(M_v S_v + M_c S_c) \\ &= M_d[c_p d\ln\theta + d(r_s(S_v - S_c) + (r_s + r_c)S_c)] \\ &= M_d[c_p d\ln\theta + d(\frac{r_s L}{T}) + (r_s + r_c)c_c d\ln T] \\ &= M_d c_p d\{\ln[\theta \exp(\frac{r_s L}{c_p T})^{\frac{r_w c_c}{c_p}}]\} \end{aligned} \quad , \qquad (1.2.35)$$

where S is the total entropy of the saturated air, S_v and S_c are, respectively, the specific entropy of water vapor and liquid water, c_c is the specific heat capacity of liquid water, and *L* is the latent heat of condensation.

The definition

$$\theta_q = \theta \exp(\frac{r_s L}{c_p T})(\frac{T}{T_0})^{\frac{r_w c_c}{c_p}} = \theta_e (\frac{T}{T_0})^{\frac{r_w c_c}{c_p}} \tag{1.2.36}$$

For the saturated air parcel, under adiabatic conditions, namely $\delta Q = 0$, the thermodynamic equation of the saturated air parcel is

$$dS = M_d c_p d(\ln \theta_q) = M_d c_p d\{\ln[\theta \exp(\frac{r_s L}{c_p T})(\frac{T}{T_0})^{\frac{r_w c_c}{c_p}}]\} = 0 \tag{1.2.37}$$

which means that $d(\ln \theta_q) = 0$ or $d\theta_q = 0$; i.e., θ_q is a conserved quantity. Although θ_q is a conserved quantity, its calculation relies on three variables, namely T, P, and r_w. r_w is difficult to estimate, mainly because it is impossible to calculate r_w from the pressure and temperature. Therefore, although this form of the expression for θ_q seems to be ideal, it is not suited to real applications. Furthermore, the assumption that none of the condensed liquid water is expelled from the air parcel is entirely unrealistic.

1.3 The Richardson Number and Its Importance

When considering the real movement of the atmosphere, as shown in the preceding analysis, using the Brunt–Väisälä frequency to determine the stability of the atmosphere may lead to incorrect results. In this case, the

Richardson number can be used instead. The Richardson number takes into account not only the thermodynamic properties of atmosphere but also the stratified shear flow; its value is often used as the stability criterion for shear instability, symmetric instability, etc. in the atmosphere, and it is of considerable importance to research into the stability of the atmosphere. It is, therefore, necessary to understand the Richardson number before giving an explanation of mesoscale stability.

1.3.1 Definition and Simple Application of the Richardson Number

British meteorologist L. F. Richardson first proposed the Richardson number as early as 1920, when he carried out research into stratified shear flow. The definition of the Richardson number is $R_i = \frac{N^2}{(d\bar{u}dz)^2}$, where N is the buoyancy frequency (Brunt–Väisälä frequency) and $\bar{u}$ is the horizontal average speed. Studies have confirmed that when Ri < 1, symmetric instability occurs; when Ri < 1/4, stratified shear instability occurs. The value of the Richardson number has become one of the important criteria for judging stability conditions. The physical essence of the Richardson number can be illustrated by the following discussion concerning the mixing of two layers of shear flow (Cushman-Roisin, 1994)1. In a stratified shear flow,

$$\rho = (\rho_1 + \rho_2)/2 \quad , \quad U = (U_1 + U_2)/2 \quad , \quad \frac{d\bar{u}}{dz} = \frac{U_1 - U_2}{H} \quad ,$$

$$N^2 = \frac{g}{\rho}\frac{\rho_2 - \rho_1}{H}, \tag{1.3.1}$$

and the Richardson number can be written as

$$R_i = \frac{N^2}{(d\bar{u}/dz)^2} = \frac{(\rho_2 - \rho_1)gH}{\rho(U_1 - U_2)^2} \tag{1.3.2}$$

Before mixing, because the density of the lower layer of air, ρ_2, is greater than the density of the upper layer, ρ_1 (Figure 1.1), the center of gravity of the whole airmass is below the center. After mixing, the light air is now mixed with heavy air, and the center of gravity rises to above the center. Thus, after sufficient mixing (Figure 1.2), the potential energy gained per unit area throughout the domain is

$$\begin{aligned} PE &= \int_0^H \rho g z dz - \int_0^H \rho_i g z dz \\ &= \frac{1}{2}\rho g H^2 - [\frac{1}{2}\rho_2 g \frac{H^2}{4} + \frac{1}{2}\rho_1 g \frac{3H^2}{4}] = \frac{1}{g}(\rho_2 - \rho_1)gH^2 . \end{aligned} \tag{1.3.3}$$

where ρ_i is initial density.

The increase in potential energy comes from the loss of kinetic energy. The loss of kinetic energy after mixing can be expressed as

$$\begin{aligned} KE &= \int_0^H \frac{1}{2}(\rho u^2)_i dz - \int_0^H \frac{1}{2}(\rho u^2)_f dz \\ &= \frac{H}{4}\rho_2 U_2^2 + \frac{H}{4}\rho_1 U_1^2 - \frac{\rho U^2}{2}H \\ &= \frac{H}{8}(U_1^2 - U_2^2)(\rho_1 - \rho_2) + \frac{H}{8}\rho(U_1 - U_2)^2 \\ &\cong \frac{H}{8}\rho(U_1 - U_2)^2 \end{aligned} \tag{1.3.4}$$

Subscripts i and f represent initial state and final state respectively.

Because $\rho_1 - \rho_2 << 1$, the first term on the right of equation (1.3.4) can be neglected as a small quantity.

From the definition of the Richardson number (1.3.2),

$$R_i = PE / KE = \frac{(\rho_2 - \rho_1)gH}{\rho(U_1 - U_2)^2} \tag{1.3.5}$$

It can be seen that the Richardson number represents the ratio of the potential energy increase to the kinetic energy loss during the mixing of different layers of the shear flow. If unstable processes can occur, that is $R_i < R_{ic}$ (R_{ic} is a critical value), then, either the density difference between the upper and lower layers is small enough to overcome the gravitational barriers when instability occurs, or the difference between the upper and lower wind speeds is large enough to supply the necessary momentum. In the absence of other sources of energy, the energy loss must be greater than the potential energy increase for instability to occur; therefore, R_i <1 is the most basic necessary condition for the occurrence of instability.

1.3.2 The Importance of the Richardson Number

That the Richardson number can be used as a tool to define many kinds of instability is not accidental but is a result of its inherent physical meaning and dynamic characteristics. The Richardson number is the unique non-dimensional parameter in the governing equation of an ageostrophic adiabatic frictionless pseudo-incompressible atmosphere. Therefore, the Richardson number can be used as a dynamic criterion for many kinds of instability. Gao, et al. (1986)[15] gave a demonstration of the importance of the Richardson number using the basic governing equations of the atmosphere.

For an adiabatic frictionless, pseudo-incompressible, stable stratified atmosphere, the basic equations are as follows:

$$\frac{du}{dt} - fv = -\frac{1}{\rho}\frac{\partial p}{\partial x} \tag{1.3.6}$$

$$\frac{dv}{dt} + fu = -\frac{1}{\rho}\frac{\partial p}{\partial y} \tag{1.3.7}$$

$$\frac{\partial p}{\partial z} = -\rho g \tag{1.3.8}$$

$$\frac{\partial u}{\partial x} + \frac{\partial v}{\partial y} + \frac{\partial w}{\partial z} = 0 \tag{1.3.9}$$

$$\frac{ds}{dt} = 0 \tag{1.3.10}$$

where s is the entropy and $s = \frac{s^*}{c_p}$, $s^* = c_p \ln \frac{\theta}{\theta_0}$. Partial differentiation of equations (1.3.6) and (1.3.7) with respect to z using the equal-entropy process gives

$$s = \frac{1}{r}\log p - \log \rho \tag{1.3.11}$$

where $r = c_p / c_v$. After some rearrangement, we have

$$(\frac{\partial}{\partial z} - \frac{\partial s}{\partial z})(\frac{du}{dt} - fv) = -g\frac{\partial s}{\partial x} \tag{1.3.12}$$

$$(\frac{\partial}{\partial z} - \frac{\partial s}{\partial z})(\frac{dv}{dt} + fu) = -g\frac{\partial s}{\partial y} \tag{1.3.13}$$

The results of a large number of observations have shown that, in the

early stages of heavy rainfall, $\frac{\partial s}{\partial z}$ is very small and is close to zero in the low levels of the atmosphere (Shou et al., 1981)[16]. As a better approximation, (1.3.12) and (1.3.13) can be rewritten as

$$\frac{\partial}{\partial z}(\frac{du}{dt} - fv) = -g\frac{\partial s}{\partial x} \tag{1.3.14}$$

and

$$\frac{\partial}{\partial z}(\frac{dv}{dt} + fu) = -g\frac{\partial s}{\partial y}, \tag{1.3.15}$$

respectively.

Using $\frac{\partial}{\partial x}$ (1.3.14)+ $\frac{\partial}{\partial y}$ (1.3.15), we obtain

$$\frac{\partial}{\partial z}\{f_0\zeta - \frac{dD}{dt} - [(\frac{\partial u}{\partial x})^2 + 2\frac{\partial u}{\partial y}\frac{\partial v}{\partial x} + (\frac{\partial v}{\partial y})^2] - (\frac{\partial w}{\partial x}\frac{\partial u}{\partial z} + \frac{\partial w}{\partial y}\frac{\partial v}{\partial z})\} = g\nabla_H^2 s \tag{1.3.16}$$

where $D = \frac{\partial u}{\partial x} + \frac{\partial v}{\partial y}, \zeta = \frac{\partial v}{\partial x} - \frac{\partial u}{\partial y}, f_0 = f, \nabla_H^2$ is a two-dimensional operator.

At the same time, the vorticity equation can be obtained from equations (1.3.6) and (1.3.7):

$$\frac{d}{dt}(f_0 + \zeta) + (\frac{\partial w}{\partial x}\frac{\partial v}{\partial z} - \frac{\partial w}{\partial y}\frac{\partial u}{\partial z}) + D(\zeta + f_0) = 0 \tag{1.3.17}$$

The results of many low-level jet-stream observations indicate that the vertical wind shear is very strong under the jet-stream axis and that the wind speed changes almost linearly with the height. Based on these results, Gao et al. (1986)[15] considered the baroclinic effect and took $U(z)$,

which can be considered as a linear function of *z*, as the wind speed of the basic field; they also took into account the entropy, $\bar{s} = Ay + Bz$, of the field. Although the low-level jet is generally super-geostrophic, this does not necessarily meet the requirements for a thermal wind relationship; however, it can be considered that the basic flow, $U(z)$, does:

$$\frac{dU(z)}{dz} = -\frac{gA}{f} \tag{1.3.18}$$

Here small disturbance,

$u = U(z) + U'(x, y, z, t)$, $v = v'(x, y, z, t)$,

$w = w'(x, y, z, t)$, $s = \bar{s}(y, z) + s'(x, y, z, t)$,

can be introduced. After substituting this into (1.3.19), (1.3.10), (1.3.16), and (1.3.17), we have

$$\frac{\partial u'}{\partial x} + \frac{\partial v'}{\partial y} + \frac{\partial w'}{\partial z} = 0 \tag{1.3.19}$$

$$f_0^2(av' + bw') + \frac{D}{Dt}(gs') = 0 \tag{1.3.20}$$

$$f_0 D' + \frac{D\zeta'}{Dt} + f_0 a \frac{\partial w'}{\partial y} = 0 \tag{1.3.21}$$

$$\frac{\partial}{\partial z}[f_0\zeta' - \frac{DD'}{Dt} + f_0 a \frac{\partial w'}{\partial x}] = \nabla_H^2(gs') \tag{1.3.22}$$

where,

$$a=\frac{gA}{f_0^2}\quad,\quad b=\frac{gB}{f_0{}^2}\quad,\quad \frac{D}{Dt}=\frac{\partial}{\partial t}+U(z)\frac{\partial}{\partial x}\quad,\quad \zeta'=\frac{\partial v'}{\partial x}-\frac{\partial u'}{\partial y}\quad,$$

$$D'=\frac{\partial u'}{\partial x}+\frac{\partial v'}{\partial y}$$

Eliminating s', v', ζ', D' from equations (1.3.19) to (1.3.22) gives

$$\begin{aligned}&\frac{D}{Dt}\left(f_0^2+\frac{D^2}{Dt^2}\right)\frac{\partial^2 w'}{\partial z^2}+2f_0^2a\left(f_0\frac{\partial}{\partial x}-\frac{D}{Dt}\frac{\partial}{\partial y}\right)\frac{\partial w'}{\partial z}\\&\quad+f_0^2\left[b\frac{D}{Dt}\left(\frac{\partial^2}{\partial x^2}+\frac{\partial^2}{\partial y^2}\right)-2f_0a^2\frac{\partial^2}{\partial x\partial y}\right]w'=0\end{aligned}\tag{1.3.23}$$

Assuming the disturbance, w', is in the form of a wave—i.e.,

$$w'=\bar{\phi}(z)e^{i(\bar{k}x+\bar{\lambda}y+\bar{\sigma}t)}\tag{1.3.24}$$

—and taking the characteristic level scale as L, the characteristic height as H, and the characteristic velocity as $U_0=-\frac{gA}{f_0}H$, then

$$(x,y)=L(x_1,y_1)\quad,\quad z=Hz_1\quad,\quad U(z)=U_0u_1=-\frac{gA}{f_0}Hz_1\quad,$$

$$\bar{\phi}(z)=\Phi(H)\phi(z_1).$$

Similarly, taking the characteristic frequency as f_0, the characteristic wave number is $\frac{f_0}{U_0}$. This then gives

$$\bar{k} = \frac{f_0}{U_0} k \ , \bar{\lambda} = \frac{f_0}{U_0} \lambda \ , \sigma = f_0 \sigma$$

where $x_1 , y_1 , z_1 , u_1 , \phi(z_1) , k , \lambda , \sigma$ are dimensionless quantities.

The dimensionless equation can then be obtained by substituting w' and these dimensionless quantities into equation (1.3.23):

$$[1-(\sigma + kz_1)^2]\frac{d^2\phi}{dz_1^2} - [\frac{2k}{\sigma + kz_1} - 2i\lambda]\frac{d\phi}{dz_1} - [Ri(k^2 + \lambda^2) + \frac{2ik\lambda}{\sigma + kz_1}]\phi = 0 \ , \tag{1.3.25}$$

where $Ri = gB \Big/ (\frac{d\bar{U}}{dz})^2$ is the Richardson number.

This equation is dimensionless and contains the unique parameter R_i, which plays an extremely important role in detecting the generation and development of different kinds of weather system and can be used as the criterion for determining different kinds of stability. Equation (1.3.25) is the same as the form given by Eady (1949)[17]; however, this equation applies to ageostrophic circumstances and so is known as the ageostrophic Eady model.

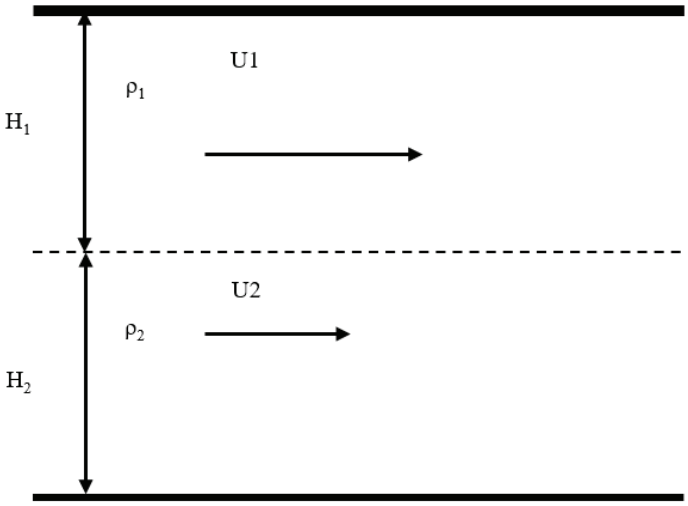

Figure 1.1 Initial shear flow

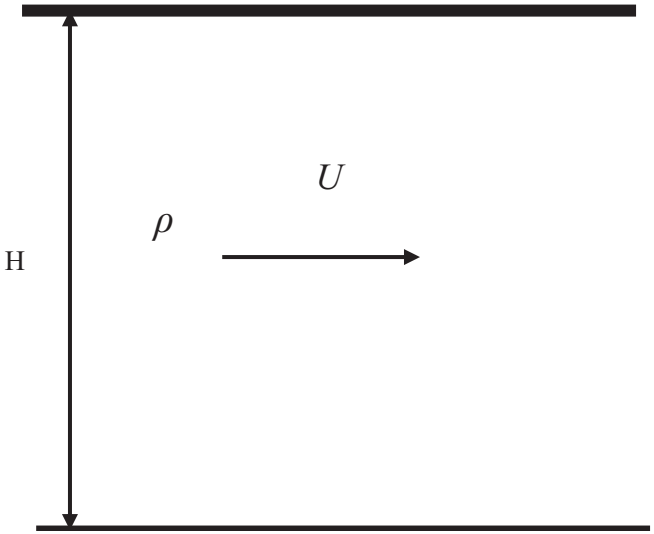

Figure 1.2 Uniform flow after mixing enough

Notes

[1]Cushman-Roisin B (1994). *Introduction to Geophysical Fluid Dynamics*, Prentice-Hall, Inc.

[2]Norbury, J. and I. Roulstone (2002). *Large-Scale Atmosphere-Ocean Dynamics Volume I: Analytical Methods and Numerical Models*. Cambridge University Press.

[3]Xu, Q. and S. Gao (1995). "An analytic model of cold air damming and its applications," *Journal of Atmospheric Sciences*, 52(3):353-365.

[4]Smith, R. B. (1988) "Linear theory of hydrostatic flow over an isolated mountain in isosteric coordinates," *Journal of Atmospheric Sciences*, 45(24):3889-3896.

[5]Fraser, A. B., R. C. Easter and P. V. Hobbs (1973) "A theoretical study of the flow of air and fallout of solid precipitation over mountainous terrain: Part I. Air flow model," *Journal of Atmospheric Sciences*, 30(5):801-812.

[6]Durran, D. R. and J. B. Klemp (1982) "On the effects of moisture on the Brunt-Väisälä frequency," *Journal of Atmospheric Sciences*, 39(10):2152-2158.

[7]Lalas, D. P. and F. Einaudi (1974) "On the correct use of the wet adiabatic lapse rate in stability criteria of a saturated atmosphere," *Journal of Applied Meteorology*, 13(3):318-324.

[8]Liu, D. and S. T. Gao (2003) "The brunt-Väisälä frequency in a saturated atmosphere and the revised equivalent potential temperature," *Acta Meteorologica Sinica*, 61(3):379-383. (in Chinese with English abstract)

[9]Bolton, D. (1980) "The computation of equivalent potential temperature," *Monthly Weather Review*, 108(7):1046-1053.

[10]Betts, A. K. and F. J. Dugan (1973) "Empirical formula for saturation pseudoadiabats and saturation equivalent potential temperature," *Journal of Applied Meteorology*, 12(4):731-732.

[11]Holton, J. R. (1972) *An Introduction to Dynamical Meteorology*, Academic Press.

[12]Simpson, R. H. (1978) "On the computation of equivalent potential temperature," *Monthly Weather Review*, 106(1):124-130.

[13]Green, J. (1999) *Atmospheric Dynamics*, Cambridge University Press.

[14]Nielsen-Gammon, J. W. and D. Keyser (2000) "Effective Stratification for Pseudo adiabatic Ascent," *Monthly Weather Review*, 128(8):3007-3010.

[15]Gao, S. T. and S. Q. Sun (1986) "Determining the instability of mesoscale perturbations with Richardson number," *Chinese Journal of Atmospheric Sciences*, 10(2) :171-182 (in Chinese).

[16]Shou, S. W. S. S. Li and X. P. Yao (2003) *Mesoscale Meteorology*, Meteorological Press, Beijing (in Chinese).

[17]Eady, E.T. (1949) "Long Waves and Cyclone Waves," *Tellus*, 1(3):33–52.

CHAPTER TWO

BASIC EQUATIONS OF MESOSCALE DYNAMICS

For large-scale systems, the primitive equations and the vortex equation are generally used. The divergence equation and potential vorticity equation can be deduced from the primitive equations to describe the strength of the large-scale atmospheric rotation and the extent of the convergence and divergence, including the atmospheric vorticity related to thermodynamic processes. Similarly, for mesoscale systems, there are corresponding basic equations as well as a vorticity equation, divergence equation, and potential vorticity equation, which are based on these basic equations. Also, due to the particular features of mesoscale systems, there are physical parameters, including the stream-line vortex and helicity, which can be used as a better description of mesoscale motion and from which the stream-line vortex equation and helicity equation can be developed. This chapter introduces some commonly used mesoscale equations together with a description of some of the features of mesoscale systems.

2.1 The Basic Equations of Mesoscale Motion

2.1.1 The Barotropic Ideal Atmosphere Equations

Many mesoscale systems are equivalent-barotropic, and so it is better to investigate mesoscale problems using shallow-water equations. This is because the shallow-water equations can reflect the barotropic

environment of the atmosphere, and also the relevant continuity equation can reflect the divergence and convergence in the overall flow. The shallow-water equations are

$$\frac{\partial u}{\partial t}+u\frac{\partial u}{\partial x}+v\frac{\partial u}{\partial y}-fv=-g\frac{\partial h}{\partial x}, \tag{2.1.1}$$

$$\frac{\partial v}{\partial t}+u\frac{\partial v}{\partial x}+v\frac{\partial v}{\partial y}+fu=-g\frac{\partial h}{\partial y}, \quad \text{and} \tag{2.1.2}$$

$$\frac{\partial h}{\partial t}+u\frac{\partial h}{\partial x}+v\frac{\partial h}{\partial y}+h\left(\frac{\partial u}{\partial x}+\frac{\partial v}{\partial y}\right)=0. \tag{2.1.3}$$

Here, u and v are the components of the horizontal speed, and h is the depth of the barotropic atmosphere. For any specific field of study, the linear form of these equations can be used to describe some of the basic characteristics of the shallow-water equations—in particular, the wave characteristics.

Assuming that the basic quantities U, V, and H (x, y) satisfy the geostrophic equilibrium relationships:

$$fV=g\frac{\partial H}{\partial x} \quad and \quad fU=-g\frac{\partial H}{\partial y}, \tag{2.1.4}$$

then, after linearization,

$$h=H+h',\ u=U+u',\ v=V+v'. \tag{2.1.5}$$

(2.1.1)–(2.1.3) can be simplified to (Durran, 1999)[1]

$$\frac{\partial \mathbf{v}}{\partial t}+A\frac{\partial \mathbf{v}}{\partial x}+B\frac{\partial \mathbf{v}}{\partial y}+C\mathbf{v}=0, \tag{2.1.6}$$

in which

$$\mathbf{v} = \begin{pmatrix} u' \\ v' \\ h' \end{pmatrix}, \quad A = \begin{pmatrix} U & 0 & g \\ 0 & U & 0 \\ H & 0 & U \end{pmatrix}, \quad B = \begin{pmatrix} V & 0 & 0 \\ 0 & V & g \\ 0 & H & V \end{pmatrix}, \quad \text{and}$$

$$C = \begin{pmatrix} 0 & -f & 0 \\ f & 0 & 0 \\ fVg & -fUg & 0 \end{pmatrix}.$$

If we set $\mathbf{v} = T^{-1}\mathbf{u}$, then

$$T^{-1} = \begin{pmatrix} C_s & 0 & 0 \\ 0 & C_s & 0 \\ 0 & 0 & g \end{pmatrix} \text{ and } C_s = \sqrt{gH}\,.$$

(2.1.6) can then be transformed to

$$\frac{\partial \mathbf{v}}{\partial t} + \overline{A}\frac{\partial \mathbf{v}}{\partial x} + \overline{B}\frac{\partial \mathbf{v}}{\partial y} + \overline{C}\,\mathbf{v} = 0\,, \tag{2.1.7}$$

where

$$\overline{A} = T^{-1}AT = \begin{pmatrix} U & 0 & C_s \\ 0 & U & 0 \\ C_s & 0 & U \end{pmatrix}, \overline{B} = T^{-1}BT = \begin{pmatrix} V & 0 & C_s \\ 0 & V & C_s \\ C_s & C_s & V \end{pmatrix}$$

and

$$\overline{C} = T^{-1}\left(A\frac{\partial T}{\partial x} + B\frac{\partial T}{\partial y} + CT\right) = \begin{pmatrix} 0 & -f & 0 \\ f & 0 & 0 \\ \frac{1}{2}fV/C_s & -\frac{1}{2}fV/C_s & 0 \end{pmatrix}.$$

It can be seen from equation (2.1.7) that both $\overline{A}$ and $\overline{B}$ are symmetric matrices. From a basic understanding of the mathematics of physical equations, it is also clear that equation (2.1.7) is a hyperbolic wave equation. Clearly, in a barotropic atmosphere, mesoscale systems are pure wave systems without any vorticity characteristics. Thus, we can write the disturbance, namely u', v', h', in the form of a wave solution and substitute this into equation (2.1.7) to investigate the wave characteristics. Further details are not given here as these can be found in more general textbooks.

2.1.2 Equations for Ideal Baroclinic Unsaturated Air

In middle-latitude regions the atmosphere is strongly baroclinic. If it is further assumed that the atmosphere is adiabatic and inviscid, the following basic equations (Gao and Cui, 2006)[2] apply:

$$\frac{d\mathbf{v}}{dt} + f\,\mathbf{k}\times\mathbf{v} = -\frac{1}{\rho}\nabla p - g\,\mathbf{k}, \tag{2.1.8}$$

$$\frac{\partial \rho}{\partial t} + \nabla\cdot(\rho\,\mathbf{v}) = 0, \tag{2.1.9}$$

$$\frac{d\theta}{dt} = 0. \tag{2.1.10}$$

Here $\frac{d(\ )}{dt} = \frac{\partial(\ )}{\partial t} + \mathbf{v}\cdot\nabla(\ )$, $\mathbf{v}$ is the three-dimensional velocity vector, ρ is the density of unsaturated air, p is the pressure, g is the acceleration due to gravity, $\mathbf{k}$ is the unit vector in the upward vertical direction, and θ is the potential temperature. Written in component form, equations (2.1.8)-(2.1.10) are actually five equations; however, there are

six unknown quantities, and so, usually, the state equation $P = \rho R T_v$ is used to make the equations close. (T_v is the virtual temperature, and generally $T_v \sim$ T: T_v is replaced by T hereafter.)

Because the potential temperature, $\theta = T(\frac{p_0}{p})^{\frac{R}{c_p}}$, and p_0 = 1000 hPa, where R is the gas constant for dry air and c_p is the specific heat at constant pressure, by making use of the state equation, we can obtain the pressure-diagnosis equation in the following form:

$$p = p_0(\frac{R}{p_0}\rho\theta)^{\frac{c_p}{c_v}}, \tag{2.1.11}$$

where c_v is the specific heat at constant volume. In order to emphasize the mesoscale thermal effect and make the calculation more convenient, we introduce the dimensionless number,

$$\pi = (\frac{p}{p_0})^{\frac{R}{c_p}}. \tag{2.1.12}$$

Using the state equation and the definition for the potential temperature, the pressure-gradient force can be written as

$$\frac{1}{\rho}\nabla p = c_p\theta\nabla\pi, \tag{2.1.13}$$

and the equation of motion becomes

$$\frac{d\mathbf{v}}{dt} + f\,\mathbf{k}\times\mathbf{v} = -c_p\theta\nabla\pi - g\,\mathbf{k}. \tag{2.1.14}$$

Using (2.1.11), equation (2.1.12) can also be written as

$$\pi = (\frac{R\rho\theta}{p_0})^{\frac{R}{c_v}}. \tag{2.1.15}$$

Taking the natural logarithms of both sides of the above equation and differentiating gives

$$\frac{d}{dt}\ln(\pi) = \frac{R}{c_v}[\frac{d\ln\rho}{dt} + \frac{d\ln\theta}{dt}]. \tag{2.1.16}$$

Using (2.1.9) and (2.1.10), equation (2.1.16) can be rewritten as

$$\frac{d\pi}{dt} + \frac{R\pi}{c_v}\nabla\cdot\mathbf{v} = 0, \tag{2.1.17}$$

where c_v is the specific heat of wet air at constant volume and $c_v = c_p - R$.

The equations suitable for application at the mesoscale are then

$$\frac{d\mathbf{v}}{dt} + f\,\mathbf{k}\times\mathbf{v} = -c_P\theta\nabla\pi - g\,\mathbf{k}, \tag{2.1.18}$$

$$\frac{d\pi}{dt} + \frac{R\pi}{c_v}\nabla\cdot\mathbf{v} = 0, \text{ and} \tag{2.1.19}$$

$$\frac{d\theta}{dt} = 0. \tag{2.1.20}$$

These equations comprise the closed equations with five unknown numbers and five equations. The biggest advantage of these equations is that the density does not appear in them and they are automatically closed. This makes the calculations more convenient. Also, the potential temperature appears explicitly in the momentum equation, thus emphasizing the role played by changes in the potential temperature field in the generation and development of mesoscale systems. This is because

observation data diagnosis, forecasting experience, and theoretical analysis (Wu et al., 1995)[3] all demonstrate that the inclination of the local isentropic surface is the important reason for the development of the vertical vorticity in mesoscale systems. Therefore, the fact that the potential temperature appears explicitly in the equations facilitates the study of the inclination of local isentropic surfaces and the generation and development of mesoscale systems. This is also the main reason for transforming the traditional equations that describe the atmosphere into the above equations, which can, then, conveniently be used in the development of a mesoscale model. The other commonly used mesoscale equations that are described in this chapter are all based on these equations.

2.1.3 The Boussinesq Approximation and the Pseudo-Incompressible Approximation

In this section, first the Boussinesq approximation and the pseudo-incompressible approximation, which are both often used in the analysis of mesoscale processes, will be introduced.

The Boussinesq approximation is the most commonly used approximation in Earth fluid dynamics. The essence of this approximation is that the influence of changes in fluid density on mass conservation in the continuity equation should be ignored, as should the effect of these changes on the inertia in the momentum equation. The influence of the changes in fluid density on buoyancy is, however, still taken into account.

In the commonly used equation for fluid motion, if ρ_0 is the reference density, then, using the Boussinesq approximation, the momentum equation can be written as:

$$\frac{d\mathbf{v}}{dt} + f\,\mathbf{k}\times\mathbf{v} + \frac{1}{\rho_0}\nabla p' = -g\frac{\rho'}{\rho_0}\mathbf{k}\,. \tag{2.1.21}$$

Here, the definition of the disturbance density is $\rho' = \rho - \bar{\rho}(z)$ rather than $\rho - \rho_0$, and the disturbance pressure, p', is given by $p' = p - \bar{p}(z)$.

If $P = \frac{p'}{\rho_0}$, $b = -g\frac{\rho - \bar{\rho}}{\rho_0}$, and $N_{b^2} = -\frac{g}{\rho_0}\frac{d\bar{\rho}}{dz}$, then, under the Boussinesq approximation, the equations can be written as

$$\frac{d\mathbf{v}}{dt} + f\,\mathbf{k}\times\mathbf{v} + \nabla P = b\,\mathbf{k}\,, \tag{2.1.22}$$

$$\frac{db}{dt} + N_b{}^2 w = 0\,, \text{ and} \tag{2.1.23}$$

$$\nabla\cdot\mathbf{v} = 0\,. \tag{2.1.24}$$

Although the Boussinesq approximation provides a qualitatively correct description of the buoyancy effect, when the fluid density in the vertical direction changes markedly—as in the case of deep convective systems, in particular, where the development can reach up to a height of over 10 km—there is a great difference between the densities of the upper and lower air. In such cases, the Boussinesq approximation no longer provides a correct quantitative description. In these circumstances, θ and π are used to represent P, b, N_b^2:

$$P = C_p\theta_o\pi',\ b = g\frac{\theta - \bar{\theta}}{\theta_o},\ N_b{}^2 = \frac{g}{\theta_o}\frac{d\bar{\theta}}{dz}\,. \tag{2.1.25}$$

Here θ_o is the standard reference potential temperature. $\pi = \overline{\pi}(z) + \pi'(x, y, z, t)$ and $\theta = \overline{\theta}(z) + \theta'(x, y, z, t)$, where $\overline{\pi}, \overline{\theta}$ represent the basic state and π', θ' represent the disturbance. The Boussinesq approximation is then fully equivalent to equations (2.1.22)–(2.1.24). The degree of approximation is then greater than that of the ordinary Boussinesq approximation because the fluid density, ρ, in the atmosphere does not approach ρ_0 as the potential temperature, θ, approaches θ_0. This is also one of the major reasons for deriving the new form of the equations (2.1.18), (2.1.19), and (2.1.20) given in this chapter. However, it is better to use an elasticity approximation or pseudo-incompressible approximation to describe the development of deep convection systems in the atmosphere.

An elasticity approximation was first put forward by Charney and Ogura (1962)[4]. Ogura and Phillips (1962)[5] used scale analysis to derive the small parameter $\varepsilon = \frac{\delta\theta}{\theta_o}$. (Here $\delta\theta$ is the deviation of the potential temperature from its reference value, θ_0.) In the equation, any quantity with a magnitude of $0(\varepsilon)$ is ignored. As a result, the ambient lapse rate can be kept close to the adiabatic lapse rate in the case of dry convection. Because ε is a small quantity, elasticity equations can be used to express the mode- filtering acoustic wave. However, in deep wet convective systems, the stability of the average state could mean that ε is no longer a small quantity—for example, for a difference in height of more than 10

km, the value of $\delta\theta$ can reach 40% of θ_0. In such circumstances, the elasticity approximation does not give a good approximation to the actual situation. Therefore, it is necessary to derive approximate equations for a deep convection system, which here are given the name pseudo-incompressible equations (Durran and Klemp, 1982)[6]. The details of their derivation follow.

From the above definitions of π and θ, we have

$$\pi = (\frac{R}{p_0}\rho\theta)^{\frac{R}{c_v}}. \tag{2.1.26}$$

Taking the logarithm of the above equation and differentiating gives

$$\frac{c_v}{R\pi}\frac{d\pi}{dt} = \frac{1}{\rho}\frac{d\rho}{dt} + \frac{1}{\theta}\frac{d\theta}{dt}, \tag{2.1.27}$$

From the above continuity equation and the thermal equation, and taking the diabatic heating effect into account, (2.1.27) can be rewritten as

$$\frac{c_v}{R\pi}\frac{d\pi}{dt} + \nabla\cdot\mathbf{v} = \frac{\dot{Q}}{c_p\rho\theta\pi}, \tag{2.1.28}$$

where $\dot{Q}$ is rate of heating per unit volume.

Separating the variables into the basic states and the disturbances, we have the following:

$$\pi = \overline{\pi}(z) + \pi'(x,y,z,t) \quad , \quad \rho = \overline{\rho}(z) + \rho'(x,y,z,t) \quad ,$$

$$\theta = \overline{\theta}(z) + \theta'(x,y,z,t)$$

Putting these expansions into (2.1.26) and (2.1.27), and using $\pi' \ll \overline{\pi}$, (2.1.28) can be written as

$$\frac{c_v}{R\bar{\pi}}\frac{d\pi'}{dt}+\frac{c_v w}{R\bar{\pi}}\frac{d\bar{\pi}}{dz}+\nabla\cdot\mathbf{v}=\frac{R\dot{Q}}{c_p p_o \bar{\pi}^{c_p/R}}. \tag{2.1.29}$$

Because $\pi' \ll \bar{\pi}$ and $\frac{d\pi'}{dt}/\bar{\pi} << \pi'\bar{\pi}$, the terms containing $\frac{d\pi'}{dt}$ in equation (2.1.29) can be neglected. Thus, (2.1.29) can be written as

$$\frac{w}{\bar{\rho}\bar{\theta}}\frac{d(\bar{\rho}\bar{\theta})}{dz}+\nabla\cdot\mathbf{v}=\frac{\dot{Q}}{c_p\bar{\rho}\bar{\theta}\bar{\pi}} \tag{2.1.30}$$

or $$\nabla\cdot(\bar{\rho}\bar{\theta}\mathbf{v})=\frac{\dot{Q}}{c_p\bar{\pi}}. \tag{2.1.31}$$

This is the pseudo-incompressible approximation equation.

Also, from the basic equations for a mesoscale baroclinic atmosphere, we can obtain the pseudo-incompressible approximation equations as follows:

$$\frac{du}{dt}-fv+c_p\theta\frac{\partial\pi'}{\partial x}=0, \tag{2.1.32}$$

$$\frac{dv}{dt}+fu+c_p\theta\frac{\partial\pi'}{\partial y}=0, \tag{2.1.33}$$

$$\frac{dw}{dt}-g\frac{\theta'}{\bar{\theta}}+c_p\theta\frac{\partial\pi'}{\partial z}=0, \tag{2.1.34}$$

$$\theta\frac{d\theta}{dt}=\frac{\dot{Q}}{c_p\bar{\rho}\bar{\theta}\bar{\pi}}, \text{ and} \tag{2.1.35}$$

$$\nabla \cdot (\overline{\rho}\overline{\theta}\,\mathbf{v}) = \frac{\dot{Q}}{c_p \overline{\pi}}. \tag{2.1.36}$$

The use of the mean variables $\overline{\rho}$, $\overline{\theta}$, and $\overline{\pi}$, means that the equation is closed and can be applied to the study of deep convection.

Overall, the Boussinesq approximation is suitable for use in the study of shallow convection (either dry or wet), the elasticity approximation can be used in the study of deep, dry convection, and the pseudo-incompressible approximation is suitable for use in the study of deep, wet convection.

2.2.1 Wind-field Decomposition

The most important atmospheric variables are the temperature, pressure, humidity, and wind. Of these, the wind is the only vector field, and so the wind field is the most important of the four. In the case of mesoscale synoptic systems for which the characteristic scale of the motion is smaller than the Rossby deformation radius, many studies have confirmed that the pressure field depends on the wind field (Rossby,1937, 1938; Oboukhov, 1949; Yeh, 1957; Zeng, 1963; Yeh and Li, 1982; Wu and Tan, 1989; Tan and Wu, 1994; Shou, 2003)[7-15]. Given the clear importance of the wind field, researchers began to discuss its differential properties as early as 1956. Petterssen pointed out that the first approximation of the Taylor expansion of the horizontal wind field can be taken at any point (u_0, v_0); in which case (Petterssen, 1956)[16],

$$u = u_0 + \frac{1}{2}(D+F)x + \frac{1}{2}(r-q)y \text{, and} \tag{2.2.1}$$

$$v = v_0 + \frac{1}{2}(r+q)x + \frac{1}{2}(D-F)y, \tag{2.2.2}$$

where $D=(\frac{\partial u}{\partial x}+\frac{\partial v}{\partial y})$, $q=(\frac{\partial v}{\partial x}-\frac{\partial u}{\partial y})$, $F=(\frac{\partial u}{\partial x}-\frac{\partial v}{\partial y})$, $r=(\frac{\partial v}{\partial x}+\frac{\partial u}{\partial y})$, D is the divergence, q is the vorticity, F is the expanded deformation term, and r is the shear deformation term. $E=\sqrt{F^2+r^2}$ is defined as the total deformation term. Thus, the divergence, D, vorticity, q, and complete deformation, E, comprise the basic differential properties of the wind field. Together, these terms combine the wind-speed components of a two-dimensional wind field with a translation term. A three-dimensional wind field is also made up of these three basic differential properties. The divergence, vorticity, and total deformation respectively correspond to the convergence and divergence effects, the rotation effect, and the deformation effect of the wind field. If we can better understand these three physical quantities, then, in turn, we will better understand the motion of the atmosphere and produce better forecasts of developments and changes in the weather. It is necessary, therefore, to study the equations of vorticity, divergence, and deformation. In the following section, the common forms of the vorticity equation and divergence equation for mesoscale systems will be introduced. The deformation field equation will be introduced in detail, together a with description of frontogenesis, in Chapter 6.

2.2.2 Vorticity Equation

From the above discussion, the basic equations that are commonly used at the mesoscale are

$$\frac{d\mathbf{v}}{dt}+f\,\mathbf{k}\times\mathbf{v}=-C_p\theta\nabla\pi-\nabla\varphi, \tag{2.2.3}$$

$$\frac{d\pi}{dt}+\frac{R\pi}{C_v}\nabla\cdot\mathbf{v}=0, \tag{2.2.4}$$

$$\frac{d\theta}{dt}=0, \tag{2.2.5}$$

where φ is the gravitational potential.

Using the relation

$$\frac{d\mathbf{v}}{dt}=\frac{\partial\mathbf{v}}{\partial t}+[\nabla(\frac{1}{2}\mathbf{v}^2)-\mathbf{v}\times(\nabla\times\mathbf{v})] \tag{2.2.6}$$

and cross-multiplying the two sides of equation (2.2.3), then

$$\frac{\partial\boldsymbol{\xi}_a}{\partial t}=-\nabla\times(\boldsymbol{\xi}_a\times\mathbf{v})-c_p\nabla\theta\times\nabla\pi\,. \tag{2.2.7}$$

This is the mesoscale absolute vorticity equation for ideal baroclinic, unsaturated wet air, which can deduced from the basic equations. In the equation

$$\boldsymbol{\xi}_a=f\,\mathbf{k}+\nabla\times\mathbf{v}\,. \tag{2.2.8}$$

This absolute vorticity equation (2.2.7) contains the potential temperature on the right-hand side, thus emphasizing the influence of the slope of the potential temperature surface on the generation and development of mesoscale systems. The first term on the right-hand side of the equation describes the advective transport of the vorticity as well as the influence of the divergence and rotation effects on the absolute vorticity change. The second term accounts for the influence of the atmospheric baroclinic effect and the solenoid effect on the generation of the absolute vorticity and on changes in the vorticity.

In real situations, the vertical component of the relative vorticity, $\nabla\times\mathbf{v}$ (called simply the vertical vorticity in the following), is usually used. From the basic mesoscale horizontal momentum equation:

$$\frac{\partial u}{\partial t}+u\frac{\partial u}{\partial x}+v\frac{\partial u}{\partial y}+w\frac{\partial u}{\partial z}-fv+c_p\theta\frac{\partial \pi}{\partial x}=0 \quad \text{and} \tag{2.2.9}$$

$$\frac{\partial v}{\partial t}+u\frac{\partial v}{\partial x}+v\frac{\partial v}{\partial y}+w\frac{\partial v}{\partial z}+fu+c_p\theta\frac{\partial \pi}{\partial y}=0. \tag{2.2.10}$$

Taking

$\frac{\partial}{\partial x}(2.2.10)-\frac{\partial}{\partial y}(2.2.9)$, then

$$\frac{\partial \zeta}{\partial t}=-\mathbf{v}\cdot\nabla\zeta-(\zeta+f)\delta+c_pJ_h(\pi,\theta)-\beta v+\frac{\partial w}{\partial y}\frac{\partial u}{\partial z}-\frac{\partial w}{\partial x}\frac{\partial v}{\partial z}. \tag{2.2.11}$$

This is the vertical vorticity equation, which is suitable for use at the mesoscale under the β-plane approximation. $\zeta=\frac{\partial v}{\partial x}-\frac{\partial u}{\partial y}$ is the vertical vorticity, $\delta=\frac{\partial u}{\partial x}+\frac{\partial v}{\partial y}$ is the horizontal divergence, $J_h(\pi,\theta)=\frac{\partial \pi}{\partial x}\frac{\partial \theta}{\partial y}-\frac{\partial \pi}{\partial y}\frac{\partial \theta}{\partial x}$ is the baroclinic effect, and $\frac{\partial w}{\partial y}\frac{\partial u}{\partial z}-\frac{\partial w}{\partial x}\frac{\partial v}{\partial z}$ is the inclination term.

2.2.3 Divergence Equation

Taking the dot product of equation (2.2.3) gives

$$\frac{\partial D}{\partial t} = -\nabla \cdot [(\mathbf{v} \cdot \nabla)\mathbf{v}] + f\,\mathbf{k} \cdot (\nabla \times \mathbf{v}) - (\nabla \times f\,\mathbf{k}) \cdot \mathbf{v} - c_p(\nabla\theta \cdot \nabla\pi + \theta\nabla^2\pi) - \nabla^2\varphi$$

. (2.2.12)

This is the mesoscale three-dimensional divergence equation deduced from the basic equations, where $D = \nabla \cdot \mathbf{v}$.

Mesoscale systems can usually be considered approximately incompressible. Therefore, for the three-dimensional divergence, usually $D \approx 0$, and so we should consider the change in the two-dimensional horizontal divergence. From the above, we can obtain the mesoscale horizontal momentum equations under the pseudo-incompressible approximation:

$$\frac{\partial u}{\partial t} + u\frac{\partial u}{\partial x} + v\frac{\partial u}{\partial y} + w\frac{\partial u}{\partial z} - fv + c_p\theta\frac{\partial \pi'}{\partial x} = 0 \qquad (2.2.13)$$

$$\frac{\partial v}{\partial t} + u\frac{\partial v}{\partial x} + v\frac{\partial v}{\partial y} + w\frac{\partial v}{\partial z} + fu + c_p\theta\frac{\partial \pi'}{\partial y} = 0. \qquad (2.2.14)$$

Taking $\frac{\partial}{\partial x}(2.2.13) + \frac{\partial}{\partial y}(2.2.14)$, we can get

$$\frac{\partial \delta}{\partial t} = -\mathbf{v} \cdot \nabla\delta - \delta^2 + 2J_h(u,v) - \nabla_h w \cdot \frac{\partial \mathbf{v}_h}{\partial z} + f\zeta - \beta u - c_p\nabla_h\theta \cdot \nabla_h\pi' - c_p\theta\nabla_h{}^2\pi' \qquad (2.2.15)$$

This is the horizontal divergence equation for a mesoscale system. The subscript "h" here means "horizontal": $J_h(u,v) = \frac{\partial u}{\partial x}\frac{\partial v}{\partial y} - \frac{\partial v}{\partial x}\frac{\partial u}{\partial y}$.

The first term on the right-hand side of equation (2.2.15) represents the divergence advection and vertical transport; the second term is the square of the divergence, which always causes an increase in the convergence or a decrease in the divergence; the third term is the deformation term, repressing the influence of the horizontal wind shear on the change in divergence; the fourth term represents the effect of the vertical shear on the horizontal wind speed; the fifth term is related to the effect produced by the Earth's rotation; and the sixth term is the β-effect term. (At the mesoscale, this last term can often be omitted). The final two terms are a joint term that accounts for the force due to the horizontal pressure gradient and potential temperature.

To determine the relative importance of each factor in the two equations, i.e., (2.2.11) and (2.2.12), it is necessary to consider specific examples. Because the sizes of these different terms, in particular the vertical motion term, vary a lot between different mesoscale systems, the sizes determined using the scale analysis method may not conform to reality. Therefore, we will not carry out a scale analysis of the terms here.

2.3 The Potential Vorticity Equation and Potential Vorticity Substance Equation for Mesoscale Systems

Vorticity is the differential physical quantity that represents the rotational characteristics of the wind field, and the vorticity equation expresses the local change in vorticity. When considering its constrained relationship, the potential vorticity should be used. Ertel (1942)[17] put forward $Q = \xi_a \cdot \nabla\theta / \rho$ as the definition of potential vorticity for adiabatic frictionless dry air. This was later given the name of “Ertel potential vorticity”. As well as being a conserved property under frictionless adiabatic conditions, The Ertel potential velocity is also reversible in an equilibrium system and so is widely used in weather

system analysis and diagnosis, including the analysis of baroclinic instability (Robinson, 1989; Gao, 1990)[18-19], extra-tropical cyclones (Hoskins and Berridford, 1988; Davis and Emanuel, 1991)[20-21], tropical cyclones (Schubert and Alworth, 1987)[22], the polar vortex (Montgomery and Farrell, 1992)[23], and frontal surfaces (Thorpe, 1990; Keyser and Rotunno, 1990)[24-25]. Pedlosky (1979)[26] pointed out that this emphasis on the importance of the potential vorticity is justified. Hoskins et al. (1985)[27] systematically analyzed the application of the Ertel potential vorticity in atmospheric diagnosis and proposed the concept of "isentropic potential vorticity thinking" (abbreviated to "IPV thinking"). The IPV is of importance to the movement and development of many mid- and high-latitude weather systems, but its significance in the lower troposphere and at middle or low latitudes is limited. In addition, the importance of the divergence cannot be ignored in mesoscale systems as the divergence is more closely related to the occurrence and development of mesoscale systems than the vorticity is (Zhao and Liu,1999)[28]. Therefore, if the effects of the convergence and divergence can be explicitly accounted for by the potential vorticity substance equation, this will be of benefit to the study of mesoscale systems and the application of this equation. Therefore, we define a new expression for the potential vorticity substance: $Q_{su} = \dfrac{\boldsymbol{\xi}_a \cdot \nabla\theta}{\pi}$. The corresponding potential vorticity substance equation is derived below.

From the commonly used mesoscale vorticity equation obtained from equation (2.2.7):

$$\frac{\partial \boldsymbol{\xi}_a}{\partial t} + \nabla \times (\boldsymbol{\xi}_a \times \mathbf{v}) = -c_p \nabla\theta \times \nabla\pi , \tag{2.3.1}$$

where $\boldsymbol{\xi}_a = f\,\mathbf{k} + \nabla \times \mathbf{v}$.

Taking the dot product of $\nabla\theta$ and equation (2.3.1) gives

$$\nabla\theta\cdot\frac{d\boldsymbol{\xi}_a}{dt}-\nabla\theta\cdot(\boldsymbol{\xi}_a\cdot\nabla)\,\mathbf{v}+\nabla\theta\cdot\boldsymbol{\xi}_a(\nabla\cdot\mathbf{v})=0\,. \tag{2.3.2}$$

If the original continuity equation is used, then $\frac{d\rho}{dt}+\rho\nabla\cdot\mathbf{v}=0$.

Substituting this into equation (2.3.2) gives

$$\nabla\theta\cdot\frac{d\boldsymbol{\xi}_a}{dt}-\nabla\theta\cdot(\boldsymbol{\xi}_a\cdot\nabla)\,\mathbf{v}-\nabla\theta\cdot\boldsymbol{\xi}_a\cdot\frac{1}{\rho}\frac{d\rho}{dt}=0\,, \tag{2.3.3}$$

and if the potential temperature is conservative, then

$$\frac{d\nabla\theta}{dt}=-\nabla\mathbf{v}\cdot\nabla\theta\,, \tag{2.3.4}$$

where $\nabla\mathbf{v}\cdot\nabla\theta=\nabla u\frac{\partial\theta}{\partial x}+\nabla v\frac{\partial\theta}{\partial y}+\nabla w\frac{\partial\theta}{\partial z}$.

Taking the dot product of $\frac{\boldsymbol{\xi}_a}{\rho}$ and the above equation, the dot product of $\frac{1}{\rho}$ and equation (2.3.3), and then adding these two equations gives

$$\frac{d}{dt}\frac{(\boldsymbol{\xi}_a\cdot\nabla\theta)}{\rho}=0\,. \tag{2.3.5}$$

This equation is the conservation equation for the Ertel potential vorticity.

Substituting (2.2.2) into (2.3.2) gives

$$\nabla\theta\cdot\frac{d\boldsymbol{\xi}_a}{dt}-\nabla\theta\cdot(\boldsymbol{\xi}_a\cdot\nabla)\,\mathbf{v}-\frac{c_v}{R}\nabla\theta\cdot\boldsymbol{\xi}_a\cdot\frac{1}{\pi}\frac{d\pi}{dt}=0\,. \tag{2.3.6}$$

Taking the dot product of $\frac{\boldsymbol{\xi}_a}{\pi}$ and the equation (2.3.4), the dot product of $\frac{1}{\pi}$ and (2.3.6), and then adding these two equations gives

$$\frac{d}{dt}\left(\frac{\boldsymbol{\xi}_a\cdot\nabla\theta}{\pi}\right)=\frac{1}{\pi}\left(\frac{R}{c_v}-1\right)(\boldsymbol{\xi}_a\cdot\nabla\theta)\nabla\cdot\mathbf{v}\,. \tag{2.3.7}$$

Defining the potential vorticity substance as $Q_{su}=\frac{\boldsymbol{\xi}_a\cdot\nabla\theta}{\pi}$, then

$$\frac{d}{dt}(Q_{su}) = \frac{1}{\pi}(\frac{R}{c_v} - 1)(\xi_a \cdot \nabla\theta)\nabla \cdot \mathbf{v}. \tag{2.3.8}$$

This is the new potential vorticity substance equation that accounts for the divergence effect and is suitable for applying to the study of mesoscale systems. In the equation, C_v is the specific heat at constant volume. The most important feature of this equation is that the divergence term clearly appears on the right-hand side (because it is frictionless adiabatic, unsaturated wet air that is being considered). Clearly, this equation is of great benefit to the study of the influence of convergence and divergence on the change in the mesoscale potential vorticity substance.

Notes

[1]Durran D.R. (1999) *Numerical methods for wave equations in*, *Geophysical Fluid Dynamics*, Springer-Verlag New York, Inc.

[2]Gao S. and X. Cui (2006) "A modified potential vorticity equation for mesoscale systems," *J Graduate School of Chinese Academy of Sciences*, 118(23):337–341.

[3]Wu G. X., Y. P. Cai and X. J. Tang (1995) "Moist potential vorticity and slantwise vorticity development," *Acta Meteorologica Sinica*, 53(4):387–405. (in Chinese with English abstract)

[4]Charney J. D. and Y. Ogura (1962) "A numerical model of thermal convection in the atmosphere," *Journal of the Meteorological Society of Japan*, 38(6):431-452.

[5]Ogura Y. and N. A. Phillips (1962) "Scale analysis of deep and shallow convection in the atmosphere," *Journal of Atmospheric Sciences*, 19(2):173–179.

[6]Durran D. R. and J. B. Klemp (1982) "On the effects of moisture on the brunt-Väisalä frequency," *Journal of Atmospheric Sciences*, 39(10):2152-2158

[7]Rossby C. G. (1937) "On the mutual adjustment of pressure and velocity distribution in certain simple current systems, I," *Journal of Marine Research*, 1(1):15-28.

[8]Rossby C. G. (1938) “On the mutual adjustment of pressure and velocity distribution in certain simple current systems, II,” *Journal of Marine Research*, 1(3):239-263.

[9]Oboukhov A. M. (1949) “The problem of geostrophic adaptation,” Izuestiya of Academy of Science USSR, *Ser, Gograhpy and Geophysics,* 13:281-289.

[10] Yeh T. C. (1957) “On the formation of quasi-geostrohpic motion in the atmosphere,” *Journal of the Meteorological Society of Japan,* 75th Anniversary Volume,35A:130-137.

[11]Zeng Q. C. (1963) “The effect of original disturbance structure on adaptation and the application of observed wind field,” *Acta Meteorol0gica Sinica,* 33(1):37–50. (in Chinese with English abstract)

[12] Yeh T. C. and M. T. Li (1982) “On the characteristics of scales of the atmospheric motions,” *Journal of the Meteorological Society of Japan, Ser. II,* 60(1):16-23.

[13] Wu R. S. and M. Z. Tan (1989) “Generalized vorticity and potential vorticity versation law and application,” *Acta Meteorologica Sinica,* 47(4):436-442. (in Chinese with English abstract)

[14]Tan M. Z. and R. S. Wu (1994) “Helicity dynamics of atmospheric flow,” *Advances in Atmospheric Science,* 11(2):175-188.

[15]Shou S. T. (2003) Mesoscale meteorology*, Meteorology Press,* Beijing. (in Chinese with English abstract)

[16]Petterssen S. (1956) Weather analysis and forecasting: *Vol I.* Science Press.

[17]Ertel H. (1942) “Ein Neuer hydrodynamischer wir-belsatz,” *Meteorologische Zeitschrift,* 59:271–281.

[18]Robinson W. A. (1989) “On the structure of potential vorticity in baroclinic instability,” *Tellus,* 41A:275–284.

[19]Gao S. T., S. Y. Tao and Y. H. Ding (1990) “The generalized E-P flux of wave-mean flow interactions,” *Science China S B,* 33(6):704–715.

[20]Hoskins B. J. and P. Berrisford (1988) “A potential vorticity perspective of the storm of 15-16 October 1987,” *Weather,* 43(3):122–129.

[21]Davis C. A. and K. A. Emanuel (1991) “Potential vorticity Diagnostics of

cyclogenesis," *Monthly Weather Review,* 119(8):1929–1953.

[22]Schubert W. H. and B. T. Alworth (1987) "Evolution of potential vorticity in tropical cyclones," *Quarterly Journal of the Royal Meteorological Society,* 113(475):147–162.

[23]Montgomery M. T. and B. F. Farrell (1992) "Polar low dynamics," *Journal of Atmospheric Sciences*, 49(24):2484–2505.

[24]Thorpe A. J. (1990) "Frontogenesis at the boundary between air-masses of different potential vorticity," *Quarterly Journal of the Royal Meteorological Society,* 116(493):561–572.

[25]Keyser D. and R. Rotunno (1990) "On the formation of potential vorticity anomalies of upper-level jet front systems," *Monthly Weather Review,* 118(9):1914–1921.

[26]Pedlosky J. (1979)*Geophsical Fluid Dynamics*, New York: Springer-Verlag

[27]Hoskins B. J., M. E. Mcintyre and Robertson A.W. (1985) "On the use and significance of isentropic potential vorticity maps," *Quarterly Journal of the Royal Meteorological Society,* 111(470):877–946.

[28]Zhao Q. and S. K. Liu (1999) "Barotropic mesoscale semi-balanced and quasi-balanced dynamic models," *Chines Journal of Atmospheric Sciences,* 23(5):559–570. (in Chinese with English abstract)

CHAPTER THREE

DYNAMIC PARAMETERS OF INHOMOGENEOUSLY SATURATED AIR AND RELATED EQUATIONS

Studies of the aerodynamics of saturated air were advocated by Xie as early as the 1970s (Xie, 1978)[1]. In response, many other researchers in China investigated different aspects of this field (e.g., Wang and Luo, 1980; Wu et al., 1995; Wang and Wu, 1999)[2-4]. Outside China, there have also been many studies of the dynamics of moist air (e.g., Holton, 1972; Betts and Dugan, 1973; Bennetts and Hoskins, 1979; Emanuel, 1979, 1994)[5-9]. In particular, Bannon recently put forward a set of equations that describe the dynamics of moist air (Bannon, 2002)[10]. Previous studies have been about either dry air or saturated air. However, the real atmosphere is neither dry nor saturated but, rather, is inhomogeneously saturated; that is, the atmosphere is a mixture of dry air and moist air and, thus, contains both saturated and unsaturated air. Even in clouds, the air is not saturated everywhere because of the entrainment of dry air. Wang and Wu (1999)[4] first put forward the concept of an inhomogeneously saturated atmosphere and has carried out several studies related to this. This work is of great importance and should be recognized as such. In this chapter, we will construct the dynamic parameters for an inhomogeneously saturated atmosphere and develop the theory of generalized potential temperature. These will be used as the theoretical basis for the study of the dynamics of the real atmosphere.

3.1 Introduction to the Generalized Potential Temperature in an Inhomogeneously Saturated Atmosphere and its Conservation

In the case of dry air, the potential temperature is a very important parameter and is conserved in dry adiabatic processes. This means that it can be used to compare the temperature differences between air parcels at different pressures, analyze the atmospheric stability, and calculate the vertical speed of the atmosphere (Shou et al., 2003; Schultz and Schumacher, 1999)[11-12]. However, in diabatic processes, such as going with rain or remarkable diabatic source, the potential temperature will not be conserved. To deal with this, we introduce the equivalent potential temperature, which is also conserved in moist diabatic processes. Therefore, it is very convenient to discuss the state change of a moist diabatic process by using the equivalent potential temperature. However, according to daily observations, the actual atmosphere is neither dry nor saturated but is a mixture of dry air and moist air and so is in an inhomogeneously saturated state. Fog is the best example of this: the relative humidity is different in the case of light fog and thick fog. Generally, the higher the relative humidity, the more easily water vapor will condense. This means that condensation will occur more easily as the humidity increases. In order to describe this and to provide a quantitative expression that describes the characteristics of a real, inhomogeneously saturated atmosphere, Gao et al. (2004)[13] introduced a dimensionless condensation weight function, $(q/q_s)^k$, in order to correctly express the idea that condensation occurs before the relative humidity reaches the point of saturation. Thus, the concept of the generalized potential temperature was obtained. The generalized potential temperature can not only be used for dry and saturated air but also in the case of an inhomogeneously saturated atmosphere. The generalized potential

temperature is also conserved in both dry and moist adiabatic processes. Furthermore, it can be used to determine the atmospheric potential stability and to trace the trajectory of air parcels in the same way as for the potential temperature and equivalent potential temperature. This concept, therefore, has wide potential application.

The potential temperature can usually be expressed as

$$\theta = T(\frac{p_0}{p})^{\frac{R}{c_p}}. \tag{3.1.1}$$

However, there are different ways of expressing the equivalent potential temperature. Bolton made a comparison of some of the expressions for the equivalent potential temperature that assumed a saturated pseudo-adiabatic process and calculated the error between them for the same temperature and pressure. The best expression for the equivalent potential temperature that was finally obtained (Bolton, 1980)[14] was

$$\theta_e = T(\frac{p_0}{p})^{0.2854(1-0.28\times10^{-3}r)} \times \mathbf{exp}[(\frac{3.376}{T_L} - 0.00254) \times r(1 + 0.81\times10^{-3}r)]$$

. (3.1.2)

This expression for the equivalent potential temperature assumes that the air parcel is saturated initially, and so the quantity that it describes can also be called the saturated equivalent potential temperature. Although it produces more accurate results, this expression is very inconvenient. Another relatively accurate expression for the equivalent potential temperature is (Cao and Cho, 1995)[15]

$$\theta_e = \theta \,\mathbf{exp}(\frac{\alpha_1 q}{T_L}), \tag{3.1.3}$$

where $T_L = \dfrac{1}{\dfrac{1}{T-\alpha_3} - \dfrac{\ln(r)}{\alpha_2}} + \alpha_3$ is the lifted condensation

temperature. Usually, $\alpha_1 = 2.675 \times 10^3 K$, which is equivalent to the value of $\frac{L}{C_p}$ at 0°C; $\alpha_2 = 2.84 \times 10^3 K$; and $\alpha_3 = 55K$. r is the mixing ratio, and q is the specific humidity. Here, $\theta = T(\frac{p_0}{p})^{\frac{R}{c_p}}$, where $p_0 = 1000hpa$, $p = \rho RT(1 + \alpha_4 q)$, and $\alpha_4 = 0.61$.

An expression such as the one above contains many parameters and is complicated, and so it is not applied widely. The most commonly used expression for the equivalent potential temperature is (Schultz and Schumacher, 1999)[12]:

$$\theta_e(T, p) = \theta(T, p) \exp(\frac{Lr_s(T, p)}{c_p T}), \tag{3.1.4}$$

where r_s is the saturated mixing ratio, and T and p denote the temperature and pressure of the original saturated air parcel, respectively. In fact, this expression was put forward by Betts and Duganas early as 1973. At that time, these authors defined this equivalent potential temperature as the saturated equivalent potential temperature and also pointed out that the equivalent potential temperature of the unsaturated airmass can be obtained by using the mixing ratio, r, instead of r_s:

$$\theta_e(T, p) = \theta(T, p) \exp(\frac{Lr(T, p)}{c_p T}). \tag{3.1.5}$$

However, this expression was meaningless, and Betts and Dugan (1973)[6] did not introduce it in detail. It is possible that, at that time, it was thought that a macroscopic unsaturated atmosphere had no latent heat to

release; also the theory of molecular statistics had not yet been introduced to meteorology.

The difference between the value of the mixing ratio, r, and the specific humidity, q, is small ($r = 0.622\frac{e}{p-e}$, $q = 0.622\frac{e}{p-0.378e}$). In China, usually the specific humidity is used in calculations (r_s has a similar relation with q_s). Therefore, here we also use the specific humidity, q (q_s), to replace the mixing ratio, r (r_s), to obtain the expressions for the saturated equivalent potential temperature and the unsaturated equivalent potential temperature:

$$\theta_e = \theta \exp(\frac{Lq_s}{c_p T}) \tag{3.1.6}$$

$$\theta_{ue} = \theta \exp(\frac{Lq}{c_p T}). \tag{3.1.7}$$

It can be seen from the above analysis that (3.1.6) and (3.1.7) are, to some extent, reasonable. In order to reflect the fact that condensation occurs more easily as the humidity increases, we introduce a weight function, $(q/q_s)^k$, that defines the equivalent potential temperature to the expression and obtain the following:

$$\theta^* = \theta \exp[\frac{Lq_s}{c_p T}(\frac{q}{q_s})^k]. \tag{3.1.8}$$

Here, θ^* is the generalized potential temperature. In the following, we will explain the physical meaning of this temperature.

The latent heat of condensation released by an inhomogeneously saturated atmosphere can be expressed as

$$\delta Q = -L\delta(q_s \cdot (q/q_s)^k) . \tag{3.1.9}$$

Substituting equation (3.1.9) into the first law of thermodynamics, $\delta U = \delta Q + \delta W$, and regarding the condensation process as irreversible, then $\delta Q = T\delta S$. The latent heat released by the condensation is removed as the liquid water is expelled from the air parcel; however, the amount of heat is very small, and so the process can still be regarded as adiabatic—alternatively, it can be considered to be a "pseudo-adiabatic process" (Andrews, 2000)[16]. We thus obtain the following form of the first law of thermodynamics:

$$c_{pm}\delta(\ln T) - R_v\delta(\ln p) = \frac{\delta Q}{T} = -\frac{L\delta(q_s \cdot (q/q_s)^k)}{T} , \tag{3.1.10}$$

where c_{pm} and R_v are the specific heat of moist air at constant pressure and the gas constant for water vapor, respectively.

When $Lq_s/(c_{pm}T) << 1$, the right-hand side of (3.1.10) can be approximated as $-\delta(Lq_s \cdot (q/q_s)^k)$. As for whether the saturated specific humidity condition is tenable, this can be determined from the distribution profile of the real atmosphere, $q_s(T, p)$; also, it was shown

that $q_s << 100g \cdot kg^{-1}$ where the concept of the equivalent potential temperature was introduced. Because the temperature of the lower atmospheric layer is usually $L/(c_{pm}T) \lesssim 10$, this approximation is valid only if $q_s(q/q_s)^k << 100g \cdot kg^{-1}$. If the variation of c_{pm} with time is also neglected, (3.1.10) can be transformed as follows:

$$\delta(c_{pm} \ln T - R_v \ln p + \frac{L(q_s \cdot (q/q_s)^k)}{T}) = 0. \tag{3.1.11}$$

Integrating equation (3.1.11) from the ground to the target height, using $\kappa = \frac{R_v}{c_{pm}}$, and taking exponentials, we get

$$\theta^*(T, p) \equiv T(\frac{p_0}{p})^{\kappa} \exp(\frac{Lq_s \cdot (q/q_s)^k}{c_{pm}T}). \tag{3.1.12}$$

Equation (3.1.12) gives the generalized potential temperature just as (3.1.8) does.

From (3.1.10) it is easy to obtain the thermodynamic equation for an inhomogeneously saturated atmosphere:

$$c_{pm} \frac{T}{\theta^*} \frac{d\theta^*}{dt} = Q_d. \tag{3.1.13}$$

Clearly, for a wet adiabatic process, i.e., $Q_d = 0$, the generalized potential temperature is conserved.

In addition, the different expressions for the equivalent potential temperature, as well as the expressions for the latent heat at a generalized potential temperature and the thermodynamic equations, assume that, once

moist air is saturated, all the vapor will condense and all the latent heat generated by the condensation process will be released (i.e., all the liquid water generated during condensation will be expelled from the air parcel); however, this is almost impossible in the real atmosphere. Further consideration of the equivalent potential temperature, generalized potential temperature, and the conservation of these quantities is necessary if the latent heat is partly retained within the air parcel.

3.2 The Generalized Moist Potential Vorticity and its Expression

The previous section introduced the condensation weight function, which can be used to express the saturated inhomogeneous characteristics of the real atmosphere. An expression for the generalized potential temperature was then also derived. In moist air dynamics, the moist potential vorticity is closely related to the equivalent potential temperature. Thus, now that the generalized potential temperature has been obtained and because it has better properties than the equivalent potential temperature, in this section we will use the generalized potential temperature instead of the equivalent potential temperature to derive the generalized moist potential vorticity.

After the concept of potential vorticity had been proposed by Ertel in 1942 (Ertel, 1942)[17], it was studied and applied extensively. Because the potential vorticity is conserved in an adiabatic frictionless atmosphere, it is one of the important dynamic parameters. However, when clouds develop and latent heat is released, the potential vorticity is no longer conserved. In such situations, the equivalent potential temperature is used to introduce the concept of moist potential vorticity instead of the potential temperature as the equivalent potential temperature is still conserved in moist adiabatic processes. Many studies of the role of dry and moist potential vorticity in the generation and development of synoptic systems have been conducted

(Bennetts and Hoskins, 1979; Emanuel, 1979; Danielsen and Hipskind, 1980; Thorpe, 1985; Hoskins and Berridford, 1988; Xu, 1992; Montgomery and Farrell, 1993; Gao el al., 2002 (a), (b))[7-8,18-24]. Here, we will focus on the generalized moist potential vorticty, which corresponds to the generalized potential temperature, and the related equation.

Taking into account the diabatic heating effect, the thermodynamic equation for an inhomogeneously saturated atmosphere can be written as

$$c_p \frac{T}{\theta}\frac{d\theta}{dt} = -L\frac{d}{dt}[(q/q_s)^k q_s] + Q_d . \tag{3.2.1}$$

We introduce the generalized potential temperature:

$$\theta^* = \theta \exp[\frac{L}{C_p}\frac{q_s}{T}(\frac{q}{q_s})^k]. \tag{3.2.2}$$

(3.2.1) can then be written as

$$c_p \frac{T}{\theta^*}\frac{d\theta^*}{dt} = Q_d . \tag{3.2.3}$$

Using the specific volume, α, the equation for the absolute vorticity is

$$\frac{d\boldsymbol{\xi}_a}{dt} = (\boldsymbol{\xi}_a \cdot \nabla)\mathbf{v} - \boldsymbol{\xi}_a \nabla \cdot \mathbf{v} - \nabla\alpha \times \nabla p , \tag{3.2.4}$$

where $\boldsymbol{\xi}_a = \nabla \times \mathbf{v} + 2\boldsymbol{\Omega}$. Setting $Q^* = \frac{\theta^*}{c_p T} Q_d$, from (3.2.3) and (3.2.4) we can derive the equation for the tendency of the generalized moist potential vorticity (Gao et al., 2004)[13]:

$$\frac{dQ_m^*}{dt} = -\alpha(\nabla\alpha \times \nabla p) \cdot \nabla\theta^* + \alpha\boldsymbol{\xi}_a \cdot \nabla Q^* . \tag{3.2.5}$$

Here, $Q_m^* = \alpha\boldsymbol{\xi}_a \cdot \nabla\theta^*$ is the generalized moist potential vorticity (GMPV), which neglects the influence of the geostrophic vorticity.

From $\alpha = \frac{R}{p}\theta(p_0/p)^{-\frac{R}{c_p}}$, we have

$$\begin{aligned}\frac{dQ_m^*}{dt} &= \alpha(\nabla p \times \nabla \alpha)\cdot\nabla\theta^* + \alpha\boldsymbol{\xi}_a\cdot\nabla Q^* \\ &= A^*(\nabla\theta\times\nabla p)\cdot\nabla q + \alpha\boldsymbol{\xi}_a\cdot\nabla Q^*\end{aligned}, \tag{3.2.6}$$

where

$$A^* = -\frac{L}{c_p}k\frac{R^2}{p^2}\left(\frac{p_0}{p}\right)^{-\frac{R}{c_p}}\left(\frac{q}{q_s}\right)^{k-1}\theta\exp\left[\frac{L}{c_p}\frac{q_s}{T}\left(\frac{q}{q_s}\right)^k\right]$$

$$= -\left[\frac{LR^2}{c_p p^2}\left(\frac{p_0}{p}\right)^{-\frac{R}{c_p}}\right]\left[k\left(\frac{q}{q_s}\right)^{k-1}\theta^*\right].$$

Clearly, the change in the GMPV is determined by the two terms on the right-hand side of equation (3.2.6): the interaction between the baroclinic solenoid and the generalized potential temperature gradient, and the interaction between the vorticity and the diabatic heating gradient. In an adiabatic atmosphere, the rate of change of the GMPV depends on the configuration of the baroclinic vector, $\nabla\theta\times\nabla p$, and the specific humidity gradient, ∇q: specifically, if a negative (positive) GMPV is generated, then $(\nabla\theta\times\nabla p)\cdot\nabla q$ takes a positive (negative) value, which means that the baroclinicity increases (decreases) in the direction of the specific humidity gradient. Therefore, in an inhomogeneously saturated atmosphere, the creation and disappearance of the GMPV is closely related to changes in the specific humidity gradient. Accordingly, Chapter 8 of this book will describe the characteristics of the GMPV and its application to dynamic nowcasting.

3.3 Moist Potential Vorticity Anomalies Caused by Thermal Forcing and Mass Forcing

It has long been known that external forcing can destroy the conservation of the potential vorticity and, as a result, cause potential vorticity anomalies (Hoskins et al., 1985; Gao et al., 1990; Zhou et al., 2002; Keyser and Rotunno, 1990)[25-28]. In large-scale systems, external forcing occurs mainly in the form of thermal forcing and frictional dissipation. For a mesoscale convective system, we should consider not only the thermal forcing, which causes potential vorticity anomalies in a similar way to those in large-scale systems, but also, more importantly, we should consider the mass forcing. Because in some mesoscale convective systems there is heavy rainfall, the change in the internal mass of the system is constrained by the significant reduction in mass that occurs as a result of the heavy rainfall as well as by the convergence and divergence of the large-scale environmental field. Therefore, when using the concept of potential vorticity to study rainstorm systems, we must note that there are two main sources of forcing that can cause potential vorticity anomalies. One is the thermal forcing, which is similar to the large-scale external forcing; the other is the mass forcing, which is not considered in large-scale systems but is very important in mesoscale systems.

The existence of potential vorticity anomalies in mesoscale convective systems was identified many years ago. For example, Fritsch and Maddox (1981)[29] pointed out that mesoscale convective systems had related potential vorticity anomalies, usually occurring as a negative potential vorticity anomaly in the upper troposphere and a positive potential vorticity anomaly in the middle troposphere. However, both Davis (Davis and Weisman, 1994)[30] and Gray (Gray et al., 1998)[31] considered that the positive potential vorticity anomaly in the middle troposphere was related to the cyclonic vortex in the middle troposphere. At the same time, some

researchers thought that the dynamic adjustment of the mass-field distribution caused by convection could also lead to a potential vorticity anomaly in the troposphere (Shutts and Gray, 1994; Fulton et al., 1995)[32-33]. Raymond and Jiang (1990)[34] developed a potential vorticity anomaly theory for long-lived mesoscale convective systems, but they did not take the mass forcing into account. Gray (1999)[35] used a mass-forcing model to study the potential vorticity anomaly. However, in this mass-forcing model, only the effect of mass transport in convection systems was considered. It is pointed that the upward (downward) transport of convection activity will produce a mass source (sink) at high levels and a mass sink (source) at low levels; however, the total mass is conserved. The loss of mass from moist air as a result of condensation and precipitation was not included in the studies by Gray. In this section, the mass forcing in a convective system is considered to consist of not only the transport of a moist airmass but also the mass lost by moist air due to heavy rainfall.

Before deriving the moist potential vorticity equation with mass forcing, first the continuity equation with mass forcing for a rainstorm system will be presented. Suppose that ρ represents the overall density of moist air and that ρ_d, ρ_m, and ρ_r represent the density of dry air, water vapor, and raindrops, respectively. We can obtain $\rho = \rho_d + \rho_m$ and then the continuity equations:

$$\frac{d\rho_d}{dt} + \rho_d \nabla \cdot \mathbf{v} = 0 , \tag{3.3.1}$$

$$\frac{d\rho_m}{dt} + \rho_m \nabla \cdot \mathbf{v} = -\dot{\rho}_v , \tag{3.3.2}$$

$$\nabla \cdot (\rho_r \mathbf{v}_T) = \dot{\rho}_v , \tag{3.3.3}$$

where $\dot{\rho}_v$ is the transfer ratio from water vapor to raindrops and $\mathbf{v}_T$ is the terminal velocity of a raindrop relative to the moist air.

Adding (3.3.1), (3.3.2), and (3.3.3), we then have

$$\frac{d\rho}{dt} + \rho\nabla\cdot\mathbf{v} = -\nabla\cdot(\rho_{\mathrm{r}}\,\mathbf{v}_T) = S_m\,, \tag{3.3.4}$$

where $S_m = -\nabla\cdot(\rho_{\mathrm{r}}\,\mathbf{v}_T)$ is the mass forcing.

Therefore, in Cartesian coordinates, the continuity equation for heavy rainfall can be written as (Gao et al., 2002)[24]

$$\frac{d\rho}{dt} + \rho\nabla\cdot\mathbf{v} = S_m\,. \tag{3.3.5}$$

The equation for the absolute vorticity is

$$\frac{\mathrm{d}\boldsymbol{\xi}_a}{\mathrm{dt}} = (\boldsymbol{\xi}_a\cdot\nabla)\,\mathbf{v} - \boldsymbol{\xi}_a\nabla\cdot\mathbf{v} + \frac{\nabla\rho\times\nabla P}{\rho^2} - \nabla\times\mathbf{F}\,, \tag{3.3.6}$$

and the thermodynamic equation is

$$\frac{d\theta_e}{dt} = \dot{\psi}\,. \tag{3.3.7}$$

In equation (3.3.6), $\boldsymbol{\xi}_a$ is the absolute vorticity vector, $\mathbf{v}$ is the velocity, $\frac{\nabla\rho\times\nabla P}{\rho^2}$ is the solenoid term, and $\mathbf{F}$ is the friction term. In equation (3.3.7), θ_e is the equivalent potential temperature.

Equation (3.3.5) includes the mass-forcing term, S_m, and (3.3.7) includes the thermal forcing term, $\dot{\psi}$. Because our area of interest is systems of heavy precipitation in saturated air, equation (3.3.7) includes

the potential temperature of saturated air, θ_e, and also the thermal forcing term in order to express the thermal forcing effects such as heating due to radiation.

Taking the dot product of $\nabla\theta_e$ and (3.3.6) gives

$$\nabla\theta_e \cdot \frac{d\boldsymbol{\xi}_a}{dt} = \nabla\theta_e \cdot (\boldsymbol{\xi}_a \cdot \nabla)\mathbf{v} - \nabla\theta_e \cdot \boldsymbol{\xi}_a(\nabla \cdot \mathbf{v}) - \nabla\theta_e \cdot \nabla \times \mathbf{F}. \tag{3.3.8}$$

By using the continuity equation (equation (3.3.5)), (3.3.8) can also be expressed as

$$\nabla\theta_e \cdot \frac{d\boldsymbol{\xi}_a}{dt} = \nabla\theta_e \cdot (\boldsymbol{\xi}_a \cdot \nabla)\mathbf{v} - \nabla\theta_e \cdot \boldsymbol{\xi}_a\left(\frac{S_m}{\rho} - \frac{1}{\rho}\frac{d\rho}{dt}\right) - \nabla\theta_e \cdot \nabla \times \mathbf{F}. \tag{3.3.9}$$

After rearranging equation (3.3.9), we have

$$\rho\frac{d}{dt}\left(\frac{\boldsymbol{\xi}_a \cdot \nabla\theta_e}{\rho}\right) - \boldsymbol{\xi}_a \cdot \frac{d\nabla\theta_e}{dt} + S_m\left(\frac{\boldsymbol{\xi}_a \cdot \nabla\theta_e}{\rho}\right) = \nabla\theta_e \cdot (\boldsymbol{\xi}_a \cdot \nabla)\mathbf{v} - \nabla\theta_e \cdot \nabla \times \mathbf{F}. \tag{3.3.10}$$

Using the consistency relation, we then obtain

$$\begin{aligned}\boldsymbol{\xi}_a \cdot \frac{d}{dt}(\nabla\theta_e) &= \boldsymbol{\xi}_a \cdot \nabla\frac{d\theta_e}{dt} + \boldsymbol{\xi}_a \cdot \mathbf{v} \cdot \nabla(\nabla\theta_e) - \boldsymbol{\xi}_a \cdot \nabla(\mathbf{v} \cdot \nabla\theta_e) \\ &= \boldsymbol{\xi}_a \cdot \nabla\dot{\psi} - \nabla\theta_e \cdot (\boldsymbol{\xi}_a \cdot \nabla)\mathbf{v}\end{aligned} \tag{3.3.11}$$

and the potential vorticity equation as

$$\frac{d}{dt}\left(\frac{\boldsymbol{\xi}_a \cdot \nabla\theta_e}{\rho}\right) = \frac{1}{\rho}\boldsymbol{\xi}_a \cdot \nabla\dot{\psi} - \frac{S_m}{\rho}\left(\frac{\boldsymbol{\xi}_a \cdot \nabla\theta_e}{\rho}\right) - \frac{1}{\rho}\nabla\theta_e \cdot \nabla \times \mathbf{F} \tag{3.3.12}$$

Here, $\frac{\boldsymbol{\xi}_a \cdot \nabla\theta_e}{\rho}$ is moist Ertel potential vorticity.

Equation (3.3.12) can be rewritten as

$$\frac{\partial}{\partial t}\left(\frac{\boldsymbol{\xi}_a \cdot \nabla\theta_e}{\rho}\right) = \frac{1}{\rho}\boldsymbol{\xi}_a \cdot \nabla\dot{\psi} - \mathbf{v} \cdot \nabla\left(\frac{\boldsymbol{\xi}_a \cdot \nabla\theta_e}{\rho}\right) - \frac{S_m}{\rho}\left(\frac{\boldsymbol{\xi}_a \cdot \nabla\theta_e}{\rho}\right) - \frac{1}{\rho}\nabla\theta_e \cdot \nabla \times \mathbf{F} \tag{3.3.13}$$

Equation (3.3.13) is the moist potential vorticity equation, which includes

thermal, mass, and frictional forcing. In the equation, $\frac{1}{\rho}\boldsymbol{\xi}_a \cdot \nabla \dot{\psi}$ is the thermal forcing term, $-\mathbf{v}\cdot\nabla(\frac{\boldsymbol{\xi}_a \cdot \nabla \theta_e}{\rho})$ is the advection term, $-\frac{S_m}{\rho}(\frac{\boldsymbol{\xi}_a \cdot \nabla \theta_e}{\rho})$ is the mass-forcing term, and $-\frac{1}{\rho}\nabla\theta_e \cdot \nabla \times \mathbf{F}$ is the frictional forcing term. In the case of frictionless adiabatic saturated air, $-\frac{1}{\rho}\nabla\theta_e \cdot \nabla \times \mathbf{F} = 0$ and $\frac{1}{\rho}\boldsymbol{\xi}_a \cdot \nabla \dot{\psi} = 0$, which means that equation (3.3.13) can then be simplified to

$$\frac{\partial}{\partial t}(\frac{\boldsymbol{\xi}_a \cdot \nabla \theta_e}{\rho}) = -\mathbf{v}\cdot\nabla(\frac{\boldsymbol{\xi}_a \cdot \nabla \theta_e}{\rho}) - \frac{S_m}{\rho}(\frac{\boldsymbol{\xi}_a \cdot \nabla \theta_e}{\rho}). \tag{3.3.14}$$

(3.3.14) is the moist potential vorticity equation with mass forcing for frictionless adiabatic, saturated air.

3.4 The Impermeability Principle for Moist Potential Vorticity Substance under Conditions with Mass Forcing

The potential vorticity itself has three major characteristics: it is conserved if there is no external source and sink; according to quasi-geostrophic and semi-geostrophic theory, it is reversible; and the potential vorticity substance is impermeable. The first two characteristics should be relatively familiar, but the concept of the impermeability of the potential vorticity substance is probably less so. The so-called impermeability of the potential vorticity substance means that it cannot diffuse or permeate from one isentropic surface to another but can only change at its isentropic surface. Haynes and McIntyre (1990)[36] proved that the potential vorticity substance of dry air is impermeable, Gao et al. (2002

(a), (b))[23-24] also proved this for the moist potential vorticity substance under conditions of thermal and mass forcing. Because this principle is of particular importance in the prediction of heavy rainfall, this section will introduce the principle of the impermeability of the moist potential vorticity substance in detail, beginning with the proof.

From the definition of the moist potential vorticity, $Q_M = \frac{\boldsymbol{\xi}_a \cdot \nabla \theta_e}{\rho}$,

$$\frac{d}{dt}(\rho Q_M) = \rho \frac{dQ_M}{dt} + Q_M \frac{d\rho}{dt}. \tag{3.4.1}$$

(3.4.1) can be rewritten as

$$\frac{\partial}{\partial t}(\rho Q_M) = \rho \frac{dQ_M}{dt} + Q_M \frac{d\rho}{dt} - \mathbf{v}\cdot\nabla(\rho Q_M). \tag{3.4.2}$$

After substituting (3.3.5) and (3.3.12) into (3.4.2), we obtain

$$\frac{\partial}{\partial t}(\rho Q_M) = \nabla\cdot(\boldsymbol{\xi}_a \dot{\psi}) - \nabla\cdot(\mathbf{F}\times\nabla\theta_e) - \nabla\cdot(\rho Q_M \mathbf{v}). \tag{3.4.3}$$

Setting $\boldsymbol{\xi}_{a\Uparrow} = \boldsymbol{\xi}_a - \frac{\boldsymbol{\xi}_a \cdot \nabla\theta_e}{(\nabla\theta_e)^2}\nabla\theta_e$ and $\dot{\psi} = \frac{d\theta_e}{dt}$, (3.4.3) can be rewritten as

$$\frac{\partial}{\partial t}(\rho Q_M) = -\nabla\cdot[\rho Q_M(\mathbf{v} - \frac{\mathbf{v}\cdot\nabla\theta_e}{(\nabla\theta_e)^2}\nabla\theta_e) - \rho Q_M \frac{\nabla\theta_e \frac{\partial\theta_e}{\partial t}}{(\nabla\theta_e)^2} - \boldsymbol{\xi}_{a\Uparrow}\frac{d\theta_e}{dt} + \mathbf{F}\times\nabla\theta_e] \tag{3.4.4}$$

Setting $\mathbf{v}_{\theta\Uparrow} = \mathbf{v} - \frac{\mathbf{v}\cdot\nabla\theta_e}{(\nabla\theta_e)^2}\nabla\theta_e$ and $\mathbf{v}_{\theta\perp} = -\frac{\nabla\theta_e \frac{\partial\theta_e}{\partial t}}{(\nabla\theta_e)^2}$, we have

$$\frac{\partial}{\partial t}(\rho Q_M) = -\nabla\cdot[\rho Q_M \mathbf{v}_{\theta\perp} + \rho Q_M \mathbf{v}_{\theta\Uparrow} - \boldsymbol{\xi}_{a\Uparrow}\frac{d\theta_e}{dt} + \mathbf{F}\times\nabla\theta_e], \tag{3.4.5}$$

where the subscript $\Uparrow$ denotes a physical quantity parallel to the θ_e

surface and $\perp$ denotes a physical quantity normal to the θ_e surface.

Clearly, the last three quantities on the right-hand side of equation (3.4.5) are all parallel to the iso-θ_e surface; however, the first term on the right-hand side, $\mathbf{v}_{\theta\perp}$, is the speed of the θ_e surface. This shows that the moist potential vorticity substance is impermeable.

If we set $\mathbf{J} = [\rho Q_M \mathbf{v}_{\theta\perp} + \rho Q_M \mathbf{v}_{\theta\uparrow\uparrow} - \boldsymbol{\xi}_{a\uparrow\uparrow} \frac{d\theta_e}{dt} + \mathbf{F} \times \nabla \theta_e]$, then we have

$$\mathbf{v}_{\theta\perp} = \frac{\mathbf{J}}{\rho Q_M} - \mathbf{v}_{\theta\uparrow\uparrow} + \frac{\boldsymbol{\xi}_{a\uparrow\uparrow} \dot{\psi}}{\rho Q_M} - \mathbf{F} \times \frac{\nabla \theta_e}{\rho Q_M}. \tag{3.4.6}$$

It can be seen from equation (3.4.6) that if the moist potential vorticity substance moves at a speed $\frac{\mathbf{J}}{\rho Q_M}$, then it will always remain on this moist isentropic surface. Air particles or chemical substances, however, can cross the moist isentropic surface under diabatic conditions. The inability of the moist potential vorticity substance to do this is termed the impermeability of the moist potential vorticity substance. Other substances do not have this attribute; hence, the diffusion theory that applies to chemical substances cannot be applied to the moist potential vorticity substance. This diffusion theory (more accurately known as the diffusion assumption) states that the chemical substance located at the point where the gradient is largest should experience the greatest amount of diffusion transport. However, even if the moist potential vorticity substance has its large gradient between moist isentropic surfaces, as a result of its impermeability, it cannot diffuse outward. This characteristic of the moist potential vorticity substance can be further demonstrated as follows.

From (3.4.5), we know that

$$\frac{\partial}{\partial t}(\rho Q_M) + \frac{\mathbf{J}}{\rho Q_M} \cdot \nabla \rho Q_M + \rho Q_M \nabla \cdot (\frac{\mathbf{J}}{\rho Q_M}) = 0 . \tag{3.4.7}$$

Equation (3.4.7) can be transformed into

$$\frac{\partial}{\partial t}(\rho Q_M) + \frac{\mathbf{J}}{\rho Q_M} \cdot \nabla \rho Q_M + \rho Q_M \nabla \cdot (\frac{\mathbf{J}}{\rho Q_M}) = 0 . \tag{3.4.8}$$

Because the moist potential vorticity substance should satisfy the mass conservation condition; that is

$$\frac{d}{dt}(\rho Q_M) + \rho Q_M \nabla \cdot \mathbf{v}_{Q_M} = 0 , \tag{3.4.9}$$

where $\mathbf{v}_{Q_M} = \frac{\mathbf{J}}{\rho Q_M}$, clearly, in the mass conservation equation, the velocity of the moist potential vorticity substance should be $\mathbf{v}_{Q_M} = \frac{\mathbf{J}}{\rho Q_M}$. Thus, it is not difficult to understand why the moist potential vorticity substance moves at a velocity of $\frac{\mathbf{J}}{\rho Q_M}$. Therefore, the velocity $\mathbf{v}_{Q_M} = \frac{\mathbf{J}}{\rho Q_M}$ is not a special choice but a fact.

In forecasting the location of heavy rain, the impermeability of the moist potential vorticity substance is very useful. If the moist potential vorticity substance could easily mix with its upper and lower surroundings in the same way as other substances, then the moist potential vorticity substance anomaly caused by the heavy rainfall would soon mix with the surroundings and it would be difficult to distinguish which fraction of the

moist potential vorticity substance was a result of the heavy rainfall and which was due to other causes. However, using the impermeability of the moist potential vorticity substance, we can easily find the moist potential vorticity anomaly caused by the heavy rainfall. The height at which latent heat is released in clouds or during raindrop formation is usually between 850 hPa and 400 hPa; the moist potential vorticity anomaly obtained from the moist potential vorticity equation is definitely in this height range and will not mix with other moist potential vorticity substance located on the adjacent moist isentropic surface. Thus, the moist potential vorticity substance anomaly in this height range is a very good dynamic tracer for tracing the location of heavy rainfall.

It has been recognized that the mixing ratio of the moist potential vorticity substance is partly the same as that of the chemical substances in the air (Hoskins et al., 1985)[25]. This is because the moist potential vorticity substance is, itself, conservative under adiabatic conditions and if there are no other non-conservative forces. This is completely equivalent to the mixing ratio of chemical substances in the air being conserved in the absence of a chemical source or sink and also the absence of diffusion. What is different is that the chemical substance can permeate the moist isentropic surface, whereas the moist potential vorticity substance cannot do so: the moist potential vorticity substance can only move between the moist isentropic surfaces that constrain it.

Notes

[1]Xie Y. B. (1978) “Synoptic Dynamic Problems of the Moist Baraclinic Atmosphere,” *Torrential Rain Corpus*. Changchun: Jilin People's Publishing House: pp. 1–15. (in Chinese with English abstract)

[2]Wang L. M. and H. B. Luo (1980) “The basic dynamic equations and main properties of the saturated moist air,” *Acta Meteorologica Sinica* , 38(1):44-50. (in Chinese with English abstract)

[3]Wu G. X., Y. P. Cai and X. J. Tang (1995) "Moist potential vorticity and slantwise vorticity development," *Acta Meteorologica Sinica,* 53(4):387–405. (in Chinese with English abstract)

[4]Wang X. R. and K. J. Wu (1999) "The introduction of condensation probability function and the dynamic equations on non-uniform saturated moist air," *Journal of Tropical Meteorology,* 15(1):64–70. (in Chinese with English abstract)

[5] Holton J. R. 1972: *An Introduction to Dynamical Meteorology*. Academic Press.

[6]Betts A. K. and F. J. Dugan (1973) "Empirical formula for saturation pseudoadiabats and saturation equivalent potential temperature," *Journal of Applied Meteorology,* 12(4):731-732.

[7]Bennetts D. A. and B. J. Hoskins (1979) "Conditional symmetric instability-A possible explanation for frontal rainbands," *Quarterly Journal of the Royal Meteorological Society,* 105(446):945–962.

[8]Emanuel K. A. (1979) "Inertial instability and mesoscale convective systems. Part I: Linear theory of inertial instability in rotating viscous fluids," *Journal of Atmospheric Sciences,* 36(12):2425-2449.

[9]Emanuel K. A. (1994) *Atmospheric Convection*. New York Oxford: Oxford University press.

[10]Bannon P. R. (2002) "Theoretical foundations for models of moist convection," *Journal of Atmospheric Sciences*, 59(12):1967-1982.

[11]Shou, S. W., S. S. Li and X. P. Yao (2003) *Mesoscale Meteorology*, Meteorological Press, Beijing. (in Chinese)

[12] Schultz D. M. and P. N. Schumacher (1999) "The use and misuse of conditional symmetric Instability," *Monthly Weather Review*, 127(12):2709–2732.

[13] Gao S. T., X. Wang and Y. Zhou (2004) "Generation of generalized moist potential vorticity in a frictionless and moist adiabatic flow," *Geophysical Research Letters,* 31(12), doi: 10.1029/2003GL019152.

[14] Bolton D. (1980) "The computation of equivalent potential temperature," *Monthly Weather Review,* 108(7):1046-1053.

[15] Cao Z. and H. Cho (1995) "Generation of moist vorticity in extratropical cyclones," *Journal of Atmospheric Sciences,* 52(18):3263–3282.

[16]Andrews D. G. (2000) *An Introduction to Atmospheric Physics*. Cambridge University Press.

[17] Ertel H.(1942) "Ein Neuer hydrodynamischer wir-belsatz," *Meteorologische Zeitschrift,* 59:271–281.

[18] Danielsen E. F. and R. S. Hipskind (1980) "Stratospheric-tropospheric exchange at polar latitudes in Summer," *Journal of Geophysical Research,* 85(C1):393-400.

[19] Thorpe A. J. (1985) "Diagnosis of balanced vortex structure using potential vorticity," *Journal of Atmospheric Sciences,* 42(4):397-406.

[20] Hoskins B. J. and P. B. Berrisford (1988) "A potential-vorticity perspective of the storm of 15-16 October 1987," *Weather,* 43(3):122–129.

[21]Xu Q. (1992) "Formation and evolution of frontal rainbands and geostrophic potential vorticity anomalies," *Journal of Atmospheric Sciences,* 49(8):629-648.

[22]Montgomery M. T. and Farrell B. F. (1993) "Tropical cyclone formation," *Journal of Atmospheric Sciences,* 50(2):285-310.

[23]Gao S. T., T. Lei, and Y. S. Zhou (2002) "Moist potential vorticity anomaly with heat and mass forcings in torrential rain system," *Chinese Physical letters,* 19(6):878-880.

[24]Gao S. T., T. Lei, Y. S. Zhou and et al. (2002) "Diagnostic analysis of moist potential vorticity anomaly torrential rain systems," *Journal of Applied Meteorological Science,* 13(6):662-670. (in Chinese with English abstract)

[25]Hoskins B. J., M. E. McIntyre and A. W. Robertson (1985) "On the use and significance of is entropic potential-vorticity maps," *Quarterly Journal of the Royal Meteorological Society,* 111(470):877-946 (Also 113, 402-404).

[26]Gao S.T., S. Y. Tao and Y. H. Ding (1990) "The generalized E-P flux of wave-mean flow Interactions," *Science China S B*, 33(6):704–715.

[27]Zhou Y. S., G. Deng, S. T. Gao and et al. (2002) "The study on the influence Characteristic of teleconnection caused by the underlying surface of the Tibetan Plateau I: data analysis," *Advances in Atmospheric Sciences,* 19(4):583–593.

[28] Keyser D. and R. Rotunno (1990) "On the formation of potential-vorticity anomalies in upper level jet front systems," *Monthly Weather Review,* 118(9):1914–1921.

[29] Fritsch J. M. and R. A. Maddox (1981) "Convectively driven mesoscale weather systems aloft. Part I: Observations," *Journal of Applied Meteorology,* 20(1):9–19.

[30]Davis C. A. and M. L. Weisman (1994) "Balanced dynamics of mesoscale vortices in simulated convective systems," *Journal of Atmospheric Sciences,* 51(14):2005–2030.

[31] Gray M. E. B., G. J. Shutts and G. C. Craig (1998) "The role of mass transfer in describing the dynamics of mesoscale convective systems," *Quarterly Journal of the Royal Meteorological Society,* 124(548):1183–1207.

[32] Shutts G. J. and M. E. B. Gray (1994) "A numerical modeling study of the geostrophic adjustment process following deep convection," *Quarterly Journal of the Royal Meteorological Society,* 120(519):1145–1178.

[33]Fulton S. R., W. H. Schubert and S. A. Hausman (1995) "Dynamical adjustment of mesoscale convective anvils," *Monthly Weather Review,* 123(11):3215–3226.

[34] Raymond D. J. and H. Jiang (1990) "A theory for long-lived mesoscale convective systems," *Journal of Atmospheric Sciences,* 47(24):3067–3077.

[35] Gray M. E. B. (1999) "An investigation into convectively generated potential-vorticity anomalies using a mass-forcing model," *Quarterly Journal of the Royal Meteorological Society,* 125(557):1589–1605.

[36] Haynes P. H. and M.E. Mcintyre (1990) "On the conservation and impermeability theorems for potential vorticity," *Journal of Atmospheric Sciences,* 47(16):2021–2031.

CHAPTER FOUR

VORTICITY: INTRODUCTION AND RELATED EQUATIONS

4.1 The Concept of Vorticity and its Computation

In Chapter 2, the vorticity was briefly introduced. The impact of the vorticity on the development of mesoscale systems is vitally important. Thus, this important concept will be discussed in depth in this chapter.

4.1.1 The Concept of Vorticity

In fluid mechanics, the vorticity is used to depict the rotation of a fluid particle, which is an important concept and can be written as

$$\boldsymbol{\xi} = \nabla \times \mathbf{v} . \tag{4.1.1}$$

Here, $\mathbf{v}$ is a three-dimensional wind vector. Due to the fact that atmospheric motion is quasi-two-dimensional, only the vertical component of the vorticity vector associated with horizontal flows is discussed in the following. The vertical component is given by

$$\zeta = \frac{\partial v}{\partial x} - \frac{\partial u}{\partial y} . \tag{4.1.2}$$

4.1.2 Vorticity Equation

The vorticity is a derived quantity. Thus, we can derive an equation for the vorticity from the primitive atmospheric momentum equation.

The primitive momentum equation for the atmosphere can be expressed as

$$\frac{\partial \mathbf{v}}{\partial t} + \mathbf{v} \cdot \nabla \mathbf{v} + f\,\mathbf{k} \times \mathbf{v} = -\frac{1}{\rho} \nabla p + \nabla \varphi + \mathbf{F} . \tag{4.1.3}$$

The use of $\mathbf{v} \cdot \nabla \mathbf{v} = \frac{1}{2} \nabla \mathbf{v}^2 + \boldsymbol{\xi} \times \mathbf{v}$ gives

$$\frac{\partial \mathbf{v}}{\partial t} + \boldsymbol{\xi} \times \mathbf{v} + f\,\mathbf{k} \times \mathbf{v} = -\frac{1}{\rho}\nabla p + \nabla(\varphi - \frac{\mathbf{v}^2}{2}) + \mathbf{F} \tag{4.1.4}$$

or

$$\frac{\partial \mathbf{v}}{\partial t} + (\boldsymbol{\xi} + f\,\mathbf{k}) \times \mathbf{v} = -\frac{1}{\rho}\nabla p + \nabla(\varphi - \frac{\mathbf{v}^2}{2}) + \mathbf{F}\,. \tag{4.1.5}$$

Using the relation

$$\nabla \times (\mathbf{a} \times \mathbf{b}) = (\mathbf{b} \cdot \nabla)\,\mathbf{a} - (\mathbf{a} \cdot \nabla)\,\mathbf{b} + \mathbf{a}\,\nabla \cdot \mathbf{b} - \mathbf{b}\,\nabla \cdot \mathbf{a}\,, \tag{4.1.6}$$

taking $\nabla \times (4.1.5)$, and using $\nabla \times \nabla(\varphi - \frac{\mathbf{v}^2}{2})$ then yields

$$\frac{\partial(\nabla \times \mathbf{v})}{\partial t} + \nabla \times [(\boldsymbol{\xi} + f\,\mathbf{k}) \times \mathbf{v}] = \frac{1}{\rho^2}\nabla\rho \times \nabla p + \nabla \times \mathbf{F}\,. \tag{4.1.7}$$

Taking $(\boldsymbol{\xi} + f\,\mathbf{k}) = \boldsymbol{\xi}_a$ as the absolute vorticity, (4.1.7) becomes

$$\frac{\partial \boldsymbol{\xi}}{\partial t} + \nabla \times (\boldsymbol{\xi}_a \times \mathbf{v}) = \frac{1}{\rho^2}\nabla\rho \times \nabla p + \nabla \times \mathbf{F}\,. \tag{4.1.8}$$

Using (4.1.6) leads to

$$\begin{aligned} \nabla \times (\boldsymbol{\xi}_a \times \mathbf{v}) &= (\mathbf{v} \cdot \nabla)\boldsymbol{\xi}_a - (\boldsymbol{\xi}_a \cdot \nabla)\,\mathbf{v} + \boldsymbol{\xi}_a \nabla \cdot \mathbf{v} - \mathbf{v}\,\nabla \cdot \boldsymbol{\xi}_a \\ &= (\mathbf{v} \cdot \nabla)\boldsymbol{\xi}_a - (\boldsymbol{\xi}_a \cdot \nabla)\,\mathbf{v} + \boldsymbol{\xi}_a \nabla \cdot \mathbf{v} \end{aligned} \tag{4.1.9}$$

and substituting (4.1.8) yields

$$\frac{\partial \boldsymbol{\xi}}{\partial t} + \mathbf{v} \cdot \nabla \boldsymbol{\xi}_a = (\boldsymbol{\xi}_a \cdot \nabla)\,\mathbf{v} - \boldsymbol{\xi}_a \nabla \cdot \mathbf{v} + \frac{1}{\rho^2}\nabla\rho \times \nabla p + \nabla \times \mathbf{F}\,. \tag{4.1.10}$$

Because $\frac{\partial \boldsymbol{\xi}_a}{\partial t} = \frac{\partial \boldsymbol{\xi}}{\partial t}$, (4.1.10) can be written as

$$\frac{d\boldsymbol{\xi}_a}{dt} = (\boldsymbol{\xi}_a \cdot \nabla)\,\mathbf{v} - \boldsymbol{\xi}_a \nabla \cdot \mathbf{v} + \frac{1}{\rho^2}\nabla\rho \times \nabla p + \nabla \times \mathbf{F}\,. \tag{4.1.11}$$

(4.1.11) is the three-dimensional vorticity equation, in which the individual changes in vorticity are determined by the four terms twisting, divergence, solenoid, and dissipation.

4.1.3 The "Freezing-in" Nature of the Vorticity

First of all, we define the concept of a "vortex line". The tangent direction at each point on a vortex line gives the direction of the vorticity at that point. A vortex line is similar to a streamline: the tangent direction at each point on a streamline is the direction of the velocity at that point. Suppose we draw a vortex line through a fluid. The vortex line is related to the fluid element vorticity, thus forming a material line. (A material line is a line connecting the material fluid elements). As the fluid moves, the material line will deform, and the vortex line will evolve; this evolution is controlled by the equation of motion. A vortex line has a remarkable nature: in a fluid without any external force or friction, the vortex line will remain aligned with the material line that it was initially connected to. That is to say, vortices always keep the same material element and the vorticity appears to be "freezing-in" within the fluid (Vallis, 2006)[1].

This nature of vortex lines can be proved as follows. Consider the evolution of an infinitesimal material line element, $\delta\mathbf{l}$. $\delta\mathbf{l}$ is the infinitesimal element of matter that connects $\mathbf{l}$ and $\mathbf{l}+\delta\mathbf{l}$. The rate of change of δl is

$$\frac{d\delta\mathbf{I}}{dt} = \frac{1}{\delta t}[\delta\mathbf{I}(t+\delta t) - \delta\mathbf{I}(t)]. \tag{4.1.12}$$

Using Taylor's formula and the definition of the velocity, we have

$$\begin{aligned}\delta\mathbf{I}(t+\delta t) &= \mathbf{I}(t) + \delta\mathbf{I}(t) + (\mathbf{v}+\delta\mathbf{v})\delta t - (\mathbf{I}(t) + \mathbf{v}\,\delta t) \\ &= \delta\mathbf{I} + \delta\mathbf{v}\,\delta t\end{aligned}. \tag{4.1.13}$$

The difference between the two above equations gives

$$\frac{d\delta\mathbf{I}}{dt} = \delta\mathbf{v}. \tag{4.1.14}$$

The use of $\delta\mathbf{v} = (\delta\mathbf{I}\cdot\nabla)\mathbf{v}$ then gives

$$\frac{d\delta\mathbf{I}}{dt} = (\delta\mathbf{I}\cdot\nabla)\mathbf{v}. \tag{4.1.15}$$

For a barotropic, frictionless, incompressible fluid, the vorticity equation can be written as

$$\frac{\partial\boldsymbol{\xi}}{\partial t} = (\boldsymbol{\xi}\cdot\nabla)\mathbf{v}. \tag{4.1.16}$$

Comparing equations (4.1.15) and (4.1.16), it can be seen that the evolution of the vorticity is consistent with that of the line element. This will be elaborated upon below.

At a certain initial time, we can find an infinitesimal material line element that is parallel to the vorticity. In this case

$$\delta \mathbf{I}(x, t=0) = A\boldsymbol{\xi}(x, t=0), \tag{4.1.17}$$

where A is a constant. In the following discussion, even if the fluid element moves to a new position, x', its vorticity is still proportional to the length of the fluid element at that point, and its direction is the same as that of the fluid element. That is to say

$$\delta \mathbf{I}(x', t) = A\boldsymbol{\xi}(x', t). \tag{4.1.18}$$

$\delta \mathbf{I} = A\boldsymbol{\xi}$ and $\delta \mathbf{I} \times \boldsymbol{\xi} = 0$. If the time derivative of $\delta \mathbf{I} \times \boldsymbol{\xi}$ is zero, we can prove that $\delta \mathbf{I}$ and $\boldsymbol{\xi}$ remain parallel.

For line elements, we have

$$\frac{d(\boldsymbol{\xi} \times \delta \mathbf{I})}{dt} = \frac{d\boldsymbol{\xi}}{dt} \times \delta \mathbf{I} - \frac{d\delta \mathbf{I}}{dt} \times \boldsymbol{\xi}; \tag{4.1.19}$$

also $\frac{d\delta \mathbf{I}}{dt} = (\delta \mathbf{I} \cdot \nabla)\mathbf{v}$ and $\frac{d\boldsymbol{\xi}}{dt} = (\boldsymbol{\xi} \cdot \nabla)\mathbf{v}$. At $t = 0$, $\delta \mathbf{I} = A\boldsymbol{\xi}$; thus,

$$\begin{aligned} \frac{d(\boldsymbol{\xi} \times \delta \mathbf{I})}{dt} &= (\boldsymbol{\xi} \cdot \nabla)\mathbf{v} \times \delta \mathbf{I} - (\delta \mathbf{I} \cdot \nabla)\mathbf{v} \times \boldsymbol{\xi} \\ &= (\boldsymbol{\xi} \cdot \nabla)\mathbf{v} \times A\boldsymbol{\xi} - (A\boldsymbol{\xi} \cdot \nabla)\mathbf{v} \times \boldsymbol{\xi} = 0 \end{aligned}. \tag{4.1.20}$$

$\boldsymbol{\xi} \times \delta \mathbf{I}$ tends to zero; thus, the vortex line remains a material line. The following analogy may be helpful here. The potential temperature of an air parcel is conserved; the vorticity also has this nature. If a material line element develops, the direction of its vorticity will always be consistent with that of the material line element and its size will be proportional to that of the element. The vorticity, thus, appears to be "freezing-in" in the fluid. This nature of vorticity enables us to use it to track the position of fluid elements.

We will now consider the more complicated case of a barotropic frictionless flow: does the "freezing-in" of the vorticity still then exist?

For a barotropic frictionless fluid, the vorticity equation can be written as

$$\frac{d\boldsymbol{\xi}}{dt} = (\boldsymbol{\xi} \cdot \nabla)\mathbf{v} - \boldsymbol{\xi}\nabla \cdot \mathbf{v}. \tag{4.1.21}$$

The continuity equation is

$$\frac{1}{\rho}\frac{d\rho}{dt} + \nabla \cdot \mathbf{v} = 0. \tag{4.1.22}$$

Substituting (4.1.22) into (4.1.21) then yields

$$\frac{d}{dt}\left(\frac{\boldsymbol{\xi}}{\rho}\right) = \left(\frac{\boldsymbol{\xi}}{\rho}\cdot\nabla\right)\mathbf{v}. \tag{4.1.23}$$

It can be seen that (4.1.23) and (4.1.16) are identical in form, and so the "freezing-in" nature of the vorticity does not require that the fluid is incompressible: therefore, this nature of the vorticity still exists in a barotropic frictionless fluid.

We can also consider a baroclinic fluid. For a baroclinic fluid, the equation of motion is

$$\frac{d\mathbf{v}}{dt} + 2\Omega\times\mathbf{v} + \frac{1}{\rho}\nabla\rho + g\,\mathbf{k} = 0. \tag{4.1.24}$$

The entropy of an air parcel can be defined as

$$S = c_p \ln\theta + C, \tag{4.1.25}$$

where c_p is the specific heat at constant pressure and C is a constant. The gradient of the entropy can then be expressed as

$$\nabla S = \frac{c_p}{\theta}\nabla\theta = \frac{c_p}{T}\nabla T - \frac{R}{p}\nabla p = \frac{c_p}{T}\nabla T - \frac{1}{T\rho}\nabla p; \tag{4.1.26}$$

thus

$$\frac{1}{\rho}\nabla p = \nabla c_p T - T\nabla S = \nabla H - T\nabla S, \tag{4.1.27}$$

where $H = c_p T$ is the enthalpy. Substituting (4.1.27) into (4.1.24) and taking the curl gives

$$\frac{d\boldsymbol{\xi}}{dt} = (\boldsymbol{\xi}\cdot\nabla)\mathbf{v} - \boldsymbol{\xi}\nabla\cdot\mathbf{v} + \nabla T\times\nabla S. \tag{4.1.28}$$

Substituting the continuity equation (equation (4.1.22)) into the above yields

$$\frac{d}{dt}\left(\frac{\boldsymbol{\xi}}{\rho}\right) = \left(\frac{\boldsymbol{\xi}}{\rho}\cdot\nabla\right)\mathbf{v} + \frac{1}{\rho}(\nabla T\times\nabla S), \tag{4.1.29}$$

and then using $T = \dfrac{d\Lambda}{dt}$ gives

$$\frac{d(\frac{1}{\rho}\nabla\Lambda\times\nabla S)}{dt}=\frac{1}{\rho}(\nabla\Lambda\times\nabla S)\cdot\nabla\mathbf{v}+\frac{1}{\rho}(\nabla T\times\nabla S) \tag{4.1.30}$$

and the following:

$$\frac{d\rho}{dt}=-\rho\nabla\cdot\mathbf{v}, \tag{4.1.31}$$

$$\frac{d\nabla S}{dt}=\nabla\frac{dS}{dt}-\nabla S\cdot\nabla\mathbf{v}-\nabla S\times\nabla\times\mathbf{v}, \tag{4.1.32}$$

$$\frac{d\nabla\Lambda}{dt}=\nabla\frac{d\Lambda}{dt}-\nabla\Lambda\cdot\nabla\mathbf{v}-\nabla\Lambda\times\nabla\times\mathbf{v}, \text{ and} \tag{4.1.33}$$

$$\frac{dS}{dt}=0. \tag{4.1.34}$$

Taking (4.1.31)–(4.1.34)

$$\frac{d(\frac{1}{\rho}\nabla\Lambda\times\nabla S)}{dt}=\frac{1}{\rho}(\nabla\Lambda\times\nabla S)\cdot\nabla\mathbf{v}+\frac{1}{\rho}(\nabla T\times\nabla S), \tag{4.1.35}$$

Above, we bring the equation (4.1.30) to the proof. And subtracting (4.1.35) from (4.1.29) gives

$$\frac{d[(\xi-\nabla\Lambda\times\nabla S)/\rho]}{dt}=(1/\rho)(\xi-\nabla\Lambda\times\nabla S)\cdot\nabla\mathbf{v}, \tag{4.1.36}$$

It can be seen that (4.1.36) and (4.1.16) are identical in form, and so the "freezing-in" nature of the vorticity is also applicable to a baroclinic fluid.

4.2 Advection Vorticity Equation

The classical vorticity equation has been widely used in earlier research and has played an important role in promoting the development of numerical weather prediction. However, experience shows that severe weather processes and climate anomalies are often closely related to atmospheric stability and baroclinic variability. These thermal factors are not considered in the classical vorticity equation, and so the application of this equation has limitations. Based on potential vorticity theory, Wu and Liu (1999)[2] obtained the following complete vertical vorticity equation:

$$\frac{d\zeta}{dt}+\beta v+(f+\zeta)(\nabla_h\cdot\mathbf{v}_h)=-\frac{1}{\alpha}\frac{1}{T}\frac{d}{dt}(\frac{p}{\theta_z}-C_d)\,, \qquad (4.1.37)$$

where $\frac{d}{dt}=\frac{\partial}{\partial t}+\mathbf{v}\cdot\nabla$ is the individual derivative, $P=\alpha\xi_a\nabla\theta$ is the potential vorticity, $\theta_z=\frac{\partial\theta}{\partial z}$ is the hydrostatic stability, and $C_d=\frac{\alpha_s\theta_s}{\theta_z}$ is the thermodynamic parameter.

This equation for the vertical vorticity overcomes the classical vorticity equation's limitation of not including a thermal factor and also includes the influence of external dynamics and thermal forcing on the vorticity change. The full vorticity can accurately represent the process of development of severe weather systems. It is obvious that the horizontal wind produces not only divergence but also advection—that is, the horizontal transport of various physical quantities such as temperature advection, vorticity advection, water-vapor advection, etc.—which are widely used in the analysis of the development of weather systems. For example, when Yao et al. (2007) [3] analyzed the influence of easterly winds in the tropical troposphere on the behavior of the western Pacific subtropical high, analysis of the vertical vorticity equation showed that the contribution of the horizontal vorticity advection was the largest. The enhancement of the horizontal vorticity advection corresponds to the enhancement of the horizontal wind field advection, but no effect of the horizontal wind field advection on the vorticity change is explicitly included in the classical vorticity equation or full vorticity equation. If the advection of the horizontal wind field has a direct effect on the vertical vorticity, what is this effect? To answer this, we derive the advection vorticity equation in pressure coordinates to reflect the effect of advection on the vorticity.

4.2.1 The Advection Vorticity Equation

In pressure coordinates, for a wind vector $\mathbf{v}_h=(u,v)$, we have $\mathbf{v}_h=u\mathbf{i}+v\mathbf{j}$, where u is the zonal wind, v the meridional wind, ω the vertical velocity, φ the geopotential, and ρ the density of the air; also $u(x,y,p,t)$, $v(x,y,p,t)$, $\omega(x,y,p,t)$, $\varphi(x,y,p,t)$, and

$\rho(x, y, p, t)$. The corresponding horizontal momentum equations can be written as

$$\frac{\partial u}{\partial t} + \mathbf{v}_h \cdot \nabla u + \omega \frac{\partial u}{\partial p} - (f + \beta y)v = -\frac{\partial \varphi}{\partial x} \tag{4.2.1a}$$

and

$$\frac{\partial v}{\partial t} + \mathbf{v}_h \cdot \nabla v + \omega \frac{\partial v}{\partial p} + (f + \beta y)u = -\frac{\partial \varphi}{\partial y} \ . \tag{4.2.1b}$$

The hydrostatic equation is expressed as

$$\frac{\partial \varphi}{\partial p} = -\frac{1}{\rho}, \tag{4.2.1c}$$

and the continuity equation is written as

$$\nabla \cdot \mathbf{v}_h + \omega \frac{\partial \omega}{\partial p} = 0 . \tag{4.2.1d}$$

Taking the derivative of (4.2.1a) with respect to y and the derivative of (4.2.1b) with respect to x and subtracting the resulting equations gives

$$\begin{aligned} \frac{\partial^2 v}{\partial x \partial t} - \frac{\partial^2 u}{\partial y \partial t} &= -\frac{\partial u}{\partial x}\frac{\partial v}{\partial x} - u\frac{\partial^2 v}{\partial x^2} - \frac{\partial v}{\partial x}\frac{\partial v}{\partial y} - v\frac{\partial^2 v}{\partial x \partial y} - \frac{\partial \omega}{\partial x}\frac{\partial v}{\partial p} \\ &- \omega\frac{\partial^2 v}{\partial x \partial p} - (f + \beta y)\frac{\partial u}{\partial x} + \frac{\partial u}{\partial x}\frac{\partial u}{\partial y} + u\frac{\partial^2 u}{\partial x \partial y} + \frac{\partial v}{\partial y}\frac{\partial u}{\partial y} \\ &+ v\frac{\partial^2 u}{\partial y^2} + \frac{\partial \omega}{\partial y}\frac{\partial u}{\partial p} + \omega\frac{\partial^2 u}{\partial y \partial p} - \beta v - (f + \beta y)\frac{\partial v}{\partial y} \end{aligned} \tag{4.2.2}$$

The vertical vorticity is defined as

$$\zeta = \frac{\partial v}{\partial x} - \frac{\partial u}{\partial y} . \tag{4.2.3}$$

Taking the derivatives of (4.2.3) in the *x*-, *y*-, and *p*- directions and adding the resulting equations yields

$$\frac{\partial \zeta}{\partial t}+u\frac{\partial \zeta}{\partial x}+v\frac{\partial \zeta}{\partial y}+\omega\frac{\partial \zeta}{\partial p}=\frac{\partial^2 v}{\partial x\partial t}-\frac{\partial^2 u}{\partial y\partial t}+u(\frac{\partial^2 v}{\partial x^2}-\frac{\partial^2 u}{\partial x\partial y})$$
$$+v(\frac{\partial^2 v}{\partial x\partial y}-\frac{\partial^2 u}{\partial y^2})+\omega(\frac{\partial^2 v}{\partial x\partial p}-\frac{\partial^2 u}{\partial y\partial p}) \quad (4.2.4)$$

Substituting $\frac{\partial^2 v}{\partial x\partial t}-\frac{\partial^2 u}{\partial y\partial t}$ of (4.2.2) into (4.2.4) yields

$$\frac{\partial \zeta}{\partial t}+u\frac{\partial \zeta}{\partial x}+v\frac{\partial \zeta}{\partial y}+\omega\frac{\partial \zeta}{\partial p}=-\frac{\partial u}{\partial x}\frac{\partial v}{\partial x}-\frac{\partial v}{\partial x}\frac{\partial v}{\partial y}-\frac{\partial \omega}{\partial x}\frac{\partial v}{\partial p}-(f+\beta y)\frac{\partial u}{\partial x}$$
$$+\frac{\partial u}{\partial x}\frac{\partial u}{\partial y}+\frac{\partial v}{\partial y}\frac{\partial u}{\partial y}+\frac{\partial \omega}{\partial y}\frac{\partial u}{\partial p}-\beta v-(f+\beta y)\frac{\partial v}{\partial y} \quad (4.2.5)$$

After rearrangement, (4.2.5) becomes

$$\frac{\partial \zeta}{\partial t}=(\frac{\partial u}{\partial x}-\frac{\partial v}{\partial y})\zeta-(\frac{\partial u}{\partial x}-\frac{\partial v}{\partial y})f-(\frac{\partial \zeta}{\partial y}+\beta)v-u\frac{\partial \zeta}{\partial x}$$
$$-\frac{\partial \omega}{\partial x}\frac{\partial v}{\partial p}-\omega\frac{\partial \zeta}{\partial p}-\beta y\frac{\partial u}{\partial x}-\frac{\partial \omega}{\partial y}\frac{\partial u}{\partial p}-\beta y\frac{\partial v}{\partial y} \quad (4.2.6)$$

Expanding $-[\nabla\cdot\mathbf{v}_h(\zeta+f+\beta y)]$ gives

$$-[\nabla\cdot\mathbf{v}_h(\zeta+f+\beta y)]=-u\frac{\partial \zeta}{\partial x}-(\zeta+f+\beta y)\frac{\partial u}{\partial x}$$
$$-(\frac{\partial \zeta}{\partial y}+\beta)v-(\zeta+f+\beta y)\frac{\partial v}{\partial y} \quad (4.2.7)$$

and substituting (4.2.3) into (4.2.7) then yields

$$-[\nabla\cdot\mathbf{v}_h(\zeta+f+\beta y)]=-u\frac{\partial^2 v}{\partial x^2}+u\frac{\partial^2 u}{\partial x\partial y}-\frac{\partial u}{\partial x}\frac{\partial v}{\partial x}+\frac{\partial u}{\partial x}\frac{\partial u}{\partial y}-f\frac{\partial u}{\partial x}$$
$$-\beta y\frac{\partial u}{\partial x}-v\frac{\partial^2 v}{\partial x\partial y}+v\frac{\partial^2 u}{\partial y^2}-\beta v-\frac{\partial v}{\partial x}\frac{\partial v}{\partial y}+\frac{\partial v}{\partial y}\frac{\partial u}{\partial y}-f\frac{\partial v}{\partial y}-\beta y\frac{\partial v}{\partial y} \quad (4.2.8)$$

The use of a unit vector, $\mathbf{k} = (0,0,1)$, in the vertical direction and the expansion of $-\mathbf{k}\cdot[\nabla\times(\omega\frac{\partial \mathbf{v}_h}{\partial p})]$ gives

$$-\mathbf{k}\cdot[\nabla\times(\omega\frac{\partial \mathbf{v}_h}{\partial p})] = -\frac{\partial\omega}{\partial x}\frac{\partial v}{\partial p} - \omega\frac{\partial^2 v}{\partial x\partial p} + \frac{\partial\omega}{\partial y}\frac{\partial u}{\partial p} + \omega\frac{\partial^2 u}{\partial y\partial p}. \tag{4.2.9}$$

Substituting (4.2.7) and (4.2.9) into (4.2.6) yields

$$\frac{\partial\zeta}{\partial t} = -[\nabla\cdot\mathbf{v}_h(\zeta + f + \beta y)] - \mathbf{k}\cdot[\nabla\times(\omega\frac{\partial \mathbf{v}_h}{\partial p})]. \tag{4.2.10}$$

$\mathbf{F}$ and $\hat{\tau}$ are respectively defined as

$$\mathbf{F} = (u - fy - \frac{1}{2}\beta y^2)\mathbf{i} + v\,\mathbf{j} \tag{4.2.11a}$$

and

$$\hat{\tau} = \mathbf{v}_h\cdot\nabla(u - fy - \frac{1}{2}\beta y^2)\mathbf{i} + \mathbf{v}_h\cdot(\nabla v)\,\mathbf{j}. \tag{4.2.11b}$$

$\hat{\tau}$ can be further expanded to give

$$\hat{\tau} = [u\frac{\partial u}{\partial x} + v(\frac{\partial u}{\partial y} - f - \beta y)]\mathbf{i} + (u\frac{\partial v}{\partial x} + v\frac{\partial v}{\partial y})\,\mathbf{j}. \tag{4.2.12}$$

$\hat{\tau}$ includes the advection terms related to the zonal wind, $u\frac{\partial u}{\partial x} + v\frac{\partial u}{\partial y}$, and the meridional wind, $u\frac{\partial v}{\partial x} + v\frac{\partial v}{\partial y}$.

The projection of the curl of $\hat{\tau}$ on to the vertical direction is

$$\begin{aligned}-\mathbf{k}\cdot(\nabla\times\hat{\tau}) = &-\frac{\partial u}{\partial x}\frac{\partial v}{\partial x} - u\frac{\partial^2 v}{\partial x^2} - \frac{\partial v}{\partial x}\frac{\partial v}{\partial y} - v\frac{\partial^2 v}{\partial x\partial y} + \frac{\partial u}{\partial x}\frac{\partial u}{\partial y}\\ &+u\frac{\partial^2 u}{\partial x\partial y} + \frac{\partial v}{\partial y}(\frac{\partial u}{\partial y} - f - \beta y) + v(\frac{\partial^2 u}{\partial y^2} - \beta)\end{aligned}. \tag{4.2.13}$$

Substituting $\mathbf{F}$ and $\hat{\tau}$ into (4.2.10), the final equation for the vertical vorticity can then be obtained as

$$\frac{\partial \zeta}{\partial t} = -\mathbf{k}\cdot(\nabla \times \hat{\tau}) - \mathbf{k}\cdot[\nabla \times (\omega \frac{\partial \mathbf{F}}{\partial p})] - (f + \beta y)\frac{\partial u}{\partial x}. \quad (4.2.14)$$

In equation (4.2.14), the first term on the right-hand side contains the influence of the horizontal wind field advection rotation effect on the vertical vorticity change, and so this term is called the advection term. The second term is similar to the pitching term in the classical vorticity equation and so is called the vorticity pitching term. Similar to the classical vorticity equation, the third term is related to the geostrophic vorticity and horizontal divergence.

Because $\hat{\tau}$ includes the advection and rotation of the horizontal wind field, the advection term is not expressed in the same form as the advection in the classical vertical vorticity equation or full vertical vorticity equation. Therefore, this vertical vorticity equation is referred to as the advection vorticity equation in this book.

4.2.2 Application of the Advection Vorticity Equation

Taking Typhoon Bilis from 2006 as an example, we introduce the application of the advection vorticity equation to the analysis of typhoons (Zhou and Ran, 2010)[4].

In 2006, tropical cyclones occurred frequently in the northwest Pacific Ocean. One of these storms, Typhoon Bilis (typhoon no. 4), developed east of the Philippines on the afternoon of 8 July and moved northwest. In the afternoon of 9 September, it intensified to a tropical storm, and by the afternoon of 11 November it had intensified to a strong tropical storm. By this time, it was close to the northeast coast of Taiwan. On 13 July, the typhoon made landfall near Yilan; after this, it moved westward through the northern part of Taiwan, entered the Taiwan Strait on the evening of 13 July, and continued to approach the northern coast of Fujian. After making landfall again in the Xiapu area of Fujian Province on 14 July, the typhoon moved westward, gradually weakening in intensity. That afternoon, it weakened into a tropical storm over Minhou County in Fujian Province but continued to move westward. It entered Jiangxi in the early morning of 15 July and weakened into a tropical depression over Jiangxi that afternoon. Following this, the system weakened into a depression and moved southwestward. After crossing Hunan, Guangxi, and Yunnan provinces, Bilis finally dissipated over the northern part of Vietnam. The strong tropical storm weakened into an area of low pressure and traveled deep into the interior of Vietnam. Bilis was an unusual typhoon in terms of the length of its life, the very intense rainfall that it produced, and the wide

range of effects that it had. Throughout its whole development, Bilis had a loose structure, the convection near the center was not strong, there was no eye wall, eye structure, or unified typhoon center, and the wind was not particularly strong. However, the water content of the typhoon was large, which caused floods over a large area in the south of China. This flooding led to secondary disasters such as landslides and mudslides, which, in the past decade, is how most casualties caused by typhoons have been caused. Figure (4.2.1) shows the path of Bilis from its generation and development into a strong tropical storm to landfall and eventual dissipation.

The wind field of Bilis had an obviously asymmetric structure. At 12:00 on 12 July, the area with the highest wind speeds was in the southern part of the typhoon. By 18:00 on 13 July, the area of highest wind speeds had transferred to the northeast quadrant of Bilis and was moving northwestward. The maximum wind speed at 850 hPa also gradually increased before landfall. At 12:00 on 12 July, the maximum wind speed was 32 m s^{-1}; by 18:00 on 13 July, it had increased to 44 m s^{-1} (Figure 4.2.2 (a) and (b)). From Figure 4.2.2, it can be seen that, in addition to the strong horizontal wind speed, the horizontal wind field of Bilis was clearly rotating, as shown by the distribution of the horizontal wind vectors.

The trend in the vorticity as Bilis moved and developed will now be examined. This will be done by comparing the terms on the right-hand side of the advection vorticity equation that was derived in the previous section and by analyzing the role of the advection term in the vorticity equation.

Figure 4.2.3 shows the vorticity field on the 850 hPa isobaric surface for 18:00 on 12 July, the trend in vorticity calculated using the classical vorticity equation, the trend in vorticity calculated using the advection vorticity equation, and the distribution of the terms on the right-hand side of the advection vorticity equation (the advection term, vorticity pitching term, geostrophic vorticity term, and horizontal divergence term). From Figure 4.2.3 (a), it can be seen that, at 18:00 on 12 July, the area of positive vorticity was located mainly in the area controlled by the circulation of Bilis and that the center of the vorticity was located in the eastern part of the circulation. The trends in vorticity calculated using the classical vorticity equation (see Figure 4.2.3 (b)) show that most of the southwestern and eastern sectors of typhoon Bilis are areas of negative vorticity trends, whereas the areas with positive vorticity trends can be divided into three parts, mainly in the northern and western sectors of the typhoon. The negative values also have significantly greater magnitudes than the positive values. In terms of the advection vorticity, Figure. 4.2.3

shows that the trend is positive in the northwestern part of the "front" of typhoon Bilis, whereas there is a region of negative values in the northeast of the typhoon at the rear of the system. The distribution of the positive and negative values is, thus, relatively clear. The results obtained using the two vorticity equations give similar values and reflect the same trends: both produce positive values for the northwestern sector of the typhoon and negative values for the southeast. These results are generally consistent with the typhoon's path: the large values produced by the advection vorticity equation have their center to the right of the typhoon's path. The distribution of the positive and negative values is also relatively simple and can be used to estimate subsequent changes in the strength of the typhoon and its movement. Further analysis of the values of the three terms that appear on the right-hand side of the advection vorticity equation (see Figure 4.2.3 (d), (e), and (f)) shows that the distribution of positive values of the advection term is basically consistent with those for the vorticity change as a whole. The central value (5×10^{-5} s^{-1}) in the range of positive values is significantly greater than that for the other two terms (2×10^{-5} s^{-1} and 0.8×10^{-5} s^{-1}, respectively). This shows that the main factor that affected the vorticity in the case of typhoon Bilis was the advection term: the effect of this term is also reflected in the advection vorticity equation but not in the classical vorticity equation. The change in the value of the pitching term (see Figure 4.2.3 (e)) at the front of the typhoon is very small and so does not give any clear indication about changes in the intensity of the typhoon or its movement. Although the magnitude of the geostrophic vorticity and horizontal divergence terms is obviously smaller than that of the advection term, the areas where these values are positive and where they are centered are consistent with the typhoon's path and so can also be used to estimate the subsequent path of the typhoon. However, the advection term is significantly larger than the other two terms and so can be used to approximate the change in vorticity of the typhoon.

4.3 Streamline Vortex Equation

The concept of a streamline vortex was developed in studies of the dynamic mechanism of supercell storms. Davies-Jones (1984)[5] first proposed the concept of streamline vorticity (defined as the component of environmental vorticity in the average wind direction relative to the storm) and then further developed this into the concept of relative helicity to explain the strong rotation of the updraft in supercell storms. Results showed that, in the reference system of the storm, if the vorticity had a component in the streamline direction, the vertical velocity would be

positively correlated with the vertical vorticity. Brandes et al. (1988)[6] discussed the influence of streamline vortices on the shape and maintenance of supercell storms. Their results showed that the relationship between velocity and vorticity causes the upward motion to have a strong rotation. Markowski et al. (1998)[7], using a three-dimensional coordinate system composed of the natural coordinate system and the vertical height above the horizontal plane, decomposed the wind field into horizontal and vertical directions to study the factors affecting individual or local changes in the streamline vortex. Scorer (1997)[8] also studied the streamline vortices or sub-vortices produced by the bending of ventilation channels and rivers. From this, it can be seen that the concept of the streamline vortex plays an important role in the study of the dynamic mechanisms of severe convective storms.

In large-scale motion, the vertical component of the vorticity is the most important contribution to the vorticity, and so in the vorticity equation describing large-scale motion we only need to consider this component. Generally, the variation in the components in the other directions is ignored, including the variation in vorticity along the streamline direction. Because the large-scale motion is quasi-horizontal and the streamline is mainly in the horizontal plane, the component corresponding to the projection of the absolute vorticity of a particle in the streamline direction is usually very small and is known as the secondary vorticity. However, in the study of mesoscale problems, for example, in strong storm systems, because the vertical component of the motion of air particles is very obvious, clear bending appears in the streamline due to the combination of horizontal and vertical motion. Also, because the vertical motion is very strong, the streamline changes from being horizontal to nearly vertical. In such cases, the vorticity in the horizontal direction can no longer be considered secondary. Because of this, in dealing with mesoscale problems, we can no longer use the method of retaining only the vertical component of the vorticity from the large-scale vorticity equation. Based on the characteristics of mesoscale motion, the new vorticity equation should be used to describe the typical characteristics of streamline bending and the change in the streamline direction from horizontal to vertical; the change in the streamline vortex then just happens. Therefore, it is very important to study the evolution of the streamline vortex (Gao and Lei, 2000)[9]. The streamline vortex is different from the general vorticity. If only a local coordinate system is used, the representation of the streamline vortex will be very complex. Therefore, here we introduce a new coordinate system—the generalized natural coordinate system. In this coordinate system, the streamline vortex

can be represented clearly, but its gradient is still defined in the local coordinate system. By jointly using the generalized natural coordinate system and the local coordinate system, the equations for the streamline vortex can be expressed easily and clearly.

4.3.1 Generalized Natural Coordinates and the Streamline Vortex

If the unit vector in the direction of the velocity is denoted by $\mathbf{t}$, we have

$$\mathbf{t} = \mathbf{v}/q_\eta \ , \ \mathbf{t}\cdot\mathbf{t} = 1 \text{ and } \mathbf{t}\cdot\partial\mathbf{t}/\partial s = 0 \tag{4.3.1}$$

Here $\partial/\partial s$ denotes the change along the streamline, $q_\eta = |\mathbf{v}|$ denotes the speed, and $\mathbf{t}$ and $\partial\mathbf{t}/\partial s$ together form a plane—usually called the osculating plane. If the unit vector of $\partial\mathbf{t}/\partial s$ is denoted by $\mathbf{n}$ and $\mathbf{n}$ is the unit normal vector, we have

$$\partial\mathbf{t}/\partial s = \kappa\mathbf{n} \tag{4.3.2}$$

where κ is the curvature of the streamline and its magnitude is

$$\kappa = \mathbf{n}\cdot\partial\mathbf{t}/\partial s$$

Because $\mathbf{t}\cdot\mathbf{n} = 0$ we have

$$\kappa = \mathbf{n}\cdot\partial\mathbf{t}/\partial s = -\mathbf{t}\cdot\partial\mathbf{n}/\partial s$$

As $\mathbf{n}$ and $\mathbf{t}$ are mutually perpendicular, $\mathbf{b}$ is known as the unit double-normal vector:

$$\mathbf{b} = \mathbf{t}\times\mathbf{n} \tag{4.3.4}$$

A right-handed coordinate system called the generalized natural coordinate system is then constructed using $\mathbf{t}$, $\mathbf{n}$, and $\mathbf{b}$. Taking the derivative of the unit vector $\mathbf{n}$ along the streamline, we have

$$\frac{\partial\mathbf{n}}{\partial s} = -\kappa\mathbf{t} + \tau\mathbf{b} \tag{4.3.5}$$

where τ is rate of rotation of $\mathbf{n}$ and $\mathbf{b}$ around $\mathbf{t}$. Because $\mathbf{t}\cdot\mathbf{b} = 0$, the use of (4.3.2) yields

$$\mathbf{t}\cdot\frac{\partial\mathbf{b}}{\partial s} = -\mathbf{b}\cdot\frac{\partial\mathbf{t}}{\partial s} = 0 \tag{4.3.6}$$

and because $\mathbf{b}\cdot\mathbf{n} = 0$ we have

$$\frac{\partial \mathbf{b}}{\partial s} = -\tau \mathbf{n} \tag{4.3.7}$$

Since the acceleration of an air particle lies within the closed plane composed of $\mathbf{t}$ and $\mathbf{n}$, the acceleration, $\mathbf{a}$, can be expressed as

$$\begin{aligned} \mathbf{a} &= \frac{D\mathbf{v}}{Dt} = \frac{\partial \mathbf{v}}{\partial t} + (\mathbf{v}\cdot\nabla)\mathbf{v} = \frac{\partial \mathbf{v}}{\partial t} + q_\eta (\mathbf{t}\cdot\nabla) q_\eta \mathbf{t} \\ &= \frac{\partial \mathbf{v}}{\partial t} + q_\eta^2 (\mathbf{t}\cdot\nabla)\mathbf{t} + q_\eta \mathbf{t}(\mathbf{t}\cdot\nabla q_\eta) \end{aligned} \tag{4.3.8}$$

From $\mathbf{t}\cdot\nabla = \partial/\partial s$ and (4.3.2), (4.3.8) becomes

$$\begin{aligned} \mathbf{a} &= \frac{D\mathbf{v}}{Dt} = \frac{\partial \mathbf{v}}{\partial t} + q_\eta^2 (\mathbf{t}\cdot\nabla)\mathbf{t} + q_\eta \mathbf{t}(\mathbf{t}\cdot\nabla q_\eta) \\ &= \frac{\partial \mathbf{v}}{\partial t} + \kappa q_\eta^2 \mathbf{n} + q_\eta \frac{\partial q_\eta}{\partial s}\mathbf{t} = \frac{\partial \mathbf{v}}{\partial t} + \kappa q_\eta^2 \mathbf{n} + a_d \mathbf{t} \end{aligned} \tag{4.3.9}$$

Here, $a_d = q_\eta \mathbf{t}\cdot\nabla q_\eta = q_\eta \partial q_\eta / \partial s$ is the tangential acceleration.

Finally, the streamline vorticity is defined as

$$\xi_s = \boldsymbol{\xi}_a \cdot \mathbf{t} = \frac{1}{q_\eta}\boldsymbol{\xi}_a \cdot \mathbf{v}. \tag{4.3.10}$$

4.3.2 Streamline Vorticity Equation

Based on the definition of the streamline vortex, the individual change can be written as

$$\begin{aligned} \frac{d\xi_s}{dt} &= \frac{\partial \xi_s}{\partial t} + (\mathbf{v}\cdot\nabla)\xi_s = \frac{\partial(\boldsymbol{\xi}_a \cdot \mathbf{t})}{\partial t} + (\mathbf{v}\cdot\nabla)(\boldsymbol{\xi}_a \cdot \mathbf{v}) \\ &= \mathbf{t}\cdot\frac{\partial \boldsymbol{\xi}_a}{\partial t} + \boldsymbol{\xi}_a \cdot \frac{\partial \mathbf{t}}{\partial t} + \boldsymbol{\xi}_a \cdot (\mathbf{v}\cdot\nabla)\mathbf{t} + \mathbf{t}\cdot(\mathbf{v}\cdot\nabla)\boldsymbol{\xi}_a \end{aligned} \tag{4.3.11}$$

Because $f\,\mathbf{k}\times\mathbf{v} = f\,\mathbf{k}\times q_\eta \mathbf{t}$ and $f\,\mathbf{k}\times\mathbf{v}$ are perpendicular to $\mathbf{t}$, so the components of $f\,\mathbf{k}\times\mathbf{v}$ are in the directions of $\mathbf{n}$ and $\mathbf{b}$. Hence the components of $f\,\mathbf{k}\times\mathbf{v}$ can be written as $f_n \mathbf{n} + f_b \mathbf{b}$. Equation (4.3.11) becomes

$$\frac{\partial \xi_s}{\partial t}+(\mathbf{v}\cdot\nabla)\xi_s=\boldsymbol{\xi}_a\cdot\frac{\partial \mathbf{t}}{\partial t}+\mathbf{t}\cdot\frac{\partial \boldsymbol{\xi}_a}{\partial t}+\boldsymbol{\xi}_a\cdot(\kappa q_\eta\,\mathbf{n})+\mathbf{t}\cdot(\mathbf{v}\cdot\nabla)\boldsymbol{\xi}_a$$
$$=\boldsymbol{\xi}_a\cdot\frac{\partial \mathbf{t}}{\partial t}+\boldsymbol{\xi}_a\cdot(\kappa q_\eta\,\mathbf{n})+\mathbf{t}\cdot[-\boldsymbol{\xi}_a(\nabla\cdot\mathbf{v})\quad,$$
$$+(\boldsymbol{\xi}_a\cdot\nabla)\mathbf{v}+\boldsymbol{\lambda}\times(\mathbf{g}-\mathbf{a}-f_n\,\mathbf{n}-f_b\,\mathbf{b})]$$

(4.3.12)

Where $\boldsymbol{\lambda}=\nabla\ln\rho$.

$\mathbf{a}$ is obtained from (4.3.9) and is substituted into (4.3.12):

$$\mathbf{t}\cdot[\boldsymbol{\lambda}\times(\mathbf{g}-\mathbf{a}-f_n\,\mathbf{n}-f_b\,\mathbf{b})]$$
$$=\mathbf{t}\cdot[\boldsymbol{\lambda}\times(\mathbf{g}-q_\eta\frac{\partial \mathbf{t}}{\partial t}-\frac{\partial q_\eta}{\partial t}\mathbf{t}+q_\eta\frac{\partial q_\eta}{\partial s}\mathbf{t}+q_\eta^2\frac{\partial \mathbf{t}}{\partial s}-f_n\,\mathbf{n}-f_b\,\mathbf{b})]$$
$$=\mathbf{t}\cdot[\boldsymbol{\lambda}\times(\mathbf{g}-q_\eta\frac{\partial \mathbf{t}}{\partial t}+q_n^2\kappa\,\mathbf{n}-f_n\,\mathbf{n}-f_b\,\mathbf{b})]$$

(4.3.13)

(4.3.12) then becomes

$$\frac{\partial \xi_s}{\partial t}+(\mathbf{v}\cdot\nabla)\xi_s=\boldsymbol{\xi}_a\cdot\frac{\partial \mathbf{t}}{\partial t}+\boldsymbol{\xi}_a\cdot(\kappa q_n\,\mathbf{n})+\mathbf{t}\cdot\frac{\partial \boldsymbol{\xi}_a}{\partial t}+\mathbf{t}\cdot(\mathbf{v}\cdot\nabla)\boldsymbol{\xi}_a$$
$$=\boldsymbol{\xi}_a\cdot\frac{\partial \mathbf{t}}{\partial t}+\boldsymbol{\xi}_a\cdot(\kappa q_\eta\,\mathbf{n})+\mathbf{t}\cdot[-\boldsymbol{\xi}_a(\nabla\cdot\mathbf{v})+(\boldsymbol{\xi}_a\cdot\nabla)\mathbf{v}\,.$$
$$+\boldsymbol{\lambda}\times(\mathbf{g}-q_\eta\frac{\partial \mathbf{t}}{\partial t}+q_\eta^2\kappa\,\mathbf{n}-f_n\,\mathbf{n}-f_b\,\mathbf{b})]$$

(4.3.14)

Equation (4.3.14) is an unsimplified streamline vortex equation. It can be seen from the equation that the change in the streamline vortex mainly depends on four factors: the fluctuations in the streamline, the change in the streamline curvature, the change in velocity along the streamline, and the projection of the vorticity gradient term in the streamline direction. The most important feature of the streamline vortex equation is that the change in the streamline vortex is closely related to the change in the streamline itself. Therefore, the importance of streamline analysis in analyzing strong storm systems should be emphasized.

4.3.3 Simplification of the Streamline Vortex Equation

Another advantage of the streamline vortex equation is that it is easy to simplify for application to different research objects and different environmental conditions. Its application to small-scale and mesoscale systems will be discussed next.

For small-scale systems such as tornadoes, squall lines, and thunderstorms, equation (4.3.14) can be simplified to

$$\frac{\partial \xi_s}{\partial t} + (\mathbf{v}\cdot\nabla)\xi_s = \boldsymbol{\xi}_a \frac{\partial \mathbf{t}}{\partial t} + \boldsymbol{\xi}_a \cdot (\kappa q_\eta \mathbf{n}) + \mathbf{t}\cdot[-\boldsymbol{\xi}_a(\nabla\cdot\mathbf{v}) + (\boldsymbol{\xi}_a\cdot\nabla)\mathbf{v} + \boldsymbol{\lambda}\times(\mathbf{g} - q_\eta \frac{\partial \mathbf{t}}{\partial t} + q_\eta^2 \kappa \mathbf{n})] \tag{4.3.15}$$

Under barotropic conditions, $\boldsymbol{\lambda} = \nabla \ln \rho = \mathbf{k}\frac{\partial \ln \rho}{\partial z}$, and $\mathbf{g} = -g\mathbf{k}$. In a Cartesian coordinate system, $\boldsymbol{\lambda}\times\mathbf{g} = 0$; thus, (4.3.15) can be further simplified to

$$\frac{\partial \xi_s}{\partial t} + (\mathbf{v}\cdot\nabla)\xi_s = \boldsymbol{\xi}_a \frac{\partial \mathbf{t}}{\partial t} + \boldsymbol{\xi}_a \cdot (\kappa q_\eta \mathbf{n}) + \mathbf{t}\cdot[-\boldsymbol{\xi}_a(\nabla\cdot\mathbf{v}) + (\boldsymbol{\xi}_a\cdot\nabla)\mathbf{v} + \boldsymbol{\lambda}\times(-q_\eta \frac{\partial \mathbf{t}}{\partial t} + q_\eta^2 \kappa \mathbf{n})] \tag{4.3.16}$$

Equation (4.3.16) is the streamline vortex equation that can be used for studying small-scale storm systems.

For a tornado with a radius of about 50 m, the speed, q_η = 25 m s^{-1}, and the second term on the right-hand side of equation (4.3.16), $\boldsymbol{\xi}_a \cdot (\kappa q_\eta \mathbf{n}) = \boldsymbol{\xi}_a \cdot \mathbf{n}\frac{25m/s}{50m} = 0.5\boldsymbol{\xi}_a \cdot \mathbf{n}/s$. If the angle between $\boldsymbol{\xi}_a$ and $\mathbf{n}$ is 45°, the rate of the individual change of the streamline vortex due to this term is

$$\frac{d\xi_s}{dt} = 0.5\boldsymbol{\xi}_a \cdot \mathbf{n} = 0.5|\boldsymbol{\xi}_a|\cdot\cos\frac{\pi}{4} = 0.5|\boldsymbol{\xi}_a|\cdot\frac{\sqrt{2}}{2} \approx 0.355|\boldsymbol{\xi}_a|$$

.

It can be seen that the effect of the streamline curvature alone will cause changes in the streamline vortex of the order of 0.355. This is

enough to show that changes in the streamline curvature play an important role in changes in the streamline vortex in strong storm systems and so cannot be ignored.

From the momentum equation, we have

$$\frac{d\mathbf{v}}{dt}+\mathbf{f}\times\mathbf{v}=\frac{\partial\mathbf{v}}{\partial t}+\nabla(\frac{1}{2}q_\eta^2)-\mathbf{v}\times\boldsymbol{\xi}+\mathbf{f}\times\mathbf{v}=\frac{\partial\mathbf{v}}{\partial t}+\nabla(\frac{1}{2}q_\eta^2)-\mathbf{v}\times\boldsymbol{\xi}_a$$
$$=-\mathbf{g}-RT\nabla(\ln\rho)-R\nabla T \tag{4.3.17}$$

Hence

$$\boldsymbol{\lambda}=\nabla\ln\rho=-\frac{1}{RT}[\frac{\partial\mathbf{v}}{\partial t}+\nabla(\frac{1}{2}q_\eta^2)+\boldsymbol{\xi}_a\times\mathbf{v}+\mathbf{g}+R\nabla T], \tag{4.3.18}$$

where $\frac{\partial\mathbf{v}}{\partial t}=\frac{\partial q_\eta}{\partial t}\mathbf{t}+q_\eta\frac{\partial\mathbf{t}}{\partial t}$. In equations (4.3.12) to (4.3.16), the term $\frac{\partial q_\eta}{\partial t}\mathbf{t}$ in λ vanishes due to the fact that this term is multiplied by a vector and dot multiplied $\vec{t}$, it must be zero. In (4.3.18), the term $q_\eta\frac{\partial\mathbf{t}}{\partial t}$ in $\frac{\partial\mathbf{v}}{\partial t}$ cannot be derived from the wind and temperature fields. However, in developing storm systems, the change of the streamline direction with time is relatively small (slow); thus, omitting this term does not introduce much of an error into the calculation. Therefore, by using equation (4.3.18) with the wind field and temperature field but without the air-pressure field, λ can be calculated accurately.

Under the condition that the streamline is quasi-stationary, (4.3.16) can be simplified to

$$\frac{\partial\xi_s}{\partial t}+(\mathbf{v}\cdot\nabla)\xi_s=\boldsymbol{\xi}_a\cdot(\kappa q_\eta\mathbf{n})+\mathbf{t}\cdot[-\boldsymbol{\xi}_a(\nabla\cdot\mathbf{v})+(\boldsymbol{\xi}_a\cdot\nabla)\mathbf{v}$$
$$+\boldsymbol{\lambda}\times q_\eta^2\kappa\mathbf{n}] \tag{4.3.19}$$

It can be seen that the change in the streamline vortex in a strong, small-scale storm system depends on the curvature of the streamline on the one hand and the change in the wind speed along the streamline on the other hand. This is very important because, if we are concerned only about the change in the streamline vortex, it is enough to consider only the curvature term of the streamline and the change in the wind speed along

the streamline in the streamline vortex equation, which greatly simplifies the problem.

In terms of the mesoscale motion, although the vertical motion is more obvious than the large-scale motion, it is still very small compared with the horizontal motion. Therefore, the streamline vortex equation can be treated in the streamline way of the large-scale motion because the Coriolis force is mainly determined by the horizontal wind. Therefore, the distribution of the wind field can be regarded as horizontal in the Coriolis force term. Under this assumption, equation (4.3.14) can be abbreviated as

$$\begin{aligned}\frac{\partial \xi_s}{\partial t}+(\mathbf{v}\cdot\nabla)\xi_s &= \boldsymbol{\xi}_a\cdot\frac{\partial \mathbf{t}}{\partial t}+\boldsymbol{\xi}_a\cdot(\kappa q_\eta \mathbf{n})+\mathbf{t}\cdot\frac{\partial \boldsymbol{\xi}_a}{\partial t}+\mathbf{t}\cdot(\mathbf{v}\cdot\nabla)\boldsymbol{\xi}_a \\ &= \boldsymbol{\xi}_a\cdot\frac{\partial \mathbf{t}}{\partial t}+\boldsymbol{\xi}_a\cdot(\kappa q_\eta \mathbf{n})+\mathbf{t}\cdot[-\boldsymbol{\xi}_a(\nabla\cdot\mathbf{v})+(\boldsymbol{\xi}_a\cdot\nabla)\mathbf{v} \\ &\quad +\boldsymbol{\lambda}\times(\mathbf{g}-q_\eta\frac{\partial \mathbf{t}}{\partial t}+q_\eta^2\kappa\mathbf{n}-f_n\mathbf{n})]\end{aligned} \tag{4.3.20}$$

Under barotropic conditions, (4.3.20) can be written as

$$\begin{aligned}\frac{\partial \xi_s}{\partial t}+(\mathbf{v}\cdot\nabla)\xi_s &= \boldsymbol{\xi}_a\cdot\frac{\partial \mathbf{t}}{\partial t}+\boldsymbol{\xi}_a\cdot(\kappa q_\eta \mathbf{n})+\mathbf{t}\cdot\frac{\partial \boldsymbol{\xi}_a}{\partial t}+\mathbf{t}\cdot(\mathbf{v}\cdot\nabla)\boldsymbol{\xi}_a \\ &= \boldsymbol{\xi}_a\cdot\frac{\partial \mathbf{t}}{\partial t}+\boldsymbol{\xi}_a\cdot(\kappa q_\eta \mathbf{n})+\mathbf{t}\cdot[-\boldsymbol{\xi}_a(\nabla\cdot\mathbf{v})+(\boldsymbol{\xi}_a\cdot\nabla)\mathbf{v} \\ &\quad +\boldsymbol{\lambda}\times(-q_\eta\frac{\partial \mathbf{t}}{\partial t}+q_\eta^2\kappa\mathbf{n}-f_n\mathbf{n})]\end{aligned} \tag{4.3.21}$$

Equations (4.3.20) and (4.3.21) are streamline vortex equations describing mesoscale motion. Particularly in the case of a steady streamline (where the three-dimensional non-divergent condition applies), we have

$$\begin{aligned}\frac{\partial \xi_s}{\partial t}+(\mathbf{v}\cdot\nabla)\xi_s &= \boldsymbol{\xi}_a\cdot(\kappa q_\eta \mathbf{n})+\mathbf{t}\cdot(\mathbf{v}\cdot\nabla)\boldsymbol{\xi}_a \\ &= \boldsymbol{\xi}_a\cdot(\kappa q_\eta \mathbf{n})+\mathbf{t}\cdot[(\boldsymbol{\xi}_a\cdot\nabla)\mathbf{v}-\boldsymbol{\xi}_a(\nabla\cdot\mathbf{v})+\boldsymbol{\lambda}\times(q_\eta^2\kappa\mathbf{n}-f_n\mathbf{n})]\end{aligned} \tag{4.3.22}$$

It can be seen that the variation in advection for the mesoscale streamline vortex is still determined by the curvature term and the velocity variation term along the streamline in the streamline vortex equation.

Generally, when studying the occurrence and development of strong

storm systems, we are not concerned with the vorticity itself but with the change in the vorticity or the change in vorticity with time. Only when the vorticity is continuously strengthening can a strong storm system be maintained and develop. So the individual change or local change in the streamline vortex is the subject of most interest in studies of strong storm systems. In the traditional vorticity equation, the individual variation in the vorticity is determined by the solenoid term as well as other terms. However, in a strong storm system, because the pressure field adapts to the wind field, there are transient changes in the pressure field, which makes it difficult to describe the pressure field accurately or to calculate the pressure-gradient force term. At the same time, because current observation data are mainly limited to isobaric surfaces at different levels, meaning that there is no continuity of data in the vertical direction, using the observation data, the solenoid term in the vorticity equation can only be calculated on these isobaric surfaces. Predicting or estimating the values between two adjacent isobaric surfaces is difficult. Therefore, it is difficult to use the traditional vorticity equation to study the vorticity development in a strong storm system. If it is used, it is likely that the change in vorticity that is calculated will be different form the true value. The streamline vortex equation avoids the shortcomings of the original vorticity equation. In the streamline vortex equation, the wind speed or the acceleration related to the wind speed is used to express the change in the streamline vortex, and the change in the curvature and direction of the streamline are also used to describe this change. Therefore, the greatest advantage of the streamline vortex equation is its dependence on the streamline and speed itself and its avoidance of the use of the pressure and pressure gradient terms. Also, the streamline diagram is easy to obtain either by data analysis or numerical simulation, and the continuity and smoothness of the streamline is good. In spaces where data are lacking, therefore, this diagram is based on the continuity of the streamline, and so it is more reliable and accurate to use the streamline and velocity to determine the development of the streamline vortex. At the same time, the effect of divergent wind is obvious in the streamline vortex equation: this can better reflect the effect of divergent wind on the development of the vortex.

4.4 Helicity and the Helicity Equation

The helicity is a physical quantity that represents the dynamic characteristics of a fluid moving in the direction of the rotation. It was first used to study turbulence in the field of hydrodynamics and is a conserved

nature in an isentropic fluid (Moffat ,1969, 1981)[10-11]. Strictly speaking, the helicity is defined as $H_e = \iiint \mathbf{v}\cdot(\nabla\times\mathbf{v})d\tau$. However, in practice, the "helicity" usually refers to the local helicity, h_e, which is defined as

$$H_e = \mathbf{v}\cdot(\nabla\times\mathbf{v}) = (\mathbf{v}_\chi+\mathbf{v}_\psi)\cdot[\nabla\times(\mathbf{v}_\chi+\mathbf{v}_\psi)] = (-\nabla\chi+\mathbf{k}\times\nabla\psi)\cdot\nabla\times(\nabla\chi+\mathbf{k}\times\nabla\psi)$$
$$= (-\nabla\chi+\mathbf{k}\times\nabla\psi)\cdot[\nabla\times(\mathbf{k}\times\nabla\psi)] = (\mathbf{v}_\chi+\mathbf{v}_\psi)\cdot\nabla\times\mathbf{v}_\psi$$

(4.3.23)

Here, $\mathbf{V}_\chi$, $\mathbf{V}_\psi$ represent the divergence and rotation components of the velocity, respectively; χ, ψ are the potential function and the stream function, respectively. It can be seen that the importance of the helicity is that it accounts for the effect of divergent wind and so can better reflect the result of the interaction between the vorticity and divergence. At the same time, it can better reflect the motion of the atmosphere, and its value reflects the degree of matching between the vorticity and velocity. Since the 1980s, meteorologists in China and in other countries have applied the helicity to studies of the development and maintenance mechanisms of severe convective storms and other related atmospheric phenomena, and have carried out numerical experiments and diagnostic analyses related to its application to the analysis and prediction of severe convective weather.

Lilly (1986)[12]first introduced the helicity into the study of severe convective storms. He pointed out that a strong convective storm is characterized by high helicity, which is derived from the environmental field and enhanced by the buoyancy effect. At the same time, this high helicity hinders the dissipation of the energy of the disturbance and plays an important role in the maintenance of supercell storms. Strong, stable convective storms often occur where there is high helicity. Etling (1985)[13] discussed and summarized several typical types of spiral flows in the atmosphere and pointed out that the fluid stability is closely related to the helicity. Wu and Tan (1989)[14] also studied the properties and applications of helicity. Wu et al. (1992, 2002)[15-16] derived the complete helicity equation and pointed out that the helicity of the atmosphere is conserved in quasi-geostrophic motion without friction. Tan and Wu (1994)[17] discussed the dynamic properties of helicity in the boundary layer and frontal regions. Liu and Liu (1997)[18] pointed out that the helicity in the steady quasi-geostrophic model is closely related to the vertical motion of the atmosphere; that is, for the steady large-scale motion of the atmosphere, ascending motion under stable stratification corresponds to positive helicity and descending motion corresponds to negative helicity. Similarly,

the helicity is closely related to the temperature advection: warm advection corresponds to positive helicity, and cold advection corresponds to negative helicity.

Helicity is important not only in theoretical research but also in the analysis and forecasting of severe convective weather. Through theoretical studies of the helicity (Lily, 1986, Davies-Jones, 1984) [12,5], later numerical simulation results (Brooks et al., 1990; Droegemeier et al., 1993; Li and Shou, 1999; Fei and Tan, 2001)[19-23], and analysis of observed data, the helicity has gradually become an important physical quantity in weather analysis and forecasting.

It is well known that the atmosphere is a dynamic system, and the trends in physical quantities that represent its motion are of more concern than the physical quantities themselves. Therefore, it is important and meaningful to study the factors that affect the helicity. When Lilly (1986)[12,24] studied the structure, energy, and propagation of a strong spiral convective storm, he derived the helicity equation under the assumption that the density was constant and the influence of Coriolis force could be ignored; it was also emphasized that the buoyancy effect has a great influence on the change in the helicity with time. In real situations, the density is not constant, and neglecting the variation in density will influence estimates of the solenoid effect in particular; that is, the baroclinic properties of the atmosphere will not be well reflected. However, observations show that severe stormy weather often occurs in places where the vertical wind shear is large: that is, where the baroclinicity is strong. (Lu and Gao, 2003)[25].

4.4.1 Helicity Equation

The governing equation of mesoscale motion can be written as

$$\frac{\partial \mathbf{v}}{\partial t} + (\mathbf{v}\cdot\nabla)\,\mathbf{v} = -c_p\theta\nabla\pi - f\,\mathbf{k}\times\mathbf{v} - g\,\mathbf{k}\,. \tag{4.4.1}$$

This equation can be simplified by assuming that any atmospheric thermodynamic variable, A, can be regarded as the sum of the basic state, $\overline{A}$, and disturbances, namely $A = \overline{A}(z) + A'$.

The equation of vertical motion can be expressed as

$$\frac{dw}{dt} = -c_p\theta\frac{\partial\pi}{\partial z} - g = -c_p(\overline{\theta}+\theta')\frac{\partial\overline{\pi}+\pi'}{\partial z} - g = -c_p\overline{\theta}\frac{\partial\pi'}{\partial z} + g\frac{\theta'}{\overline{\theta}} \tag{4.4.2}$$

The governing equation of motion can then be written as

$$\frac{\partial \mathbf{v}}{\partial t} + (\mathbf{v}\cdot\nabla)\,\mathbf{v} = -c_p\,\bar{\theta}\nabla\pi' - f\,\mathbf{k}\times\mathbf{v} + b\,\mathbf{k}, \tag{4.4.3}$$

where $b = g\dfrac{\theta'}{\bar{\theta}}$.

Cross multiplying (4.4.3), and the relative vorticity $\xi = \nabla\times\mathbf{v}$, $\mathbf{T} = -c_p\,\bar{\theta}\nabla\pi' - f\,\mathbf{k}\times\mathbf{v} + b\,\mathbf{k}$, the equation of relative vorticity can be written as

$$\frac{\partial \xi}{\partial t} + (\mathbf{v}\cdot\nabla)\xi + \xi(\nabla\cdot\mathbf{v})\,\mathbf{v} - (\xi\cdot\nabla)\,\mathbf{v} = \nabla\times\mathbf{T} \tag{4.4.4}$$

Taking the dot product of (4.4.3) and (4.4.4) with ξ and $\mathbf{v}$, respectively, gives

$$\xi\cdot\frac{\partial \mathbf{v}}{\partial t} + \xi\cdot[(\mathbf{v}\cdot\nabla)\,\mathbf{v}] = \xi\cdot\mathbf{T} \quad \text{and} \tag{4.4.5}$$

$$\mathbf{v}\cdot\frac{\partial \xi}{\partial t} + \mathbf{v}\cdot[(\mathbf{v}\cdot\nabla)\xi + \xi(\nabla\cdot\mathbf{v}) - (\xi\cdot\nabla)\,\mathbf{v}] = \mathbf{v}\cdot(\nabla\times\mathbf{T}) \tag{4.4.6}$$

Given $H_e = \xi\cdot\mathbf{v}$ and adding (4.4.5) and (4.4.6) yields

$$\frac{\partial h_e}{\partial t} + (\mathbf{v}\cdot\nabla)H_e + H_e(\nabla\cdot\mathbf{v}) - \mathbf{v}\cdot[(\xi\cdot\nabla)\,\mathbf{v}] = \mathbf{v}\cdot(\nabla\times\mathbf{T}) + \xi\cdot\mathbf{T}; \tag{4.4.7}$$

that is,

$$\frac{\partial H_e}{\partial t} + \nabla\cdot(\mathbf{v}\,H_e) - \frac{1}{2}\nabla\cdot(\xi\,|\,\mathbf{v}\,|^2) = \mathbf{v}\cdot(\nabla\times\mathbf{T}) + \xi\cdot\mathbf{T}. \tag{4.4.8}$$

The right-hand side of (4.4.8) can be expanded as

$$\boldsymbol{\xi}\cdot\mathbf{T}=\boldsymbol{\xi}\cdot(-c_p\overline{\theta}\nabla\pi'-f\,\mathbf{k}\times\mathbf{v}+b\,\mathbf{k})$$
$$=-\boldsymbol{\xi}\cdot c_p\overline{\theta}\nabla\pi'-\boldsymbol{\xi}\cdot(f\,\mathbf{k}\times\mathbf{v})+b\zeta$$
$$=-\boldsymbol{\xi}\cdot c_p\overline{\theta}\nabla\pi'-f\,\mathbf{k}\cdot(\mathbf{v}\times\boldsymbol{\xi})+b\zeta$$
$$=-\boldsymbol{\xi}\cdot c_p\overline{\theta}\nabla\pi'-f\,\mathbf{k}\cdot[\frac{1}{2}\nabla(\mathbf{v}\cdot\mathbf{v})-(\mathbf{v}\cdot\nabla)\,\mathbf{v}]+b\zeta$$
$$\mathbf{v}\cdot(\nabla\times\mathbf{T})=\mathbf{v}\cdot[\nabla\times(-c_p\overline{\theta}\nabla\pi'-f\,\mathbf{k}\times\mathbf{v}+b\,\mathbf{k})]\cdot$$
$$=\mathbf{v}\cdot(\nabla\pi'\times\nabla c_p\overline{\theta})-\mathbf{v}\cdot[\nabla\times(f\,\mathbf{k}\times\mathbf{v})]+\mathbf{v}\cdot(\nabla\times b\,\mathbf{k})$$
$$=\mathbf{v}\cdot(\nabla\pi'\times\nabla c_p\overline{\theta})-\mathbf{v}\cdot[f\,\mathbf{k}(\nabla\cdot\mathbf{v})-(f\,\mathbf{k}\cdot\nabla)\,\mathbf{v}]+\mathbf{v}\cdot(\nabla b\times\mathbf{k})$$

(4.4.9)

For mesoscale systems, $f\,\mathbf{k}$ can be considered constant. The helicity equation can then be written as

$$\frac{\partial H_e}{\partial t}=-\nabla\cdot(H_e\,\mathbf{v})+\frac{1}{2}\nabla\cdot(\boldsymbol{\xi}\,|\,\mathbf{v}\,|^2)+\mathbf{v}\cdot(\nabla\pi'\times\nabla c_p\overline{\theta})-\boldsymbol{\xi}\cdot c_p\overline{\theta}\nabla\pi'$$
$$\mathbf{(1)}\qquad\mathbf{(2)}\qquad\mathbf{(3)}\qquad\mathbf{(4)}$$
$$+b\zeta-f[\mathbf{k}\cdot\mathbf{v}(\nabla\cdot\mathbf{v})-\mathbf{k}\cdot(\mathbf{v}\cdot\nabla)\,\mathbf{v}]+\mathbf{v}\cdot(\nabla b\times\mathbf{k})$$
$$\mathbf{(5)}\qquad\mathbf{(6)}\qquad\mathbf{(7)}$$

(4.4.10)

From this equation, it can see that the change in helicity is not only related to the divergence (1), the divergence of the kinetic energy (2), and baroclinic solenoid (3) but also to the vorticity and pressure-gradient force (4), buoyancy (5), geostrophic deflection force (6), and buoyancy gradient (7).

Next, the helicity equation derived above is discussed using the method of scale analysis.

Assume that U , V , and W are the characteristic scales of the wind speed in the x-, y-, and z-directions, respectively; L_x , L_y , and D_z are the horizontal and vertical scales of the disturbance, respectively; θ and Θ are the characteristic scales of θ' and $\overline{\theta}$, respectively; and $\Delta_h\theta$ is the

characteristic scale of the horizontal variation in θ'. Also, $\Delta_z\Theta$ is the characteristic scale of the horizontal variation in $\overline{\theta}$, H is the height of the corresponding Θ in an isentropic atmosphere, $H = \frac{c_p\Theta}{g}$, and $\Delta_h\pi$ and $\Delta_z\pi$ is π' are the characteristic scales of the horizontal and vertical variations, respectively. For simplicity, $L_x \sim L_y \sim L$, and $V \sim U$.

We will now consider the right-hand side of equation (4.4.10) in more detail.

$$\text{Term 1} = -\nabla\cdot(H_e\,\mathbf{v}) = -\left(\frac{\partial uH_e}{\partial x} + \frac{\partial vH_e}{\partial y}\right) - \frac{\partial wH_e}{\partial z}$$

$$\frac{U^3}{LD_z} \qquad \frac{WU^2}{D_z^2}$$

$$\text{Term 2} = \frac{1}{2}\nabla\cdot(\boldsymbol{\xi}|\mathbf{v}|^2)$$

$$= \frac{1}{2}\left[\frac{\partial w}{\partial y}\frac{\partial(u^2+v^2)}{\partial x} - \frac{\partial w}{\partial x}\frac{\partial(u^2+v^2)}{\partial y} - \frac{\partial v}{\partial z}\frac{\partial w^2}{\partial x} + \frac{\partial u}{\partial z}\frac{\partial w^2}{\partial y} + \left(\frac{\partial v}{\partial x} - \frac{\partial u}{\partial y}\right)\frac{\partial w^2}{\partial z} + \right.$$

$$\frac{WU^2}{2L^2} \qquad \frac{UW^2}{2LD_z}$$

$$\left.\frac{\partial u}{\partial z}\frac{\partial(u^2+v^2)}{\partial y} - \frac{\partial v}{\partial z}\frac{\partial(u^2+v^2)}{\partial x} + \left(\frac{\partial v}{\partial x} - \frac{\partial u}{\partial y}\right)\frac{\partial(u^2+v^2)}{\partial z} + \frac{\partial w}{\partial y}\frac{\partial w^2}{\partial x} - \frac{\partial w}{\partial x}\frac{\partial w^2}{\partial y}\right]$$

$$\frac{U^3}{2LD_z} \qquad \frac{W^3}{2L^2}$$

$$\text{Term 3} = \mathbf{v}\cdot(\nabla\pi'\times\nabla c_p\overline{\theta})$$

$$\frac{C_pU\Delta_z\Theta\Delta_h\pi}{LD_z}$$

Term 4 $= -\boldsymbol{\xi} \cdot c_p \bar{\theta} \nabla \pi'$

$$= c_p \bar{\theta} \frac{\partial \pi'}{\partial z}\left(\frac{\partial u}{\partial y} - \frac{\partial v}{\partial x}\right) + c_p \bar{\theta}\left(\frac{\partial \pi'}{\partial x}\frac{\partial v}{\partial z} - \frac{\partial \pi'}{\partial y}\frac{\partial u}{\partial z}\right) + c_p \bar{\theta}\left(\frac{\partial \pi'}{\partial y}\frac{\partial w}{\partial x} - \frac{\partial \pi'}{\partial x}\frac{\partial w}{\partial y}\right)$$

$$\frac{c_p U \Theta \Delta_z \pi}{L D_z} \qquad \frac{c_p U \Theta \Delta_h \pi}{L D_z} \qquad \frac{c_p W \Theta \Delta_h \pi}{L^2}$$

Term 5 $= b\zeta = g\frac{\theta'}{\bar{\theta}}\left(\frac{\partial v}{\partial x} - \frac{\partial u}{\partial y}\right)$,

$$g\frac{\theta}{\Theta}\frac{U}{L} = \frac{c_p \theta}{HL}\frac{U}{L}$$

Term 6 $= -f\,\mathbf{k}\cdot\mathbf{v}\nabla\cdot\mathbf{v} + f\,\mathbf{k}\cdot(\mathbf{v}\cdot\nabla)\mathbf{v}$ （$f = 2\Omega\sin\varphi$）

$$= -fw\left(\frac{\partial u}{\partial x} + \frac{\partial v}{\partial y}\right) + f\left(u\frac{\partial w}{\partial x} + v\frac{\partial w}{\partial y}\right)$$

$$\frac{fWU}{L}$$

Term 7 $= \mathbf{v}\cdot(\nabla b \times \mathbf{k}) = u\frac{\partial b}{\partial y} - v\frac{\partial b}{\partial x} = u\frac{g}{\bar{\theta}}\frac{\partial \theta'}{\partial y} - v\frac{g}{\bar{\theta}}\frac{\partial \theta'}{\partial x}$

$$g\frac{\Delta_h \theta}{\Theta}\frac{U}{L}$$

The magnitude of each fundamental scale of the mesoscale motion at mid-latitudes can be taken as $c_p \sim 10^3 J \cdot K^{-1} \cdot kg^{-1}$, $\Theta \sim 3\times 10^2 K$, $H = c_p \Theta / g \sim 10^4 m$, $U \sim 10 m \cdot s^{-1}$, $\theta \sim \Delta_h \Theta \sim 10^0 - 10^1 K$, $\Delta_z \Theta \sim 10^1 K$, $W \sim 10^{-1} - 10^1 m \cdot s^{-1}$, and $f \sim 10^{-4} s^{-1}$.

In general, the pressure gradient in a mesoscale system is larger than that in large-scale systems; however, the main reason for this is that the horizontal and vertical scales of a mesoscale system are different, and the horizontal and vertical changes in pressure are equivalent to those in a large-scale system. This means that we can use the horizontal and vertical changes in a large-scale system to make estimates of the gradients in a mesoscale system. For large-scale motion, the geostrophic relation is $c_p\Theta\frac{\Delta_h\pi}{L}\sim f_0U\sim10^{-3}$, where $L\sim10^6m$. Thus, $\Delta_h\pi\sim10^{-2}$. In a similar way as for the static equilibrium relationship, we can estimate $\Delta_Z\pi\sim10^0m$.

Lilly (1986)[12,24] emphasized that buoyancy has an important effect on the helicity; we therefore divide each term of the helicity equation by $b\zeta$ and then discuss the magnitudes of these terms in different cases.

Case (A) In the case of deep convection $\frac{D_Z}{H}<1$, but not very small, strong vertical motion, for the convergence and divergence of atmosphere and advection of helicity. Whatever the size of the temperature disturbance, generally these two terms are negligible relative to the buoyancy term. In some cases, however, the size of the advection term can be equal to that of the buoyancy term when the horizontal scale is large.

Although, generally speaking, the pressure gradient in a mesoscale system is larger than that in a large-scale system, the main reason for this is that the scales of the horizontal and vertical directions of the system are different. Also, the horizontal and vertical changes in pressure are equivalent to those in a large-scale system, and so these can be estimated from the horizontal and vertical changes in a large-scale system. Therefore, by using the large-scale geostrophic and static equilibrium relationships, we can deduce that, in the case of deep convection, the joint effect of the pressure gradient and vorticity has an important influence on the change in helicity and that this influence is even greater than the buoyancy effect emphasized by Lilly. The effect due to the potential temperature disturbance is far less than that due to the potential temperature except near to fronts.

(B) For shallow convection, $\frac{D_z}{H}\ll1$, and we can obtain the following results by scale analysis.

In the case of shallow convection, the pressure gradient, vorticity, and solenoid term still have an important joint effect on the changes in helicity.

The influence of the uneven horizontal distribution of buoyancy on the helicity in the front area cannot be ignored, and the influence of the transportation of helicity, as well as the divergence and convergence of the atmosphere, on the helicity is greater than in the case of deep convection. The effect of the geostrophic force is only when the vertical motion is very strong and the horizontal scale is large. However, the influence of the potential temperature disturbance is still very small except in the front area.

Based on the above analysis, the simplified helicity equation can be written as

$$\frac{\partial H_e}{\partial t} = c_p u \frac{\partial \bar{\theta}}{\partial z}\frac{\partial \pi'}{\partial y} - c_p v \frac{\partial \bar{\theta}}{\partial z}\frac{\partial \pi'}{\partial x} + c_p \bar{\theta}\frac{\partial \pi'}{\partial x}\frac{\partial v}{\partial z} + c_p \bar{\theta}\frac{\partial \pi'}{\partial y}\frac{\partial u}{\partial z} - c_p \bar{\theta}\frac{\partial \pi'}{\partial z}\zeta + b\zeta \tag{4.4.11}$$

It is not difficult to see from the above formula that the change in helicity is related not only to the current wind field and vorticity but also to the source term of the wind field and vorticity. It is interesting that the helicity reflects the degree of coordination between the vorticity and speed, and the factors affecting the change in helicity can also be said to be quantities that reflect this degree of coordination. When the horizontal wind field and the solenoid term (the vorticity source term), the vorticity and pressure gradient (the wind source term), and the buoyancy (another source term for the vertical wind) work together with the vertical vorticity, this tends to increase the helicity. The first four terms in equation (4.4.10) are related to the horizontal solenoid term, the vorticity, and the pressure gradient, whereas the last two terms are related to the vertical vorticity, buoyancy field, and pressure gradient. The first five terms are larger than the sixth term, which is the buoyancy-effect term.

4.4.2 Discussion

According to the definitions used in vector analysis, the helicity is considered to be a pseudo- scalar.

The three terms on the right-hand side of (4.4.10) have different meanings and are related to the components of the wind speed and vorticity in the *x*-, *y*-, and *z*-directions. These terms may have different motion forms even when their values are the same. Therefore, it is necessary to discuss further how the helicity evolves in different directions during rainstorms and severe convective weather; the relationship between the helicity and the factors that influence it will also be discussed. For convenience, the *x*-, *y*-, and *z*-components of the helicity will be denoted by h_{e1}, h_{e2}, and h_{e3}, respectively.

The horizontal helicity is the product of the horizontal wind speed and the horizontal vorticity. An abnormal positive increase in the horizontal helicity (meaning that the horizontal wind speed and vorticity both have the same sign) can be due to an increase in the horizontal wind speed, an increase in the horizontal vorticity, or an increase in both. This corresponds to an abnormal state of the atmosphere and may be related to parameters that are important in forecasting severe convective storms and, thus, be predictive. On the one hand, an increase in horizontal wind speed can be due to the jet stream, which is often associated with rainstorms. A southwesterly low-level jet can cause strong transport of warm and humid air, strengthen the stratification instability and low-level disturbances, and then trigger unstable energy release. Water-vapor convergence at the left of fronts and cyclonic shear on the left-hand side can generate or increase the vertical vorticity. In such situations, the high-altitude jet can enhance the vertical wind shear and the value of helicity may be reduced, which is conducive to the development of convection and an increase in the horizontal vorticity. On the other hand, the amount of horizontal vorticity is mainly determined by the vertical shear of the horizontal wind field, and the vertical shear of the horizontal wind is an important parameter in the prediction of strong storms as it is closely related to atmospheric instability and strong convection. In addition, and perhaps more importantly, a large horizontal vorticity indicates that the air can form a strong vertical circulation under appropriate conditions and contribute to the maintenance of the vertical circulation. The horizontal vorticity can increase the vertical vorticity by "twisting" the rising convective motion, thus promoting the development of the system. For this reason, the horizontal vorticity can be an important source of vertical vorticity.

In terms of magnitude, the horizontal helicity is larger than the vertical helicity (at least in the early stages of a storm) and, to a large extent, determines the total helicity. Diagnosis and research work have also confirmed this (Li and Shou, 1999; Fei and Tan, 2001; Yang et al., 1994)[22-23,26]. At the same time, the predictability and importance of the horizontal helicity are fully reflected in operational forecasts. Generally, the helicity that is calculated is essentially the horizontal helicity, which ignores the related horizontal helicity of the storm under an uneven horizontal distribution of the vertical motion: $H_e = \int_0^h (\overline{\mathbf{v}}_H - \mathbf{C}) \cdot \boldsymbol{\zeta}_H dz$, where $\overline{\mathbf{v}}_H = (u(z), v(z))$ is the environmental wind, $\mathbf{C} = (C_x + C_y)$ is

the speed of movement of the storm, $\zeta_H = \mathbf{k} \times \frac{d\bar{\mathbf{v}}}{dz}$ is the horizontal vorticity vector, and h is the depth of the layer of air (usually 3 km). In practice, wind sounding data from a single station are often used to calculate the helicity $H_e = \sum_{n=0}^{N-1} (u_{n+1} - C_x)(v_n - C_y) - (u_n - C_x)(v_{n+1} - C_y)$, where $H_e = 150 m^2 \cdot s^{-2}$, is often considered to be the critical value for the genesis and development of a severe convective storm (Davies-Jones et al., 1990)[27].

The vertical helicity is the product of the vertical vorticity and the vertical velocity. Systems with a large vertical vorticity are closely related to severe weather phenomena such as mesocyclones, and so the change in the vertical vorticity has always been a focus of meteorological research and operational forecasting. In addition, the vertical velocity is the most direct cause of weather phenomena in the real atmosphere. There are vortices without vertical upward motion as well as atmospheric divergence and convergence and so cannot produce weather phenomenon; whereas, if there is only vertical upward motion and atmospheric divergence or convergence, the motion will be difficult to maintain, the system will not endure for long, and its impact will be small. Therefore, although the magnitude of the vertical helicity is generally smaller than that of the horizontal helicity and is often ignored when calculating the helicity, in practice, it fully reflects the coordination between two physical quantities closely related to certain weather phenomena. To a certain extent, the vertical helicity not only reflects the degree to which a system can maintain itself but also reflects the development of the system and the severity of the related weather phenomena. Many practical studies (Yang et al., 1994; Wu et al., 1996; Tan and Yang, 2000; Liu and Zeng, 2002)[26,28-30] have shown that the distribution of the vertical helicity matches well with the area of rainfall.

To investigate this topic further, we can consider the component equations (4.4.1) and (4.4.2) that describe the relationship between the horizontal and vertical helicity and their respective functions and then derive the helicity equations in the three directions $\xi = (\zeta_1, \zeta_2, \zeta)$:

$$\frac{\partial H_{e1}}{\partial t} = -(\mathbf{v}\cdot\nabla)H_{e1} - H_{e1}(\frac{\partial v}{\partial y} + \frac{\partial w}{\partial z}) - u(\frac{\partial u}{\partial y}\frac{\partial w}{\partial x} - \frac{\partial u}{\partial z}\frac{\partial v}{\partial x}) + c_p u\frac{\partial \overline{\theta}}{\partial z}\frac{\partial \pi'}{\partial y} -$$
$$c_p\overline{\theta}\zeta_1\frac{\partial \pi'}{\partial x} + u\frac{\partial b}{\partial y} + f(u\frac{\partial u}{\partial z} + \zeta_1 v), \quad (4.4.12)$$

$$\frac{\partial H_{e2}}{\partial t} = -(\mathbf{v}\cdot\nabla)H_{e2} - H_{e2}(\frac{\partial u}{\partial x} + \frac{\partial w}{\partial z}) - v(\frac{\partial v}{\partial z}\frac{\partial u}{\partial y} - \frac{\partial v}{\partial x}\frac{\partial w}{\partial y}) - c_p v\frac{\partial \overline{\theta}}{\partial z}\frac{\partial \pi'}{\partial x} -$$
$$c_p\overline{\theta}\zeta_2\frac{\partial \pi'}{\partial x} - v\frac{\partial b}{\partial x} + f(v\frac{\partial v}{\partial z} - \zeta_2 u), \text{ and} \quad (4.4.13)$$

$$\frac{\partial H_{e3}}{\partial t} = -(\mathbf{v}\cdot\nabla)H_{e3} - H_{e3}(\frac{\partial u}{\partial x} + \frac{\partial v}{\partial y}) - w(\frac{\partial v}{\partial z}\frac{\partial w}{\partial x} - \frac{\partial w}{\partial y}\frac{\partial u}{\partial z}) - c_p\overline{\theta}\zeta\frac{\partial \pi'}{\partial z}$$
$$+b\zeta - f(w\frac{\partial u}{\partial x} + w\frac{\partial v}{\partial y}). \quad (4.4.14)$$

Using the scale analysis that was described earlier, equations (4.4.12)–(4.4.14) can be simplified to

$$\frac{\partial H_{e1}}{\partial t} = c_p u\frac{\partial \overline{\theta}}{\partial z}\frac{\partial \pi'}{\partial y} + c_p\overline{\theta}\frac{\partial v}{\partial z}\frac{\partial \pi'}{\partial x}, \quad (4.4.15)$$

$$\frac{\partial H_{e2}}{\partial t} = -c_p v\frac{\partial \overline{\theta}}{\partial z}\frac{\partial \pi'}{\partial x} - c_p\overline{\theta}\frac{\partial u}{\partial z}\frac{\partial \pi'}{\partial y}, \text{ and} \quad (4.4.16)$$

$$\frac{\partial H_{e3}}{\partial t} = b\zeta - c_p\overline{\theta}\zeta\frac{\partial \pi'}{\partial z}. \quad (4.4.17)$$

It is not difficult to see that the factors that affect the helicity in different directions can be clearly distinguished. In contrast to the simplified helicity equation discussed in Section (4.4.2), the total helicity change is a comprehensive reflection of the helicity change in different directions: the first four factors in the simplified helicity equation, which are related to the solenoid, vorticity, and pressure gradient in the horizontal direction, all appear in the horizontal helicity equation The last two factors in the simplified equation are associated with the vorticity, buoyancy, and pressure fields in the vertical direction. When these factors work together, the horizontal and vertical helicity tend to increase.

From the above equation, it can also be seen that the two main factors that affect the change in the horizontal helicity are related to the horizontal

wind and horizontal vorticity, which make up the horizontal helicity. The two main factors that affect the change in the vertical helicity are related to the vertical vorticity and not directly to the vertical velocity; however, they are all from the vertical motion path. Therefore, the initial vertical vorticity is very important. In addition, as Lilly (1986) emphasized, the buoyancy effect also plays an important role in the growth of the helicity, both by increasing the vertical velocity and by promoting the increase in vertical helicity in combination with the vertical vorticity.

From the above analysis, we can conclude the following. The helicity in the horizontal direction is different from the helicity in the vertical direction. However, these are related to each other and play different roles in rainstorms and severe convective weather. The horizontal helicity is more predictive, indicating the possibility of severe storms; the vertical helicity is more likely to reflect the ability of the system to maintain itself, the development of the system, and the severity of the related weather phenomena. Because the horizontal helicity provides favorable conditions for the formation or growth of the vertical helicity, the effect of the horizontal vortex on the horizontal helicity cannot be ignored. At the same time, the trigger for the vertical motion, the buoyancy effect, and the twisting due to the horizontal helicity all play an important role in the formation and development of the vertical helicity.

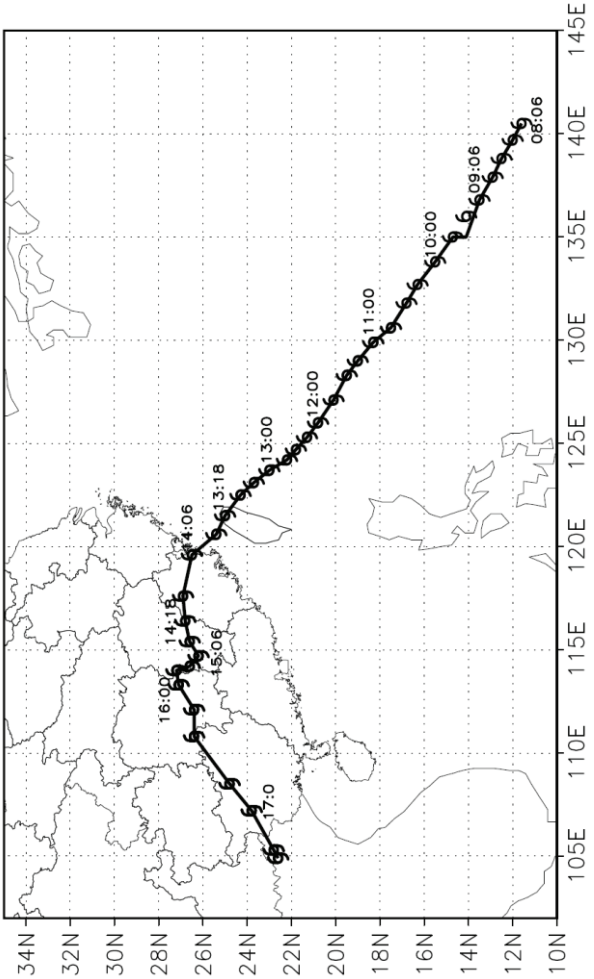

Fig. 4.2.1. Path of typhoon Bilis

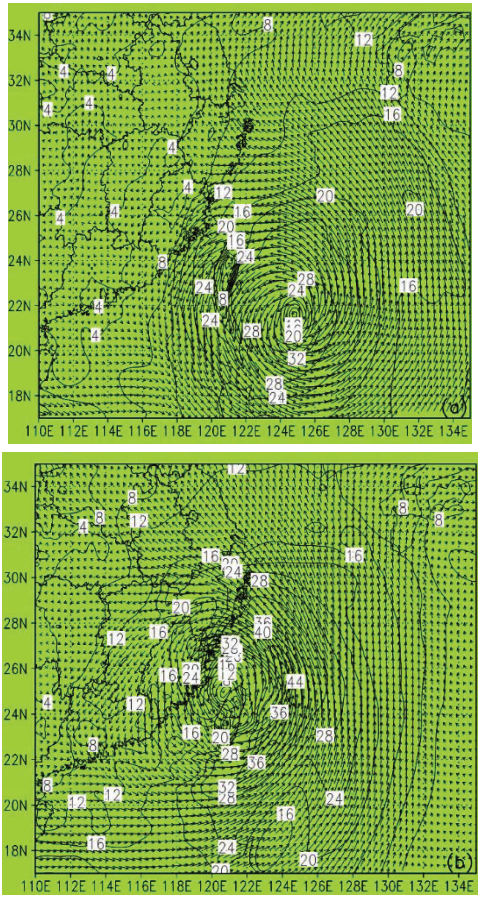

Fig. 4.2.2. Horizontal distribution of winds in typhoon Bilis at 850 hPa at (a) 12:00 on 12 July 2006 and (b) 18:00 on 13 July 2006

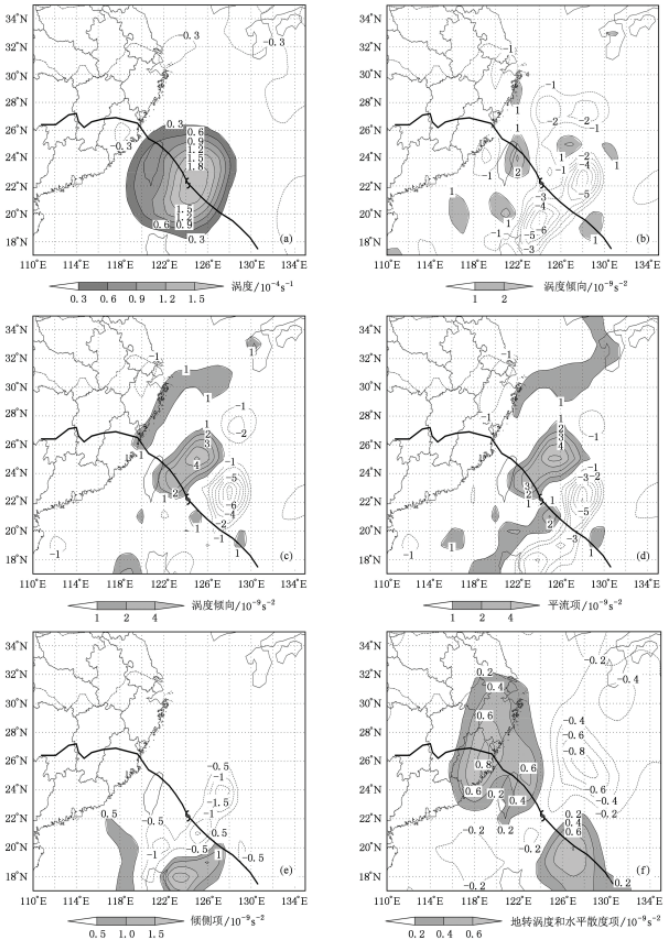

Fig. 4.2.3. Distribution of vorticity and trend in vorticity on the 850-hPa isobaric surface for 18:00 LST on 12 July 2006. The shaded area denotes positive values, the thick line marks the path of typhoon Bilis, and the typhoon symbol indicates the central position of the typhoon: (a) vorticity, (b) vorticity trend calculated using the classical vorticity equation, (c) vorticity trend calculated using the advection vorticity equation, (d) advection term, (e) pitching term, and (f) geostrophic vorticity and water advection term in the advection vorticity equation.

Notes

[1]Vallis G. K. (2006) *Atmospheric and Oceanic Fluid Dynamics: Fundamentals and Large-Scale Circulation*. Cambridge University Press.
[2]Wu G. X. and H. Z. Liu (1999) "Complete form of vertical vorticity tendency equation and slantwise vorticity development," *Acta Meteorogica Sinica,* 57(1):1–15. (in Chinese with English abstract)
[3] Yao X. P., G. X. Wu, Y. M. Liu and et al. (2007) "Case study on the impact of the vortex in the easterlies over the tropical upper troposphere on the subtropical anticyclone over the western Pacific Ocean," *Acta Meteorogica Sinica,* 65(2):198–207. (in Chinese with English abstract)
[4] Zhou Y. and L. Ran (2010) "Advective vorticity equation and its application to the vorticity variation of Typhoon Bilis in 2006," *Acta Physica Sinica*, 59(2):1366–1377.
[5]Davies-Jones R. (1984) "Streamwise vorticity: the origin of updraft rotation in supercell storms," *Journal of Atmospheric Sciences,* 41(20):2991–3006.
[6] Brandes E. A., R. P. Davies-Jones and B. C. Johnson (1988) "Streamwise vorticity effects on supercell morphology and persistence," *Journal of Atmospheric Sciences,* 45(6):947–963.
[7] Markowski P. M., J. M. Straka, E. N. Rasmussen and et al. (1998) "Variability of storm-relative helicity during vortex," *Monthly Weather Review,* 126(11):2959–2971.
[8]Scorer R. S. (1997) *Dynamics of Meteorology and Climate.* Praxis Publishing Ltd.
[9]Gao S. T. and T. Lei (2000) "Streamwise vorticity equation," *Advances in Atmospheric Science,* 17(3):339–347.
[10]Moffatt H. K. (1969) "The degree of knottedness of tangled vortex lines," *Journal of Fluid Mechanics,* 35(1):117–129.
[11]Moffatt H. K. (1981) "Some developments in the theory of turbulence," *Journal of Fluid Mechanics,* 106(1) :27–47.
[12]Lilly D. K. (1986) "The structure, energetics and propagation of rotating convective storms, Part II: Helicity and storm stabilization," *Journal of Atmospheric Sciences,* 43(2):126–140
[13]Etling D. (1985) "Some aspects of helicity in atmosphere flows," *Beiträge zur Physik Der Atmosphäre,* 58(1):88–100.
[14]Wu R. S. and Z. M. Tan (1989) "Conservation laws on generalized vorticity and potential vorticity and its application," *Acta Meteorogica Sinica,* 47(4):436–442.
[15]Wu W. S., D. K. Lilly and R. M. Kerr (1992) "Helicity and thermal convection with shear," *Journal of Atmospheric Sciences,* 49(19) :1800–1809.
[16]Wu R. S. (2002) *Atmospheric Dynamics,* High Education Press.
[17]Tan Z.M. and R. S. Wu (1994) "Helicity dynamics of atmospheric flow," *Advances in Atmospheric Science,* 11(2):175-188
[18]Liu S. K. and S. D. Liu (1997) "Toroidal-poloidal decomposition and Beltrami flows in atmosphere motions," *Chinese Journal of Atmospheric Science,* 21(2):151–160.
[19]Brooks H. E., C. A. Doswell III and R. P. Davies-Jones (1990) "Environmental helicity and the maintenance and evolution of low-level meso-cyclones," the

Tornado: its Structure, Dynamics, Prediction, and Hazards, Geophysics, Monograph, *American Geophysical Union,* 79:97–104.
[20]Brooks H. E. and R. B. Wilhelmson (1990) "The effect of low-level hodograph curvature on supercell structure," *Preprints 16th Conference on Severe Local Storms, Kananaskis Park, Alberta, Canada*, American Meteorological Society, 34–39.
[21]Droegemeier K. K., S. M. Lazarus and R. P. Davies-Jones (1993) "The influence of helicity on numerically simulated convective storms," *Monthly Weather Review,* 121(7):2005–2029.
[22]Li Y. H. and S. W. Shou (1999) "Rotational wind helicity and its effects on torrential rain process," *Transactions of Atmospheric Sciences,* 22(1):95–102.
[23]Fei S. Q. and Z. M. Tan (2001) "On the helicity dynamics of severe convective storms", *Advances in Atmospheric Science,* 18(1):67–86.
[24]Lilly D. K. (1986) "The structure, energetics and propagation of rotating convective storms, Part I: Energy exchange with the mean flow," *Journal of Atmospheric Sciences,* 43(2):113–125.
[25] Lu H. J. and S. T. Gao (2003) "On the helicity and the helicity equation", *Acta Meteorogica Sinica,* 61(6):684-691.
[26]Yang Y. K., Y. L. Liu, Z. S. Wan and *et al.* (1994) "The helicity analysis of Mei-yu front storm rainfall during July 1991," *Acta Meteorogica Sinica,* 52(3):379–384.
[27]Davies-Jones R., D. W. Burgess and M. Foster (1990) "Test of helicity as a forecast parameter," *Preprints 16th Conference on Severe Local Storms, Kananaskis Park, Alberta, Canada*, American Meteorological Society, 588–592.
[28]Wu B. J., C. H. Xu, Y. Y. Liu and et al. (1996) "Applying helicity to analysis of torrential rain over the Changjiang Gorges," Quarterly *Journal of Applied Meteorology,* 7(1):108–112.
[29]Tan Z. H. and X. X. Yang (2000) "Helicity analysis on the torrential rain in Shandong in August 1999," *Meteorological Monthly,* 26(9):7–11.
[30]Liu H. M. and L. Z. Zheng (2002) "Helicity diagnosis and short-time extraordinary area rainfall forecast," *Meteorological Monthly,* 28(10):37–40.

CHAPTER FIVE

DIVERGENCE: INTRODUCTION AND RELATED EQUATIONS

During the summer, China is often affected by torrential rainfall, which leads to floods and mudslides and causes tremendous loss of life and property. Thus, accurate forecasting of torrential rainfall is one of the most important components of operational forecasts during the monsoon season. Torrential rainfall is a mesoscale phenomenon, and its occurrence is intimately associated with the development of mesoscale weather systems. Meteorologists have made many advances through the analysis of vorticity and potential vorticity, but recent observations indicate that the development of torrential rainfall is intimately related to strong convergence in the lower troposphere. Analyzing the evolution of the divergence associated with systems of torrential rainfall enhances the understanding of the physical processes that are responsible for the formation and development of mesoscale torrential rainfall. This chapter, therefore, looks at the concept of divergence and related equations.

5.1 Divergence and the Divergence Equation

5.1.1 Divergence

In fluid mechanics, the divergence is a quantity that is used to measure the expansion or contraction of a volume of fluid and can be written as

$$D = \nabla \cdot \mathbf{v} = \frac{\partial u}{\partial x} + \frac{\partial v}{\partial y} + \frac{\partial w}{\partial z}. \tag{5.1.1}$$

A small cube with sides of length δx, δy, and δz has a volume $\delta x \delta y \delta z$. When the fluid is in motion, the rate of volume expansion per unit volume is called the volume expansivity; i.e.,

$$\text{volume expansivity} = \frac{1}{\delta x \delta y \delta z} \frac{d}{dt}(\delta x \delta y \delta z) \ . \tag{5.1.2}$$

Equation (5.1.2) can be simplified as

$$\text{volume expansivity} = \frac{\delta}{\delta x}\frac{dx}{dt} + \frac{\delta}{\delta y}\frac{dy}{dt} + \frac{\delta}{\delta z}\frac{dz}{dt}$$

$$= \frac{\delta u}{\delta x} + \frac{\delta v}{\delta y} + \frac{\delta v}{\delta z} = \nabla \cdot \mathbf{v} . \tag{5.1.3}$$

Thus, the divergence of a fluid is the rate of expansion or contraction of a unit volume of the fluid.

5.1.2 Divergence Equation

The quasi-hydrostatic approximation is valid for mesoscale and large-scale motions with lengths of over 100 km. The horizontal momentum equation can be expressed as

$$\frac{\partial \mathbf{v}_h}{\partial t} + (\mathbf{v}_h \cdot \nabla_h)\mathbf{v}_h + \omega\frac{\partial \mathbf{v}_h}{\partial p} - f\,\mathbf{v}_h \times \mathbf{k} = -\nabla_h \varphi , \tag{5.1.4}$$

where $\mathbf{v}_h$ is a two-dimensional wind vector and ∇_h is the two-dimensional derivative operator $\nabla_h = \frac{\partial}{\partial x}\mathbf{i} + \frac{\partial}{\partial y}\mathbf{j}$. With the following derivative calculation of vector:

$$(\mathbf{v}_h \cdot \nabla_h)\mathbf{v}_h = \nabla_h\left(\frac{\mathbf{v}_h \cdot \mathbf{v}_h}{2}\right) - \mathbf{v}_h \times \nabla_h \times \mathbf{v}_h \tag{5.1.5}$$

and substituting (5.1.5) into (5.1.4) gives

$$\frac{\partial \mathbf{v}_h}{\partial t} + \omega\frac{\partial \mathbf{v}_h}{\partial p} - (f + \zeta)\mathbf{v}_h \times \mathbf{k} = -\nabla_h\left(\varphi + \frac{\mathbf{v}_h \cdot \mathbf{v}_h}{2}\right), \tag{5.1.6}$$

where $\zeta = \mathbf{k} \cdot \nabla_h \times \mathbf{v}_h$ is the vertical component of the vorticity. The use of $\nabla \cdot (5.1.6)$ then gives

$$\frac{\partial(\nabla_h \cdot \mathbf{v}_h)}{\partial t} + \nabla_h \cdot (\omega\frac{\partial \mathbf{v}_h}{\partial p}) - \nabla_h \cdot (f + \zeta)\mathbf{v}_h \times \mathbf{k} = -\nabla_h^2\left(\varphi + \frac{\mathbf{v}_h \cdot \mathbf{v}_h}{2}\right), \tag{5.1.7}$$

where $\delta = \nabla_h \cdot \mathbf{v}_h$ is the horizontal divergence and $E_{pe} = \varphi + \frac{\mathbf{v}_h \cdot \mathbf{v}_h}{2}$ is the pressure energy. Equation (5.1.7) then becomes

$$\frac{\partial \delta}{\partial t} = -\nabla_h \omega \cdot \frac{\partial \mathbf{v}_h}{\partial p} - \omega \cdot \frac{\partial \delta}{\partial p} + \mathbf{k} \cdot [\nabla_h \times (f + \zeta) \mathbf{v}_h] - \nabla_h^2 E_{pe} . \tag{5.1.8}$$

This is a typical two-dimensional divergence equation. The equation shows that the change in divergence is mainly associated with the mass and wind fields. The thermodynamic factors are not considered here, which constitutes a weakness in the divergence equation. It is difficult to use this equation directly to analyze the impacts of atmospheric thermodynamics and thermal stratification on the divergence. Chen et al. (2009)[1] derived a new two-dimensional divergence equation that included an equivalent potential temperature term. However, the derivation of this equation is rather complex.

Here, we derive a simple form of the three-dimensional divergence equation that includes thermodynamic effects. It is better to use Cartesian coordinates rather than polar coordinates for studying mesoscale motion. In Cartesian coordinates, the vertical momentum equation can be written

$$\frac{\partial \mathbf{v}}{\partial t} + (\mathbf{v} \cdot \nabla) \mathbf{v} - f \mathbf{v} \times \mathbf{k} = -\nabla \varphi + T \nabla S - \nabla H , \tag{5.1.9}$$

where $\mathbf{v}$ is a three-dimensional wind vector, ∇ is the three-dimensional derivative operator, $\nabla = \frac{\partial}{\partial x}\mathbf{i} + \frac{\partial}{\partial y}\mathbf{j} + \frac{\partial}{\partial z}\mathbf{k}$, and S and H are the entropy and enthalpy, respectively.

Substituting $(\mathbf{v} \cdot \nabla) \mathbf{v} = \nabla(\frac{\mathbf{v} \cdot \mathbf{v}}{2}) - \mathbf{v} \times \nabla \times \mathbf{v}$ into (5.1.9) yields

$$\frac{\partial \mathbf{v}}{\partial t} - f \mathbf{v} \times \mathbf{k} - \mathbf{v} \times \boldsymbol{\xi} = T \nabla S - \nabla H - \nabla(\varphi + \frac{\mathbf{v} \cdot \mathbf{v}}{2}) , \tag{5.1.10}$$

where $\boldsymbol{\xi} = \nabla \times \mathbf{v}$ is a three-dimensional vorticity vector. Taking $\nabla \cdot (5.1.10)$ we obtain

$$\frac{\partial (\nabla \cdot \mathbf{v})}{\partial t} - \nabla \cdot (f \mathbf{v} \times \mathbf{k}) - \nabla \cdot (\mathbf{v} \times \boldsymbol{\xi}) = \nabla \cdot (T \nabla S - \nabla H) - \nabla^2 (\varphi + \frac{\mathbf{v} \cdot \mathbf{v}}{2}) , \tag{5.1.11}$$

where $D = \nabla \cdot \mathbf{v}$ is the divergence, $E_{pe} = \varphi + \frac{\mathbf{v} \cdot \mathbf{v}}{2}$ is the pressure energy, and

$$\nabla \cdot (\mathbf{a} \times \mathbf{b}) = \mathbf{b} \cdot (\nabla \times \mathbf{a}) - \mathbf{a} \cdot (\nabla \times \mathbf{b}) . \tag{5.1.12}$$

a and **b** are vectors, and (5.1.11) becomes

$$\frac{\partial D}{\partial t} = f\zeta - \boldsymbol{\xi}^2 + \mathbf{v}\cdot(\nabla\times\boldsymbol{\xi}) + \nabla^2 E_{pe} - \nabla\cdot(T\nabla S - \nabla H) \quad (5.1.13)$$

Equation (5.1.13) includes thermodynamic effects in the form of the entropy and enthalpy.

5.2 Potential Divergence

When considering the effects of divergence, the potential divergence is defined as the projection of the vorticity vector of the horizontal wind vector rotated by 90° on the gradient of to the generalized potential temperature. The density of the wave activity related to the potential divergence is considered to be a second-order perturbation of the potential divergence, which represents transport of perturbed heat and is associated with the development of potential stability. The relevant definitions and applications are discussed in the following (Ran et al., 2013)[2].

5.2.1 Potential Divergence and the Equation for the Wave-activity Density of the Potential Divergence

The moist potential vorticity is an important physical quantity that has been widely applied in studies of various weather phenomena. In local Cartesian coordinates, it can be written as

$$q^* = -\frac{\partial v}{\partial z}\frac{\partial \theta^*}{\partial x} + \frac{\partial u}{\partial z}\frac{\partial \theta^*}{\partial y} + \left(\frac{\partial v}{\partial x} - \frac{\partial u}{\partial y} + f\right)\frac{\partial \theta^*}{\partial z}, \quad (5.2.1)$$

where θ^* is the generalized potential temperature. Tao et al. (2012)[3] showed that the potential vorticity mainly represents the coupling effect of the vorticity and potential stability. As with the vorticity, the potential divergence is introduced to reflect the dynamic nature of the horizontal divergence during torrential rainfall. The potential divergence is given by

$$M^* = -\left(\frac{\partial u}{\partial z}\frac{\partial \theta^*}{\partial x} + \frac{\partial v}{\partial z}\frac{\partial \theta^*}{\partial y}\right) + \left(\frac{\partial u}{\partial x} + \frac{\partial v}{\partial y}\right)\frac{\partial \theta^*}{\partial z}. \quad (5.2.2)$$

Although the definitions of q^* and M^* are similar, their physical meanings are different. Equation (5.2.2) can be rewritten as

$$M^* = \left[\nabla\times\left(\mathbf{v}_h\times\mathbf{k}\right)\right]\cdot\nabla\theta^*, \quad (5.2.3)$$

where $\mathbf{v}_h = (u, v, 0)$ is the horizontal wind speed. M^* denotes the projection of the vorticity vector of the horizontal wind vector rotated by 90° on the gradient of the generalized potential temperature, whereas q^* represents the projection of the vorticity of the horizontal wind vector on the gradient of the generalized potential temperature. q^* represents the dynamic nature of the vertical relative vorticity, $(\frac{\partial v}{\partial x} - \frac{\partial u}{\partial y})$, whereas M^* reflects the dynamic effects of the horizontal divergence $(\frac{\partial u}{\partial x} + \frac{\partial v}{\partial y})$.

M^* can be partitioned into three parts: the basic state, first-order perturbation, and second-order perturbation.

$$M^* = M_0 + M_e + A,$$

where

$$M_0 = [\nabla \times (\mathbf{v}_{0h} \times \mathbf{k})] \cdot \nabla \theta_0^*, \tag{5.2.4}$$

$$M_e = [\nabla \times (\mathbf{v}_{0h} \times \mathbf{k})] \cdot \nabla \theta_e^* + [\nabla \times (\mathbf{v}_{eh} \times \mathbf{k})] \cdot \nabla \theta_0^* \text{,and} \tag{5.2.5}$$

$$A = [\nabla \times (\mathbf{v}_{eh} \times \mathbf{k})] \cdot \nabla \theta_e^*. \tag{5.2.6}$$

Here, the subscript "$_0$" denotes the basic state, and "$_e$" denotes the perturbation. M_0 describes the large-scale dynamic and thermodynamic characteristics, whereas M_e contains large-scale and mesoscale information. A is a second-order perturbation and denotes the perturbed energy and coupling effects due to the vertical shear of the horizontal wind, the perturbed divergence, and the perturbed gradient of the generalized potential temperature. A is defined as the wave-activity density of the potential divergence (or simply the wave-activity density). Since this book focuses on mesoscale disturbances, we focus attention on A in the discussions that follow.

Equation (5.2.6) can be also written as

$$A = \frac{\partial}{\partial x}(u_e \frac{\partial \theta_e^*}{\partial z}) + \frac{\partial}{\partial y}(v_e \frac{\partial \theta_e^*}{\partial z}) - \frac{\partial}{\partial z}(u_e \frac{\partial \theta_e^*}{\partial x} + v_e \frac{\partial \theta_e^*}{\partial y}). \tag{5.2.7}$$

The first two terms on the right-hand side of (5.2.7) are the horizontal flux divergence, which represents the thermodynamic characteristics (the vertical gradient of the generalized potential temperature perturbation); the third term denotes the vertical gradient of the perturbed horizontal advection of the perturbation heat.

Taking the derivative of (5.2.7) with respect to time gives

$$\frac{\partial A}{\partial t} = -\frac{\partial}{\partial x}\left(\frac{\partial \theta_e^*}{\partial t}\frac{\partial u_e}{\partial z} + \theta_e^* \frac{\partial^2 u_e}{\partial z \partial t}\right) - \frac{\partial}{\partial y}\left(\frac{\partial \theta_e^*}{\partial t}\frac{\partial v_e}{\partial z} + \theta_e^* \frac{\partial^2 v_e}{\partial z \partial t}\right) + \frac{\partial}{\partial z}\left[\frac{\partial \theta_e^*}{\partial t}\left(\frac{\partial u_e}{\partial x} + \frac{\partial v_e}{\partial y}\right) + \theta_e^*\left(\frac{\partial^2 u_e}{\partial x \partial t} + \frac{\partial^2 v_e}{\partial y \partial t}\right)\right] \quad . \tag{5.2.8}$$

The linearization of the basic equations of atmospheric motion in local Cartesian coordinates using the perturbation method yields

$$\frac{\partial u_e}{\partial t} = -\mathbf{v}_e \cdot \nabla u_0 - \mathbf{v}_0 \cdot \nabla u_e + f v_{ae}, \tag{5.2.9}$$

$$\frac{\partial v_e}{\partial t} = -\mathbf{v}_e \cdot \nabla v_0 - \mathbf{v}_0 \cdot \nabla v_e - f u_{ae}, \tag{5.2.10}$$

$$\frac{\partial \theta_e^*}{\partial t} = -\mathbf{v}_e \cdot \nabla \theta_0^* - \mathbf{v}_0 \cdot \nabla \theta_e^* + S_{\theta^*}, \tag{5.2.11}$$

where $\mathbf{v}_e = (u_e, v_e, w_e)$, $\mathbf{v}_0 = (u_0, v_0, w_0)$, and $\mathbf{v}_{ae} = (u_{ae}, v_{ae}, 0)$.

Eliminating the local change term on the right-hand side of (5.2.8) and using (5.2.9)–(5.2.11) to construct the divergence form of the equation for the wave-activity density gives

$$\frac{\partial A}{\partial t} = \nabla \cdot \mathbf{F}_1 + \nabla \cdot \mathbf{F}_2 + \nabla \cdot \mathbf{F}_e + \nabla \cdot [S_{\theta_e^*} \nabla \times (\mathbf{k} \times \mathbf{v}_{he})], \tag{5.2.12}$$

where

$$\mathbf{F}_1 = f \mathbf{v}_{ae} \times \nabla \theta_e^*, \tag{5.2.13}$$

$$\mathbf{F}_2 = \begin{pmatrix} \left[\left(u_0\frac{\partial\theta_e^*}{\partial x}+v_0\frac{\partial\theta_e^*}{\partial y}+u_e\frac{\partial\theta_0^*}{\partial x}+v_e\frac{\partial\theta_0^*}{\partial y}\right)\frac{\partial u_e}{\partial z}-\left(u_0\frac{\partial u_e}{\partial x}+v_0\frac{\partial u_e}{\partial y}+u_e\frac{\partial u_0}{\partial x}+v_e\frac{\partial u_0}{\partial y}\right)\frac{\partial\theta_e^*}{\partial z}\right] \\ \left[\left(u_0\frac{\partial\theta_e^*}{\partial x}+v_0\frac{\partial\theta_e^*}{\partial y}+u_e\frac{\partial\theta_0^*}{\partial x}+v_e\frac{\partial\theta_0^*}{\partial y}\right)\frac{\partial v_e}{\partial z}-\left(u_0\frac{\partial v_e}{\partial x}+v_0\frac{\partial v_e}{\partial y}+u_e\frac{\partial v_0}{\partial x}+v_e\frac{\partial v_0}{\partial y}\right)\frac{\partial\theta_e^*}{\partial z}\right] \\ \left[\left(v_0\frac{\partial u_e}{\partial y}+w_0\frac{\partial u_e}{\partial z}+v_e\frac{\partial u_0}{\partial y}+w_e\frac{\partial u_0}{\partial z}\right)\frac{\partial\theta_e^*}{\partial x}+\left(u_0\frac{\partial v_e}{\partial x}+w_0\frac{\partial v_e}{\partial z}+u_e\frac{\partial v_0}{\partial x}+w_e\frac{\partial v_0}{\partial z}\right)\frac{\partial\theta_e^*}{\partial y}-\right. \\ \left.\left(v_0\frac{\partial\theta_e^*}{\partial y}+w_0\frac{\partial\theta_e^*}{\partial z}+v_e\frac{\partial\theta_0^*}{\partial y}+w_e\frac{\partial\theta_0^*}{\partial z}\right)\frac{\partial u_e}{\partial x}-\left(u_0\frac{\partial\theta_e^*}{\partial x}+w_0\frac{\partial\theta_e^*}{\partial z}+u_e\frac{\partial\theta_0^*}{\partial x}+w_e\frac{\partial\theta_0^*}{\partial z}\right)\frac{\partial v_e}{\partial y}\right] \end{pmatrix} \tag{5.2.14}$$

$$\mathbf{F}_e = \mathbf{F}_{eD} + \mathbf{F}_{eT}, \tag{5.2.15}$$

$$\mathbf{F}_{eD} = \begin{pmatrix} w_e\frac{\partial u_e}{\partial z}\frac{\partial\theta_0^*}{\partial z} \\ w_e\frac{\partial v_e}{\partial z}\frac{\partial\theta_0^*}{\partial z} \\ -u_e\frac{\partial u_e}{\partial x}\frac{\partial\theta_0^*}{\partial x}-v_e\frac{\partial v_e}{\partial y}\frac{\partial\theta_0^*}{\partial y} \end{pmatrix}, \text{ and} \tag{5.2.16}$$

$$\mathbf{F}_{eT} = \begin{pmatrix} -w_e\frac{\partial\theta_e^*}{\partial z}\frac{\partial u_0}{\partial z} \\ -w_e\frac{\partial\theta_e^*}{\partial z}\frac{\partial v_0}{\partial z} \\ u_e\frac{\partial\theta_e^*}{\partial x}\frac{\partial u_0}{\partial x}+v_e\frac{\partial\theta_e^*}{\partial y}\frac{\partial v_0}{\partial y} \end{pmatrix}. \tag{5.2.17}$$

The left-hand side of (5.2.12) is the local change in A, the first three terms on the right-hand side of the equation represent the divergence of the second-order perturbation flux, and the fourth term is the source or sink of A. Since A denotes the perturbation energy, (5.2.12) describes the evolution of the perturbation energy. Equation (5.2.12) can only be applied to the study of perturbations with small amplitudes since the small-perturbation method is used to derive it.

5.2.2 Application of the Potential Divergence

In the following, the concept of potential divergence is applied to an analysis of Typhoon Morakot. Tropical storm Morakot formed over the northwest Pacific in the early morning of 4 August 2009 and strengthened into a typhoon on 5 August. The typhoon first made landfall at Hualian, Taiwan at 23:45 BT (Beijing time) on 7 August and made a second landfall at Xiapu, Fujian at 16:20 BT on 9 August. Morakot weakened to a tropical storm on 10 August and dissipated at 02:00 BT on 12 August. Morakot produced torrential rainfall in many cities across China; this led to severe floods, particularly in Zhejiang and Fujian provinces.

At 18:00 UTC on 7 August, as Morakot made landfall on Taiwan, its western eye wall was located over the Taiwan Strait. Light rain occurred over the coasts of Zhejiang and Fujian. This rainfall was associated with low values of wave-activity density, representing the weak transport of perturbation heat. At 18:00 UTC on 8 August, Morakot moved out over the Taiwan Strait, and its western eye wall then covered the coast of southeastern China. The rainfall was increasing at this stage.

The evolution of the rainfall and wave-activity density (Figure 5.2.1) shows that the areas of high rainfall and high values of $\langle |A| \rangle$ over China (north of 25°N) were similar and both were moving northward; their centers also coincided, which indicates that there was significant transport of perturbation heat. Due to the lack of observational data, however, the areas of rainfall and high values of wave-activity density do not show any consistency.

In order to analyze the major factors that are responsible for the evolution of the wave-activity density, the activity flux divergence, $\nabla \cdot \mathbf{F} = \nabla \cdot \mathbf{F}_1 + \nabla \cdot \mathbf{F}_2 + \nabla \cdot \mathbf{F}_e$, is calculated here. As shown in Figure 5.2.2, at 18:00 UTC on 7 August, the anomalies in the wave-activity density were mainly located in the middle and lower troposphere; these anomalies correspond to local changes in the wave-activity density caused by the wave-activity flux divergence after the landfall of Morakot at Hualian, Taiwan. The typhoon center moved over the Taiwan Strait at 18:00 UTC on 8 August. The divergence maintained its strength within the area of rainfall, implying that there was some development of the wave-activity density. After the second landfall at 18:00 UTC on 9 August, the anomalies in the wave-activity flux divergence moved to the north of the area of heavy rain and their values decreased, suggesting a weakening of the wave-activity density. Note that the sign of the wave-activity density also changed. Thus, whether the divergence（$\nabla \cdot \mathbf{F} > \mathbf{0}$）or convergence

（$\nabla \cdot \mathbf{F} < \mathbf{0}$）of the wave-activity flux enhances or suppresses the development of a disturbance depends on the sign of the wave-activity density.

As shown in Figure 5.2.3, the wave-activity flux divergence increased rapidly after the typhoon made landfall at Hualian, Taiwan at 12:00 UTC on 7 August, reached a second maximum at 12:00 UTC on 8 August, and then decreased. At 00:00 UTC on 9 August, the divergence was increasing again and reached its maximum at 06:00 on 9 August. It decreased again after the second landfall of the typhoon. The maximum value of the potential vorticity term of the perturbation ageostrophic wind, $\left\langle \left| \nabla \cdot \mathbf{F}_1 \right| \right\rangle$, was larger than the term representing the coupling of the first-order perturbation advection and the perturbation shear, $\left\langle \left| \nabla \cdot \mathbf{F}_2 \right| \right\rangle$, and also larger than the term representing the coupling of the second-order perturbation advection and the shear of the basic state, $\left\langle \left| \nabla \cdot \mathbf{F}_e \right| \right\rangle$. Thus, the potential vorticity term of the perturbation ageostrophic wind is a major forcing term for the wave-activity density. The coupling term for the first-order perturbation advection and perturbation shear is next in terms of its effect, and the coupling term for the second-order perturbation advection and the shear of the basic state is the least important.

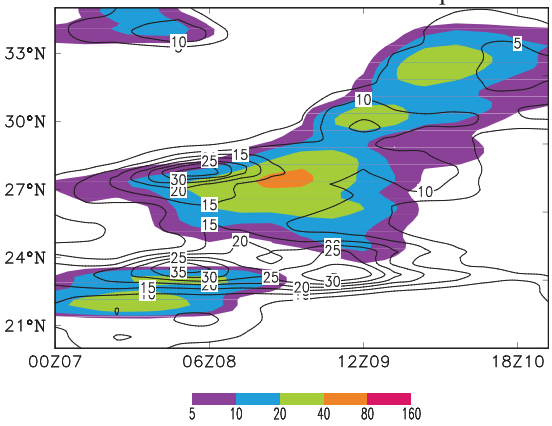

Fig. 5.2.1. Meridional–temporal cross-section of the wave-activity density, $\left\langle \left| A \right| \right\rangle$, along the 120°E meridian (contour spacing: 10^{-5} K s^{-2}). The shadow area in the background denote the six-hour cumulative observed rainfall amount (mm).

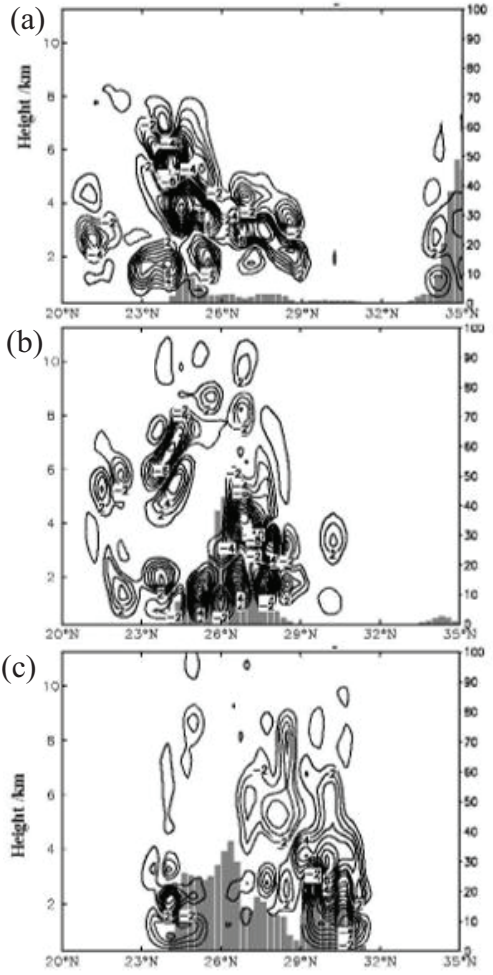

Fig. 5.2.2. Meridional–vertical cross-section of the wave-activity flux divergence, $\nabla \cdot \mathbf{F}$, along the 119°E meridian (contour spacing: 10^{-11} K m^{-1} s^{-2}) at: (a) 18:00 UTC, 7 August, (b) 18:00 UTC, 8 August, and (c) 18:00 UTC, 9 August 2009. The gray bars denote the six-hour cumulative observed rainfall amount (mm).

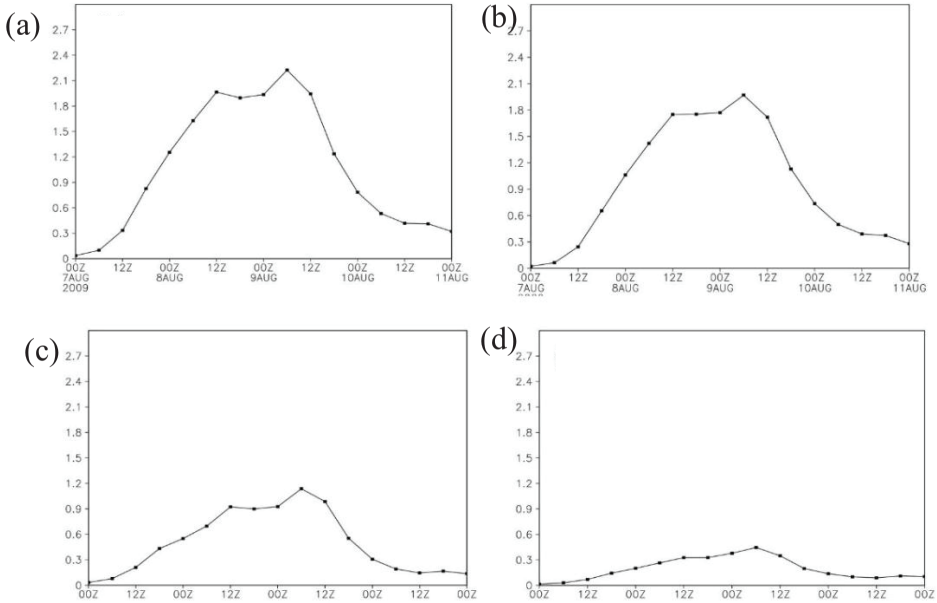

Fig. 5.2.3. The ti me evolution of: (a) $\left\langle \left| \nabla \cdot \mathbf{F} \right| \right\rangle$, (b) $\left\langle \left| \nabla \cdot \mathbf{F}_1 \right| \right\rangle$, (c) $\left\langle \left| \nabla \cdot \mathbf{F}_2 \right| \right\rangle$, and (d) $\left\langle \left| \nabla \cdot \mathbf{F}_e \right| \right\rangle$. Units: 10^{-7} K s^{-2}, at the center region of the typhoon morakot.

Notes

[1]Chen Z. M., K. Q. Yang and H. Y. Wu (2009) "Mechanism of heavy rainfall maintenance and increment in convergence excited by coupling forces between dynamic and thermodynamic fields," *Acta Physica Sinica,* 58(6):4362-4371.

[2]Ran L. K., L. Liu, N. Li and *et al.* (2013) "The analysis of the potential-divergence wave activity density and its application to typhoon precipitation," *Chinese Journal of Geophysics,* 56(10):3285-3301.

[3]Tao Z. Y., X. G. Zhou and Y. G. Zheng (2012) "Vorticity, potential vorticity and stratospheric dry intrusion: origin, application and misuse of potential vorticity concept," *Meteorological Monthly,* 38(1):28-40.

CHAPTER SIX

DEFORMATION: INTRODUCTION AND RELATED EQUATIONS

Among the basic variables that describe the atmosphere, namely, temperature, pressure, humidity, and wind velocity, only the wind velocity is a vector quantity. At the mesoscale, where the characteristic scale is less than the Rossby radius of the deformation, it is known that the wind field determines the mass field through geostrophic adjustment (Rossby, 1937, 1938; Yeh, 1957; Yeh and Li, 1982; Zeng, 1963 (a), (b), and (c))[1-7]. At the even smaller scale of convective storms, the importance of the wind field is even more evident, and it is known that the environmental wind profile has a strong effect on the storm type (Weisman and Klemp, 1982)[8] and storm dynamics (e.g., Fernandez and Thorpe, 1979)[9].

The importance of the wind field has been recognized by many researchers. Petterssen (1956)[10] showed that a 2D linear wind field could be expressed as a combination of the translation, divergence, deformation, and vorticity components. Other researchers, including Wiin-Nielsen (1973)[11] have also discussed these characteristics of wind fields in some detail. Traditionally, the divergence and vorticity are the two quantities that have received the most attention. The prognostic equations for vorticity and divergence derived from the equations of motion have been used extensively in the literature as well as in textbooks for studying dynamics of fluid flows and various atmospheric phenomena. The deformation has, in comparison, received much less attention, except in studies of frontogenesis. For certain types of precipitation systems, such as those associated with the "meiyu" front in eastern China, the large-scale flow pattern often exhibits a dominant deformation pattern at low levels, whereas the divergence and vorticity may have smaller magnitudes. For these types of systems, it is important to understand the role of the deformation in triggering and maintaining the precipitation, and in order to gain insight into the evolution of the deformation field with time. In order to gain some insight into this, in this chapter, the equation for the deformation trend will be derived and discussed.

In meteorology, the deformation is considered mainly in relation to the

process of frontogenesis (Petterssen, 1956; Yang et al., 2014; Yang et al., 2015)[10,12-13] However, a large number of observations and clear, simple theories show that the deformation also plays important roles in other physical processes such as storm-track dynamics, the formation and maintenance of the moat structure in tropical cyclones, symmetric instability, and the onset of blocking (e.g., Whitaker and Dole, 1995; Elhmaidi et al., 2004; Rivière and Joly, 2006 (a) and (b); Wang, 2008; Gao et al., 2008; Thomas, 2012; Moon and Nolan, 2015)[14-21]. In this chapter, another important aspect that will be discussed is the role of the deformation in the development of disturbance or vortices. This has been the subject of many studies. Based on the traditional exponential growth problem of normal modes (Charney, 1947; Eady, 1949; Kuo, 1949)[22-24], Farrell (1989)[25] demonstrated that, although the deformational flow does not support any exponentially growing solution, a disturbance embedded in the deformational flow undergoes transient development. Mak and Cai (1989)[26] obtained a general condition for the stability of a perturbation embedded in a non-divergent 2D barotropic flow. It was stated that "to optimally extract (kinetic) energy from the basic flow, a perturbation must be elongated locally along the axis of contraction of the basic deformation field". (This was given a physical interpretation by Cai (1992)[27].) In addition, Cai and Mak (1990)[28] derived a complete set of energy equations for local perturbations in a zonally inhomogeneous baroclinic jet streak as part of a two-layer, quasi-geostrophic beta-plane channel model (equations (10)–(13) in Cai and Mak (1990)[28]). Using these equations, Mak (1991)[29] verified the "eddy straining" mechanism proposed by Shutts (1983)[30], which argues that, due to the impact of the deformation, a transient eddy is stretched in the north–south direction and compressed in the zonal direction, causing transfer of momentum and energy to the blocking flow and stimulating the onset of blocking. As well as discussing the perturbation growth mode within the deformation field, Weiss (1991)[31] obtained a condition necessary for an increase in the vorticity gradient (the Okubo–Weiss condition) that explained the vortex filament phenomenon by using the conserved vertical vorticity equation in a barotropic and non-divergent atmosphere. According to this condition, the vertical vorticity gradient increases when the size of the square of the deformation is larger than the square of the vorticity and changes periodically when the square of the vorticity is larger than the square of the deformation. This theory was used to explain the mechanism behind the moat structure in tropical cyclones by Rozoff et al. (2006)[32] and Wang (2008)[18].

While most of the research described above is concerned with the deformation of a barotropic atmosphere, the relation between the

deformation and disturbances in a baroclinic atmosphere has also received great attention. Bishop and Thorpe (1994 (a) and (b))[33-34] indicated that the deformation has a key influence on the unstable development of frontal waves but may simultaneously suppress these waves. Renfrew et al. (1997)[35] argued that the magnitude of the stretching of the environmental flow (Bishop, 1996 (a) and (b))[36-37] is crucial to frontal stability. Wang and Wu (2001)[38] found that a symmetric disturbance tends to develop under the ascending flow of the transverse circulation caused by deformational frontogenesis. Using a two-dimensional shallow-water model, Jiang et al. (2011)[39-40] investigated the formation and evolution of a meso-β-scale low vortex embedded in the deformational flow. In addition, these authors proposed an index that described the interaction between the vortex and the deformational flow. This index was shown to be able to indicate the direction of the short-term movement of a tropical cyclone. These investigations provide a significant insight into vortex development in a baroclinic atmosphere and imply that the deformation plays an important role in the evolution of baroclinic vortices. In the following, based on these theories, the impact of the deformation on vortex development will be discussed.

6.1 The Total Deformation and the Equation for the Trend in the Total Deformation

6.1.1 The Total Deformation

Petterssen (1956)[10] applied the Taylor expansion to the horizontal wind (u,v) and obtained the following equations by retaining the first-order approximation:

$$u = u_0 + \frac{1}{2}(\delta + F_{st})x + \frac{1}{2}(F_{sh} - \zeta)y \tag{6.1.1}$$

$$v = v_0 + \frac{1}{2}(F_{sh} + \zeta)x + \frac{1}{2}(\delta - F_{st})y\,. \tag{6.1.2}$$

Here, u_0 and v_0 are the wind velocities in the origin of coordinate system, $\delta = \frac{\partial u}{\partial x} + \frac{\partial v}{\partial y}$ is the horizontal divergence, $\zeta = \frac{\partial v}{\partial x} - \frac{\partial u}{\partial y}$ is the vertical vorticity, $E_{st} = \frac{\partial u}{\partial x} - \frac{\partial v}{\partial y}$ is the stretching deformation, and

$E_{sh} = (\frac{\partial v}{\partial x} + \frac{\partial u}{\partial y})$ is the shearing deformation. $E = \sqrt{E_{st}{}^2 + E_{sh}{}^2}$ is the total deformation (Petterssen, 1956; Keyser et al., 1986, 1988)[10,41-42] Rotating the coordinates (x, y) counterclockwise by an angle θ gives the new coordinates (x', y'). The relations for the coordinate transformation are $x' = x\cos\theta + y\sin\theta$, $y' = y\cos\theta - x\sin\theta$, $x = x'\cos\theta - y'\sin\theta$, and $y = x'\sin\theta + y'\cos\theta$. Using these relations, we obtain $u = u'\cos\theta - v'\sin\theta$ and $v = u'\sin\theta + v'\cos\theta$. Therefore,

$$\begin{pmatrix} \frac{\partial u}{\partial x} \\ \frac{\partial v}{\partial y} \end{pmatrix} = \begin{pmatrix} (\frac{\partial u'}{\partial x'}\cdot\cos\theta - \frac{\partial v'}{\partial x'}\sin\theta)\cos\theta + (\frac{\partial u'}{\partial y'}\cdot\cos\theta - \frac{\partial v'}{\partial y'}\sin\theta)\cdot(-\sin\theta) \\ (\frac{\partial u'}{\partial x'}\cdot\sin\theta + \frac{\partial v'}{\partial x'}\cos\theta)\sin\theta + (\frac{\partial u'}{\partial y'}\cdot\sin\theta + \frac{\partial v'}{\partial y'}\cos\theta)\cdot\cos\theta \end{pmatrix}, \tag{6.1.3}$$

and the following expressions can be derived:

$$\begin{aligned} E_{st} &= \frac{\partial u}{\partial x} - \frac{\partial v}{\partial y} = (\frac{\partial u'}{\partial x'} - \frac{\partial v'}{\partial y'})\cos 2\theta - (\frac{\partial v'}{\partial x'} + \frac{\partial u'}{\partial y'})\sin 2\theta \quad \text{and} \\ &= E'_{st}\cos 2\theta - E'_{sh}\sin 2\theta \end{aligned} \tag{6.1.4}$$

$$\begin{aligned} E_{sh} &= \frac{\partial v}{\partial x} + \frac{\partial u}{\partial y} = (\frac{\partial u'}{\partial x'} - \frac{\partial v'}{\partial y'})\sin 2\theta + (\frac{\partial v'}{\partial x'} + \frac{\partial u'}{\partial y'})\cos 2\theta \quad . \\ &= E'_{st}\sin 2\theta + E'_{sh}\cos 2\theta \end{aligned} \tag{6.1.5}$$

Therefore, we can obtain $E^2 = E_{st}^2 + E_{sh}^2 = E'^2_{st} + E'^2_{sh}$, where E'_{st} and E'_{sh} are, respectively, the stretching deformation and shearing deformation in the rotated coordinates. This indicates that the total deformation does not change with the coordinate rotation.

6.1.2 Equation for the deformation trend

In this section, we will derive the equation for the trend in the total deformation for horizontal motion in pressure coordinates. We have

$$\frac{\partial u}{\partial t}+u\frac{\partial u}{\partial x}+v\frac{\partial u}{\partial y}+\omega\frac{\partial u}{\partial p}-fv=-g\frac{\partial z}{\partial x}+F_x \quad \text{and} \tag{6.1.6}$$

$$\frac{\partial v}{\partial t}+u\frac{\partial v}{\partial x}+v\frac{\partial v}{\partial y}+\omega\frac{\partial v}{\partial p}+fu=-g\frac{\partial z}{\partial y}+F_y . \tag{6.1.7}$$

Applying the operator $\frac{\partial}{\partial x}$ (6.1.6) $-\frac{\partial}{\partial y}$ (6.1.7) gives

$$\frac{\partial E_{st}}{\partial t}+\mathbf{v}\cdot\nabla E_{st}+E_{st}\delta+(\frac{\partial\omega}{\partial x}\frac{\partial u}{\partial p}-\frac{\partial\omega}{\partial y}\frac{\partial v}{\partial p})-f(\frac{\partial v}{\partial x}+\frac{\partial u}{\partial y})-u\frac{\partial f}{\partial y}$$
$$=-g(\frac{\partial^2 z}{\partial x^2}-\frac{\partial^2 z}{\partial y^2})+(\frac{\partial F_x}{\partial x}-\frac{\partial F_y}{\partial y}) \tag{6.1.8}$$

Applying the operator $\frac{\partial}{\partial y}$(6.1.6)$+\frac{\partial}{\partial x}$(6.1.7) gives

$$\frac{\partial E_{sh}}{\partial t}+\mathbf{v}\cdot\nabla E_{sh}+E_{sh}\delta+(\frac{\partial\omega}{\partial y}\frac{\partial u}{\partial p}+\frac{\partial\omega}{\partial x}\frac{\partial v}{\partial p})+f(\frac{\partial u}{\partial x}-\frac{\partial v}{\partial y})-v\frac{\partial f}{\partial y}$$
$$=-2g\frac{\partial^2 z}{\partial x\partial y}+(\frac{\partial F_x}{\partial y}+\frac{\partial F_y}{\partial x}) \tag{6.1.9}$$

Next, using $\frac{E_{st}}{\sqrt{{E_{st}}^2+{E_{sh}}^2}}$(6.1.8)$+\frac{E_{sh}}{\sqrt{{E_{st}}^2+{E_{sh}}^2}}$(6.1.9) gives the equation for the trend in the total deformation (Gao et al., 2008):

$$\frac{\partial E}{\partial t}=T_1+T_2+T_3+T_4+T_5+T_6 \ , \tag{6.1.10}$$

where

$$T_1=-\mathbf{v}\cdot\nabla E , \tag{6.1.11}$$

$$T_2=-E\nabla_h\cdot\mathbf{v} , \tag{6.1.12}$$

$$T_3 = \frac{uE_{st} + vE_{sh}}{E}\frac{\partial f}{\partial y}, \tag{6.1.13}$$

$$T_4 = -\frac{E_{st}}{E}\left(g\frac{\partial^2 z}{\partial x^2} - g\frac{\partial^2 z}{\partial y^2}\right) - \frac{E_{sh}}{E}\left(2g\frac{\partial^2 z}{\partial x \partial y}\right), \tag{6.1.14}$$

$$T_5 = \frac{E_{st}}{E}\left(\frac{\partial \omega}{\partial x}\frac{\partial u}{\partial p} - \frac{\partial \omega}{\partial y}\frac{\partial v}{\partial p}\right) + \frac{E_{sh}}{E}\left(\frac{\partial \omega}{\partial y}\frac{\partial u}{\partial p} + \frac{\partial \omega}{\partial x}\frac{\partial v}{\partial p}\right), \text{ and} \tag{6.1.15}$$

$$T_6 = \frac{E_{st}}{E}\left(\frac{\partial F_x}{\partial x} - \frac{\partial F_y}{\partial y}\right) + \frac{E_{sh}}{E}\left(\frac{\partial F_x}{\partial y} + \frac{\partial F_y}{\partial x}\right). \tag{6.1.16}$$

Here, $\mathbf{v}$ is the 3D wind vector, $\nabla_h \cdot \mathbf{v}$ is the horizontal divergence, and $\omega = dp/dt$ is the vertical velocity in pressure coordinates. From equation (6.1.10), we can see that the local change in the total deformation is caused by advection (T_1), horizontal divergence (T_2), the term related to the β-effect (T_3), the pressure-gradient term (T_4), contributions due to the vertical velocity (T_5), and the term related to the frictional force and/or turbulent mixing (T_6).

6.1.3 The Physical Meaning of Each Term

For convenience, we can choose our coordinate system so that the shearing deformation is zero. We consider a pure stretching deformation field defined by $u = ax$ and $v = -ay$. The flow described by this set of equations in the region nearby is the typical flow pattern associated with a saddle field formed by two areas of high pressure and two areas of low pressure. For this flow, $\partial u/\partial x > 0$ and $\partial v/\partial y < 0$; in the first quadrant, $u > 0$ and $v < 0$.

T_1 in equation (6.1.10) represents the advection for the total deformation. The sign of this term, ($-\mathbf{v}\cdot\nabla E$), is determined by the angle between the velocity vector and the gradient of the total deformation. When the angle is less than 90°, the projection of $\mathbf{v}$ on $-\nabla E$ is positive and so T_1 is positive; otherwise, the term is negative.

T_2 represents the change in the total deformation due to the horizontal divergence. For a pure deformation field, $\nabla_h \cdot \mathbf{v} = 0$ and so this term is zero.

T_3 is a term that is related to the *β*-effect or the longitudinal gradient of the Coriolis parameter, *f*. Its sign is determined by the interaction between *u* and $\frac{\partial f}{\partial y}$ in the new coordinate system (which means that E_{sh} = 0).

T_4 represents the effect of the pressure force. Assuming that the flow pattern for the deformation corresponds to pure stretching, this can be rewritten as $-(g\frac{\partial^2 z}{\partial x^2} - g\frac{\partial^2 z}{\partial y^2})$. The contribution of this term to the total deformation is determined by the combination of the shear in the *x* and *y* directions of the pressure force. (*x* and *y* represent the new coordinate axes under which the shearing deformation is zero.)

T_5 combines the horizontal shear of the vertical velocity with the vertical shear of the horizontal velocity in the new coordinate system. Under the above assumption (E_{sh} = 0), T_5 can be rewritten as $\frac{\partial \omega}{\partial x}\frac{\partial u}{\partial p} - \frac{\partial \omega}{\partial y}\frac{\partial v}{\partial p}$. Its contribution to the change in the total deformation is determined by the interaction between the signs of its components.

T_6 describes the effect of the friction or turbulent mixing on the total deformation.

6.2 Interactions Between the Vorticity, Divergence, and Deformation

The vorticity, divergence, and deformation describe, respectively, the changes in the angle, area, and shape of the continuous atmosphere and denote differential properties of its motion. As has been demonstrated by numerous observations and theoretical studies, these different properties of motion have a significant relationship with the evolution of weather systems.

As well being used directly to measure and identify a vortex system

(Sadarjoen and Post, 2000; Hoskins and Hodges, 2002; Luo and Dai, 2008)[43-45], the vorticity is also used in the potential vorticity theorem to explain the dynamics of cyclogenesis, the interactions between the upper-level and lower-level atmosphere, tropical cyclogenesis, the long-term persistence of mesoscale convective systems (MCSs) (Danielsen, 1968; Hoskins et al., 1985; Haynes and McIntyre, 1987; Davis and Emanuel, 1991; Montgomery and Enagonio, 1998)[46-50], barotropic instability (Mak and Cai 1989), and the turbulent dynamics due to the conservation of vorticity in a barotropic non-divergent environment (Okubo, 1970; Weiss, 1991; Rozoff et al., 2006; Wang, 2008)[51,31-32,18]. The divergence, which is based on the continuity equation, is highly relevant to phenomena involving vertical motion, such as the initiation or intensification of convection due to moisture accumulation, the pumping effect, or the passage of gravity waves. In addition, it is also a basis for nonlinear balance theory, which is often used to study the inner dynamics of the evolution of MCSs or to confirm the existence of gravity waves. Compared to the vorticity and divergence, the effects of the deformation on the development of weather systems are less frequently considered. In atmospheric dynamics, the deformation is mainly considered in relation to frontogenesis: this is based on the well-known theorem that the deformation drives frontogenesis when the angle between the dilatation axis and the isentropes is less than 45° (Petterssen, 1956; Keyser et al., 1988)[10,42]. Mak and Cai (1989)[26] and Cai (1992)[27] discussed the stability of a disturbance in the deformation field and found that a perturbation must be properly configured with the deformation field to optimally extract (kinetic) energy from the basic flow. In a climatological study of deformation, Spensberger and Spengler (2014)[52] demonstrated that the deformation is also related to the movement and evolution of the upper-level jet stream, orographic blocking, and Rossby wave-breaking.

While most previous studies have paid attention to the separate effects of vorticity, divergence, and deformation on the evolution of weather systems, the roles of the combination of these three factors has been less well studied and remains more elusive. A single quantity (vorticity, divergence, or deformation) only describes a portion of the flow features and cannot reflect the holistic structure of the flow. Combinations of the vorticity, divergence, and deformation in different proportions result in different flow patterns, which then persist and develop into different weather phenomena. In fact, it can be anticipated that a change in one property of motion (e.g., the divergence) will also cause changes in the other properties (e.g., the vorticity and deformation), given that these three properties are derived from the same description of the motion. These

changes will affect the structure of the flow and the subsequent evolution of the weather conditions. It is thus natural to question how the different properties of motion interact with one another and what roles these interactions play in the evolution of weather systems. Some studies concerning the interaction between the vorticity and divergence have already been made. From the equations for the vorticity and divergence, it can be seen that the vorticity includes the divergence on the right-hand side of its trend equation and that the divergence also includes the vorticity in the forcing term of its trend equation. This means that, on the one hand, the divergence influences the evolution of the vorticity, while, on the other hand, a change in the vorticity further impacts the evolution of the divergence. This, then, constitutes a feedback process. However, there are no clearly interactive terms in the vorticity and divergence equations, which limits the ability to make a quantitative measurement of the vorticity–divergence interaction and its impact on weather systems. Moreover, apart from the vorticity–divergence interaction, it is not clear whether there is any interaction between the deformation and vorticity or between the deformation and divergence. If there is any interaction, it is still not clear what impact this interaction has on weather systems. This section is mainly concerned with these questions.

6.2.1 Enstrophy and the Enstrophy Trend Equations

When discussing the changes in some variables, absolute values or the squares of the variables are usually used instead of the original values as the different signs can complicate the discussion. For example, positive values of the change in vorticity ($\frac{d\zeta}{dt} > 0$) not only represent an increase in cyclonic vorticity but may also indicate a decrease in anticyclonic vorticity. The squared vorticity, therefore, can better represent a change in the intensity of the rotation. In addition, as stated in the introduction, the shear deformation, E_{sh}, and stretching deformation, E_{st}, change with the coordinate. Therefore, the total deformation, E, which is the square root of the sum of the square of the shearing deformation and the square of the stretching deformation is usually used to measure the intensity of the deformation. It is also much easier to discuss the square of the deformation than the deformation itself. For these reasons, we use the squared forms of the vorticity, divergence, and the deformation to discuss the interactions between them. These squared forms are defined as follows:

$$\varepsilon_e = \frac{1}{2}\zeta^2 = \frac{1}{2}(\frac{\partial v}{\partial x})^2 + \frac{1}{2}(\frac{\partial u}{\partial y})^2 - \frac{\partial v}{\partial x}\frac{\partial u}{\partial y} \quad , \tag{6.2.1}$$

$$\delta_e = \frac{1}{2}\delta^2 = \frac{1}{2}(\frac{\partial u}{\partial x})^2 + \frac{1}{2}(\frac{\partial v}{\partial y})^2 + \frac{\partial u}{\partial x}\frac{\partial v}{\partial y}, \text{ and} \tag{6.2.2}$$

$$\sigma_e = \frac{1}{2}E^2 = \frac{1}{2}(E_{sh}^2 + E_{st}^2)$$
$$= \frac{1}{2}(\frac{\partial v}{\partial x})^2 + \frac{1}{2}(\frac{\partial u}{\partial y})^2 + \frac{\partial v}{\partial x}\frac{\partial u}{\partial y} + \frac{1}{2}(\frac{\partial u}{\partial x})^2 + \frac{1}{2}(\frac{\partial v}{\partial y})^2 - \frac{\partial u}{\partial x}\frac{\partial v}{\partial y} \quad . \tag{6.2.3}$$

In the above, ε_e is half of the squared vorticity and is known as the enstrophy of the vorticity; δ_e is half of the squared divergence and is called the enstrophy of the divergence; and σ_e is half of the squared deformation and is known as the enstrophy of the deformation. σ_e is composed of half of the square of the shearing deformation and half of the square of the stretching deformation. Here, the "half" operation is used to make the subsequent interactive terms simpler and does not change the results of the analysis. The three squared quantities represent the intensity of the rotation, divergence, and deformation, respectively.

In pressure coordinates, the basic equations of the horizontal motion of the atmosphere in a plane, f, without friction can be written as

$$\frac{\partial u}{\partial t} + \mathbf{v}\cdot\nabla u = fv - g\frac{\partial z}{\partial x} \quad \text{and} \tag{6.2.4}$$

$$\frac{\partial v}{\partial t} + \mathbf{v}\cdot\nabla v = -fu - g\frac{\partial z}{\partial y} \quad , \tag{6.2.5}$$

where $\mathbf{v} = (u, v, \omega)$ is the three-dimensional velocity vector, z is the geopotential height, g is the gravitational acceleration, and f is the Coriolis parameter, which is a constant here. Taking the partial derivatives

of equations (6.2.4)–(6.2.5) with respect to t, we obtain

$$\frac{\partial \varepsilon_e}{\partial t} = \zeta \frac{\partial \zeta}{\partial t} = \zeta [\frac{\partial}{\partial x}(\frac{\partial v}{\partial t}) - \frac{\partial}{\partial y}(\frac{\partial u}{\partial t})], \tag{6.2.6}$$

$$\frac{\partial \delta_e}{\partial t} = D \frac{\partial D}{\partial t} = D \frac{\partial}{\partial x}(\frac{\partial u}{\partial t}) + \frac{\partial}{\partial y}(\frac{\partial v}{\partial t}), \text{ and} \tag{6.2.7}$$

$$\begin{aligned} \frac{\partial \sigma_e}{\partial t} &= E_{sh} \frac{\partial E_{sh}}{\partial t} + E_{st} \frac{\partial}{\partial t} E_{st} \\ &= E_{sh} [\frac{\partial}{\partial x}(\frac{\partial v}{\partial t}) + \frac{\partial}{\partial y}(\frac{\partial u}{\partial t})] + E_{st} [\frac{\partial}{\partial x}(\frac{\partial u}{\partial t}) - \frac{\partial}{\partial y}(\frac{\partial v}{\partial t})] \end{aligned}. \tag{6.2.8}$$

Substituting equations (6.2.4) and (6.2.5) into equations (6.2.6)–(6.2.8) produces the equations for the trends in the enstrophy of the vorticity, divergence, and deformation:

$$\frac{\partial \varepsilon_e}{\partial t} = -\mathbf{v} \cdot \nabla \varepsilon_e - f\zeta\delta - \zeta^2\delta + \zeta(\frac{\partial \omega}{\partial y}\frac{\partial u}{\partial p} - \frac{\partial \omega}{\partial x}\frac{\partial v}{\partial p}), \tag{6.2.9}$$

$$\begin{aligned} \frac{\partial \delta_e}{\partial t} = &-\mathbf{v} \cdot \nabla \delta_e - \delta(\frac{\partial u}{\partial x})^2 - \delta(\frac{\partial v}{\partial y})^2 - 2\frac{\partial v}{\partial x}\frac{\partial u}{\partial y}\delta \\ &- \delta(\frac{\partial \omega}{\partial x}\frac{\partial u}{\partial p} + \frac{\partial \omega}{\partial y}\frac{\partial v}{\partial p}) + f\zeta\delta - \delta g \nabla_h^2 z \end{aligned} \tag{6.2.10}$$

$$\begin{aligned} \frac{\partial \sigma_e}{\partial t} = &-\mathbf{v} \cdot \nabla \sigma_e - E^2\delta - E_{sh}(\frac{\partial \omega}{\partial y}\frac{\partial u}{\partial p} + \frac{\partial \omega}{\partial x}\frac{\partial v}{\partial p}) \\ &-E_{st}(\frac{\partial \omega}{\partial x}\frac{\partial u}{\partial p} - \frac{\partial \omega}{\partial y}\frac{\partial v}{\partial p}) - 2E_{sh}g\frac{\partial^2 z}{\partial x \partial y} - E_{st}g\frac{\partial^2 z}{\partial x^2} + E_{st}g\frac{\partial^2 z}{\partial y^2} \end{aligned} \tag{6.2.11}$$

In order to discuss the interactions between the vorticity, divergence, and deformation, terms with the same absolute values but opposite signs (given the name "opposite-sign terms" in the following), which may be

sources or sinks of the quantity in equation, are identified as the interaction terms. (For a further, detailed discussion, see Li et al., 2019)[53].

6.3 Impact of the Interaction Between the Vorticity, Divergence, and Deformation on Vortex Evolution

The effects of the interactions between the vorticity, divergence, and deformation on the evolution of a precipitation vortex can be used to illustrate the possible role of deformation during the processes that lead to heavy rainfall.

In order to illustrate the evolution of a particular vortex, Figure 6.3.1 shows the horizontal distributions of the streamlines, vorticity enstrophy (VorE), and precipitation at 800 hPa. At 18:00 UTC on 16 August 2009, a vortex began to form near 113.5°E, 35.5°N from the weak cyclonic shear of a south-southeast wind (black rectangle). Figure 6.3.2 (a) shows the situation as the vortex developed. The VorE–DefE interaction term is mainly positive within the vortex area, indicating a transition from deformation enstrophy to vorticity enstrophy. During this process, the deformation enstrophy is consumed, whereas the VorE tends to increase, which is favorable for the initiation of a vortex. Also, during the vortex initiation, the VorE–DivE interaction term is also positive, meaning that the divergence enstrophy is transformed into vorticity enstrophy, which favors the vortex development.

The VorE–DivE interaction term is

$$\frac{d\varepsilon_e}{dt} \sim -f\zeta\delta + \frac{\partial v_1}{\partial x}\frac{\partial u_1}{\partial y}\delta \text{, and} \tag{6.3.1}$$

$$\frac{d\delta_e}{dt} \sim f\zeta\delta - \frac{\partial v_1}{\partial x}\frac{\partial u_1}{\partial y}\delta . \tag{6.3.2}$$

Equations (6.3.1) and (6.3.2) show that the interaction between the VorE and divergence enstrophy can be described by two terms. The first term is the Coriolis parameter term, which is determined by the configuration of the vorticity and the divergence. $\mathbf{v}_{h1} = (u_1, v_1)$ is the purely rotational wind. For example, for a cyclonic convergent circulation ($\zeta > 0, \delta < 0$), the Coriolis parameter term is negative ($f\zeta\delta < 0$). The divergence enstrophy is thus transformed into VorE and increases the positive cyclonic vorticity. The second term on the right-hand side of

equations (6.3.1) and (6.3.2) is the coupling of the divergence and the shear of the rotational wind $\frac{\partial v_1}{\partial x}$, $\frac{\partial u_1}{\partial y}$, which is determined by the distribution of the flow.

Figure 6.3.3 shows the relative distributions of the two sub-terms in the VorE–DivE interaction term. It can be seen that the term $f\zeta\delta$ determines the basic distribution of the VorE–DivE interaction. Given that, within the vortex area, the vertical vorticity, ζ, is generally positive, the divergence becomes the decisive factor for the sign of the VorE–DivE interaction. When the flow is convergent ($\delta < 0$), which makes $f\zeta\delta$ negative, the divergence enstrophy is transformed into VorE, which drives the development of the vortex. When the flow becomes divergent and the term $f\zeta\delta$ is positive, the VorE is transformed into divergence enstrophy and weakens the vortex. This means that the divergence is a crucial factor in the evolution of a vortex and implies that there is a need to analyze the evolution of the divergence enstrophy.

As in Figure 6.3.2, the DivE–DefE interaction term has positive values in the area of vortex formation, which tends to produce divergence enstrophy and thus increase the convergence. The intensification of the convergence then promotes an increase in the vorticity enstrophy through the VorE–DivE interaction term, which leads to further intensification of the vortex development. This indicates that the deformation can interact with the vorticity to affect the vortex directly. In addition, the deformation interacts with the divergence and influences the vortex development in an indirect way. These results provide a new insight into vortex development that is worth further investigating in the future.

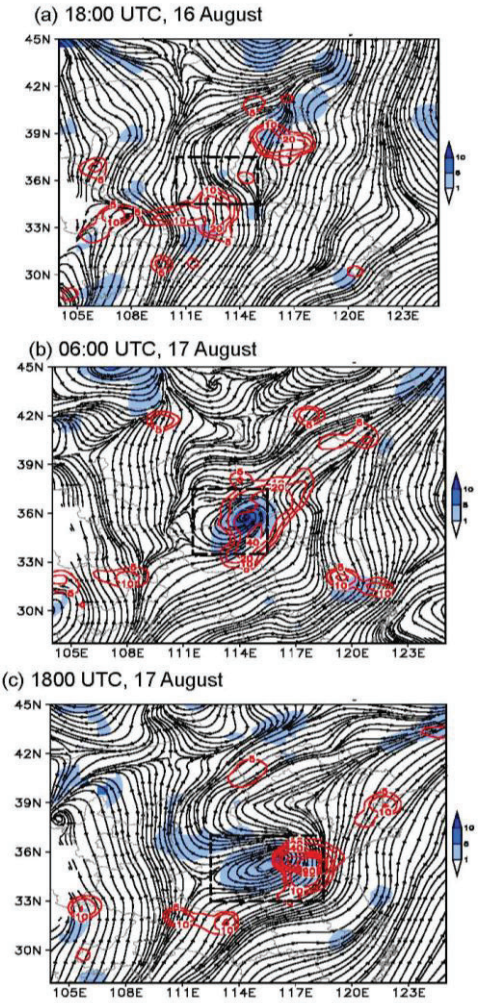

Fig. 6.3.1. Vorticity enstrophy (color-shaded area; units: 10^{-9} s^{-2}) and streamlines at 800 hPa. The black boxes enclose the whole vortex area. The red lines are the six-hour accumulated rainfall amount (mm). The triangle indicates the location of the formation of the vortex.

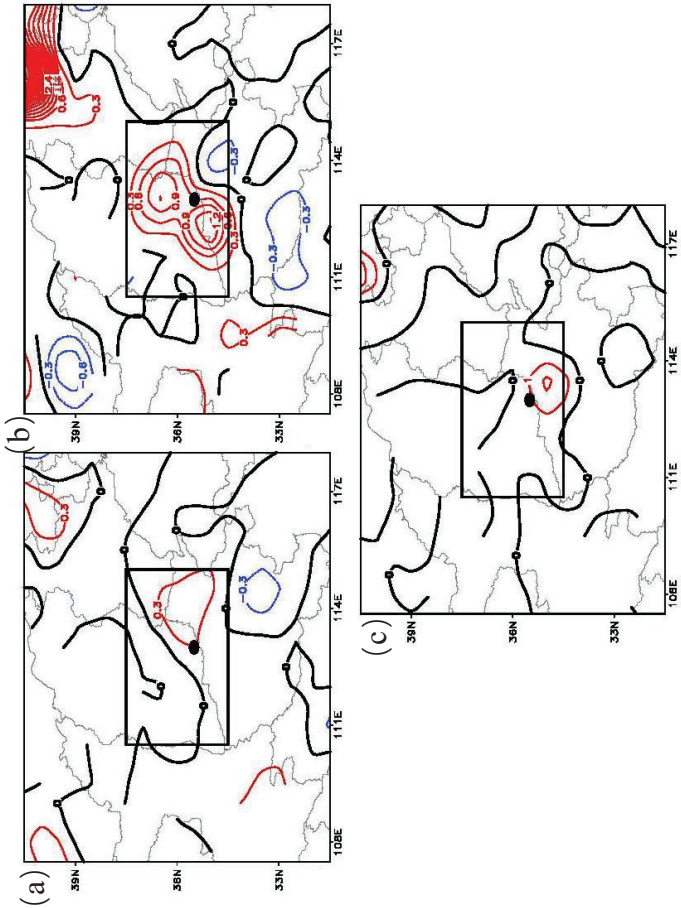

Fig. 6.3.2. Distribution of (a) the VorE–DefE interaction term, (b) the VorE–DivE interaction term, and (c) the DivE–DefE interaction term at 800 hPa for 18:00 UTC, 16 August 2009. Units: 10^{-13} s^{-3}

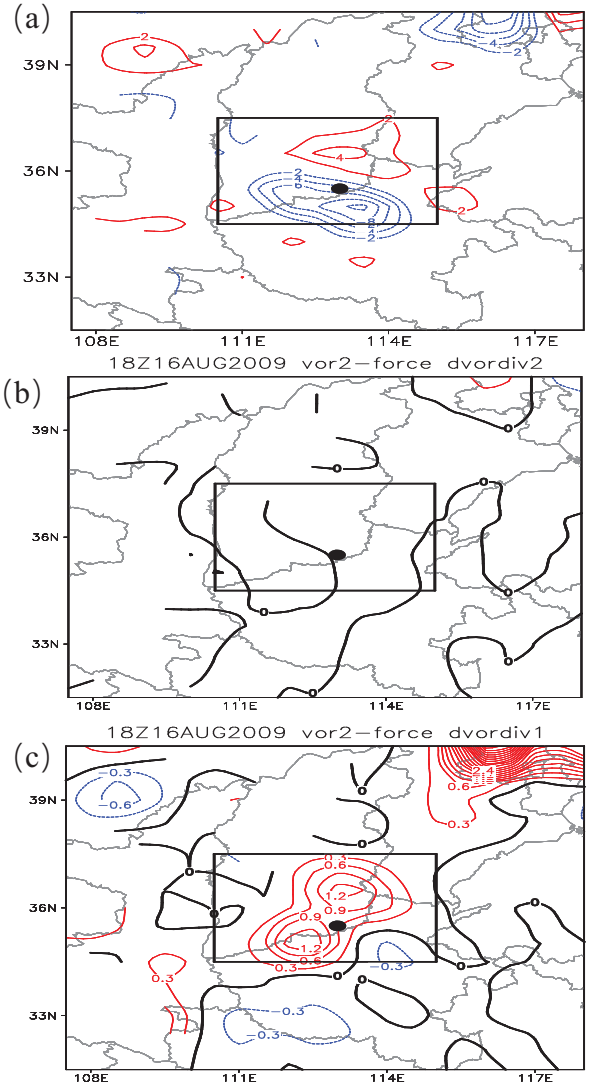

Fig. 6.3.3. Horizontal distributions of the two sub-terms of the VorE–DefE interaction term: (a) the term related to the Coriolis parameter and (b) the coupling of the divergence and the shear of the rotational wind (units: 10^{-13} s^{-2}). (c) The divergence at 800 hPa at 18:00 UTC, 16 August 2009.

Notes

[1]Rossby C. G. (1937) "On the mutual adjustment of pressure and velocity distribution in certain simple current systems, I," *Journal of Marine Research*, 1(1):15-28.
[2]Rossby C. G. (1938) "On the mutual adjustment of pressure and velocity distribution in certain simple current systems, II," *Journal of Marine Research,* 1(3):239-263.
[3]Yeh T. C. (1957) "On the formation of quasi-geostrophic motion in the atmosphere," *Journal of the Meteorological Society of Japan*. 75th Anniversary Volume,35A:130-137.
[4]Yeh T. C. and M. Li (1982) "On the characteristics of scales of the atmospheric motions," *Journal of the Meteorological Society of Japan,* 60(1):16-23.
[5]Zeng Q. C. (1963a) "The effect of original disturbance structure on adaptation and the application of observed wind field," *Acta Meteorologica Sinica,* 33(1):37–50. (in Chinese with English abstract)
[6]Zeng Q. C. 1963b: "The adaptation and development in atmosphere," *Acta Meteorologica Sinica,* 33(2):163-174. (in Chinese with English abstract)
[7]Zeng Q. C. 1963c: "The adaptation and development in atmosphere," *Acta Meteorologica Sinica,* 33(8):281-189. (in Chinese with English abstract)
[8]Weisman M. L. and J. B. Klemp (1982) "The dependence of numerically simulated convective storms on vertical wind shear and buoyancy," *Monthly Weather Review,* 110(6):504-520.
[9]Fernandez W. and A. J. Thorpe (1979) "An evaluation of theories of storm motion using observations of tropical convective systems," *Monthly Weather Review,* 107(10):1306-1319.
[10]Petterssen S. (1956) Weather analysis and forecasting, Vol.1: *Motion and Motion Systems*, 2nd edition, McGraw-Hill, 428pp.
[11]Wiin-Nielsen A. (1973) Compendium of meteorology: *Vol I.,* World Meteorological Organization. *No.364.*
[12]Yang S., S. T. Gao and C. G. Lu (2014) "A generalized frontogenesis function and its Application," *Advances in Atmospheric Sciences,* 31(5):1065-1078.
[13]Yang S., S. T. Gao and C. G. Lu (2015) "Investigation of the Mei-yu front using a new deformation frontogenesis function," *Advances in Atmospheric Sciences,* 32(5):635-647.
[14]Whitaker J. S. and R. M. Dole (1995) "Organization of storm tracks in zonally varying Flows," *Journal of Atmospheric Sciences,* 52(8):1178-1191.
[15]Elhmaidi D., A. Provenzale, T. Lili and *et al.* (2004) "Stability of two-dimensional vorticity Filaments," *Physical Letters A,* 333(1-2):85-90.
[16]Rivière G. and A. Joly (2006a) "Role of the low-frequency deformation field on the explosive growth of extratropical cyclones at the jet exit. Part I: Barotropic critical region," *Journal of Atmospheric Sciences,* 63(8):1965–1981.
[17]Rivière G. and A. Joly (2006b) "Role of the low-frequency deformation field on the explosive growth of extratropical cyclones at the jet exit. Part II: Baroclinic critical region," *Journal of Atmospheric Sciences,* 63(8):1982–1995.
[18]Wang Y. Q. (2008) "Rapid filamentation zone in a numerically simulated

tropical cyclone," *Journal of Atmospheric Sciences,* 65(4):1158-1181.
[19]Gao S. T., S. Yang, M. Xue and *et al.* (2008) "Total deformation and its role in heavy precipitation events associated with deformation-dominant flow patterns," *Advances in Atmospheric Sciences,* 25(1):11-23.
[20]Thomas L. N. (2012) "On the effects of frontogenetic strain on symmetric instability and inertia-gravity waves," *Journal of Fluid Mechanics,* 711:620-640.
[21]Moon Y. and D. S. Nolan (2015) "Spiral rainbands in a numerical simulation of Hurricane Bill (2009). Part II: Propagation of inner rainbands," *Journal of Atmospheric Sciences,* 72(1):191-215.
[22]Charney J. G. (1947) "The dynamics of long waves in a baroclinic westerly current," *Journal of Meteorology,* 4(5):136–162.
[23]Eady E. T. (1949) "Long waves and cyclone waves," *Tellus,* 1(3):33-52.
[24]Kuo H. L. (1949) "Dynamics instability od two-dimensional non-divergent flow in a barotropic atmosphere," *Journal of Meteorology,* 6(2):105-122.
[25]Farrell B. F. (1989) "Transient development in confluent and diffluent flow," *Journal of Atmospheric Sciences,* 46(21):3279-3288.
[26]Mak M. and M. Cai (1989) "Local barotropic instability," *Journal of Atmospheric Sciences,* 46(21):3289-3311.
[27]Cai M. (1992) "A physical interpretation of the stability property of a localized disturbance in a deformation flow," *Journal of Atmospheric Sciences,* 49(23):2177-2182.
[28]Cai M. and M. Mak (1990) "On the basic dynamics of regional cyclogenesis," *Journal of Atmospheric Sciences,* 47(12):1417-1442.
[29]Mak M. (1991) "Dynamics of an atmospheric blocking as deduced from its local Energetics," *Quarterly Journal of the Royal Meteorological Society,* 117(499):477-493.
[30]Shutts G. J. (1983) "The propagation of eddies in diffluent jet-streams: eddy vorticity forcing of "blocking" flow fields," *Quarterly Journal of the Royal Meteorological Society,* 109(462):737-761.
[31]Weiss J. (1991) "The dynamics of enstrophy transfer in two-dimensional hydrodynamics," *Physica D,* 48(2-3):273-294.
[32]Rozoff C. M., W. H. Schubert, B. D. McNoldy and et al. (2006) "Rapid filamentation zones in intense tropical cyclones," *Journal of Atmospheric Sciences,* 63(1):325-340.
[33]Bishop C. H. and A. J. Thorpe(1994a) "Frontal wave stability during moist deformation frontogenesis. Part I: Linear wave dynamics," *Journal of Atmospheric Sciences,* 51(6):852-873.
[34]Bishop C. H. and A. J. Thorpe (1994b) "Frontal wave stability during moist deformation frontogenesis. Part II: The suppression of nonlinear wave development," *Journal of Atmospheric Sciences,* 51(6):874-888.
[35]Renfrew I. A., A. J. Thorpe and C. H. Bishop (1997) "The role of the environmental flow in the development of secondary frontal cyclones," *Quarterly Journal of the Royal Meteorological Society,* 123(542):1653-1675.
[36]Bishop C. H. (1996a) "Domain-independent attribution. Part I: Reconstructing the wind from estimates of vorticity and divergence using free space green's functions," *Journal of Atmospheric Sciences,* 53(2):241-252.

[37]Bishop C. H. (1996b) "Domain-independent attribution. Part II: its value in the verification of dynamical theories of frontal waves and frontogenesis," *Journal of Atmospheric Sciences,* 53(2):253-262.
[38]Wang X. B. and R. S. Wu (2001) "The development of symmetric disturbance superposed on baroclinic frontal zone under the action of deformation field," *Acta Meteorologica Sinica,* 15(4):420-435.
[39]Jiang Y. Q., Y. Wang, Z. G. Zhou and et al. (2011) "Interaction index of vortex and deformation Field," *Journal of PLA University of Science and Technology*, 12(6):685-689.
[40]Jiang Y. Q. Study on the dynamic mechanism of formation of mesoscale weather systems triggered by wind perturbations [*Ph.D dissertation of Nanjing University*], 2011.
[41]Keyser D., M. J. Pecnick and M. A. Shapiro (1986) "Diagnosis of the role of vertical deformation in a two-dimensional primitive equation model of upper-level frontogenesis," *Journal of Atmospheric Sciences,* 43(8):839-850.
[42]Keyser D., M. J. Reeder and R. J. Reed (1988) "A generalization of Pettersen's frontogenesis function and its relation to the forcing of vertical motion," *Monthly Weather Review,* 116(3):762–781.
[43]Ari Sadarjoen I. and F. H. Post (2000) "Detection, quantification, and tracking of vortices using streamline geometry," *Journal of Computational and Graphical statistics,* 24(3):333-341.
[44]Hoskins B.J. and K. I. Hodges (2002) "New perspectives on the Northern Hemisphere winter storm tracks," *Journal of Atmospheric Sciences,* 59(6):1041-1061.
[45]Luo Z. X. and K. Dai (2008) "A climatological investigation of the activity of summer subtropical vortices", *Acta Meteorologica Sinica,* 22(1):1-7.
[46]Danielsen E. F. (1968) "Stratospheric-tropospheric exchange based on radioactivity, ozone and potential vorticity," *Journal of Atmospheric Sciences,* 25(3):502–518.
[47]Hoskins BJ, M. E. McIntyre and A. W. Robertson (1985): "On the use and significance of isentropic potential vorticity maps," *Quarterly Journal of the Royal Meteorological Society,* 111(470):877-946.
[48]Haynes P. H. and M. E. McIntyre (1987) "On the evolution of vorticity and potential vorticity in the presence of diabatic heating and frictional or other forces," *Journal of Atmospheric Sciences,* 44(5):828-841.
[49]Davis C. A. and K. A. Emanuel (1991) "Potential vorticity diagnostics of cyclogenesis," *Monthly Weather Review,* 119(8):1929-1953.
[50]Montgomery M. T. and J. Enagonio (1998) "Tropical cyclogenesis via convectively forced vortex Rossby waves in a three-dimensional quasigeostrophic model," *Journal of Atmospheric Sciences,* 55(20):3176–3207.
[51]Okubo A. (1970) "Horizontal dispersion of floatable particles in the vicinity of velocity singularity such as convergences," *Deep Sea Research,* 17(3):445–454.
[52]Spensberger C. and T. Spengler (2014) "A new look at deformation as a diagnostic for large-scale flow," *Journal of Atmospheric Sciences,* 71(11):4221-4234.
[53]Li N., L. K. Ran and S. T. Gao (2019) "On the interactions of vorticity,

divergence and deformation in a meso-α scale vortex," *Meteorology and Atmospheric Physics,* 132:203–223.

CHAPTER SEVEN

GENERALIZED FRONTOGENESIS THEORY

In the past, extensive studies on generalized frontogenesis theory have been performed by meteorologists both inside and outside China; these studies have been concerned with fronts dynamics and the analysis of weather situations. These studies, including those by Petterssen (1936)[1] and Miller (1948)[2], started from the perspective of motion and discussed the intensity changes in fronts by analyzing changes in the potential temperature gradient. Petterssen (1956)[3] pointed out that vorticity, divergence, and deformation are all conducive to frontogenesis. Some researchers have considered that the growth of baroclinic instability is closely related to frontogenesis and have emphasized that low-level frontogenesis is due to the vertical circulation caused by wave growth and the strength of the deformation (Palmin, 1948; Phillips, 1956; Williams, 1967)[4-6]. Hoskins and Bretherton (1972)[7] also put forward a semi-geostrophic theoretical model that concerned nonlinear baroclinic fluctuations and frontogenesis, analytically confirming how the Eady wave created a discontinuity in temperature in a limited time. Both Davies-Jones (1982, 1985)[8-9] and Doswell (1985)[10] studied the role of deformation in frontogenesis. Ninomiya (1984, 2000)[11-12] showed that the deformation and horizontal convergence in subtropical zones are primary contributors to meiyu frontogenesis. This frontogenesis produces vertical circulation. Ninomiya (1984)[11] calculated the size of the terms in the frontogenesis equation and showed that transport of water vapor along the periphery of

the subtropical high from the western Pacific to the meiyu front favored the formation of the front.

Zeng (1979)[13] showed that the acceleration of the high-level jet can lead to frontogenesis in the middle troposphere. Wu et al. (2004)[14] made progress starting from the findings of Petterssen (1936)[1] and Miller (1948)[2]. Wu et al. looked at the intensity changes in frontal systems by utilizing the local and Lagrange frontogenesis functions. They further studied the problem about the relation between adaptation and frontogenesis.

In these earlier studies, the change in the potential temperature gradient was often used as the criterion for frontogenesis and frontolysis. However, in the vicinity of the front, except in the case of the polar front, which has a larger temperature gradient, fronts at low and middle latitudes are dew-point fronts with large water-vapor gradients. The deformation induces the convergence of different airflows, which can provide rich sources of water vapor. This makes the water-vapor gradient more intense and is conducive to frontogenesis. Therefore, this chapter starts with a discussion of the deformation of the wind field, analyzes the quantitative contributions of the vorticity, divergence, and deformation to the frontogenesis in detail, and focuses on frontogenesis caused by the deformation field as this field is conducive to frontogenesis. The generalized frontogenesis function represented by the local rate of change of the deformation gradient is also derived.

7.1 Generalized Scalar Frontogenesis Function

7.1.1 An Idealized Flow-field Model

We can start from the horizontal gradient change of potential temperature and equivalent potential temperature in the vicinity of a front when studying frontogenesis and frontolysis. The situation in which the absolute value of the potential temperature, θ, or equivalent potential

temperature, θ_e, is increasing with time is called frontogenesis; the opposite is called frontolysis. It is known that in the vicinity of a front, except in the case of the polar front, which has a larger temperature gradient, fronts at low and middle latitudes are dew-point fronts with larger water-vapor gradients. The deformation induces the convergence of different airflows, which can provide rich sources of water vapor. Next, an idealized flow-field model will be used to verify that the deformation field is the driving force behind the water-vapor and temperature gradients.

A purely 2D deformational flow is non-divergent and irrotational. For this reason, by itself, such a flow does not produce vertical lifting at low levels or create convergence through the Ekman pumping effect. However, deformation is important in frontogenesis because of the shearing and stretching effects. These cause increases in the horizontal temperature gradient and also the baroclinicity through advection, which leads to frontogenesis. In addition, the deformational flow can play an important role in advecting moisture into a region of precipitation.

To illustrate the role of a deformation-dominated flow field—a typical flow pattern associated with the Meiyu front—we can construct an idealized flow field with a typical "saddle" pattern. Our idealized flow field is constructed using a linear combination of two functions. Equation (7.1.1) defines a vortex:

$$V_{\mathrm{T}}(R) = V_0\left(\frac{\Phi_1 + \Phi_2}{2}\right) \quad , \tag{7.1.1}$$

where $\Phi_n(R, R_0) = \dfrac{2nR_0^{2n-1}R}{(2n-1)R_0^{2n} + R^{2n}}$; $n = 1, 2$.

This vortex contains two free parameters, n and R_0, where n is an integer, R_0 is a characteristic radius, and R is the distance from the vortex center. This vortex is a smoothed version of the Rankine combined vortex (Harasti and List, 2005)[15]. Its main feature is that it avoids the singularity

associated with the Rankine combined vortex at $R = R_0$ (Figure 7.1.1).

Note that, here, V_T is the tangential wind speed of the vortex, V_0 is the maximum value of V_T at radius R_0, and R is the radius for the constructed high- and low-level circulations.

We can specify a pure deformational flow:

$$\begin{cases} u = bx, \\ v = -by \end{cases},$$

where b is a positive constant. A linear combination of them gives

$$\begin{pmatrix} u \\ v \end{pmatrix} = \alpha K(m) V_T(R) \begin{pmatrix} -\sin\theta \\ \cos\theta \end{pmatrix} + (1-\alpha) \begin{pmatrix} bx \\ -by \end{pmatrix}, \tag{7.1.2}$$

where $K(m) = \begin{cases} 1, & \text{when } m = 1 \text{ or } 3 \\ -1, & \text{when } m = 2 \text{ or } 4 \end{cases}$ (m = 1, 2, 3, 4 denotes the quadrant), $\tan\theta = (y - Y_{0m})/(x - X_{0m})$, $\sin\theta = (y - Y_{0m})/R$, $\cos\theta = (x - X_{0m})/R$, $x = (i - 51)\Delta x$, and $y = (j - 51)\Delta y$, where i is the grid index in the x direction and j is the grid index in the y direction. The total number of grid points is 101×101.

We then have $R = R(x, y) = \sqrt{(x - X_{0m})^2 + (y - Y_{0m})^2}$.

$$(X_{0m}, Y_{0m}) = \begin{cases} (X_{01}, Y_{01}) = (25\Delta x, 25\Delta y) & \text{when } m=1 \\ (X_{02}, Y_{02}) = (-25\Delta x, 25\Delta y) & \text{when } m=2 \\ (X_{03}, Y_{03}) = (-25\Delta x, -25\Delta y) & \text{when } m=3 \\ (X_{04}, Y_{04}) = (25\Delta x, -25\Delta y) & \text{when } m=4 \end{cases}$$

are the four centers of the constructed high- and low-level circulations. The deformation coefficient, $b = 1.6 \times 10^{-5}$. The center of the flow region is at the origin of the coordinate system. The velocity is calculated on a 101×101 grid with a grid spacing of 60 km (i.e., $\Delta x = \Delta y = 60$ km).

In equation (7.1.2), α is a weight, which is determined as

$$\alpha = \begin{cases} 0, & R_{i,j} > R_0 \\ \dfrac{R_{i,j}}{25\Delta x}, & R_1 < R_{i,j} \le R_0 \\ 1, & 0 < R_{i,j} \le R_1 \end{cases},$$

where R_0 = 1200 km and R_1 = 900 km.

This idealized flow consists of two areas of high pressure (anticyclones) and two low-pressure areas (cyclones). An east–west confluence zone exists between the high–low couplets in the north and the low–high couplets in the south. Within the confluence zone, both the vorticity and divergence are very small and approach zero(Figure 7.1.2).

In typical Meiyu frontal systems, the horizontal temperature gradient is usually weak, and classical frontogensis processes are therefore less important. We assume a uniform background potential temperature and an initial background relative humidity field (q) that is a function of y only: q = 0.9–0.008 (y – 1), where y is the grid location in the y direction. As a result of the advection due to this flow, after six hours, the isolines of relative humidity are noticeably concentrated toward the confluence of the "saddle" field; after 12 hours, the isolines have become even more concentrated (Figure 7.1.3 (b)). After 36 hours, the isolines have become

yet more concentrated (Figure 7.1.3 (d)), indicating the buildup of a strong moisture gradient along the confluence zone. In the three-dimensional case, vertical motion along the confluence zone will cause upward transport of the moisture brought in by the horizontal deformational flow.

Often, the moisture gradient zone is not parallel to the confluence zone. An example of this is when the initial relative humidity (q) is given by $q = 0.9 + 0.008\ (x - y)$, where x is the grid location in the x direction. Figure 7.1.4 shows the evolution of this humidity field subject to the advection by the same idealized flow. The contours of relative humidity become more and more concentrated as in the previous case. Moreover, the orientation of these contours becomes more and more parallel to the confluence zone (Figure 7.1.4). Eventually, the zone with a strong moisture gradient becomes parallel to the confluence zone.

In the real atmosphere, this type of "saddle" flow is frequently observed and is often related to precipitation. In a flow such as this, the vorticity and divergence are small, whereas the deformation is large. In the above example, the value of the deformation is 3.2×10^{-5} in the middle part of the idealized "saddle" domain, whereas both the divergence and vorticity are zero in this region (not shown). Therefore, even in the absence of a distinct temperature gradient, heavy precipitation can result from the confluence associated with the deformation, which drives the moisture field. The richness of moisture in the confluence zone provides favorable conditions for moist convection—although the actual trigger for the convection is usually provided by something else, such as upper-level lifting by a shortwave trough (Hoxit et al., 1978; Maddox et al., 1978; Caracena et al., 1979; Maddox et al., 1980 (a) and (b))[16-20.]

7.1.2 Derivation of the Generalized Scalar Frontogenesis Function

From the above analyses of an idealized flow-field model, it is

apparent that the confluence associated with the deformation promotes frontogenesis through moisture convergence. In this section, a new, generalized scalar frontogenesis function that depends on the local rate of change of $|\nabla E|$ with time is defined. This function is expressed as

$$F_E = \frac{\partial}{\partial t}|\nabla E|, \tag{7.1.3}$$

where E is the total deformation and $|\nabla E|$ represents the absolute value of the horizontal gradient of the total deformation, which can be written

$$|\nabla E| = \sqrt{(\frac{\partial E}{\partial x})^2 + (\frac{\partial E}{\partial y})^2}\,. \tag{7.1.4}$$

The total deformation and its equation will be used here. These have already been discussed in Chapter 6.

Based on Petterssen's velocity decomposition (1956)[3] and the classical Clebsch velocity potential, the 2D velocity tensor derivative can be written as

$$\frac{\partial u_i}{\partial x_j} = \nabla \mathbf{v} = \frac{1}{2}\begin{pmatrix} E_{st} & E_{sh} \\ E_{sh} & -E_{st} \end{pmatrix} + \frac{1}{2}\begin{pmatrix} D & 0 \\ 0 & D \end{pmatrix} + \frac{1}{2}\begin{pmatrix} 0 & \zeta \\ -\zeta & 0 \end{pmatrix}, \tag{7.1.5}$$

where

$u_i = (u,v)$ and $\partial x_j = (\partial x, \partial y)$, $D = (\partial u/\partial x + \partial v/\partial y)$,

$\zeta = (\partial v/\partial x - \partial u/\partial y)$, $E_{st} = (\partial u/\partial x - \partial v/\partial y)$, and

$E_{sh} = (\partial v/\partial x + \partial u/\partial y)$. These quantities are, respectively, the divergence, vorticity, stretching deformation, and shearing deformation.

For the first matrix on the right-hand side of equation (7.1.5), we

define the total deformation to generalize the overall result of the stretching and shearing deformations. In order to do so, we take

$$\det\left|\begin{pmatrix} E_{st} & E_{sh} \\ E_{sh} & -E_{st} \end{pmatrix}\right| = E_{st}^2 + E_{sh}^2 ,$$

and the total deformation can thus be defined as

$$E = \sqrt{E_{st}^2 + E_{sh}^2} . \tag{7.1.6}$$

The total deformation has been used by meteorologists for many decades (e.g., Petterssen 1956)[3]. When the (x, y) coordinate system is rotated to a new coordinate system (x', y'), it can be shown that the total deformation preserves its symmetry under the rotation. In other words, the total deformation is independent of the rotation of the coordinate system.

Beginning from the horizontal motion equations, a prognostic equation for the total horizontal deformation can be derived (see Chapter 6):

$$\begin{aligned}
&\frac{\partial E}{\partial t} + \mathbf{v}_h \cdot \nabla E + \omega \frac{\partial E}{\partial p} + ED - E^{-1}\beta(uE_{st} + vE_{sh}) + E^{-1}E_{st}\left(\frac{\partial^2 \varphi}{\partial x^2} - \frac{\partial^2 \varphi}{\partial y^2}\right) + E^{-1}E_{sh}\left(2\frac{\partial^2 \varphi}{\partial x \partial y}\right) \\
&-E^{-1}E_{st}\left(\frac{\partial \omega}{\partial x}\frac{\partial u}{\partial p} - \frac{\partial \omega}{\partial y}\frac{\partial v}{\partial p}\right) - E^{-1}E_{sh}\left(\frac{\partial \omega}{\partial y}\frac{\partial u}{\partial p} + \frac{\partial \omega}{\partial x}\frac{\partial v}{\partial p}\right) \\
&+E^{-1}E_{st}\left(\frac{\partial F_x}{\partial x} - \frac{\partial F_y}{\partial y}\right) + E^{-1}E_{sh}\left(\frac{\partial F_x}{\partial y} + \frac{\partial F_y}{\partial x}\right) = 0
\end{aligned} \tag{7.1.7}$$

It can be seen from equation (7.1.7) that the local rate of change of the total deformation with time is related to the advection of the deformation (both horizontally and vertically: terms 2 and 3), is affected by the interaction between the deformation and divergence (term 4), depends on the β-effect (term 5), and is related to various second-order derivatives of the geopotential acting on the stretching and shearing deformations (terms 6 and 7), the tilting effect (terms 8 and 9), and the friction and/or

turbulent mixing (terms 10 and 11).

Based on the above equation for the total deformation, the generalized scalar frontogenesis function is derived in detail below. First $\left|\nabla E\right|$ is rewritten as $\sqrt{(\nabla E)^2}$; using the chain rule for differentiation, equation (7.1.3) can be decomposed as

$$F_E = \frac{\partial}{\partial t}\left|\nabla E\right| = \frac{1}{\left|\nabla E\right|}\left[\frac{\partial E}{\partial x}\frac{\partial}{\partial t}\left(\frac{\partial E}{\partial x}\right) + \frac{\partial E}{\partial y}\frac{\partial}{\partial t}\left(\frac{\partial E}{\partial y}\right)\right]. \tag{7.1.8}$$

Equation (7.1.7) can be written in the following form:

$$\frac{\partial E}{\partial t} = T_2 + T_3 + T_4 + T_5 + T_6 + T_7 + T_8 + T_9 + T_{10} + T_{11}, \tag{7.1.9}$$

where $T_2, T_3, \cdots, T_{11}$ represent the original terms in equation (7.1.7).

Thus, equation (7.1.8) becomes

$$\begin{aligned}
F_E &= \frac{1}{\left|\nabla E\right|}\left\{\frac{\partial E}{\partial x}\left[\frac{\partial}{\partial x}\left(\frac{\partial E}{\partial t}\right)\right] + \frac{\partial E}{\partial y}\left[\frac{\partial}{\partial y}\left(\frac{\partial E}{\partial t}\right)\right]\right\} \\
&= \frac{1}{\left|\nabla E\right|}\left[\nabla E \cdot \nabla (T_2 + T_3 + T_4 + T_5 + T_6 + T_7 + T_8 + T_9 + T_{10} + T_{11})\right] \\
&= -\mathbf{v}\cdot\nabla_3\left|\nabla E\right| - \frac{1}{\left|\nabla E\right|}\left[\frac{\partial E}{\partial x}\left(\frac{\partial \mathbf{v}_h}{\partial x}\cdot\nabla E\right) + \frac{\partial E}{\partial y}\left(\frac{\partial \mathbf{v}_h}{\partial y}\cdot\nabla E\right)\right] - \frac{1}{\left|\nabla E\right|}\left[\frac{\partial E}{\partial x}\frac{\partial \omega}{\partial x} + \frac{\partial E}{\partial y}\frac{\partial \omega}{\partial y}\right]\frac{\partial E}{\partial p} \\
&+ \frac{1}{\left|\nabla E\right|}\left[\frac{\partial E}{\partial x}\frac{\partial}{\partial x} + \frac{\partial E}{\partial y}\frac{\partial}{\partial y}\right](T_4 + T_5 + T_6 + T_7 + T_8 + T_9 + T_{10} + T_{11}) \\
&= -\mathbf{v}\cdot\nabla_3\left|\nabla E\right| - \frac{1}{\left|\nabla E\right|}\left[\frac{1}{2}E_{st}\left(\frac{\partial E}{\partial x}\right)^2 + E_{sh}\left(\frac{\partial E}{\partial x}\frac{\partial E}{\partial y}\right) - \frac{1}{2}E_{st}\left(\frac{\partial E}{\partial y}\right)^2\right] - \frac{1}{2}D\left|\nabla E\right| \\
&- \frac{1}{\left|\nabla E\right|}\left[\frac{\partial E}{\partial x}\frac{\partial \omega}{\partial x} + \frac{\partial E}{\partial y}\frac{\partial \omega}{\partial y}\right]\frac{\partial E}{\partial p} \\
&+ \frac{1}{\left|\nabla E\right|}\left[\frac{\partial E}{\partial x}\frac{\partial}{\partial x} + \frac{\partial E}{\partial y}\frac{\partial}{\partial y}\right](T_4 + T_5 + T_6 + T_7 + T_8 + T_9 + T_{10} + T_{11}) \\
&= F_1 + F_2 + F_3 + F_4 + F_5 + F_6 + F_7
\end{aligned}, \tag{7.1.10}$$

where

$$F_1 = -\mathbf{v}\cdot\nabla_3\left|\nabla E\right|$$

$$F_2 = -\frac{1}{\left|\nabla E\right|}\left[\frac{1}{2}E_{st}\left(\frac{\partial E}{\partial x}\right)^2 + E_{sh}\left(\frac{\partial E}{\partial x}\frac{\partial E}{\partial y}\right) - \frac{1}{2}E_{st}\left(\frac{\partial E}{\partial y}\right)^2\right]$$

$$F_3 = \frac{1}{\left|\nabla E\right|}\left[\frac{\partial E}{\partial x}\frac{\partial}{\partial x} + \frac{\partial E}{\partial y}\frac{\partial}{\partial y}\right]T_4 - \frac{1}{2}D\left|\nabla E\right| = -\frac{3}{2}D\left|\nabla E\right| - \frac{E}{\left|\nabla E\right|}\left[\nabla E\cdot\nabla D\right]$$

$$F_4 = \frac{1}{\left|\nabla E\right|}\left[\frac{\partial E}{\partial x}\frac{\partial}{\partial x} + \frac{\partial E}{\partial y}\frac{\partial}{\partial y}\right]T_5 = \frac{1}{\left|\nabla E\right|}\left[\nabla E\cdot\nabla T_5\right]$$

$$F_5 = \frac{1}{\left|\nabla E\right|}\left[\frac{\partial E}{\partial x}\frac{\partial}{\partial x} + \frac{\partial E}{\partial y}\frac{\partial}{\partial y}\right](T_6 + T_7) = \frac{1}{\left|\nabla E\right|}\left[\nabla E\cdot\nabla(T_6 + T_7)\right]$$

$$F_6 = \frac{1}{\left|\nabla E\right|}\left[\frac{\partial E}{\partial x}\frac{\partial}{\partial x} + \frac{\partial E}{\partial y}\frac{\partial}{\partial y}\right](T_8 + T_9) - \frac{1}{\left|\nabla E\right|}\left[\frac{\partial E}{\partial x}\frac{\partial \omega}{\partial x} + \frac{\partial E}{\partial y}\frac{\partial \omega}{\partial y}\right]\frac{\partial E}{\partial p}$$

$$= \frac{1}{\left|\nabla E\right|}\left[\nabla E\cdot\nabla(T_8 + T_9) - (\nabla E\cdot\nabla\omega)\frac{\partial E}{\partial p}\right]$$

$$F_7 = \frac{1}{\left|\nabla E\right|}\left[\frac{\partial E}{\partial x}\frac{\partial}{\partial x} + \frac{\partial E}{\partial y}\frac{\partial}{\partial y}\right](T_{10} + T_{11}) = \frac{1}{\left|\nabla E\right|}\left[\nabla E\cdot\nabla(T_{10} + T_{11})\right] \quad . \tag{7.1.11}$$

In (7.1.9), (7.1.10), and (7.1.11), the following notation was used:

$$T_2 = -\mathbf{v}_h\cdot\nabla E\,, \tag{7.1.12a}$$

$$T_3 = -\omega\frac{\partial E}{\partial p}\,, \tag{7.1.12b}$$

$$T_4 = -E\nabla_h\cdot\mathbf{v}\,, \tag{7.1.12c}$$

$$T_5 = \frac{uE_{st} + vE_{sh}}{E}\frac{\partial f}{\partial y}\,, \tag{7.1.12d}$$

$$T_6 = -\frac{E_{st}}{E}\left(g\frac{\partial^2 z}{\partial x^2} - g\frac{\partial^2 z}{\partial y^2}\right), \tag{7.1.12e}$$

$$T_7 = -\frac{E_{sh}}{E}\left(2g\frac{\partial^2 z}{\partial x \partial y}\right), \tag{7.1.12f}$$

$$T_8 = \frac{E_{st}}{E}\left(\frac{\partial \omega}{\partial x}\frac{\partial u}{\partial p} - \frac{\partial \omega}{\partial y}\frac{\partial v}{\partial p}\right), \tag{7.1.12g}$$

$$T_9 = \frac{E_{sh}}{E}\left(\frac{\partial \omega}{\partial y}\frac{\partial u}{\partial p} + \frac{\partial \omega}{\partial x}\frac{\partial v}{\partial p}\right), \tag{7.1.12h}$$

$$T_{10} = -\frac{E_{st}}{E}\left(\frac{\partial F_x}{\partial x} - \frac{\partial F_y}{\partial y}\right), \tag{7.1.12i}$$

$$T_{11} = -\frac{E_{sh}}{E}\left(\frac{\partial F_x}{\partial y} + \frac{\partial F_y}{\partial x}\right). \tag{7.1.12j}$$

Here, $\mathbf{v}$ is a three-dimensional velocity vector, $\nabla_h \cdot \mathbf{v}$ is the horizontal divergence, and $\omega = dp/dt$ is the vertical velocity in the pressure coordinate system.

According to equation (7.1.10), the generalized frontogenesis function is associated with the advection (F_1), horizontal deformation (F_2), horizontal divergence (F_3), β-effect (F_4), pressure-gradient force (F_5), tilting effect (F_6), and friction and/or turbulent mixing (F_7).

7.1.3 The Physical Meaning of Each Term in the Generalized Scalar Frontogenesis Function

For the convenience of discussion and to simplify the problem, we now rotate our coordinate system so that the shearing deformation is zero. We consider a purely stretching deformational field defined by u = bx and v = –by. For the region close to the origin, the flow described by this set of equations is the typical flow pattern associated with a "two-high and two-low" saddle field. For this pattern, $\partial u/\partial x > 0$ and $\partial v/\partial y < 0$, and in the first quadrant u > 0 and v < 0.

Therefore, equation (7.1.10) is simplified to,

$$
\begin{aligned}
F_1 &= -\mathbf{v}\cdot\nabla_3\left|\nabla E\right| \\
F_2 &= -\frac{E}{2\left|\nabla E\right|}\left[\left(\frac{\partial E}{\partial x}\right)^2-\left(\frac{\partial E}{\partial y}\right)^2\right] \\
F_3 &= 0 \\
F_4 &= \frac{1}{\left|\nabla E\right|}\left[\nabla E\cdot\nabla\left(u\frac{\partial f}{\partial y}\right)\right] \\
F_5 &= \frac{1}{\left|\nabla E\right|}\left[\nabla E\cdot\nabla\left(g\left(\frac{\partial^2 z}{\partial y^2}-\frac{\partial^2 z}{\partial x^2}\right)\right)\right] \\
F_6 &= \frac{1}{\left|\nabla E\right|}\left[\nabla E\cdot\nabla\left(\frac{\partial\omega}{\partial x}\frac{\partial u}{\partial p}-\frac{\partial\omega}{\partial y}\frac{\partial v}{\partial p}\right)\right]-\frac{1}{\left|\nabla E\right|}\left[\nabla E\cdot\nabla\omega\right]\frac{\partial E}{\partial p} \\
F_7 &= \frac{1}{\left|\nabla E\right|}\left[\nabla E\cdot\nabla\left(\frac{\partial F_x}{\partial x}-\frac{\partial F_y}{\partial y}\right)\right]
\end{aligned}
\quad . \tag{7.1.13}
$$

According to equation (7.1.13), F_1 represents the contribution of the advection of the absolute value of the horizontal total deformation

gradient to the local frontogenesis. The sign of this term is determined by the projection of the three-dimensional velocity vector on the gradient of $|\nabla E|$: if the angle between $\mathbf{v}$ and $\nabla_3 |\nabla E|$ is less than $\frac{\pi}{2}$, the projection is positive, $F_1 < 0$ and the advection leads to frontolysis; otherwise, $F_1 > 0$ and the advection leads to frontogenesis. F_2 represents the role of the horizontal total deformation and its second-order derivatives in the frontogenesis. Its sign is determined by the angle between the isolines of E and the *x*-axis: this angle is η ($0 < \eta < \pi$). If $\frac{\pi}{4} < \eta < \frac{3\pi}{4}$, then $\left|\frac{\partial E}{\partial x}\right| < \left|\frac{\partial E}{\partial y}\right|$ and $F_2 > 0$, and this term leads to frontogenesis. If $0 < \eta < \frac{\pi}{4}$ or $\frac{3\pi}{4} < \eta < \pi$, it leads to frontolysis. When $\eta = 0$ or $\eta = \pi$, $F_2 = -\frac{E}{2}\left|\frac{\partial E}{\partial x}\right|$ decreases to its minimum value; when $\eta = \frac{\pi}{2}$, $F_2 = \frac{E}{2}\left|\frac{\partial E}{\partial y}\right|$ reaches its maximum value and the frontogenesis induced by the horizontal total deformation reaches its strongest. F_3 represents the frontogenesis due to the horizontal convergence or divergence. For a pure deformational field, $\nabla_h \cdot \mathbf{v} = 0$, and so this term is zero. F_4 is a term that is related to the β-effect; that is, the effect of the longitudinal gradient of the Coriolis parameter, *f*. Its

sign is determined by the angle between the horizontal gradient of the total deformation and the horizontal gradient of ($u\frac{\partial f}{\partial y}$) in the new coordinate system (which makes $E_{sh}=0$). F_5 represents the effect of various second-order derivatives of the geopotential on the frontogenesis. Its contribution to the frontogenesis is determined by the combination of the horizontal gradients of the total deformation and various second-order derivatives of the geopotential. F_6 represents the contribution of the term related to the vertical velocity to the frontogenesis. Assuming that $E_{sh}=0$, F_6 can be simplified to $\frac{1}{|\nabla E|}[\frac{\partial E}{\partial x}(\frac{\partial}{\partial x}(\frac{\partial \omega}{\partial x}\frac{\partial u}{\partial p}-\frac{\partial \omega}{\partial y}\frac{\partial v}{\partial p}))+\frac{\partial E}{\partial y}(\frac{\partial}{\partial y}(\frac{\partial \omega}{\partial x}\frac{\partial u}{\partial p}-\frac{\partial \omega}{\partial y}\frac{\partial v}{\partial p}))]$. The signs of several of these components and their interactions determine the influence of this term on the frontogenesis. F_7 describes the effect of friction and/or turbulent mixing on the frontogenesis in the new coordinate system.

In this section, the generalized scalar frontogenesis function and the Lagrange rate of the total deformation gradient, $|\nabla E|$,. are described. Keyser et al(1988)[21] to extend Pettersen frontogenesis into a form suitable for applying the horizontal potential temperature gradient vector: the result was called the vector frontogenesis function. This means that the generalized vector frontogenesis function can be defined based on the generalized scalar frontogenesis function: it represents the local rate of change of the horizontal gradient of the total deformation. The expression

for this is

$$F_E = \frac{\partial}{\partial t}(\nabla E), \tag{7.1.14}$$

where ∇E represents the horizontal gradient of the total deformation.

7.2 The Scalar Frontogenesis Function in a Non-uniformly Saturated Atmosphere

Traditionally, the Lagrange change of the gradients of θ or T (the potential temperature or temperature) is used as the criterion for frontogenesis in a dry atmosphere. In a saturated atmosphere, frontogenesis drives the θ_e isoline density. However, the real atmosphere is neither absolutely dry nor completely saturated everywhere but is non-uniformly saturated (as is the case near a humidity front). Therefore, the generalized potential temperature, which is suitable for use in the case of non-uniform saturation (Gao et al., 2004)[22] is used to derive the generalized frontogenesis function in a non-uniformly saturated atmosphere. Based on this new variable, the generalized frontogenesis function in a non-uniformly saturated atmosphere is defined as

$$F^* = \frac{d}{dt}\left|\nabla\theta^*\right|, \tag{7.2.1}$$

which gives the Lagrange rate of change of the absolute value of the horizontal gradient of the generalized potential temperature. $\theta^* = \theta \exp[\frac{Lq_s}{c_p T}(\frac{q}{q_s})^k]$, and $\left|\nabla\theta^*\right|$ is the absolute value of the horizontal gradient of the generalized potential temperature:

$$\left|\nabla\theta^*\right| = \sqrt{(\frac{\partial\theta^*}{\partial x})^2 + (\frac{\partial\theta^*}{\partial y})^2}. \tag{7.2.2}$$

The generalized frontogenesis function will be analyzed in detail in the next section.

7.2.1 The Scalar Frontogenesis Function in a Non-uniformly Saturated Atmosphere

$$F^* = \frac{d}{dt}\left|\nabla\theta^*\right| = \frac{1}{\left|\nabla\theta^*\right|}\left[\frac{\partial\theta^*}{\partial x}\frac{d}{dt}\left(\frac{\partial\theta^*}{\partial x}\right) + \frac{\partial\theta^*}{\partial y}\frac{d}{dt}\left(\frac{\partial\theta^*}{\partial y}\right)\right] \quad (7.2.3)$$

Given that $\frac{d\theta^*}{dt} = Q^*$, the following can be derived from equation (7.2.3):

$$\frac{d}{dt}\left(\frac{\partial\theta^*}{\partial x}\right) = \frac{\partial Q^*}{\partial x} - \frac{\partial \mathbf{v}}{\partial x}\cdot\nabla\theta^* \quad \text{and} \quad (7.2.4a)$$

$$\frac{d}{dt}\left(\frac{\partial\theta^*}{\partial y}\right) = \frac{\partial Q^*}{\partial y} - \frac{\partial \mathbf{v}}{\partial y}\cdot\nabla\theta^*. \quad (7.2.4b)$$

$\mathbf{v}$ is the three-dimensional wind vector, and Q^* represents the diabatic heat except for the latent heat of condensation.

Therefore, equation (7.2.3) becomes

$$F^* = \frac{1}{\left|\nabla\theta^*\right|}\{\frac{\partial\theta^*}{\partial x}[\frac{\partial Q^*}{\partial x} - \frac{\partial \mathbf{v}}{\partial x}\cdot\nabla\theta^*] + \frac{\partial\theta^*}{\partial y}[\frac{\partial Q^*}{\partial y} - \frac{\partial \mathbf{v}}{\partial y}\cdot\nabla\theta^*]\}$$

$$= \frac{1}{\left|\nabla\theta^*\right|}[\frac{\partial\theta^*}{\partial x}(-\frac{\partial \mathbf{v}}{\partial x}\cdot\nabla\theta^*) + \frac{\partial\theta^*}{\partial y}(-\frac{\partial \mathbf{v}}{\partial y}\cdot\nabla\theta^*)]$$

$$+ \frac{1}{\left|\nabla\theta^*\right|}[\frac{\partial\theta^*}{\partial x}\frac{\partial Q^*}{\partial x} + \frac{\partial\theta^*}{\partial y}\frac{\partial Q^*}{\partial y}]$$

$$= -\frac{1}{\left|\nabla\theta^*\right|}[\frac{\partial\theta^*}{\partial x}(\frac{\partial \mathbf{v}_h}{\partial x}\cdot\nabla\theta^*) + \frac{\partial\theta^*}{\partial y}(\frac{\partial \mathbf{v}_h}{\partial y}\cdot\nabla\theta^*)]$$

$$- \frac{1}{\left|\nabla\theta^*\right|}[(\frac{\partial\theta^*}{\partial x}\frac{\partial w}{\partial x} + \frac{\partial\theta^*}{\partial y}\frac{\partial w}{\partial y})\frac{\partial\theta^*}{\partial z}]$$

$$+ \frac{1}{\left|\nabla\theta^*\right|}[\frac{\partial\theta^*}{\partial x}\frac{\partial Q^*}{\partial x} + \frac{\partial\theta^*}{\partial y}\frac{\partial Q^*}{\partial y}] \quad (7.2.5)$$

where $\mathbf{v}$ is the horizontal velocity.

From equation (7.2.5), it can be seen that the generalized frontogenesis function is associated with the horizontal shear of the three-dimensional wind vector, friction, and/or turbulent mixing.

7.2.2 The Physical Meaning of Each Term in the Generalized Frontogenesis Function

(A) Contribution of the term associated with horizontal motion to frontogenesis

For the convenience of discussion, the isolines of θ^* are assumed to be parallel to the *x*-axis. Thus the *y*-axis is orientated along the gradient of

θ^*, $\frac{\partial \theta}{\partial x} = 0$, and $\frac{\partial \theta}{\partial y} = \nabla \theta$. Therefore, the term related to the horizontal motion, $-\frac{1}{\left|\nabla \theta^*\right|}[\frac{\partial \theta^*}{\partial x}(\frac{\partial \mathbf{v}_h}{\partial x} \cdot \nabla \theta^*) + \frac{\partial \theta^*}{\partial y}(\frac{\partial \mathbf{v}_h}{\partial y} \cdot \nabla \theta^*)]$, becomes $-\frac{1}{\left|\nabla \theta^*\right|}[(\frac{\partial \theta^*}{\partial y})^2 \frac{\partial v}{\partial y}]$. Since *v* is the velocity component in the *y*-direction, it is orthogonal to the isolines of θ^*. As *v* decreases in the direction of the horizontal gradient of θ^*, i.e., $\frac{\partial v}{\partial y} < 0$, then $-\frac{1}{\left|\nabla \theta^*\right|}[(\frac{\partial \theta^*}{\partial y})^2 \frac{\partial v}{\partial y}] > 0$ and frontogenesis occurs. In contrast, if $\frac{\partial v}{\partial y} > 0$, frontolysis occurs. This reveals the contribution of the term associated with horizontal motion to frontogenesis: as the isolines of θ^* becomes denser because of horizontal convergence, frontogenesis occurs; as they become less dense, frontolysis occurs.

(B) Contribution of the term related to vertical motion to frontogenesis

As for the term associated with the horizontal velocity, the isolines of θ^* are also assumed to be parallel to the *x*-axis. Therefore the term related to the vertical motion, $-\frac{1}{\left|\nabla \theta^*\right|}[(\frac{\partial \theta^*}{\partial x}\frac{\partial w}{\partial x} + \frac{\partial \theta^*}{\partial y}\frac{\partial w}{\partial y})\frac{\partial \theta^*}{\partial z}]$, becomes

$-\frac{1}{\left|\nabla\theta^*\right|}\left[\frac{\partial\theta^*}{\partial y}\frac{\partial w}{\partial y}\frac{\partial\theta^*}{\partial z}\right]$ or $\frac{\partial w}{\partial y}\frac{\partial\theta^*}{\partial z}$. If the stratification is stable (i.e., $\frac{\partial\theta^*}{\partial z}>0$), then if a moist, warm air parcel descends ($w<0$) or cold, dry air ascends ($w>0$), then $\frac{\partial w}{\partial y}>0$ and the contribution of the vertical motion to frontogenesis is positive, i.e., $\frac{\partial w}{\partial y}\frac{\partial\theta^*}{\partial z}>0$, and frontogenesis occurs. The opposite occurs when warm air ascends or cold air descends. If the stratification is unstable, however, frontolysis occurs if ascending motion descends in the *y*-direction.

(C) Contribution of diabatic heat to frontogenesis

The term related to the diabatic heat, $\frac{1}{\left|\nabla\theta^*\right|}\left[\frac{\partial\theta^*}{\partial x}\frac{\partial Q^*}{\partial x}+\frac{\partial\theta^*}{\partial y}\frac{\partial Q^*}{\partial y}\right]$, can be simplified to $\frac{1}{\left|\nabla\theta^*\right|}\left[\frac{\partial\theta^*}{\partial y}\frac{\partial Q^*}{\partial y}\right]$, i.e., $-\frac{\partial Q^*}{\partial y}$, if the above assumption holds. As cold, dry air moves southward and rises above warm, moist air, heat and water vapor will be transferred into the cold air by physical processes such as turbulence, convection, radiation, and heat exchange. This will cause the cold, dry air to become warmer and the generalized potential temperature to increase; i.e., $\frac{d\theta^*}{dt}>0$ （$Q^*>0$）.The diabatic heat will change the properties of the cold air

and produce a descending gradient for the generalized potential temperature between the cold and warm air; i.e., $-\frac{\partial Q^*}{\partial y} < 0$ and frontolysis occurs. Similarly, if warm air moves northward and cools diabatically, then $\frac{d\theta^*}{dt} < 0$ ($Q^* < 0$), which also produces a downward generalized potential temperature gradient, and $-\frac{\partial Q^*}{\partial y} < 0$; therefore, frontolysis again occurs. However, in a free atmosphere, the ascent of a warm, moist air parcel will cause latent heat to be released by condensation, which will favor strengthening of the horizontal gradient of the generalized potential temperature between the cold and warm air; i.e., frontogenesis occurs.

7.2.3 Another Form of the Generalized Frontogenesis Function in a Non-uniformly Saturated Atmosphere

$$F^* = \frac{1}{\left|\nabla\theta^*\right|}\left[\frac{\partial\theta^*}{\partial x}\left(-\frac{\partial \mathbf{v}}{\partial x}\cdot\nabla\theta^*\right)+\frac{\partial\theta^*}{\partial y}\left(-\frac{\partial \mathbf{v}}{\partial y}\cdot\nabla\theta^*\right)\right]$$
$$+\frac{1}{\left|\nabla\theta^*\right|}\left[\frac{\partial\theta^*}{\partial x}\frac{\partial Q^*}{\partial x}+\frac{\partial\theta^*}{\partial y}\frac{\partial Q^*}{\partial y}\right] \quad . \qquad (7.2.6)$$
$$= T_1 + T_2 + T_3 + T_4$$

$$T_1 = \frac{1}{\left|\nabla\theta^*\right|}\left(\frac{\partial\theta^*}{\partial x}\frac{\partial Q^*}{\partial x}+\frac{\partial\theta^*}{\partial y}\frac{\partial Q^*}{\partial y}\right) = -\mathbf{n}\cdot\nabla Q^*, \qquad (7.2.7a)$$

$$T_2 = -\frac{1}{\left|\nabla\theta^*\right|}\left(\frac{\partial w}{\partial x}\frac{\partial\theta^*}{\partial x} + \frac{\partial w}{\partial y}\frac{\partial\theta^*}{\partial y}\right)\frac{\partial\theta^*}{\partial z} = \frac{\partial\theta^*}{\partial z}\mathbf{n}\cdot\nabla w, \qquad (7.2.7b)$$

$$T_3 = -\frac{D}{2}\left|\nabla\theta^*\right|, \text{ and} \qquad (7.2.7c)$$

$$T_4 = -\frac{1}{2\left|\nabla\theta^*\right|}\left(E_{st}\left(\frac{\partial\theta^*}{\partial x}\right)^2 + 2E_{sh}\left(\frac{\partial\theta^*}{\partial x}\frac{\partial\theta^*}{\partial y}\right) - E_{st}\left(\frac{\partial\theta^*}{\partial y}\right)^2\right). \qquad (7.2.7d)$$

where $\mathbf{n}$ is the unit vector along the direction of $(-\nabla\theta^*)$.

Ninomiya (1984, 2000)[11-12] derived the frontogenesis function that is traditionally used. His derivation was consistent with the form of equations (7.2.7a)–(7.2.7d) except that, in Ninomiya's derivation, θ_e was replaced by θ^* since the background atmosphere used was a saturated rather than a non-uniformly saturated one.

The physical meanings of the terms in equation (7.2.6) are analyzed below.

(A) The term related to diabatic heat, T_1

T_1 represents the contribution to frontogenesis of the projection of the horizontal gradient of the diabatic heat on the direction of the horizontal gradient of the generalized potential temperature.

(B) The vertical motion term, T_2

T_2 represents the effect on frontogenesis of the projection of the horizontal gradient of the vertical velocity in the direction of the horizontal gradient of the generalized potential temperature.

In a stable, stratified atmosphere $\left(\frac{\partial\theta^*}{\partial z} > 0\right)$, the coupling between the

descent of warm air ($w < 0$), and the ascent of cold air ($w > 0$) means that $\mathbf{n}\cdot\nabla w > 0$, so that $T_2 > 0$ and frontogenesis occurs. Vice versa.

(C) The horizontal convergence/divergence term, T_3

T_3 represents the increase or decrease in the horizontal gradient of the generalized potential temperature (i.e., frontogenesis or frontolysis) induced by the horizontal convergence ($D < 0$) or divergence ($D > 0$).

(D) The horizontal deformation term, T_4

T_4 denotes the contribution of the horizontal deformation to the frontogenesis. For simplicity, ideal conditions are assumed. For adiabatic conditions ($T_1 = 0$) and a horizontal airflow ($T_2 = 0$) (for example, on a rigid horizontal boundary such as the Earth's surface), a typical deformation field (e.g., pure stretching deformation) can be chosen. This assumption is made so that the shearing deformation vanishes locally. x is the axis of dilation and y the axis of contraction. The angle between the generalized potential temperature and the x-axis is β (Figure 7.2.1); therefore, the angle between $-\nabla\theta^*$ and the x-axis, $\phi = \beta + \frac{\pi}{2}$. The gradient of the generalized potential temperature can then be expressed as

$$-\nabla\theta^* = \left|\nabla\theta^*\right|[(-\sin\beta)\,\mathbf{i} + \cos\beta\,\mathbf{j}], \tag{7.2.8}$$

$$\text{where } \nabla\theta^* = \frac{\partial\theta^*}{\partial x}i + \frac{\partial\theta^*}{\partial y}j. \tag{7.2.9}$$

Combining equation (7.2.8) and equation (7.2.9) gives the following:

$$\frac{\partial\theta^*}{\partial x} = \left|\nabla\theta^*\right|\sin\beta, \text{ and } \frac{\partial\theta^*}{\partial y} = -\left|\nabla\theta^*\right|\cos\beta. \tag{7.2.10}$$

Combining equation (7.2.10) with equation (7.2.7d), the expression for T_4 becomes

$$T_4 = -\frac{\left|\nabla\theta^*\right|}{2}(E_{st}\sin^2\beta - 2E_{sh}\sin\beta\cos\beta - E_{st}\cos^2\beta)$$
$$= \frac{\left|\nabla\theta^*\right|}{2}(E_{st}\cos 2\beta + E_{sh}\sin 2\beta) \quad (7.2.11)$$

For a purely stretching deformation (i.e., the shearing deformation, $E_{sh} = 0$), equation (7.2.11) can be simplified to

$$T_4 = \frac{1}{2}\left|\nabla\theta^*\right| E\cos 2\beta, \quad (7.2.12)$$

where E ($E^2 = E_{st}^2 + E_{sh}^2$) is the total deformation.

If $\beta < \frac{\pi}{4}$, then $T_4 > 0$ and frontogenesis occurs. If $\beta = \frac{\pi}{4}$, then $T_4 = 0$; if $\beta > \frac{\pi}{4}$, then $T_4 < 0$ and frontolysis occurs. When $\beta = 0$, the frontogenesis reaches its peak strength. Therefore, deformation is the pattern most favorable to frontogenesis in a non-uniformly saturated atmosphere. This is consistent with the results of analyses of both dry air and saturated air.

7.2.4 A Case Study Using the Generalized Scalar Frontogenesis Function in a Non-uniformly Saturated Atmosphere

In this section, a frontal precipitation process that occurred in northern China in August 2004 is discussed. The applicability of the generalized frontogenesis function in a non-uniformly saturated moist atmosphere is considered by using $1^\circ \times 1^\circ$ NCEP/NCAR data.

Figure 7.2.2 shows the temporal mean frontal surface (the region of

concentrated isolines of θ^*) at 00:00 UTC on 11 August 2004 and the values of the different terms in the frontogenesis function (equation (7.2.6)). Figure 7.2.2 (a) shows the relative sizes of the correlations between the generalized frontogenesis function and the components of equation (7.2.6). The trends in the different terms (Figure 7.2.2) and their distributions at different levels show that, although the vertical velocity term is negative near to the front (not shown), the large-scale convergence and deformation of the horizontal wind and also the diabatic heating within the frontal zone combine to sustain the strong gradient of θ^* against the decrease in θ^* caused by the tilting/twisting effect. This example thus illustrates the main features of the generalized frontogenesis function.

In this section, a real inhomogeneous saturated atmosphere has been considered using the generalized potential temperature. This is an appropriate way of deriving the scalar frontogenesis function for an inhomogeneous saturated atmosphere. This is not only a more suitable method of solving the frontogenesis problem theoretically, it can also be used to describe a real case of frontogenesis in an inhomogeneous saturated moist atmosphere.

Traditionally, the Lagrange change in the gradients of θ or T (the potential temperature or temperature) has been used as the criterion for frontogenesis in a dry atmosphere. In the case of a saturated atmosphere, frontogenesis derives θ_e isolines dense; However, the real atmosphere is neither absolutely dry nor completely saturated everywhere but is non-uniformly saturated (such as near to a humidity front). Therefore, the generalized potential temperature, which is suitable for application to a situation where the saturation is non-uniform (Gao et al., 2004) can be

used to derive the generalized frontogenesis function in a non-uniformly moist atmosphere. Using this new variable, the generalized frontogenesis function in a non-uniformly saturated moist atmosphere is

$$F^* = \frac{d}{dt}\left|\nabla\theta^*\right|, \tag{7.2.13}$$

Where $\nabla\theta^*$ represents the horizontal gradient of the generalized potential temperature. The derivation of equation (7.2.13) is left as an exercise for the reader.

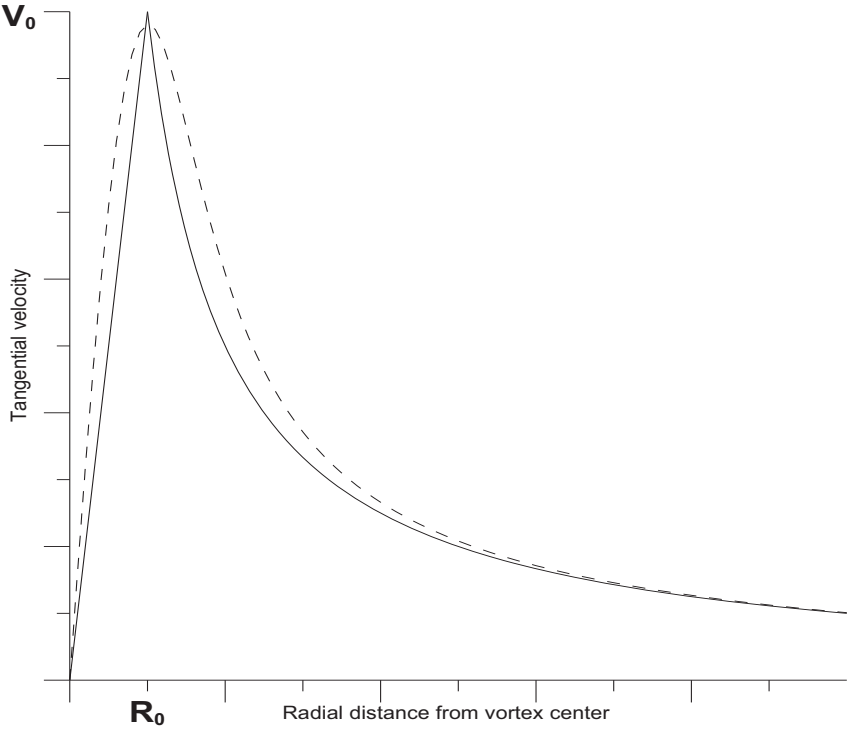

Fig. 7.1.1. The tangential velocity derived from the traditional Rankine combined vortex (solid line) and vortex (dashed line) which has a similar appearance to a smoothed version of the Rankine combined vortex.

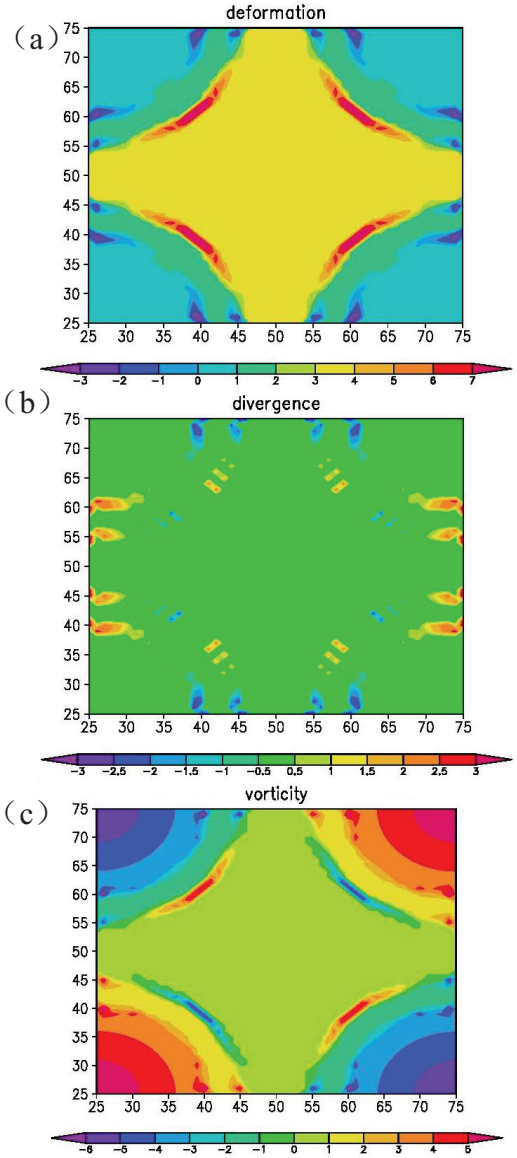

Fig. 7.1.2. (a) Deformation, (b) divergence, and (c) vorticity fields (units: 10^{-5} s^{-1}) of the idealized flow shown in Fig. 7.1.1

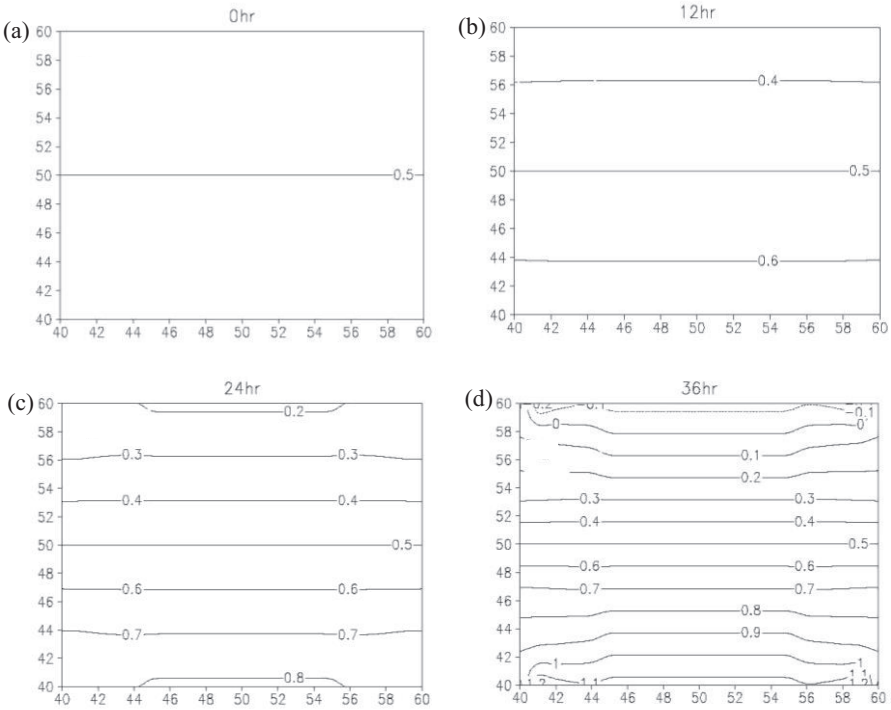

Fig. 7.1.3. A 2D relative humidity field subject to advection by an idealized deformational flow field at (a) 0 nours, (b) 12 hours, (c) 24 hours, and (d) 36 hours. The contour intervals have a spacing of 0.1, and all contours at time zero have an east–west orientation.

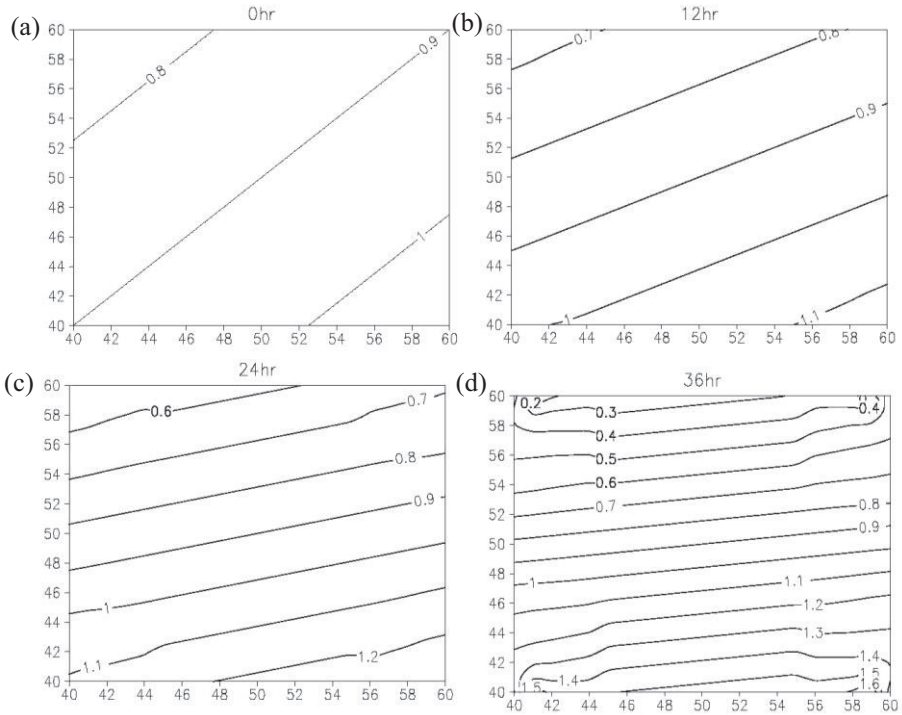

Fig. 7.1.4. A 2D relative humidity field subject to advection by an idealized deformational flow field at (a) 0 hours, (b) 12 hours, (c) 24 hours, and (d) 36 hours. The contours have a spacing of 0.1, and all contours at time zero have a southwest–northeast orientation.

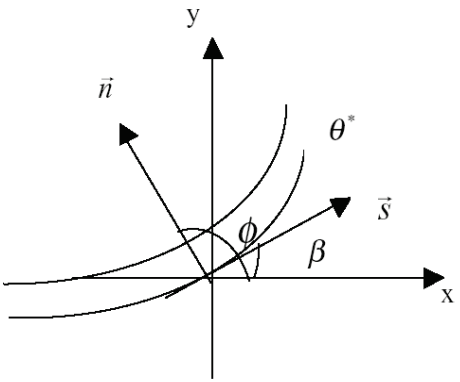

Fig. 7.2.1. Schematic illustrating right-handed Cartesian coordinate systems (*x, y*) and (*s, n*) defined locally by rotating the standard (*x, y*) Cartesian coordinates system through an angle β to give the (*s,n*) system. The *s*-axis is tangent to an isoline of θ^* and is directed such that the *n*-axis points toward colder air. The angle between $\vec{n}$ and the *x*-axis is ϕ.

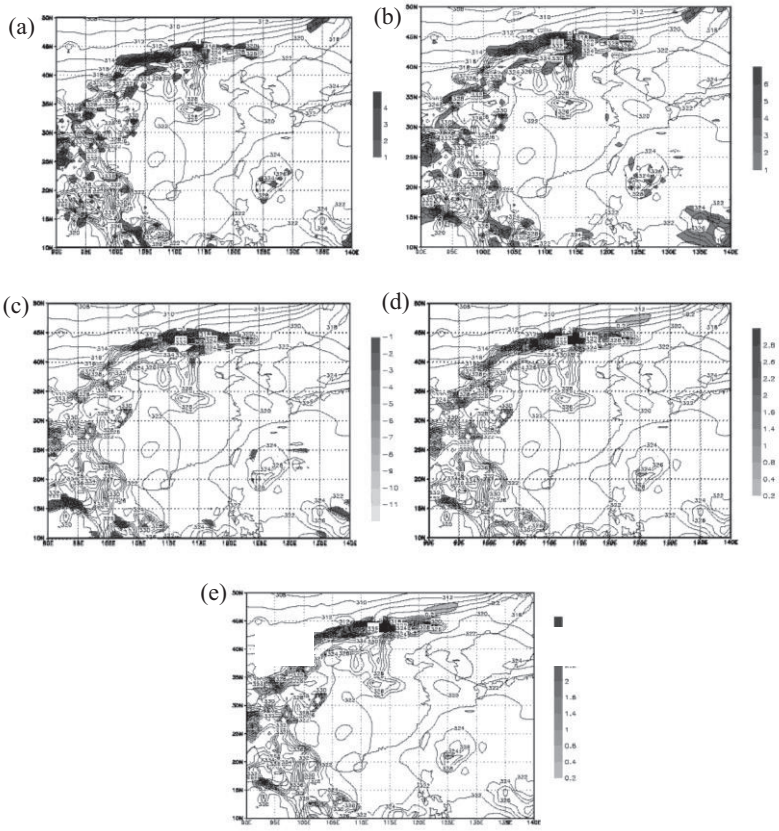

Fig. 7.2.2. The temporal mean frontal surface (the region of intense iso-θ^*) at 00:00 UTC, 11 August 2004 together with the values of the different terms in the frontogenesis function (equation (7.2.6)). Thick real isoline is iso-θ^* (units: K). The shading denotes the regions where the intensity of the different terms in the frontogenesis function satisfies: (a) $T_{1234} > 1$, (b) $T_1 > 1$, (c) $T_2 < -1$, (d) $T_3 > 0.2$, and (e) $T_4 > 0.2$ (units: 10^{-9} K m^{-1} s^{-1}).

Notes

[1]Petterssen S.(1936) "Contribution to the theory of frontogenesis," *Geofys Publ,* 11(6):1-27.

[2] Miller J. E. (1948) "On the concept of frontogenesis," *Journal of Meteorology,* 5(4):169-171.

[3]Petterssen S. (1956) Weather analysis and forecasting, Vol.1: *Motion and Motion Systems*, 2 nd ed. McGraw-Hill, 428pp.

[4]Palmin E. and C. W. Newton (1948) "A study of the mean wind and temperature distribution in the vicinity of the polar front in winter," *Journal of Meteorology,* 5(5):220–226.

[5]Phillips N. A. (1956) "The general circulation of the atmosphere, a numerical experiment," *Quarterly Journal of the Royal Meteorological Society,* 82(352):123–164.

[6]Williams R. T. (1967) "Atmosphere frontogenesis, a numerical experiment," *Journal of Atmospheric Sciences,* 24(6):627–641.

[7]Hoskins B. J. and F. P. Bretherton (1972) "Atmospheric frontogenesis models: mathematical formulation and Solution," *Journal of Atmospheric Sciences,* 29(1):11–37.

[8]Davies-Jones R. P. (1982) *Observational and Theoretical Aspects of Tornadogenesis. Intense Atmospheric Vortices*, L. Bengtsson and J. Lighthill, Eds. Springer-Verlag: pp. 175-189.

[9]Davies-Jones R. P. (1985) "Comments on "A kinematic analysis of frontogenesis associated with a nondivergent vortex," *Journal of Atmospheric Sciences,* 42(19):2073-2075.

[10]Doswell III C. A. (1984) "A kinematic analysis of frontogenesis associated with a nondivergent vortex," *Journal of Atmospheric Sciences*, 41(7):1242-1248.

[11]Ninomiya K.(1984) "Characteristics of Baiu front as a predominant subtropical front in the summer northern hemisphere," *Journal of the Meteorological Society of Japan,* 62(6):880–894.

[12]Ninomiya K. (2000) “Large- and meso-scale characteristics of Meiyu/Baiu front associated with intense rainfalls in 1-10 July 1991,” *Journal of the Meteorological Society of Japan,* 78(2):141-157.

[13]Zeng Q. C. (1979) *Mathematical and Physical Basis of the Numerical Weather Forecast*. Beijing: Science Press: pp. 237–314.

[14]Wu R. S., S. T. Gao, Z. M. Tan and et al. (2004) *Frontal Processes and Mesoscale Disturbances*. Beijing: Meteorological Press: pp. 6-57.

[15]Harasti P. R. and R. List (2005) “Principal component analysis of Doppler radar data. Part I: Geometric connections between eigenvectors and the core region of atmosphere vortices,” *Journal of Atmospheric Sciences,* 62(11):4027-4042.

[16]Hoxit L.R., J. M. Fritsch and C. F. Chappell (1978) [Reply]: Reply, *Monthly Weather Review,* 106(7):1034-1034.

[17]Maddox R. A., L. R. Hoxit, C. F. Chappell and *et al.* (1978) “Comparison of meteorological aspects of the big Thompson and rapid city flash floods,” *Monthly Weather Review,* 106(3):375–389.

[18]Caracena F., R. A. Maddox, L. R. Hoxit and *et al.* (1979) “Mesoanalysis of the big Thompson storm,” *Monthly Weather Review,* 107(1):1-17.

[19]Maddox R. A., F. Canova and L. R. Hoxit (1980a) “Meteorological characteristics of flash flood events over the western United States,” *Monthly Weather Review,* 108(11):1866-1877.

[20]Maddox R. A., L. R. Hoxit and C. F. Chappell (1980b) “A study of tornadic thunderstorm interactions with thermal boundaries,” *Monthly Weather Review,* 108(3):322-336.

[21]Keyser D., M. J. Reeder and R. J. Reed (1988) “A generalization of Petterssen’s frontogenesis function and its relation to the forcing of vertical motion,” *Monthly Weather Review,* 116(3):762–781.

[22]Gao S. T., X. R. Wang and Y. S. Zhou (2004) “Generation of generalized moist potential vorticity in a frictionless and moist adiabatic flow,” *Geophysical Research Letters,* L12113, 31(12), doi: 10.1029/2003GL019152.

CHAPTER EIGHT

ATMOSPHERIC POTENTIAL VORTICITY

Wind, temperature, pressure, and water vapor are the basic elements used to describe atmospheric states, and their associated equations are derived in order to form a framework for studying the atmosphere. Theoretically, a weather forecast is made by accurately solving these atmospheric equations with accurate initial conditions. However, the complexity of atmospheric processes, the accuracy of the initial conditions, the way in which computing methods are constructed, and the parameterization of subscale atmospheric processes mean that numerical modeling does not describe the evolution of weather systems well. In addition to the solution of primitive equations, the physical quantities associated with the movement and development of weather systems are diagnosed in atmospheric dynamics and synoptic meteorology. These quantities are mainly related to the key physical processes that are responsible for the development of weather systems and thus are predicted based on typical dynamic and thermodynamic structures. The conservation of these quantities is very important; in particular, the conservation of potential vorticity has been widely applied and is one of most important derived quantities in modern dynamic meteorology.

8.1 Potential Vorticity and its Trend Equation

The concept of potential vorticity was introduced by Rossby (1940)[1]. Ertel (1942)[2] gave a complete definition of the potential vorticity in a baroclinic atmosphere. In order to derive the equation for the potential vorticity and to demonstrate its conservation, the equations for the vorticity vector, the continuity, and its thermodynamics are first introduced here:

$$\frac{d\boldsymbol{\xi}_a}{dt} = (\boldsymbol{\xi}_a \cdot \nabla)\mathbf{v} - (\nabla \cdot \mathbf{v})\boldsymbol{\xi}_a + \nabla p \times \nabla \alpha + \nabla \times \mathbf{F} \quad , \tag{8.1.1}$$

$$\frac{1}{\rho}\frac{d\rho}{dt} = -\nabla \cdot \mathbf{v} \text{, and} \tag{8.1.2}$$

$$\frac{d\theta}{dt} = Q_d \tag{8.1.3}$$

In the above, $\boldsymbol{\xi}_a = \nabla \times \mathbf{v} + 2\boldsymbol{\Omega}$ is the absolute vorticity vector, p is the pressure, α is the specific volume, ρ is the density of the air, θ is the potential temperature, and Q_d is the diabatic heating. From (8.1.3) and using $\nabla(\mathbf{v} \cdot \nabla\theta) = \mathbf{v} \cdot \nabla(\nabla\theta) + \nabla\mathbf{v} \cdot \nabla\theta$, the equation for the potential temperature gradient is derived as

$$\frac{d\nabla\theta}{dt} = -\nabla\mathbf{v} \cdot \nabla\theta + \nabla Q_d \,. \tag{8.1.4}$$

$\frac{1}{\rho} \times$ (8.1.1) – $\frac{1}{\rho}\boldsymbol{\xi}_a \times$ (8.1.2) yields

$$\frac{d}{dt}(\frac{\boldsymbol{\xi}_a}{\rho}) = (\frac{\boldsymbol{\xi}_a}{\rho} \cdot \nabla)\mathbf{v} - \frac{1}{\rho}\nabla p \times \nabla\alpha + \frac{1}{\rho}\nabla \times \mathbf{F} \,. \tag{8.1.5}$$

Taking the dot product of $\frac{\boldsymbol{\xi}_a}{\rho}$ and (8.1.5) gives

$$\frac{\boldsymbol{\xi}_a}{\rho} \cdot \frac{d\nabla\theta}{dt} = -\frac{\boldsymbol{\xi}_a}{\rho} \cdot (\nabla\mathbf{v} \cdot \nabla\theta) + \frac{\boldsymbol{\xi}_a}{\rho} \cdot \nabla Q_d \,, \tag{8.1.6}$$

and taking the dot product of $\nabla\theta$ and (8.1.4) gives

$$\nabla\theta \cdot \frac{d}{dt}(\frac{\boldsymbol{\xi}_a}{\rho}) = \nabla\theta \cdot (\frac{\boldsymbol{\xi}_a}{\rho} \cdot \nabla)\mathbf{v} - \frac{1}{\rho}\nabla p \times \nabla\alpha \cdot \nabla\theta + \frac{1}{\rho}\nabla \times \mathbf{F} \cdot \nabla\theta \,. \tag{8.1.7}$$

As θ is a function of p and α, we have

$$\nabla\theta = \frac{\partial\theta}{\partial p}\nabla p + \frac{\partial\theta}{\partial\alpha}\nabla\alpha \,, \tag{8.1.8}$$

and thus $\nabla p \times \nabla\alpha \cdot \nabla\theta = 0$. Also, as

$\nabla\theta \cdot (\frac{\boldsymbol{\xi}_a}{\rho} \cdot \nabla)\mathbf{v} = \frac{\boldsymbol{\xi}_a}{\rho} \cdot (\nabla\mathbf{v} \cdot \nabla\theta)$, equation (8.1.6) plus (8.1.7) becomes

$$\frac{d}{dt}(\frac{\boldsymbol{\xi}_a}{\rho} \cdot \nabla\theta) = \frac{1}{\rho}\nabla \times \mathbf{F} \cdot \nabla\theta + \frac{\boldsymbol{\xi}_a}{\rho} \cdot \nabla Q_d \,. \tag{8.1.9}$$

In (8.1.9), the potential vorticity is defined as the dot product of the vorticity vector and the gradient of the potential temperature; i.e., as

$$Q = \frac{\boldsymbol{\xi}_a}{\rho} \cdot \nabla\theta . \tag{8.1.10}$$

In an adiabatic frictionless atmosphere, the potential vorticity is conserved ($Q_d = 0$ and $\mathbf{F} = 0$).

The conservation of potential vorticity has important applications in atmospheric dynamics and the application of the isentropic potential vorticity to the diagnostic analysis of weather processes in particular. As the horizontal gradient of the potential temperature on an isentropic surface is zero, the potential vorticity consists only of the component of the vorticity perpendicular to the isentropic surface. Large-scale motions are usually quasi-two-dimensional, and the isentropic surface is horizontal. Thus, the isentropic potential vorticity basically describes the evolution of the vertical vorticity. The evolution of cyclones and anticyclones can be detected by tracking areas of anomalous potential vorticity, which is the concept on which IPV is based. With regard to the conservation of potential vorticity and potential temperature in an adiabatic and frictionless atmosphere, air parcels move along their cross line. Because the isentropic potential vorticity represents the state of motion of an air parcel, the potential vorticity can be used to effectively trace air parcel motion. In addition, the potential vorticity is retrievable since it excludes gravity waves and gravity–inertial waves. (The gravity potential and associated buoyancy are not included in the vorticity equation.) The equilibrium fields retrieved by potential vorticity are usually called “slow fold”.

8.2 Second-order Potential Vorticity

During an adiabatic process, the potential temperature is conserved. Following Gao et al. (2014)[3], we have

$$\frac{\partial\theta}{\partial t} = -\mathbf{v} \cdot \nabla\theta . \tag{8.2.1}$$

A local change in the potential temperature results only from the advection of potential temperature. If the wind vector in (8.2.1) is replaced by the vorticity vector, the potential vorticity, which is conserved for a diabatic and frictionless atmosphere, can be derived. Thus,

$$\frac{\partial Q}{\partial t} = -\mathbf{v} \cdot \nabla Q . \tag{8.2.2}$$

The wind vector in the advection term in (8.2.2) is replaced by the vorticity, and a new physical quantity is introduced:

$$Q_S = \frac{1}{\rho} \boldsymbol{\xi}_a \cdot \nabla Q . \tag{8.2.3}$$

Although this new quantity has a form similar to that of the potential vorticity, Q_s contains the potential vorticity gradient and is known as the second-order potential vorticity. The question is: Is the second-order potential vorticity conserved? To answer this question, consider the following momentum equation for a compressible, adiabatic, and frictionless atmosphere:

$$d_t \mathbf{v} + 2\boldsymbol{\Omega} \times \mathbf{v} + \frac{1}{\rho} \nabla p + \boldsymbol{g} = 0 \tag{8.2.4}$$

Introducing the entropy ($s = c_p \ln \theta + C$) and the enthalpy ($H = c_p T$) and using the equation of the state, the pressure gradient in the momentum equation takes the form of the entropy and enthalpy:

$$-\frac{1}{\rho} \nabla p = T \nabla s - \nabla c_p T = T \nabla s - \nabla H . \tag{8.2.5}$$

Substituting (8.2.5) into (8.2.4) yields another form of the momentum equation:

$$d_t \mathbf{v} + 2\boldsymbol{\Omega} \times \mathbf{v} - T \nabla s + \nabla H + \boldsymbol{g} = 0 . \tag{8.2.6}$$

Taking the cross product of (8.2.6) and combining continuity equation (8.1.2), the vorticity equation is derived:

$$d_t \left(\frac{\boldsymbol{\xi}_a}{\rho} \right) = \frac{\boldsymbol{\xi}_a}{\rho} \cdot \nabla \mathbf{v} - \frac{1}{\rho} \nabla T \times \nabla s . \tag{8.2.7}$$

In a barotropic atmosphere, (8.2.7) becomes

$$d_t \left(\frac{\boldsymbol{\xi}_a}{\rho} \right) = \frac{\boldsymbol{\xi}_a}{\rho} \cdot \nabla \mathbf{v} . \tag{8.2.8}$$

For a baroclinic atmosphere, a similar form of the vorticity equation can be derived:

$$d_t \left(\frac{\boldsymbol{\xi}_g}{\rho} \right) = \frac{\boldsymbol{\xi}_g}{\rho} \cdot \nabla \mathbf{v} , \tag{8.2.9}$$

where $\boldsymbol{\xi}_g = \boldsymbol{\xi}_a - \nabla\Lambda \times \nabla s$ is the generalized vorticity or barotropic vorticity, $\nabla\Lambda \times \nabla s$ is the baroclinic vorticity, Λ denotes Lagrangian integration of the temperature, T ($d_t\Lambda = T$), and $s = c_p \ln\theta$ is the entropy.

$$d_t\left(\frac{\nabla\Lambda \times \nabla s}{\rho}\right) = \left(\frac{\nabla\Lambda \times \nabla s}{\rho}\right) \cdot \nabla \mathbf{v} + \frac{\nabla T \times \nabla s}{\rho} \tag{8.2.10}$$

(A detailed derivation can be found in Gao et al. (2012)[4]; otherwise, this is left as an exercise for the reader.) Based on (8.2.9), any tracing function, λ, has the following equation:

$$d_t\left(\frac{1}{\rho}\boldsymbol{\xi}_g \cdot \nabla\lambda\right) = \frac{1}{\rho}\boldsymbol{\xi}_g \cdot \nabla d_t\lambda\,. \tag{8.2.11}$$

(8.2.11) is important for a new conserved quantity. When $\lambda = s$, we have

$$d_t\left(\frac{1}{\rho}\boldsymbol{\xi}_g \cdot \nabla s\right) = \frac{1}{\rho}\boldsymbol{\xi}_g \cdot \nabla d_t s\,. \tag{8.2.12}$$

During an adiabatic process, the entropy is conserved ($d_t s = 0$) and we have

$$d_t\left(\frac{1}{\rho}\boldsymbol{\xi}_g \cdot \nabla s\right) = 0\,. \tag{8.2.13}$$

Taking into account that

$$\boldsymbol{\xi}_g \cdot \nabla s = \left(\boldsymbol{\xi}_a - \nabla\Lambda \times \nabla s\right) \cdot \nabla s = \boldsymbol{\xi}_a \cdot \nabla s\,, \tag{8.2.14}$$

we have shown that the potential vorticity is conserved:

$$Q = \frac{1}{\rho}\boldsymbol{\xi}_a \cdot \nabla s\,. \tag{8.2.15}$$

This provides a new method for deriving the potential vorticity. Notice that although the potential vorticity contains the complete absolute vorticity vector, the fact that $(\nabla\Lambda \times \nabla s) \cdot \nabla s = 0$ means that the baroclinic vorticity is excluded from the potential vorticity; i.e., the vorticity accumulated by baroclinic processes is not included in the potential vorticity.

The conservation of entropy was used in the above derivation of the potential vorticity. Similarly, when $\lambda = Q$, we have

$$d_t(\frac{1}{\rho}\boldsymbol{\xi}_g \cdot \nabla Q) = \frac{1}{\rho}\boldsymbol{\xi}_g \cdot \nabla d_t Q. \tag{8.2.16}$$

The conservation of the potential vorticity ($d_t Q = 0$) in an adiabatic frictionless atmosphere leads to

$$d_t(\frac{1}{\rho}\boldsymbol{\xi}_g \cdot \nabla Q) = 0. \tag{8.2.17}$$

A new, conserved quantity is constructed:

$$Q_s = \frac{1}{\rho}\boldsymbol{\xi}_g \cdot \nabla Q. \tag{8.2.18}$$

This new quantity is known as the second-order potential vorticity because it contains the gradient of the potential vorticity. In contrast to (8.2.3), the second-order potential vorticity in (8.2.18) is the dot product of the generalized vorticity vector and the potential vorticity gradient. Although the second-order potential vorticity is derived from the potential vorticity, the two quantities have different physical meanings. The potential vorticity contains the gradient of the potential temperature only, whereas the second-order potential vorticity includes the gradient of the potential vorticity. Thus, the potential vorticity depicts the evolution of disturbances along the isentropic surface, whereas the second-order potential vorticity denotes the evolution of disturbances along the isotimic surface of the potential vorticity.

8.3 The Potential Vorticity and Second-order Potential Vorticity in Terrain-following Coordinates

The potential vorticity is usually analyzed using pressure coordinates or isentropic coordinates. Since mesoscale models (e.g., the WRF model) use terrain-following coordinates, their outputs need to be converted from terrain-following coordinates to pressure (or isentropic) coordinates. These outputs are then used to calculate the potential vorticity. This conversion between two coordinate systems introduces interpolation errors, which can cause errors in the calculation of the potential vorticity. Thus, it is useful to derive the potential vorticity in terrain-following coordinates. Following the WRF model, Cao and Xu (2011)[5] defined the terrain-following coordinates:

$$\eta^* = \frac{p - p_t}{\mu} \tag{8.3.1}$$

and

$$\mu = p_s - p_t . \tag{8.3.2}$$

Here, p is the pressure, p_s is the surface pressure, and p_t is the pressure at the upper boundary:

$$\frac{\partial F}{\partial p} = \frac{\partial F}{\partial \eta^*}\frac{\partial \eta^*}{\partial p} \text{ and} \tag{8.3.3}$$

$$\left.\frac{\partial F}{\partial s}\right|_{\eta^*} = \left.\frac{\partial F}{\partial s}\right|_{p} + \left.\frac{\partial F}{\partial \eta^*}\frac{\partial \eta^*}{\partial p}\frac{\partial p}{\partial s}\right|_{\eta^*} \tag{8.3.4}$$

Cao and Xu (2011) also derived the potential vorticity in terrain-following coordinates as

$$Q_{\eta^*} = -(g/\mu)(f\,\mathbf{k} + \nabla_{\eta^*} \times \mathbf{v}) \cdot \nabla_{\eta^*}\theta . \tag{8.3.5}$$

The results of numerical experiments show that, if the potential vorticity is directly calculated in terrain-following coordinates, it depicts weather systems much better than if it is transferred from other coordinate systems.

As with the potential vorticity, using data transferred from a different coordinate system produces errors in the calculated second-order potential vorticity. Thus, here, the second-order potential vorticity is introduced in terrain-following coordinates. The second-order potential vorticity can be written in pressure coordinates as

$$Q_{sp} = -g(f\,\mathbf{k} + \nabla_p \times \mathbf{v}) \cdot \nabla_p Q . \tag{8.3.6}$$

The baroclinic vorticity is excluded from (8.3.6) because it is hard to calculate this accurately when carrying out a synoptic diagnosis as a result of the limitations of the temporal and spatial resolutions of the data. Although it is no longer conserved due to the exclusion of the baroclinic vorticity, the second-order potential vorticity is still important in diagnosing severe weather systems. Based on (8.3.3)–(8.3.4), the second-order potential vorticity in terrain-following coordinates can be written as

$$
\begin{aligned}
Q_{s\eta^*} &= -g[-\frac{\partial v}{\partial \eta^*}\frac{\partial \eta^*}{\partial p}(\frac{\partial Q_{\eta^*}}{\partial x}-\frac{\partial Q_{\eta^*}}{\partial \eta^*}\frac{\partial \eta^*}{\partial p}\frac{\partial p}{\partial x})+\frac{\partial u}{\partial \eta^*}\frac{\partial \eta^*}{\partial p}(\frac{\partial Q_{\eta^*}}{\partial y}-\frac{\partial Q_{\eta^*}}{\partial \eta^*}\frac{\partial \eta^*}{\partial p}\frac{\partial p}{\partial y}) \\
&\quad +(\frac{\partial v}{\partial x}-\frac{\partial v}{\partial \eta^*}\frac{\partial \eta^*}{\partial p}\frac{\partial p}{\partial x}-\frac{\partial u}{\partial y}+\frac{\partial u}{\partial \eta^*}\frac{\partial \eta^*}{\partial p}\frac{\partial p}{\partial y}+f)\frac{\partial Q_{\eta^*}}{\partial \eta^*}\frac{\partial \eta^*}{\partial p}] \\
&= -g\frac{\partial \eta^*}{\partial p}(-\frac{\partial v}{\partial \eta^*}\frac{\partial Q_{\eta^*}}{\partial x}+\frac{\partial u}{\partial \eta^*}\frac{\partial Q_{\eta^*}}{\partial y}+(\frac{\partial v}{\partial x}-\frac{\partial u}{\partial y}+f)\frac{\partial Q_{\eta^*}}{\partial \eta^*}) \\
&= -g/\mu(f\mathbf{k}+\nabla_{\eta^*}\times\mathbf{v})\cdot\nabla_{\eta^*}Q_{\eta^*}
\end{aligned}
\tag{8.3.7}
$$

8.4 The Generalized Moist Potential Vorticity

In Chapter 3, the condensation probability function and generalized potential temperature were derived. The generalized potential temperature is more useful than the equivalent potential temperature. Due to the close relationship between the moist potential vorticity and equivalent potential temperature in moist atmospheric dynamics, the equivalent potential temperature is replaced by the generalized potential temperature when deriving the generalized moist potential vorticity.

The potential vorticity has been widely used in atmospheric studies and applications since it was introduced by Ertel (1942)[2]. As it is conserved in an adiabatic frictionless atmosphere, the potential vorticity is one of the most important thermodynamic parameters. However, the potential vorticity is not conserved when latent heat is released during the development of clouds. It *is* conserved in moist adiabatic processes when the moist potential vorticity is introduced by replacing the potential temperature by the equivalent potential temperature. The concept of the moist potential vorticity has been used to study the formation and development of weather systems in Bennetts and Hoskins (1979)[6], Emanuel (1979)[7], Danielsen and Hipskind (1980)[8], Thorpe (1985)[9], Hoskins and Berridford (1988)[10], Xu (1992)[11], Montgomery and Farrell (1993)[12], and Gao et al. (2002)[13-14]. In the following, the generalized potential vorticity is discussed.

8.4.1 The Generalized Moist Potential Vorticity and the Equation for the Trend in the Generalized Moist Potential Vorticity

If there is diabatic heating, the thermodynamic equation in a non-uniformly saturated atmosphere can be written as

$$c_p \frac{T}{\theta}\frac{d\theta}{dt} = -L\frac{d}{dt}[(q/q_s)^k q_s] + S_d \tag{8.4.1}$$

Introducing the generalized potential temperature,

$$\theta^* = \theta \exp[\frac{L}{c_p}\frac{q_s}{T}(\frac{q}{q_s})^k], \tag{8.4.2}$$

(8.4.1) becomes

$$c_p \frac{T}{\theta^*}\frac{d\theta^*}{dt} = Q_d \tag{8.4.3}$$

Using the specific volume, α, the absolute vorticity equation is expressed as

$$\frac{d\boldsymbol{\xi}_a}{dt} = (\boldsymbol{\xi}_a \cdot \nabla)\mathbf{v} - \boldsymbol{\xi}_a \nabla \cdot \mathbf{v} - \nabla\alpha \times \nabla p, \tag{8.4.4}$$

where $\boldsymbol{\xi}_a = \nabla \times \mathbf{v} + 2\Omega$. Using $Q^* = \frac{\theta^*}{c_p T} Q_d$. Eqs.(8.4.3) and (8.4.4) are used to construct the equation for the trend in the generalized moist potential vorticity as

$$\frac{dQ_m^*}{dt} = -\alpha(\nabla\alpha \times \nabla p) \cdot \nabla\theta^* + \alpha\boldsymbol{\xi}_a \cdot \nabla Q^* \tag{8.4.5}$$

Here, $Q_m^* = \alpha\boldsymbol{\xi}_a \cdot \nabla\theta^*$ is the generalized moist potential vorticity (GMPV).

From $\alpha = \frac{R}{p}\theta(p_0/p)^{-\frac{R}{c_p}}$, we obtain

$$\frac{dQ_m^*}{dt} = Q_m^*(A+B)/Q_*, \tag{8.4.6}$$

where, $A = [\frac{R}{p}(p_0/p)^{-\frac{R}{c_p}}] \cdot (\nabla p \times \nabla \theta) \cdot \nabla \theta^*$, $B = \xi_a \cdot \nabla Q^*$, and $Q_* = \xi_a \cdot \nabla \theta^*$. A and B denote the combination of the baroclinicity and the gradient of the generalized potential temperature and the diabatic heating, respectively.

8.4.2 Generation of the Generalized Moist Potential Vorticity

(1) Generation of GMPV from term A in an unsaturated area

For a moist adiabatic atmosphere, excluding friction and radiation, S = 0, and B = 0. Within a moisture-free area, $q = 0$, $(q/q_s)^k = 0$, and $\theta^* = \theta$; thus, A = 0. In a saturated area, $q = q_s$, $(q/q_s)^k = 1$, and $\theta^* = \theta_e$; thus, again, A = 0. Therefore, no GPMV is generated.

In the unsaturated area, $0 < q < q_s$, $0 < (q/q_s)^k < 1$, $\theta^* \neq \theta$, and $\theta^* \neq \theta_e$; thus, $A \neq 0$. This implies that GMPV is generated by term A only.

(2) Generation of GMPV by term A in a nearly saturated area

In the condensation probability function, k = 9. In an unsaturated area, $(\frac{q}{q_s}) < 0.7$, $(\frac{q}{q_s})^9 < 0.05 \approx 0$, and $\theta^* \approx \theta$. In a saturated area, $(\frac{q}{q_s}) > 0.995$, $(\frac{q}{q_s})^9 > 0.96 \approx 1$, and $\theta^* \approx \theta_e$. Thus, $A \neq 0$ but $A \approx 0$.

In a nearly saturated area ($0.7 < (\frac{q}{q_s}) < 0.995$), $0.04 < (\frac{q}{q_s})^9 < 0.96$, and condensation occurs. Thus, in a nearly saturated area in a frictionless adiabatic moist atmosphere, GMPV can be generated by term A.

(3) Generation of GMPV by the term A associated with the condensation.

Using the generalized potential temperature (3.1.12), (8.4.6) can be written as

$$\frac{dQ_m^*}{dt} = Q_m^*(A+B)/Q_* = \frac{LR}{c_p p}\{k(\frac{q}{q_s})^{k-1}\exp[\frac{L}{c_p}\frac{q_s}{T}(\frac{q}{q_s})^k]\}\cdot(\nabla p\times\nabla\theta)\cdot\nabla q = \frac{LR}{c_p p}[k(\frac{q}{q_s})^{k-1}\frac{\theta^*}{\theta}]\cdot(\nabla p\times\nabla\theta)\cdot\nabla q + B/\theta^* \tag{8.4.7}$$

In order to simplify term A, we use A':

$$A' = [\frac{R}{p}(p/p_0)^{-\frac{R}{c_p}}]\cdot(\nabla p\times\nabla\theta)\cdot\nabla\{\theta\exp(\frac{L}{c_p}\frac{q}{T})\} = [\frac{LR}{c_p p}(p/p_0)^{-\frac{2R}{c_p}}][\exp(\frac{L}{c_p}\frac{q}{T})](\nabla p\times\nabla\theta)\cdot\nabla q = [\frac{LR}{c_p p}(p/p_0)^{-\frac{2R}{c_p}}]\frac{\theta_{ue}}{\theta}\cdot(\nabla p\times\nabla\theta)\cdot\nabla q \tag{8.4.8}$$

where A' is associated with the baroclinicity and equivalent potential temperature of the unsaturated moist air and $\theta_e = \theta\exp(\frac{Lq}{c_p T})$.

Using (8.4.8), (8.4.7) becomes

$$A = k(\frac{q}{q_s})^{k-1}\frac{\theta^*}{\theta_{ue}}A' = k(\frac{q}{q_s})^{k-1}\exp(\frac{Lq_s}{c_p T}((\frac{q}{q_s})^k - (\frac{q}{q_s})))A' = \Psi(rh)A' \tag{8.4.9a}$$

where

$$\Psi(rh) = \Psi(\frac{q}{q_s}) = k(\frac{q}{q_s})^{k\text{-}1}\exp(\frac{Lq}{c_p T}((\frac{q}{q_s})^k - (\frac{q}{q_s}))) \tag{8.4.9b}$$

and $rh = q / q_s$. (8.4.9a) shows that, in an adiabatic and frictionless atmosphere, the generation of GMPV is determined by the covariance between $\Psi(rh)$ and A'. $\Psi(rh)$ is a function of the specific humidity, and A' is a function of the moisture gradient. For T = 280 K, p = 1000 hPa, and $q_s = 6 \times 10^{-3}$ g g^{-1}; the change of $\Psi(rh)$ with rh is shown in Figure 8.1. When $rh < rh_1$ (rh_1 = 0.53), $\Psi(rh) < 0.05 \approx 0$, and GMPV cannot be generated. When $rh < rh_2$ (rh_2 = 0.7), $\Psi(rh) < 0.5$, the generation rate of the GMPV is small; when $rh_2 < rh < rh_3$ (rh_3 = 0.77), $0.5 < \Psi(rh) < 1$ and the generation of GMPV is negligible. Finally, when $rh > rh_3$, $\Psi(rh) > 1$ before q approaches q_s , and $\Psi(rh)$ increases quickly with increasing rh. Thus, the generation of GMPV is enhanced as rh increases.

8.5 Thermodynamic and Mass Forcing of the Moist Potential Vorticity

Many researchers have realized that external forcing can lead to anomalous potential vorticity (Hoskins et al., 1985; Gao et al., 1990; Zhou et al., 2002; Keyser and Rotunno, 1990)[15-18]. The main types of external forcing in the case of large-scale systems are thermodynamic forcing and frictional dissipation. For a mesoscale convective system, the large-scale thermodynamic forcing as well as mass forcing are responsible for anomalies in the potential vorticity. The mass fields of a convective system that produces torrential rainfall are largely determined by large-scale convergence or divergence as well as by the reduction in mass due to the rainfall. Thus, studies of torrential rainfall produced by anomalous potential vorticity focus on these two sources of forcing: large-scale thermodynamic forcing and mass forcing.

Meteorologists have paid a lot of attention to anomalous potential vorticity in mesoscale convective systems. For mesoscale convective systems with anomalous potential vorticity, Fritsch and Maddox (1981)[19] demonstrated the association between negative potential vorticity in the upper troposphere and positive potential vorticity in the middle troposphere. Davis and Weisman (1994)[20] and Gray et al. (1998)[21] showed that a positive anomaly in the potential vorticity in the middle troposphere is associated with a mid-level cyclone. The dynamic adjustment of mass fields caused by convection may lead to anomalous potential vorticity in

the middle troposphere (Shutts and Gray, 1994; Fulton et al., 1995)[22-23]. Raymond and Jiang (1990)[24] developed a theory of anomalous potential vorticity for a long-lasting mesoscale convective system; however, they did not consider the mass forcing. Gray (1999)[25] used a mass-forcing model to study the anomalous potential vorticity with mass forcing only; this model only included the effects due to mass transport in a convective system. It was found that the upward (downward) transport of mass resulting from convective activity can produce a mass source (sink) in the upper troposphere and a mass sink (source) in the lower troposphere and that the total mass is conserved. However, the mass loss associated with condensation and rainfall was not considered in the studies by Gray (1999)[25] and Shutts and Gray (1994)[22]. In the discussion of a convective system that follows here, the transport of water vapor and also the mass reduction as a result of rainfall is considered.

Before the equation for moist potential vorticity with mass forcing is derived, the continuity equation with mass forcing will be presented.

Given moist air with a density ρ, and where ρ_d, ρ_m, and ρ_r are the densities of dry air, water vapor, and the condensate, respectively, we have $\rho = \rho_d + \rho_m$. The continuity equation then takes the following forms:

$$\frac{d\rho_d}{dt} + \rho_d \nabla \cdot \mathbf{v} = 0, \tag{8.5.1}$$

$$\frac{d\rho_m}{dt} + \rho_m \nabla \cdot \mathbf{v} = -\dot{\rho}_v, \text{ and} \tag{8.5.2}$$

$$\nabla \cdot (\rho_r \mathbf{v}_T) = \dot{\rho}_v, \tag{8.5.3}$$

where $\dot{\rho}_v$ is the condensation rate and $\mathbf{v}_T$ is the terminal velocity of the rain droplet.

The addition of (8.5.1), (8.5.2), and (8.5.3) gives

$$\frac{d\rho}{dt} + \rho \nabla \cdot \mathbf{v} = -\nabla \cdot (\rho_r \mathbf{v}_T) = S_m, \tag{8.5.4}$$

where $S_m = -\nabla \cdot (\rho_r \mathbf{v}_T)$ is the mass forcing associated with condensation.

In Cartesian coordinates, the continuity equation that takes into account the phase change from water vapor to hydrometeors can be written as (Gao et al., 2002)[13-14]

$$\frac{d\rho}{dt} + \rho\nabla \cdot \mathbf{v} = S_m \tag{8.5.5}$$

The equation for the absolute vorticity is

$$\frac{\mathrm{d}\xi_a}{\mathrm{dt}} = (\xi_a \cdot \nabla)\mathbf{v} - \xi_a \nabla \cdot \mathbf{v} + \frac{\nabla\rho \times \nabla P}{\rho^2} - \nabla \times \mathbf{F} \tag{8.5.6}$$

The thermodynamic equation is

$$\frac{d\theta_e}{dt} = \dot{\psi} \tag{8.5.7}$$

In (8.5.6), ξ_a is the absolute vorticity vector, $\mathbf{v}$ is the wind vector, $\frac{\nabla\rho \times \nabla P}{\rho^2}$ is the solenoid term, and $\mathbf{F}$ is the frictional term; in (8.5.7), θ_e is the equivalent potential temperature.

The mass-forcing term S_m is included in (8.5.5), and the thermodynamic forcing term $\dot{\psi}$ is included in (8.5.7). In studies of severe weather systems in a saturated atmosphere, the moist potential temperature, θ_e, is used and the thermodynamic forcing is included in (8.5.7).

Taking the dot product of $\nabla\theta_e$ and (8.5.6) gives

$$\nabla\theta_e \cdot \frac{d\xi_a}{dt} = \nabla\theta_e \cdot (\xi_a \cdot \nabla)\mathbf{v} - \nabla\theta_e \cdot \xi_a(\nabla \cdot \mathbf{v}) - \nabla\theta_e \cdot \nabla \times \mathbf{F}. \tag{8.5.8}$$

Using the continuity equation (equation (8.5.5)), (8.5.8) becomes

$$\nabla\theta_e \cdot \frac{d\xi_a}{dt} = \nabla\theta_e \cdot (\xi_a \cdot \nabla)\mathbf{v} - \nabla\theta_e \cdot \xi_a\left(\frac{S_m}{\rho} - \frac{1}{\rho}\frac{d\rho}{dt}\right) - \nabla\theta_e \cdot \nabla \times \mathbf{F}, \tag{8.5.9}$$

and

$$\rho\frac{d}{dt}\left(\frac{\xi_a \cdot \nabla\theta_e}{\rho}\right) - \xi_a \cdot \frac{d\nabla\theta_e}{dt} + S_m\left(\frac{\xi_a \cdot \nabla\theta_e}{\rho}\right) = \nabla\theta_e \cdot (\xi_a \cdot \nabla)\mathbf{v} - \nabla\theta_e \cdot \nabla \times \mathbf{F} \tag{8.5.10}$$

By using the relation as follows

$$\xi_a \cdot \frac{d}{dt}(\nabla\theta_e) = \xi_a \cdot \nabla\frac{d\theta_e}{dt} + \xi_a \cdot \mathbf{v} \cdot \nabla(\nabla\theta_e) - \xi_a \cdot \nabla(\mathbf{v} \cdot \nabla\theta_e)$$

$$= \xi_a \cdot \nabla\dot{\psi} - \nabla\theta_e \cdot (\xi_a \cdot \nabla)\mathbf{v} \tag{8.5.11}$$

we get the following potential vorticity equation:

$$\frac{d}{dt}\left(\frac{\xi_a \cdot \nabla\theta_e}{\rho}\right) = \frac{1}{\rho}\xi_a \cdot \nabla\dot{\psi} - \frac{S_m}{\rho}\left(\frac{\xi_a \cdot \nabla\theta_e}{\rho}\right) - \frac{1}{\rho}\nabla\theta_e \cdot \nabla \times \mathbf{F} \tag{8.5.12}$$

Here $\frac{\xi_a \cdot \nabla\theta_e}{\rho}$ is the moist Ertel potential vorticity.

(8.5.12) can be rewritten as

$$\frac{\partial}{\partial t}\left(\frac{\xi_a \cdot \nabla\theta_e}{\rho}\right) = \frac{1}{\rho}\xi_a \cdot \nabla\dot{\psi} - \mathbf{v} \cdot \nabla\left(\frac{\xi_a \cdot \nabla\theta_e}{\rho}\right) - \frac{S_m}{\rho}\left(\frac{\xi_a \cdot \nabla\theta_e}{\rho}\right) - \frac{1}{\rho}\nabla\theta_e \cdot \nabla \times \mathbf{F} \tag{8.5.13}$$

(8.5.13) is the moist potential vorticity equation with thermodynamic, frictional, and mass forcing. Here $\frac{1}{\rho}\xi_a \cdot \nabla\dot{\psi}$ is the thermodynamic forcing excluding latent heating; $-\mathbf{v} \cdot \nabla\left(\frac{\xi_a \cdot \nabla\theta_e}{\rho}\right)$ is the advection term, $-\frac{S_m}{\rho}\left(\frac{\xi_a \cdot \nabla\theta_e}{\rho}\right)$ represents the mass forcing, and $-\frac{1}{\rho}\nabla\theta_e \cdot \nabla \times \mathbf{F}$ is the frictional forcing. For a frictionless adiabatic saturated atmosphere, we have $-\frac{1}{\rho}\nabla\theta_e \cdot \nabla \times \mathbf{F} = 0$ and $\frac{1}{\rho}\xi_a \cdot \nabla\dot{\psi} = 0$; (8.5.13) can then be simplified to

$$\frac{\partial}{\partial t}\left(\frac{\xi_a \cdot \nabla\theta_e}{\rho}\right) = -\mathbf{v} \cdot \nabla\left(\frac{\xi_a \cdot \nabla\theta_e}{\rho}\right) - \frac{S_m}{\rho}\left(\frac{\xi_a \cdot \nabla\theta_e}{\rho}\right) \tag{8.5.14}$$

(8.5.14) is the moist potential vorticity equation with mass forcing in a frictionless adiabatic saturated atmosphere.

8.6 The Second-order Moist Potential Vorticity

Similarly to the GMPV, the second-order moist potential vorticity is introduced to depict the dynamic and thermodynamic processes of the moist atmosphere. From (8.4.5), under adiabatic and frictionless conditions, the GMPV can be expressed by the following equation:

$$\frac{dQ_m^*}{dt} = -\alpha(\nabla\alpha \times \nabla p) \cdot \nabla\theta^* \tag{8.6.1}$$

Since the dot product of solenoid term and the generalized potential temperature gradient appears on the right-hand side of this equation, the generalized moist potential vorticity cannot be conserved. To derive the second-order moist potential vorticity, the conserved GMPV is derived first. λ is replaced by θ^* in (8.2.11) to obtain

$$\frac{d}{dt}(\alpha\boldsymbol{\xi}_g \cdot \nabla\theta^*) = 0 \tag{8.6.3}$$

Here

$$Q_{mg} = \alpha\boldsymbol{\xi}_g \cdot \nabla\theta^* \tag{8.6.3}$$

is defined as the GMPV, which is conserved. Also, $\lambda = Q_{mg}$ in (8.2.11) to get

$$\frac{d}{dt}(\alpha\boldsymbol{\xi}_g \cdot \nabla Q_{mg}) = 0 \tag{8.6.4}$$

From (8.7.4), we can obtain the second-order moist potential vorticity in a non-uniformly saturated atmosphere:

$$Q_{ms} = \alpha\boldsymbol{\xi}_g \cdot \nabla Q_{mg}\,. \tag{8.6.5}$$

The second-order moist potential vorticity is an application of the generalized potential vorticity gradient to atmospheric dynamics. The generalized potential vorticity is a physical quantity that includes dynamic, thermodynamic, and water vapor processes, whereas the second-order moist potential vorticity combines the dynamic gradient and the thermodynamic gradient. Severe weather is intimately associated with atmospheric boundary processes such as fronts, dry lines, and convergence lines. The associated gradients were depicted using the gradient of only one physical quantity (temperature, moisture, or wind) in previous studies. Gradients in several different physical quantities often exist at same time. Thus, the second-order moist potential vorticity can be used to more completely diagnose dynamic and thermodynamic processes associated

with severe weather. Applications to the diagnosis and forecasting of torrential rainfall will be discussed in the following chapters.

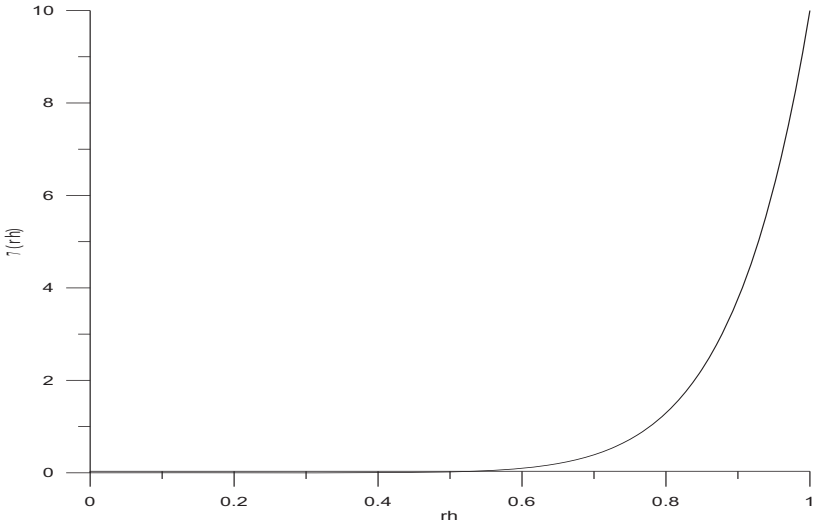

Fig. 8.1. The change in $\psi(rh)$ with rh (k = 9, T = 280 K, p = 1000 hPa, and $q_s = 6 \times 10^{-3}$ g g^{-1})

Notes

[1]Rossby, C. G. (1940) "Planetary flow patterns in the atmosphere," *Journal of the Royal Meteorological Society,* 66(1940):68-97.

[2] Ertel H. (1942) "Ein Neuer hydrodynamischer wir-belsatz," *Meteorologische Zeitschrift,* 59:271–281.

[3]Gao, S.T., P. C. Xu, N. Li and et al. (2014) "Second-order potential vorticity and its potential applications," *Science China Earth Science,* 57(10):2428-2434.

[4]Gao S.T., P. C. Xu, L. K. Ran and et al. (2012) "On the generalized Ertel–Rossby invariant," *Advances in Atmospheric Sciences,* 29(4):690–694.

[5]Cao J. and Q. Xu (2011) "Computing hydrostatic potential vorticity in terrain-following coordinates," *Monthly Weather Review,* 139(9):2955-2961.

[6]Bennetts, D. A. and B. J. Hoskins (1979) "Conditional symmetric instability-A possible explanation for frontal rainbands," *Quarterly Journal of the Royal Meteorological Society,* 105(446):945–962.

[7]Emanuel K. A. (1979) "Inertial instability and mesoscale convective systems. Part I: Linear theory of inertial instability in rotating viscous fluids," *Journal of Atmospheric Sciences,* 36(12):2425-2449.

[8]Danielsen E. F. and R. S. Hipskind (1980) "Stratospheric-tropospheric exchange at polar latitudes in summer," *Journal of Geophysical Research,* 85(NC1):393-400.
[9]Thorpe A. J. (1985) "Diagnosis of balanced vortex structure using potential vorticity," *Journal of Atmospheric Sciences,* 42(4):397-406.
[10]Hoskins B. J. and P. B. Berrisford (1988) "A potential-vorticity perspective of the storm of 15-16 October 1987," *Weather,* 43:122–129.
[11]Xu Q. (1992) "Formation and evolution of frontal rainbands and geostrophic potential vorticity anomalies," *Journal of Atmospheric Sciences,* 49(8):629-648.
[12]Montgomery, M. T. and B. F. Farrell (1993) "Tropical cyclone formation," *Journal of Atmospheric Sciences,* 50:285-310.
[13]Gao, S. T., Lei, T., Zhou, Y. S. and et al. (2002) "Diagnostic analysis of moist potential vorticity anomaly torrential rain systems" *Quarterly Journal of Applied Meteorlolgy,* 13(006):662-670. (in Chinese with English abstract)
[14] Gao, S. T., T. Lei and Y. S. Zhou (2002) "Moist potential vorticity anomaly with heat and mass forcings in torrential rain system," *Chinese Physics Letters,* 19(6):878-880.
[15]Hoskins, B. J., McIntyre, M. E. and Robertson, A. W. (1985) "On the use and significance of is entropic potential-vorticity maps," *Quarterly Journal of the Royal Meteorological Society,* 111(470):877-946.
[16]Gao, S. T., S. Y. Tao and Y. H. Ding (1990) "The generalized E-P flux of wave-mean flow interactions," *Science in China Ser. B,* 33(6):704–715.
[17]Zhou, Y. S., G. Deng, S. T. Gao and et al. (2002) "The study on the influence Characteristic of teleconnection caused by the underlying surface of the Tibetan Plateau I: data analysis," *Advances in Atmospheric Sciences,* 19(4):583–593.
[18]Keyser, D. and R. Rotunno (1990) "On the formation of potential-vorticity anomalies in upper level jet front systems," *Monthly Weather Review,* 118(9):1914–1921.
[19]Fritsch J. M. and R. A. Maddox (1981) "Convectively driven mesoscale weather systems aloft. Part I: Observations," *Journal of Applied Meteorology,* 20(1):9–19.
[20]Davis, C. A. and M. L. Weisman (1994) "Balanced dynamics of mesoscale vortices in simulated convective systems," *Journal of the Atmospheric Sciences,* 51(14):2005–2030.
[21]Gray, M. E. B., G. J. Shutts and G. C. Craig (1998) "The role of mass transfer in describing the dynamics of mesoscale convective systems," *Quarterly Journal of the Royal Meteorological Society,* 124(548):1183–1207.
[22] Shutts, G. J. and M. E. B. Gray (1994) "A numerical modeling study of the geostrophic adjustment process following deep convection," *Quarterly Journal of the Royal Meteorological Society,* 120(519):1145–1178.
[23]Fulton, S. R., W. H. Schubert and S. A. Hausman (1995) "Dynamical adjustment of mesoscale convective anvils," *Monthly Weather Review,* 123(11):3215–3226.
[24]Raymond, D. J. and H. Jiang (1990) "A theory for long-lived mesoscale convective systems," *Journal of Atmospheric Sciences,* 47(24):3067–3077.
[25]Gray, M. E. B. (1999) "An investigation into convectively generated potential-vorticity anomalies using a mass-forcing model," *Quarterly Journal of the Royal Meteorological Society,* 125(557):1589–1605.

CHAPTER NINE

MESOSCALE INSTABILITY AND ANALYSIS METHODS

In the study of hydrodynamics, in order to explain how fluid flow changes from laminar to turbulent, the stability problem for fluid motion was considered (Helmholtz, 1868; Kelvin, 1871; Rayleigh 1880)[1-3]. Later, this problem was developed into a fundamental theory that went beyond the scope of fluid motion and became one of the basic problems of atmospheric dynamics rather than a purely hydrodynamic one. Atmospheric stability theory is not only of important theoretical value but also has important applications, and so it is important to study this theory.

There have been many studies concerning stability, which has been discussed in various books and papers (Beer and Tolstoy, 1975; Holton, 1979; Pedlosky, 1979; Scorer, 1997; Stone, 1966; Ooyama, 1966; Krishnamurti, 1968; Buizza and Palmer, 1995)[4-11]. Therefore, we will not focus on stability here. Instability, however, is one of the basic concepts in mesoscale dynamics, and so, in this chapter, some basic methods for analyzing instability and several common types of mesoscale instability will be introduced.

9.1 Introduction to Methods for Classifying and Analyzing Instability

9.1.1 Classification of Stability

In the field of physics, the stability of an object refers to a potential

property of the object; that is, whether it will move further away from its equilibrium position or return to the original location after it has been disturbed from its equilibrium position. In the case of the atmosphere, stability refers to the possible motion of an air parcel or layer of air that has been disturbed from its equilibrium state.

Under the simultaneous action of horizontal and vertical forces, stability can be classified as vertical static stability, horizontal inertial stability, or symmetric stability. Also, based on the configuration of pressure and temperature fields, the stability can be classified as barotropic stability or baroclinic stability. In addition, if we are considering discontinuities in density and the horizontal or vertical wind shear, there is also shear instability (Kelvin–Helmholtz instability), vortex-layer shear instability, and so on. If the concept of stability is used to discuss the development of long waves and short waves in the context of the atmospheric wave problem, then this instability is called dynamic instability. In the case of saturated air, static stability (also called stratified stability) is called conditional instability—for more details of this see Section 3. When the uplift of unsaturated moist air over a large area is being considered, conditional instability is known as convective instability or potential instability. When conditional instability refers to the interaction between cumulus convection and synoptic-scale fluctuation, it is given the name “conditional instability of the second kind” (CISK). According to the methods used to analyze instability, the instability can also be classified as being linear or nonlinear. Similarly, according to the approximation classification, it can be classified as geostrophic or ageostrophic; in addition, the ageostrophic instability can be classified as super-high velocity instability or generalized barotropic instability (Zeng, 1979)[12]. It should be noted that the various kinds of stability are interrelated. For instance, symmetric instability occurs in a baroclinic atmosphere and is, in fact, a kind of baroclinic instability (Stone, 1966)[8]; the difference is that the energy of the baroclinic instability comes from

the available potential energy of the basic flow, whereas the energy of the symmetric instability comes from the kinetic energy of the basic flow. According to the traditional view, therefore, these are still separate. Also, the inertial instability belongs to the scope of generalized barotropic instability.

Among the types of instability mentioned above, the types related to mesoscale convection are mainly static instability, convective instability, conditional instability, and symmetric instability. The latter part of this chapter will focus on introducing these types of instability together with analytical methods that can be applied to them.

9.1.2 Method of Analyzing Instability

The main methods used to analyze instability are known as the parcel method, normal-mode method, singular-vector decomposition, the $\overline{\mathrm{A}}-\mathrm{B}$ hybrid method, and the WKBJ method. The instability criteria obtained using these methods are often expressed using the Richardson number (Ri); this number, therefore, can be used to distinguish between different kinds of instability.

(1) The parcel method

As its name implies, the parcel method describes the atmospheric instability based on the motion of an air parcel. It is mainly used to distinguish between static instability, inertial instability, and symmetric instability. In order to apply the parcel method, certain conditions need to be satisfied. These conditions are: (1) when the air parcel moves, the surrounding atmosphere should remain in an equilibrium state; (2) the air parcel should not mix with the surroundings—i.e., no mass or heat exchange should occur; and (3) at any moment the pressure within the air parcel should be equal to the pressure of the surrounding atmosphere at the same height, thus meeting the quasi-static condition.

Specifically, this method involves selecting a random parcel from the atmosphere and assuming that the air parcel is displaced to a new location under the effect of a transient external force. The forcing conditions at the new location are then analyzed. The type of instability is determined by looking at whether the acceleration of the particle at the new location is positive or negative.

It should be pointed out that the parcel method involves a relatively brief analysis. When considering the perturbation of the basic flow, whether the perturbation develops depends on whether it can obtain energy from the basic flow, whereas the transform condition of this energy is that the basic flow should be dynamically unstable. However, the parcel method cannot be used to consider the dynamic instability problem for the basic flow.

(2) The normal-mode method

The normal-mode method is the method most commonly used for analyzing linear stability. It is an analytical method and can be used to build a complete characteristic function for instability problems: in fact, it turns the instability problem into one of solving the characteristic value problem. The normal-mode method is also known as the standard-model method or the free-wave method.

The so-called normal mode refers to the wave solution of orthogonal normalization. It is used to analyze stability theory through the solution of the linearization equations. Specifically, it refers to a basic zonal flow, $\bar{u}(y,z)$, overlapping a small fluctuation. The small fluctuation, $e^{i(kx+\lambda y+\sigma t)}$, is in the form of a linear equation, where k is the latitudinal wave number and l is the longitudinal wave number; these numbers are both real. $\sigma=\sigma_r+i\sigma_i$ is the plural frequency. The perturbed wave

solutions can be put back into the governing linear equations to find $|\sigma_i|$, which is also known as the unstable wave of growth (Scorer, 1997)[7].

It should be noted that there are limitations to the application of the normal-mode method. Firstly, the exponential growth that is involved means that important changes will occur in the basic flow. This exponential growth is the result of linearity, and the normal-mode method is effective only when the disturbance is very small. As time passes, the amplitude of the initial small disturbance increases continuously and the linear stability problem becomes a theoretical nonlinear limited-amplitude problem. The application of the normal-mode method is then no longer appropriate. Secondly, the normal-mode method is only appropriate for applying to wave-like disturbances: it is not appropriate for disturbances with a non-wave-like form caused by unsteady, continuous forcing (Pedlosky, 1979)[6]. Furthermore, the normal-mode method considers only the development of the disturbance itself; it does not take into account the possible conditions under which the disturbance develops—such as whether there is sufficient kinetic or potential energy to make the disturbance develop. Also, not all stability problems relate to eigenfunctions and eigenvalues, and the normal-mode method is not appropriate for problems not involving eigenvalues (Ooyama,1966)[9].

(3) The WKBJ method

The WKBJ method, also known as the perturbation method or small-parameter expansion method, is a common method of solving nonlinear equations, higher-order equations, and equations with variable coefficients. It is also one of the methods used to detect nonlinear instability. The WKBJ method can be used in situations where the basic flow varies slowly.

The steps involved in this method are listed below.

i. Make the problem dimensionless.

A small parameter, ε, is chosen. We then have the following equation:

$$\frac{dx_i}{dt} = \varepsilon F_i(t, x_1, \cdots, x_i, \varepsilon) + G_i(t, x_1, \cdots, x_i, \varepsilon) . \tag{9.1.1}$$

ii. Choose an asymptotic sequence, $\delta_n(\varepsilon)$, which satisfies

① $\lim_{\varepsilon \to 0} \delta_n(\varepsilon) = 0$ ② $\lim_{\varepsilon \to 0} \delta_{n+1}(\varepsilon) / \delta_n(\varepsilon) = 0$

③ $o(\varepsilon)$=1 ;

for example, $\delta_n(\varepsilon) = \varepsilon^n$ can be chosen.

iii. Asymptotically expand $x_i = x_{i0} + \sum_{n=1}^{N} \delta_n(\varepsilon) x_{in}$.

$$F_i = F_{i0} + \sum_{n=1}^{N} \delta_n(\varepsilon) F_{in} , \quad G_i = G_{i0} + \sum_{n=1}^{N} \delta_n(\varepsilon) G_{in}$$

iv. Substitute (iii) into the equation $\frac{d}{dt} x_i = \varepsilon F_i + G_i$ and assume $\delta_n(\varepsilon) = \varepsilon^n$; then

$$\frac{d}{dt}(x_{i0} + \varepsilon x_{i1} + \cdots) = \varepsilon(F_{i0} + \varepsilon F_{i1} + \cdots) + (G_{i0} + \varepsilon G_{i1} + \cdots) . \tag{9.1.2}$$

v. Obtain the approximation for each order of the expansion by ε: for example, from (9.1.2), we can obtain

$$\varepsilon^0 : \frac{d}{dt} x_{i0} = G_{i0}$$

$$\varepsilon^1 : \frac{d}{dt} x_{i1} = F_{i0} + G_{i1} .$$
$$\vdots$$

vi. Solve

The development of the amplitude in the solution is used to describe the instability.

For multiple time-scales, the WKBJ method needs adjustment as follows. The time used to describe the development of the wave's amplitude and the propagation time of the wave phase speed are separated because the former corresponds to "slow time" ($T = \varepsilon t$) and the latter to "fast time" ($\tau = t$). The stream function for the disturbance is $\psi = \psi(x, y, \tau, T)$, and so we have $\frac{\partial \psi}{\partial t} = \frac{\partial \psi}{\partial \tau} + \varepsilon \frac{\partial \psi}{\partial T}$.

Furthermore, we expand the stream function into the form of the small parameter (ε), substitute it into the original (nonlinear) equation，and obtain the approximation for each order, with the two layer mode. The structure, stability, and development of the disturbance can then be considered.

(4) The $\overline{\mathrm{A}} - \mathrm{B}$ hybrid method

The $\overline{\mathrm{A}} - \mathrm{B}$ hybrid method is a new nonlinear method for analyzing stability that was introduced in research into wave-flow interactions (Dodd et al., 1982)[13]. It is actually a method for reducing the amplitude equation to the Lorentz system of equations so that the amplitude of the disturbance can be studied in phase space. As well as being important in wave-flow interactions, the $\overline{\mathrm{A}} - \mathrm{B}$ method can also be used to analyze the stability of atmospheric motion. This is because every problem in meteorology can be reduced to two equations that describe the amplitude of the disturbance,

$\overline{\mathrm{A}}$, and the basic flow, B. The specific $\overline{\mathrm{A}}-\mathrm{B}$ equations are different for different situations; however, they all have the same form, which can be written as follows (Dodd et al，1982):

$$\frac{d^2\overline{A}}{dT_1^2}+\Delta_1\frac{d\overline{A}}{dT_1}=\alpha\overline{A}-\tilde{\alpha}\overline{A}B \quad \text{and} \tag{9.1.3}$$

$$\frac{dB}{dT_1}+\Delta_2 B=(\frac{d}{dT_1}+\Delta_3)\left|\overline{A}\right|^2. \tag{9.1.4}$$

In these equations, $\Delta_1,\Delta_2,\Delta_3,\alpha,\tilde{\alpha}$ are coefficients whose particular forms depend on the particular physical problem being studied.

Next, we introduce the following transforms:

$$\tau=\Omega T_1 \ , \tag{9.1.5}$$

$$X=(2\tilde{\alpha})^{1/2}\Omega^{-1}\overline{A}, \tag{9.1.6}$$

$$Y=(\frac{1}{2}\Delta_3)\Omega\dot{X}+X \text{, and} \tag{9.1.7}$$

$$Z=(2\tilde{\alpha})\Omega^{-1}\Delta_3^{-1}B. \tag{9.1.8}$$

Usually, Ω is considered to be a function of Δ_1 and Δ_2. By using certain transformational relations, we can transform the $\overline{\mathrm{A}}-\mathrm{B}$ hybrid equation into the Lorentz system. The value of the Rayleigh number, $\tilde{r}$, in the Lorentz system is then used to determine the system stability.

The $\overline{\mathrm{A}}-\mathrm{B}$ hybrid equation method makes use of the basic concept behind the high-spectrum method used by Charney and Devore (1979)[14] and also the basic concept behind the amplitude-evolution method created

by Beardsley and Winant (1979)[15] and Pedlosky (1979)[6]. These ideas are combined with Dodd's treatment of the mathematics of the wave-flow interaction. This method is used in the nonlinear stability in the wave-flow interaction. This is a powerful tool for studying a baroclinic atmosphere in particular.

This method involves some rules, and the transformation method is relatively stable. It is, therefore, easy to use.

9.2 Static Instability

In the last section, some of the methods that are used for classifying and analyzing instability were introduced. In this section, we will introduce the instability problem as it relates to mesoscale systems.

Static instability relates to the situation in which an air parcel that exists in an atmosphere in static equilibrium departs from its original position and moves vertically under the influence of an external force. If the external force is removed, the air parcel will continue to accelerate in the original direction. This is known as static instability. If the air parcel gradually returns to its original position, the layer of the atmosphere where this parcel is located is said to be statically stable. If the air parcel is stationary, then this layer of the atmosphere is called the neutral atmospheric layer. In the absence of an external force, this atmospheric layer can either maintain its original position or continue to ascend or descend. Here is known as the degree of atmospheric static stability.

This way in which the atmosphere tends to move is related to the atmospheric stratification. The stratification refers to the vertical distribution of temperature and humidity in the atmosphere. The degree of atmospheric static stability is a measurement of the potential stability due to the atmospheric stratification. Therefore, static stability, instability, and neutral stability are known as stratified stability, instability, and neutral stability, respectively. In other words, static stability and stratified stability

are equivalent.

The Richardson number is the basis on which the stratified stability is classified. When $Ri < 0$, the stratification is unstable; when $Ri > 0$, the stratification is stable. We can also use the Brunt–Vaisala frequency, N^2, mentioned in the Chapter 1 to decide whether the stratification is stable. When $N^2 > 0$, the stratification is stable; when $N^2 < 0$, the stratification is unstable.

The basic methods used to analyze static stability are the air-parcel method and the whole- layer lift method, with the air-parcel method being the more widely used of the two. These two methods are discussed in detail in other books on meteorology and atmospheric dynamics, and so, here, we only list the static stability criteria for dry air or unsaturated moist air. These criteria are:

$$r \begin{cases} > r_d & \text{unstable} \\ = r_d & \text{neutral} \\ < r_d & \text{stable} \end{cases} \tag{9.2.1}$$

where r is the lapse rate of the environmental temperature and r_d is the dry adiabatic lapse rate.

In the T-lnp map (Fig. 9.2.1), r is called the stratification curve, and r_d is the state curve (also known as the dry adiabatic line).

When the air is saturated, the wet adiabatic lapse rate, r_m, is used to replace r_d, and the stability criteria for saturated air are obtained:

$$r \begin{cases} > r_m & \text{unstable} \\ = r_m & \text{neutral} \\ < r_m & \text{stable} \end{cases} \tag{9.2.2}$$

Based on the complete set of criteria for dry air and saturated air, the atmospheric static stability criteria may be classified into five types (Fig. 9.2.2):

(1) $r > r_d$: "absolute instability"—both dry air and saturated air are unstable

(2) $r < r_m$: "absolute stability"—both dry air and saturated air are stable

(3) $r_m < r < r_d$: "conditional instability"—dry air is stable; saturated air is unstable

(4) $r = r_d$: neutral conditions for dry air; saturated air is unstable

(5) $r = r_m$ dry air is stable; neutral conditions for saturated air

In the above, a comparison of the values of r and r_d (or r_m) is used to determine the type of atmospheric stability; however, this is only appropriate for a thin layer. When the atmospheric layer is thick, r, r_d, and r_m are no longer constant and the unstable energy is used to define the criteria for the stability of the layer.

In meteorology, the more commonly used thermodynamic parameter is the potential temperature. In terms of the potential temperature, the atmospheric static stability criteria can be expressed as:

$$\frac{\partial \theta}{\partial z}\begin{cases} >0 & \text{stable} \\ =0 & \text{neutral} \\ <0 & \text{unstable} \end{cases} \tag{9.2.3}$$

When considering saturated air, the equivalent potential temperature, θ_e, replaces the potential temperature:

$$\frac{\partial \theta_e}{\partial z}\begin{cases} >0 & \text{stable} \\ =0 & \text{neutral} \\ <0 & \text{unstable} \end{cases} \tag{9.2.4}$$

and so the conditional instability criteria may also be expressed using $\frac{\partial \theta_e}{\partial z} < 0$.

9.3 Symmetric Instability

Symmetric instability is a kind of instability in which an air parcel exhibits inclined upward motion caused by both buoyancy and rotation under static equilibrium, geostrophic equilibrium, and vertical wind shear (or horizontal wind shear). It is also known as buoyancy– inertial instability and, in essence, describes the instability of an inclined rising flow. Specifically, symmetric instability relates the problem of a quasi-geostrophic basic flow to ageostrophic–parallel mesoscale disturbances. This type of instability is known as symmetric instability because the disturbance is symmetric about one axis (Eliassen et al, 1957; Stone, 1966)[16,8]. If the isentropic surface is regarded as the horizontal surface, then the symmetric instability is equivalent to inertial instability on an isentropic surface.

Symmetric instability has a range from tens to hundreds of kilometers. It is generally considered that this type of instability is the direct cause of many rain- and snow-producing bands. These bands, which are a type of mesoscale system, usually occur in warm and occluded fronts. If the front has an east–west orientation and the basic flow in the north–south direction is zero, only the zonal basic flow, *U*, is considered. The basic flow acts as the axis of symmetry, and the disturbance is oriented north–south. The isophase surface will be parallel to the direction of the basic flow, and so symmetric instability is also known as parallel instability. In such circumstances, the direction in which the mesoscale

perturbation propagates, and the direction of the basic flow will be perpendicular to each other. If the direction normal to the isophase surface of the mesoscale linear disturbance is defined as the disturbance axis and the direction of the basic airflow as the axis of symmetry, then the disturbance axis and axis of symmetry will be perpendicular to each other.

The criterion for symmetric instability is $0.25 < Ri < 0.95$.

9.3.1. The Air-parcel Method

To decide whether symmetric instability is present, we can use either the air-parcel method or the normal-mode method. We will consider the use of the air-parcel method first. Symmetric instability relates to an air particle rising "slantwise", as shown in Figure 9.3.1. The basic geostrophic flow for the air parcel located at $(0,0)$ is $\mathbf{v} = v\,\mathbf{j} + \omega\,\mathbf{k}$; also

$$\bar{u}_g(\Delta y, \Delta z) = \bar{u}_g(0,0) + \left(\frac{\partial \bar{u}_g}{\partial z}\right)_0 \Delta z + \left(\frac{\partial \bar{u}_g}{\partial y}\right)_0 \Delta y \tag{9.3.1}$$

and

$$u(\Delta y, \Delta z) = u(0,0) + \left(\frac{\partial u}{\partial z}\right)_0 \Delta z + \left(\frac{\partial u}{\partial y}\right)_0 \Delta y\,. \tag{9.3.2}$$

We can make the approximation

$$u(\Delta y) = \bar{u}_g(0) + f\,\Delta y\,. \tag{9.3.3}$$

Because we are considering the *y*–*z* plane, the equations of motion are

$$\frac{dv}{dt} = f(\bar{u}_g - u) \tag{9.3.4}$$

$$\frac{dw}{dt} = -\frac{1}{\rho}\frac{\partial p}{\partial z} - g\,. \tag{9.3.5}$$

Putting (9.3.1) and (9.3.3) into (9.3.4), we get

$$\frac{dv}{dt} = f(\bar{u}_g - u) = f[\bar{u}_g(0) + (\frac{\partial \bar{u}_g}{\partial z})_0 \Delta z + (\frac{\partial \bar{u}_g}{\partial y})_0 \Delta y - \bar{u}_g(0) - f\Delta y]$$

$$= f[\frac{\partial \bar{u}_g}{\partial z}\Delta z - (f - \frac{\partial \bar{u}_g}{\partial y})\Delta y] = f^2(\frac{1}{R_i} - \frac{\zeta_a}{f})\Delta y \tag{9.3.6}$$

where $\zeta_a = f - \frac{\partial \bar{u}_g}{\partial y}$ is the absolute vorticity, $R_i = N^2 \Big/ (\frac{\partial \bar{u}_g}{\partial z})^2$ is the Richardson number, $N^2 = \frac{g}{\theta}\frac{\partial \theta}{\partial z}$ is the stratified stability, and $(\frac{\Delta z}{\Delta y})_\theta = \frac{\partial \theta / \partial y}{\partial \theta / \partial z} = f\frac{\partial u_g}{\partial z} / N^2$.

From (9.3.6) we can see that when $\Delta y > 0$, namely the movement is toward the north, if $\frac{\zeta_a R_i}{f} < 1$ is unstable, the air parcel will accelerate northwards. If $\frac{\zeta_a R_i}{f} > 1$ is stable, the air parcel will decelerate.

In the northern hemisphere, $f > 0$, and so as $\frac{\zeta_a R_i}{f} < 1 \Rightarrow Ri < \frac{f}{\zeta_a}$; $N^2 \Big/ (\frac{\partial \bar{u}_g}{\partial z})^2 < \frac{f}{\zeta_a}$.

This has the following implications. (1) If the stratified stability is decreasing or there is increasing vertical wind shear, Ri will decrease. This

promotes the occurrence of symmetric instability. (2) Anti-cyclonic shear in the basic flow will tend to make the Richardson number increase. (3) If there is stratified stability and inertial stability, inclined convection will develop only if the vertical wind shear is sufficiently large.

9.3.2. The Normal-mode Method

To simplify the problem, we restrict the symmetric disturbance to the *y*–*z* plane and take the *x*-axis as the axis of symmetry: $\partial/\partial x = 0$. Then, in the Boussinesq approximation, we can obtain the following linear equations:

$$\frac{\partial u'}{\partial t} = fv' - (v'\frac{\partial}{\partial y} + w'\frac{\partial}{\partial z})\overline{U}, \tag{9.3.7}$$

$$\frac{\partial v'}{\partial t} = -fu' - \frac{1}{\overline{\rho}}\frac{\partial p'}{\partial y}, \tag{9.3.8}$$

$$\frac{\partial w'}{\partial t} = -\frac{1}{\overline{\rho}}\frac{\partial p'}{\partial z} + \frac{\theta'}{\overline{\theta}}g, \tag{9.3.9}$$

$$\frac{\partial v'}{\partial y} + \frac{\partial w'}{\partial z} = 0, \tag{9.3.10}$$

$$\frac{\partial \theta'}{\partial t} = -(v'\frac{\partial}{\partial y} + w'\frac{\partial}{\partial z})\overline{\theta}. \tag{9.3.11}$$

Because in the *y*–*z* plane the velocity of the disturbance is non-divergent ($\frac{\partial v'}{\partial y} + \frac{\partial w'}{\partial z} = 0$), we can introduce the perturbed stream function, ψ,

and we have $v' = -\frac{\partial \psi}{\partial z}$, $w' = \frac{\partial \psi}{\partial y}$. Removing the perturbed pressure, p', from equations (9.3.8) and (9.3.9), we obtain

$$\frac{\partial}{\partial t}\left(\frac{\partial^2 \psi}{\partial y^2} + \frac{\partial^2 \psi}{\partial z^2}\right) = \frac{\partial}{\partial y}\left(\frac{\theta'}{\overline{\theta}} g\right) + \frac{\partial}{\partial z}(fu') . \tag{9.3.12}$$

Here, we assume that both the potential temperature of the basic state, $\overline{\theta}$, and the density, $\overline{\rho}$, are constant: $\theta = \overline{\theta} + \theta'$.

From the balance relation for the thermal wind, we have

$$f \frac{\partial \overline{U}}{\partial z} = -\frac{g}{\overline{\theta}} \frac{\partial \theta'}{\partial y} . \tag{9.3.13}$$

If the stratified instability parameter is assumed to be $N^2 = \frac{g}{\overline{\theta}} \frac{\partial \theta'}{\partial z}$, the inclined instability parameter to be $S^2 = f \frac{\partial \overline{U}}{\partial z} = -\frac{g}{\overline{\theta}} \frac{\partial \theta'}{\partial y}$, and the inertial stability parameter to be $F^2 = f\left(f - \frac{\partial \overline{U}}{\partial y}\right)$, and noting that

$\frac{F^2}{S^2} = \frac{f\left(f - \frac{\partial \overline{U}}{\partial y}\right)}{f \frac{\partial \overline{U}}{\partial z}} = \frac{\left(f - \frac{\partial \overline{U}}{\partial y}\right)}{\frac{\partial \overline{U}}{\partial z}}$ is the slope of the absolute vorticity

vector, then from the momentum equation, $\frac{du}{dt} - fv = 0$, it can be shown that $\frac{d}{dt}(u - fy) = 0$. In this way, we obtain the absolute momentum as $M = \overline{U} - fy$. It is also clear that the slope of the absolute momentum is $\frac{F^2}{S^2}$. The slope of the absolute vorticity vector is also the slope of iso-momentum surface, and $\frac{S^2}{N^2} = -\frac{\overline{\frac{\partial \theta'}{\partial y}}}{\overline{\frac{\partial \theta'}{\partial z}}}$ is the slope of the isentropic surface in the basic environmental flow.

From (9.3.7), (9.3.11), and (9.3.12) we have

$$\frac{\partial^2}{\partial t^2}\left(\frac{\partial^2 \psi}{\partial y^2} + \frac{\partial^2 \psi}{\partial z^2}\right) + N^2 \frac{\partial^2 \psi}{\partial y^2} + 2S^2 \frac{\partial^2 \psi}{\partial y \partial z} + F^2 \frac{\partial^2 \psi}{\partial z^2} = 0 \quad (9.3.14)$$

For symmetric instability, because the stability of the disturbance is related to the direction of the displacement, in an unbounded domain, we can set the wave solution as

$$\psi = e^{i[m(y \sin\alpha + z\cos\alpha) - \sigma t]}, \quad (9.3.15)$$

where m is the wave number and α is the angle between the perturbed displacement and the horizontal. Putting (9.3.15) into (9.3.14) we obtain

$$\sigma^2 = N^2 \sin^2 \alpha + 2S^2 \sin\alpha \cos\alpha + F^2 \cos^2 \alpha . \quad (9.3.16)$$

When $\sigma^2 < 0$, the disturbance is not stable. In order to find the condition necessary for instability, we need to find the minimum value of

σ^2, which is negative. To get the minimum value of σ^2 from the extreme value principal $\frac{\partial \sigma^2}{\partial \alpha} = 0$, we get

$$\tan 2\alpha = -2S^2 / (N^2 - F^2). \tag{9.3.17}$$

Then, combining (9.3.16) with (9.3.17) and eliminating α, we can obtain the minimum value of σ^2:

$$2\sigma_{\min}^2 = N^2 + F^2 - [(N^2 + F^2)^2 - 4q]^{\frac{1}{2}}, \tag{9.3.18}$$

where $q = F^2 N^2 - S^4$.

If there is instability, we must have $\sigma_{\min}^2 < 0$. From (9.3.18), it can be see that, usually, $N^2 > 0, F^2 > 0$; if this is the case, then only if $q < 0$ will instability occur.

$$q = F^2 N^2 - S^4 < 0 \Rightarrow \frac{q}{S^4} = \frac{F^2 N^2}{S^4} - 1 < 0,$$

That is $\frac{F^2 N^2}{S^4} < 1$

Based on $Ri = \frac{F^2 N^2}{S^4} = \frac{f^2 N^2}{f^2 (\frac{\partial \overline{U}}{\partial z})^2} = \frac{N^2}{(\frac{\partial \overline{U}}{\partial z})^2}$,

we get $Ri < 1$.

instability occurs:

$$Ri = \frac{F^2 N^2}{S^4} = \frac{F^2 / S^2}{S^2 / N^2} < 1$$

Because $\frac{F^2}{S^2}$ and $\frac{S^2}{N^2}$ are, respectively, the slopes of the iso-momentum surface and the isentropic surface, when the slope of the iso-momentum surface is smaller than the slope of the isentropic surface, symmetric instability may occur. This will be explained below using a graph.

Usually, the potential temperature and momentum increase as the height increases and decrease with increasing latitude. As a result, as Figure 9.3.1 shows, the slope of the isentropic surface is bigger than the slope of the iso-momentum surface.

As shown in the figure, the air parcel initially at A moves vertically, and, because $\frac{\partial \theta}{\partial z} > 0$, it is statically stable. If it moves horizontally, then, because $\frac{\partial M}{\partial y} < 0$, it is inertially stable. However, when the air parcel moves in an inclined way from A to B, then the momentum of the air parcel is smaller than the environmental momentum and the potential temperature of the air parcel is bigger than the environmental potential temperature. As a result, the air parcel accelerates toward the north and also vertically upward, which causes instability.

When $\left.\frac{\partial z}{\partial y}\right|_{\theta} > \left.\frac{\partial z}{\partial y}\right|_{M}$; that is, the slope of the isentropic surface is bigger than that of the iso-momentum surface, symmetric instability occurs.

When $\left.\frac{\partial z}{\partial y}\right|_{\theta} < \left.\frac{\partial z}{\partial y}\right|_{M}$; that is, the slope of the isentropic surface is smaller than that of the iso-momentum surface, symmetric stability occurs.

Therefore, for symmetric instability to occur, this requires the isentropic surface to be sufficiently inclined or the iso-momentum surface to be almost horizontal. In other words, the temperature difference across the whole layer in the vertical direction must be small and the horizontal motion stronger than the vertical motion. These conditions are not easily satisfied in real weather systems.

9.3.3. The Range of the Scale of the Symmetric Instability

When an air parcel rises along the iso-θ line shown in Figure 9.3.1, for the isentropic surface, $\left.\frac{\partial M}{\partial y}\right|_{\theta} > 0$, and so in this situation the symmetric instability can be considered to be the inertial instability on the isentropic surface. Namely, $f - \left.\frac{\partial \overline{U}}{\partial y}\right|_{\theta} < 0$ or $\delta y < \frac{\delta \overline{U}}{f}$. Therefore, we can obtain the range of the scale of the symmetric instability as

$$\delta y < \frac{\delta \overline{U}}{\delta z}\frac{\delta z}{f} \Rightarrow L < \overline{U}_z \frac{D}{f}, \tag{9.3.19}$$

where L and D represent the horizontal scale and the vertical scale, respectively.

The time scale for the symmetric instability is

$$\tau = \frac{L}{\overline{U}} \sim \overline{U}_z \frac{D}{f\overline{U}} \sim \frac{1}{f} \tag{9.3.20}$$

From the above analysis, it can be seen that the symmetric instability and inertial instability have the same time scale and horizontal scale. Here, $R_0 = \frac{\overline{U}}{fL} \sim 1$ and so the symmetric instability is a kind of mesoscale instability.

9.3.4. Conditional Symmetric Instability

When considering moist air, Bennettes and Hoskins (1979)[17] included the release of latent heat in the symmetric instability and thereby introduced the concept of conditional symmetric instability (CSI). This refers to the transformation of a symmetrically stable atmosphere into a symmetrically unstable one due to the release of the heat.

Here, we use the wet-bulb potential temperature to replace the potential temperature and write the stratified stability parameter as $N_w^{\,2} = \frac{g}{\overline{\theta}} \frac{\partial \theta_w}{\partial z}$ and the baroclinicity stability parameter as $S_w^{\,2} = f \frac{\partial \overline{U}}{\partial z} = -\frac{g}{\overline{\theta}} \frac{\partial \theta_w}{\partial y}$. By utilizing the same method as above, we can derive the minimum-frequency equation as follows:

$$2\sigma_{\mathbf{min}}^2 = N_w^{\,2} + F^2 - [(N_w^{\,2} + F^2)^2 - 4q_w]^{\frac{1}{2}}, \tag{9.3.21}$$

where

$$q_w = F^2 N_w^{\,2} - S_w^{\,2} S^2 \tag{9.3.22}$$

The criterion for CSI is $q_w < 0$, or $F^2 N_w^{\,2} - S_w^{\,2} S^2 < 0$, or

$$Ri = \frac{F^2 N_w^{\ 2}}{S_w^{\ 2} S^2} = \frac{F^2 / S^2}{S_w^{\ 2} / N_w^{\ 2}} < 1 . \tag{9.3.23}$$

Because $\frac{F^2}{S^2}$ and $\frac{S_w^{\ 2}}{N_w^{\ 2}}$ are, respectively, the slopes of the iso-momentum surface and iso-wet-bulb potential temperature surface, when the slope of the iso-momentum surface is smaller than that of the iso-wet-bulb potential temperature surface, symmetric instability occurs. In a similar way, CSI is equivalent to inertial instability on a wet isentropic surface; therefore

$$\left.\frac{\partial M}{\partial y}\right|_{\theta_w} < 0 \text{ or } f\left(f - \left.\frac{\partial \overline{U}}{\partial y}\right)\right|_{\theta_w} < 0 . \tag{9.3.24}$$

(9.3.23) and (9.3.24) are the criteria for CSI.

9.3.5 Characteristics of the Symmetric Instability, and the Similarity Between the Buoyancy Instability and the Inertial Instability

From the above discussion, for situations where there is only buoyancy, it can be seen that the angle $\alpha = \frac{\pi}{2}$: this is the angle between the disturbance displacement in the case of symmetric instability and the horizontal direction. From (9.3.16), if the frequency of the disturbance frequency $\sigma^2 = N^2$, buoyancy oscillation or instability will occur. When there is only an inertial force, the angle between the disturbance displacement in the case of symmetric instability and the horizontal direction is $\alpha = 0$. In this case, if the disturbance frequency in equation

(9.3.16), σ^2, is equal to F^2, inertial fluctuation or inertial instability will occur. The stratified instability and inertial instability, therefore, are just special cases of the symmetric instability.

9.4 Shear Instability

Shear instability occurs at an interface where there is a discontinuity in the density and a vertical shear in the velocity. This type of instability is also known as Kelvin–Helmholtz instability (K–H instability) and is, in fact, due to instability in the internal gravity wave (Helmholtz, 1868; Tritton, 1977)[1,18]. In research, an interface such as the one described above is usually regarded as being a thin, horizontal layer with a strong vortex and to be made up of a large number of small, discrete eddies, with each eddy having the same direction of rotation. The situation is illustrated in Figure 9.4.1 (Scorer, 1997)[7].

Thus, at the boundary, the velocities of adjacent vortices counteract each other, leaving only the velocity profile on the two sides of the vortex sheet. The result is that a shear line forms along the center of the vortex. Clearly, shear instability is a typical example of the use of a discrete model instead of a continuous model in studies of instability. It should be noted that two conditions should be satisfied at the interface: both sides should have the same streamline, and the pressure should be continuous across the boundary. This situation can be treated as a linear problem. The reason why the interface can be seen as a thin vortex sheet is that K–H instability is equivalent to a kind of long-wave approximation for a continuous stratified fluid. If the wavelength is sufficiently long, the mixing layer can be considered to be a vortex sheet. By using a discrete model instead of a continuous model, we can study the instability mechanism and estimate the growth rate for the disturbance. However, discrete models sometimes produce false instability; also, because of the use of the long-wave approximation, cases of real instability cannot be explored in this way.

A vortex sheet is a situation where a discontinuity across an interface produces a layer with a strong wind shear. The velocity in the vortex sheet can produce an induced velocity and thereby change the stability of the vortex sheet. The vortex-sheet instability plays an important role when the stability of the north–south shear flow is being considered. In this case, the method used for the instability analysis is similar to the general method used for the shear instability but with some differences concerning how the boundary problems are dealt with. Correspondingly, the methods of mathematical analysis are also different. In addition, the horizontal disturbance due to the horizontal shear flow is not limited by the stratified stability. It should be pointed out that when shear and rotation occur simultaneously, a new mechanism caused by the Coriolis force induces shear instability; if there is no rotation, shear instability (such as a K–H wave) is more likely to occur (Pedlosky, 1979)[6].

In this section, the vertical wind-shear instability is analyzed as being the shear instability, and the horizontal wind-shear instability is analyzed as being the vortex-sheet shear instability.

For shear instability, Ri < 0.25; however, the vortex-sheet instability cannot be repressed by a single value of the Ri number. We will discuss the situations corresponding to different values of Ri in later sections.

9.4.1 Shear Instability

Two layers of a uniform incompressible fluid are considered here. For the sake of simplicity, the motion is restricted to the (x, z) plane, and the interface between the two layers is located at z = 0. The situation where a disturbance $z = h(x,t)$ occurs at the interface is shown in Figure 9.4.2.

Using the normal-mode method, we assume that

$$u_j = \overline{U}_j + u_j^{'}, w_j = w_j^{'}, p_j = \overline{p}_j + p_j^{'} \ (j = 1,2)$$

and that the basic state satisfies the static balance condition:

$$\frac{\partial \overline{p}_j}{\partial z} = -\overline{\rho}_j g \qquad (j = 1,2). \tag{9.4.1}$$

Ignoring the effect of the Earth's rotation, the linearized motion equations may be written as

$$(\frac{\partial}{\partial t} + \overline{U}_j \frac{\partial}{\partial x})u_j^{'} = -\frac{1}{\overline{\rho}_j}\frac{\partial p_j^{'}}{\partial x} \tag{9.4.2}$$

and

$$(\frac{\partial}{\partial t} + \overline{U}_j \frac{\partial}{\partial x})w_j^{'} = -\frac{1}{\overline{\rho}_j}\frac{\partial p_j^{'}}{\partial z} \quad , \tag{9.4.3}$$

and the continuity equation as

$$\frac{\partial u_j^{'}}{\partial x} + \frac{\partial v_j^{'}}{\partial y} = 0 \quad . \tag{9.4.4}$$

Eliminating $p_j^{'}$ and $u_j^{'}$, the equation for $w_j^{'}$ can be written as

$$(\frac{\partial}{\partial t} + \overline{U}_j \frac{\partial}{\partial x})(\frac{\partial^2}{\partial x^2} + \frac{\partial^2}{\partial z^2})w_j^{'} = 0 . \tag{9.4.5}$$

At the interface, the pressure is continuous; therefore, we have

$$z = h, \quad \frac{dp_1^{'}}{dt} = \frac{dp_2^{'}}{dt} . \tag{9.4.6}$$

Also, using the static balance condition (9.4.1), we get

$$z = h, \quad (\frac{\partial}{\partial t} + \overline{U}_j \frac{\partial}{\partial x})(p_1^{'} - p_2^{'}) - g(\overline{\rho}_1 - \overline{\rho}_2)w_j^{'} = 0 . \qquad (9.4.7)$$

The infinite distance satisfies the natural boundary conditions

$$z \to -\infty \text{ if } w_1^{'} \text{ is limited,} \qquad (9.4.8)$$

$$z \to \infty \text{ if } w_2^{'} \text{ is limited.} \qquad (9.4.9)$$

We suppose that equation (9.4.5) has the wave solution,

$$w_j^{'} = \tilde{W}_j(z)e^{i(kx-\sigma t)} \qquad j = 1, 2 . \qquad (9.4.10)$$

Substituting equation (9.4.10) into equation (9.4.5), we then have

$$\frac{d^2\tilde{W}_j(z)}{dz^2} - k^2\tilde{W}_j(z) = 0 , \qquad (9.4.11)$$

and by using boundary conditions (9.4.8) and (9.4.9) we obtain

$$\tilde{W}_1(z) = Ae^{kz}, \quad \tilde{W}_2(z) = Be^{-kz} \qquad (9.4.12)$$

where A and B are arbitrary constants. Substituting these two solutions into (9.4.10) gives $w_j^{'}$. If

this is then substituted into the initial linearized equations, we have

$$\begin{aligned} u_1^{'} &= iAe^{kz} \cdot e^{ik(x-ct)} \\ w_1^{'} &= Ae^{kz} \cdot e^{ik(x-ct)} \\ p_1^{'} &= i\overline{\rho}_1(c - \overline{U}_1)Ae^{kz} \cdot e^{ik(x-ct)} \end{aligned} \qquad (9.4.13)$$

and

$$\begin{aligned} u_2^{'} &= -iBe^{-kz} \cdot e^{ik(x-ct)} \\ w_2^{'} &= Be^{-kz} \cdot e^{ik(x-ct)} \\ p_2^{'} &= -i\overline{\rho}_2(c - \overline{U}_2)Be^{-kz} \cdot e^{ik(x-ct)} \end{aligned} \qquad (9.4.14)$$

(Note that the constant of integration is zero during the process of

integration.)

By utilizing the interface conditions ((9.4.7)–(9.4.9)), we can obtain the homogeneous linear algebraic equations for A and B. The condition for a non-zero solution is that the determinant of the coefficient is zero, and so we have

$$(\overline{\rho}_1+\overline{\rho}_2)c^2-2(\overline{\rho}_1\overline{U}_1+\overline{\rho}_2\overline{U}_2)c+[\overline{\rho}_1\overline{U}_1{}^2+\overline{\rho}_2\overline{U}_2{}^2-\frac{g}{k}(\overline{\rho}_1-\overline{\rho}_2)]=0 \quad . \tag{9.4.15}$$

The wave velocity is

$$c=\frac{\overline{\rho}_1\overline{U}_1+\overline{\rho}_2\overline{U}_2}{\overline{\rho}_1+\overline{\rho}_2}\pm\sqrt{\frac{g(\overline{\rho}_1-\overline{\rho}_2)}{k(\overline{\rho}_1+\overline{\rho}_2)}-\frac{\overline{\rho}_1\overline{\rho}_2(\overline{U}_1-\overline{U}_2)^2}{(\overline{\rho}_1+\overline{\rho}_2)^2}} \quad . \tag{9.4.16}$$

The occurrence of instability requires that

$$\frac{(\overline{\rho}_1-\overline{\rho}_2)(\overline{\rho}_2+\overline{\rho}_1)}{\overline{\rho}_1\overline{\rho}_2}\frac{g}{k}<(\overline{U}_1-\overline{U}_2)^2 . \tag{9.4.17}$$

Therefore: (1) when the velocity of the upper layer and the velocity of the lower layer are not equal（$\overline{U}_1\neq\overline{U}_2$）then there are always some wavelengths that satisfy the conditions for instability; (2) when $\overline{\rho}_2<\overline{\rho}_1$—i.e., the stratification is stable—clearly all wavelengths satisfy the conditions for instability, the vertical shear flow must be unstable; and (3) when the difference in density across the interface is small and the stratification is stable, (9.4.17) becomes

$$k>k_C=2g\frac{\Delta\rho}{\overline{\rho}}\Big/(\Delta U)^2 , \tag{9.4.18}$$

where $\overline{\rho}=(\overline{\rho}_1+\overline{\rho}_2)/2$, $\overline{\rho}_2-\overline{\rho}_1=\Delta\rho$, $\overline{\rho}_1\overline{\rho}_2=\overline{\rho}^2$. Therefore

$$R_i = \frac{2g\Delta\rho}{k\overline{\rho}(\Delta U)^2} = \frac{k_C}{k} < 1 .$$

9.4.2. Vortex-layer Instability

When we consider the north–south horizontal wind-speed shear, the stratification effect deceases. However, the viscous effect caused by the velocity gradient and the vortex-layer effect caused by the increase in the velocity gradient strengthen the discontinuity. We know that the velocity of the flow in the vortex layer may cause an induced velocity, which may produce a change in the stability of the vortex layer. In the following, therefore, we will consider the problem of the stability in the vortex layer (see Figure 9.4.3).

At point B in Figure 9.4.3, the induced velocity of the vortex-layer element, δx, in the *x*-direction is

$$u_i = \frac{\eta\Delta y\delta x}{2\pi\sqrt{x^2 + (A(t)(\cos kx - 1))^2}} \cdot \frac{A(t)(1-\cos kx)}{\sqrt{x^2 + (A(t)(\cos kx - 1))^2}} \approx \frac{\eta\Delta y\delta x}{2\pi x} \cdot \frac{A(t)(1-\cos kx)}{x} . \tag{9.4.19}$$

For a small disturbance, $A(t)$ is very small, and so here we neglect $A^2(t)$. The induced velocity at point B in the vortex layer is

$$\begin{aligned} u_0 &= \int_{-\infty}^{\infty} \frac{\eta\Delta y A(t)(1-\cos kx)}{2\pi x^2} dx = \frac{\eta\Delta y A(t)}{\pi} \int_{-\infty}^{\infty} \frac{\sin\frac{1}{2}kx}{x^2} dx \\ &= -\frac{\eta\Delta y A(t)}{\pi} \left| \frac{1}{x}\sin^2\frac{1}{2}kx \right|_{-\infty}^{\infty} + \frac{\eta\Delta y A(t)}{2\pi} \int_{-\infty}^{\infty} k\frac{\sin kx}{x} dx \\ &= \frac{\eta\Delta y A(t)}{2\pi} \int_{-\infty}^{\infty} k\frac{\sin kx}{x} dx \end{aligned} . \tag{9.4.20}$$

Because $\int_{-\infty}^{\infty} k \frac{\sin kx}{x} dx = k\pi$, then (9.4.20) can also be written as

$$u_0(y,t) = \frac{\eta \Delta y A(t) k}{2}.$$

(9.4.21)

Because of symmetry, the induced velocity in the *y*-direction at point B is canceled out and so the integral of the velocity in the *y*-direction is zero.

Therefore, at any point x_1 within the vortex layer, the velocity component in the *x*-direction is

$$u(x_1, y, t) = \int_{-\infty}^{+\infty} \frac{\eta \Delta y A(t)(\cos kx_1 - \cos kx)}{2\pi (x - x_1)^2} dx = \frac{1}{2} \eta \Delta y A(t) k \cos kx_1$$

. (9.4.22)

Replacing x_1 with x we get

$$u(x, y, t) = u_0 \cos kx = \frac{1}{2} \eta \Delta y A(t) k \cos kx \quad (9.4.23)$$

As the induced velocity is non-divergent, we have $\partial u / \partial x + \partial v / \partial y = 0$, and so

$$v = -\int (\partial u / \partial x) dy + c(x,t) = -\frac{1}{2} \Delta y A(t) k \cos kx \int \eta dy + c(x,t) \quad ,$$

(9.4.24)

where $\eta = \partial U(y,t) / \partial y$ is the environmental vorticity. (9.4.24) can also be written as

$$v = \frac{1}{2} \Delta y U(y,t) A(t) k \cos kx + c(x,t). \quad (9.4.25)$$

As the disturbance is symmetric about the *y*-axis, the induced velocity

component, v, is zero when $x = k\pi + \frac{\pi}{2}, k\pi + \frac{3\pi}{2}$ and 2кл ($k = 0,1,2,3\cdots$). Therefore, $c(x,t)$ in equation (9.4.25) is given by

$$c(x,t) = -\frac{1}{2}\Delta y U(A(t))A(t)k\cos kx\,. \tag{9.4.26}$$

Here, we use U(A(t)) = U(-A(t)): this condition means that the velocities at points that are the same distance from the shear line are equal but that the velocities on the two sides of the line have opposite directions. Equation (9.4.25) can then be written as

$$v(x,y,t) = \frac{1}{2}\Delta y U(y,t)A(t)k\cos kx - \frac{1}{2}\Delta y U(A(t))A(t)k\cos kx \tag{9.4.27}$$

.

The vorticity equation is

$$\frac{\partial \boldsymbol{\xi}}{\partial t} = -(\mathbf{v}\cdot\nabla)\boldsymbol{\xi} - \boldsymbol{\xi}\nabla\cdot\mathbf{v} + (\boldsymbol{\xi}\cdot\nabla)\mathbf{v} + \mathbf{R}\times(\mathbf{g} - \mathbf{a})\,. \tag{9.4.28}$$

We are considering the horizontal motion, and so $\boldsymbol{\xi} \approx \xi\mathbf{k}$,

$$\mathbf{R} = \frac{1}{\rho}\nabla\rho = \frac{1}{\rho}\frac{\partial\rho}{y}\mathbf{j}\,,\quad \mathbf{g} = -g\mathbf{k}\,,$$

$$\mathbf{a} = \frac{d\,\mathbf{v}}{dt} \approx (\mathbf{v}\cdot\nabla)\mathbf{v} = [(\bar{u} + u)\frac{\partial}{\partial x} + v\frac{\partial}{\partial y}][(\bar{u} + u)\mathbf{i} + v\,\mathbf{j}]\,,$$

$\bar{u}(y,t) = \frac{U_1(y,t) + U_2(y,t)}{2}$, and

$$\xi(x,y,t) = [\eta + f + (\frac{\partial v}{\partial x} - \frac{\partial u}{\partial y})]\mathbf{k}$$

$$= (\eta + f + \frac{1}{2}\Delta y U(A(t))A(t)k^2\sin kx - \frac{1}{2}\Delta y U(y,t)A(t)k^2\sin kx - \frac{1}{2}\frac{\partial\eta}{\partial y}\Delta y A(t)k\cos kx)\mathbf{k}$$

.

Using the horizontal non-divergence condition, and ∇ is two dimensional operator $(\boldsymbol{\xi}\cdot\nabla)\,\mathbf{v}=0$, (9.4.28) can be written as

$$\frac{\partial\boldsymbol{\xi}}{\partial t}=-(\mathbf{v}\cdot\nabla)\boldsymbol{\xi}+\mathbf{R}\times(\mathbf{g}-\mathbf{a}). \tag{9.4.29}$$

Because $\mathbf{R}\times\mathbf{g}=-g\dfrac{1}{\rho}\dfrac{\partial\rho}{\partial y}\mathbf{i}$ makes no contribution to the vertical vorticity and because

$$((\bar{u}+u)\frac{\partial}{\partial x}(\bar{u}+u)+v\frac{\partial}{\partial y}(\bar{u}+u))\mathbf{i}\approx[\bar{u}\frac{\partial u}{\partial x}+v\frac{\partial\bar{u}}{\partial y}]\mathbf{i}$$

$$=-\bar{u}A(t)\frac{1}{2}\Delta y\eta k^2\sin kx+\frac{1}{2}\Delta yU(y,t)\frac{\partial\bar{u}}{\partial y}A(t)k\cos kx-\frac{1}{2}\Delta yU(A(t))\frac{\partial\bar{u}}{\partial y}A(t)k\cos kx$$

,

then

$$\mathbf{R}\times\mathbf{a}=R(\bar{u}\frac{\partial u}{\partial x}+v\frac{\partial\bar{u}}{\partial y})\mathbf{k}$$

$$=R[-\frac{1}{2}\bar{u}A(t)\eta\Delta yk^2\sin kx+\frac{1}{2}\Delta yU(y,t)\frac{\partial\bar{u}}{\partial y}A(t)k\cos kx-\frac{1}{2}\Delta yU(A(t))\frac{\partial\bar{u}}{\partial y}A(t)A(t)k\cos kx]$$

.

Also, because

$$-(\mathbf{v}\cdot\nabla)\xi$$

$$=-[(\bar{u}+u)\frac{\partial}{\partial x}+v\frac{\partial}{\partial y}](\eta+f+\frac{1}{2}\Delta yU(A(t))A(t)k^2\sin kx-\frac{1}{2}\Delta yU(y,t)A(t)k^2\sin kx-\frac{1}{2}\frac{\partial\eta}{\partial y}\Delta yA(t)k\cos kx)\mathbf{k}$$

$$=-\frac{1}{2}\bar{u}\Delta yU(A(t))A(t)k^3\cos kx+\frac{1}{2}\bar{u}\Delta yU(y,t)A(t)k^3\cos kx-\frac{1}{2}\bar{u}\frac{\partial\eta}{\partial y}\Delta yA(t)k^2\sin kx$$

$$=-\frac{1}{2}\Delta yU(y,t)\frac{\partial\eta}{\partial y}A(t)k\cos kx+\frac{1}{2}\Delta yU(A(t))\frac{\partial\eta}{\partial y}A(t)k\cos kx$$

(9.4.29) can be written as

$$\frac{\partial \boldsymbol{\xi}}{\partial t} = -(\mathbf{v}\cdot\nabla)\boldsymbol{\xi} + \mathbf{R}\times(\mathbf{g}-\mathbf{a})$$
$$= \{-\frac{1}{2}\bar{u}\Delta y U(A(t))A(t)k^3\cos kx + \frac{1}{2}\bar{u}\Delta y U(y,t)A(t)k^3\cos kx - \frac{1}{2}\bar{u}\frac{\partial \eta}{\partial y}\Delta y A(t)k^2\sin kx$$
$$-\frac{1}{2}\Delta y U(y,t)\frac{\partial \eta}{\partial y}A(t)k\cos kx + \frac{1}{2}\Delta y U(A(t))\frac{\partial \eta}{\partial y}A(t)k\cos kx$$
$$+R\left[-\frac{1}{2}\bar{u}\Delta y\eta A(t)k^2\sin kx + \frac{1}{2}\Delta y U(y,t)\frac{\partial \bar{u}}{\partial y}A(t)k\cos kx - \frac{1}{2}\Delta y U(A(t))\frac{\partial \bar{u}}{\partial y}A(t)k\cos kx\right]\}\mathbf{k}$$

The above equation implies that when $\Delta y > 0$ at the point (tan kx = 0, cos kx = 1) then the condition which satisfies $\partial\xi/\partial t > 0$ is

$$-\bar{u}U(A(t))k^2 + \bar{u}U(y,t)k^2 - U(y,t)\frac{\partial \eta}{\partial y} + U(A(t))\frac{\partial \eta}{\partial y} + U(y,t)\frac{\partial \bar{u}}{\partial y}R - U(A(t))\frac{\partial \bar{u}}{\partial y}R > 0$$

.

The above equation can be simplified to

$$(-U(A(t)) + U(y,t))(\bar{u}k^2 - \frac{\partial \eta}{\partial y} + \frac{\partial \bar{u}}{\partial y}R) > 0 \quad . \tag{9.4.30}$$

In order to get better understanding of (9.4.30), the two terms on its left-hand-side can be discussed as follows:

(1) If $\bar{u}k^2 - \frac{\partial \eta}{\partial y} + \frac{\partial \bar{u}}{\partial y}R > 0$, then $-U(A(t)) + U(y,t) > 0$,

meaning that

$$U(y,t) > U(A(t)) . \tag{9.4.31}$$

Also $\bar{u}k^2 - \frac{\partial \eta}{\partial y} + \frac{\partial \bar{u}}{\partial y}R > 0$, and so

$$1-\frac{\partial \eta}{\bar{u}k^2\partial y}+\frac{\partial \bar{u}}{\bar{u}k^2\partial y}R>0 \tag{9.4.32}$$

or

$$(1-R_v+R_{id})>0 \ , \tag{9.4.33}$$

where R_v is the shear Richardson number and R_{id} is the mixed Richardson number.

If we do not take the horizontal gradient of the density into account, the mixed Richardson number is 0, and so (9.4.33) implies that

$$R_v<1. \tag{9.4.34}$$

This result is similar to the result for the shear instability. Therefore, the essential conditions for the instability of a vortex are

$$\begin{cases}(1-R_v+R_{id})>0\\ \dfrac{U(y,t)}{U(A(t))}>1\end{cases}, \tag{9.4.35}$$

where $U\left(A(t)\right)\neq 0$.

(2)If $\bar{u}k^2-\dfrac{\partial \eta}{\partial y}+\dfrac{\partial \bar{u}}{\partial y}R<0$, then

$$\begin{cases}(1-R_v+R_{id})<0\\ \dfrac{U(y,t)}{U(A(t))}<1\end{cases}. \tag{9.4.36}$$

Also, because $\bar{u}k^2>>\dfrac{\partial \eta}{\partial y}$ generally holds, the condition

$\frac{U(y,t)}{U(A(t))} < 1$ is easily satisfied, which means that $(1-R_v+R_{id}) < 0$ may not be true and (9.4.36) cannot be considered as the instability criterion.

From (9.4.30), the unstable wave number must satisfy

$$k^2 > \frac{1}{u}(\frac{\partial \eta}{\partial y} - \frac{\partial \bar{u}}{\partial y} R) . \tag{9.4.37}$$

Therefore, the shorter the wavelength, the more easily shear instability occurs.

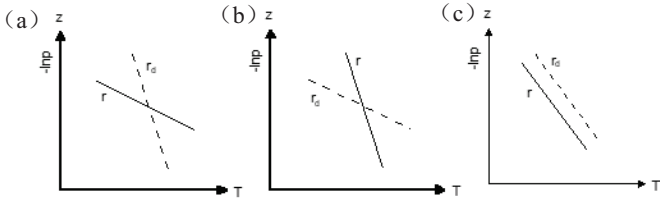

Fig 9.2.1. The T-lnp map: r and r_d are used to determine the atmospheric stability. (a), (b), and (c) illustrate, respectively, $r > r_d$, $r < r_d$, and $r = r_d$, which are the three types of stratified stability.

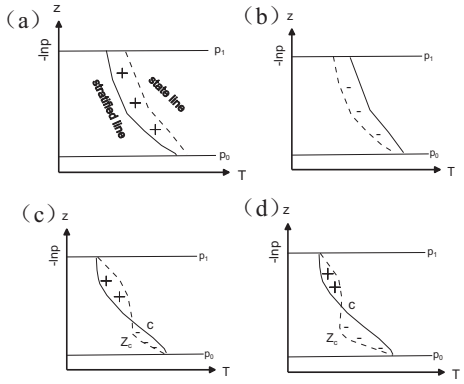

Fig. 9.2.2. Illustration of types of unstable energy: (a) absolute instability, (b) absolute stability, (c) real potential instability (the area above point c is larger than the area below point c), and (d) pseudo-potential instability (the area above point c is smaller than the area below point c)

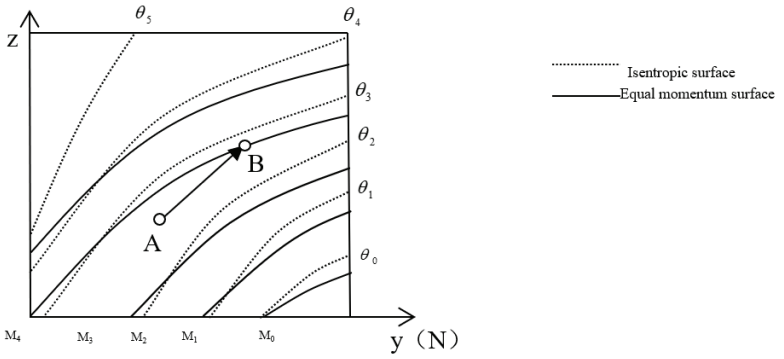

Fig. 9.3.1. Unstable symmetric unstable situation; momentum, $M = \bar{U} - fy$

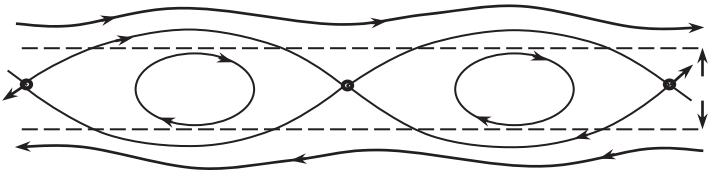

Fig. 9.4.1. Sketch of a vortex sheet

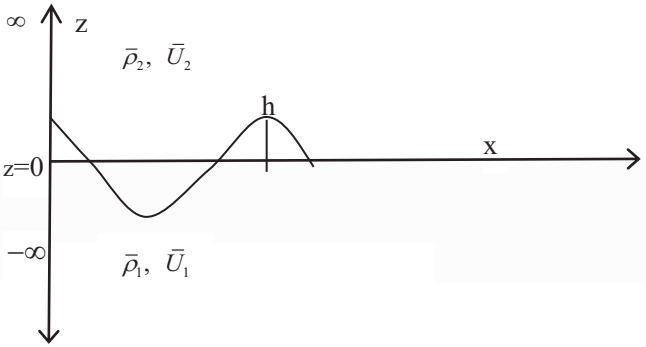

Fig. 9.4.2. Disturbance at a discontinuous interface

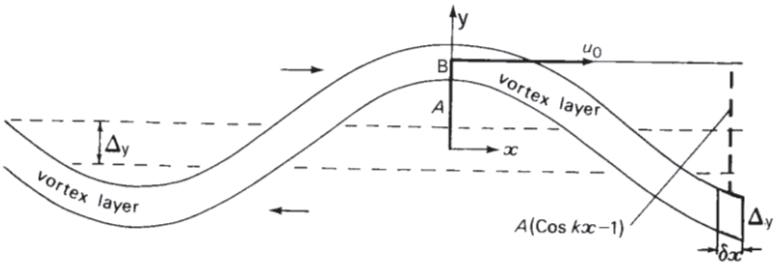

Fig. 9.4.3. Sketch of the vortex layer in a shear line

Notes

[1]Helmholtz, H. (1868) "On the discontinuous movement of fluids," *Philosophical Magazine,* 36(4):337-346.

[2]Kelvin, W. (1871) "The influence of wind on waves in water supposed frictionless," *Philosophical Magazine,* 42:368-374.

[3]Rayleigh, L. (1880) "On the stability, or instability, of certain fluid motions," *Proceedings of the London Mathematical Society*, s1-11(1):57–72.

[4]Beer, T. and I. Tolstoy (1975) "Atmospheric waves," *Physics Today,* 28(11):70–71.

[5]Holton, J. R. (1979) *An introduction to dynamic meteorology*. Academic Press, Inc:391.

[6]Pedlosky, J. (1979) *Geophysical Fluid Dynamics*. Springer-Verlag New York Inc. pp626.

[7]Scorer, R. S. (1997) *Dynamics of Meteorology and Climate*. Praxis Publishing Ltd. pp686.

[8]Stone, P. H. (1966) "On the non-geostrophic baroclinic stability," *Journal of Atmospheric Sciences,* 23(4):390-400.

[9]Ooyama, K. (1966) "On the stability of the baroclinic circular vortex: a sufficient criterion for instability," *Journal of Atmospheric Sciences,* 23(4):43-53.

[10]Krishnamurti, T. N. (1968) "A diagnostic balance model for studies of weather systems of low and high latitudes, Rossby number less than 1," *Monthly Weather Review,* 96(4):197–207.

[11]Buizza, R. and T. N. Palmer (1995) "The singular-vector structure of the atmospheric global circulation," *Journal of Atmospheric Sciences,* 52(9):1434-1456.

[12]Zeng, Q. C. (1979) *The Basis of Math and Physics for Numerical Weather Prediction.* Beijing Science Press. (in Chinese)

[13]Dodd, K. R., J. C. Elibeck, J. D. Gibbon and *et al.* (1982) *Solitons and Nonlinear Wave Equations*. London: Academic Press.

[14]Charney, J. G. and J. G. Devore (1979) "Multiple flow equilibria in the

atmosphere and blocking," *Journal of Atmospheric Sciences,* 36(7):1205-1216.

[15]Beardsley, R. C. and C. D. Winant(1979) "On the mean circulation in the Mid-Atlantic Bight," *J Phys Oceanogr,* 9(3):612-619.

[16]Eliassen, A. and E. Kleinschmidt (1957) *Handbuch der Physik*.Berlin: Springer-Verlag.

[17]Bennetts, D. A. and B. J. Hoskins (1979) "Conditional symmetric instability: A possible explanation for Frontal rain bands," *Quarterly Journal of the Royal Meteorological Society,* 105:945-962.

[18]Tritton, D. J. (1977) *Physical Fluid Dynamics*. Van Nostrand Reinhold Company.

CHAPTER TEN

ATMOSPHERIC GRAVITY WAVES

Gravity waves are ubiquitous in the atmosphere. Their horizontal wavelengths range from a few hundred meters to thousands of kilometers. Gravity waves play a very important role in the atmosphere and in the evolution of weather systems. They are often closely related to the meso-scale convection systems. This chapter is focused on the three-dimensional inertia-gravity waves and symmetric inertia-gravity waves. The wave characteristics, polarization properties and wave activity density are introduced. In addition, the wavelet and cross spectral method for analyzing and reconstructing gravity waves are addressed.

10.1 Overview of Gravity Waves

10.1.1 Classification of Gravity Waves and Formation Mechanism

Gravity waves are common in the Earth's atmosphere and oceans and play an important role in the transmission of momentum and energy. Gravity waves can be divided into external gravity waves and internal gravity waves. The external gravity waves often appear on the ocean surface, atmospheric free surface, and lower boundary of atmosphere. The shallow-water equations are usually used to describe the waves. Internal gravity waves are caused by the combination of gravity and buoyancy when air parcel is disturbed, and then deviates from equilibrium position on a discontinuous surface (such as a discontinuous shear line or density

front) in a stable atmosphere.

In the following, the mechanisms of external gravity waves and internal gravity waves are illustrated. A free surface is taken as an example to illustrate the formation of external gravity waves. If a point on a free surface is disturbed, the free surface will rise at that point. Since the free surface at that point is higher than those around it, the pressure at the point increases because of gravity and a pressure-gradient force directed outward from that point is generated. Due to the pressure-gradient force, the fluid at that point diverges outward. The divergence necessarily causes the free surface at that point to fall, whereas the free surface surrounding that point will rise. The divergence and convergence in adjacent region and free surface fluctuation together form an external gravity wave. Therefore, gravity is intrinsic to external gravity waves. However, if the free surface is fixed, and there is no vertical disturbance, no external gravity waves are generated.

In the case of internal gravity waves, it is assumed that atmosphere is adiabatic and stable, and that upper and lower boundaries are fixed. At initial moment, an air parcel at a certain point is disturbed, and then, begins to ascend. According to the first thermodynamic laws, the temperature of air parcel must fall with adiabatic ascending. Therefore, after the parcel has risen to a certain height, the parcel temperature will be lower than the ambient temperature and the buoyancy that the parcel is subject to will be less than the gravity. Under the influence of downward total force, the parcel gradually begins to descend. After the parcel reaches the equilibrium position, it will continue to move downward due to inertia. In the descending process, due to adiabatic warming, the parcel will descend to a certain height where the buoyancy is greater than the gravity. The total force is now directed upward, and the parcel will begin to ascend again. This process repeats itself, and the air parcel oscillates vertically around the equilibrium position, which forms internal gravity wave.

Gravity waves are transverse waves. Generally speaking, external

gravity waves belong to fast wave type. Like sound waves, external gravity waves have no significant influence on weather. However, internal gravity waves have an important impact on local weather changes and are of great significance to meso-scale weather systems.

Since atmosphere is a rotating fluid, the Coriolis force due to the Earth's rotation makes air parcel to horizontally oscillate. Therefore, the gravity wave under the influence of Coriolis force, which is named inertia-gravity wave, is not necessarily oscillated in vertical direction. Therefore, in general, inertia-gravity waves are not limited to propagating vertically and may also aslant propagate. However, whether they propagate horizontally or obliquely, gravity waves can only occur in a stably stratified atmosphere. If the stratification is unstable, no gravity waves will be formed.

10.1.2 Factors that Trigger Gravity Waves

There are many factors exciting gravity waves. It is generally believed that the processes generating gravity waves are mainly related to terrain, shear instability, and cumulus convection. Topographic waves such as mountain waves and lee waves easily form due to airflows over mountains. Lilly and Kennedy (1973)[1] showed that the characteristic horizontal wavelength of leeward waves is equivalent to the terrain width. The vertical shear instability of basic airflow can also generate gravity waves. Lindzen (1974)[2] showed that such gravity waves disperse unstable energy outwards, thereby stabilizing basic airflow. The characteristic horizontal wavelength of such a gravity wave is $\pi\sqrt{2}(\Delta U)/N$, where ΔU is the vertical shear of basic airflow. For a typical shear value in the atmosphere (10 m s^{-1}), the horizontal wavelength of a gravity wave due to vertical shear instability is a few kilometers. The generation of gravity waves by cumulus convection is a complicated and difficult problem. Up

until now, three mechanisms with cumulus convection have been proposed. The first is a purely thermal forcing mechanism. Piani et al. (2000)[3] pointed out that the vertical thickness of latent-heat heating layer is comparable to vertical wavelength of a gravity wave excited by thermal forcing. The second is the blocking effect. Clark et al. (1986)[4] considered that cumulus convection produced a similar terrain blocking effect when studying the excitation of gravity waves due to boundary-layer convection, which is a kind of "instantaneous terrain". Fovell et al. (1992)[5] showed that the frequency of gravity waves is the same as the frequency of momentum forcing and so proposed a "mechanical oscillator" mechanism. In addition, nonlinear wave–wave interactions can cause wave-energy exchange, wave-amplitude development, and spectrum evolution of gravity waves.

10.1.3 Methods of Observing Gravity Waves

As detection technology has developed, observations of gravity waves in real atmosphere have been continuously enhanced. Current methods of observing gravity waves mainly include radiosonde, remote-sensing satellite, radar observations, and aircraft observations.

It can be seen from the polarization properties of monochromatic gravity waves that if the end trajectory of horizontal wind is an ellipse, then inertia-gravity wave propagates upward. The height difference corresponding to horizontal wind vector around a circle should be equal to the vertical wavelength of inertia-gravity wave. The ratio of short axis to long axis of ellipse is equal to the ratio of Coriolis parameter to frequency. Because of these properties of gravity waves, radiosonde observations can be used to analyze the characteristic parameters of large-scale low-frequency inertia-gravity waves, including horizontal and vertical wavelengths, phase velocity, and propagation direction. It is also possible to analyze regional changes of gravity waves, as well as seasonal

and interannual variations (Vincent et al., 1997; Vincent and Alexander, 2000; Zink and Vincent, 2001 (a))[6-8]. Hirota and Niki (1985)[9] used radiosonde observations to perform statistical analysis of climatic characteristics of inertia-gravity waves with wavelengths of 25–65 km. The results showed that the propagation of inertia-gravity waves is generally isotropic and that the energy is mainly transmitted upwards. The gravity-wave intensity shows obvious seasonal changes at high latitudes and is stronger in winter than in summer.

There are many methods of observing gravity waves by satellite remote sensing. For example, satellites can provide large-scale gravity-wave observations at fixed time interval, however, small-scale waves will be missed. The observation data from the LIMS (Limb Infrared Monitoring of the Stratosphere) instrument can be inverted to temperature. After processing by a Kalman filter, a temperature disturbance containing gravity-wave information can be obtained. Fetzer and Gille (1994)[10] argued that this temperature disturbance is mainly determined by low-frequency inertia-gravity waves with a vertical wavelength of about 6–50 km and a horizontal wavelength of more than 200 km. Preusse et al. (1999)[11] used CRISTA (Cryogenic Infrared Spectrometers and Telescopes for the Atmosphere) data, which have a finer horizontal and vertical resolution than LIMS, to analyze temperature disturbances produced by gravity waves and obtained similar results. Tsuda et al. (2000)[12] used GPS data to analyze the energy of gravity waves. It was also found that the gravity-wave energy in the convection zone at low latitudes is particularly strong and that the energy over land in mid-latitude regions is greater than that over the oceans. McLandress et al. (2000)[13] used MLS (Microwave Limb Sounder) data to analyze the temperature changes due to stratospheric and mesospheric gravity waves. The results showed that, in summer, the forcing source for gravity waves in the northern hemisphere is deep convection, whereas, for mid-latitudes in the southern hemisphere, the forcing source is topography.

Hirota and Niki (1985) study changes of gravity waves with season and latitude in stratosphere. It was shown that the gravity waves at 40°N–80°N presented obvious periodic, seasonal changes and mainly propagated upwards.

10.2 The Governing Equations

The dynamic characteristics of a typical meso-scale system are non-hydrostatic and non-geostrophic balances. The dynamic equations suitable for meso-scale systems are the filtered sound-wave modes. Here, the equations describing gravity waves will be derived from the non-hydrostatic primitive equations in Cartesian (x, y, z) coordinate system.

The equations for an adiabatic frictionless and incompressible atmosphere are:

$$\frac{\partial u}{\partial t}+u\frac{\partial u}{\partial x}+v\frac{\partial u}{\partial y}+w\frac{\partial u}{\partial z}-fv=-\frac{1}{\rho}\frac{\partial p}{\partial x}, \tag{10.2.1}$$

$$\frac{\partial v}{\partial t}+u\frac{\partial v}{\partial x}+v\frac{\partial v}{\partial y}+w\frac{\partial v}{\partial z}+fu=-\frac{1}{\rho}\frac{\partial p}{\partial y}, \tag{10.2.2}$$

$$\frac{\partial w}{\partial t}+u\frac{\partial w}{\partial x}+v\frac{\partial w}{\partial y}+w\frac{\partial w}{\partial z}=-\frac{1}{\rho}\frac{\partial p}{\partial z}-g, \tag{10.2.3}$$

$$\frac{\partial u}{\partial x}+\frac{\partial v}{\partial y}+\frac{\partial w}{\partial z}=0, \tag{10.2.4}$$

$$\frac{\partial \theta}{\partial t}+u\frac{\partial \theta}{\partial x}+v\frac{\partial \theta}{\partial y}+w\frac{\partial \theta}{\partial z}=0, \tag{10.2.5}$$

$p=\rho RT$, and (10.2.6)

$$\theta = T(\frac{p_s}{p})^{\frac{R}{c_p}}, \tag{10.2.7}$$

where u, v, w, ρ, T, p, and θ are, respectively, the velocity in the *x*-, *y*-, and *z*-directions and the density, temperature, pressure, and potential temperature. g is the gravity acceleration, p_s is the reference pressure, and $f = f(y)$ is the Coriolis parameter.

We assume that the physical quantities can be decomposed into the basic state and the disturbance, namely,

$$u = \bar{u}(y,z) + u', \quad v = v', \quad w = w', \quad \rho = \bar{\rho}(y,z) + \rho',$$

$$p = \bar{p}(y,z) + p', \; T = \bar{T}(y,z) + T', \; \theta = \bar{\theta}(y,z) + \theta'. \tag{10.2.8}$$

Here, "$\bar{}$" denotes the basic state, which is the function of y and z, and "$'$" represents the disturbance, which is expressed as the function of x, y, z, and t. It is assumed that the basic state is a set of stable solutions to Eqs. (10.2.1)–(10.2.7) and that the density disturbance in the horizontal motion Eqs. (10.2.1) and (10.2.2) is negligible. However, the density disturbance in the vertical motion Eq. (10.2.3) is very important. After (10.2.8) is substituted into Eqs. (10.2.1)–(10.2.7), with Boussinesq approximations, the linearized equations can be obtained:

$$\frac{\partial u'}{\partial t} + \bar{u}\frac{\partial u'}{\partial x} + v'\frac{\partial \bar{u}}{\partial y} + w'\frac{\partial \bar{u}}{\partial z} - fv' = -\frac{1}{\bar{\rho}}\frac{\partial p'}{\partial x}, \tag{10.2.9}$$

$$\frac{\partial v'}{\partial t}+\bar{u}\frac{\partial v'}{\partial x}+fu'=-\frac{1}{\bar{\rho}}\frac{\partial p'}{\partial y}, \tag{10.2.10}$$

$$\frac{\partial w'}{\partial t}+\bar{u}\frac{\partial w'}{\partial x}=-\frac{1}{\bar{\rho}}\frac{\partial p'}{\partial z}+g\frac{\theta'}{\bar{\theta}}, \tag{10.2.11}$$

$$\frac{\partial u'}{\partial x}+\frac{\partial v'}{\partial y}+\frac{\partial w'}{\partial z}=0, \tag{10.2.12}$$

$$\frac{\partial \theta'}{\partial t}+\bar{u}\frac{\partial \theta'}{\partial x}+v'\frac{\partial \bar{\theta}}{\partial y}+w'N^2\frac{\bar{\theta}}{g}=0, \tag{10.2.13}$$

where $N^2=\frac{g}{\bar{\theta}}\frac{\partial \bar{\theta}}{\partial z}$ is the buoyancy oscillation frequency.

At the same time, the basic state satisfies the following equations:

$$f\bar{u}=-\frac{1}{\bar{\rho}}\frac{\partial \bar{p}}{\partial y}, \tag{10.2.14}$$

$$\frac{\partial \bar{p}}{\partial z}=-\bar{\rho}g, \tag{10.2.15}$$

$$\bar{p}=\bar{\rho}R\bar{T}, \tag{10.2.16}$$

$$\bar{\theta}=\bar{T}\left(\frac{p_s}{p}\right)^{\frac{R}{c_p}}. \tag{10.2.17}$$

It can be seen from (10.2.14) and (10.2.15) that the stable state satisfies the geostrophic balance and hydrostatic balance. Taking partial derivative of (10.2.14) with z, and using (10.2.15), we can obtain

$$f\frac{\partial \bar{u}}{\partial z} = -\frac{g}{\bar{\theta}}\frac{\partial \bar{\theta}}{\partial y} + f\bar{u}\frac{\partial \bar{\theta}}{\partial z}. \tag{10.2.18}$$

The above equation describes the relation between the vertical shear of basic-state zonal velocity and the spatial gradient of basic-state potential temperature. If $f\bar{u}\frac{\partial \bar{\theta}}{\partial z}$ is relatively small and so can be ignored, then the above equation represents the thermal wind balance in Cartesian coordinates.

The linear Eqs. (10.2.9)–(10.2.13) describe inertial gravity mixing waves. Next, based on these equations, we will discuss the wave characteristics, polarization properties, and wave-activity equation for three-dimensional inertia-gravity waves and symmetric inertia-gravity waves.

10.3 Gravity Wave Characteristics

In physics, a wave denotes the propagation of disturbances or vibrations in space that are periodic in time and space. The wavefront is an important concept for describing fluctuations. This refers to the surface composed by the points with the same phase at a certain moment. If the wavefront is a plane, then the wave is called a plane wave; if the wavefront is a spherical surface, then the wave is called spherical wave.

In general, three-dimensional wave can be expressed as

$$q = A_m e^{i(kx+ly+nz-\omega t)},$$

where A_m is the complex amplitude, $kx + ly + nz - \omega t = \phi$ is the phase, ω is the frequency, and k, l, and n are the wave numbers in the x-, y-, and z-directions, respectively. The velocity at which the wavefront

propagates through space is called the wave velocity or phase velocity. Since the wave-number vector (k,l,n) is perpendicular to the iso-phase surface, the phase velocity can be said to represent the distance that the iso-phase surface moves in the direction of wave-number vector per unit time. Therefore, the wave-number vector represents the direction of phase velocity. The phase velocity can be written as

$$C = \frac{\omega}{\sqrt{k^2 + l^2 + n^2}}. \tag{10.3.1}$$

The phase velocities, Cx, Cy and Cz, in the x-, y-, and z-directions are:

$$Cx = \frac{\omega}{k},\ Cy = \frac{\omega}{l},\ \text{and}\ Cz = \frac{\omega}{n}. \tag{10.3.2}$$

As shown in Figure 10.1, the phase velocity, C, and also Cx, Cy, and Cz, do not satisfy the vector synthesis rule.

The waves in real atmosphere are usually not monochromatic, but rather are mixing of various monochromatic waves. In terms of dynamics, the wave train consists of two parts: a high-frequency carrier and a low-frequency wave packet. Carriers vary rapidly in time and space, whereas wave packets change slowly. Generally, the wave-train phase velocity refers to the propagation speed of the carrier—that is, the propagation speed of a given phase point. The propagation velocity of the wave packet (the envelope of the carrier)—that is, the propagation velocity of a given amplitude point—is called group velocity and represents the propagation of energy. The group velocity is a vector whose components conform to the vector synthesis. The group-velocity components Cgx, Cgy, and Cgz in the x-, y-, and z-directions are

$$Cgx = \frac{\partial \omega}{\partial k},\ Cgy = \frac{\partial \omega}{\partial l} \text{ and } Cgz = \frac{\partial \omega}{\partial n} \tag{10.3.3}$$

If phase velocity is a function of wave number and is not equal to group velocity, the wave is dispersive.

We assume that the linear Eqs. (10.2.9)–(10.2.13) have plane-wave solutions in the following form:

$$\begin{pmatrix} u'(x,y,z,t) \\ v'(x,y,z,t) \\ w'(x,y,z,t) \\ \theta'(x,y,z,t) \\ p'(x,y,z,t) \end{pmatrix} = \begin{pmatrix} \tilde{u} \\ \tilde{v} \\ \tilde{w} \\ \tilde{\theta} \\ \tilde{p} \end{pmatrix} e^{i(kx+ly+nz-\omega t)}. \tag{10.3.4}$$

Here, the wave parameters ω, k, l, and n are all real, and the amplitude $(\tilde{u}, \tilde{v}, \tilde{w}, \tilde{\theta}, \tilde{p})$ may be complex.

10.3.1 Inertia-gravity Waves

Assuming that the basic zonal airflow is stationary ($\bar{u} = 0$), the other basic states are only function of height, (z), and the atmosphere is stable ($N^2 > 0$), and taking into consideration the effect of the Earth's rotation ($f = f(y)$), then the linearized equations describing a three-dimensional inertia-gravity wave can be written as

$$\frac{\partial u'}{\partial t} - fv' = -\frac{1}{\rho}\frac{\partial p'}{\partial x}, \tag{10.3.5}$$

$$\frac{\partial v'}{\partial t} + fu' = -\frac{1}{\rho}\frac{\partial p'}{\partial y}, \tag{10.3.6}$$

$$\frac{\partial w'}{\partial t} = -\frac{1}{\bar{\rho}}\frac{\partial p'}{\partial z} + g\frac{\theta'}{\bar{\theta}}, \tag{10.3.7}$$

$$\frac{\partial u'}{\partial x} + \frac{\partial v'}{\partial y} + \frac{\partial w'}{\partial z} = 0, \tag{10.3.8}$$

$$\frac{\partial \theta'}{\partial t} + w' N^2 \frac{\bar{\theta}}{g} = 0. \tag{10.3.9}$$

Substituting the plane-wave solution (10.3.4) into Eqs. (10.3.5)–(10.3.9) gives

$$-i\omega\tilde{u} - f\tilde{v} + ik\frac{\tilde{p}}{\bar{\rho}} = 0, \tag{10.3.10}$$

$$-i\omega\tilde{v} + f\tilde{u} + il\frac{\tilde{p}}{\bar{\rho}} = 0, \tag{10.3.11}$$

$$-i\omega\tilde{w} + in\frac{\tilde{p}}{\bar{\rho}} - g\frac{\tilde{\theta}}{\bar{\theta}} = 0, \tag{10.3.12}$$

$$k\tilde{u} + l\tilde{v} + n\tilde{w} = 0, \tag{10.3.13}$$

$$-i\omega\tilde{\theta} + N^2\frac{\bar{\theta}}{g}\tilde{w} = 0. \tag{10.3.14}$$

If non-zero solutions to Eqs. (10.3.10)–(10.3.14) exist, then the coefficient determinant must be zero, i.e.,

$$\begin{vmatrix} -i\omega & -f & 0 & \frac{ik}{=\rho} & 0 \\ f & -i\omega & 0 & \frac{il}{=\rho} & 0 \\ 0 & 0 & -i\omega & \frac{in}{=\rho} & -\frac{g}{=\theta} \\ k & l & n & 0 & 0 \\ 0 & 0 & N^2\frac{\bar{\theta}}{g} & 0 & -i\omega \end{vmatrix} = 0 \quad .$$

(10.3.15)

By solving the determinant (10.3.15), the dispersion relation for three-dimensional inertia-gravity waves can be found

$$\omega^2(k^2+l^2+n^2) = N^2(k^2+l^2) + f^2n^2 \,. \tag{10.3.16}$$

This dispersion relation contains the term f^2n^2, which represents the influence of the Earth's rotation.

The corresponding phase velocity and group velocity are given by the following

$$Cx = \frac{N^2(k^2+l^2)+f^2n^2}{\omega k(k^2+l^2+n^2)}, \tag{10.3.17}$$

$$Cy = \frac{N^2(k^2+l^2)+f^2n^2}{\omega l(k^2+l^2+n^2)}, \tag{10.3.18}$$

$$Cz = \frac{N^2(k^2+l^2)+f^2n^2}{\omega n(k^2+l^2+n^2)}, \tag{10.3.19}$$

$$Cgx = \frac{(\omega^2 - f^2)n^2 k}{\omega(k^2 + l^2 + n^2)(k^2 + l^2)}, \tag{10.3.20}$$

$$Cgy = \frac{(\omega^2 - f^2)n^2 l}{\omega(k^2 + l^2 + n^2)(k^2 + l^2)}, \tag{10.3.21}$$

$$Cgz = -\frac{(\omega^2 - f^2)n}{\omega(k^2 + l^2 + n^2)}. \tag{10.3.22}$$

It can be proved with the group-velocity expressions ((10.3.20)–(10.3.22)) that

$$(k, l, n) \cdot (Cgx, Cgy, Cgz) = 0. \tag{10.3.23}$$

The above equation shows that the wave-number vector for a three-dimensional inertia-gravity wave in stationary basic airflow is perpendicular to the group velocity. This means the wave energy propagates on the iso-phase plane.

We consider a simple two-dimensional (y, z) situation to discuss the relation between wave-number vector and group velocity. Assuming that the disturbance is independent of the x-axis, i.e. $k = 0$, then (10.3.21) and (10.3.22) become

$$Cgy = -\lambda_y l \tag{10.3.24}$$

$$Cgz = \lambda_z n, \tag{10.3.25}$$

where $\lambda_y = \frac{(f^2 - \omega^2)n^2}{\omega(l^2 + n^2)l^2}$ and $\lambda_z = \frac{(f^2 - \omega^2)}{\omega(l^2 + n^2)}$. Clearly, the wave-number vector (l, n) and the direction of group velocity

(Cgy, Cgz) are still perpendicular in the *y*–*z* plane. If $l > 0$ and $n > 0$, the group velocity direction of high-frequency inertia-gravity waves ($\lambda_y < 0$ and $\lambda_z < 0$) is to the right of wave-number vector direction, and the wave energy propagates to the right of the wave-number vector direction.

We assume that $k = K\cos\alpha\sin\gamma$, $l = K\cos\alpha\cos\gamma$, and $n = K\sin\alpha$, where $K = (k^2 + l^2 + n^2)^{\frac{1}{2}}$, α is the angle between the wave-number vector (k, l, n) and the horizontal plane, and γ is the angle between the horizontal component of wave-number vector (k, l) and the y-axis. Substituting the above wave numbers into the dispersion relation (10.3.16), we obtain

$$\omega^2 = f^2 + (N^2 - f^2)\cos^2\alpha. \tag{10.3.26}$$

It can be seen that the wave frequency is mainly determined by the buoyancy oscillation frequency, N^2, the Coriolis parameter, f, and the angle, α, and does not depend on wave numbers. If the other parameters remain unchanged and $N^2 > f^2$ (which, in general, is the case for real atmosphere), the high-frequency three-dimensional inertia-gravity waves propagate close to the horizontal direction and the low-frequency three-dimensional inertia-gravity waves propagate close to the vertical direction. In addition, if $N^2 > f^2$, the frequency range is given by:

$$f^2 \le \omega^2 \le N^2. \tag{10.3.27}$$

From Eqs. (10.3.10)–(10.3.14), we obtain

$$\tilde{u} = -\frac{(k\omega + ilf)n}{\omega(k^2 + l^2)}\tilde{w}. \tag{10.3.28}$$

$$\tilde{v} = -\frac{(l\omega - ikf)n}{\omega(k^2 + l^2)}\tilde{w}. \tag{10.3.29}$$

Substituting (10.3.28)–(10.3.29) into (10.3.4) gives the velocity disturbance as follows

$$\begin{pmatrix} u'(x,y,z,t) \\ v'(x,y,z,t) \\ w'(x,y,z,t) \end{pmatrix} = \begin{pmatrix} -\dfrac{(k\omega + ilf)n}{\omega(k^2 + l^2)} \\ -\dfrac{(l\omega - ikf)n}{\omega(k^2 + l^2)} \\ 1 \end{pmatrix} \tilde{w} e^{i(kx+ly+nz-\omega t)}. \tag{10.3.30}$$

Tt is easy to show from (10.3.30) that

$$(k,l,n) \cdot \begin{pmatrix} u'(x,y,z,t) \\ v'(x,y,z,t) \\ w'(x,y,z,t) \end{pmatrix} = 0. \tag{10.3.31}$$

The above equation indicates that wave-number vector is perpendicular to velocity disturbance. This means that three-dimensional inertia-gravity wave in a stationary basic airflow is a transverse wave.

10.3.2 Symmetric Inertia-gravity Waves

Suppose that the atmosphere is symmetrical about the x-axis ($\frac{\partial}{\partial x} = 0$), all the basic states are functions of y and z, and that the

atmosphere is stratified ($N^2 > 0$). Taking into account the Earth's rotation effect ($f = f(y)$), the linearized perturbation equations describing the symmetric inertia-gravity waves can be written as

$$\frac{\partial u'}{\partial t} + v' \frac{\partial \bar{u}}{\partial y} + w' \frac{\partial \bar{u}}{\partial z} - fv' = 0, \tag{10.3.32}$$

$$\frac{\partial v'}{\partial t} + fu' = -\frac{1}{\bar{\rho}} \frac{\partial p'}{\partial y}, \tag{10.3.33}$$

$$\frac{\partial w'}{\partial t} = -\frac{1}{\bar{\rho}} \frac{\partial p'}{\partial z} + g \frac{\theta'}{\bar{\theta}}, \tag{10.3.34}$$

$$\frac{\partial v'}{\partial y} + \frac{\partial w'}{\partial z} = 0, \tag{10.3.35}$$

$$\frac{\partial \theta'}{\partial t} + v' \frac{\partial \bar{\theta}}{\partial y} + w' N^2 \frac{\bar{\theta}}{g} = 0. \tag{10.3.36}$$

With $k = 0$, substituting the plane-wave solution (10.3.4) into the above equations gives

$$-i\omega\tilde{u} - (f - \frac{\partial \bar{u}}{\partial y})\tilde{v} + \frac{\partial \bar{u}}{\partial z}\tilde{w} = 0, \tag{10.3.37}$$

$$-i\omega\tilde{v} + f\tilde{u} + il\frac{\tilde{p}}{\bar{\rho}} = 0, \tag{10.3.38}$$

$$-i\omega\tilde{w} + in\frac{\tilde{p}}{\bar{\rho}} - g\frac{\tilde{\theta}}{\bar{\theta}} = 0, \tag{10.3.39}$$

$$l\tilde{v} + n\tilde{w} = 0\,, \tag{10.3.40}$$

$$-i\omega\tilde{\theta} + \frac{\partial\bar{\theta}}{\partial y}\tilde{v} + N^2\frac{\bar{\theta}}{g}\tilde{w} = 0\,. \tag{10.3.41}$$

If there is non-zero solution to Eqs. (10.3.37)–(10.3.41), the coefficient determinant of these equations must be zero, i.e.,

$$\begin{vmatrix} -i\omega & -(f - \frac{\partial\bar{u}}{\partial y}) & \frac{\partial\bar{u}}{\partial z} & 0 & 0 \\ f & -i\omega & 0 & \frac{il}{\bar{\rho}} & 0 \\ 0 & 0 & -i\omega & \frac{in}{\bar{\rho}} & -\frac{g}{\bar{\theta}} \\ 0 & l & n & 0 & 0 \\ 0 & \frac{\partial\bar{\theta}}{\partial y} & N^2\frac{\bar{\theta}}{g} & 0 & -i\omega \end{vmatrix} = 0\,. \tag{10.3.42}$$

After solving the determinant, we can obtain the dispersion relation for symmetric inertia-gravity waves:

$$\omega^2(l^2 + n^2) = N^2 l^2 + (f\frac{\partial\bar{u}}{\partial z} - \frac{g}{\bar{\theta}}\frac{\partial\bar{\theta}}{\partial y})nl + f(f - \frac{\partial u}{\partial y})n^2\,. \tag{10.3.43}$$

Since the basic states adopted here varies in the y- and z-directions, the frequency is related to the static stability parameter (N^2), baroclinic parameter $f\frac{\partial\bar{u}}{\partial z} - \frac{g}{\bar{\theta}}\frac{\partial\bar{\theta}}{\partial y}$, and inertial stability parameter $f^2 - f\frac{\partial\bar{u}}{\partial y}$.

According to the dispersion relation (10.3.43), the phase velocity and group velocity are given by the following:

$$Cy = \frac{N^2 l^2 + (f\frac{\partial \bar{u}}{\partial z} - \frac{g}{\bar{\theta}}\frac{\partial \bar{\theta}}{\partial y})nl + f(f - \frac{\partial \bar{u}}{\partial y})n^2}{\omega l(l^2 + n^2)}, \qquad (10.3.44)$$

$$Cz = \frac{N^2 l^2 + (f\frac{\partial \bar{u}}{\partial z} - \frac{g}{\bar{\theta}}\frac{\partial \bar{\theta}}{\partial y})nl + f(f - \frac{\partial \bar{u}}{\partial y})n^2}{\omega n(l^2 + n^2)}, \qquad (10.3.45)$$

$$Cgy = \frac{1}{2}\frac{(n^2 - l^2)\omega^2 - f(f - \frac{\partial \bar{u}}{\partial y})n^2 + N^2 l^2}{\omega l(l^2 + n^2)}, \text{ and} \qquad (10.3.46)$$

$$Cgz = -\frac{1}{2}\frac{(n^2 - l^2)\omega^2 - f(f - \frac{\partial \bar{u}}{\partial y})n^2 + N^2 l^2}{\omega n(l^2 + n^2)}. \qquad (10.3.47)$$

With the expressions for group velocity ((10.3.44)–(10.3.47)), it can be shown that

$$(l,n)\cdot(Cgy, Cgz) = 0. \qquad (10.3.48)$$

This indicates that the wave-number vector of symmetric inertia-gravity wave is perpendicular to the group velocity, that is, the wave energy propagates along iso-phase plane.

Assuming that

$$l = K\cos\alpha \quad \text{and} \quad n = K\sin\alpha, \qquad (10.3.49)$$

where $K = (l^2 + n^2)^{\frac{1}{2}}$ and α is the angle between wave-number vector (l,n) and y-axis. Substituting (10.3.49) into (10.3.43), we

obtain

$$\omega^2 = N^2 \cos^2\alpha + (f\frac{\partial \bar{u}}{\partial z} - \frac{g}{\bar{\theta}}\frac{\partial \bar{\theta}}{\partial y})\sin\alpha\cos\alpha + f(f - \frac{\partial \bar{u}}{\partial y})\sin^2\alpha \ . \tag{10.3.50}$$

It can be seen from the above equation that the frequency of symmetrical inertia-gravity wave depends on the angle, α, but does not depend on wave numbers.

From Eqs. (10.3.32)–(10.3.36), we obtain

$$\tilde{v} = -\frac{n}{l}\tilde{w}. \tag{10.3.51}$$

Substituting (10.3.51) into (10.3.4), the velocity perturbation in y- and z-directions can be written as

$$\begin{pmatrix} v'(x,y,z,t) \\ w'(x,y,z,t) \end{pmatrix} = \begin{pmatrix} -\frac{n}{l} \\ 1 \end{pmatrix} \tilde{w} e^{i(ly+nz-\omega t)} . \tag{10.3.52}$$

We also get

$$(l,n)\cdot\begin{pmatrix} v'(x,y,z,t) \\ w'(x,y,z,t) \end{pmatrix} = 0 . \tag{10.3.53}$$

It is proved that symmetric inertia-gravity wave is also transverse wave.

10.4 Gravity-wave Polarization Theory

Polarization is an important property of gravity waves and a basis for detecting gravity waves from observational data. This section begins with a brief introduction to physical concept of polarization and then discusses the polarization properties of inertia-gravity waves and symmetric inertia-gravity waves.

A characteristic of light is that the vibration direction is generally perpendicular to the direction of light propagation. In electromagnetic wave theory, this is known as light polarization. Light can be categorized as unpolarized light, fully polarized light, and partially polarized light.

In a plane perpendicular to light propagation, if the vibrations occur in all directions, the amplitudes are the same, and there is no fixed phase relation among individual vibrations, then this light is called natural light (Figure 10.4.1 (a)). If the light vibrates in a fixed direction in a perpendicular plane, then the light is said to be linearly polarized (Figure 10.4.1 (b)). The plane composed of vibration direction of linearly polarized light and light propagation direction is referred to as vibration plane. If the light vibrations rotate uniformly around the light propagation direction with a constantly changing amplitude and the projection of vibration end point trajectory on the perpendicular plane is an ellipse, then the light is said to be elliptically polarized (Fig. 10.4.1 (c)). If the vibration amplitude is constant and the projection of end point trajectory on a perpendicular plane is a circle, then the light is said to be circularly polarized. Light that is a mixture of natural light and polarized light is called partially polarized light.

The concept of light polarization is also applicable to atmospheric gravity waves. It is assumed that the two vibrations perpendicular to each other can be expressed as

$$E_x = E_{xm}\cos(kx + ly + nz - \omega t + \phi_x) \tag{10.4.1}$$

$$E_y = E_{ym}\cos(kx + ly + nz - \omega t + \phi_y), \tag{10.4.2}$$

where E_{xm} and E_{ym} are the amplitudes of two vibrations, E_x and E_y, respectively, k, l, and n are the wave numbers in the x-, y-,

and z - directions, respectively, ω is the wave frequency, and ϕ_x and ϕ_y are the initial phases of E_x and E_y, respectively.

Using trigonometric formula, (10.4.1) and (10.4.2) can be combined into

$$\frac{E_1^{\ 2}}{E_{1m}^{\ 2}} + \frac{E_2^{\ 2}}{E_{2m}^{\ 2}} - 2\frac{E_1 E_2}{E_{1m} E_{2m}} \cos\phi_m = \sin^2\phi, \tag{10.4.3}$$

where $\phi = \phi_x - \phi_y$ is the initial phase difference between E_x and E_y. Eq. (10.4.3) is a general elliptic equation. The angle β between the long axis of ellipse and the x-axis (Fig. 10.4.2) satisfies the following relation

$$\tan 2\beta = 2\frac{E_{xm} E_{ym}}{E_{xm}^{\ 2} - E_{ym}^{\ 2}} \cos\phi. \tag{10.4.4}$$

It can be seen from (10.4.3) and (10.4.4) that when $\phi = n\pi, n = 0, \pm 1, \pm 2, \cdots$, $E_y = \pm\frac{E_{ym}}{E_{xm}} E_x$, indicating that the end point of combination vibration moves along a straight line. When $\phi = (2n+1)\frac{\pi}{2}, n = 0, \pm 1, \pm 2, \cdots$, $\frac{E_x^2}{E_{xm}^2} + \frac{E_y^2}{E_{ym}^2} = 1$ and $\beta = 0$ or $\frac{\pi}{2}$, indicating that the end point trajectory of combined vibrations is ellipse. The two focus points lie on the coordinate axis. When

$\phi = (2n+1)\frac{\pi}{2}, n = 0, \pm 1, \pm 2, \cdots$ and $E_{xm} = E_{ym}$, then $\frac{E_x^2}{E_{xm}^2} + \frac{E_y^2}{E_{xm}^2} = 1$, indicating the end point trajectory of synthetic vibrations is a circle, which corresponds to circular polarization. For other values of ϕ, although (10.4.3) represents an elliptically polarized wave, the end point trajectory presents an ellipse with a long axis at an angle β to horizontal axis.

10.4.1 Inertia-gravity Waves

From Eqs. (10.3.10)–(10.3.14), we can obtain the following expressions for complex amplitude of three-dimensional inertia-gravity wave

$$\tilde{u} = -\frac{n(ifl + \omega k)}{\omega(l^2 + k^2)}\tilde{w}, \tag{10.4.5}$$

$$\tilde{v} = \frac{n(ifk - \omega l)}{\omega(l^2 + k^2)}\tilde{w}, \tag{10.4.6}$$

$$\tilde{u} = -\frac{ifl + \omega k}{ifk - \omega l}\tilde{v}, \tag{10.4.7}$$

$$\tilde{p} = \frac{\overline{\rho}}{n}(\omega - \frac{N^2}{\omega})\tilde{w}, \tag{10.4.8}$$

$$\tilde{\theta} = -i\frac{\overline{\theta}}{g}\frac{N^2}{\omega}\tilde{w}. \tag{10.4.9}$$

If Eqs. (10.4.5)–(10.4.9) hold, there must be the following phase differences between various disturbance amplitudes

$$\varphi_u - \varphi_w = m\pi + \mathbf{arctan}(\frac{fl}{\omega k}), m = 0, \pm 1, \pm 2, \cdots, \quad (10.4.10)$$

$$\varphi_v - \varphi_w = m\pi + \mathbf{arctan}(-\frac{fk}{\omega l}), m = 0, \pm 1, \pm 2, \cdots, \quad (10.4.11)$$

$$\varphi_u - \varphi_v = (2m+1)\pi + \mathbf{arctan}[\frac{\omega f(l^2+k^2)}{(\omega^2 - f^2)kl}], m = 0, \pm 1, \pm 2, \cdots, \quad (10.4.12)$$

$$\varphi_p - \varphi_w = m\pi, m = 0, \pm 1, \pm 2, \cdots, \quad (10.4.13)$$

$$\varphi_\theta - \varphi_w = 2m\pi + \frac{3\pi}{2}, m = 0, \pm 1, \pm 2, \cdots. \quad (10.4.14)$$

The initial phase difference among disturbance velocities is related to the Coriolis parameter, and wave parameter, indicating elliptical polarization. Also, the phase difference between pressure and vertical velocity is $m\pi$, and the phase difference between potential temperature and vertical velocity is $2m\pi + \frac{3\pi}{2}$.

Similarly, the phase difference between horizontal divergence ($\frac{\partial u'}{\partial x} + \frac{\partial v'}{\partial y} = -inw_0 e^{i\varphi_w} e^{i(kx+ly+nz-\omega t)}$) and vertical velocity is $m\pi + \frac{\pi}{2}$. Substituting the plane-wave solution

($u' = u_0 e^{i\varphi_u} e^{i(kx+ly+nz-\omega t)}$, $v' = v_0 e^{i\varphi_u} e^{i(kx+ly+nz-\omega t)}$) into the perturbation vertical vorticity and using (10.4.9) and (10.4.10), we obtain

$$\frac{\partial v'}{\partial x} - \frac{\partial u'}{\partial y} = -\frac{fn}{\omega} w_0 e^{i\varphi_w} e^{i(kx+ly+nz-\omega t)}. \tag{10.4.15}$$

It is shown that the phase difference between vorticity and vertical velocity for three-dimensional inertia-gravity wave is $m\pi$. It can be inferred that the phase difference between vertical vorticity and horizontal divergence is $\frac{\pi}{2}$.

10.4.2 Symmetric Inertia-gravity Wave

From Eqs. (10.3.37)–(10.3.41), we can obtain the following expressions of complex amplitude for symmetric inertia-gravity wave

$$\tilde{u} = [\frac{\partial \bar{u}}{\partial z} - \frac{n}{l}(\frac{\partial \bar{u}}{\partial y} - f)]\frac{\tilde{w}}{i\omega}, \tag{10.4.16}$$

$$\tilde{v} = -\frac{n}{l}\tilde{w}, \tag{10.4.17}$$

$$\frac{\tilde{p}}{\bar{\rho}} = \frac{1}{in}[i\omega + (N^2 - \frac{n}{l}\frac{g}{\theta_0}\frac{\partial \bar{\theta}}{\partial y})\frac{1}{i\omega}]\tilde{w}, \tag{10.4.18}$$

$$\tilde{\theta} = (\frac{\theta_0}{g}N^2 - \frac{n}{l}\frac{\partial \bar{\theta}}{\partial y})\frac{\tilde{w}}{i\omega}. \tag{10.4.19}$$

It can be seen that if Eqs. (10.4.16)–(10.4.19) hold, there must be the following phase difference among various disturbance amplitudes

$$\varphi_u - \varphi_w = m\pi + \frac{\pi}{2}, m = 0, \pm 1, \pm 2, \cdots, \tag{10.4.20}$$

$$\varphi_v - \varphi_w = m\pi, m = 0, \pm 1, \pm 2, \cdots, \tag{10.4.21}$$

$$\varphi_u - \varphi_v = m\pi + \frac{\pi}{2}, m = 0, \pm 1, \pm 2, \cdots, \tag{10.4.22}$$

$$\varphi_p - \varphi_w = m\pi, m = 0, \pm 1, \pm 2, \cdots, \tag{10.4.23}$$

$$\varphi_\theta - \varphi_w = m\pi + \frac{\pi}{2}, m = 0, \pm 1, \pm 2, \cdots. \tag{10.4.24}$$

For symmetric inertia-gravity wave, the phase differences between u' and v', and between u' and w' are $m\pi + \frac{\pi}{2}$, indicating that these velocity components are elliptically polarized. The phase difference between v' and w' is $m\pi$, indicating that they are linearly polarized. The phase difference between ρ' and w' is $m\pi$, and the phase difference between θ' and w' is $m\pi + \frac{\pi}{2}$.

Using (10.4.17), the vorticity disturbance can be written as

$$\frac{\partial w'}{\partial y} - \frac{\partial v'}{\partial z} = i\frac{l^2 + n^2}{l} w'. \tag{10.4.25}$$

It is shown the phase difference between vorticity and vertical velocity for symmetric inertia-gravity wave is $m\pi + \frac{\pi}{2}$.

10.5 Gravity Wave Identification and Analysis

10.5.1 Fourier Analysis

Fourier analysis is an important method to analyze atmospheric waves (Wheeler and kiladis, 1999; Zhang et al., 2001). Two-dimensional Fourier analysis can convert a two-dimensional spatial and temporal field of a physical variable into a two-dimensional frequency-wave number energy spectrum.

When an array satisfies certain conditions, it can be expanded by Fourier series as

$$x_t = a_0 + \sum_{k=1}^{l} (a_k \cos \omega_k t + b_k \sin \omega_k t) \tag{10.5.1}$$

where k is the wave number, L is the total number of harmonics, $\omega_k = \frac{2\pi}{n} k$ is the angular frequency and $A_k = \sqrt{a_k{}^2 + b_k{}^2}$ is the harmonic amplitude. It describes the variation of harmonic amplitude with frequency. $\theta_k = \arctan(-\frac{b_k}{a_k})$ is the phase while a_0 , a_k , b_k are Fourier coefficients with the following expressions as

$$a_0 = \frac{1}{n} \sum_{t=1}^{n} x_t \tag{10.5.2}$$

$$a_k = \frac{2}{n} \sum_{t=1}^{n} x_t \cos \omega_t t \tag{10.5.3}$$

$$b_k = \frac{2}{n} \sum_{t=1}^{n} x_t \sin \omega_t t \tag{10.5.4}$$

The two-dimensional Fourier transform and the two-dimensional inverse Fourier transform can be written as

$$\mathbf{F}(\omega,\tau)=\int\int_{-\infty}^{+\infty} f(x,y)\,\mathbf{exp}(-\mathbf{j}2\pi(\omega x+\tau y))dxdy \qquad (10.5.5)$$

$$f(x,y)=\int\int_{-\infty}^{+\infty} F(\omega,\tau)\,\mathbf{exp}(\mathbf{j}2\pi(\omega x+\tau y))d\omega d\tau \qquad (10.5.6)$$

in which ω is the frequency and τ is the period.

Take a heavy rain in Sichuan on August 17, 2014 for example. The wave characteristics such as period and wavelength in the heavy rain event can be preliminarily understood by decomposing and converting the vertical velocity through the two-dimensional Fourier analysis method. A single-peak narrow-spectrum structure is obvious in Figure 10.5.1. In other words, the area with concentrated spectral energy presents a band-like distribution. It proves the existence of wave characteristics. High energy mainly locates in the area with the frequency of 0.0083~0.0125 min^{-1} (period 80~120 min^{-1}) and positive wave number of 0.0133~0.0267 km^{-1} (wavelength 37.5~75 km), which indicates that the wave propagates eastward. The black solid line in the figure represents the phase velocity ($c=\omega/k$). It can be seen that the vertical motions of different scale features almost propagate eastward at the same phase velocity with wave velocity between 10 and 25 m/s and average velocity of 15 m/s.

10.5.2 Cross-spectrum Analysis

Gravity waves are common atmospheric waves in topographic rainstorms. They have the property of polarization (Polarization is the property that the vibration direction is perpendicular to the propagation direction). Lu et al. (2005a, b) discussed the polarization of gravity waves and proposed the semi-polarization theory of gravity waves. In the Cartesian coordinates, under the Boussinesq approximation, the disturbance horizontal divergence and vertical vorticity of the

three-dimensional inertial gravity wave can be written as:

$$\frac{\partial u'}{\partial x}+\frac{\partial v'}{\partial y}=-inw', \tag{10.5.7}$$

$$\frac{\partial v'}{\partial x}-\frac{\partial u'}{\partial y}=-\frac{fn}{\omega}w'. \tag{10.5.8}$$

Where u', D' and w' are the perturbation speeds, ω is the circular frequency, n is the vertical wave number, and f is the Coriolis parameter. The above equations show that the phase difference between the disturbance horizontal divergence and the disturbance vertical velocity is $m\pi+\frac{\pi}{2}$, while the phase difference between the disturbance vertical vorticity and the disturbance vertical velocity is $m\pi$. Therefore the time and space difference between the disturbance vertical vorticity and the disturbance horizontal divergence is $\frac{\pi}{2}$ (Gao Shouting, 2005). This is an important polarization property of inertial gravity waves, and it is also an important basis for identifying inertial gravity waves from observation and simulation data.

(1) Traditional cross spectrum

The cross-spectrum method is an important method for analyzing waves. It can clearly determine the phase difference relationship between two different arrays. The results such as the amplitude spectrum and condensed spectrum can reflect the energy of the wave. The calculation process of the cross spectrum method is as follows（Cho，1995；Lu et al.，2005）:

First, Fourier transform is performed on the physical variables, and the two physical variables x and y are converted into functions of wave numbers and frequencies. On this basis, the amplitude spectrum, phase difference spectrum and cohesion spectrum are calculated. The amplitude spectrum represents the energy relationship of the vibration of a certain

frequency of the two arrays. The larger the amplitude spectrum, the higher the energy at a certain frequency. The calculation formula for the amplitude can be written as:

$$A(\omega) = [(\mathbf{X}^R\mathbf{Y}^R + \mathbf{X}^I\mathbf{Y}^I)^2 + (\mathbf{X}^I\mathbf{Y}^R - \mathbf{X}^R\mathbf{Y}^I)^2]^{1/2} \tag{10.5.9}$$

Here X and Y represent the arrays of the physical variables after Fourier transform, while the superscript R and I represent the real and imaginary parts of the physical variables respectively. The phase difference spectrum represents the phase difference relationship between two arrays of different frequencies, and its value varies among -90°~90°. The calculation formula for the phase difference spectrum is：

$$P(\omega) = \mathbf{arctan}\left(\frac{\mathbf{X}^I\mathbf{Y}^R - \mathbf{X}^R\mathbf{Y}^I}{\mathbf{X}^R\mathbf{Y}^R + \mathbf{X}^I\mathbf{Y}^I}\right) \tag{10.5.10}$$

Cohesion spectrum represents the correlation between different frequencies of two sequences, and the correlation coefficient varies between 0 and 1. The calculation formula is：

$$\mathbf{C}(\omega) = \frac{\left\|\mathbf{X}\mathbf{Y}^*\right\|^2}{\left\|\mathbf{X}\right\|^2\left\|\mathbf{Y}\right\|^2} \tag{10.5.11}$$

where Y* represents the conjugate of a complex number, and ||Y|| and ||X|| represent the modulus of the complex number, respectively. The larger the cohesion spectrum value, the stronger the correlation between the two sequences.

Figure 10.5.2 uses the cross-spectrum method to calculate the phase spectra and the corresponding cohesion spectra of vorticity and divergence of different wave numbers. It can be seen that both the phase difference is about 90°, and the characteristic wave numbers [0.02~0.023, 0.04 and 0.066 (km^{-1})] correspond to the larger condensed spectrum values, indicating that the waves of these wave numbers are gravity waves.

(2) Wavelet cross spectrum

Through Cross-spectrum analysis, we can only know the existence of gravity waves and their corresponding frequencies. We cannot distinguish where and when the gravity waves occur. In order to solve this problem, one-dimensional continuous wavelet analysis and wavelet cross-spectrum can be used to perform wavelet analysis on different frequencies of gravity waves, and then reconstruct the wave of certain frequency, so that the occurrence and development of gravity waves can be observed more intuitively.

The difference between the wavelet cross spectrum method and the traditional cross spectrum one is that the traditional cross spectrum method analyzes the cross relationship based on the Fourier transform, while the wavelet cross spectrum first performs one-dimensional continuous wavelet decomposition on the two arrays of the physical variables, and then calculate the cross correlate coefficients. The wavelet cross-spectrum can reflect where and when the waves occur, and thus provides a better description for studying the development and evolution of the wave. The calculation formulas for the wavelet cross spectrum are as follows:

$$C(a,b,f(t),\psi(t)) = \int_{-\infty}^{\infty} f(t)\frac{1}{\sqrt{a}}\psi^{*}(\frac{t-b}{a})dt \qquad (10.5.12)$$

$$C_{xy}(a,b) = S(C_x^{*}(a,b)C_y(a,b)) \qquad (10.5.13)$$

In the formulas, $C_x(a,b)$ and $C_y(a,b)$ represent the continuous wavelet transform of two physical variables X and Y, a and b are respectively the scale function and position function of the continuous wavelet transform, the superscript * represents the conjugate of the complex number, and S represents smooth.

$C_{xy}(a,b)$ can be written as (Liu, 1994, Ge, 2008):

$$C_{xy} = \left|C_{xy}\right| \exp i(\theta_y(a,b) - \theta_x(a,b)) \tag{10.5.14}$$

where $\theta_y(a,b) - \theta_x(a,b)$ is the phase difference. Condensed spectrum can be written as:

$$R_{xy}(a) = \frac{\left|\int_T C_x^*(a,b) C_y(a,b) db\right|^2}{\int_T \left|C_x(a,b)\right|^2 db \int_T \left|C_y(a,b)\right|^2 db} \tag{10.5.15}$$

Its physical meaning is consistent with that in the traditional cross spectrum.

Wavelet cross-spectrum analysis is performed on vorticity and divergence, and the basic wavelet is selected as Gaus complex wavelet. It can be seen in Figure 10.5.3 that there is a 90° phase difference in a large and relatively stable area near 102.9°-103.8°E, indicating the existence of the wave characteristics of gravity waves. The corresponding condensed spectrum value is very strong and close to 1, indicating the high correlation between vorticity and divergence at this frequency. At the same time, it corresponds to the large energy region of the amplitude spectrum, indicating that the energy of the wave is very strong.

10.5.3 Gravity Wave Reconstruction

Comprehensive usage of the information obtained from cross-spectrum analysis and wavelet cross-spectrum analysis, together with the inverse Fourier transform formula in (10.5.6), gravity waves can be reconstructed. In Figure 10.5.4, we can clearly see the wave characteristics of gravity waves at key scales in the process of heavy rain. The distribution of vertical velocity presents the positive and negative change, mainly at the height of 12-15 km. It also can be seen that the gravity wave propagates

eastward with time. Therefore, the reconstructed gravity waves can be used to analyze the local structures of the wave more clearly.

10.5.4 Conclusion

This section takes a torrential rain in a mountainous area in Sichuan as an example, and introduces how to use the cross-spectrum analysis method and the Fourier transform method to identify and extract gravity waves. Through the two-dimensional Fourier spectrum analysis, the period and wave number range of the gravity wave, as well as the propagation direction and speed of the wave can be obtained preliminary. According to the traditional cross spectrum method with the usage of the polarization property of the gravity wave, it is proved that the waves of the key frequencies and wave numbers are gravity waves. The cross spectrum method is firstly to determine whether it conforms to the polarization property of the gravity wave by analyzing the condensed spectrum and phase spectrum of the time series of two meteorological elements, and then to determine the frequency and wave number of the gravity wave. Finally, the wavelet cross-spectrum method is used to analyze where and when the gravity waves of key frequencies and wave numbers occur. The major advantage of the wavelet cross-spectrum method is that it can not only display the spectral characteristics, but also show where and when the waves occur. With the frequency and wave number of gravity waves determined by the cross spectrum method, and the two-dimensional inverse Fourier transform to transform meteorological elements into the space-time field, the gravity wave structure is reconstructed and used to analyze the development and evolution characteristics, location changes and sources of gravity waves with key frequencies and wave numbers.

10.6 Gravity-wave Breaking Parameterization Theory

10.6.1 Gravity-wave Breaking Theory

The so-called breaking of gravity waves simply refers to the process by which the gravity wave amplitude of does not grow with height during upwards propagation.

In the pressure-logarithmic coordinate system, we have

$$\frac{\partial u'}{\partial t}+\frac{\partial \Phi'}{\partial x}=0, \tag{10.6.1}$$

$$\frac{\partial u'}{\partial x}+\frac{1}{=\rho}\frac{\partial}{\partial Z}(\overline{\rho w'})=0, \tag{10.6.2}$$

$$\frac{\partial}{\partial t}(\frac{\partial \Phi'}{\partial Z})+N^2 w'=0, \tag{10.6.3}$$

where $\frac{\partial \Phi'}{\partial Z}=\frac{RT'}{H}$. Asuming a wave-like solution

$$(u', w', \Phi')=e^{z/2H}\,\mathrm{Re}[(u', w', \Phi')e^{i(kx+mZ-\omega t)}], \tag{10.6.4}$$

and substituting it into. (10.6.1)–(10.6.3) yields a dispersion relation:

$$\omega^2=\frac{N^2k^2}{k^2+m^2+1/(4H^2)}. \tag{10.6.5}$$

Since the vertical wave number is much smaller than the scale height, H, and the horizontal wave number is much smaller than the vertical wave number—that is, $1/(4H^2)\ll m^2,\ k\ll m$ —equation (10.6.5) can be simplified to $\omega=\pm Nk/m$. For the upwards propagation, $C_{gz}>0$,

and so the vertical group velocity is

$$C_{gz} = -\frac{\partial \omega}{\partial m} = \frac{Nk}{m^2} = \frac{\omega^2}{Nk}. \tag{10.6.6}$$

Due to the existence of basic-state wind, $\overline{U}$, the frequency after polarization to be $\omega = k(\overline{U} - c)$; the vertical group velocity is therefore

$$C_{gz} = \frac{k}{N}(\overline{U} - c)^2. \tag{10.6.7}$$

When $(\overline{U} - c)$ is large—that is, when $\overline{U}$ and c are opposite, C_{gz} is also large, and the gravity wave is obviously upwards propagates. When $\overline{U}$ and c have the same direction, the vertical group velocity is small, which is not conducive to the upwards propagation. At the same time, amplitude is $(u', w') \propto \rho^{-1/2} \propto e^{Z/2H}$; thus, when gravity wave upwards propagates, the wave amplitude must increase with height, meaning that the potential temperature gradient becomes steep. The following will occur when a certain height is reached:

$$\frac{\partial \theta}{\partial Z} = \frac{\partial \overline{\theta}}{\partial Z} + \frac{\partial \theta'}{\partial Z} = 0. \tag{10.6.8}$$

When this occurs, the isentropic surface becomes vertical. The wave then begins to break due to instability. Because

$$\frac{\partial \Phi}{\partial T} = RTH^{-1} = R(\theta e^{-\kappa Z/H})H^{-1}, \tag{10.6.9}$$

Potential temperature gradient can be expressed as

$$\frac{\partial \theta}{\partial Z} \approx \frac{H}{R} e^{-\kappa Z/H} [N^2 + \Phi_{zz}]; \tag{10.6.10}$$

therefore,

$$\frac{\partial \theta}{\partial Z} = 0 \rightarrow N^2 = m^2 \Phi e^{Z/2H} \quad . \tag{10.6.11}$$

The breaking height can then be estimated by

$$Z_b \approx 2H \ln \left| \frac{N^2}{m^2 \Phi} \right|, \tag{10.6.12}$$

where Φ is the wave amplitude.

10.6.2 Gravity-wave Drag Theory

An important feature of gravity-wave propagation is that gravity waves can carry momentum flux generated from source region to upper level as well as—in particular—to mesosphere. The momentum flux carried by gravity wave is dissipated in breaking zone and affects middle atmospheric circulation in the form of gravity-wave drag. Many meteorologists have studied this (Holton, 1975; Lindzen, 1981; Fritts, 1984; Matsuno, 1982). Because gravity-wave breaking is so important, McFarlane (1987) first parameterized gravity-wave drag scheme. Gao et al. (1998, 2003) then improved on McFarlane's parameterization scheme. It is introduced in detail below.

The basic idea behind the parameterization scheme proposed by McFarlane (1987) is that the terrain can be represented by

$$z = h \cos \mu, \tag{10.6.13}$$

where h is the terrain height. The terrain is a fixed source exciting steady gravity waves. The non-viscous, adiabatic, dimensionless anelastic equations that describe steady gravity waves are

$$\bar{u}\frac{\partial u}{\partial x}+w\frac{\partial \bar{u}}{\partial Z}=-\frac{\partial \pi}{\partial x}, \tag{10.6.14}$$

$$\frac{\partial \pi}{\partial Z}=g\frac{\theta}{\bar{\theta}}, \tag{10.6.15}$$

$$\frac{\partial u}{\partial x}+\frac{1}{\bar{\rho}}\frac{\partial}{\partial Z}(\bar{\rho}w)=0, \tag{10.6.16}$$

$$\bar{u}\frac{\partial \theta}{\partial x}+w\frac{\partial \bar{\theta}}{\partial Z}=0, \tag{10.6.17}$$

where $\pi = c_p p_0 \theta_0 (p/p_0)^{\kappa} + gz$ is the Exner function (Ogura and Phillips., 1962), and "-" denotes the latitudinal average. The averaged variables are functions of z only. u, w, and θ represent disturbances. Based on (10.6.16) and (10.6.17), we introduce the following relationship:

$$w=\bar{u}\frac{\partial \psi}{\partial x},\ u=-\frac{1}{\bar{\rho}}\frac{\partial}{\partial Z}(\bar{\rho}\bar{u}\psi),\ \theta=-\psi\frac{\partial \bar{\theta}}{\partial Z}, \tag{10.6.18}$$

where ψ is the stream function.

Substituting (10.6.18) into (10.6.14) and (10.6.17), eliminating π, integrating x, and taking the integration constant to be zero, we get

$$\frac{\partial}{\partial Z}[\frac{\bar{u}^2}{\bar{\rho}}\frac{\partial}{\partial Z}(\bar{\rho}\psi)+N^2\psi=0, \tag{10.6.19}$$

where $N^2=\frac{g}{\bar{\theta}}\frac{\partial \bar{\theta}}{\partial Z}$. It is assumed that the formal solution for ψ is

$$\psi(Z,x)=A(Z)\cos[\mu x+\int_0^z \phi(Z')dZ']. \tag{10.6.20}$$

Substituting (10.6.20) into (10.6.19) and setting the coefficient of trigonometric function to zero, we also have

$$\frac{N^2}{\bar{u}^2} - \phi^2 + o\left(\frac{1}{A}\frac{d^2A}{dZ^2}\right) = 0 \tag{10.6.21}$$

$$2\frac{dA}{dZ} + A\left(\frac{1}{\bar{\rho}\phi\bar{u}^2}\frac{d(\bar{\rho}\phi\bar{u}^2)}{dZ}\right) = 0\,. \tag{10.6.22}$$

By taking the first approximation, omitting the third term in (10.6.21), integrating Z on both sides of (10.6.22), and using the lower boundary condition, we have the following approximate solution:

$$\phi = \frac{N}{\bar{u}}, A = h\left[\frac{\bar{\rho}(0)N(0)\bar{u}(0)}{\bar{\rho}N\bar{u}}\right]^{\frac{1}{2}}. \tag{10.6.23}$$

The vertical momentum flux by wave can be defined as

$$\tau = \frac{1}{L}\int_{-\frac{L}{2}}^{\frac{L}{2}} \bar{\rho}uwdx\,, \tag{10.6.24}$$

where L is the x-direction wavelength.

Next, substituting (10.6.18), (10.6.20), and (10.6.23) into (10.6.24), and assuming that average amount changes very slowly in vertical direction, then (10.6.24) can be approximately written as

$$\tau \approx -\frac{\mu h^2}{2}\bar{\rho}(0)N(0)\bar{u}(0)\,. \tag{10.6.25}$$

Eq. (10.6.25) indicates that, outside the zone of gravity-wave breaking, the momentum flux carried by upward propagation of gravity wave does not vary with height. When the gravity wave reaches the saturated layer, the gravity wave will break and the resulting turbulence will cause energy dissipation, which limits the increase of wave amplitude. In order to consider the effect of vertical diffusion on wave, an attenuation factor is introduced. The perturbation stream function can then be written as

$$\psi(Z,x)=\psi_1(Z,x)\exp[-\int_0^z D(Z')dZ'], \tag{10.6.26}$$

where $\psi_1(Z,x)$ is given by (10.6.20), $D(Z)=N^3K/(\mu\overline{U}^4)$, and K is the vortex diffusivity. Correspondingly, in the wave-breaking zone, the vertical momentum flux can be expressed as

$$\tau=\tau(0)\exp[-2\int_0^z D(Z')dZ'], \tag{10.6.27}$$

where $\tau(0)$ is given by (10.6.25). In the wave-breaking zone, taking $D(Z)=\frac{1}{F}\frac{dF}{dZ}$, (10.6.27) becomes

$$\tau=\frac{\tau(0)}{F^2}=-\frac{1}{2}\frac{\overline{\rho}\overline{\mu}\overline{\mu}^3}{N}. \tag{10.6.28}$$

Therefore, in the wave-breaking zone, the local variation of averaged airflow caused by gravity-wave drag is

$$\frac{\partial\overline{u}}{\partial t}=-\frac{1}{\overline{\rho}}\frac{\partial\tau}{\partial Z}=-\frac{\mu}{2}\frac{\overline{\mu}^3}{N}\max[\frac{d\ln F^2}{dZ},0], \tag{10.6.29}$$

which is the basic idea in McFarlane's gravity-wave drag parameterization scheme.

Although McFarlane proposed a reasonable parameterization scheme for the influence of momentum flux by gravity wave on zonal mean airflow, he did not consider the effect of turbulent dissipation caused by gravity-wave breaking on airflow. This dissipation not only reduces the momentum of gravity wave but also affects the zonal mean flow. In the gravity-wave breaking zone, the gravity-wave equations with dissipation are, in fact

$$\bar{u}\frac{\partial u}{\partial x}+w\frac{\partial \bar{u}}{\partial Z}=-\frac{\partial \pi}{\partial x}+D\frac{\partial^2 u}{\partial Z^2}, \tag{10.6.30}$$

$$\frac{\partial \pi}{\partial Z}=g\frac{\theta}{\bar{\theta}}, \tag{10.6.31}$$

$$\frac{\partial u}{\partial x}+\frac{1}{\bar{\rho}}\frac{\partial}{\partial Z}(\bar{\rho}w)=0, \tag{10.6.32}$$

$$\bar{u}\frac{\partial \theta}{\partial x}+w\frac{\partial \bar{\theta}}{\partial Z}=D\frac{\partial^2 \theta}{\partial Z^2}, \tag{10.6.33}$$

where D is the dissipation coefficient, which is still to be determined. By eliminating π from (10.6.30) and (10.6.31), we obtain

$$\begin{aligned}&\frac{\partial \bar{u}}{\partial Z}\frac{\partial u}{\partial x}+\bar{u}\frac{\partial^2 u}{\partial Z\partial x}+\frac{\partial \bar{u}}{\partial Z}\frac{\partial w}{\partial Z}+w\frac{\partial^2 u}{\partial Z^2}\\&=-\frac{g}{\bar{\theta}}\frac{\partial \theta}{\partial x}+\frac{\partial D}{\partial Z}\frac{\partial^2 u}{\partial Z^2}+D\frac{\partial^3 u}{\partial Z^3}\end{aligned}. \tag{10.6.34}$$

Assuming that the form solution is

$$u=ue^{i(kx+mZ)},\quad w=we^{i(kx+mZ)},\quad \theta=\theta e^{i(kx+mZ)}, \tag{10.6.35}$$

and substituting (10.6.35) into (10.6.32)–(10.6.34), we get

$$(ik\frac{\partial \bar{u}}{\partial Z}-km\bar{u}+\frac{\partial D}{\partial Z}m^2+im^3D)u+(\frac{\partial^2 \bar{u}}{\partial Z^2}+i\frac{\partial \bar{u}}{\partial Z}m)w=-ik\frac{g}{\bar{\theta}}\theta \tag{10.6.36}$$

$$\mathrm{i}ku+(\mathrm{i}m+N_1^2)w=0, \tag{10.6.37}$$

$$(ik\bar{u}+m^2D)\theta+\frac{\partial \bar{\theta}}{\partial Z}w=0, \tag{10.6.38}$$

where $N_1^2 = \dfrac{\partial \ln \bar{\rho}}{\partial Z}$. By eliminating u, w, θ from (10.6.36)–(10.6.38), the following relation can be obtained:

$$\begin{aligned}&[i(k\frac{\partial \bar{u}}{\partial Z} + Dm^3) - (km\bar{u} - \frac{\partial D}{\partial Z}m^2)](ik\bar{u} + Dm^2)(im + N_1^2) \\ &-ik(\frac{\partial^2 \bar{u}}{\partial Z^2} + i\frac{\partial \bar{u}}{\partial Z}m)(ik\bar{u} + Dm^2) = N^2k^2\end{aligned} \tag{10.6.39}$$

Separating the real and imaginary parts in (10.6.39), we obtain

$$\begin{aligned}&(-k^2\bar{u}\frac{\partial \bar{u}}{\partial Z} - 2Dm^3k\bar{u} + D\frac{\partial D}{\partial Z}m^4)N_1^2 \\ &+(-m^6D^2 + k^2m^2\bar{u}^{-2} - \frac{\partial D}{\partial Z}m^3k\bar{u} + k^2\bar{u}\frac{\partial^2 \bar{u}}{\partial Z^2}) = k^2N^2\end{aligned} \tag{10.6.40}$$

$$\begin{aligned}&(k\frac{\partial \bar{u}}{\partial Z}Dm^2 + m^5D^2 - k^2m\bar{u}^{-2} + \frac{\partial D}{\partial Z}m^2k\bar{u})N_1^2 \\ &+(-k\frac{\partial^2 \bar{u}}{\partial Z^2}Dm^2 - 2Dm^4k\bar{u} + D\frac{\partial D}{\partial Z}m^5) = 0\end{aligned} \tag{10.6.41}$$

Multiplying both sides of (10.6.40) by $\dfrac{N_1^2}{m}$ and then adding the result to (10.6.41), we obtain

$$\begin{aligned}&-(2m^2k\bar{u}N_1^4 - k\frac{\partial \bar{u}}{\partial Z}m^2N_1^2 + 2m^4k\bar{u} + k\frac{\partial^2 \bar{u}}{\partial Z^2}m^2)D + D\frac{\partial D}{\partial Z}(m^3N_1^4 + m^5) \\ &= \frac{k^2N^2N_1^2 + k^2\bar{u}\dfrac{\partial \bar{u}}{\partial Z}N_1^4 - k^2\bar{u}\dfrac{\partial^2 \bar{u}}{\partial Z^2}N_1^2}{m}\end{aligned} \tag{10.6.42}$$

In the saturated layer where the gravity-wave breaking occurs, the atmosphere becomes relatively uniform in the vertical direction due to the turbulence mixing. It can, therefore, be considered that the dissipation coefficient, D, changes slowly with height and so (10.6.42) can be abbreviated as

$$\begin{aligned} &-(2m^2k\bar{u}N_1^4 - k\frac{\partial\bar{u}}{\partial Z}m^2N_1^2 + 2m^4k\bar{u} + k\frac{\partial^2\bar{u}}{\partial Z^2}m^2)D \\ &= \frac{k^2N^2N_1^2 + k^2\bar{u}\frac{\partial\bar{u}}{\partial Z}N_1^4 - k^2\bar{u}\frac{\partial^2\bar{u}}{\partial Z^2}N_1^2}{m} \end{aligned} . \qquad (10.6.43)$$

Thus, (10.6.43) can also be written as

$$D = \frac{k(N^2N_1^2 + \bar{u}\frac{\partial\bar{u}}{\partial Z}N_1^4 - \bar{u}\frac{\partial^2\bar{u}}{\partial Z^2}N_1^2)}{m^3(2\bar{u}N_1^4 - \frac{\partial\bar{u}}{\partial Z}N_1^2 + 2m^2\bar{u} + \frac{\partial^2\bar{u}}{\partial Z^2})} . \qquad (10.6.44)$$

Therefore, the dissipation of the zonal mean flow caused by gravity-wave breaking can be expressed as

$$D\frac{\partial^2\bar{u}}{\partial Z^2} = \frac{k(N^2N_1^2 + \bar{u}\frac{\partial\bar{u}}{\partial Z}N_1^4 - \bar{u}\frac{\partial^2\bar{u}}{\partial Z^2}N_1^2)}{m^3(2\bar{u}N_1^4 - \frac{\partial\bar{u}}{\partial Z}N_1^2 + 2m^2\bar{u} + \frac{\partial^2\bar{u}}{\partial Z^2})}\frac{\partial^2\bar{u}}{\partial Z^2} . \qquad (10.6.45)$$

Thus, the dissipation can be completely represented by the physical quantities and wave number at an appropriate scale.

Therefore, in the mid-latitude region, the dragging effect of complete gravity wave on zonal mean flow consists of two parts: (1) the momentum flux of gravity wave and (2) the dissipation effect. The result can be expressed as

$$\frac{\partial \bar{u}}{\partial t} = -\frac{1}{\bar{\rho}}\frac{\partial \tau}{\partial Z} + D\frac{\partial^2 \bar{u}}{\partial Z^2} = -\frac{\mu}{2}\frac{\bar{u}^3}{N}\mathbf{max}[\frac{d\ln F^2}{dZ}, 0]$$
$$-\frac{k(N^2 N_1^2 + \bar{u}\frac{\partial \bar{u}}{\partial Z}N_1^4 - \bar{u}\frac{\partial^2 \bar{u}}{\partial Z^2}N_1^2)}{m^3(2\bar{u}N_1^4 - \frac{\partial \bar{u}}{\partial Z}N_1^2 + 2m^2\bar{u} + \frac{\partial^2 \bar{u}}{\partial Z^2})}\frac{\partial^2 \bar{u}}{\partial Z^2} \quad . \qquad (10.6.46)$$

It should be pointed out that although this parameterization scheme can reasonably describe the drag effect of gravity-wave breaking on zonal mean flow. In fact, in many cases, the thermal dissipation coefficient and the viscous dissipation coefficient are both functions of height. The ratio of these coefficients is represented by the Prandtl number, which ranges from 1 to 50. In the above parameterization scheme, the two coefficients are considered to be equal, which is a weakness. In addition, the upward propagation of gravity wave is generally unsteady, and the parameterization for unsteady gravity waves in the middle atmosphere remains to be investigated.

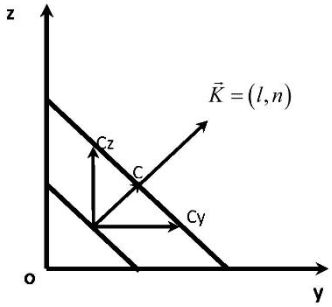

Fig. 10.1. The phase velocity (C) and the phase-velocity components (Cy and Cz)

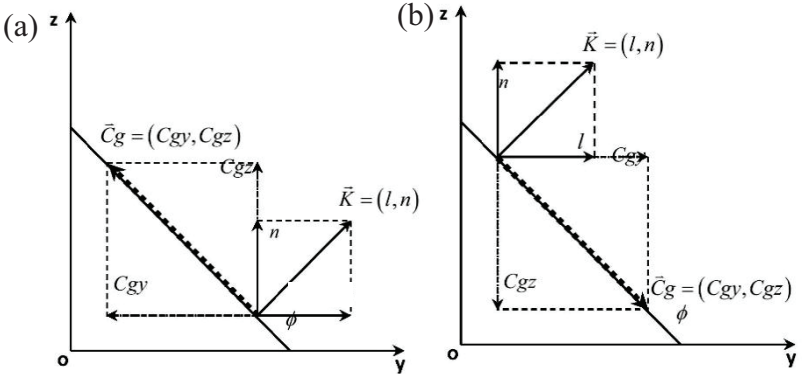

Fig. 10.2. The relationship between the wave-number vector, $\mathbf{K} = (l, n)$, and the group-velocity, $\mathbf{C}g = (Cgy, Cgz)$. (a) $\lambda_y > 0$ and $\lambda_z > 0$; (b) $\lambda_y < 0$ and $\lambda_z < 0$

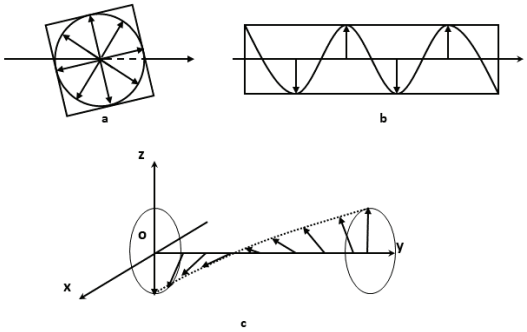

Fig. 10.4.1 Schematic diagram of (a) natural light, (b) linearly polarized light, and (c) elliptically polarized light

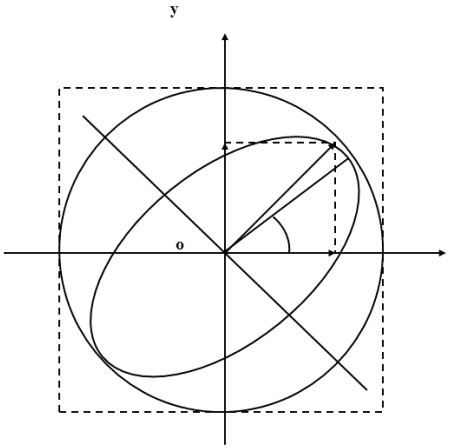

Fig. 10.4.2. Polarization diagram

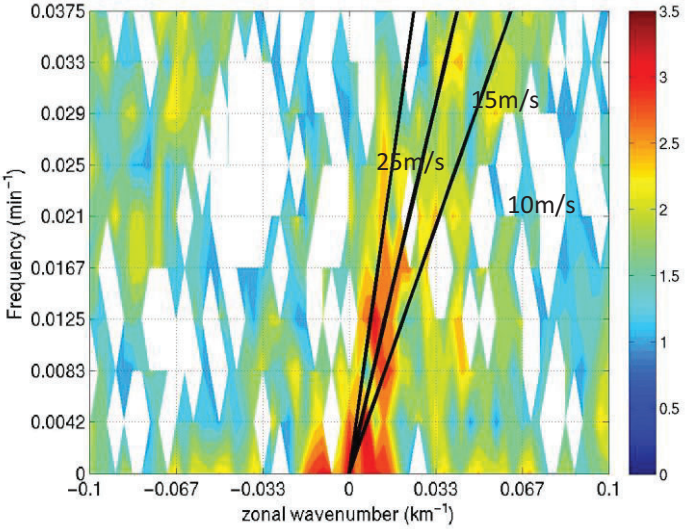

Fig. 10.5.1 The power spectral density of the vertical velocity. The contour represents the phase velocity $c = \omega / k$, which are 10m/s, 15m/s and 25m/s respectively.

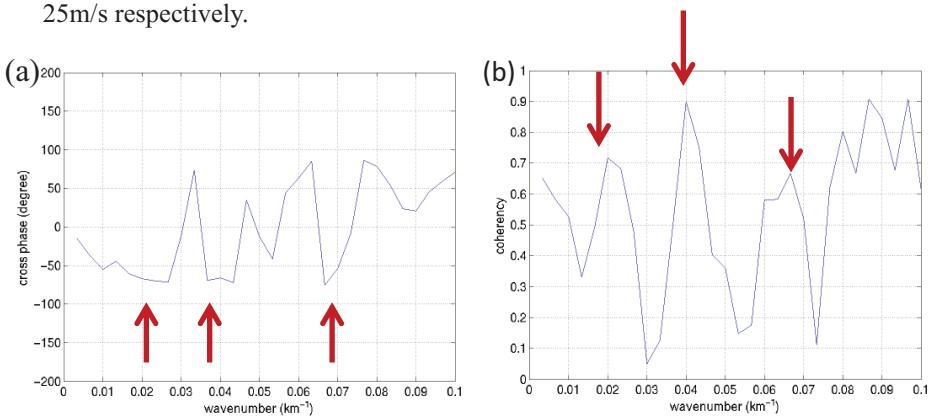

Fig. 10.5.2 (a)Phase spectrum and (b)condensation spectrum of vorticity and divergence.

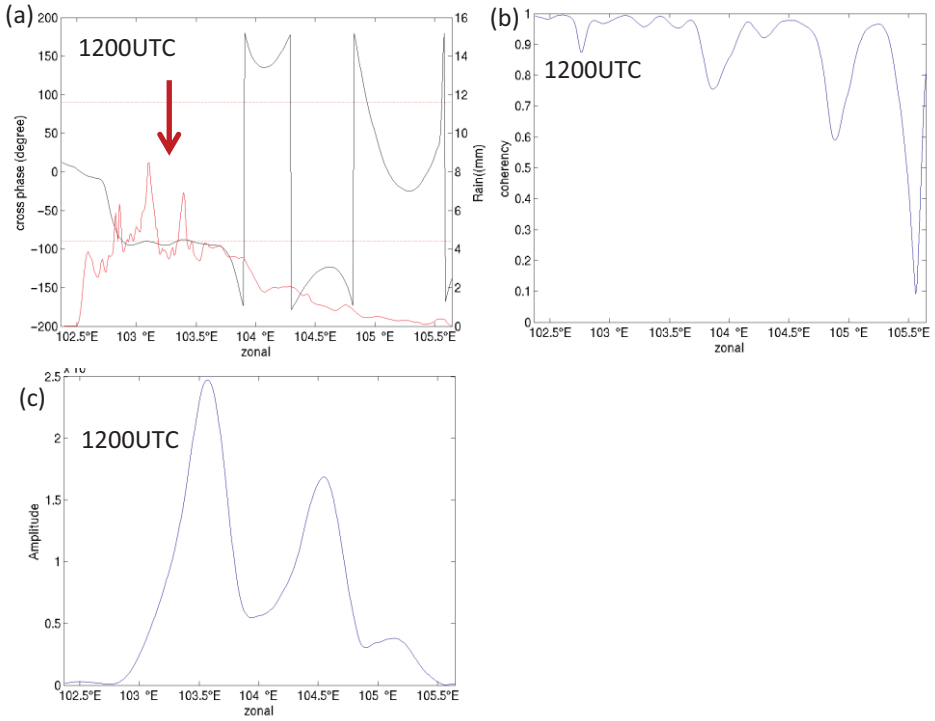

Fig. 10.5.3 Phase difference (a), cohesion spectrum (b) and amplitude spectrum (c) of vorticity and divergence with a frequency of 0.025 and cumulative precipitation (red line in a).

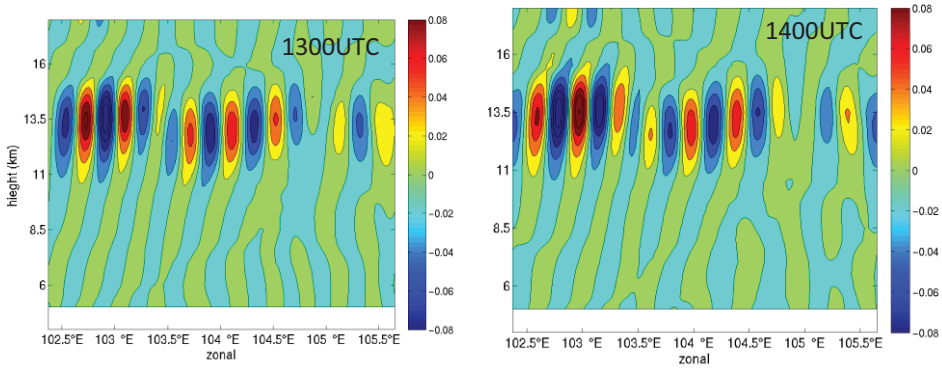

Fig. 10.5.4 The height-zonal profile of vertical velocity of the gravity wave reconstructed by selecting the range of wavelength 40~50km and cycle 80~100 min.

Notes

[1]Lilly, D. K. and P. J. Kennedy (1973) "Observations of a stationary mountain wave and its associated momentum flux and energy dissipation," *Journal of Atmospheric Sciences*, 30(6):1135-1152.

[2]Lindzen, R. S. (1974) "Stability of a helmholtz velocity profile in a continuously stratified, Infinite Boussinesq fluid—applications to clear air turbulence," *Journal of Atmospheric Sciences*, 31(6):1507-1514.

[3]Piani, C., D. Durran, M. J. Alexander, et al. (2000) "A numerical study of three- dimensional gravity waves triggered by deep tropical convection and their role in the dynamics of the QBO," *Journal of Atmospheric Sciences*, 57(22):3689-3702.

[4]Clark, T. L., T. Hauf, and J. P. Kuettner (1986) "Convectively forced internal gravity waves: results from twodimensional numerical experiments," *Quarterly Journal of the Royal Meteorological Society*, 112(474):899-925.

[5]Fovell, R., D. Durran, and J. R. Holton (1992) "Numerical simulations of convectively generated stratospheric gravity waves," *Journal of Atmospheric Sciences*, 49(16):1427-1442.

[6]Vincent, R. A., S. J. Allen, and S. D. Eckermann (1997) Gravity-wave parameters in the lower stratosphere In *Gravity Wave Processes and Their Parameterization in Global Climate Models, Gravity Wave Processes*. Hamilton, K. Ed. Heidelberg, Springer-Verlag.

[7]Vincent, R. A. and M. J. Alexander (2000) "Gravity waves in the tropical lower stratosphere: an observational study of seasonal and interannual variability," *Journal of Geophysical Research*, 105(27):17,971-17,982.

[8]Zink, F. and R. A. Vincent (2001) "Wavelet analysis of stratospheric gravity wave packets over Macquarie Island1. Wave parameters," *Journal of Geophysical Research*, 106(D10):275-210,288.

[9]Hirota, I. and T. Niki (1985) "A statistical study of inertia-gravity waves in the middle atmosphere," *Journal of the Meteorological Society of Japan*,

63(6):1055-1066.

[10]Fetzer, E, J. and J. C. Gille (1994) "Gravity wave variance in LIMS temperatures. Part I. Variability and comparison with background winds," *Journal of Atmospheric Sciences*, 51(17):2461-2483.

[11]Preusse, P., B. Schaeler, J. T. Bacmeister et al. (1999) "Evidence for gravity waves in CRISTA temperatures," *Advances in Space Research*, 24(11):1601-1604.

[12]Tsuda, T., M. Nishida, C. Rocken et al. (2000) "A global morphology of gravity wave activity in the stratosphere revealed by the GPS occultation data (GPS/MET)," *Journal of Geophysical Research*, 105(D6):7257-7273.

[13]McLandress, C., M. J. Alexander, and D. L. Wu (2000) "Microwave Limb Sounder observations of gravity waves in the stratosphere: A climatology and interpretation," *Journal of Geophysical Research*, 105(D9):11,947-11, 967.

[14]Andrews, D. G. (1983). "Finite-amplitude Eliassen-Palm theorem in isentropic coordinates," *Journal of Atmospheric Sciences*, 40(8):1877-1883.

[15]Andrews, D. G. (1987) "On the interpretation of the Eliassen-Palm flux divergence," *Quarterly Journal of the Royal Meteorological Society*, 113(475):323-338.

[16]Brunet, G. and P. H. Haynes (1996) "Low-latitude reflection of Rossby wave trains," *Journal of Atmospheric Sciences*, 53(3):482-496.

[17]Durran, D. R. (1995) "Pseudomomentum diagnostics for two-dimensional stratified compressible flow," *Journal of Atmospheric Sciences*, 52(22):3997-4009.

[18]Gao, S. T. and H. D. Zhang and W. S. Lu (2004) "Ageostrophic generalized e–p flux in baroclinic atmosphere," *Chinese Physics Letters*, 21(3):576-579.

[19]Haynes, P. H. (1988) "Forced, dissipative generalizations of finite-amplitude wave activity conservation relations for zonal and nonzonal basic flows," *Journal of Atmospheric Sciences*,

45(16):2352-2362.

[20]Magnusdottir, G. and P. H. Haynes (1996) "Application of wave-activity diagnostics to baroclinic-wave life cycles," *Journal of Atmospheric Sciences*, 53(16):2317-2353.

[21]McIntyre, M. E. (1980) "An introduction to the generalized Lagrangian-mean description of wave, mean-flow interaction," *Pure and Applied Geophysics*, 118:152-176.

[22]McIntyre, M. E. and T. G. Shepherd (1987) "An exact local conservation theorem for finite amplitude disturbances to non-parallel shear flows, with remarks on Hamiltonian structure and on Arnol'd 's stability theorems," *Journal of Fluid Mechanics*, 181(1):527-565.

[23]MacKay, M. D. (1998) "A pseudoenergy conservation law for the two-dimensional primitive equations," *Journal of Atmospheric Sciences*, 55(13):2261-2269.

[24]Ren, S. (2000) "Finite-amplitude wave-activity invariants and nonlinear stability theorems for shallow water semigeostrophic dynamics," *Journal of Atmospheric Sciences*, 57(20):3388-3397.

[25]Scinocca, J. F. and T. G. Shepherd (1992) "Nonlinear wave-activity conservation laws and Hamiltonian structure for the two-dimensional anelastic equations," *Journal of Atmospheric Sciences*, 49(1):5–28.

[26]Holton, J. R. (1975) *The Dynamic Meteorology of the Stratosphere and Mesosphere*, American Meteorological Society.

[27]Lindzen, R. S. (1981) "Turbulence and stress owing to gravity wave and tidal breakdown," *Journal of Geophysical Research*, 86(C10):9707-9714.

[28]Fritts, D. C. (1984) "Gravity wave saturation in the middle atmosphere:a review of theory and observations," *Reviews of Geophysics*, 22(3):275-308.

[29]Matsuno, T. (1982) "A quasi one-dimensional model of the middle atmospheric circulation interacting with internal gravity waves," *Journal of the Meteorological Society of Japan*, 60(1):215–226.

[30]McFarlane, N. A. (1987) "The effect of orographically exited gravity wave drag on the general circulation of the lower stratosphere and

troposphere," *Journal of Atmospheric Sciences*, 44(14):1776-1800.

[31]Gao, S. T. and K. R. Liu (1998) "A study of the effect of gravitly wave breaking on middle atmospheric circulation," *Acta Meteorologica Sinica*, 12(4):479-485.

[32]Ogura, Y. and N. A. Phillips (1962) "Scale analysis of deep and shallow convection in the atmosphere," *Journal of Atmospheric Sciences*, 19(2):173-179.

[33]Torrence, C. and G. P. Compo (1998) "A practical guide to wavelet analysis," *Bulletin of the American Meteorological Society*, 79(1):61-78.

[34]Grivet-Talocia, S., F. Einaudi, W. L. Clark et al. (1999) "A 4-yr climatology of pressure disturbances using a barometer network in central Illinois," *Monthly Weather Review*, 127(7):1613-1629.

[35]Cho, J. Y. N. (1995) "Inertia-gravity wave parameter estimation from cross-spectral analysis," *Journal of Geophysical Research*, 100(D9):18,727-18,737.

[36]Whitcher, B., P. Guttorp and D. B. Percival (2000) "Wavelet analysis of covariance with application to atmospheric time series," *Journal of Geophysical Research*, 105(D11):14,941-14,962.

[37]Schöch, A., G. Baumgarten, D. C. Fritts et al. (2004) "Gravity waves in the troposphere and stratosphere during the MaCWAVE/MIDAS summer rocket program," *Geophysical Research Letters*, 31(24): L24S04, doi: 10.1029/2004GL019837.

[38] Lu, C., S. E. Koch and N. Wang (2005): "Determination of temporal and spatial characteristics of gravity waves using cross-spectral analysis and wavelet transformation," *Journal of Geophysical Research*, 110(D01), doi: 10.1029/2004JD004906.

[39]Jenkins, G. M. and D. G. Watts (1969) "Spectral Analysis and Its Applications," *Journal of the American Statal Association*, 64(328): 1668-1669.

[40]Lu, C., S. E. Koch and N. Wang (2005) "Stokes parameter analysis of a packet of turbulence-generating gravity waves," *Journal of Geophysical*

Research, 110(D20), doi: 10.1029/2004JD005736.

[41]Wheeler M, and Kiladis G N.1999. Convectively coupled equatorial waves: Analysis of clouds and temperature in the wavenumber-frequency domain. J. Atmos. Sci., 56:374-399.

[42]Zhang F Q, and Koch S E. Davis C A, Kaplan M L.2001. Wavelet analysis and the governing dynamics of a large-amplitude meso-scale gravity-wave event along the east coast of the united states. Quart. J. R. meteor. Soc., 127:2209-2245.

CHAPTER ELEVEN

MESOSCALE BALANCE AND UNBALANCE

Balance in meteorology usually refers to the relationship between wind and mass. This relationship does not vary with time. However, individually, the wind or mass can change with time; thus, the balance is the movable state balance. The balance most commonly encountered in meteorology is the hydrostatic balance. Synoptic-scale weather systems and most mesoscale weather systems must satisfy the hydrostatic balance conditions. However, because of strong ageostrophic, the quasi-geostrophic approximation is not always satisfied in mesoscale weather systems. The following questions are, therefore, important. Does the balance relation apply in mesoscale systems? If so, does the influence of mesoscale divergence winds play a role in the balance? What is unbalance?

In this chapter, based on various large-scale balance equations and balance models, balance and unbalance are defined, and the associated equations are derived. The potential-vorticity retrieval technique and mesoscale motion are discussed in terms of the mesoscale balance model.

11.1 Balance and Unbalance in a Quasi-geostrophic Framework

Large-scale motion in the atmosphere is usually quasi-geostrophic, and so this type of motion usually meets the geostrophic balance and thermal wind balance conditions:

$$\mathbf{v}_g = \mathbf{k}\times\frac{1}{\rho f}\nabla p \quad \text{and} \tag{11.1.1}$$

$$\frac{\partial \mathbf{v}_g}{\partial \ln p} = -\frac{R}{f}\mathbf{k}\times(\nabla T)\,. \tag{11.1.2}$$

Charney (1955, 1962)[1-2] derived the following nonlinear balance equation for frictionless conditions in pressure coordinates:

$$\nabla^2\phi - \nabla\cdot(f\nabla\psi) - 2[\frac{\partial^2\psi}{\partial x^2}\frac{\partial^2\psi}{\partial y^2} - (\frac{\partial^2\psi}{\partial x\partial y})^2] = 0 \tag{11.1.3}$$

Here, $\phi = gz$ is the geopotential height and ψ is the stream function. This equation is valid when gravity waves are weak—i.e., Fr (Froude number) << 1 and Ro (Rossby number) << 1 and when the local change in the horizontal divergence ($\frac{\partial D}{\partial t}$) has a similar order of magnitude to min (Fr2, Ro2) and can be neglected.

For the divergence winds, taking $u = -\frac{\partial\psi}{\partial y} - \frac{\partial\chi}{\partial x}$ and $v = \frac{\partial\psi}{\partial x} - \frac{\partial\chi}{\partial y}$, where χ is the velocity potential, for a small Rossby number ($R_0 = \varepsilon$), Allen et al. (1990)[3] derived the following nonlinear balance equation:

$$\nabla^2\phi - \nabla^2\psi - 2\varepsilon[\frac{\partial^2\psi}{\partial x^2}\frac{\partial^2\psi}{\partial y^2} - (\frac{\partial^2\psi}{\partial x\partial y})^2] = 0 \tag{11.1.4}$$

Including terms with $O(\varepsilon^2)$, the nonlinear balance equation becomes

$$\nabla^2\phi - \nabla^2\psi - 2\varepsilon[\frac{\partial^2\psi}{\partial x^2}\frac{\partial^2\psi}{\partial y^2} - (\frac{\partial^2\psi}{\partial x\partial y})^2] - \varepsilon^2(\frac{\partial\nabla^2\psi}{\partial x}\frac{\partial\chi}{\partial y} - \frac{\partial\nabla^2\psi}{\partial y}\frac{\partial\chi}{\partial x}) = 0 \tag{11.1.5}$$

All of the above balance equations are constructed for $R_0\ (or\ \varepsilon) <<$ 1—i.e., for conditions where the Coriolis force is much more important than the inertial force—and so are only applicable to large-scale analysis.

The balance models are constructed using a set of balance equations. It should be noted that, in addition to the balance equations, the balance models contain a slow-time tendency equation as well as the hydrostatic equation, thermodynamic equation, vorticity equation, and continuity equation. The large-scale quasi-geostrophic approximation, semi-geostrophic approximation, and geostrophic momentum approximation are types of balance models. Thus, the balance models can be used not only to depict the different types of balance motion but also to completely depict the evolution of systems in the movable state balance.

Unbalanced large-scale motion is motion that does not meet geostrophic balance, thermal wind balance, or nonlinear balance conditions. Diagnostic tools for detecting unbalanced motion exist. The direct way to detect unbalanced motion is to start from a derived equation from a balance equation (e.g., the large-scale divergence equation) by, for example, calculating and comparing the balance terms and residuals. The divergence and vertical velocity are computed for reference. In this way, the evolution of unbalanced processes can be diagnosed (James et al. 1988)[4]. In addition, the following tools for detecting large-scale unbalance exist (Zhang et al. 2000)[5].

(1) Lagrangian Rossby number

The Lagrangian Rossby number for a frictionless fluid is given by

(Koch and Dorian 1988)

$$R_0 = \frac{d\,\mathbf{v}/\,dt}{f\left|\mathbf{v}\right|} = \frac{\left|f\,\mathbf{v}_{ag}\times\mathbf{k}\right|}{f\left|\mathbf{v}\right|} = \frac{\left|\mathbf{v}_{ag}\right|}{\left|\mathbf{v}\right|}. \tag{11.1.6}$$

In fact, Ro is an ageostrophic measure for depicting departure from the geostrophic balance. The larger Ro is, the larger the departure.

(2) Psi vector ($\boldsymbol{\psi}$)

The psi vector ($\boldsymbol{\psi}$) is defined as (Keyser et al. 1989)[6]

$$V_{agirr} = -\frac{\partial\boldsymbol{\psi}}{\partial p}, \quad \omega = \nabla_p \cdot \boldsymbol{\psi}, \quad \boldsymbol{\psi} = -\nabla\chi \tag{11.1.7}$$

where χ is the velocity potential, V_{agirr} is the non-rotational component of the ageostrophic wind, and ω is the vertical velocity in pressure coordinates. The divergence of the ageostrophic winds and the associated vertical velocity are calculated using the Psi vector so that the degree of unbalance can be determined.

(3) ω equation

In pressure coordinates, the ω equation for adiabatic, frictionless, quasi-geostrophic flow is written as

$$\sigma\nabla^2\omega + f_0^2\frac{\partial^2\omega}{\partial p^2} = f_0\frac{\partial}{\partial p}[\mathbf{v}_g\cdot\nabla(f_0\nabla^2\varphi + f)] + \nabla^2[\mathbf{v}_g\cdot\nabla(-\frac{\partial\varphi}{\partial p})]$$

. (11.1.8)

The first term on the right-hand side of (11.1.8) denotes the vertical difference in the absolute vorticity advection, and the second term denotes the temperature advection. Generally, if a forcing is larger than zero, upward motion is produced. For instance, upward motion is easily produced ahead of a trough (the first term is larger than zero) or warm advection (the second term is larger than zero). Conversely, subsidence is easily generated ahead of a ridge or cold advection. The intensity of the

unbalance can be determined by analyzing the vertical motion.

(4) Potential-vorticity retrieval

The detection of unbalanced flows from retrievals of the potential vorticity can be used to retrieve field variables under balanced conditions. These retrieved variables can be compared to the results of observations in order to determine the degree of unbalance in a system. The retrieval of potential vorticity is an important technique in meteorology

11.2 Definitions of Balance and Unbalance Equations

Before the balance and unbalance equations are defined, we need to ask whether vertical motion is balanced or unbalanced. Krishnamurti et al. (1968)[7] and Zhang et al. (2000)[5] showed that the quasi-geostrophic ω equation is derived by applying the geostrophic balance and thermal wind balance to the quasi-geostrophic vorticity equation and the thermodynamic equation. Thus, vertical motion is one of basic elements in the recovery of geostrophic balance and, thus, is an element of the balance system. However, Chen (1987)[8] argued that vertical motion contributes to the unbalance because it is caused by the unbalance flow through the adjustment from the unbalance to the balance. Therefore, for weather systems (large-scale, mesoscale, or micro-scale), the vertical motion can be partitioned into balanced and unbalanced parts. According to Krishnamurti et al. (1968)[7], the vertical motion can be considered part of the balance model, whereas, according to Chen (1987)[8], the unbalanced motion consist of two stages: (1) a breakdown stage associated with the advection of horizontal circulations and (2) a rebuilding stage, which is a result of the adjustment between pressure, temperature, and winds by the vertical motion. Chen (1987)[8] also called the two phases as the advection change and the adjustment change. The vertical motions are attributable to the balanced part of the system when they are included as one of the basic elements of the diagnostic balance equation, whereas these movements are

attributable to the unbalanced part of the system when they are included in the unbalance equation and undergo the adjustment from unbalance to balance.

Based on an analysis of the balance and unbalance situations, the balance and unbalance equations are defined as follows (Gao et al. 2006)[9].

First of all, as a result of atmospheric motion, the balance and unbalance consist of movable state balance and unbalance; i.e., these are the balance motions and unbalance motions. Thus, the balance and unbalance equations should be derived from the momentum equations and satisfy the following conditions.

（1） The balance equation: this equation does not contain a time derivative and only includes terms with relatively large magnitudes. In addition, as the balance system is maintained by vortices, rotational winds (denoted by the stream function) are major parts of the balance equation. Thus, the dispersion terms for high-frequency oscillations such as gravity waves are excluded.

（2） Unbalance equation: this equation contains a time derivative and also includes terms with relatively small magnitudes; the primitive equation can be used as the unbalance equation. In addition, due to the fact that the unbalance terms mainly represent the adjustment processes of systems, such processes contain the dispersion energy of high-frequency waves. Therefore, the unbalance equation should include these dispersion effects.

Note that the balance and unbalance equations are not unique. The balanced and unbalanced motions within systems can be depicted by various physical quantities and associated equations.

As the Coriolis force, inertial force, and pressure-gradient force are equally important, these three forces determine the formation and development of systems. Thus, the balance equations (11.1.3)–(11.1.5) are not suitable for mesoscale analysis. Raymond (1992)[10] derived a nonlinear balance equation for a large Rossby number by making the assumption

that the magnitudes of the velocity potential, divergence, and vertical velocity were much less than 1; this led to the derivation of the nonlinear balance equation (for example, 11.1.3), and the pressure-gradient force was denoted by the dimensionless variable π. This equation cannot be applied to mesoscale systems with strong divergence and a high vertical velocity. In a similar way to the nonlinear balance equations, quasi-balance equations, linear balance equations, double linear balance equations, semi-balance equations, near-balance equations, and mixed-balanced equations have been derived (Allen et al., 1990; Barth et al., 1990; Xu, 1994)[3,11-12]. All of these equations are derived by simplifying the divergence equation, or by using $R_0 << 1$, or by assuming that some quantities (e.g., the divergence, vertical velocity, or velocity potential) are small. These equations can be used to study synoptic or shallow mesoscale systems, but they are not suitable for studying mesoscale systems with strong divergence winds. Dewell (1987)[13] argued that mesoscale systems lack the balance that synoptic systems have.

Observational studies and modeling of mesoscale convective systems (MCSs) and mesoscale convective complexes (MCCs) (Houze et al., 1990; Bartels and Maddox, 1991; Rutledge, 1991; Leary and Rappaport, 1987; Zhang and Fritch, 1988; Brandes, 1990; Fritsch et al., 1994)[14-20] have shown that systems such as these contain mesoscale convective vortices (MCVs). This type of vortex has a warm-core structure, similar to that of tropical cyclones. The warm core strengthens the inertial stability; i.e., causes the rotational flows induced by diabatic heating to balance more efficiently. In some studies (Raymond, 1992; Davis and Weisman, 1994; Jiang and Raymond, 1995) [10,21-22], it was shown that these flows are balanced; i.e., that the thermodynamic structures and mesoscale circulations evolve under quasi-balanced conditions.

Studies have also revealed that balanced motions exist in mesoscale

systems and that the associated equations apply. Vortices plays an important role in the mesoscale balance, but the effects of divergence are not neglected. In mesoscale systems, both divergent and rotational winds are important; thus, the balance equation includes both rotational and divergent winds. The mesoscale vertical motion is also important and should not be omitted from the balance equation. The large-scale balance equations mentioned earlier are not adequate for studying mesoscale balance motion. Therefore, in contrast to the divergence and vorticity equations, the mesoscale balance equation should be derived from the helicity equation and include the effects of both the divergent and rotational winds

11.3 Mesoscale Balance Equation

In this section, based on the previous discussion, the balance equation and balance model for depicting mesoscale characteristics are constructed from the helicity equation.

Keeping the terms in the helicity equation that are similar in size to or larger than buoyancy force, the helicity equation can be simplified to (Lu et al., 2003)[23]

$$\frac{\partial H_e}{\partial t} = c_p u \frac{\partial \bar{\theta}}{\partial z}\frac{\partial \pi'}{\partial y} - c_p v \frac{\partial \bar{\theta}}{\partial z}\frac{\partial \pi'}{\partial x} + c_p \bar{\theta}\frac{\partial \pi'}{\partial x}\frac{\partial v}{\partial z} - c_p \bar{\theta}\frac{\partial \pi'}{\partial y}\frac{\partial u}{\partial z} - c_p \bar{\theta}\frac{\partial \pi'}{\partial z}\zeta + b\zeta \quad . \tag{11.3.1}$$

In vector form, (11.3.1) can be written as

$$\frac{\partial H_e}{\partial t} = \mathbf{v}_h \cdot (\nabla_3 \pi' \times \nabla_3 c_p \bar{\theta}) - \nabla_3 \times \mathbf{v}_h \cdot c_p \bar{\theta} \nabla_3 \pi' + b\zeta \, . \tag{11.3.2}$$

Because

$$\frac{\partial H_e}{\partial t} = \frac{\partial}{\partial t}(\mathbf{v}\cdot\nabla\times\mathbf{v}) = \frac{\partial}{\partial t}[u(\frac{\partial v}{\partial z}-\frac{\partial w}{\partial y})+v(\frac{\partial w}{\partial x}-\frac{\partial u}{\partial z})+w(\frac{\partial v}{\partial x}-\frac{\partial u}{\partial y})]$$
$$= \frac{\partial}{\partial t}(u\frac{\partial v}{\partial z}-v\frac{\partial u}{\partial z})+\frac{\partial}{\partial t}[-u\frac{\partial w}{\partial y}+v\frac{\partial w}{\partial x}+w(\frac{\partial v}{\partial x}-\frac{\partial u}{\partial y})] \quad , \tag{11.3.3}$$

scale analysis (Lu et al., 2003) shows that the local change of the helicity (H_e) and the advection of the helicity (H_e) have the same orders of magnitudes and that both are small. The first five terms on the right-hand side of equation (11.1.3) are larger than the sixth term (which accounts for buoyancy effects), and $\frac{\partial H_e}{\partial t}$ and $b\zeta$ are small. Thus, keeping the largest term leads to the balance equation:

$$c_p u\frac{\partial\bar{\theta}}{\partial z}\frac{\partial\pi'}{\partial y}-c_p v\frac{\partial\bar{\theta}}{\partial z}\frac{\partial\pi'}{\partial x}+c_p\bar{\theta}\frac{\partial\pi'}{\partial x}\frac{\partial v}{\partial z}-c_p\bar{\theta}\frac{\partial\pi'}{\partial y}\frac{\partial u}{\partial z}-c_p\bar{\theta}\frac{\partial\pi'}{\partial z}\zeta=0 \tag{11.3.4}$$

which in vector form can be written as

$$\mathbf{v}_h\cdot(\nabla_3\pi'\times\nabla_3 c_p\bar{\theta})-\nabla_3\times\mathbf{v}_h\cdot c_p\bar{\theta}\nabla_3\pi'=0 \tag{11.3.5}$$

where the subscript h denotes the horizontal component and the subscript 3 denotes the derivative in the x-, y-, and z-directions. If the terms associated with the vertical velocity are included, (11.3.5) can be simplified to

$$\mathbf{v}\cdot(\nabla\pi'\times\nabla c_p\bar{\theta})-\nabla\times\mathbf{v}\cdot c_p\bar{\theta}\nabla\pi'=0 \tag{11.3.6}$$

where $\mathbf{v}$ denotes the three-dimensional wind vector and ∇ denotes a three-dimensional operator.

The horizontal winds in (11.3.5) or three-dimensional winds in (11.3.6) account for the effects of the divergent winds. Furthermore,

$\mathbf{v} = \mathbf{v}_h + w\mathbf{k}$ and $\mathbf{v}_h = \mathbf{v}_\psi + \mathbf{v}_\chi$, which means that (11.3.5) and (11.3.6) can, respectively, be written as

$$\mathbf{v}_\chi \cdot (\nabla \pi' \times \nabla c_p \bar{\theta}) + \mathbf{v}_\psi \cdot (\nabla \pi' \times \nabla c_p \bar{\theta}) = \nabla \times \mathbf{v}_\psi \cdot c_p \bar{\theta} \nabla \pi' \text{ and} \tag{11.3.7}$$

$$(\mathbf{v}_\psi + \mathbf{v}_\chi) \cdot (\nabla \pi' \times \nabla c_p \bar{\theta}) + w\mathbf{k} \cdot (\nabla \pi' \times \nabla c_p \bar{\theta}) = \nabla \times \mathbf{v}_\psi \cdot c_p \bar{\theta} \nabla \pi' + \nabla \times w\mathbf{k} \cdot c_p \bar{\theta} \nabla \pi' \tag{11.3.8}$$

The helicity-derived balance equations (equations (11.3.5) and (11.3.6)) include the effects of both divergent and rotational winds, demonstrating the interaction between divergent winds and rotational winds. Equation (11.3.8) shows that the balance equation (equation (11.3.6)) accounts for vertical motion and better reflects the mutual interactions between divergent winds, rotational winds, and the vertical velocity in systems of mesoscale balance. Equations (11.3.7) and (11.3.8) show that rotational winds are dominant—there are two terms associated with rotational winds. Thus, equations (11.3.5) and (11.3.6) will be used as the mesoscale balance equations in this book.

11.4 Mesoscale Unbalance Equation

In the last section, the mesoscale balance equations ((11.3.5) and (11.3.6)) were derived from the helicity equation. Naturally, the unbalance can also be discussed from the point of view of the helicity equation; this concerns the development of the helicity after the balance condition (11.3.5) is broken.

For an unbalanced system we have

$$\mathbf{v}_h \cdot (\nabla_3 \pi' \times \nabla_3 c_p \bar{\theta}) - \nabla_3 \times \mathbf{v}_h \cdot c_p \bar{\theta} \nabla_3 \pi' = O(\varepsilon), \tag{11.4.1}$$

where $O(\varepsilon)$ denotes the residual between the two large terms. The helicity equation can be written as

$$\frac{\partial H_e}{\partial t} = -\nabla\cdot(H_e\,\mathbf{v}) + \frac{1}{2}\nabla\cdot(\boldsymbol{\xi}|\mathbf{v}|^2) - f\,\mathbf{k}\cdot\mathbf{v}(\nabla\cdot\mathbf{v}) + f\,\mathbf{k}\cdot(\mathbf{v}\cdot\nabla)\,\mathbf{v} + \mathbf{v}\cdot(\nabla b\times\mathbf{k}) + b\zeta + w\mathbf{k}\cdot(\nabla\pi'\times\nabla c_p\bar{\theta}) - \nabla\times w\mathbf{k}\cdot c_p\bar{\theta}\nabla\pi' + O(\varepsilon) \tag{11.4.2}$$

The unbalance processes can be divided into two phases: the breakdown phase from the balanced state and recovery phase. The equations for the two different phases can be expressed by using the partitioning analysis method (Chen 1987):

$$\frac{\partial H_{e1}}{\partial t} = -(\mathbf{v}_h\cdot\nabla_h)H_e - H_e\nabla_h\cdot\mathbf{v}_h + \mathbf{v}_h\cdot[(\boldsymbol{\xi}\cdot\nabla_h)\,\mathbf{v}_h] + \mathbf{v}_h\cdot(\nabla_h b\times\mathbf{k}) + b\zeta + O(\varepsilon) \tag{11.4.3}$$

$$\frac{\partial H_{e2}}{\partial t} = -w\frac{\partial H_e}{\partial z} - H_e\frac{\partial w}{\partial z} - f\,\mathbf{k}\cdot\mathbf{v}_h\frac{\partial w}{\partial z} + w[(\boldsymbol{\xi}\cdot\nabla)w] - fw(\nabla\cdot\mathbf{v}) + f(\mathbf{v}\cdot\nabla)w + w\mathbf{k}\cdot(\nabla\pi'\times\nabla c_p\bar{\theta}) - \nabla\times w\mathbf{k}\cdot c_p\bar{\theta}\nabla\pi' \tag{11.4.4}$$

$$H_e = H_{e1} + H_{e2}\,. \tag{11.4.5}$$

Equation (11.4.3) shows the effect of the breakdown of the balanced state by horizontal advection and the effect of horizontal divergence on the local change in helicity. Equation (11.4.4) describes the evolution of the helicity from the unbalanced to the balanced phases caused by the vertical velocity after the balanced state breaks down. It can be used as tools for detecting unbalanced mesoscale flows.

Due to the change in divergence during the unbalance processes, the divergence equation can be directly used as the unbalance equation. Thus, the divergence equation can be considered to be one of the mesoscale unbalance equations.

The horizontal divergence equation can be written as

$$\frac{\partial D}{\partial t} = -\mathbf{v}\cdot\nabla D - D^2 + 2J_h(u,v) - \nabla_h w\cdot\frac{\partial \mathbf{v}_h}{\partial z} + f\zeta - \beta u - c_p\nabla_h\theta\cdot\nabla_h\pi' - c_p\theta\nabla_h{}^2\pi' \tag{11.4.6}$$

Generally, the magnitude of the square of the divergence is smaller than that of the other terms. Thus, equation (11.4.6) can be simplified to

$$\frac{\partial D}{\partial t} = -\mathbf{v}\cdot\nabla D - \nabla_h w\cdot\frac{\partial \mathbf{v}_h}{\partial z} - \nabla_h{}^2 c_p\theta_0\pi' + 2J_h(u,v) + f\zeta - \beta u \tag{11.4.7}$$

The change in the divergence and also the unbalance can be determined by calculating each term on the right-hand side of equation (11.4.7). James et al. (1988)[24] diagnosed unbalance using the divergence equation. Although the formulations are different, the divergence equation diagnosed by James et al (1988)[24]can be deduced from (11.4.6). The continuity equation is used to determine the vertical motions that are occurring during the unbalance processes.

Because the mesoscale motions are quasi-incompressible, we have

$$\nabla\cdot\mathbf{v} = D + \frac{\partial w}{\partial z} \approx 0 \quad \text{and}$$

$$\frac{\partial w}{\partial z} \approx -D \tag{11.4.8}$$

Thus, the change in horizontal divergence can be used to diagnose the change in vertical motion with height.

The atmospheric baroclinicity is included in equation (11.4.7). Taking into account the thermodynamic forcing, the adiabatic thermodynamic equation can be expressed as

$$\frac{\partial\theta}{\partial t} + (\mathbf{v}_h\cdot\nabla_h)\theta + w\frac{\partial\theta}{\partial z} = 0\,. \tag{11.4.9}$$

Taking ∇_h of (11.4.9), we have

$$\frac{\partial \nabla_h \theta}{\partial t} + \nabla_h[(\mathbf{v}_h \cdot \nabla_h)\theta] + \nabla_h(w\frac{\partial \theta}{\partial z}) = 0 \tag{11.4.10}$$

the use of the vector derivative then gives

$$\nabla_h[(\mathbf{v}_h \cdot \nabla_h)\theta] = (\mathbf{v}_h \cdot \nabla_h)\nabla_h\theta + (\nabla_h\theta \cdot \nabla_h)\,\mathbf{v}_h + \mathbf{v}_h \times (\nabla_h \times \nabla_h\theta) + \nabla_h\theta \times (\nabla_h \times \mathbf{v}_h) \tag{11.4.11}$$

We know $\nabla_h \times \nabla_h \theta = 0$, Equation (11.4.11) can be simplified:

$$\nabla_h[(\mathbf{v}_h \cdot \nabla_h)\theta] = (\mathbf{v}_h \cdot \nabla_h)\nabla_h\theta + (\nabla_h\theta \cdot \nabla_h)\,\mathbf{v}_h + \nabla_h\theta \times \boldsymbol{\xi}. \tag{11.4.12}$$

As $$\nabla_h(w\frac{\partial \theta}{\partial z}) = \frac{\partial \theta}{\partial z}\nabla_h w + w\frac{\partial \nabla_h \theta}{\partial z}, \tag{11.4.13}$$

substituting (11.4.12) and (11.4.13) into (11.4.11) yields

$$\frac{\partial \nabla_h \theta}{\partial t} + (\mathbf{v}_h \cdot \nabla_h)\nabla_h\theta + (\nabla_h\theta \cdot \nabla_h)\,\mathbf{v}_h + \nabla_h\theta \times \boldsymbol{\xi} + \frac{\partial \theta}{\partial z}\nabla_h w + w\frac{\partial \nabla_h \theta}{\partial z} = 0 \tag{11.4.14}$$

Using $\mathbf{F} = \frac{\partial \nabla_h \theta}{\partial t} + (\mathbf{v}_h \cdot \nabla_h)\nabla_h\theta + w\frac{\partial \nabla_h \theta}{\partial z} = \frac{d\nabla_h \theta}{dt}$, equation (11.4.14) becomes

$$\mathbf{F} + (\nabla_h\theta \cdot \nabla_h)\,\mathbf{v}_h + \nabla_h\theta \times \boldsymbol{\xi} + \frac{\partial \theta}{\partial z}\nabla_h w = 0. \tag{11.4.15}$$

Equations (11.4.9) and (11.4.15) show that the atmospheric stratification ($\frac{\partial \theta}{\partial z}$) affects the thermodynamic field. When $\frac{\partial \theta}{\partial z} = 0$, the atmospheric stratification is neutral and the thermodynamic field does not have any impact on the vertical velocity. Equation (11.4.8) shows that the thermodynamic field does not affect the horizontal divergence. Thus, the horizontal divergence is controlled by the dynamic forcing. In fact, neutral

stratification ($\frac{\partial \theta}{\partial z} = 0$) cannot exist over a large area but occurs in a shallow layer in the mid-troposphere. Generally, $\frac{\partial \theta}{\partial z} \neq 0$.

When $\frac{\partial \theta}{\partial z} \neq 0$, equation (11.4.15) becomes

$$\nabla_h w = \frac{1}{\frac{\partial \theta}{\partial z}} [\mathbf{F} + (\nabla_h \theta \cdot \nabla_h) \mathbf{v}_h + \nabla_h \theta \times \boldsymbol{\xi}]. \tag{11.4.16}$$

Here $\frac{\partial \theta}{\partial z} \neq 0$.

Substituting (11.4.16) into divergence equation (11.4.7) yields

$$\frac{\partial D}{\partial t} = -\mathbf{v} \cdot \nabla D - \frac{1}{\frac{\partial \theta}{\partial z}} [\mathbf{F} + (\nabla_h \theta \cdot \nabla_h) \mathbf{v}_h + \nabla_h \theta \times \boldsymbol{\xi}] \cdot \frac{\partial \mathbf{v}_h}{\partial z} + \nabla_h^2 c_p \theta_0 \pi' + 2J_h(u, v) + f\zeta - \beta u \tag{11.4.17}$$

This is the equation for the unbalance including atmospheric baroclinic and thermodynamic forcing under non-neutral stratification (the divergence-trend equation).

11.5 The Mesoscale Barotropic Balance Model and the Potential-vorticity Retrieval Technique

In the previous sections, the balance and unbalance equations were discussed. In this section, we will look at a technique used to retrieve the potential vorticity.

Given the potential vorticity on an isentropic surface together with the boundary conditions, the retrieval of the potential vorticity allows other fields such as the wind, temperature, and pressure, as well as the height on the isentropic surface, to be calculated. All of this is based on the balance

condition and does not account for gravity waves and inertial gravity waves. This is because the potential vorticity on an isentropic surface contains all of the dynamic information except that of gravity waves. Thus, potential-vorticity retrieval is intimately associated with the balance model.

First, we will discuss the large-scale barotropic balance model and potential-vorticity retrieval technique. For large-scale motion, the barotropic balance model on the f-plane is constructed using the following equations:

$$\frac{dQ_h}{dt} = 0\,, \tag{11.5.1}$$

$$\nabla^2\varphi' - f\zeta = -\nabla\cdot(\mathbf{v}\cdot\nabla\mathbf{v})\,, \tag{11.5.2}$$

$$Q = \frac{\zeta + f}{h} = g\frac{\zeta + f}{\bar{\varphi} + \varphi'}\,, \tag{11.5.3}$$

$$\mathbf{v} = \mathbf{k}\times\nabla\psi\,, \text{ and} \tag{11.5.4}$$

$$\psi = (\nabla^2)^{-1}\zeta\,. \tag{11.5.5}$$

Here $\mathbf{v}$ is the horizontal wind vector (called the horizontal wind in this section), in which divergent winds are neglected in the first-order approximation. ψ is the stream function; $\varphi = gh$ is the potential height; and $\bar{\varphi}$ is the reference constant potential height of φ ($\bar{\varphi} = g\bar{h}$, where $\bar{h}$ is the atmospheric isentropic depth: $\bar{h} \approx 8km$). φ' is the deviation of φ from $\bar{\varphi}$; ζ is the vertical component of the relative vorticity; and Q is the barotropic potential vorticity. (11.5.1) describes the

conservation of the potential vorticity; (11.5.2) is a divergence equation derived from barotropic shallow-water equations and is a nonlinear balance equation in which the local change in divergence is neglected. (11.5.3) defines the barotropic shallow-water potential vorticity. ∇ is the two-dimensional form of ∇_h.

The conservation of the barotropic potential vorticity ($\frac{dQ_h}{dt} = 0$) leads to $\frac{\partial Q_h}{\partial t} = -\mathbf{v}\cdot\nabla Q_h$, which can be written as $\frac{Q_{hn+1} - Q_{hn}}{\Delta t} = -\mathbf{v}_n \cdot \nabla Q_{hn}$ in differential form. If $\mathbf{v}_n$ and Q_{hn} at step n are known, Q_{hn+1} can be calculated at step n+1. The following equations are then constructed:

$$\nabla^2 \phi'_{n+1} - f\zeta_{n+1} = -\nabla\cdot(\mathbf{v}_{n+1}\cdot\nabla\mathbf{v}_{n+1}), \tag{11.5.6}$$

$$\mathbf{v}_{n+1} = \mathbf{k}\times\nabla\psi_{n+1}, \tag{11.5.7}$$

$$\psi_{n+1} = (\nabla^2)^{-1}\zeta_{n+1}, \text{ and} \tag{11.5.8}$$

$$Q_{hn+1} = g\frac{\zeta_{n+1} + f}{\bar{\phi} + \phi'_{n+1}}. \tag{11.5.9}$$

Here, Q_{hn+1} is known. (11.5.6)–(11.5.9) are used to obtain φ'_{n+1}, $\mathbf{v}_{n+1}$, ψ_{n+1}, and ζ_{n+1} at step n+1 using an iterative method.

The potential-vorticity retrieval technique mentioned above uses the wind (as denoted by the stream function) in the balance model, which is acceptable for large-scale motion. However, modifications are needed for

application to mesocale motion.

McIntyre et al. (2000)[25] neglected the local change in divergence in the divergence equation:

$$\nabla^2\varphi' - f\zeta = -\nabla\cdot(\mathbf{v}\cdot\nabla\mathbf{v})\,. \tag{11.5.10}$$

Here the wind field is defined as

$$\mathbf{v} = curl^{-1}\zeta + div^{-1}D\,. \tag{11.5.11}$$

In addition to the variables that appear in (11.5.10) and (11.5.11), some new variables are introduced. The barotropic shallow-water equations (equations (2.1.1)–(2.1.3)) are used to obtain the vorticity, divergence, and continuity equations:

$$\frac{\partial\zeta}{\partial t} + fD = -\mathbf{v}\cdot\nabla\zeta - \zeta D\,, \tag{11.5.12}$$

$$\frac{\partial D}{\partial t} + \nabla^2\varphi' - f\zeta = -\nabla\cdot(\mathbf{v}\cdot\nabla\mathbf{v})\,, \text{ and} \tag{11.5.13}$$

$$\frac{\partial\varphi'}{\partial t} + \bar{\varphi}D = -\mathbf{v}\cdot\nabla\varphi - \varphi' D\,. \tag{11.5.14}$$

Taking the derivative of (11.5.13) with respect to time gives

$$\frac{\partial^2 D}{\partial t^2} - f\frac{\partial\zeta}{\partial t} + \nabla^2\frac{\partial\varphi'}{\partial t} = -\frac{\partial}{\partial t}[\nabla\cdot(\mathbf{v}\cdot\nabla\mathbf{v})]\,, \tag{11.5.15}$$

and substituting (11.5.12) and (11.5.14) into (11.5.15) then gives

$$\frac{\partial^2 D}{\partial t^2} - f[-\nabla\cdot(\mathbf{v}\zeta) - \beta v - fD] + \nabla^2[-\nabla\cdot(\mathbf{v}\varphi') - \bar{\varphi}D] = -\frac{\partial}{\partial t}[\nabla\cdot(\mathbf{v}\cdot\nabla\mathbf{v})]$$

. (11.5.16)

(11.5.16) can also be written as

$$\frac{\partial^2 D}{\partial t^2} + (f^2 - \overline{\varphi}\nabla^2)D = -f[\nabla\cdot(\mathbf{v}\zeta)] + \nabla^2[\nabla\cdot(\mathbf{v}\varphi')] - \frac{\partial}{\partial t}[\nabla\cdot(\mathbf{v}\cdot\nabla\mathbf{v})]$$
$$= -\nabla\cdot[f\zeta\,\mathbf{v} + \frac{\partial}{\partial t}(\mathbf{v}\cdot\nabla\mathbf{v}) - \nabla^2(\phi'\,\mathbf{v})] \tag{11.5.17}$$

Taking $\frac{\partial \mathbf{v}}{\partial t} = \mathbf{v}_t$ and $\frac{\partial \zeta}{\partial t} = \zeta_t$, we assume that $\mathbf{v}_t = curl^{-1}\zeta_t$ (McIntyre et al., 2000), where $curl^{-1}\zeta$ denotes the rotational component of the wind: $curl^{-1}\zeta = \mathbf{k}\times\nabla\psi = \mathbf{v}_\psi$. $div^{-1}D$ denotes the divergent component of the wind: $div^{-1}D = -\nabla\chi = \mathbf{v}_\chi$. Taking $u_t = \frac{\partial u}{\partial t} = \mathbf{v}_t\cdot\mathbf{i} = curl^{-1}\zeta_t\cdot\mathbf{i}$ gives the following equations:

$$\nabla^2\varphi' - f\zeta = -\nabla\cdot(\mathbf{v}\cdot\nabla\mathbf{v}), \tag{11.5.18}$$

$$(f^2 - \overline{\varphi}\nabla^2)D = -\nabla\cdot[f\zeta\,\mathbf{v} + \mathbf{v}_t\cdot\nabla\mathbf{v} + \mathbf{v}\cdot\nabla\mathbf{v}_t - \nabla^2(\varphi'\,\mathbf{v})], \tag{11.5.19}$$

$$\zeta_t + fD = -\nabla\cdot(\mathbf{v}\zeta) - \beta v, \tag{11.5.20}$$

$$\mathbf{v} = curl^{-1}\zeta + div^{-1}D, \tag{11.5.21}$$

$$\mathbf{v}_t = curl^{-1}\zeta_t, \tag{11.5.22}$$

$$Q_h = \frac{\zeta + f}{h} = g\frac{\zeta + f}{\overline{\varphi} + \varphi'}, \text{ and} \tag{11.5.23}$$

$$\frac{dQ_h}{dt} = 0 . \tag{11.5.24}$$

The conservation of the barotropic potential vorticity (Q_h) leads to $\frac{\partial Q_h}{\partial t} = -\mathbf{v}\cdot\nabla Q_h$. If the wind and potential vorticity at step n are known, the potential vorticity at step n+1 can be constructed by integration with respect to time: thus, Q_{hn+1} at step n+1 is calculated from the wind field at step n. Equations (11.5.18)–(11.5.23) are used to obtain φ', $\mathbf{v}$, ζ, D, $\mathbf{v}_t$, and ζ_t using an iterative method. The equation for the trend in the potential-vorticity tendency is integrated with respect to time to obtain the potential-vorticity. Because the wind term partially accounts for the effects of the divergent wind, equations (11.5.18)–(11.5.23), together with the potential-vorticity conservation equation, are used to construct a balance model for the slow fold. Because this model is derived from the large-scale barotropic balance model, McIntyre called the model of the large-scale barotropic balance as the first-order model and also this balance model as the second-order model.

McIntyre et al. also introduced a third-order balance model, which includes the derivatives with respect to time of the divergence equation (11.5.15) and vorticity equation (11.5.12) and where $\mathbf{v}_t = curl^{-1}\zeta_t + div^{-1}D_t$ and $\mathbf{v}_2 = \frac{\partial^2 \mathbf{v}}{\partial t^2} = curl^{-1}\zeta_2$. As for the first- and second-order models, the vorticity equation and potential-vorticity equation are included to construct a closed equation set. The effects of the divergent wind increase as the model order increases, and so the higher-order models are more appropriate for application to mesoscale

studies.

11.6 The Mesoscale Baroclinic Balance Model and the Potential-vorticity Retrieval Technique

The balance equation is derived from the helicity for mesoscale baroclinic systems, and the mesoscale baroclinic balance model is thus obtained. To reduce the number of physical variables, the atmospheric thermodynamic variables are not partitioned into reference variables and perturbation variables, and the helicity equation is directly derived.

The momentum equation for a baroclinic atmosphere is written as

$$\frac{\partial \mathbf{v}}{\partial t} + (\mathbf{v}\cdot\nabla)\,\mathbf{v} = -c_p\theta\nabla\pi - f\,\mathbf{k}\times\mathbf{v} - \nabla\varphi \tag{11.6.1}$$

and the associated vorticity equation as

$$\frac{\partial \boldsymbol{\xi}}{\partial t} + (\mathbf{v}\cdot\nabla)\boldsymbol{\xi} + \boldsymbol{\xi}(\nabla\cdot\mathbf{v}) - (\boldsymbol{\xi}\cdot\nabla)\,\mathbf{v} = \nabla\times\mathbf{T}\,, \tag{11.6.2}$$

where $\boldsymbol{\xi} = \nabla\times\mathbf{v} = (\xi_1, \xi_2, \zeta)$ and $\mathbf{T} = -c_p\bar{\theta}\nabla\pi' - f\,\mathbf{k}\times\mathbf{v} - \nabla\varphi$.

Taking the dot product of equation (11.6.1) with $\boldsymbol{\xi}$ and the dot product of equation (11.6.2) with $\mathbf{v}$ gives

$$\boldsymbol{\xi}\cdot\frac{\partial \mathbf{v}}{\partial t} + \boldsymbol{\xi}\cdot[(\mathbf{v}\cdot\nabla)\,\mathbf{v}] = \boldsymbol{\xi}\cdot\mathbf{T} \quad \text{and} \tag{11.6.3}$$

$$\mathbf{v}\cdot\frac{\partial \boldsymbol{\xi}}{\partial t} + \mathbf{v}\cdot[(\mathbf{v}\nabla)\boldsymbol{\xi} + \boldsymbol{\xi}(\nabla\cdot\mathbf{v}) - (\boldsymbol{\xi}\cdot\nabla)\,\mathbf{v}] = \mathbf{v}\cdot(\nabla\times\mathbf{T}) \tag{11.6.4}$$

$H_e = \boldsymbol{\xi}\cdot\mathbf{v}$, and so (11.6.3) plus (11.6.4) gives

$$\frac{\partial H_e}{\partial t} + (\mathbf{v}\cdot\nabla)H_e + H_e(\nabla\cdot\mathbf{v}) - \mathbf{v}\cdot[(\boldsymbol{\xi}\cdot\nabla)\,\mathbf{v}] = \mathbf{v}\cdot(\nabla\times\mathbf{T}) + \boldsymbol{\omega}\cdot\mathbf{T} \tag{11.6.5}$$

i.e.,

$$\frac{\partial H_e}{\partial t} + \nabla \cdot (\mathbf{v} H_e) - \frac{1}{2} \nabla \cdot (\boldsymbol{\xi} |\mathbf{v}|^2) = \mathbf{v} \cdot (\nabla \times \mathbf{T}) + \boldsymbol{\xi} \cdot \mathbf{T} \,. \quad (11.6.6)$$

The right-hand side of (11.6.6) can be expanded as

$$\begin{aligned} \boldsymbol{\xi} \cdot \mathbf{T} &= \boldsymbol{\xi} \cdot (-c_p \theta \nabla \pi - f \, \mathbf{k} \times \mathbf{v} - \nabla \varphi) \\ &= -\boldsymbol{\xi} \cdot c_p \theta \nabla \pi - f \, \mathbf{k} \cdot [\frac{1}{2} \nabla (\mathbf{v} \cdot \mathbf{v}) - (\mathbf{v} \cdot \nabla) \mathbf{v}] - \boldsymbol{\xi} \cdot \nabla \varphi \end{aligned}$$

$$\begin{aligned} \mathbf{v} \cdot (\nabla \times \mathbf{T}) &= \mathbf{v} \cdot [\nabla \times (-c_p \theta \nabla \pi - f \, \mathbf{k} \times \mathbf{v} - \nabla \varphi)] \\ &= \mathbf{v} \cdot (\nabla \pi \times \nabla c_p \theta) - \mathbf{v} \cdot [f \, \mathbf{k} (\nabla \cdot \mathbf{v}) - (f \, \mathbf{k} \cdot \nabla) \mathbf{v}] \end{aligned}$$

Taking the f-plane approximation, the helicity equation can be written as

$$\begin{aligned} \frac{\partial H_e}{\partial t} &= -\nabla \cdot (H_e \mathbf{v}) + \frac{1}{2} \nabla \cdot (\boldsymbol{\xi} |\mathbf{v}|^2) + \mathbf{v} \cdot (\nabla \pi \times \nabla C_P \theta) \\ &\quad (1) \qquad (2) \qquad (3) \\ &\quad - \boldsymbol{\xi} \cdot c_p \theta \nabla \pi - \boldsymbol{\xi} \cdot \nabla \varphi - f [\mathbf{k} \cdot \mathbf{v} (\nabla \cdot \mathbf{v}) - \mathbf{k} \cdot (\mathbf{v} \cdot \nabla) \mathbf{v}] \\ &\quad (4) \qquad (5) \qquad (6) \end{aligned} \quad .(11.6.7)$$

Unlike the helicity equation in Chapter 4, this equation excludes the perturbation potential temperature term. By applying scale analysis to equation (11.6.7) and keeping the terms that are similar to or larger than the buoyancy term in the helicity equation, the simplified helicity equation is obtained:

$$\frac{\partial H_e}{\partial t} = \mathbf{v} \cdot (\nabla \pi \times \nabla c_p \theta) - \nabla \times \mathbf{v} \cdot c_p \theta \nabla \pi - \boldsymbol{\xi} \cdot \nabla \varphi \,. \quad (11.6.8)$$

This analysis shows that $\frac{\partial H_e}{\partial t}$ and $\boldsymbol{\xi} \cdot \nabla \varphi$ are smaller than the buoyancy term. Keeping the largest term, the balance equation can be written as

$$\mathbf{v}\cdot(\nabla\pi\times\nabla c_p\theta)-\nabla\times\mathbf{v}\cdot c_p\theta\nabla\pi=0. \tag{11.6.9}$$

Based on expressions of the potential vorticity, potential temperature, absolute vorticity, potential vorticity, and π, the mesoscale baroclinic balance equations can be expressed as

$$\mathbf{v}\cdot(\nabla\pi\times\nabla c_p\theta)-\nabla\times\mathbf{v}\cdot c_p\theta\nabla\pi=0, \tag{11.6.10}$$

$$\pi=(\frac{R}{p_o}\rho\theta)^{\frac{R}{c_v}}, \tag{11.6.11}$$

$$\xi_a=\nabla\times\mathbf{v}+f\,\mathbf{k}, \tag{11.6.12}$$

$$Q_\theta=\frac{\xi_a\cdot\nabla\theta}{\rho}, \tag{11.6.13}$$

$$\frac{dQ_\theta}{dt}=0, \tag{11.6.14}$$

$$\frac{d\theta}{dt}=0. \tag{11.6.15}$$

There are six equations for the six unknown variables $\mathbf{v}$, π, θ, Q_θ, ξ, ρ; however, $\mathbf{v}$ is a vector that has three components, and this means that the set of equations is unclosed: additional equations are needed to form a closed set. Given the importance of divergence in mesoscale systems, the divergence equation is introduced:

$$\frac{\partial D}{\partial t}+\nabla_h\cdot(\mathbf{v}_h\cdot\nabla_h\mathbf{v}_h)+\nabla\cdot(w\frac{\partial\mathbf{v}}{\partial z})-f\zeta+c_p\nabla_h\theta\cdot\nabla_h\pi+c_p\theta\nabla_h{}^2\pi=0. \tag{11.6.16}$$

In addition, during the formation and development of mesoscale systems, the local change in divergence with time may be small although

the divergence itself is large. Thus, $\frac{\partial D}{\partial t}$ can be neglected and the divergence equation simplified to

$$\nabla_h \cdot (\mathbf{v}_h \cdot \nabla_h \mathbf{v}_h) + \nabla \cdot (w \frac{\partial \mathbf{v}}{\partial z}) - f\zeta + c_p \nabla_h \theta \cdot \nabla_h \pi + c_p \theta \nabla_h^2 \pi = 0. \tag{11.6.17}$$

It is assumed that the atmosphere is incompressible under the balance conditions; therefore, we have

$$\nabla_h \cdot \mathbf{v}_h + \frac{\partial w}{\partial z} = 0, \tag{11.6.18}$$

and the vertical vorticity can be written as

$$\zeta = \frac{\partial v}{\partial x} - \frac{\partial u}{\partial y} = \nabla_h \times \mathbf{v}_h. \tag{11.6.19}$$

Equations (11.6.10)–(11.6.19) form a closed set of equations. Note that $\mathbf{v}$ here comprises the three-dimensional divergent winds and rotational winds.

The conservation of the potential vorticity ($\frac{dQ_\theta}{dt} = 0$) yields $\frac{\partial Q_\theta}{\partial t} = -\mathbf{v} \cdot \nabla Q_\theta$, which has the differential form $\frac{Q_{\theta n+1} - Q_{\theta n}}{\Delta t} = -\mathbf{v}_n \cdot \nabla Q_{\theta n}$. If $\mathbf{v}_n$ and the potential vorticity, $Q_{\theta n}$, at step n are known, $Q_{\theta n+1}$ at step n+1 can be calculated. Similarly, the conservation of the potential temperature ($\frac{d\theta}{dt} = 0$) yields $\frac{\partial \theta}{\partial t} = -\mathbf{v} \cdot \nabla \theta$, which has the differential form

$\frac{\theta_{n+1}-\theta_n}{\Delta t} = -\mathbf{v}_n \cdot \nabla\theta_n$. If $\mathbf{v}_n$ and the potential temperature, θ_n, at step n are known, θ_{n+1} at step n+1 can be calculated. Thus, the equations for the retrieval of the potential vorticity can be written as:

$$\mathbf{v}_{n+1} \cdot (\nabla\pi_{n+1} \times \nabla c_p\theta_{n+1}) - \nabla \times \mathbf{v}_{n+1} \cdot c_p\theta_{n+1}\nabla\pi_{n+1} = 0, \quad (11.6.20)$$

$$\pi_{n+1} = (\frac{R}{p_o}\rho_{n+1}\theta_{n+1})^{R/C_v}, \quad (11.6.21)$$

$$\xi_{a_{n+1}} = \nabla \times \mathbf{v}_{n+1} + f\,\mathbf{k}, \quad (11.6.22)$$

$$Q_{\theta n+1} = \frac{\xi_{a_{n+1}} \cdot \nabla\theta_{n+1}}{\rho_{n+1}}. \quad (11.6.23)$$

$$\nabla_h \cdot (\mathbf{v}_{hn+1} \cdot \nabla_h \mathbf{v}_{hn+1}) + \nabla \cdot (w_{n+1}\frac{\partial \mathbf{v}_{n+1}}{\partial z}) - f\nabla_h \times \mathbf{v}_{hn+1} + c_p\nabla_h\theta_{n+1} \cdot \nabla_h\pi_{n+1} + c_p\theta_{n+1}\nabla_h{}^2\pi_{n+1} = 0 \quad (11.6.24)$$

$$\nabla_h \cdot \mathbf{v}_h + \frac{\partial w}{\partial z} = 0 \quad (11.6.25)$$

Here $Q_{\theta n+1}$ and θ_{n+1} are known, and π_{n+1}, $\mathbf{v}_{\theta n+1}$, $\xi_{a_{n+1}}$, and ρ_{n+1} at step n+1 can be obtained using an iterative method.

The balance model and associated potential-vorticity retrieval technique described above can be used to diagnose unbalanced mesoscale flows. The fields obtained from the retrieval of the potential vorticity correspond to balanced states. A comparison between the calculated fields and observations can be used to diagnose the unbalance in a system.

Notes

[1]Charney, J. G. (1962) "Integration of the primitive and the balance equations," *Proc. International Symposium of Numerical Weather Prediction, Tokyo*, Meteorological Society of Japan:131-152.

[2]Charney, J. G. (1955) "The use of primitive equations of motion in numerical prediction," *Tellus*, 7(1):22-26.

[3]Allen, J. S., J. A. Barth and P. A. Newberger (1990) "On intermediate models for barotropic continental shelf and slope flow fields. Part I: Formulation Comparison Exact Solutions," *Journal of Physical Oceanography*, 20(7):1017-1042.

[4]Koch, S. E. and P. B. Dorian (1988) "A mesoscale gravity wave event observed durntain CCOPE. Part III: Wave environment and probable source mechanisms," *Monthly Weather Review*, 116(12):2570-2592.

[5]Zhang, F., S. E. Koch, C. A. Davis, et al. (2000) "A survey of unbalanced flow diagnostics and their application," *Advances in Atmospheric Sciences*, 17(2):165-183.

[6]Keyser, D., B. D. Schmidt and D. G. Duffy (1989) "A technique for representing three-dimensional vertical circulations in baroclinic disturbances," *Monthly Weather Review*, 117(11):2463–2494.

[7]Krishnamurti, T. N. (1968) "A diagnostic balance model for studies of weather systems of low and high latitudes. Rossby Number less than 1," *Monthly Weather Review*, 96(4):197-207.

[8]Chen, Q. (1987) Dynamics of Synoptic and Sub-Synoptic Systems. Science Press. (in Chinese)

[9]Gao, S. and F. Zhou (2006) "Mesocale balance equation and the diagnostic method of unbalanced flow based on helicity," *Chinese Journal of Atmospheric Sciences*, 30(5):854-862. (in Chinese with English abstract)

[10]Raymond, D. J. (1992) "Nonlinear balance and potential vorticity thinking at large Rossby Number," *Quarterly Journal of the Royal Meteorological Society*, 118(507):987-1015.

[11]Barth, J. A., J. S. Allen and P. A. Newberger (1990) "On intermediate models for

barotropic continental shelf and slope flow fields, Part II: Comparison of Numerical Model Solutions in Doubly Periodic Domains," *Journal of Physical Oceanography*, 27(20):1044-1076.

[12]Xu, Q. (1994) "Semibalance Model-Connection between geostrophic type and balanced type intermediate models," *Journal of Atmospheric Sciences*, 51(7):953-970.

[13]Doswell, C. A. (1987) "The distinction between large-scale and mesoscale contribution to severe convection: A case study example," *Weather & Forecasting*, 2(1):3-16.

[14]Houze, R. A., B. F. Smull and P. Dodge (1990) "Mesoscale organization of springtime storms in Oklahoma," *Monthly Weather Review*, 118(3):613-654.

[15]Bartels, D. L and R. A. Maddox (1991) "Midlevel cyclonic vortices generated by mesoscale convective systems," *Monthly Weather Review*, 119(1):104-118.

[16]Rutledge, S. A. (1991) "Middle latitude and tropical mesoscale convective systems," *Reviews of Geophysics*, 29(S1):88-97.

[17]Leary, C. A. and E. N. Rappaport (1987) "The lifecycle and internal structure of a mesoscale Convective complex," *Monthly Weather Review*, 115(8):1503-1527.

[18]Zhang, D.-L. and J. M. Fritsch (1988) "A numerical investigation of a convectively generated Inertially stable, extratropical warm-core mesovortex over land. Part I," *Monthly Weather Review*, 116(12):2660-2687.

[19]Brandes, E. A. (1990) "Evolution and structure of the 6-7 May 1985 mesoscale convective system and associated vortex," *Monthly Weather Review*, 118(1):109-127.

[20]Fritsch, J. M., J. D. Murphy and J. S. Kain (1994) "Warm-core vortex amplification over land," *Journal of Atmospheric Sciences*, 51(13):1780-1807.

[21]Davis, C. A. and M. L. Weisman (1994) "Balanced dynamics of mesoscale vortices in simulated Convective system," *Journal of Atmospheric Sciences*, 51(14):2005-2030.

[22]Jiang, H. and D. J. Raymond (1995) "Simulation of a mature mesoscale convective system using a nonlinear balance model," *Journal of Atmospheric Sciences*, 52(2):161-175.

[23]Lu, H. and S. Gao (2003): "On the helicity and the helicity equation," *Acta Meteorological Sinica*, 61(6):684-691. (in Chinese with English abstract)

[24]James, T. M. and W. A. Abeling (1988) "A diagnosis of unbalanced flow in upper levels during the AVE-SESAME 1 period," *Monthly Weather Review*, 116(12):2425-2436.

[25]McIntyre, M. E. and W. A. Norton (2000) "Potential vorticity inversion on a hemisphere," *Journal of Atmospheric Sciences*, 57(9):1214–1235.

CHAPTER TWELVE

DYNAMIC FORECASTING METHODS BASED ON SCALAR FIELD THEORY

Vorticity, divergence, and deformation are three different basic aspects of the wind field that can describe the effects of the atmospheric rotation, the convergence and divergence, and the deformation, respectively. Many studies of these basic aspects of the wind field have been conducted. These studies have considered new combined physical quantities such as the scalar field of the potential vorticity, the moist potential vorticity, and the generalized moist potential vorticity, as well as the divergence, and deformation themselves. The earlier chapters of this book introduced the dynamic theory of the scalar field. This chapter will focus on dynamic forecasting methods based on the scalar field theory.

12.1 A Dynamic Forecasting Method for Hot and Humid Weather in Large Urban Areas in Summer

12.1.1 Definition of Hot and Humid Weather

In recent years, there has been an increasing tendency for hot and humid weather to occur in large cities. For example, from 30 July to 4 August 2002, a period of unprecedentedly hot, humid weather affected the city of Beijing and the surrounding areas. This type of weather is commonly called “sauna weather” in China and is characterized by high humidity and a lack of wind. (The relative humidity in such events is commonly more than 70%, whereas the normal value is about 50%). In these conditions, heat cannot be radiated by the human body, and moisture

cannot be lost in the form of vapor or sweat. In fact, as a result of the high temperature, the human body receives heat radiated by the atmosphere, resulting in very uncomfortable conditions. In the summer of 2004, weather conditions such as these occurred in several large cities; e.g., in Beijing (from 18 July to 24 July), Shanghai (on July 22), Nanjing (from 15 July to 17 July), and Guangzhou (from 20 July to 22 August). As a result, attention was again focused on this type of weather event.

Year-to-year changes in the annual mean temperature in Beijing and Tianjin show that periods of above- and below-average temperatures both occurred in the 1960s and 1970s. Since the 1980s, the temperature has tended to increase. The records of annual mean relative humidity indicate that the humidity in Beijing was relatively low from 1981 to 1995 but started to slowly increase from 1996 onwards. Although the humidity during this period was still lower than in the period between 1964 and 1981, it was clearly higher than it was during the 1980s. In Tianjin, after 1990, the humidity was higher than in the 1980s. At the same time, the relative humidity in Tianjin was higher than it was in Beijing (with an annual mean value of more than 60%). Therefore, the probability of high humidity occurring in large cities in China, such as Beijing and Tianjin, has increased since the 1980s (Fig 12.1.1).

It is still not clear what causes this kind of abnormally hot and humid weather, and there are no definite criteria defining its occurrence. Many studies of heatwaves have been carried out outside China. Karl and Knight (1997)[1] diagnosed and analyzed heatwaves in the United States and looked at their effects. In order to produce a standard definition of a heatwave, as well as to take into account the reaction of the human body to the temperature and humidity, the United States National Meteorological Academy amended the thermodynamic index using an index proposed by Steadman that was based on the concept of the apparent temperature (T_a). Later, Driscoll (1985)[2] derived a total of 11 independent thermodynamic indexes; Kalkstein and Valimont (1986)[3] and Hoppe (1999)[4] also produced

new indexes. Because a clear definition of a heatwave is lacking and because there is no meteorological equipment that can measure the complex interactions between the human body and the environment, and given that there is also no standard meteorological variable for measuring a heatwave, Robinson (2001)[5] produced a heatwave index, H_i, which was a measure of the predicted heat stress. It was pointed out that when H_i is higher than a critical value for two consecutive days or when H_i is lower than a critical value for two consecutive nights, a heatwave alert can be issued. Because this index is an approximation to the environmental and temperature conditions that are being experienced, the critical value of a heat index is only a general estimate of the heat stress and cannot be used at a large scale. For instance, for the same critical value of a heat index, the heat stress that is experienced can vary due to personal factors, the environment, an individual's adaptation capability, and other factors. Conversely, in cooler areas, this critical value may never be reached even though so-called heatwaves may still occur there. Therefore, different critical values should be defined for different areas. Based on this idea, Robinson (2001)[5] analyzed the critical values of the hourly heat index for 178 American stations from 1951 to1990.

In China, clear definitions and methods relating to hot, humid weather are still lacking, and, as yet, no relevant results have been published. Lin et al. produced a simple summary of the hot and humid weather events that occurred in Beijing during the summer flood season in 2002. The period of hot, humid weather that affected Beijing from 30 July to 4 August 2002 will be analyzed in more detail below.

12.1.2 Circulation Characteristics of Temperature and Humidity During Hot and Humid Weather in the Beijing Area

From 30 July to 4 August 2002, the Beijing area experienced a period of unprecedentedly hot and humid "sauna" weather. This event differed

from the hot weather that is routinely experience in Beijing in summer, which is mainly caused by a high-pressure ridge over the mainland. In these typical hot-weather situations, strong descending motion is very evident and atmospheric moisture is low. However, the hot weather that occurred in Beijing in 2002 was produced by a subtropical anticyclone. The western Pacific subtropical anticyclone extended westward to around 120°E so that northern China lay on its periphery. This led to the temperature and relative humidity in northern China being higher than normal.

The weather over northern China was controlled by the subtropical anticyclone during this period of hot, humid weather. In Figure 12.1.2, the 588-gpdm line, which represents the boundary of the subtropical anticyclone at 500 hPa, extends westward and dominates the whole of northern China, reaching as far as 95°E on 1 August 2002. At this point, the northwest as well as the north of China was under the influence of the anticyclone. The southerly airflow along the periphery of the anticyclone transported warm, moist air from the Pacific to the north of China: this can be seen clearly from the transport of moisture plotted at 850 hPa (Figure 12.1.3). A distinct moisture flux occurred over northern China east of 110°E, which resulted in Beijing and the surrounding areas being a center of moisture convergence. (From Figure 12.1.3, a zone of moisture convergence can be seen lying at 40°N, between 110°E and 120°E.) The presence of this confluence center over Beijing and its surrounding areas can also be seen from the average vertical velocity distribution (Figure 12.1.4). In Figure 12.1.4, the center of the vertical speed confluence at 850 hPa lies at about 40°N, 117°E; i.e., over the Beijing area. At the same time, downdraft dominated the middle and lower troposphere within the area enclosed by the 588-gpdm line (not shown).

From plots of the vertical velocity (Figure 12.1.4), it can be seen that, during this period of hot and humid weather, the middle and lower troposphere over Beijing was basically controlled by downdraft. From the

analysis of the sounding made at the Beijing station during this period, it can be seen that the humidity in the lower troposphere was high, with the relative humidity being above 90% between 1000 hPa and 850 hPa. The middle atmosphere, however, was drier. There was an inversion layer (see Figure 12.1.5) above the low-level layer of high humidity. The existence of the inversion layer made the lower troposphere more stable. The amount of convective control energy reached 32 J kg^{-1}, but the amount of convective available potential energy reached 2834 J kg^{-1} above the inversion layer. Since the downdraft within the subtropical anticyclone blocked the upward transport of low-level water vapor, the humidity near the ground was high. With the addition of heating from the ground, hot, humid conditions resulted.

12.1.3 Dynamic Identification of Hot, Humid Weather in the Beijing Area

From the expression for the generalized moist potential vorticity (GMPV) that was given in Chapter 3, we have

$$Q_m^* = \alpha_a \boldsymbol{\xi}_a \cdot \nabla \theta^* = \alpha \boldsymbol{\xi}_a \cdot \nabla [\theta \exp(\frac{Lq_s}{c_p T}(\frac{q}{q_s})^k)]$$
$$= \alpha \boldsymbol{\xi}_a \cdot \nabla \theta \cdot \exp(\frac{Lq_s}{c_p T}(\frac{q}{q_s})^k) + \alpha \boldsymbol{\xi}_a \theta \exp(\frac{Lq_s}{c_p T}(\frac{q}{q_s})^k) \cdot \frac{L}{c_p T}(\frac{q}{q_s})^{k-1} \nabla q \tag{12.1.1}$$

Clearly, the generalized moist potential vorticity is related to the atmospheric temperature and relative humidity. The negative anomaly in this potential vorticity is located mainly in the lower atmosphere, where the relative humidity is large and the angles between the absolute vorticity and the potential temperature gradient and humidity gradient are greater than 90°. Hence, hot, humid weather encourages the generation of generalized moist potential vorticity.

The GMPV can be calculated using NCEP/NCAR 1° × 1° data. Figure 12.1.6 shows the distribution of the GMPV and relative humidity at 925 hPa at 00:00 UTC on 31 July 2002. Taking a GMPV of less than or equal to −0.25 as being anomalous, a negative GMPV anomaly can be seen covering three main areas: Beijing, the Heilong River and Jilin Province in between, and the Korean Peninsula. Beijing lay in the center of a large negative GMPV anomaly. Up to 00:00 UTC on 4 August, a negative GMPV anomaly also existed in the central part of Inner Mongolia. There was also a negative anomaly lying across Jiangsu, Hubei, and Henan provinces. However, the large negative GMPV anomaly centered at Beijing (and covering parts of Tianjin as well as Hebei Province) persisted and became stronger. The negative GMPV anomaly was concentrated in the lower troposphere during this period and generated an area where the relative humidity was over 70%. (It was more noticeable where the relative humidity exceeded 80%.)

Figure 12.1.7(a) is the GMPV meridional–vertical section along 116.3°E, and Figure 12.1.7(b) is the zonal–vertical section along 39.9°N in the Beijing area. From both vertical sections, it can be seen that the large negative GMPV anomalies are concentrated in the middle and lower troposphere. This shows that, due to the transport and confluence of moisture in the middle and lower troposphere, there were considerable increases in moisture and relative humidity in the atmosphere in Beijing. (If the relative humidity increases, this produces a humidity gradient with the surrounding relatively dry air.) As a result, a GMPV anomaly was formed. This is consistent with the theoretical analyses given in the previous section. At the same time, it can be seen from Figure 12.1.7 that the negative GMPV values mainly lie under 850 hPa, which is also consistent with the region where the relative humidity reaches 90% being mostly located under 850 hPa (see Figure 12.1.6). This indicates that the GMPV is representative of high humidity. By definition, the GMPV takes into account both the temperature and relative humidity. During the period

being analyzed here, moisture transport and confluence were concentrated in the Beijing area, which led to an increase in the relative humidity in Beijing. In combination with the effect of sinking heat in the subtropical anticyclone, high temperatures and high humidity then occurred in the lower troposphere, and a GMPV anomaly was generated. From Figure 12.1.6, it can be seen that there were also GMPV anomalies in other regions (shaded in the figure) as well as in Beijing and the surrounding areas. In all these other regions, the relative humidity was over 80%, sometimes 90%, and the quantity of water vapor in the atmosphere was large. Based on the GMPV anomalies, we would also expect to find that hot and humid weather had occurred in these areas.

12.1.4. The Forecasting of Hot and Humid Weather

It is not enough only to point out that a GMPV anomaly will be generated when hot and humid weather occurs. If such anomalies can be detected before the occurrence of hot, humid weather, it may be possible to use this to make forecasts of this type of weather. Therefore, we will consider whether trends in the GMPV can be used in forecasting.

From the equation for the trend of the generalized moist potential vorticity, we have

$$\frac{\partial Q_m^*}{\partial t} = -\mathbf{v}\cdot\nabla Q_m^* + Q_m^*(A+B)/Q_*, \tag{12.1.2}$$

Where $A = [\frac{R}{p}(p_0/p)^{-\frac{R}{c_p}}]\cdot(\nabla p\times\nabla\theta)\cdot\nabla\theta^*$ is the baroclinicity term and the covariance of the generalized potential temperature gradient; $B = \xi_a\cdot\nabla Q^*$ is the diabatic heating term, and $Q_* = \xi_a\cdot\nabla\theta^*$.

In hot, humid weather, the wind field is very weak and the effect of the

advection term $-\mathbf{v}\cdot\nabla Q_m^*$ can be neglected. Hence equation (12.1.2) can be simplified to

$$\frac{\partial Q_m^*}{\partial t} = Q_m^*(A+B)/Q_* . \tag{12.1.3}$$

Clearly, the anomaly in the generalized moist potential vorticity is also affected by the A term as well as by the friction and diabatic heating (the B term). From the expression for the A term, $A = \Psi(rh)A' = \Psi(\frac{q}{q_s})\cdot\frac{LR}{c_p p}\cdot\frac{\theta_{ue}}{\theta}\cdot(\nabla p\times\nabla\theta)\cdot\nabla q$, it is clear that the temperature, humidity, and the covariances of their gradients can all cause anomalies in the generalized moist potential vorticity. It can be predicted that hot, humid weather will occur when there is an anomaly in the generalized moist potential vorticity.

Figure 12.1.8 (a) shows that, before 00:00 UTC on 30 July when the period of hot, humid weather began in the Beijing area, a distinct drop in the 6-hour GMPV trend occurred in the Beijing and Tianjin areas. This means that the GMPV anomaly was strengthening at that time, and the possible occurrence of hot, humid weather in the Beijing and Tianjin areas could have been predicted. This negative anomaly in the GMPV trend disappeared at 18:00 on 4 August (Figure 12.8(b)), indicating that the period of hot, humid weather was over. In fact, this weather event in Beijing basically coincided with the GMPV anomaly.

Based on the definition of the GMPV and the equation for the trend in the GMPV, an anomaly in the GMPV includes the effects of the atmospheric dynamic field, the thermodynamic field, and the moisture. In contrast to conventional physical variables such as the temperature and humidity, the GMPV can reflect the interaction between the wind, temperature, and moisture to some extent. The GMPV trend term can be calculated by using

equation (12.1.2). Based on the size of this term, the occurrence and short-term intensity of hot and humid weather in areas such as Beijing can be predicted. Thus, the GMPV is a quantity that can be used in the dynamic identification of hot and humid weather. However, due to the low resolution of the data used in the above example, large value area of GMPV covers in a larger range. From observations of the heat-island effect in Beijing in recent years, it has been found that temperature in the city is 2°C–3°C higher than in the surrounding areas. Thus, the influence of the urban heat island should also be taken into account in the GMPV equation.

12.2 A Dynamic Forecasting Method for Cyclone Motion

In saturated air, the moist potential vorticity (MPV) can be used to trace the surface track of a cyclone (Cao and Zhang, 2005)[6]. However, the real atmosphere is inhomogeneously saturated, and so cyclones can be more efficiently tracked using the GMPV. Based on an observed example, in the following, we will analyze the relationship between the generalized moist potential vorticity anomaly and cyclone motion.

12.2.1 Theory

For an adiabatic, inhomogeneous atmosphere, the equation for the GMPV trend can be written as

$$\frac{dQ_m^*}{dt} = \alpha(\nabla p \times \nabla \alpha) \cdot \nabla \theta^* = A^*(\nabla \theta \times \nabla p) \cdot \nabla q, \tag{12.2.1}$$

where $$A^* = -[\frac{LR^2}{c_p p^2}(\frac{p_0}{p})^{-\frac{R}{c_p}}][k(\frac{q}{q_s})^{k-1}\theta^*]. \tag{12.2.2}$$

In contrast to the vorticity equation,

$$\frac{d\boldsymbol{\xi}_a}{dt} = (\boldsymbol{\xi}_a \cdot \nabla)\mathbf{v} - \boldsymbol{\xi}_a \nabla \cdot \mathbf{v} - \nabla\alpha \times \nabla p, \tag{12.2.3}$$

it can be seen that the baroclinic vector, $\nabla p \times \nabla \alpha$, appears in both equations (12.2.1) and (12.2.3). Hence, the physical mechanism that produces the variation in the absolute vorticity is the same as the one that leads to the formation and dissipation of the GMPV—namely, they are both associated with the baroclinic term. From the right-hand side of equation (12.2.1), it can be seen that the rate of change of the GMPV depends on the configuration of the baroclinic vector, $\nabla p \times \nabla \alpha$, and the specific humidity gradient, ∇q. To be specific, if negative (positive) GMPV is generated, then $(\nabla\theta \times \nabla p) \cdot \nabla q$ will be positive (negative), indicating that the baroclinity increases (decreases) in the direction of the specific humidity gradient. Therefore, in an inhomogeneous saturated atmosphere, the formation and dissipation of GMPV are closely related with the absolute vorticity change, which is a reflection of the movement of a cyclone.

12.2.2 Forecasting of Cyclone Motion

Taking the southwest Pacific cyclone that occurred from 7 April to 9 April 2001 as an example and using the 1.0°×1.0° NCEP data to compute the three-dimensional GMPV fields, from the resulting 700 hPa isobaric chart it is clear that there is some coherence between the surface cyclone centers and the regions of NGMPV (negative general moist potential vorticity). There are two main reasons for using the NGMPV here. The first reason is that the frictional effect plays an important role in the

boundary layers, and so it is not appropriate to use the GMPV or MPV. The other reason is that the amount of water vapor in the upper atmosphere is small, and thus the value of the GMPV is too small to be useful.

Figure 12.2.1 shows the horizontal distribution of the NGMPV on the 700-hPa surface (shaded) superimposed on the horizontal geopotential heights on the 1000-hPa surface for the period from 00:00 UTC on 7 April to 18:00 UTC on 8 April, 2001. The cyclone shown here experienced three major phases. During the first phase from 00:00 UTC to 12:00 UTC on 7 April, the cyclone extended northward and deepened; however, there was no obvious movement of the center (Figure 12.2.1 (a), (b), and (c)). The second phase began at 12:00 UTC on 7 April when the center moved quickly eastward toward southeast China (Fig. 12.2.1 (e)). Meanwhile, heavy rain fell in Fujian province. The last phase, from 06:00 UTC to 18:00 UTC on 8 April was the dissipative stage. The cyclone moved over the Taiwan Straits during the first six hours (Figure 12.2.1 (g)) and then swiftly moved eastward into the sea and dissipated(Figure 12.2.1 (h)). From 06:00 UTC on 7 April to 12:00 UTC on 8 April, 2001, this cyclone traveled about 3000 km from southwest China to the Taiwan Strait.

From 00:00 UTC to 06:00 UTC on 7 April 2001, a north–south area of low NGMPV developed but its center did not move much (Figure 12.2.1 (a) and (b)). Later, this area expanded, and its center moved quickly, reaching southeast China around 12:00–18:00 UTC on 7 April (Figure 12.2.1 (c) and (d)). After the area of low NGMPV had moved close to the Taiwan Strait around 06:00 UTC on 8 April, it then swiftly moved over the sea and dissipated (Figure 12.2.1 (f)). The horizontal distribution of the GMPV over southeast China became positive after 12:00 UTC on 8 April (Figure 12.2.1 (g) and (h)). From 12:00 UTC on 7 April to 12:00 UTC on 8 April, the area of low NGMPV was located to the east of the cyclone center and moved ahead of the cyclone. The two centers became coincident from 12:00 UTC on 8 April onward as the cyclone began to fill

over land. At 06:00 UTC on 8 April, a new vortex appeared downstream of this cyclone. Interestingly, a new region of low NGMPV also appeared along with this vortex.

It should be noted that the regions of low NGMPV were located on the periphery of the cyclone throughout this period, rather than being coincident with the surface center of the cyclone. Another thing to point out is that the NGMPV region expanded and formed several centers of low NGMPV as the surface cyclone developed between 06:00 UTC on 7 April and 00:00 UTC on 8 April (Figure 12.2.1 (b), (c), (d), and e). These centers quickly combined and the whole region contracted again when the cyclone began to dissipate (Fig. 12.2.1 (f) and (g)). Finally, the NGMPV band broke up as the cyclone died out (Figure 12.2.1 (h)).

Computation of the MPV field for comparison with the distribution of GMPV at 700 hPa shows that many differences began to occur between the two quantities once the cyclone began to expand at 18:00 UTC on 7 April. In other words, after the cyclone had reached the mature stage, the regions of low negative MPV values no longer matched up with the movement and development of the cyclone (see Figure 12.2.2 (e), (f), (g), and h). This may be because the influence of the humidity is not appropriately taken into account: the use of the condensation probability function $(q/q_s)^k$ is, therefore, very important.

Taking the location of the minimum pressure as the cyclone center, we can draw tracks of the centers of the low NGMPV regions and tracks of the surface cyclone centers from 06:00 UTC on 7 April to 18:00 UTC on 8 April 2001. These are drawn as dashed lines and solid lines, respectively, in Figure 12.2.3. It can be seen that the track of the low NGMPV is similar to that of the surface cyclone during the development of the cyclone and also that, throughout, the low NGMPV center coincides with where the cyclone center is located six hours later. Clearly, then, the use of the NGMPV is a good method of tracking cyclones. It should be pointed out

that the positions of the low NGMPV centers in Figure 12.2.3 were determined by considering the specific humidity gradient vectors together with the potential temperature gradient vectors.

12.3 Determining the Region Affected by a Rainstorm and the Movement of the Storm Using a Dynamic Forecasting Method

Due to the impermeability of the MPVS (moist potential vorticity substance), the MPVS anomaly caused by intense precipitation cannot cross adjacent moist isentropic surfaces. This may provide the basis for a method of forecasting regions of heavy rainfall. Since the iso-θ_e line can easily be drawn on an isobaric chart based on current data, the iso-θ_e line represents the intersection between the moist isentropic surface and the isobaric surface. Besides, an MPVS anomaly located between two different moist isentropic surfaces must move along the moist isentropic surface pipeline bound by these two moist isentropic surfaces; in other words, on a fixed isobaric surface, the MPVS anomaly has to move between the two iso-$\boldsymbol{\theta_e}$ lines that have been identified. Also, the MPVS anomaly, which is a consequence of the processes producing the heavy rainfall, is a strong signal marking the location of the rainstorm system. Thus, the movement of the MPVS anomaly exactly represents the movement of the system. This provides the scientific basis for using the movement of MPVS anomalies to forecast rainstorms. Meanwhile, from research into MPVS anomalies, it has been found that, in the analysis of synoptic charts, there are weaknesses in the traditional method of emphasizing the tracing of troughs and ridges using contour line analysis and that more emphasis should be put on the alignment and distribution of iso-$\boldsymbol{\theta_e}$ lines, which can be considered to "control" the rainstorm. Therefore, forecasting the region that will be affected by a rainstorm and the direction in which the storm will move can be achieved by focusing on the

distribution of the iso-θ_e lines and the MPVS anomaly.

To make the forecast method specific, we calculated the MPVS at various levels between 1000 hPa and 100hPa using NCEP/NCAR reanalysis data of the Yangtze River basin during the rainy season (resolution 1° × 1°; 22 June to 2 July 1999) and found that the most obvious MPVS anomaly in the rainstorms that affected this region was found between 850 hPa and 500 hPa. The average MPVS distribution corresponded to the distribution of the total precipitation in the Yangtze River basin and neighboring regions for the rainy season as a whole (see Figure 12.3.1). It can be seen that the total precipitation and the MPVS anomaly both have a zonal, southwest–northeast distribution, with the precipitation being concentrated mainly in the south of the Yangtze River basin and the MPVS anomaly stretching from west to east along the Yangtze River, which means that it lies along and to the south of the meiyu front. The MPVS anomaly in the Yangtze River basin stretches from 105°E to 130°E and is centered at 30°N between 110°E and 125°E. These high MPVS values correspond to the location of the precipitation belt shown in the chart (Figure 12.3.1), and the precipitation center (where the precipitation is more than 800 mm) has a location that is essentially the same as the center of the region of high MPVS values.

Figure 12.3.2 (a) and (b) show the distribution of the moist potential vorticity substance at 00:00 UTC on 23 June at 700 hPa together with the precipitation distribution in the Yangtze river valley and the surrounding regions. It can be seen from Figure 12.3.2 (a) that, in the Yangtze river valley (from 110°E to 120°E), there is a band of unusually high values of the moist potential vorticity substance stretching from southwest to northeast; the central value in this band is possibly 0.6×10^{-6} K m^{-1} s^{-1}. This band corresponds to the location of the precipitation zone, which is also oriented southwest to northeast. The center of the area with the highest precipitation and the center of the area with high values of the moist potential vorticity substance also overlap. Figure 12.3.2 (a) also

shows that the iso-θ_e lines on both sides of the moist potential vorticity substance anomaly are aligned southwest to northeast. Based on the principal of the impenetrability of the moist potential vorticity substance, subsequently, the moist potential vorticity substance anomaly will keep this orientation, which means that the storm zone corresponding to this anomaly will also remain aligned in this way.

The corresponding relation between the moist potential vorticity substance in the Yangtze River valley and the precipitation zone over land is clearly shown in Figure 12.3.3 (a) and (b). Figure 12.3.3 (a) shows that, in the Yangtze river valley and the area to the east, there is a zone of moist potential vorticity substance lying from southwest to northeast, centered between 108°E and 120°E at around 30°N as before. The central value of the moist potential vorticity substance exceeds 0.9 x10^{-6} K m^{-1} s^{-1}. Based on the distribution of the moist potential vorticity substance, we can predict that the precipitation zone corresponding to high values of the moist potential vorticity substance will also be aligned from southwest to northeast and that the precipitation center will coincide with the center of the area with high values of moist potential vorticity substance. As shown in Figure 12.3.3 (b), in the Yangtze river valley between 115°E and 120°E, there is no major precipitation center and the highest value of precipitation is about 100 mm. In the southwest between 110°E and 115°E, a large area with rainfall of 50 mm exists. From Figure 12.3.3 (a), it can also be seen that the iso-θ_e line of the area of abnormal moist potential vorticity substance is oriented west-southwest and has a smooth variation on 23 June. The corresponding main anomaly in the moist potential vorticity substance is aligned in a similar way to the iso-θ_e line; however, the northeast corner of this anomalous area (120°E–124°E, 33°N–36°N) is

clearly at an angle to the iso-θ_e line, which has the same orientation here as elsewhere (see Figure 12.3.4 (a)). On 24 June, the precipitation zone still has a southwest–northeast alignment and is clearly at an angle to the iso-θ_e line. However, based on the orientation of the moist potential vorticity substance produced by the rainstorm system and the impermeability of this substance, subsequently the precipitation band may turn and become aligned east to west.

Figure 12.3.4 (a) shows that, at 00:00 UTC on 25 June, an area of anomalous moist potential vorticity substance was located between two iso-θ_e lines. A zone of anomalously high moist potential vorticity substance stretched from the east of the Qinghai–Tibet plateau to the southwest of Japan along the Yangtze River valley This zone was aligned more east to west than on the previous day, but the center is still shown as lying between 108°E and 130°E at 30°N in the precipitation chart from the same time (Figure 12.3.4 (b)). The precipitation band still has a southwest-to-northeast orientation but is closer to lying west to east than previously.

After 26 June (Figure 12.3.5 (a)), the moist potential vorticity substance anomaly and also the iso-θ_e line became oriented east–west; the center of this anomaly lay between 110°N and 125°E at 30°N, as shown in the precipitation chart for the same time (Figure 12.3.5(b)). The precipitation zone also lies east–west and so there is a clear latitudinal distribution of precipitation distribution. The center of the precipitation zone corresponds to the center of the moist potential vorticity substance anomaly.

From 26 June to 30 June, the precipitation band maintained this latitudinal distribution and remained oriented east–west with the center of

the precipitation located over the Yangtze River valley. The band of abnormally high values of moist potential vorticity substance also remained oriented east–west with its center lying between 110°N and 125°E at 30°N, coinciding with the center of the precipitation zone. The moist potential vorticity substance anomaly was also usually parallel to the isentropes and, in fact, was trapped between them, thus verifying the impermeability of the moist potential vorticity substance.

Because of the impermeability of the moist potential vorticity substance, an area of high values of moist potential vorticity caused by precipitation has to remain between two iso-θ_e lines: if the iso-θ_e line has an east–west orientation, then the moist potential vorticity substance which is trapped between the iso-θ_e lines must move in this direction and the rainfall zone must also be aligned east–west band. Longitudinal rainstorms cannot then occur. These facts form the basis of a dynamic method of forecasting rainstorms using the alignment and location of the center of anomalies in the moist potential vorticity substance.

In the above example, the precipitation band was originally aligned northeast–southwest but this alignment became latitudinal from 26 June onwards; the distribution of the moist potential vorticity substance was similar. From this analysis of a rainfall event in the Yangtze River valley and also the analysis of the moist potential vorticity substance, we have found that, during such events, the moist potential vorticity substance produced by the mass force is located between 850 hPa and 500 hPa.

Therefore, the change in the moist potential vorticity substance with time in a system producing heavy rainfall is due to mass forcing as well as thermal forcing. These two types of forcing produce anomalous values of the moist potential vorticity substance. The impermeable moist potential vorticity substance is also the best dynamic tracer for following the

movement of rainstorms. In the isobaric plane, an iso-θ_e line corresponds to the isentropic surface of moist air as the moist potential vorticity substance cannot penetrate the moist isentropic surface. Thus, the moist potential vorticity substance has to remain in the area between two iso-θ_e lines. If the iso-θ_e lines are aligned east–west, then the rainfall area must have the same alignment. Similarly, if the iso-θ_e lines are aligned north–south, the rainfall area will have the same orientation and a longitudinal rainstorm will result. Therefore, a combination of the moist potential vorticity substance and the orientation of the iso-θ_e lines suggests a possible method for forecasting rainstorms based on the importance of the iso-θ_e lines in the isobaric plane. This is a move away from the traditional method of emphasizing the analysis of the iso-height lines and offers a dynamic method for forecasting rainfall.

12.4 Forecasting Heavy Precipitation Using the Mass Divergence Method

Usually, the two-dimensional horizontal divergence field only takes into account the divergence and convergence of the horizontal wind field. However, for a storm system that produces a large amount of precipitation, large changes occur in the mass field, which leads to the mass conservation law being broken. The continuity equation then also contains a source–sink term and becomes

$$\frac{\partial \rho}{\partial t} + \nabla \cdot (\rho \mathbf{v}) = -\nabla \cdot (\rho_r \mathbf{v}_t) = S_r, \tag{12.4.1}$$

where ρ is the density the of moist atmosphere, $S_r = -\nabla \cdot (\rho_r \mathbf{v}_t)$ is the mass sink (or source) term, and ρ_r and $\mathbf{v}_t$ are the density and terminal velocity of the raindrops, respectively. At the same time, this change in mass field produces an anomaly in the moist potential vorticity (Qiu et al., 1993; Gao et al., 2004)[7-8]. Clearly then, in precipitation systems, mass forcing is very important. If we include mass in the divergence, then we can consider not only the convergence and divergence effects of the horizontal wind field but also precipitation-induced mass forcing, thus accounting for the effect of both the momentum and mass fields. This variable is an improvement on the horizontal divergence, which we call the mass divergence: it is defined as $D_M = \nabla \cdot (\rho \mathbf{v})$.

In order to introduce the mass divergence method, we will use the example of a typical meiyu-front rainstorm that occurred in the Yangtze River region in China from 00:00 UTC on 4 July to 12:00 UTC on 5 July 2003. This event was numerically simulated using a WRF model. Reliable model output that had a high spatial and temporal resolution and which could be used to diagnose mass divergence were obtained.

Figure 12.4.1 (a) shows that, at the 700 hPa level, there is a zone of high equivalent potential temperature, θ_e, that clearly indicates the meiyu frontal zone and stretches from northeast to southwest between 27°N and 36°N. Within this zone, especially near the northern edge, a line of strong confluence exists (Figure 12.4.1 (b)); this is also a shear zone. At the 200-hPa level, the precipitation region is dominated by a divergent flow along the northeast edge of the south Asian high (not shown). Therefore, the low-level confluence and the upper-level divergence together constitute a favorable circulation pattern for heavy precipitation along the Meiyu front.

Fig.12.4.2 (a) and (b) show the observed and simulated 36-hour precipitation, respectively, for the period 00:00 UTC, 4 July to 12:00 UTC, 5 July 2003. From the figure, it can be seen that the predicted and observed centers of maximum precipitation in mainland China in MRYR (Meiyu rainstorm Yangtze river) are located at 119.5°E and 32.5°N and 119°E and 32°N, respectively; two other precipitation centers located at 114°E and 30.5°N and 116.5°E and 31.5°N are also simulated well. However, the simulated precipitation amounts are less than the amounts that were actually observed.

In general, the precipitation along the Yangtze River is well reproduced by the model. The model results are therefore credible and can be used for more detailed diagnoses.

The model output data can be used to calculate the mass divergence and its relationship with the six-hour surface precipitation.

In this example of Meiyu frontal rainfall, the zone of negative values of the three-dimensional mass divergence (Dm) at the 6.379-km level and the zone of non-zero values of Dm at the 3.247- and 4.287-km levels (Figure 12.4.2 (a), (b), and (c)) can be used to detect the occurrence and evolution of precipitation (Figure 12.4.3).

In this case, the precipitation began after 00:00 UTC on 4 July 2003, and a rain band formed within the zone of non-zero values of Dm at the 4.287-km level. The rain band and this zone moved in a similar way, from north of 33°N to the region between 33°N to 31.5°N and then to around 30°N (Figure 12.4.3). Two extremes of precipitation occurred: one between 17:00 UTC on 4 July and 00:00 UTC on 5 July and the other between 23:00 UTC on 4 July and 08:00 UTC on 5 July. Two peak values of Dm were located at 32°N at 21:00 UTC on 4 July and at 31.5°N at 23.50 UTC on 4 July (Figure (2.4.4)); these can be used to predict the occurrence of two subsequent precipitation maxima well. The absolute value of Dm increased as the amount of precipitation in the next six hours increased. It can also be seen from Figure 12.4.4 and Figure 12.4.2 (b) that

there is a clear positive correlation between the two. From 00:00 UTC to 06:00 on 5 July, the accumulated six-hour precipitation rate reached its maximum of 30 mm/6 hours (Figure 12.4.5 (a)). The six-hour mean of the absolute value of Dm reached its peak of about 6.8×10^{-5} kg s^{-1} m^{-3} between 18:00 UTC on 4 July and 00:00 UTC on 5 July ((Figure 12.4.5 (b)), which was in advance of the precipitation peak. This analysis shows that value of Dm is a good predictor of the precipitation within the following six-hour period.

Since the maximal six-hour precipitation occurred between 00:00 UTC and 06:00 UTC on 5 July, the meridional–vertical section of Dm along 118°E for 00:00 UTC on 5 July (Figure 12.4.6) should also be analyzed. From Figure 12.4.6, it can be seen that the zone of high absolute values of the mass divergence are close to being vertically aligned above the precipitation region (located at around 31.7°N and 118°E). The mass divergence below 6 km (about 500 hPa) is positive, which means that this is a layer of mass divergence, and the center of the divergence is located at around the 3.5-km level at 31.7°N. Between 6 and 12 km the mass divergence is negative, meaning that this is a layer of mass convergence. The absolute value of the mass divergence at the 3-km (about 700-hPa) level is a maximum (Figure 12.4.6), and the mass divergence is strongest here. Note that the strong mass divergence at the 3-km level results in strong mass convergence on both sides.This is especially clear within the precipitation regions between 20:00 UTC on 4 July and 03:00 UTC on 5 July.

Can the correlation between the zone of non-zero values of Dm in the lower troposphere and the zone of negative values of Dm in the upper troposphere be used to better predict the subsequent six-hour precipitation? To examine this, we can analyze the meridional–vertical sections of the horizontal and vertical components of Dm along 118°E (Figure 12.4.7 (a) and (b)) together with the vertical velocity at 00:00 on 5 July (Figure 12.4.8).

From Figure 12.4.7 (a), it can be seen that the horizontal mass convergence in the lower troposphere is coupled with the horizontal mass divergence in the upper troposphere. However, the vertical component of Dm (Figure 12.4.7 (b)) is exactly out of phase with the horizontal component, which is a result of the distribution of the vertical velocity. Below the 7-km level, the increase in the updraft with height produces vertical mass divergence, whereas the opposite trend produces mass convergence above this level.

The above analysis shows that Dm takes into account the mass field as well as the horizontal convergence and divergence effects of the wind field and the shear in the vertical velocity: that is, it reflects the interaction between the three-dimensional wind vector (the atmospheric dynamic effect) and the mass field. Thus, in theory, Dm is of more importance than the pure horizontal divergence. In the frontal rainfall case analyzed above, although the horizontal divergence is generally negative within the precipitation region, the negative divergence extends well beyond this region. Therefore, it can be seen that in the case of heavy rainfall events, the mass divergence is more useful than the horizontal divergence in the diagnosis of precipitation.

The signs of the condensation rate (R_{cm}) (Figure 12.4.9) and Dm (Fig. 12.4.6) are opposite. Above the 3-km level, strong updraft (Figure 12.4.8) cools the air and leads to the condensation of vapor (shown by the zone of positive values of R_{cm} above the 3-km level in Figure 12.4.9). This then leads to the formation of clouds and, subsequently, rain (in the shaded regions in Figure 12.4.10 (b)). As a result of the condensation of water vapor, the mass convergence in this region is enhanced (corresponding to the zone with negative values of Dm in Figure 12.4.6). At the same time, the downdraft below 3 km warms the air and causes the evaporation of

water vapor (corresponding to the zone of negative values of R_{cm} below the 4-km level in Figure 12.4.9). This causes the amount of cloud and rain in the lower troposphere to be greatly reduced (Fig.12.4.10 (a)), and the height of the cloud nuclei rises from 5 km to 6 km (Figures 12.4.10 (a) and (b)). Due to evaporation, there is plentiful moisture, which results in the mass divergence in the lower troposphere (the region of positive values of Dm in Fig. 12.4.6).

From the above analyses, it can be seen that mass divergence is a useful physical variable for diagnosing precipitation. We therefore need an equation for the mass divergence. This can be derived as

$$\frac{\partial D_M}{\partial t} = \underset{1}{-\mathbf{v}\cdot\nabla D_M} \underset{2}{-\rho\mathbf{v}\cdot\nabla D} \underset{3}{-DD_M} \underset{4}{-[\nabla(\rho u)\cdot\frac{\partial \mathbf{v}}{\partial x}+\nabla(\rho v)\cdot\frac{\partial \mathbf{v}}{\partial y}+\nabla(\rho w)\cdot\frac{\partial \mathbf{v}}{\partial z}]}$$

$$\underset{5}{+f\varsigma_M} \underset{6}{-\beta\rho u} \underset{7}{-g\frac{\partial \rho}{\partial z}} \underset{8}{-(\nabla\alpha\cdot\nabla p+\alpha\nabla^2 p+\alpha\nabla\rho\cdot\nabla p)} \underset{9}{-(DR_{cm}+\mathbf{v}\cdot\nabla R_{cm})} \underset{10}{+(\nabla\cdot\mathbf{F}-\nabla\rho\cdot\mathbf{F})} \quad (12.4.2)$$

From equation (12.4.2), it can be seen that the local change in the mass divergence is associated with the advection of mass divergence (term 1), the advection of three-dimensional divergence (term 2), the interaction between three-dimensional divergence and the mass divergence (term 3), the three-dimensional shear in the wind vector (term 4), the interaction between the Coriolis force and the mass vorticity (term 5), the β-effect (term 6), the change in density (term 7), the pressure force (term 8), mass sinks (or sources) (term 9), and friction (term 10). The main factors affecting the change in the mass divergence are analyzed below using output data from the WRF model that has a high spatial and temporal resolution.

From Figure 12.4.2, it can be seen that the precipitation within the region 114°E–120°E and 30°N–33°N was the highest and was also the

best simulated. Therefore, this region was selected for analysis and the area-mean curves of the terms in equation (12.4.1) (apart from the friction and mass sink term and the sum (sum = term 1 + term 2+ … + term 8)) were plotted for the period 00:00 UTC, 4 July to 12:00 UTC, 5 July 2003.

Calculations shown that term 6 is two to three orders of magnitude smaller than the sum of the terms. Therefore, in Figure 12.4.10, term 6 is plotted as a zero line. The other terms are similar in magnitude to the sum: that is, of the order of 10^{-8}. To clarify the relative contribution of the different terms to the sum, the correlation coefficient between terms 1–8 and the sum were calculated along with the root-mean-square deviations; the values are shown in Table 12.4.1. From the table, it can be seen that term 5, term 6, and term 8 have a negative correlation with the sum, whereas the other terms have a positive correlation. Of all the terms, term 4 has the best correlation with the sum, and the root-mean-square deviation between this term and the sum is minimal. In terms of the correlation, term 4 is followed by term 1, term 2, and term 7. This indicates that the quantities that make the largest contribution to the change in the mass divergence are the shear in the three-dimensional wind vector, the advection of the mass divergence, the advection of the three-dimensional divergence, and the pressure-force.

It can be seen from Table 12.4.1 that term 8 is well correlated with the sum and has a low deviation. This is in agreement with the observation.

The above analysis shows that the mass divergence leads heavy precipitation by about six hours and so the mass-divergence method is very effective for the short-term forecasting of heavy precipitation.

12.5 The Deformation Forecasting Method

The deformation field is very important in many problems, especially with regard to the confluence of flows on the elongation axis, where it can form a narrow band with sharp changes in temperature and humidity. The

deformation field, therefore, plays an important driving role in frontogenesis. In addition, many phenomena, in particular storm rainfall, are related to the deformation field. In the following, some particular cases are analyzed, and the deformation forecasting method is introduced.

The 1 July 2003 Yangtze storm provides an example of rain bands oriented approximately east–west. This rainfall began after 06:00 UTC on 4 July 2003, and the largest amount of six-hour precipitation occurred between 18:00 UTC on 4 July and 00:00 UTC on 5 July, 2003 (Figure 12.5.1), when the rain band was aligned approximately east–west. The front appeared around the time of the onset of the precipitation, and there was always a convergence of the wind in the lower troposphere in the vicinity of the rain area; thus, this front was a typical example of precipitation.

As early as 00:00 UTC on 4 July 2003, before the onset of the precipitation, there was a region of large deformation values aligned northeast–southwest in the troposphere above the area of the later precipitation (Fig. 12.5.2); the deformation values were of the order of 10^{-5}. After 00:00 UTC on 4 July 2003, precipitation began to occur, and the rain band formed within the zone of large total deformation. The value of the total deformation increased along with the amount of later six-hour precipitation, meaning that these were positively correlated with one another. At 00:00 UTC on 5 July when the amount of six-hourly cumulative precipitation was greatest, the deformation field reached its peak, with a magnitude of 10^{-4}. During the period of precipitation, the center of the zone of large values of total deformation lay slightly to the north of the center of the cumulative six-hour precipitation center, and these two quantities had similar trends (Figures 12.5.1 and 12.5.3). The best correlation between the deformation field and the precipitation zone was at 00:00 UTC on 5 July, when the amount of precipitation was the largest.

As an example of a case of rain bands with a nearly north–south

orientation, the storm that affected northern China on 10 October 2003 can be used. In this case, the rainfall began after 00:00 UTC on 10 October, with the largest amount of precipitation falling between 18:00 UTC on 10 October and 00:00 UTC on 11 October (see Figure 12.5.4). The rain band was oriented approximately north–south. Around the time of the onset of the precipitation, fronts and an obvious shear line can be seen in the equivalent potential temperature chart at 900 hPa—i.e. the lower troposphere—in the vicinity of the rain area (see Figure 12.5.5). This case is thus typical of precipitation caused by the interaction between a front and a shear line.

Both the orientation and location of the zone of large total deformation (not shown) coincided with the confluent shear line in the lower troposphere (Figures 12.5.5 and 12.5.6), which was where the precipitation later occurred. The rain band lay a little to the south of the zone of large total deformation but had the same orientation. Similar to the case of July 2003, during the course of the precipitation event, the center of the area with large values of total deformation lay slightly to the north of center of the cumulative six-hour precipitation. The value of the total deformation also increased as the amount of later six-hour precipitation increased. The six-hour cumulative precipitation reached its peak between 00:00 UTC and 06:00 UTC on 11 October 2003. This was also when the deformation field had its best correlation with the rain area; the total deformation also had its maximum value at this time (Figure 12.5.6).

From the above analysis of two different rainfall events with rain bands that had different orientations, we can draw some conclusions. Before and during the precipitation event, both the location and alignment of the bands of large total deformation and the confluent shear line overlapped in the lower troposphere. The rain bands were located slightly to the southwest of these bands and generally had the same alignment as the zone of large deformation values. The value of the total deformation in the lower troposphere began to increase before the precipitation reached its

maximum intensity, with the former leading the latter by six hours or more. The magnitudes of both the low-level divergence and the vorticity were smaller than that of the total deformation in the two cases that were examined, suggesting that the total deformation is an important precursor of heavy precipitation of the type analyzed here.

From chapter 6, we know that, in the equation for the deformation trend, the local change term and the convection term for the deformation field (term 1), the horizontal divergence term (term 2), and the β-effect term (term 3) are related to the horizontal pressure-gradient term (term 4), the vertical velocity term (term 5), and the friction force term (term 6), respectively. By calculating all of the terms that appear in the equation for the deformation field, we can learn which terms have an important impact on the local change in the deformation and thus find out which factors are the most important in terms of the the generation and development of the deformation field. In the following, we will calculate the size of all of the terms in the equation for the trend in the horizontal deformation apart from the local change term and the friction term.

Figures 12.5.7 to 12.5.12 show the latitude–time section for term 1 (Figure 12.5.7), term 2 (Figure 12.5.8), term 3 (Figure 12.5.9), term 4 (Figure 12.5.10), and term 5 (Figure 12.5.11) in the equation for the trend in the deformation field for 00:00 UTC on 3 July to 00:00 UTC on 6 July 2003 at 700 hPa along 119°E. The sum of these terms is shown in Figure 12.5.12.

The results of the calculations show that at 31.5°N–36.0°N the advection term is negative (Figure 12.5.7), whereas the rest of the terms are positive. The β-effect term is an order of magnitude smaller than the other terms. Among the other terms, the bands with large positive values of the horizontal divergence (Figure 12.5.8) and the horizontal pressure gradient (Figure 12.5.10) as well as the terms related to the vertical velocity (Figure 12.5.11) correspond best to the temporal and spatial

distribution of the sum of all the terms in the zone between 31.5°N and 36.0°N; this is especially so at 00:00 UTC on 5 July. Clearly, the horizontal divergence term, the horizontal pressure gradient term, and the terms related to the vertical velocity are important factors.

From the analysis of the rainstorm that affected northern China between 00:00 UTC on 10 October and 12:00 UTC on 11 October 2003, we have found that the horizontal divergence term, the horizontal pressure-gradient term, and the terms related to the vertical velocity are the most important. The specific process related to this analysis will not be introduced in detail here.

From the analysis of the cases above, we can see that the use of the equation for the trend in the deformation can help in predicting the occurrence of rainstorms and the precipitation trend. Taking the six-hour integral of the total deformation trend, it has been seen that the locations of the bands of large values of the total deformation basically coincide with the precipitation regions; also, the increasing or decreasing trend in the total deformation field is positively correlated with the precipitation. Clearly, then, the deformation can be used as a dynamic factor for predicting precipitation, especially in the case of frontal rainfall. Dynamic forecasting methods based on the deformation are based on calculating the future trend in the total deformation.

12.6 Vapor Potential Vorticity and its Application

The so-called vapor potential vortex, which is the physical property obtained by replacing the gradient of the potential temperature by the gradient of the specific humidity in the definition of the potential vorticity, describes the interaction between the dynamic function and the vapor distribution. In the systems of strong convection with strong vertical development, the value of the potential vorticity is very small and so cannot be used to reflect the development of this kind of system. In this

case, the use of the vapor potential vorticity is much more appropriate. In this section we will begin with the theory behind the equation for the trend in the vapor potential vorticity and the conservation of the vapor potential vorticity. A practical example of the application of the vapor potential vorticity will then be given.

12.6.1 Theory

From equation for the absolute vorticity, we have

$$\frac{d\boldsymbol{\xi}_a}{dt} - (\boldsymbol{\xi}_a \cdot \nabla)\mathbf{v} + (\nabla \cdot \mathbf{v})\boldsymbol{\xi}_a = -\nabla\alpha \times \nabla p + \nabla \times \mathbf{F} . \qquad (12.6.1)$$

Substituting the continuity equation, $\nabla \cdot \mathbf{v} = \frac{1}{\alpha}\frac{d\alpha}{dt}$, into the above equation gives

$$\frac{d}{dt}(\alpha\boldsymbol{\xi}_a) - (\alpha\boldsymbol{\xi}_a \cdot \nabla)\mathbf{v} = -\alpha(\nabla\alpha \times \nabla p) + \alpha\nabla \times \mathbf{F} \qquad (12.6.2)$$

The water vapor equation can be written as

$$\frac{\partial q}{\partial t} + \mathbf{v} \cdot \nabla q = S_v \qquad (12.6.3)$$

Taking the gradient of both sides of equation (12.6.3) gives

$$\frac{\partial \nabla q}{\partial t} + \nabla(\mathbf{v} \cdot \nabla q) = \nabla S_v \qquad (12.6.4)$$

Making use of

$$\nabla(\mathbf{A} \cdot \mathbf{B}) = \mathbf{A} \times (\nabla \times \mathbf{B}) + (\mathbf{A} \cdot \nabla)\mathbf{B} + (\mathbf{B} \cdot \nabla)\mathbf{A} + \mathbf{B} \times (\nabla \times \mathbf{A}),$$

Then we have

$$\frac{\partial \nabla q}{\partial t} + (\mathbf{v} \cdot \nabla)\nabla q + (\nabla q \cdot \nabla)\mathbf{v} + \nabla q \times (\nabla \times \mathbf{v}) = \nabla S_v ,$$

that is

$$\frac{d\nabla q}{dt} + (\nabla q \cdot \nabla)\,\mathbf{v} + \nabla q \times (\nabla \times \mathbf{v}) = \nabla S_v \qquad (12.6.5)$$

Taking the dot product of (12.6.5) and $\alpha\boldsymbol{\xi}_a$, the dot product of (12.6.2) and ∇q, and then adding the results, and using this together with the fact that

$$\mathbf{A}\cdot(\mathbf{B}\cdot\nabla)\mathbf{C}=\mathbf{B}\cdot(\mathbf{A}\cdot\nabla)\mathbf{C}+\mathbf{B}\cdot\mathbf{A}\times(\nabla\times\mathbf{C}),$$

we then have

$$\frac{d}{dt}\left(\alpha\boldsymbol{\xi}_a\cdot\nabla q\right)=\alpha\left(-\nabla\alpha\times\nabla p\right)\cdot\nabla q+\alpha\nabla q\cdot\nabla\times\mathbf{F}+\alpha\boldsymbol{\xi}_a\cdot\nabla S_v. \tag{12.6.6}$$

Defining $Q_q=\alpha\boldsymbol{\xi}_a\cdot\nabla q$, the above equation can be simplified to

$$\frac{dQ_q}{dt}=\alpha\left(-\nabla\alpha\times\nabla p\right)\cdot\nabla q+\alpha\nabla q\cdot\nabla\times\mathbf{F}+\alpha\boldsymbol{\xi}_a\cdot\nabla S_v. \tag{12.6.7}$$

Equation (12.6.7) is the equation for the trend in vapor potential vorticity, which is derived from using the vorticity equation, continuity equation, and vapor equation. The right-hand side of equation (12.6.7) means that the development and change in the vapor potential vorticity is affected by the baroclinic term, the effect of friction, and the vapor resource term. The vapor potential vorticity differs from the potential vorticity as it has its source in the water vapor. Also, the vapor potential vorticity is not conserved and is influenced by both the specific humidity gradient and the baroclinic solenoid term. Taking these effects into account, equation (12.6.7) becomes

$$\frac{dQ_q}{dt}=-\alpha(\nabla\alpha\times\nabla p)\cdot\nabla q. \tag{12.6.8}$$

Given $\alpha = \frac{1}{\rho} = \frac{RT}{p} = \theta \frac{R}{p} (\frac{p_0}{p})^{-\frac{R}{c_p}}$, we obtain

$$\frac{dQ_q}{dt} = A^* (\nabla\theta \times \nabla p) \cdot \nabla q, \tag{12.6.9}$$

Where, A^* is a function related to θ and p and which has a value that is always less than zero. Therefore, in a baroclinic atmosphere with no source of water vapor and no friction, if the specific humidity gradient has a component in the direction (or inverse direction) of the baroclinic vector, then the vapor potential vorticity is decreasing (or increasing). In a barotropic atmosphere with no source of water vapor and without friction, the vapor potential vorticity is conserved.

12.6.2 Application

The vapor potential vorticity can be used to analyze Typhoon Pu Gong Ying, which occurred between 23 June and 4 July 2004. The period between 27 June and 1 July is considered here. Figure 12.6.1 shows the path of the vapor potential vorticity along with the path of the typhoon. These paths can be seen to correspond well, which suggests that the vapor potential vorticity can be used to trace the movement of a typhoon. Figure 12.6.2 shows the distribution of the vapor potential vorticity field and the associated flow field in the horizontal plane. It is noticeable that the negative center of the advection of the vapor potential vorticity always coincides with the later center of the vapor potential vorticity. This is because, usually, the term for the vapor potential vorticity advection can be used to predict the development of the vapor potential vorticity, and so, by calculating the advection term, the path of the typhoon can be forecast.

12.7 Applications of the Second Order Moist Potential Vorticity

Whether it is a large-scale system with a spatial scale of several thousand kilometers or a convective system with a scale of only a few kilometers, gradients are typical characteristics of the evolution of the system. For example, a large-scale frontal system with a temperature gradient, shear line with wind gradient and dry line with humidity gradients, etc. These areas with strong gradient are occurance areas of rainstorms. In the past, these gradient boundaries were usually characterized by potential temperature gradients, water vapor gradients etc. But in actual processes, especially in areas where precipitation occurs, these gradients often exist at the same time. The second-order moist potential vorticity is a physical quantity that comprehensively includes atmospheric thermal gradient and dynamic gradient, so it has important applications in the diagnosis and forecast of heavy rain. As we all know, the existence of updraft and downdraft in the rainstorm system is often accompanied by stronger momentum and heat exchange between the upper and lower layers, as well as the exchange of potential vortices. The high-level potential vorticity and the low-level ones are quite different, so that there is a large potential vorticity gradient in the heavy rain system, and the second-order moist potential vorticity including the potential vorticity gradient also has an abnormally large value area in the heavy rainfall area. To illustrate this point, we applied it to the extreme rainstorm that occurred in Beijing on July 21, 2012. It is worth noting that in the diagnosis of the actual precipitation process, since the baroclinic vorticity in the second-order moist potential vorticity is difficult to calculate accurately, it is usually omitted, and the second-order moist potential vorticity is directly written as:

$$Q_{ms} = \alpha \boldsymbol{\xi}_a \cdot \nabla Q_m \tag{12.7.1}$$

That is, the scalar product of the absolute vorticity vector and the generalized moist potential vorticity gradient. As shown in Figure 12.7.1a, the 24-hour precipitation on July 21, 2012 was distributed in a northeast-southwest direction. There were mainly three precipitation centers, located in the Beijing area of North China (about 40°N, 116°E), the southwest of Shanxi (about 34°N, 106°E) and the southeast of Sichuan (30°N, 105°E), the precipitation in Beijing is the strongest. Corresponding to the rain belt, there is a circular convective cloud system in Beijing from the TBB distribution at 1200 UTC on July 21 (Figure 12.7.1b). This cloud system has been maintained in Beijing for a long time and also caused extreme precipitation in Beijing. The main factor. From the large-scale configuration of superimposed and infrared cloud images (Figure 12.7.1c), this precipitation is the result of the combined effects of cold fronts, low-level vortices, low-level jets, and high-level jets moving to the northeast. Figure 12.7.2 shows the distribution of the second-order moist potential vorticity from 0000 UTC on July 21, 2012 to 0000 UTC on July 22, 2012. It is worth noting that the second-order moist potential vorticity here is the vertical integral of its absolute value, that is $\left\langle \left| Q_{ms} \right| \right\rangle = \int_{p=975}^{p=500} \left| Q_{ms} \right| dp$, the purpose is to be able to include all factors related to precipitation in the entire atmosphere. As shown in Figure 12.7.2a, at 0000 UTC on July 21, the heavy rainfall was distributed in a northeast-southwest direction. The two precipitation centers were located at approximately (37°N, 107°E) and (40°N, 111°E) respectively. At 0600 UTC, the length of the rain band was significantly increased, and the two centers moved in opposite directions. With the movement of the precipitation center in the northern part of the rain belt, Beijing and its surrounding areas were gradually affected, and heavy precipitation occurred around 1200 UTC. As shown in Figure 12.7.2c, there is a mass precipitation area in North China. The heavy precipitation in northern Beijing reached 70mm/6h. After that, the precipitation area began to move

to the southeast and began to affect Tianjin and eastern Hebei. During the entire precipitation process, the most significant feature of the second-order moist potential vorticity distribution is that it appears as an abnormally high value area in the precipitation area, and the abnormal value area moves with the movement of precipitation. This feature is also reflected in the longitude-time variation graph of the second-order moist potential vorticity. As shown in Figure 12.7.3, precipitation along 40°N began at 1200 UTC on July 20, 2012, and experienced two precipitation peaks. The distribution of the abnormal value of the second-order moist potential vorticity has similar characteristics to the distribution of precipitation, especially in the process of heavy precipitation in Beijing on July 21 at 1200 UTC, the second-order moist potential vorticity has a strong center near Beijing (about 116.5°E, 10× 10-8 m^3 K s^{-2} kg^{-2}). The above analysis shows that there is a close relationship between the second-order moist potential vorticity and heavy precipitation, and it has great potential in the application of precipitation diagnosis and forecasting.

Term	1	2	3	4	5	6	7	8
Correlation coefficient	0.41	0.32	0.19	0.79	−0.10	−0.02	0.31	−0.41
RMS (10^{-8} kg m^{-3} s^{-2})	6.63	6.86	7.15	4.75	8.98	9.53	7.20	9.14

Table 12.4.1. The correlation coefficient and the root-mean-square deviation between terms 1–8 and the sum of the terms in equation (12.4.1)

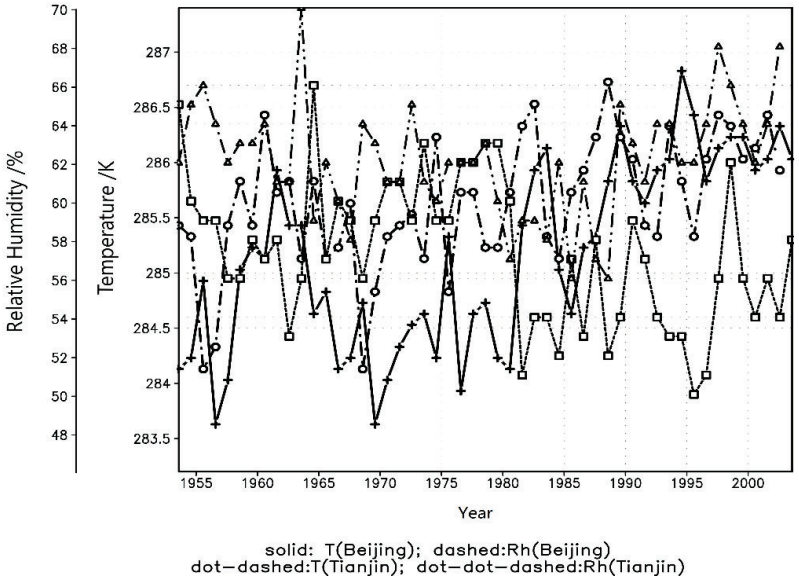

Fig. 12.1.1. The year-to-year change in annual mean temperature (K) and relative humidity (%) in Beijing and Tianjin from 1953 to 2003

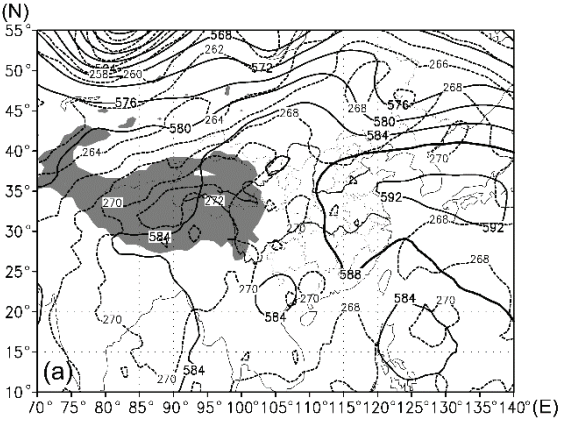

Fig. 12.1.2. Geopotential height (gpdm) and temperature (K) at 500 hPa at 00:00 UTC on 31 July 2002. The shaded area is the Tibetan Plateau.

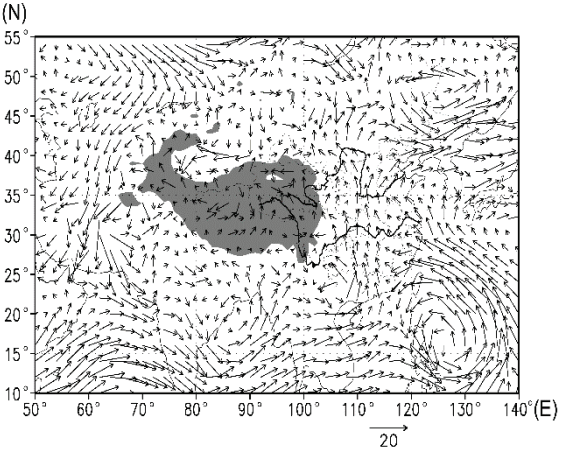

Fig.12.1.3. Moisture transport at 850 hPa (based on the $\vec{vq}$ vector; gm g^{-1} s^{-1}) on 31 July 2002. The shaded area is the Tibetan Plateau.

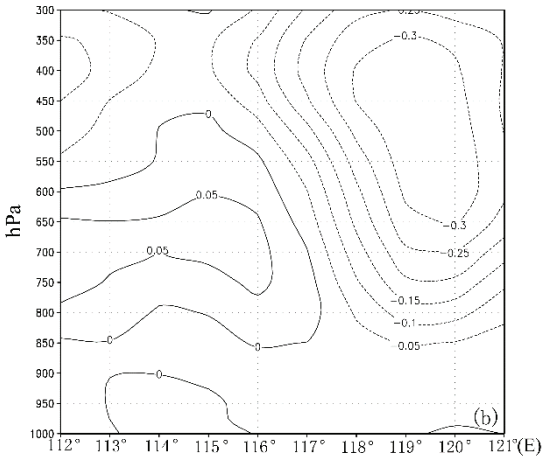

Fig. 12.1.4. Distribution of the average vertical velocity (Pa s^{-1}) from 31 July to 4 August 2002: zonal–vertical section along 39.9°N

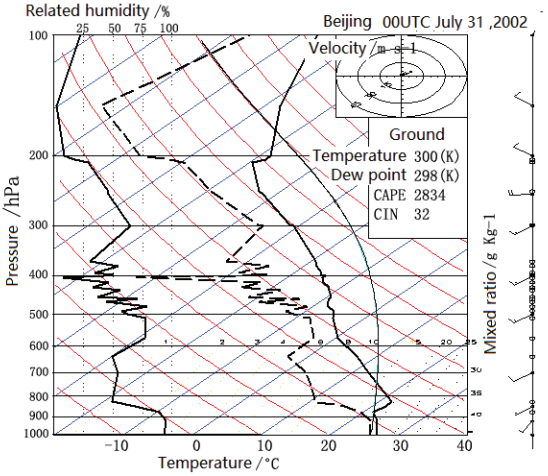

Fig. 12.1.5. Plot of T–ln p from observations made at 00:00 UTC at the Beijing station on 31 July 2002. The solid line at the left-hand side denotes the relative humidity (%), the dashed line denotes the dew-point temperature (K), and the thick and thin solid lines on the right hand side represent the state and stratification curves, respectively.

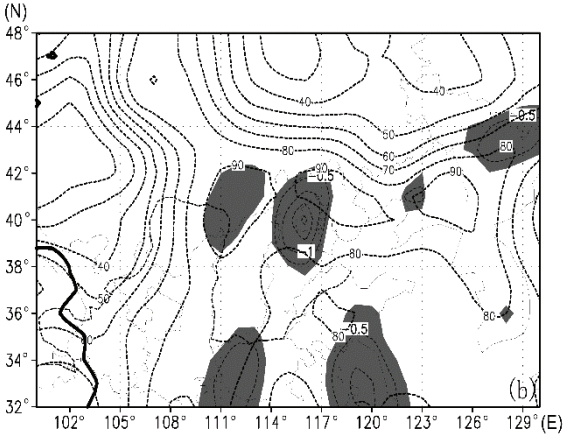

Fig. 12.1.6. Generalized moist potential vorticity (GMPV: solid line with an interval of 0.2 PVU) and relative humidity (RH: dashed lines with an interval of 10%) at 925 hPa at 00:00 UTC on 31 July 31 2002. The shaded regions are regions where GMPV ≤ -0.25.

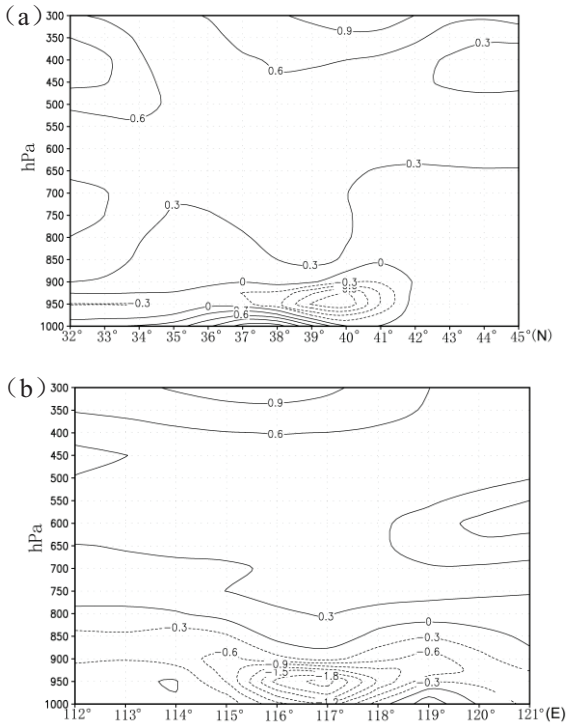

Fig. 12.1.7. Vertical sections of GMPV at 00:00 UTC on 2 August 2 (units: PVU): (a) meridional–vertical section along 116.3°E; (b) zonal–vertical section along 39.9°N

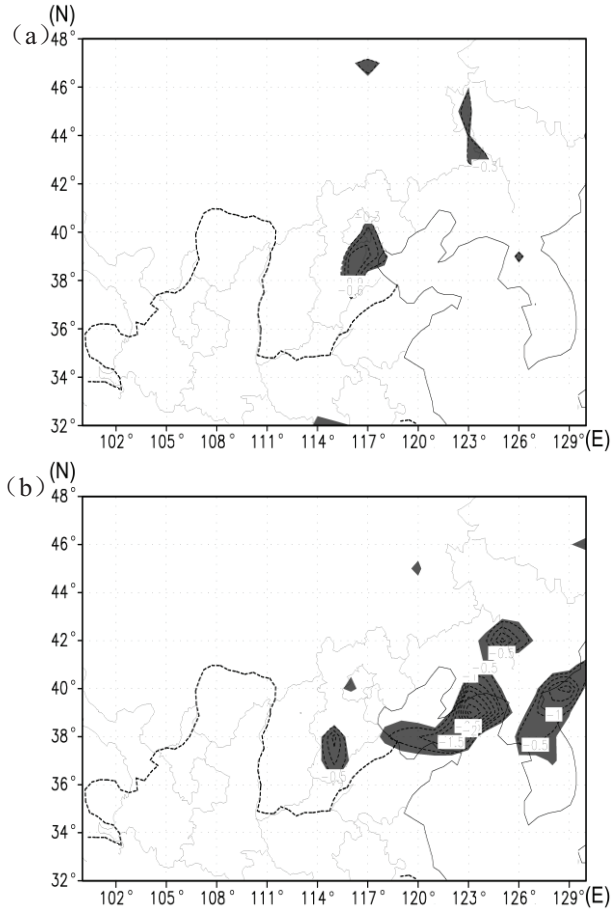

Fig. 12.1.8. The GMPV trend at 950 hPa (units: 10^{-4} PVU s^{-1}) from (a) 18:00 UTC on 29 July to 00:00 UTC on 30 July 2002 and from (b) 18:00 UTC on 4 August to 00:00 UTC on 5 August 2002. Shaded regions have values less than −0.25.

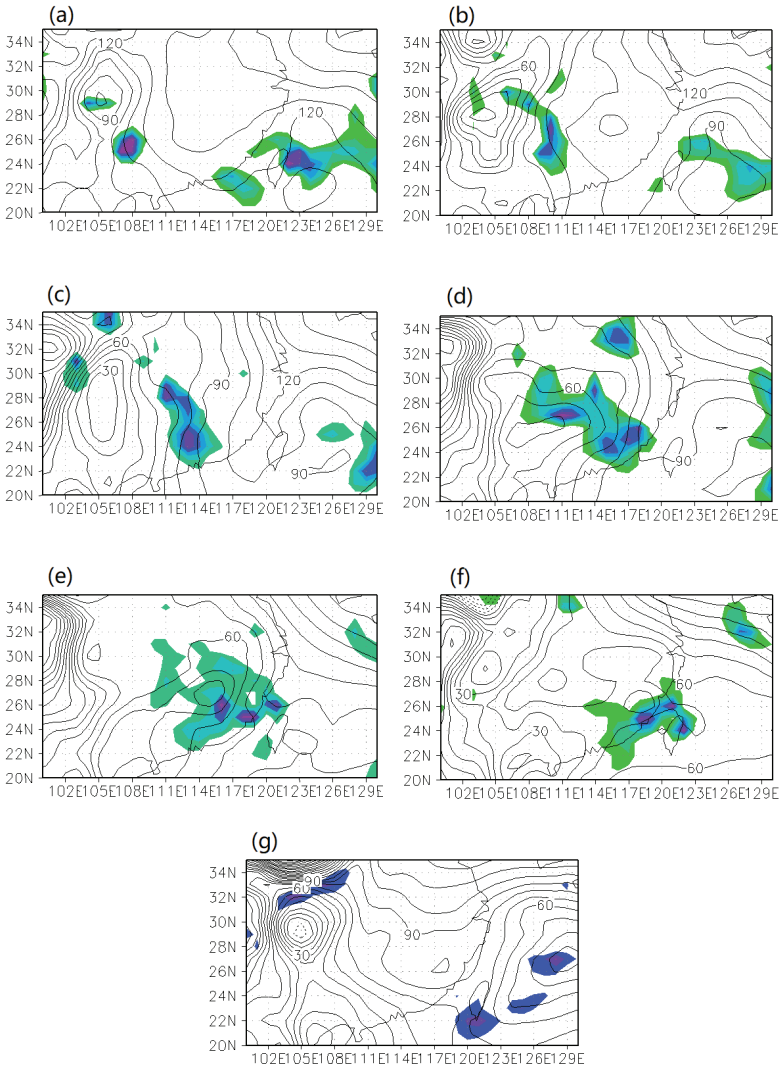

Fig. 12.2.1. Horizontal distribution of the NGMPV on the 700-hPa surface (shaded), superimposed on the geopotential height on the 1000-hPa surface (interval: 10 gpdm) for (a) 00:00 UTC, 7 April; (b) 06:00 UTC, 7 April; (c) 12:00 UTC, 7 April; (d) 18:00 UTC, 7 April; (e) 00:00 UTC, 8 April; (f) 06:00 UTC, 8 April; and (g) 18:00 UTC 8 April 2001

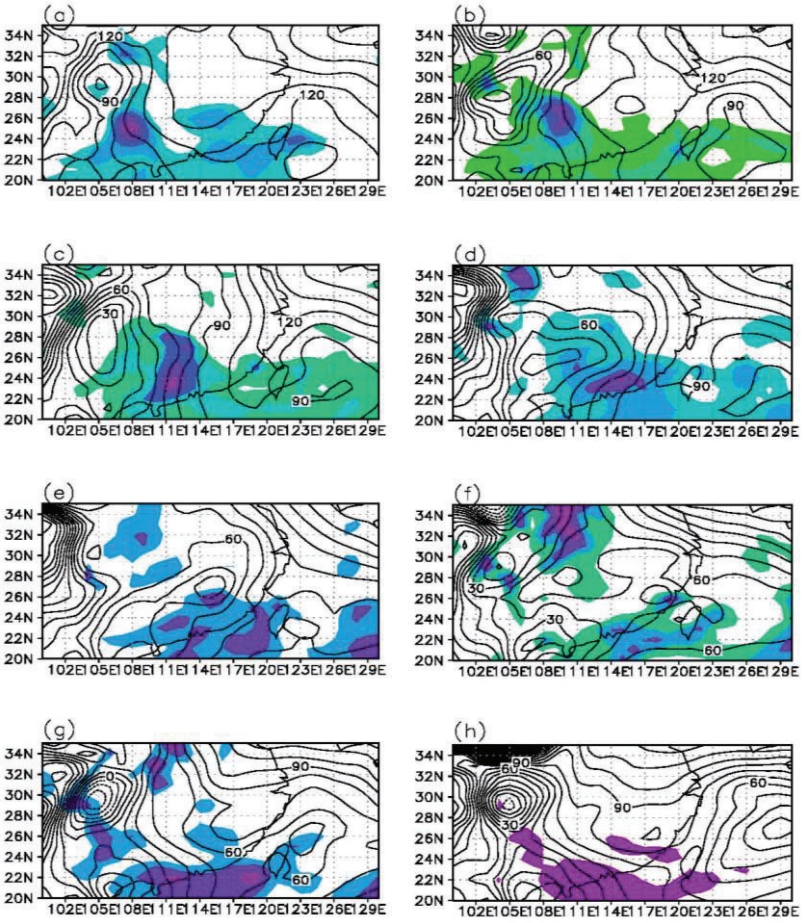

Fig. 12.2.2. Horizontal distribution of the NGMPV on the 700-hPa surface (shaded), superimposed on the geopotential height on the 1000-hPa surface (interval: 10 gpdm) for (a) 00:00 UTC, 7 April; (b) 06:00 UTC, 7 April; (c) 12:00 UTC, 7 April; (d) 18:00 UTC, 7 April; (e) 00:00 UTC, 8 April; (f) 06:00 UTC, 8 April; (g) 12:00 UTC, 8 April; and (h) 18:00 UTC, 8 April 2001

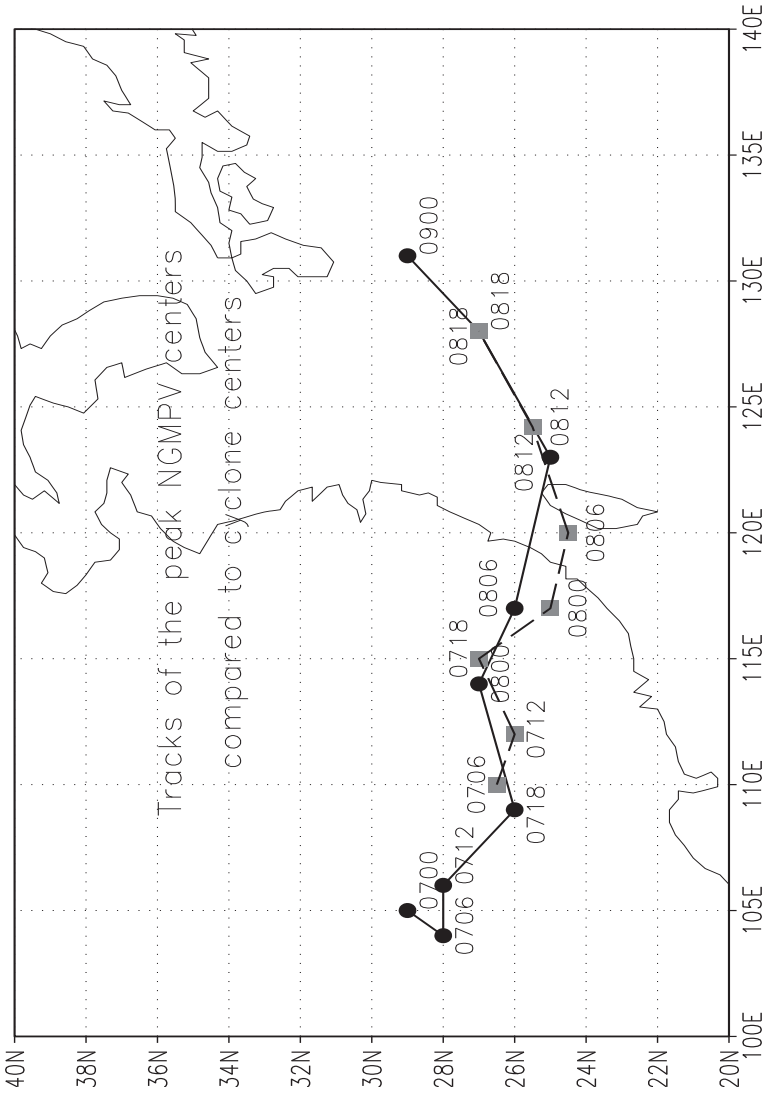

Fig. 12.2.3. Track of the low NGMPV center from 06:00 UTC on 7 April to 18:00 UTC on 8 April 2001 (dashed lined with rectangles) together with the surface track of the cyclone (solid line with circles).

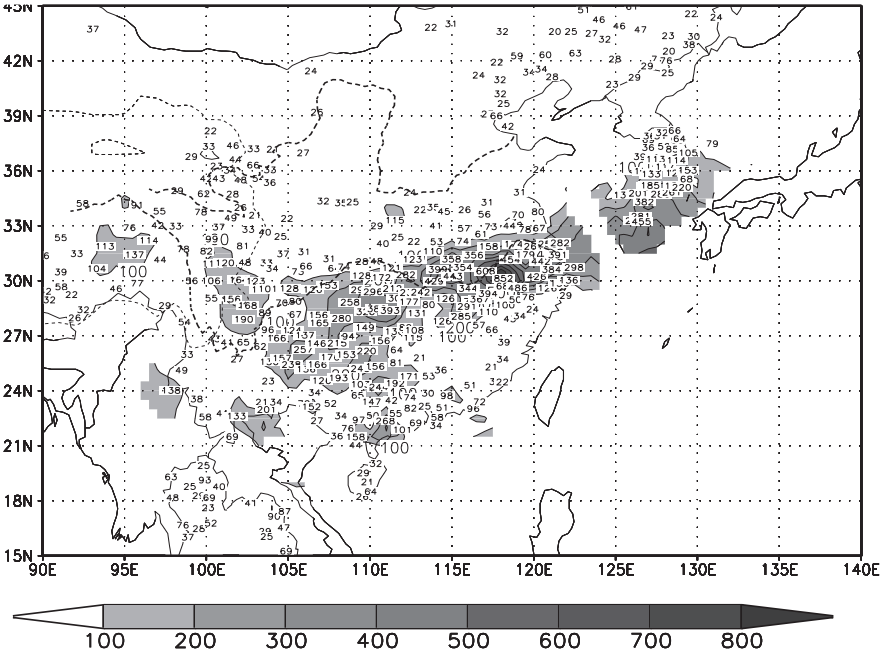

Fig. 12.3.1. Total precipitation from 22 June to 2 July 1999 (mm) and the distribution of the moist potential vorticity substance (shaded area)

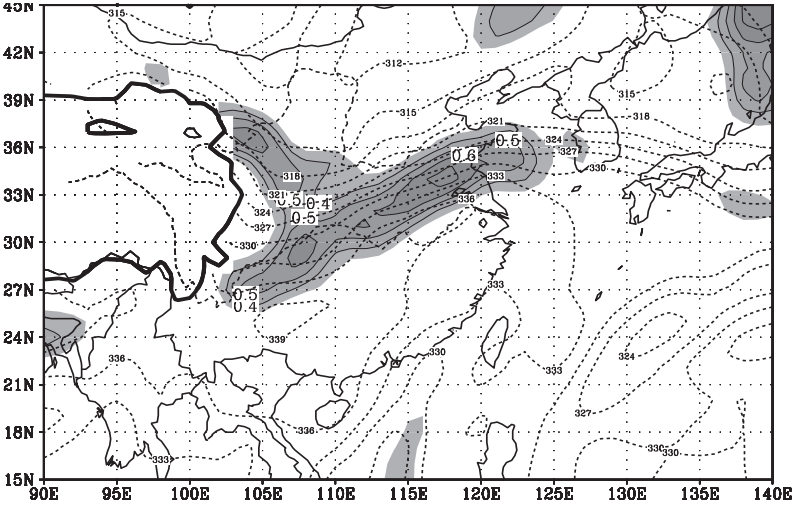

Fig. 12.3.2 (a). Distribution of moist potential vorticity substance at 700 hPa at 00:00 UTC on 23 June 1999 (units: 10^{-6} K m^{-1} s^{-1}; solid line: moist potential vorticity substance; dashed line: θ_e; the shaded area marks where the value of the moist potential vorticity substance ≤ −2.)

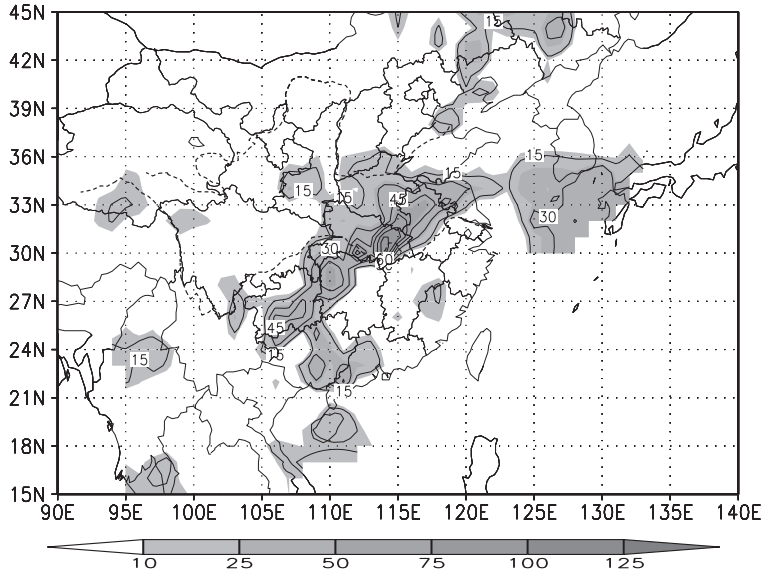

Fig. 12.3.2 (b). 24-hour precipitation as observed at 00:00, 23 June 1999 (mm)

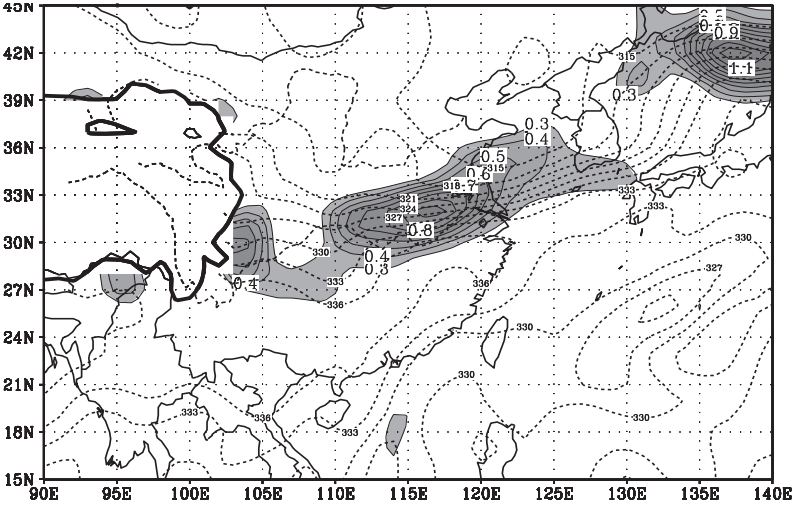

Fig. 12.3.3 (a). As for Fig. 12.3.2 (a) but for 00:00 UTC, 24 June 1999

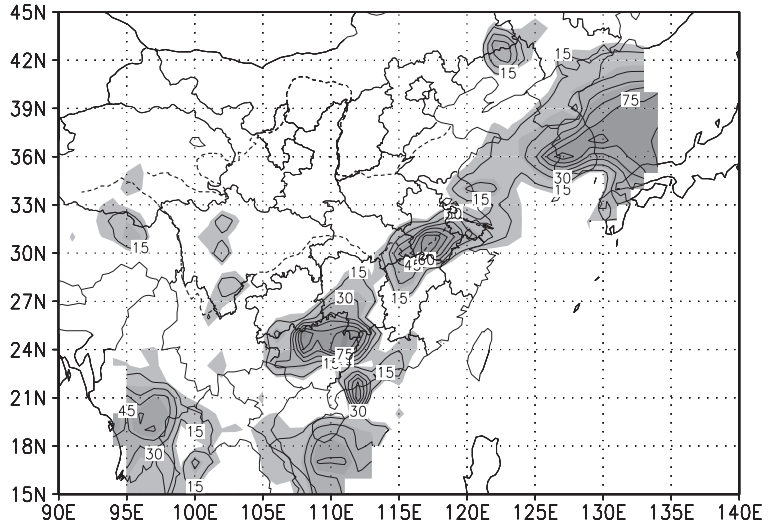

Fig. 12.3.3 (b). As for Fig. 12.3.2 (b) but for 00:00 UTC, 24 June 1999

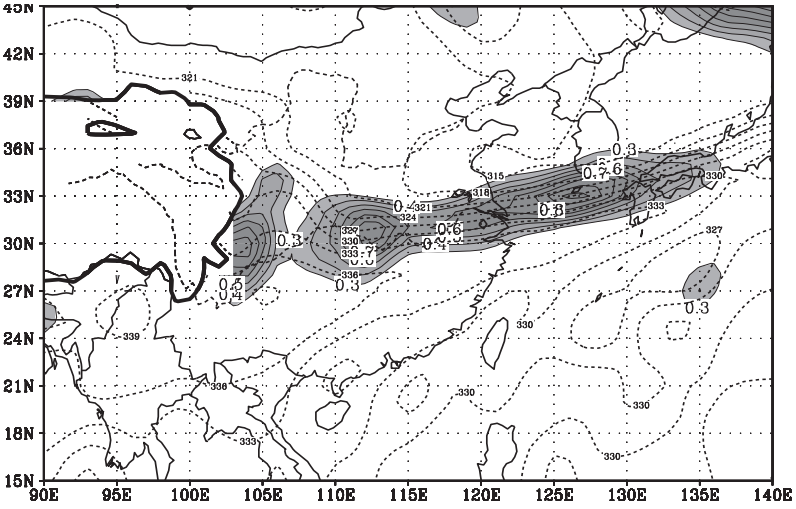

Fig. 12.3.4 (a). As for Fig. 12.3.2 (a) but for 00:00 UTC, 25 June 1999

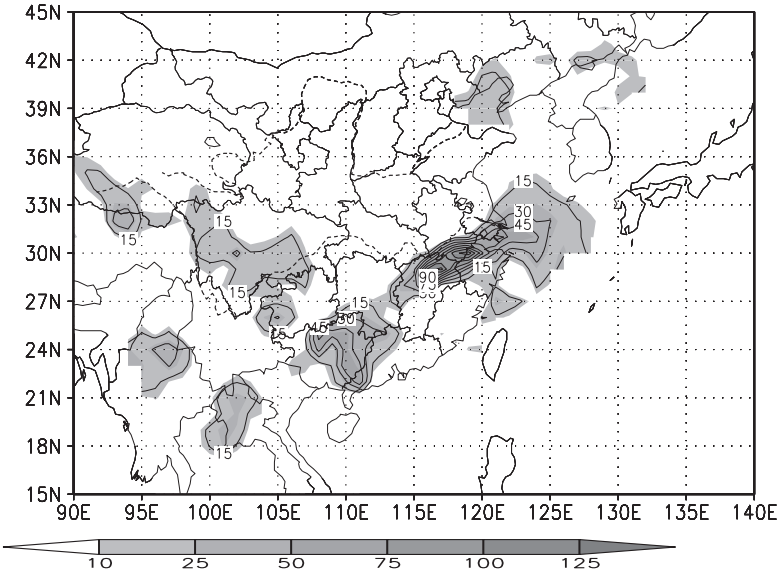

Fig. 12.3.4 (b). As for Fig. 12.3.2 (b) but for 00:00 UTC, 25 June 1999

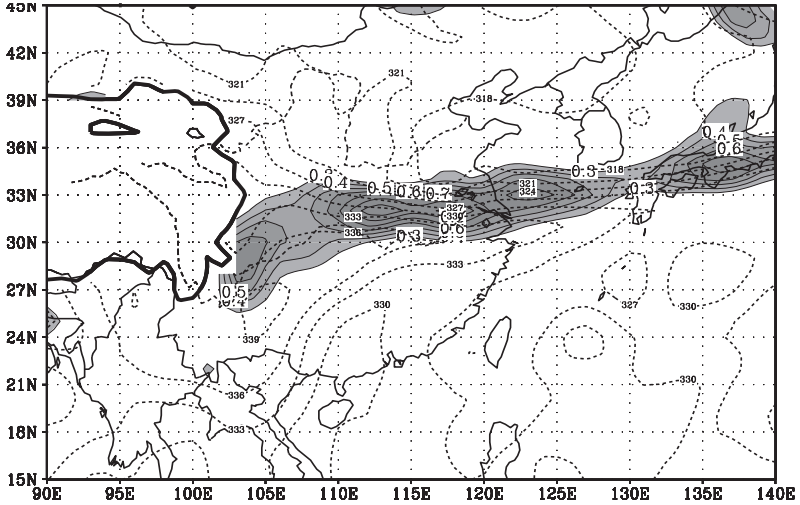

Fig. 12.3.5 (a). As for Fig. 12.3.2 (a) but for 00:00 UTC, 26 June 1999

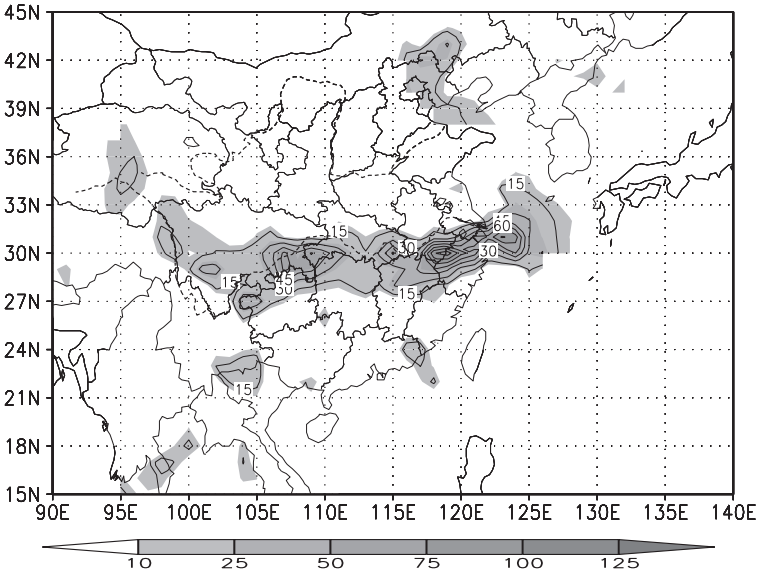

Fig. 12.3.5 (b). As for Fig. 12.3.2 (b) but for 00:00 UTC, 26 June 1999

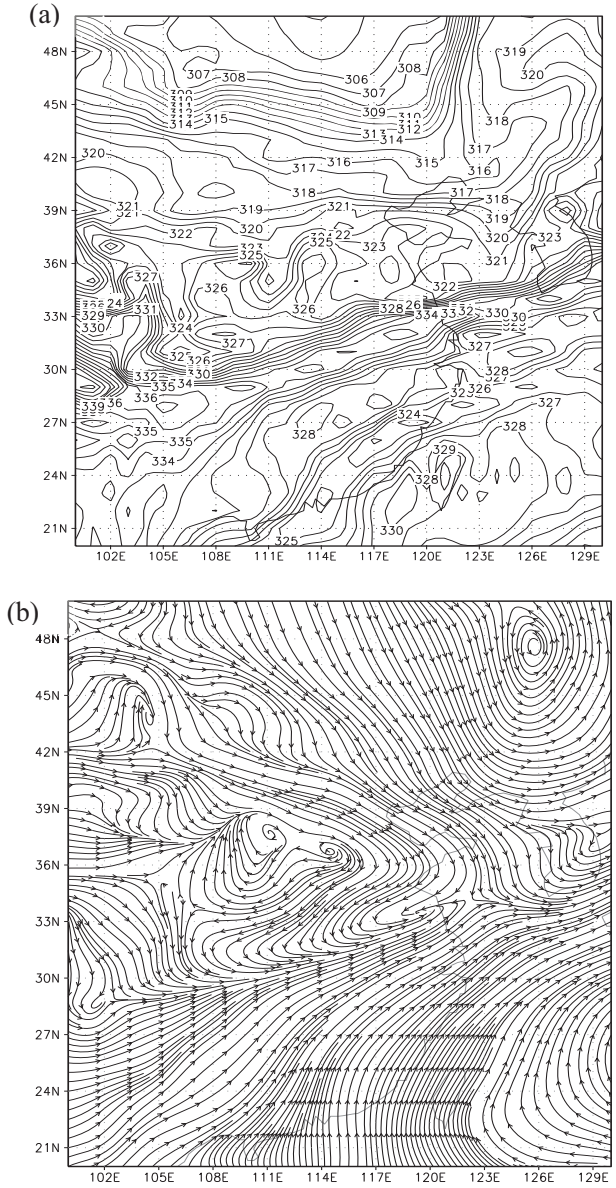

Fig. 12.4.1. The (a) equivalent potential temperature (K) and (b) streamline fields at the 700-hPa level at 00:00 UTC, 5 July 2003

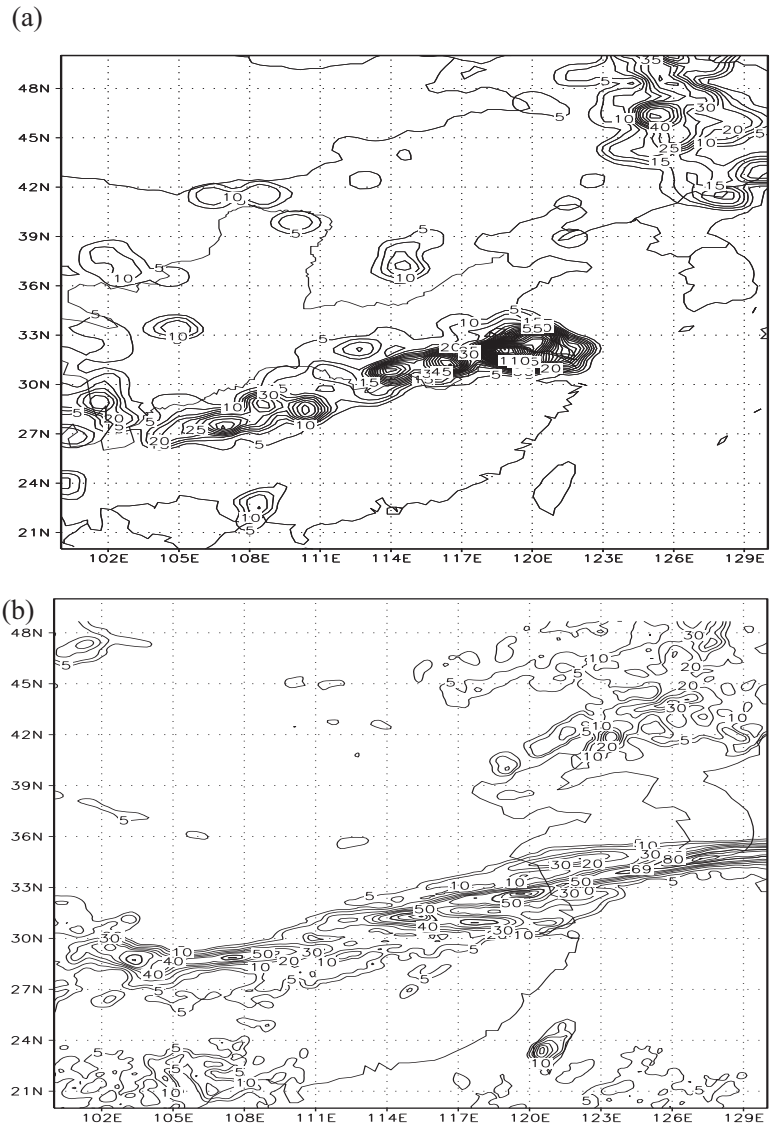

Fig. 12.4.2 (a) Observed and (b) predicted 36-hour total rainfall (mm) in the middle and lower reaches of the Yangtze River from 00:00 UTC, 4 July to 12:00 UTC, 5 July 2003

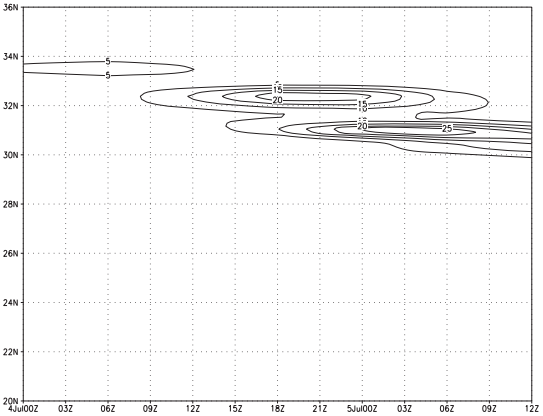

Fig. 12.4.3. Time–latitude cross-sections of 6-hour accumulated precipitation (mm) along 118°E from 00:00 UTC, 4 July to 12:00 UTC, 5 July 2003

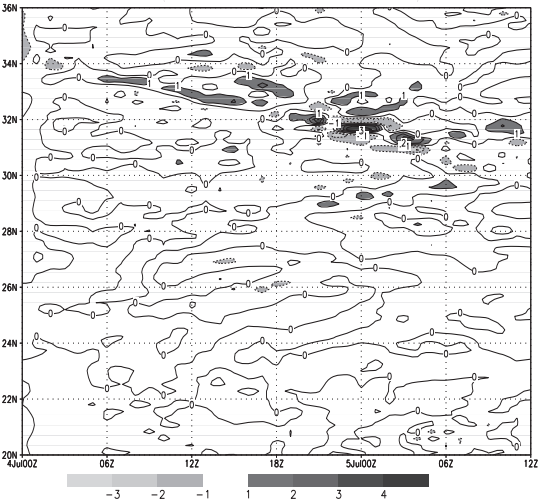

Fig. 12.4.4. Time–latitude cross-sections of mass divergence (10^{-5} kg m^{-3} s^{-1}) at the 4.287-km level along 118°E from 00:00 UTC, 4 July to 12:00 UTC, 5 July 2003

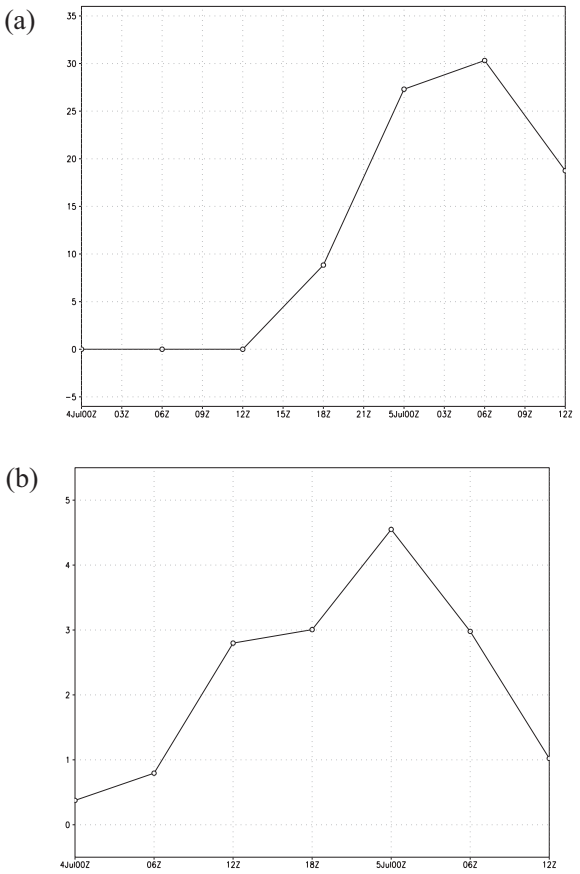

Fig. 12.4.5. (a) The six-hour precipitation (mm) and (b) the absolute value of the six-hour mass divergence (10^{-5} kg s^{-1} m^{-3}) at the 4.287-km level at the center of the precipitation zone (119°E, 32°N)

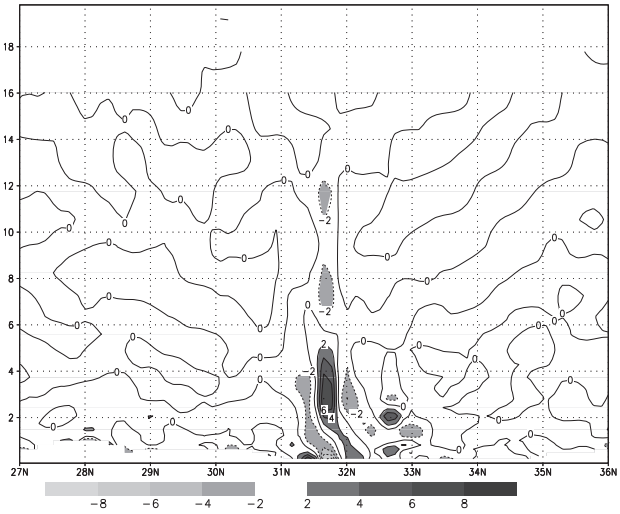

Fig. 12.4.6. Meridional–vertical section of the mass divergence along 118°E (10^{-5} kg m^{-3} s^{-1}) at 00:00 UTC, 5 July 2003. The shaded regions denote where the absolute value of the mass divergence is greater than 2.

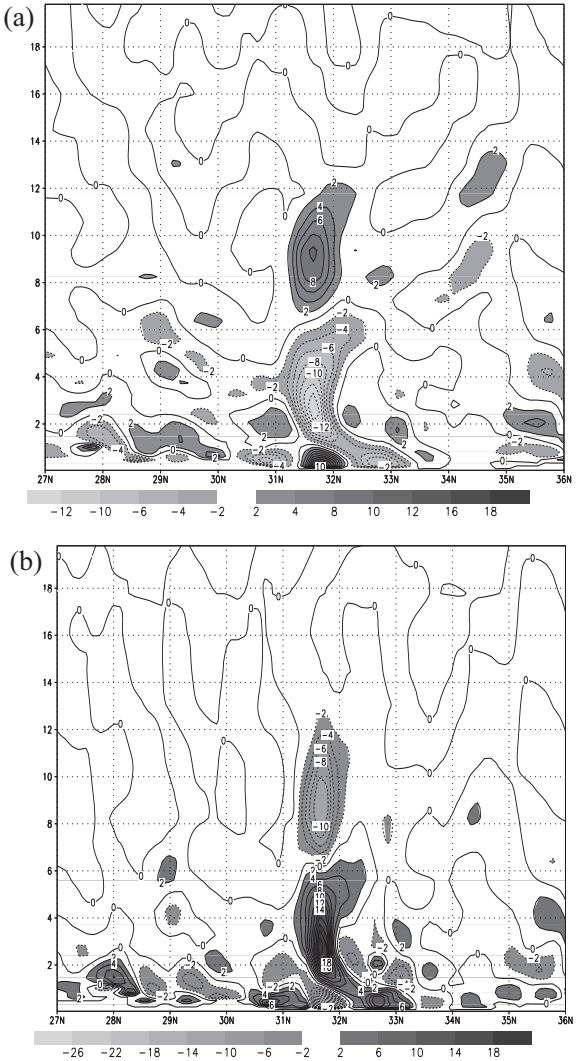

Fig. 12.4.7. Meridional–vertical sections along 118°E of (a) the horizontal component and (b) the vertical component of the mass divergence (10^{-5} kg $s^{-1} m^{-3}$) at 00:00 UTC, 5 July, 2003. The shaded regions denote where the absolute value of the mass divergence is greater than 2.

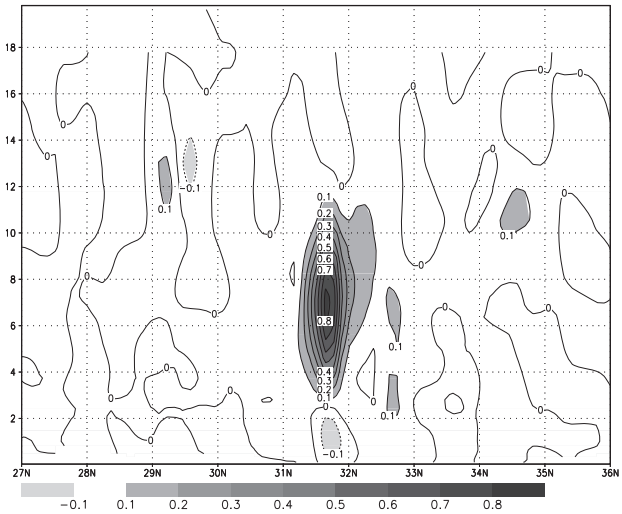

Fig. 12.4.8. Meridional–vertical section of the vertical velocity (m s^{-1}) along 118°E at 00:00 UTC, 5 July 2003. The shaded regions denote where the absolute value of the vertical velocity is greater than 2.

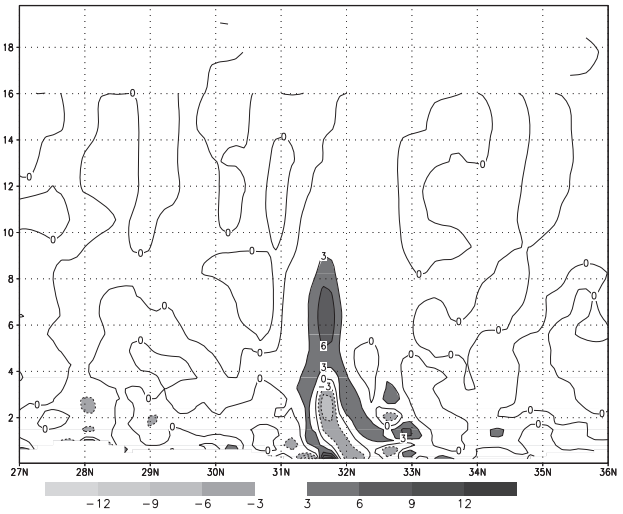

Fig. 12.4.9. Meridional–vertical section of R_{cm} along 118°E (10^{-6} kg m^{-3} s^{-1}) at 00:00 UTC, 5 July 2003. The shading denotes regions where the absolute value of R_{cm} is greater than 3.

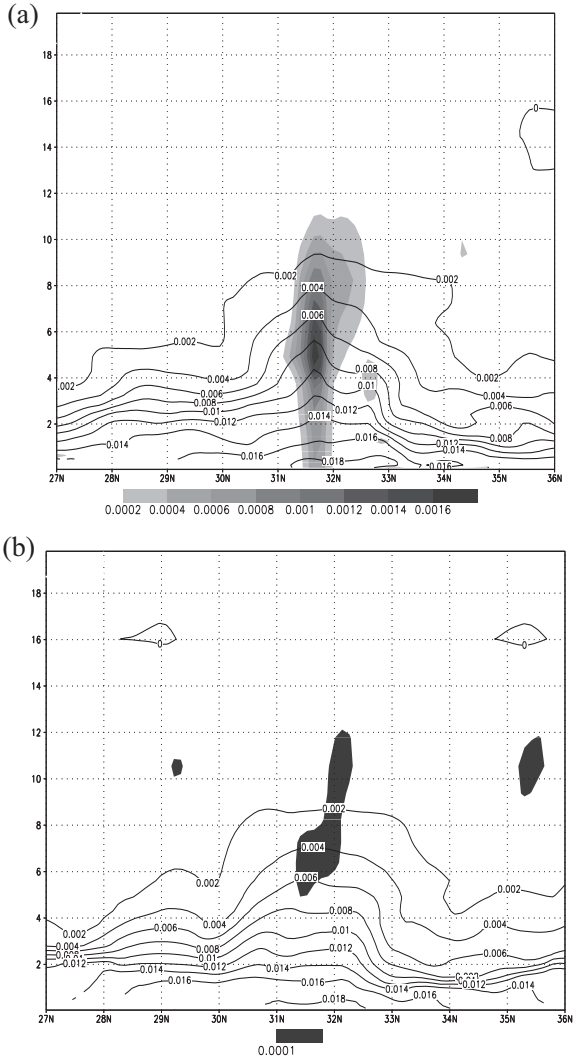

Figure 12.4.10. Meridional–vertical section of q_{con} (the sum of the mixing ratios of cloud water, raindrops, ice, snow, and graupel; shown as isolines) along 118°E and q (the sum of the mixing ratio of water condensate and vapor; shown as shaded regions; units: g g^{-1} for (a) 00:00 UTC and (b) 06:00 UTC, 5 July 2003.

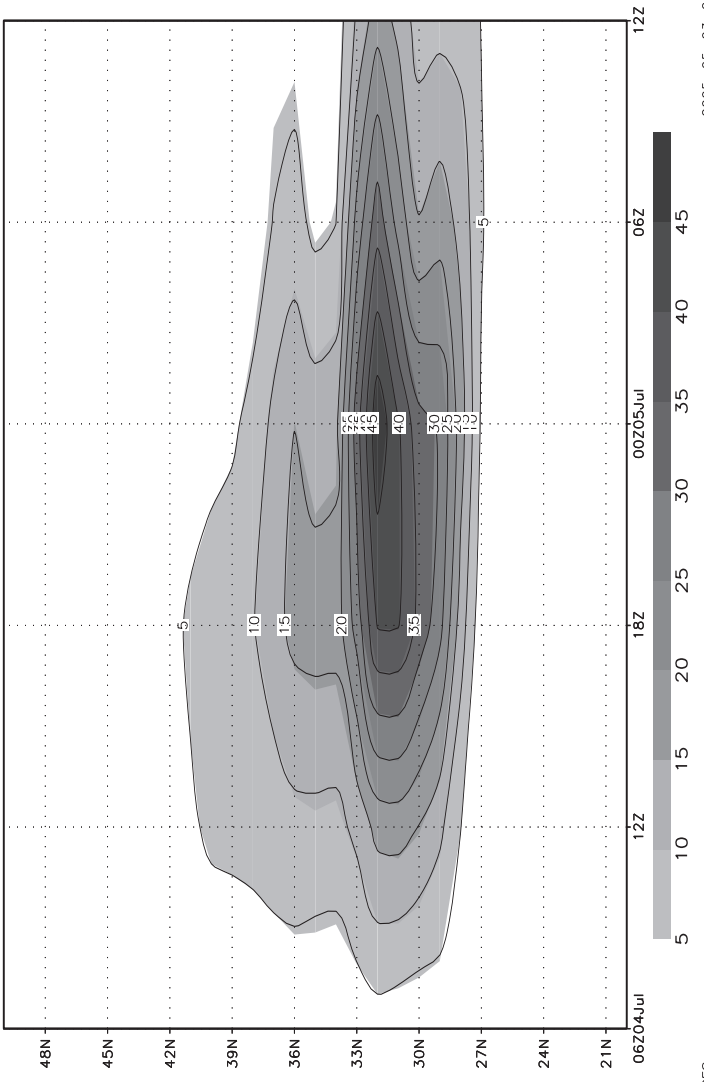

Fig.12.5.1. Time–latitude cross-section along 119°E for the six-hour cumulative precipitation (mm) from 06:00 UTC on 4 July to 12:00 UTC on 5 July 2003

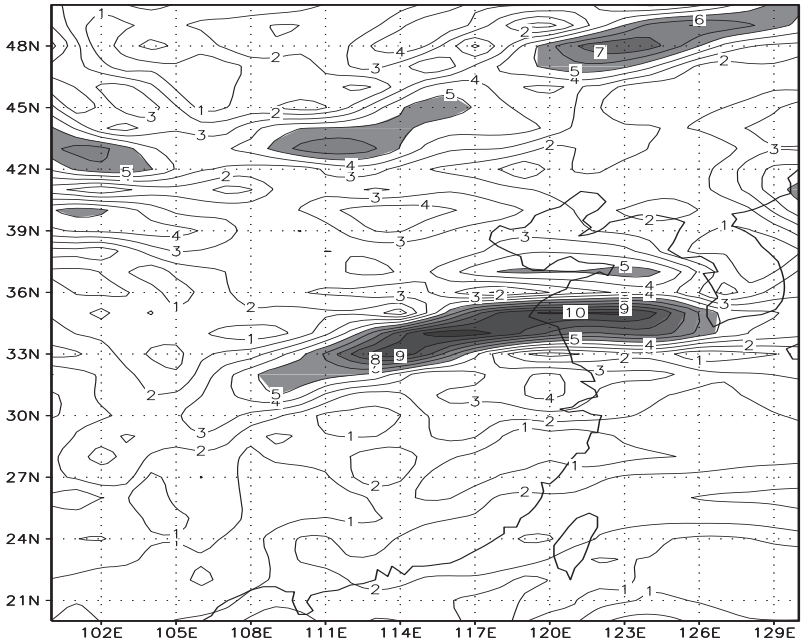

Fig. 12.5.2. Total deformation (10^{-5} s^{-1}) at 700 hPa at 00:00 UTC on 4 July 2003. The shaded areas are areas where the total deformation exceeds 5×10^{-5} s^{-1}.

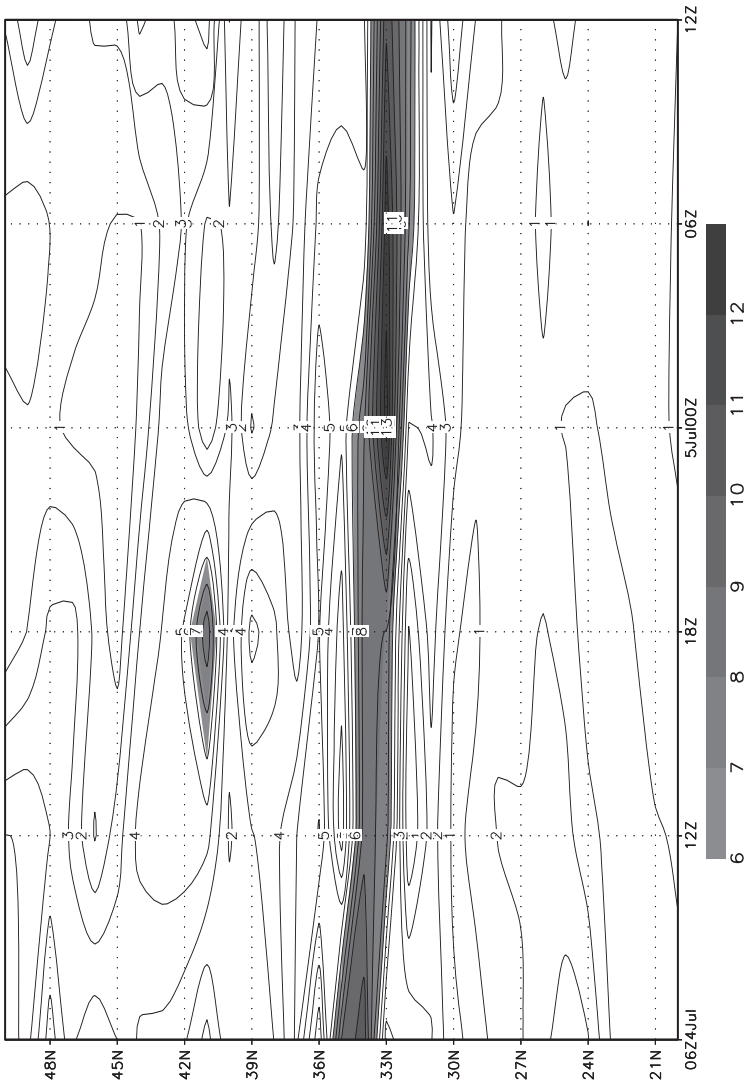

Fig. 12.5.3. Time–latitude cross-section of the total deformation (10^{-5} s^{-1}) along 119°E at 700 hPa from 06:00 UTC on 4 July to 12:00 UTC on 5 July 2003. The shaded areas are areas where the total deformation exceeds 6×10^{-5} s^{-1}.

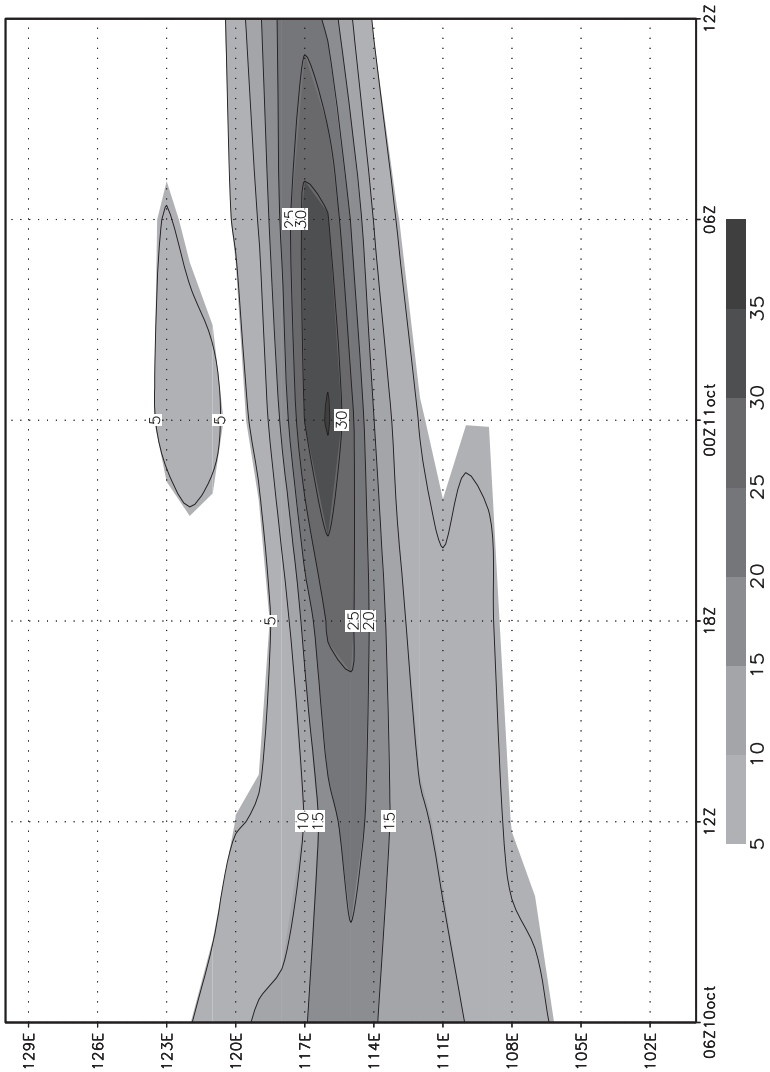

Fig. 12.5.4. Time–longitude cross-section along 37°N for the six-hour cumulative precipitation (mm) from 06:00 UTC, 10 October to 12:00 UTC, 11 October 2003.

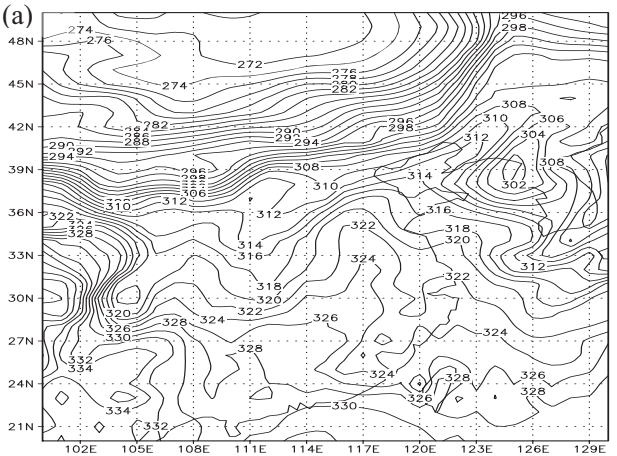

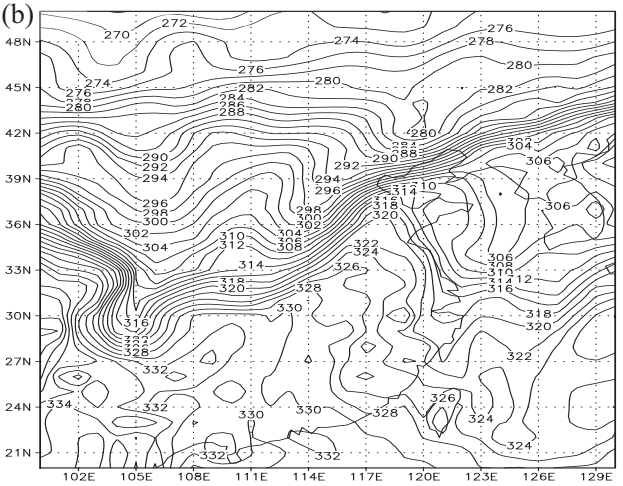

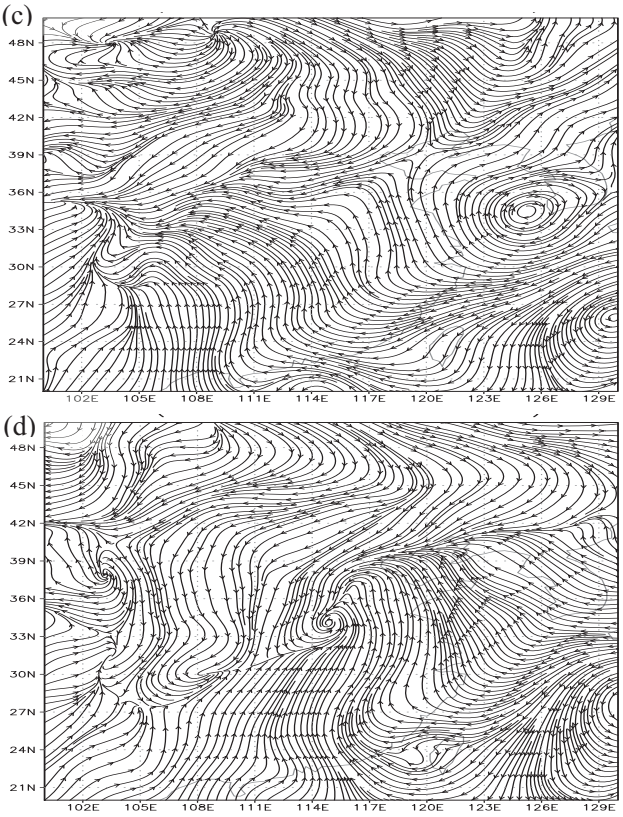

Fig. 12.5.5. Equivalent potential temperature (K) at (a) 00:00 UTC on 10 October and (b) 00:00 UTC on 11 October and the streamline at (c) 00:00 UTC on 10 October and (d) 00:00 UTC on 11 October 2003. The fields at 900 hPa are shown.

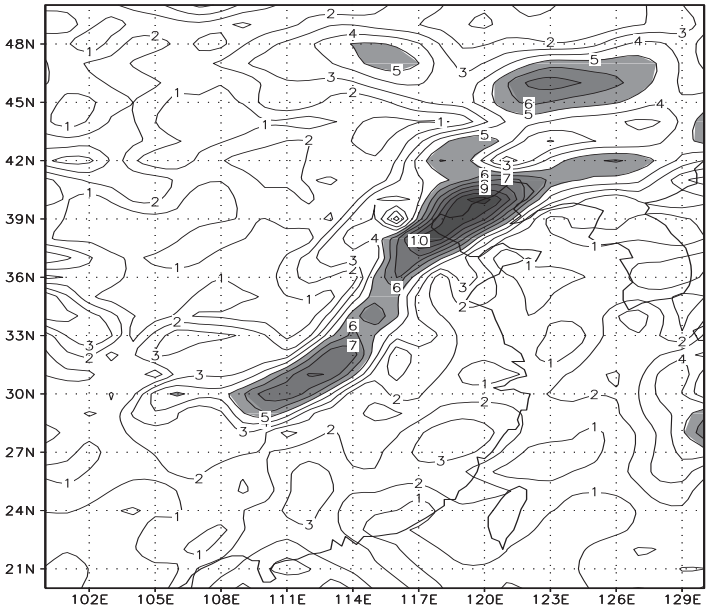

Fig. 12.5.6. Total deformation (10^{-5} s^{-1}) at 900 hPa at 00:00 UTC, 11 August 2003. The shaded areas are areas where the value of the total deformation exceeds 5×10^{-5} s^{-1}.

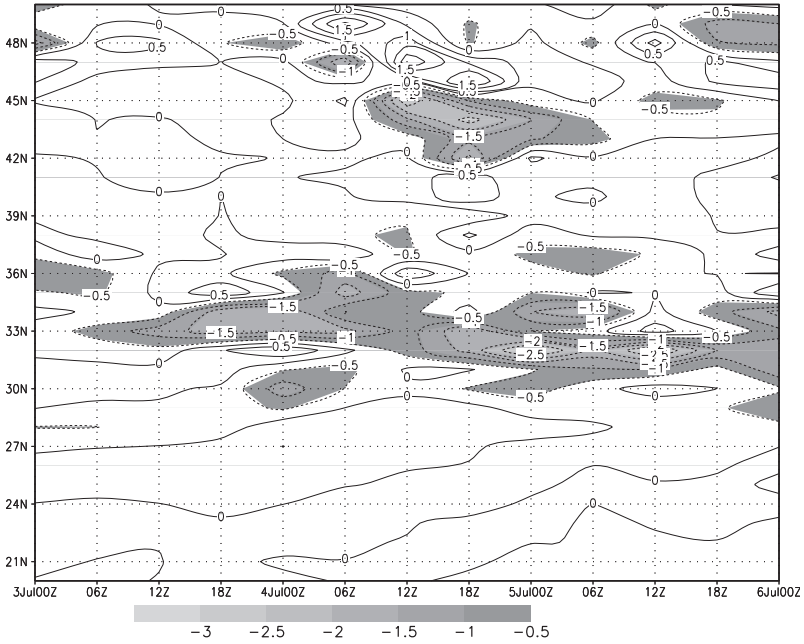

Fig. 12.5.7. Time–latitude cross-section of the advection term (10^{-9} s^{-2}) along 119°E at 700 hPa from 00:00 UTC on 3 July to 00:00 UTC on 6 July 2003.The shaded areas are areas where the total deformation is smaller than −0.5.

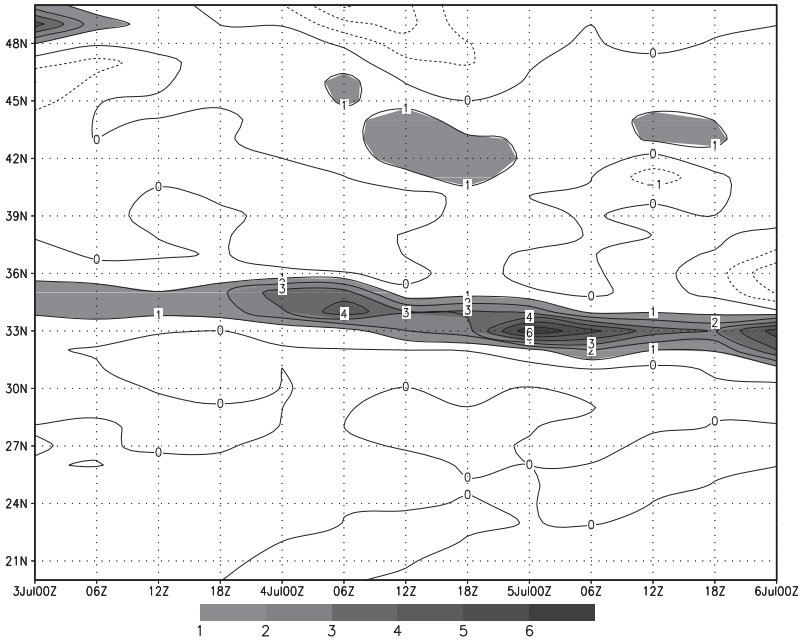

Fig. 12.5.8. Time–latitude cross-section of the horizontal divergence term (10^{-9} s^{-2}) along 119°E at 700 hPa from 00:00 UTC on 3 July to 00:00 UTC on 6 July 2003. The shaded areas are areas where the total deformation exceeds 1.

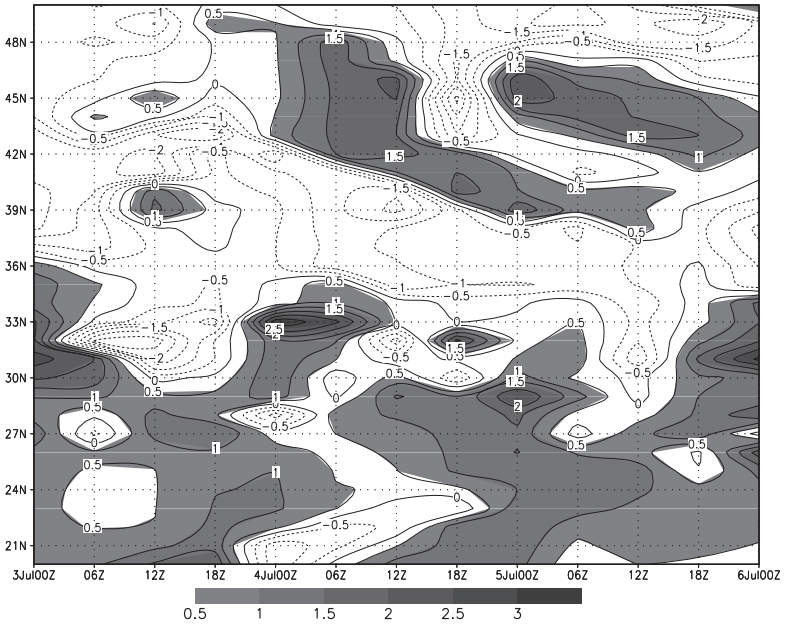

Fig. 12.5.9. Time–latitude cross-section of the β-effect term (10^{-10} s^{-2}) along 119°E at 700 hPa from 00:00 UTC on 3 July to 00:00 UTC on 6 July 2003.The shaded areas are areas where the total deformation exceeds 0.5.

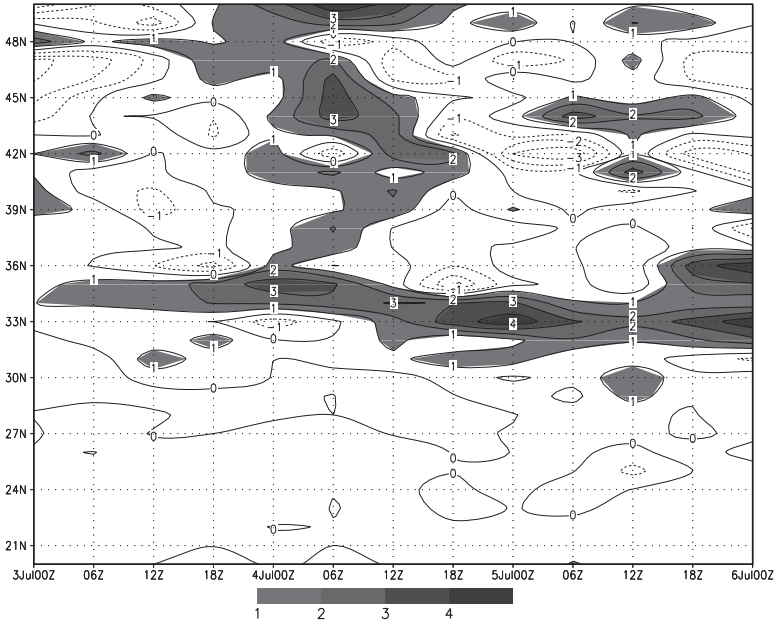

Fig. 12.5.10. Time–latitude cross-section of the horizontal pressure term (10^{-9} s^{-2}) along 119°E at 700 hPa from 00:00 UTC on 3 July to 00:00 UTC on 6 July 2003.The shaded areas are areas where the total deformation exceeds 1.

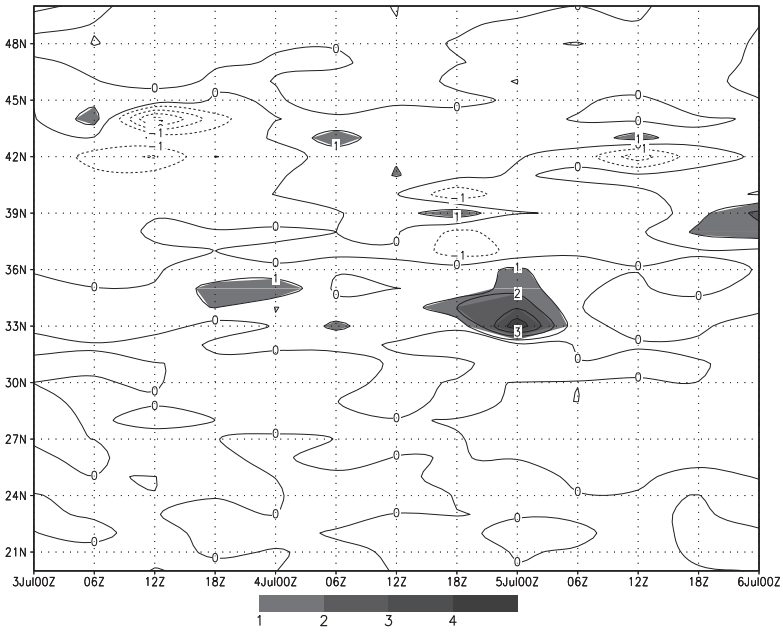

Fig. 12.5.11. Time–latitude cross-section of the vertical velocity term (10^{-9} s^{-2}) along 119°E at 700 hPa from 00:00 UTC on 3 July to 00:00 UTC on 6 July 2003. The shaded areas are areas where the total deformation exceeds 1.

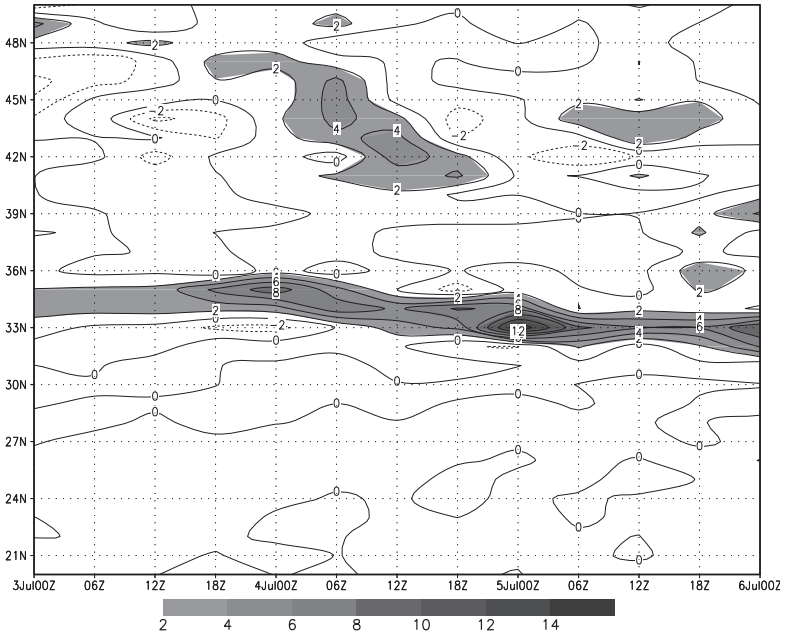

Fig. 12.5.12. Time–latitude cross-section of the sum of the terms on the right-hand side of the equation for the deformation trend (10^{-9} s^{-2}) along 119°E at 700 hPa from 00:00 UTC on 3 July to 00:00 UTC on 6 July 2003. The shaded areas are areas where the total deformation exceeds 2.

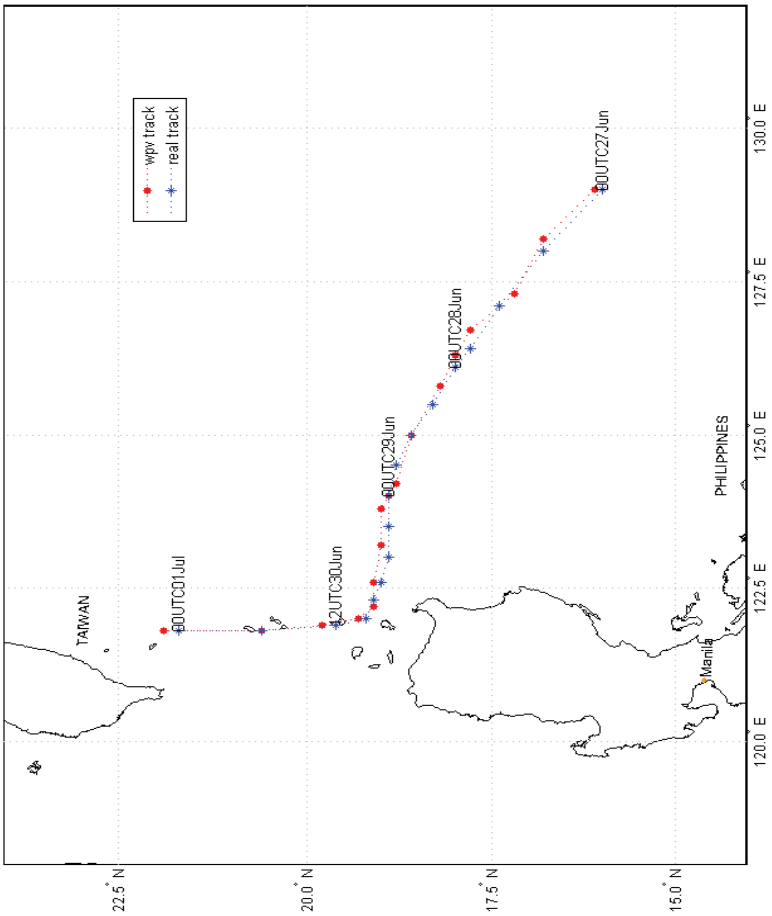

Fig. 12.6.1. Path of the vapor potential vortex (in red) and the path of Typhoon Pu Gong Ying (in blue) from 27 June to 1 July 2004

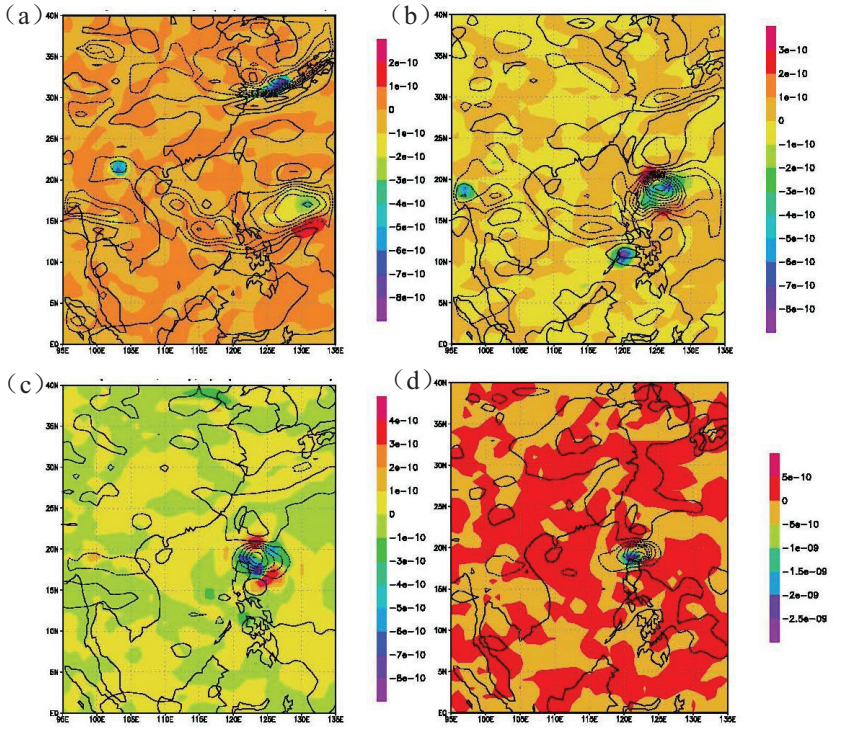

Fig. 12.6.2. The distribution of vapor potential vorticity advection at 00:00 UTC (shaded) and the vapor potential vorticity at 06:00 UTC (real line) at 500 hPa from 27 June to 1 July 2004

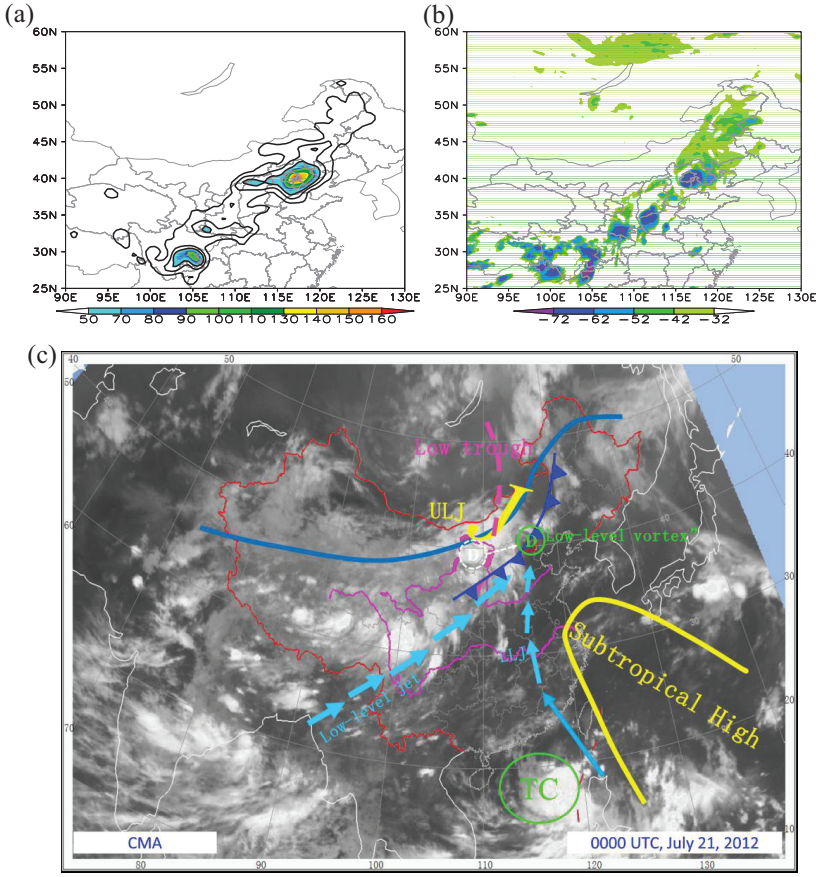

Fig. 12.7.1 On July 21, 2012, (a) 24-hour cumulative precipitation, (b) TBB distribution of 1200 UTC, and (c) large-scale situation configuration of 0000 UTC superimposed on infrared cloud image

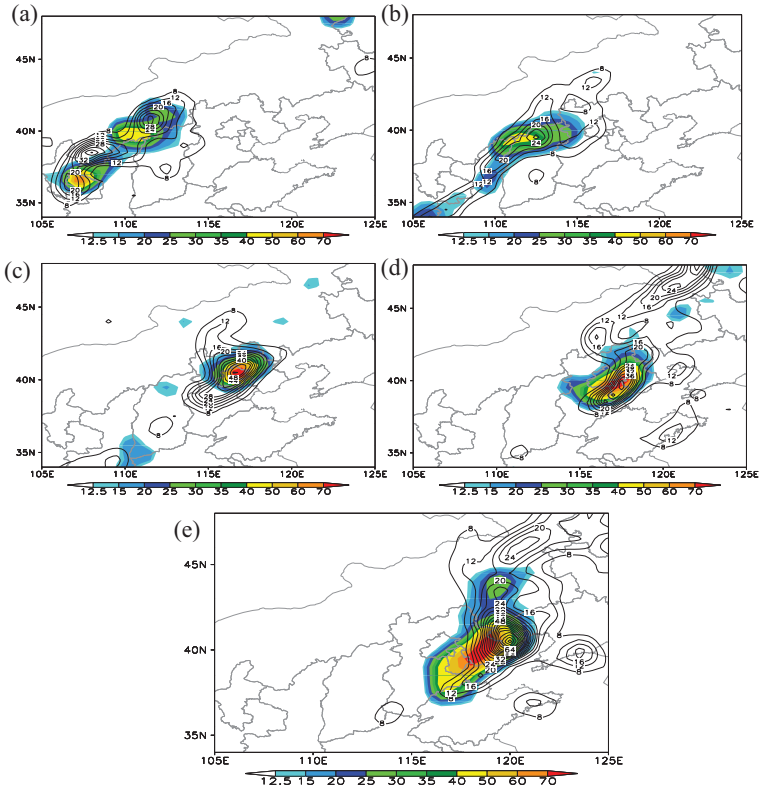

Fig. 12.7.2 Horizontal distribution of the Q_{ms} absolute value by vertically integrating ($\left\langle \left| Q_{ms} \right| \right\rangle$ unit: 10^{-8} m^3 K s^{-2} kg^{-2}) of the second-order moist potential vorticity at 0000 UTC from 21 July 2012 to 22 July 2012 at 0000 UTC. The shaddow area shows 6-hour cumulative precipitation (unit: mm).

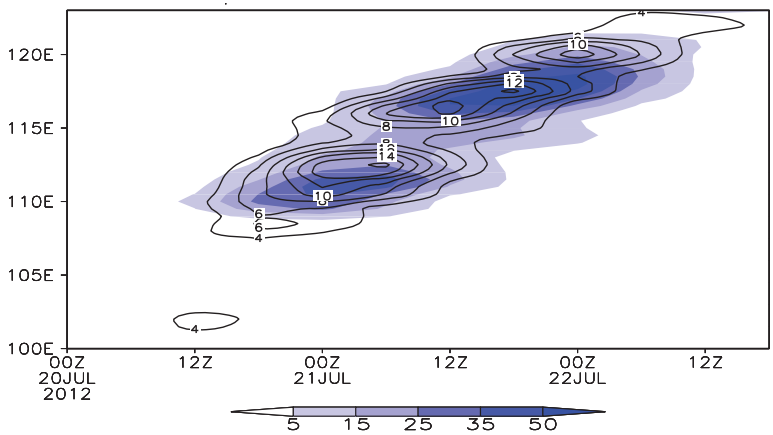

Fig. 12.7.3 Time section of second-order moist potential vorticity along 40°N 0000 UTC-22 July 2012 (Unit: 10^{-8} m^3 K s^{-2} kg^{-2}). The shaddow area is 6-hour accumulated precipitation.

Notes

[1]Karl, T. R. and R. W. Knight (1997) "The 1995 Chicago heat wave: How likely is a recurrence?" *Bulletin of the American Meteorological Society*, 78(6):1107-1119.

[2]Driscoll, D. M. (1985) Handbook of Applied Meteorology, *D. D. Houghton, Ed. John Wiley and Sons*.

[3]Kalkstein, L. S. and K. M. Valimont (1986) "An Evaluation of Summer Discomfort in the United State Using a Relative Climatological Index," *Bulletin of the American Meteorological Society*, 67(7):842-848.

[4]Höppe, P. (1999) "The Physiological equivalent temperature – a universal index for the biometeorological assessment of the thermal environment," *International Journal of Biometeorology*, 43(2):71-75.

[5]Robinson, P. J. (2001) "On the definition of a heat wave," *Journal of Applied Meteorology*, 40(4):762-775.

[6]Cao, Z. H. and D. L. Zhang (2005) "Sensitivity of cyclone tracks to the initial moisture distribution moist potential vorticity perspective," *Advances in Atmospheric Sciences*, 22(6):807-820.

[7]Qiu, C., J. Bao and Q. Xu (1993) "Is the mass sink due to precipitation negligible?" *Monthly Weather Review*, 121(3):853-857.

[8]Gao, S., Y. Zhou, X. Cui et al. (2004) "Impacts of cloud-induced mass forcing on the development of moist potential vorticity anomaly during torrential rains," *Advances in Atmospheric Sciences*, 21(6):923-927.

CHAPTER THIRTEEN

DYNAMIC FORECASTING METHODS BASED ON VECTOR FIELD THEORY

The characteristics of atmospheric motion are mainly depicted by vector fields such as the wind field and vorticity field. The pressure gradient and temperature gradient (atmospheric baroclinicity) are also vector fields. The most important equation among the basic atmospheric equations is the momentum equation, which is also a vector equation. As studies of the atmosphere have advanced, greater attention has been paid to the study of scalar fields such as the potential vorticity, potential temperature, helicity, and streamline vorticity. Although some scalar quantities are conserved and reversible, they do not contain all of the important information that vector quantities do. As a result, vector fields cannot be completely replaced by scalar fields. Vector fields have received little attention recently, and so, given the importance of vector fields, this chapter examines vector field theory and associated dynamic forecasting methods.

13.1 The Convective Vorticity Vector

The potential temperature surface of large-scale weather systems is quasi-horizontal (except in the frontal zone), and the potential temperature (θ) increases with height. Thus, the potential temperature gradient ($\nabla\theta$) is aligned vertically, and the motion in the atmosphere is quasi-horizontal. The absolute vorticity vector is usually vertical. This leads to a large value

of the Ertel potential vorticity (denoted by Q_θ: $Q_\theta = \frac{\boldsymbol{\xi}_a \cdot \nabla\theta}{\rho}$), which is an important physical quantity in large-scale systems. Due to the conservation of potential vorticity in an adiabatic frictionless atmosphere and the reversibility in a balanced system, the potential vorticity has been widely applied in studies of atmospheric dynamics and is considered the core of the dynamics of balanced systems (Hoskins et al., 1985; McIntyre, 1987; McIntyre et al., 2000)[1-3]. For mesoscale deep-convective systems associated with torrential rainfall, strong convection and saturation cause the iso-equivalent potential temperature surface to be vertical, which then means that the equivalent temperature gradient ($\nabla\theta_e$) is quasi-horizontal.

As a result, the dot product of the absolute vorticity vector and the equivalent potential temperature gradient is small (Figure 13.1.1). Thus, the potential vorticity cannot be used to trace atmospheric motion. In addition, the potential vorticity is a scalar quantity and does not include all of the information about an important vector field. Gao et al. (2004)[4], therefore, proposed the use of the convective vorticity vector ($\mathbf{C} = \frac{\boldsymbol{\xi}_a \times \nabla\theta}{\rho}$) to depict the formation and development of mesoscale deep-convective systems. It was shown that, in deep-convective systems, the convective vorticity vector has a large value and is an important physical quantity that contains important information about the vector fields.

At point A in Figure 13.1.1., $Q_m = \frac{\boldsymbol{\xi}_a \cdot \nabla\theta_e}{\rho} = 0$ and

$\mathbf{C} = \dfrac{\boldsymbol{\xi}_a \times \nabla \theta_e}{\rho} \neq 0$; at point B, $Q_m = \dfrac{\boldsymbol{\xi}_a \cdot \nabla \theta_e}{\rho} \neq 0$ and

$\mathbf{C} = \dfrac{\boldsymbol{\xi}_a \times \nabla \theta_e}{\rho} = 0$.

In order to examine the correlation between the convective vorticity vector and convection, a torrential rainfall event that occurred over northern China between 00:00 UTC on 12 August and 12:00 UTC on 13 August 2004 was simulated using the ARPS model, and the modeling data were used to carry out a diagnostic analysis (Gao et al., 2007)[5].

For convenience, the convective vorticity vector can be partitioned according to

$$\mathbf{C} = \frac{\boldsymbol{\xi}_a \times \nabla \theta_e}{\overline{\rho}} = C_x \mathbf{i} + C_y \mathbf{j} + C_z \mathbf{k}, \tag{13.1.1}$$

where

$C_x = \dfrac{1}{\overline{\rho}}(\xi_2 \dfrac{\partial \theta_e}{\partial z} - \zeta \dfrac{\partial \theta_e}{\partial y})$, $C_y = \dfrac{1}{\overline{\rho}}(\zeta \dfrac{\partial \theta_e}{\partial x} - \xi_1 \dfrac{\partial \theta_e}{\partial z})$, $C_z = \dfrac{1}{\overline{\rho}}(\xi_1 \dfrac{\partial \theta_e}{\partial y} - \xi_2 \dfrac{\partial \theta_e}{\partial x})$

are the zonal, meridional, and vertical components of the vector, respectively; $\overline{\rho} = \overline{\rho}(z)$ is the height-dependent atmospheric density.

The absolute vorticity is defined as

$$\boldsymbol{\xi}_a = \nabla \times (u\mathbf{i} + v\mathbf{j} + w\mathbf{k}) + f\mathbf{k} = \xi_1 \mathbf{i} + \xi_2 \mathbf{j} + \zeta \mathbf{k}, \tag{13.1.2}$$

where $\xi_1 = \dfrac{\partial w}{\partial y} - \dfrac{\partial v}{\partial z}, \xi_2 = \dfrac{\partial u}{\partial z} - \dfrac{\partial w}{\partial x}, \zeta = \dfrac{\partial v}{\partial x} + f - \dfrac{\partial u}{\partial y}$, and f is the Coriolis parameter.

Vertically integrating the components of the convective vorticity vector, we have

$$[C_x]=\int_{z_1}^{z_2}\overline{\rho}C_x dz, \qquad [C_y]=\int_{z_1}^{z_2}\overline{\rho}C_y dz, \qquad [C_z]=\int_{z_1}^{z_2}\overline{\rho}C_z dz \ , \tag{13.1.3}$$

where $z_1=600m,\ z_2=17000m$.

The vertical integral of the sum of the mixing ratios of cloud water, raindrops, cloud ice, snow, and graupel is used to denote the convection. We thus have

$$[CH]=\int_{z_1}^{z_2}\overline{\rho}[q_c+q_r+q_s+q_i+q_g]dz\ , \tag{13.1.4}$$

where q_c, q_r, q_i, q_s, and q_g are the mixing ratios of cloud water, raindrops, cloud ice, snow, and graupel, respectively. In addition, the potential vorticity (PV) can also be vertically integrated and compared with the convective vorticity vector.

Figure 13.1.2 shows the horizontal distributions of $[C_x]$, $[C_y]$, $[C_z]$, PV, and CH at 00:00 UTC on 13 August 2004. CH was oriented northeast–southwest, which was consistent with the orientation of the rain bands (not shown). The centers of these distributions were located at (36°N, 112.5°E) and (38°N, 117°E). The components of the convective vorticity vector have similar orientations, but the distribution of the potential vorticity is slightly different from that of the convection. This suggests that the convective vorticity vector may be a better indicator than the potential vorticity.

Figure 13.1.3 shows the evolution of the meridional distribution of $[C_x]$, $[C_y]$, $[C_z]$, and CH averaged from 112°E to 119°E over the period 00:00 UTC on 12 August to 12:00 UTC on 13 August 2004. The

maxima of $[C_y]$ and $[C_z]$ were aligned with the maximum of CH, which moved southward.

The correlation between the convective vorticity vector, potential vorticity, and cloud hydrometeors can be further examined using Figure 13.1.4, which shows the evolution of $[C_x]$, $[C_y]$, $[C_z]$, PV, and CH averaged over the area 37°N–42°N and 112°E–119°E. The linear correlation coefficients between $[C_x]$ and CH, $[C_y]$ and CH, $[C_z]$ and CH, and PV and [CH] are −0.44, 0.52, 0.89, and −0.70, respectively. The linear correlation coefficients between $[C_x]$ and the rainfall rate, $[C_y]$ and the rainfall rate, $[C_z]$ and the rainfall rate, and PV and the rainfall rate are −0.20, 0.55, 0.91, and -0.85, respectively.

The t-test gives the critical value of the correlation coefficient for freedom degree of 70 in this case as 0.3. Thus, the relations between $[C_y]$ and [CH] and between $[C_z]$ and CH are statistically significant. The root-mean-squared (RMS) differences between $[C_x]$ and CH, between $[C_y]$ and CH, between $[C_z]$ and CH, and between PV and CH are 0.19, 0.27, 0.79, and 0.49, respectively. The RMS differences between $[C_x]$ and the rainfall rate, between $[C_y]$ and the rainfall rate, between $[C_z]$ and the rainfall rate, and between PV and the rainfall rate are 0.04, 0.30, 0.82, and 0.72, respectively. This indicates that the correlation coefficient between the vertical component of the convective

vorticity vector and the surface rainfall rate, which represents the interaction between the horizontal vorticity and the horizontal temperature gradient, has the largest linear correlation coefficient. In the next section, the trend equation of the vertical component of the convective vorticity vector will be applied to the nowcasting of the real atmosphere.

13.2 A Dynamic Prediction Method Based on the Convective Vorticity Vector

In the last section, it was demonstrated that there is a close relationship between the convective vorticity vector (CVV) and the formation and development of convective systems. How can this be applied to dynamic predictions? In this section, the equation for the trend in the vertical component of the CVV is used to analyze a real rainfall event.

The three-dimensional primitive equations of motion are expressed as

$$\frac{\partial u}{\partial t}+u\frac{\partial u}{\partial x}+v\frac{\partial u}{\partial y}+w\frac{\partial u}{\partial z}-fv=-\frac{1}{\rho}\frac{\partial p'}{\partial x}, \tag{13.2.1}$$

$$\frac{\partial v}{\partial t}+u\frac{\partial v}{\partial x}+v\frac{\partial v}{\partial y}+w\frac{\partial v}{\partial z}+fu=-\frac{1}{\rho}\frac{\partial p'}{\partial y}, \tag{13.2.2}$$

$$\frac{\partial w}{\partial t}+u\frac{\partial w}{\partial x}+v\frac{\partial w}{\partial y}+w\frac{\partial w}{\partial z}=-\frac{1}{\rho}\frac{\partial p'}{\partial z}+B_b, \tag{13.2.3}$$

$$\frac{\partial u}{\partial x}+\frac{\partial v}{\partial y}+\frac{1}{\rho}\frac{\partial \overline{\rho}w}{\partial z}=0, \tag{13.2.4}$$

$$\frac{d\theta}{dt}=\frac{\theta}{c_pT}Q_d, \text{ and} \tag{13.2.5}$$

$$\frac{\partial q_v}{\partial t}+u\frac{\partial q_v}{\partial x}+v\frac{\partial q_v}{\partial y}+w\frac{\partial q_v}{\partial z}=S_{q_v}, \tag{13.2.6}$$

where $p'=p-\overline{p}(z)$ is the deviation from the mean pressure, $\overline{\rho}=\rho(z)$ is the mean density, $B_b=-g\frac{\rho'}{\overline{\rho}}$ is the buoyancy term, Q_d is the diabatic heating term, q_v is the specific humidity, and S_{q_v} is the source/sink of water vapor.

The equivalent potential temperature is defined as

$$\theta_e=\theta e^{\frac{L_v q_v}{c_p T}}, \tag{13.2.7}$$

where θ and T are the potential temperature and temperature, respectively, L_v is the latent heat of condensation, and c_p is the heat capacity of dry air at constant pressure.

From (13.2.5) and (13.2.6), the equation for the equivalent potential temperature can be expressed as

$$\frac{\partial \theta_e}{\partial t}+u\frac{\partial \theta_e}{\partial x}+v\frac{\partial \theta_e}{\partial y}+w\frac{\partial \theta_e}{\partial z}=\frac{\theta_e}{c_p T}\tilde{Q}_s, \tag{13.2.8}$$

where $\tilde{Q}_s=Q_d+L_v S_{q_v}-\frac{L_v q_v}{T}\frac{dT}{dt}$ and $\mathbf{v}=u\mathbf{i}+v\mathbf{j}+w\mathbf{k}$.

The absolute vorticity is defined as

$$\boldsymbol{\xi}_a=\nabla\times(u\mathbf{i}+v\mathbf{j}+w\mathbf{k})+f\mathbf{k}=\xi_1\mathbf{i}+\xi_2\mathbf{j}+\zeta\mathbf{k}, \tag{13.2.9}$$

where $\xi_1=\frac{\partial w}{\partial y}-\frac{\partial v}{\partial z};\xi_2=\frac{\partial u}{\partial z}-\frac{\partial w}{\partial x};\zeta=\frac{\partial v}{\partial x}+f-\frac{\partial u}{\partial y}$. Thus, the

trend equations for the three components of the absolute vorticity can be constructed:

$$\frac{\partial \xi_1}{\partial t} + \mathbf{v} \cdot \nabla \xi_1 = \boldsymbol{\xi}_a \cdot \nabla u + \frac{\partial B_b}{\partial y} + (\xi_1 w - \frac{1}{\overline{\rho}} \frac{\partial p'}{\partial y}) \frac{\partial \ln \overline{\rho}}{\partial z}, \quad (13.2.10)$$

$$\frac{\partial \xi_2}{\partial t} + \mathbf{v} \cdot \nabla \xi_2 = \boldsymbol{\xi}_a \cdot \nabla v - \frac{\partial B_b}{\partial x} + (\xi_2 w + \frac{1}{\overline{\rho}} \frac{\partial p'}{\partial x}) \frac{\partial \ln \overline{\rho}}{\partial z} \quad (13.2.11)$$

$$\frac{\partial \zeta}{\partial t} + \mathbf{v} \cdot \nabla \zeta = \boldsymbol{\xi}_a \cdot \nabla w + \zeta w \frac{\partial \ln \overline{\rho}}{\partial z}. \quad (13.2.12)$$

The vertical component of the CVV is defined as

$$C_z = \frac{1}{\overline{\rho}} (\xi_1 \frac{\partial \theta_e}{\partial y} - \xi_2 \frac{\partial \theta_e}{\partial x}). \quad (13.2.13)$$

The use of (13.2.8) and (13.2.10)–(13.2.12) yields the equation for the trend in the vertical component of the CVV:

$$\begin{aligned} \frac{\partial}{\partial t} C_z = & -\mathbf{v} \cdot \nabla C_z + \frac{1}{\overline{\rho}} [\xi_2 \frac{\partial u}{\partial x} - \xi_1 \frac{\partial u}{\partial y} - \boldsymbol{\xi}_a \cdot \nabla v + \frac{\partial p'}{\partial x} \frac{\partial}{\partial z} (\frac{1}{\rho}) + \frac{\partial B_b}{\partial x}] \frac{\partial \theta_e}{\partial x} \\ & + \frac{1}{\rho} [\xi_2 \frac{\partial v}{\partial x} - \xi_1 \frac{\partial v}{\partial y} + \boldsymbol{\xi}_a \cdot \nabla u + \frac{\partial p'}{\partial y} \frac{\partial}{\partial z} (\frac{1}{\rho}) + \frac{\partial B_b}{\partial y}] \frac{\partial \theta_e}{\partial y} \\ & + \frac{1}{\rho} (\xi_2 \frac{\partial w}{\partial x} - \xi_1 \frac{\partial w}{\partial y}) \frac{\partial \theta_e}{\partial z} + \frac{1}{\rho} [\xi_1 \frac{\partial}{\partial y} (\frac{\theta_e}{c_p T} \tilde{Q}) - \xi_2 \frac{\partial}{\partial x} (\frac{\theta_e}{c_p T} \tilde{Q})] \end{aligned} \quad (13.2.14)$$

Equation (13.2.14) states that the local change in the vertical component of the CVV (CZT) is associated with the advection term (CZ1), with the interaction between the vertical gradient of the equivalent potential temperature and the dynamics related to dynamic, thermodynamic, and microphysical processes (which are represented by the second (CZ2), third (CZ3), and fourth (CZ4) terms on the right-hand side), and also with

the term related to diabatic heating (CZ5).

Figure 13.2.1 shows the evolution of the area averages of these terms for 34°N–43°N and 112°E–119°E from 00:00 UTC, 12 August to 12:00 UTC, 13 August 2004. The linear correlation coefficients between CZ1 and CZT, CZ2 and CZT, CZ3 and CZT, CZ4 and CZT, and between CZ5 and CZT are −0.29, 0.39, 0.46, −0.24, and 0.36, respectively. The corresponding RMS differences are 0.77, 1.82, 2.35, 2.13, and 0.51×10^{-8} s^{-2} K, respectively. The standard deviation of CZT is 0.53×10^{-8} s^{-2} K. The largest linear correlation coefficient and the smallest RMS difference indicate that the diabatic heating term is mainly responsible for the trend in $[C_z]$.

Figure 13.2.2 shows the evolution of the zonal distribution of the six-hour cumulative rainfall amount and the vertical component of the CVV from 00:00 UTC, 12 August to 12:00 UTC, 13 August 2004. The two distributions are spatially and temporally similar. The maximum of the vertical component of the CVV was located to the east of the maximum of the six-hour cumulative rainfall amount, implying that the vertical component of CVV is a precursor of the six-hour cumulative rainfall amount. Thus, it may be possible to use the vertical component of the CVV for nowcasting through integration of the trend equation.

These results show that the CVV is an important parameter in two- and three-dimensional analysis of convective development and can be applied to the nowcasting of tropical and mid-latitude convective systems. The short-term integration of the trend equation for the vertical component of the CVV can be used in nowcasting of the formation and development of torrential rainfall systems.

13.3 The Moist Vorticity Vector (MVV) and Dynamic Vorticity Vector (DVV)

The vorticity and the potential temperature gradient can be cross- and dot-multiplied to obtain the potential vorticity, moist potential vorticity, generalized moist potential vorticity, and convective vorticity vectors, and these can be applied in the study of the formation and development of mesoscale weather systems. These quantities account for the disposition between atmospheric motion and temperature. In fact, during the formation and development of a weather system, the disposition between the wind field and the temperature field is important and is indicative of whether the system will develop or dissipate. In mesoscale weather systems, in particular, when precipitation occurs, the disposition between the water vapor field and the wind field is also an important indicator of the development of the weather systems. Thus, similarly to the potential vorticity and convective vorticity vectors, Gao et al. (2005)[6] proposed two new vectors: the moist vorticity vector (MVV: $\boldsymbol{\xi}_q = \alpha \boldsymbol{\xi}_a \times \nabla q$) and the dynamic vorticity vector (DVV: $\boldsymbol{\xi}_v = \alpha \boldsymbol{\xi}_a \times \mathbf{v}$), which are based on the water vapor potential vorticity ($Q_q = \alpha \boldsymbol{\xi}_a \cdot \nabla q$).

13.3.1 The Moist Vorticity Vector

The moist vorticity vector is constructed by replacing the potential temperature by the specific humidity in the expression of vorticity (Gao et al., 2005).

Taking the cross product of (12.6.1) with ∇q, we get

$$\nabla q \times \frac{\partial \boldsymbol{\xi}_a}{\partial t} + \nabla q \times (\mathbf{v} \cdot \nabla)\boldsymbol{\xi}_a = \nabla q \times (\boldsymbol{\xi}_a \cdot \nabla)\mathbf{v} - \nabla q \times \boldsymbol{\xi}_a (\nabla \cdot \mathbf{v}) - \nabla q \times (\nabla \alpha \times \nabla p)$$

, (13.3.1)

and taking the cross product of (12.6.4) with $\boldsymbol{\xi}_a$ gives

$$\boldsymbol{\xi}_a \times \frac{\partial \nabla q}{\partial t} + \boldsymbol{\xi}_a \times \nabla(\mathbf{v} \cdot \nabla q) = \boldsymbol{\xi}_a \times \nabla S_v . \tag{13.3.2}$$

As

$$\begin{aligned} \nabla(\mathbf{v} \cdot \nabla q) &= \mathbf{v} \times (\nabla \times \nabla q) + (\mathbf{v} \cdot \nabla)\nabla q + \nabla q \times (\nabla \times \mathbf{v}) + (\nabla q \cdot \nabla)\mathbf{v}\mathbf{v} \\ &= (\mathbf{v} \cdot \nabla)\nabla q + \nabla q \times (\nabla \times \mathbf{v}) + (\nabla q \cdot \nabla)\mathbf{v}\mathbf{v} \end{aligned}$$

, (13.3.2)

becomes

$$\boldsymbol{\xi}_a \times \frac{\partial \nabla q}{\partial t} + \boldsymbol{\xi}_a \times [(\mathbf{v} \cdot \nabla)\nabla q + \nabla q \times (\nabla \times \mathbf{v}) + (\nabla q \cdot \nabla)\mathbf{v}] = \boldsymbol{\xi}_a \times \nabla S_v$$

. (13.3.3)

Defining $\boldsymbol{\xi}_q = \alpha \boldsymbol{\xi}_a \times \nabla q$ as the moist vorticity vector, we get

$$\frac{d\boldsymbol{\xi}_q}{dt} = \frac{\partial}{\partial t}(\alpha \boldsymbol{\xi}_a \times \nabla q) + (\mathbf{v} \cdot \nabla)(\alpha \boldsymbol{\xi}_a \times \nabla q) ,$$

from which

$$\begin{aligned} \frac{d\boldsymbol{\xi}_q}{dt} = {} & \alpha \boldsymbol{\xi}_a \times \frac{\partial}{\partial t}\nabla q - \alpha \nabla q \times \frac{\partial \boldsymbol{\xi}_a}{\partial t} + (\boldsymbol{\xi}_a \times \nabla q)\frac{\partial \alpha}{\partial t} + \alpha \boldsymbol{\xi}_a \times (\mathbf{v} \cdot \nabla)\nabla q \\ & - \alpha \nabla q \times (\mathbf{v} \cdot \nabla)\boldsymbol{\xi}_a + (\boldsymbol{\xi}_a \times \nabla q)(\mathbf{v} \cdot \nabla)\alpha \end{aligned} .$$

(13.3.4)

Equation (13.3.4) becomes

$$\frac{d}{dt}(\boldsymbol{\xi}_q) = -\alpha \boldsymbol{\xi}_a \times \nabla q \times (\nabla \times \mathbf{v}) - \alpha \boldsymbol{\xi}_a \times (\nabla q \cdot \nabla)\mathbf{v}$$

（1） （2）

$$+\alpha(\boldsymbol{\xi}_a \cdot \nabla)\mathbf{v} \times \nabla q - \alpha(\nabla\alpha \times \nabla p) \times \nabla q + \alpha\boldsymbol{\xi}_a \times \nabla S_v \quad . \qquad (13.3.15)$$

（3） （4） （5）

The first term on the right-hand side is the local change in the moist vorticity vector induced by the vorticity, the second and third terms account for the wind-shear effects, and the fourth term represents the interaction between the solenoid term and the water-vapor gradient. If this gradient is less than 90°, the development of the moist vorticity vector is suppressed; if it is larger than 90°, the development of the moist vorticity vector is enhanced.

13.3.2 The Dynamic Vorticity Vector

The dynamic vorticity vector is defined as $\boldsymbol{\xi}_v = \alpha\boldsymbol{\xi}_a \times \mathbf{v}$ (Gao et al., 2005)[6]. The absolute vorticity equation and momentum equation are, respectively,

$$\frac{\partial \boldsymbol{\xi}_a}{\partial t} + \mathbf{v}\cdot\nabla\boldsymbol{\xi}_a = (\boldsymbol{\xi}_a \cdot \nabla)\,\mathbf{v} - \boldsymbol{\xi}_a(\nabla \cdot \mathbf{v}) - \nabla\alpha \times \nabla p \text{ and} \qquad (13.3.16)$$

$$\frac{\partial \mathbf{v}}{\partial t} + (\mathbf{v}\cdot\nabla)\,\mathbf{v} + f\,\mathbf{k}\times\mathbf{v} = -\alpha\nabla p - g\,\mathbf{k} \ . \qquad (13.3.17)$$

Taking (13.3.16)$\times\mathbf{v}$, we get

$$\frac{\partial \boldsymbol{\xi}_a}{\partial t} \times \mathbf{v} + (\mathbf{v}\cdot\nabla)\boldsymbol{\xi}_a \times \mathbf{v} = (\boldsymbol{\xi}_a \cdot \nabla)\,\mathbf{v} \times \mathbf{v} - \boldsymbol{\xi}_a(\nabla \cdot \mathbf{v}) \times \mathbf{v} - \nabla\alpha \times \nabla p \times \mathbf{v} \quad , \qquad (13.3.18)$$

taking $\boldsymbol{\xi}_a \times (13.3.17)$ gives

$$\boldsymbol{\xi}_a \times \frac{\partial \mathbf{v}}{\partial t} + \boldsymbol{\xi}_a \times (\mathbf{v}\cdot\nabla)\,\mathbf{v} + \boldsymbol{\xi}_a \times (f\,\mathbf{k}\times\mathbf{v}) = -\boldsymbol{\xi}_a \times \alpha\nabla p - \boldsymbol{\xi}_a \times g\,\mathbf{k}\,, \qquad (13.3.19)$$

and taking (13.3.18) + 13.3.19, we get

$$\frac{\partial}{\partial t}(\xi_a \times \mathbf{v}) + (\mathbf{v}\cdot\nabla)(\xi_a \times \mathbf{v}) \quad .$$
$$= -\xi_a \times (f\,\mathbf{k}\times\mathbf{v}) + (\xi_a \cdot \nabla)\,\mathbf{v}\times\mathbf{v} - \xi_a(\nabla\cdot\mathbf{v})\times\mathbf{v} - \nabla\alpha\times\nabla p\times\mathbf{v} - \xi_a\times\alpha\nabla p - \xi_a\times g\,\mathbf{k} \tag{13.3.20}$$

From the continuity equation, $\frac{d\rho}{dt} + \rho\nabla\cdot\mathbf{v} = 0$, we also have

$$\nabla\cdot\mathbf{v} = -\frac{1}{\rho}\frac{d\rho}{dt}. \tag{13.3.21}$$

Substituting equation (13.3.21) into equation (13.3.20) yields

$$\frac{d}{dt}(\alpha\xi_a\times\mathbf{v}) = -\alpha\xi_a\times(f\,\mathbf{k}\times\mathbf{v}) + \alpha(\xi_a\cdot\nabla)\,\mathbf{v}\times\mathbf{v} - \alpha\nabla\alpha\times\nabla p\times\mathbf{v} - \alpha^2\xi_a\times\nabla p - \alpha\xi_a\times g\,\mathbf{k}\cdot \tag{13.3.22}$$

Equation (13.3.22) is the equation for the trend in the dynamic vorticity vector. The local change in the dynamic vorticity vector is determined by both the wind-related terms (terms 1, 4, and 5) and the vorticity-related terms (terms 2 and 3).

Gao et al. (2005)[6] used the MVV and DVV in the diagnosis of two-dimensional tropical convective systems. The short-term integration of the trend equations for MVV and DVV can be applied in the nowcasting of convective systems.

13.4 The Ageostrophic Q Vector in a Non-uniformly Saturated Atmosphere

Hoskins (1978)[7] derived a quasi-geostrophic ω equation that included forcing of the divergence of the **Q** vector. The theories related to the quasi-geostrophic **Q** vector have been widely applied (Lawrence,1991; Huang et al., 1997)[8], and various new forms such as the semi-geostrophic **Q** vector, ageostrophic **Q** vector (Davies-Jones,1991)[9], moist **Q** vector

(Yao et al., 2004)[10], generalized **Q** vector (Davies-Jones, 1991)[9], and the **C** vector (Xu, 1992)[11] have been proposed and used. These vectors have been widely applied in the diagnosis of vertical motion, frontogenesis, and secondary circulations. However, the assumption is made that the air is either absolutely dry or saturated. Later, the ageostrophic moist **Q** vector ($\vec{Q}_m$) was used to study the latent-heat effect on torrential rainfall in the case of typhoon 9608 (Yao et al., 2004)[10]. However, such analysis cannot be applied to the transition zone between saturated and non-saturated air.

In this section, as with the derivation of the generalized moist potential vorticity (GMPV) in a non-uniformly saturated atmosphere (Gao et al., 2004)[12], the condensation probability function, $(q/q_s)^k$ (k = 9), is introduced to the thermodynamic equation to reformulate $\mathbf{Q}_m$ as $\mathbf{Q}_{um}$.

13.4.1 The Ageostrophic Q Vector in a Frictionless and Non-uniformly Saturated Atmosphere

The thermodynamic equation in a non-uniformly saturated atmosphere can be expressed as

$$\frac{d\theta^*}{dt} = -\frac{L\theta^*}{c_pT}\frac{d}{dt}[(q/q_s)^k q_s] + \frac{\theta^*}{c_pT}Q_d \quad . \tag{13.4.1}$$

Taking $H^* = -\frac{L\theta^*}{c_pT}\frac{d}{dt}(q/q_s)^k q_s + \frac{\theta^*}{c_pT}Q_d$, this becomes

$\frac{d\theta^*}{dt} = H^*$, where $\theta^* = \theta \exp[\frac{Lq_s}{c_pT}(\frac{q}{q_s})^k]$.

The ageostrophic momentum equations in pressure coordinates can be

written as

$$\frac{du}{dt} = fv_a, \tag{13.4.2}$$

$$\frac{dv}{dt} = -fu_a, \tag{13.4.3}$$

$$\frac{\partial \phi}{\partial p} = -\alpha, \tag{13.4.4}$$

$$\frac{\partial u}{\partial x} + \frac{\partial v}{\partial y} + \frac{\partial \omega}{\partial p} = 0, \tag{13.4.5}$$

$$\frac{d\theta^*}{dt} = H^*, \tag{13.4.6}$$

where $u_a = u - u_g$ and $v_a = v - v_g$ are the zonal and meridional deviations from the geostrophic flows. α is the specific volume, ϕ is the geopotential, *u* and *v* are the zonal and meridional winds, respectively, and ω is the vertical velocity in pressure coordinates.

Taking $f\frac{\partial}{\partial p}(13.4.2)$, we get

$$f\frac{d}{dt}(\frac{\partial u}{\partial p}) = -f(\frac{\partial v}{\partial p}\frac{\partial u}{\partial y} - \frac{\partial v}{\partial y}\frac{\partial u}{\partial p}) + f^2\frac{\partial v_a}{\partial p}, \tag{13.4.7}$$

taking $f\frac{\partial}{\partial p}(13.4.3)$ gives

$$f\frac{d}{dt}(\frac{\partial v}{\partial p})=f(\frac{\partial v}{\partial p}\frac{\partial u}{\partial x}-\frac{\partial v}{\partial x}\frac{\partial u}{\partial p})-f^2\frac{\partial u_a}{\partial p}, \tag{13.4.8}$$

and taking $\frac{\partial}{\partial x}(13.4.6)$, we get

$$\frac{d}{dt}(\frac{\partial \theta^*}{\partial x})=\frac{\partial H^*}{\partial x}-\frac{\partial \mathbf{v}_h}{\partial x}\cdot\nabla_h\theta^*-\frac{\partial \omega}{\partial x}\cdot\frac{\partial \theta^*}{\partial p}, \tag{13.4.9}$$

where $\mathbf{v}_h$ is the horizontal wind vector,

$$\mathbf{v}_h=u\,\mathbf{i}+v\,\mathbf{j},\nabla_h=\frac{\partial}{\partial x}\mathbf{i}+\frac{\partial}{\partial y}\mathbf{j}.$$

From $\theta=T(\frac{p_0}{p})^{\frac{R}{c_p}}$, $p=\rho RT$, we get $\theta=\frac{p}{\rho R}(\frac{p_0}{p})^{\frac{R}{c_p}}$.

Defining $h_\pi=\frac{R}{p}(\frac{p_0}{p})^{\frac{R}{c_p}}$ gives $\theta=\frac{1}{\rho h_\pi}=-\frac{1}{h_\pi}\frac{\partial \phi}{\partial p}$

As $v_g=\frac{1}{f}\frac{\partial \phi}{\partial x}$, equation (13.4.9) becomes

$$\frac{d}{dt}(\frac{\partial \theta}{\partial x})=-[\frac{\partial}{\partial t}(\frac{f}{h_\pi}\frac{\partial v_g}{\partial p})+u\frac{\partial}{\partial x}(\frac{f}{h_\pi}\frac{\partial v_g}{\partial p})+v\frac{\partial}{\partial y}(\frac{f}{h_\pi}\frac{\partial v_g}{\partial p})+\omega\frac{\partial}{\partial p}(\frac{f}{h_\pi}\frac{\partial v_g}{\partial p})]$$
. (13.4.10)

Substituting h_π into equation (13.4.10), the last term of (13.4.10) becomes

$$\omega\frac{\partial}{\partial p}(\frac{f}{h_\pi}\frac{\partial v_g}{\partial p})=\omega f\frac{\partial v_g}{\partial p}(\rho\frac{\partial \theta}{\partial p})+\omega f\frac{\partial v_g}{\partial p}(\theta\frac{\partial \rho}{\partial p})+\omega\frac{f}{h_\pi}\frac{\partial}{\partial p}(\frac{\partial v_g}{\partial p})$$

,

and equation (13.4.10) can then be written as

$$\frac{d}{dt}(\frac{\partial\theta}{\partial x}) = -[\frac{\partial}{\partial t}(\frac{f}{h_\pi}\frac{\partial v_g}{\partial p}) + u\frac{\partial}{\partial x}(\frac{f}{h_\pi}\frac{\partial v_g}{\partial p}) + v\frac{\partial}{\partial y}(\frac{f}{h_\pi}\frac{\partial v_g}{\partial p}) + \omega f\frac{\partial v_g}{\partial p}(\rho\frac{\partial\theta}{\partial p}) + \omega f\frac{\partial v_g}{\partial p}(\theta\frac{\partial\rho}{\partial p}) + \omega\frac{f}{h_\pi}\frac{\partial}{\partial p}(\frac{\partial v_g}{\partial p})]$$

(13.4.11)

Neglecting the small terms $\omega f\frac{\partial v_g}{\partial p}(\theta\frac{\partial\rho}{\partial p})$ and $\omega\frac{f}{h_\pi}\frac{\partial}{\partial p}(\frac{\partial v_g}{\partial p})$,

equation (13.4.11) can be simplified to

$$\frac{d}{dt}(\frac{\partial\theta}{\partial x}) = -\frac{f}{h_\pi}\frac{d}{dt}(\frac{\partial v_g}{\partial p}). \tag{13.4.12}$$

Equation (13.4.9) can also be written as

$$-\frac{f}{h_\pi}\frac{d}{dt}(\frac{\partial v_g}{\partial p}) = \frac{\partial H^*}{\partial x} - \frac{\partial \mathbf{v}_h}{\partial x}\cdot\nabla_h\theta - \frac{\partial\omega}{\partial x}\cdot\frac{\partial\theta}{\partial p}. \tag{13.4.13}$$

Similarly, taking $\frac{\partial}{\partial y}(13.4.6)$ and using $u_g = -\frac{1}{f}\frac{\partial\phi}{\partial y}$ gives

$$\frac{f}{h_\pi}\frac{d}{dt}(\frac{\partial u_g}{\partial p}) = \frac{\partial H^*}{\partial y} - \frac{\partial \mathbf{v}_h}{\partial y}\cdot\nabla_h\theta - \frac{\partial\omega}{\partial y}\cdot\frac{\partial\theta}{\partial p}. \tag{13.4.14}$$

Next, taking $(13.4.8)/h_\pi + (13.4.13)$ and $v_a = v - v_g$, we obtain

$$\frac{f}{h_\pi}\frac{d}{dt}(\frac{\partial v_a}{\partial p}) = \frac{f}{h_\pi}(\frac{\partial v}{\partial p}\frac{\partial u}{\partial x} - \frac{\partial v}{\partial x}\frac{\partial u}{\partial p}) - \frac{f^2}{h_\pi}\frac{\partial u_a}{\partial p} + \frac{\partial H^*}{\partial x} - \frac{\partial \mathbf{v}_h}{\partial x}\cdot\nabla_h\theta - \frac{\partial\omega}{\partial x}\cdot\frac{\partial\theta}{\partial p}$$

, (13.4.15)

and taking $(13.4.7)/h_\pi - (13.4.14)$ and $u_a = u - u_g$, we obtain

$$\frac{f}{h_\pi}\frac{d}{dt}\left(\frac{\partial u_a}{\partial p}\right) = -\frac{f}{h_\pi}\left(\frac{\partial v}{\partial p}\frac{\partial u}{\partial y} - \frac{\partial v}{\partial y}\frac{\partial u}{\partial p}\right) + \frac{f^2}{h_\pi}\frac{\partial v_a}{\partial p} - \frac{\partial H^*}{\partial y} + \frac{\partial \mathbf{v}_h}{\partial y}\cdot\nabla_h\theta + \frac{\partial \omega}{\partial y}\cdot\frac{\partial \theta}{\partial p}$$

. (13.4.16)

Using approximation: $\frac{d}{dt}\left(\frac{\partial v_a}{\partial p}\right) = 0$ and $\frac{d}{dt}\left(\frac{\partial u_a}{\partial p}\right) = 0$,

equations (13.4.15) and (13.4.16) become

$$\frac{f}{h_\pi}\left(\frac{\partial v}{\partial p}\frac{\partial u}{\partial x} - \frac{\partial v}{\partial x}\frac{\partial u}{\partial p}\right) - \frac{f^2}{h_\pi}\frac{\partial u_a}{\partial p} + \frac{\partial H^*}{\partial x} - \frac{\partial \mathbf{v}_h}{\partial x}\cdot\nabla_h\theta - \frac{\partial \omega}{\partial x}\cdot\frac{\partial \theta}{\partial p} = 0$$

(13.4.17)

$$\frac{f}{h_\pi}\left(\frac{\partial v}{\partial p}\frac{\partial u}{\partial y} - \frac{\partial v}{\partial y}\frac{\partial u}{\partial p}\right) - \frac{f^2}{h_\pi}\frac{\partial v_a}{\partial p} + \frac{\partial H^*}{\partial y} - \frac{\partial \mathbf{v}_h}{\partial y}\cdot\nabla_h\theta - \frac{\partial \omega}{\partial y}\cdot\frac{\partial \theta}{\partial p} = 0\,.$$

(13.4.18)

Using $\sigma_\pi = -h_\pi\frac{\partial \theta}{\partial p}$, equations (13.4.17) and (13.4.18) can be

written as

$$f\left(\frac{\partial v}{\partial p}\frac{\partial u}{\partial x} - \frac{\partial v}{\partial x}\frac{\partial u}{\partial p}\right) - h_\pi\cdot\frac{\partial \mathbf{v}_h}{\partial x}\cdot\nabla_h\theta + \frac{\partial(h_\pi H^*)}{\partial x} = f^2\frac{\partial u_a}{\partial p} - \sigma_\pi\frac{\partial \omega}{\partial x}$$

and (13.4.19)

$$f\left(\frac{\partial v}{\partial p}\frac{\partial u}{\partial y} - \frac{\partial v}{\partial y}\frac{\partial u}{\partial p}\right) - h_\pi\cdot\frac{\partial \mathbf{v}_h}{\partial y}\cdot\nabla_h\theta + \frac{\partial(h_\pi H^*)}{\partial y} = f^2\frac{\partial v_a}{\partial p} - \sigma_\pi\frac{\partial \omega}{\partial y}\cdot$$

. (13.4.20)

Defining

$$Q_{umx} = \frac{1}{2}[f(\frac{\partial v}{\partial p}\frac{\partial u}{\partial x} - \frac{\partial u}{\partial p}\frac{\partial v}{\partial x}) - h_\pi \frac{\partial \mathbf{v}_h}{\partial x}\cdot\nabla_h\theta + \frac{\partial(h_\pi H^*)}{\partial x}] \quad (13.4.21)$$

$$Q_{umy} = \frac{1}{2}[f(\frac{\partial v}{\partial p}\frac{\partial u}{\partial y} - \frac{\partial u}{\partial p}\frac{\partial v}{\partial y}) - h_\pi \frac{\partial \mathbf{v}_h}{\partial y}\cdot\nabla_h\theta + \frac{\partial(h_\pi H^*)}{\partial y}] \quad (13.4.22)$$

and substituting H^* into equations (13.4.21) and (13.4.22), we get

$$Q_{umx} = \frac{1}{2}[f(\frac{\partial v}{\partial p}\frac{\partial u}{\partial x} - \frac{\partial u}{\partial p}\frac{\partial v}{\partial x}) - h_\pi \frac{\partial \mathbf{v}_h}{\partial x}\cdot\nabla_h\theta - \frac{\partial}{\partial x}(\frac{LR}{c_pP}\frac{d}{dt}(q_s(\frac{q}{q_s})^k) - \frac{R}{c_pP}Q_d)] \quad (13.4.23)$$

$$Q_{umy} = \frac{1}{2}[f(\frac{\partial v}{\partial p}\frac{\partial u}{\partial y} - \frac{\partial u}{\partial p}\frac{\partial v}{\partial y}) - h_\pi \frac{\partial \mathbf{v}_h}{\partial y}\cdot\nabla_h\theta - \frac{\partial}{\partial y}(\frac{LR}{c_pP}\frac{d}{dt}(q_s(\frac{q}{q_s})^k) - \frac{R}{c_pP}Q_d)]. \quad (13.4.24)$$

We then have

$$Q_{umx} = \frac{1}{2}f^2(\frac{\partial u_a}{\partial p} - \sigma_\pi \frac{\partial \omega}{\partial x}) \quad \text{and} \quad (13.4.25)$$

$$Q_{umy} = \frac{1}{2}f^2(\frac{\partial v_a}{\partial p} - \sigma_\pi \frac{\partial \omega}{\partial y}). \quad (13.4.26)$$

Here, σ is a static stability parameter ($\sigma_\pi = -h_\pi \frac{\partial \theta}{\partial p}$, $h_\pi = \frac{\alpha}{\theta}$).

Taking $\frac{\partial(14.4.25)}{\partial x} + \frac{\partial(14.4.26)}{\partial y}$ leads to

$$\frac{\partial Q_{umx}}{\partial x} + \frac{\partial Q_{umy}}{\partial y} = -\frac{1}{2}(f^2\frac{\partial^2\omega}{\partial p^2} + \sigma_\pi\nabla^2\omega),$$

and taking $\mathbf{Q}_{um} = Q_{umx}\,\mathbf{i} + Q_{umy}\,\mathbf{j}$ leads to

$$\nabla \cdot \mathbf{Q}_{um} = \frac{\partial Q_{umx}}{\partial x} + \frac{\partial Q_{umy}}{\partial y}.$$

The ageostrophic ω equation including diabatic heating can be expressed as

$$f\frac{\partial^2 \omega}{\partial p^2} + \nabla_h{}^2(\sigma_\pi \omega) = -2\nabla_h \cdot \mathbf{Q}_{um}. \tag{13.4.27}$$

Equation (13.4.27) shows that $\nabla_h \cdot \mathbf{Q}_{um}$ is a only forcing term in the ageostrophic diabatic ω equation. If the vertical velocity has a wave-like solution— $\omega \propto \nabla_h \cdot \mathbf{Q}_{um}$ —then when $\nabla_h \cdot \mathbf{Q}_{um} > 0$, $\omega > 0$ and when $\nabla_h \cdot \mathbf{Q}_{um} < 0$, $\omega < 0$. Subsidence corresponds to the divergence of $\mathbf{Q}_{um}$, whereas ascent corresponds to the convergence of $\mathbf{Q}_{um}$. As for $\mathbf{Q}_{um}$, the direction of $\mathbf{Q}_{um}$ is in the direction of upward motion. Equation (13.4.27) shows that there is a close relation between $\nabla_h \cdot \mathbf{Q}_{um}$ and rainfall; $\nabla_h \cdot \mathbf{Q}_{um}$ is also the forcing of the ageostrophic ω equation. Thus, the convergence of $\mathbf{Q}_{um}$ enhances upward motion and secondary circulations, which is favorable to the generation of torrential rainfall.

13.4.2 Simplified Formulations of the Q Vector

If diabatic heating is excluded ($Q_d = 0$), (13.4.23) and (13.4.24) become

$$Q_{umx} = \frac{1}{2}[f(\frac{\partial v}{\partial p}\frac{\partial u}{\partial x} - \frac{\partial u}{\partial p}\frac{\partial v}{\partial x}) - h_\pi \frac{\partial \mathbf{v}_h}{\partial x}\cdot\nabla_h\theta - \frac{\partial}{\partial x}(\frac{LR}{c_p p}\frac{d}{dt}(q_s(\frac{q}{q_s})^k))] \tag{13.4.28}$$

$$Q_{umy} = \frac{1}{2}[f(\frac{\partial v}{\partial p}\frac{\partial u}{\partial y} - \frac{\partial u}{\partial p}\frac{\partial v}{\partial y}) - h_\pi \frac{\partial \mathbf{v}_h}{\partial y}\cdot\nabla_h\theta - \frac{\partial}{\partial y}(\frac{LR}{c_p p}\frac{d}{dt}(q_s(\frac{q}{q_s})^k))] \cdot \tag{13.4.29}$$

These equations represent the moist **Q** vector ($\mathbf{Q}_{um}$) in an adiabatic, frictionless, non-uniform, saturated atmosphere.

In dry air, $q = 0$, $(q/q_s)^k = 0$, $\theta^* = \theta$, and $\nabla_h\cdot(\frac{LR}{c_p p}\frac{d}{dt}(q_s(\frac{q}{q_s})^k) = 0$; thus, $\mathbf{Q}_{um}$ is not a function of q or q_s. Hence, (13.4.28) and (13.4.29) can be further simplified to

$$Q_{umx} = \frac{1}{2}[f(\frac{\partial v}{\partial p}\frac{\partial u}{\partial x} - \frac{\partial u}{\partial p}\frac{\partial v}{\partial x}) - h_\pi \frac{\partial \mathbf{v}_h}{\partial x}\cdot\nabla_h\theta] \tag{13.4.30}$$

$$Q_{umy} = \frac{1}{2}[f(\frac{\partial v}{\partial p}\frac{\partial u}{\partial y} - \frac{\partial u}{\partial p}\frac{\partial v}{\partial y}) - h_\pi \frac{\partial \mathbf{v}_h}{\partial y}\cdot\nabla_h\theta]. \tag{13.4.31}$$

Equations (13.4.30) and (13.4.31) represent the Q vector in a dry atmosphere.

In a saturated atmosphere, $q = q_s$, $(q/q_s)^k = 1$, $\theta^* = \theta_e$, and

$\nabla_h \cdot (\frac{LR}{c_p p} \frac{d}{dt}(q_s (\frac{q}{q_s})^k)) = \nabla_h \cdot (\frac{LR}{c_p p} \frac{dq_s}{dt}) \sim \nabla_h \cdot (\frac{LR\omega}{c_p p} \frac{\partial q_s}{\partial p})$; thus,

$\mathbf{Q}_{um}$ is not a function of q. Hence, (13.4.28) and (13.4.29) become

$$Q_{umx} = \frac{1}{2}[f(\frac{\partial v}{\partial p}\frac{\partial u}{\partial x} - \frac{\partial u}{\partial p}\frac{\partial v}{\partial x}) - h_\pi \frac{\partial \mathbf{v}_h}{\partial x} \cdot \nabla_h \theta - \frac{\partial}{\partial x}(\frac{LR\omega}{c_p p}\frac{\partial q_s}{\partial p})] \tag{13.4.32}$$

$$Q_{umy} = \frac{1}{2}[f(\frac{\partial v}{\partial p}\frac{\partial u}{\partial y} - \frac{\partial u}{\partial p}\frac{\partial v}{\partial y}) - h_\pi \frac{\partial \mathbf{v}_h}{\partial y} \cdot \nabla_h \theta - \frac{\partial}{\partial y}(\frac{LR\omega}{c_p p}\frac{\partial q_s}{\partial p})]. \tag{13.4.33}$$

Equations (13.4.32) and (13.4.33) represent the moist **Q** vector in a saturated atmosphere.

In an unsaturated atmosphere, $0 < q < q_s$, $0 < (q/q_s)^k < 1$, $\theta^* \neq \theta$, and $\theta^* \neq \theta_e$; thus, $\nabla_h \cdot (\frac{LR}{C_p p} \frac{d}{dt}(q_s (\frac{q}{q_s})^k)$ is a function of q and q_s, which is favorable to the generation of $\mathbf{Q}_{um}$. This suggests that $\mathbf{Q}_{um}$ plays a role in an unsaturated atmosphere through $\nabla_h \cdot (\frac{LR}{c_p p} \frac{d}{dt}(q_s (\frac{q}{q_s})^k)$.

$\mathbf{Q}_{um}$ denotes the **Q** vector in dry air, unsaturated air, or saturated air

and can be applied to investigations of the driving role of vertical motion in the transition zone between saturated and unsaturated air.

13.5 A Dynamic Forecasting Method Based on the Q Vector

In the last section, the ageostrophic **Q** vector ($\mathbf{Q}_{um}$) in a non-uniformly saturated atmosphere was introduced. This vector accounts for the release of latent heat as well as relative humidity and has a more complete physical meaning than the saturated **Q** vector ($\mathbf{Q}_{um}$).

To demonstrate the application of $\mathbf{Q}_{um}$ in nowcasting, a torrential rainfall event that occurred between 00:00 UTC on 4 July and 12:00 UTC on 5 July 2003 is analyzed here.

Figure 13.5.1 shows the evolution with time of the meridional distribution of the six-hour cumulative rainfall amount along 118°E from 00:00 UTC on 4 July to 12:00 UTC on 5 July 2003, as calculated using WRF modeling data. The maximum six-hour rainfall occurred between 00:00 and 06:00 UTC on 5 July. This comparison between Q_{umx} and Q_{umy} and the relative humidity shows that $\mathbf{Q}_{um}$ appeared in the region where the relative humidity was over 70%.

Yao (2004) used the ageostrophic moist Q vector ($\mathbf{Q}_m$) to diagnose the torrential rainfall associated with typhoon 9608 and found that the collocation between the divergence of $\mathbf{Q}_m$ and the rainfall area was better than that between the dry **Q** vector in the lower troposphere and the rainfall area, thus demonstrating the effect of latent heat on rainfall. As the

saturation of the atmosphere is non-uniform, it is reasonable to introduce the relative humidity into the **Q** vector to give $\mathbf{Q}_{um}$. During meiyu torrential rainfall events, the divergence of $\mathbf{Q}_{um}$ in the lower troposphere is a better precursor of the formation and development of rainfall than either the divergence of the dry **Q** vector, the divergence of $\mathbf{Q}_m$, or the vertical velocity, ω (see Figures 13.5.2 (a) and (b), 13.5.3 (a), (b), and (c), and 13.5.4. Figures 13.5.3 (b) and 13.5.3 (c) show the evolution of the meridional distribution of $\nabla_h \cdot \mathbf{Q}_{dry}$ and $\mathbf{Q}_m$ along 118°E at 750 hPa. Although the rainfall area contains the convergence zones of the dry **Q** vector and the ageostrophic moist **Q** vector ($\mathbf{Q}_m$), these two zones are much smaller than the rainfall area. The distributions of the non-uniformly saturated **Q** vector ($\mathbf{Q}_{um}$) and the rainfall are well matched, which demonstrates the advantage of using the non-uniformly saturated **Q** vector.

A comparison of Figures 13.5.1 and 13.5.3 (a) shows that the rainfall began after 00:00 UTC on 4 July 2003. Rain bands formed over the zone of strong convergence of $\mathbf{Q}_{um}$ (i.e., the zone of large $-\nabla_h \cdot \mathbf{Q}_{um}$). The rain bands moved together with this zone from north of 33°N to be located around 33.0°N–31.5°N and 30°N. The two rainfall maxima occurred between 17:00 UTC, 4 July and 00:00 UTC, 5 July and between 23:00 UTC, 4 July and 08:00 UTC, 5 July, whereas the two strong convergence centers of the non-uniformly saturated **Q** vector ($-\nabla_h \cdot \mathbf{Q}_{um}$) were located at 32°N at 17:00 UTC on 4 July and at 31°N at 23:00 UTC on 4

July. This indicates that $\mathbf{Q}_{um}$ can be used to provide good predictions of the center of the area of maximum rainfall. As shown in Figures 13.5.1 and 13.5.3 (a), the horizontal convergence of the non-uniformly saturated **Q** vector ($-\nabla_h \cdot \mathbf{Q}_{um}$) increases with increasing subsequent six-hour rainfall. The six-hour cumulative rainfall amount reached its maximum of 30 mm between 00:00 and 06:00 UTC on 5 July (Figure 13.5.5 (a)), whereas the six-hour average of $-\nabla_h \cdot \mathbf{Q}_{um}$ reached its maximum value (-9×10^{-16} hPa^{-1} s^{-3}) between 08:00 UTC on 4 July and 00:00 UTC on 5 July (Figure 13.5.5 (b)) and thus was ahead of the rainfall. This suggests that $\nabla_h \cdot \mathbf{Q}_{um}$ is a good indicator of future six-hour rainfall and can be used as the basis of a dynamic forecasting method.

As $\nabla_h \cdot \mathbf{Q}_{um}$ constitutes the forcing in the ageostrophic ω equation, the horizontal convergence of the non-uniformly saturated **Q** vector may enhance upward motion and secondary circulation, thus leading to the generation of torrential rainfall. This demonstrates the application of the **Q** vector.

13.6 The E Vector

The interactions between motion at different scales is important. For example, cyclonic convergence favors the formation and development of mesoscale systems, whereas anticyclonic divergence does not favor their formation and development. In this section, the E vector (James 1995)[13] is introduced into the synoptic background favorable to the development of mesoscale systems

First, motion can be partitioned into its mean and perturbation

components:

$$u = \bar{u} + u' \tag{13.6.1}$$

$$v = \bar{v} + v', \tag{13.6.2}$$

where $\bar{u}$, $\bar{v}$ denote the mean zonal and meridional components of the wind and u', v' denote the zonal and meridional perturbation components of the wind, respectively. The quasi-geostrophic theory is applicable to synoptic systems.

The horizontal momentum equations can be expressed as

$$\frac{\partial u}{\partial t} + \mathbf{v}\cdot\nabla u = -\frac{1}{\rho}\frac{\partial p}{\partial x} + fv \quad \text{and} \tag{13.6.3}$$

$$\frac{\partial v}{\partial t} + \mathbf{v}\cdot\nabla v = -\frac{1}{\rho}\frac{\partial p}{\partial y} - fu. \tag{13.6.4}$$

Based on the assumption of geostrophic balance, taking the time averages of the horizontal momentum equations gives

$$\overline{\mathbf{v}\cdot\nabla u} = fv_a, \tag{13.6.5}$$

$$\overline{\mathbf{v}\cdot\nabla v} = -fu_a, \tag{13.6.6}$$

where u_a, v_a are the deviations from the geostrophic flows:

$$u_a = u - u_g, \quad v_a = v - v_g. \tag{13.6.7}$$

Equation (13.6.5) shows that the entrance zone of the high-level jet has a poleward ageostrophic flow, whereas, in the exit zone, the flow is directed toward the equator. Thus, high-level convergence is generated on

the equator side of the exit zone, and high-level divergence is generated on the poleward side of this zone. As a result of the conservation of mass, upward motion is induced in the middle troposphere over the divergence zone, and subsidence is generated in the lower stratosphere to compensate for the mass loss. Conversely, downward motion is induced in the middle troposphere over the convergence zone, and upward motion is generated in the lower stratosphere to offset the mass gain. Because the stratosphere has a high degree of static stability, the vertical motion in the stratosphere are rather weak. Meridional circulations with opposite directions are also produced in the troposphere at the entrance and exit of the jet (Figure 13.6.1). The updrafts induce cyclonic vortices in the lower troposphere and anticyclonic vortices in the upper troposphere; these generate the transient vortices near jets that are observed in synoptic charts.

The formation and transport of the transient vorticity in turn affect the mean circulations. Given that the transient vortices in the upper troposphere are two-dimensional and non-divergent (note that, although the transient vortices are produced by convergence, the vortices themselves are non-divergent), we have

$$\frac{\partial u'}{\partial x} + \frac{\partial v'}{\partial y} = 0 . \tag{13.6.8}$$

The covariance between horizontal winds of the transient vortices can be written in matrix form:

$$C = \begin{pmatrix} \overline{u'^2} & \overline{u'v'} \\ \overline{u'v'} & \overline{v'^2} \end{pmatrix} . \tag{13.6.9}$$

(13.6.9) can be re-written as the sum of a diagonal matrix and a symmetric matrix:

$$C=\begin{pmatrix} K & 0 \\ 0 & K \end{pmatrix}+\begin{pmatrix} M & N \\ N & -\mathrm{M} \end{pmatrix}, \tag{13.6.10}$$

where $K=(\overline{u'^2+v'^2})/2,\quad M=(\overline{u'^2-v'^2})/2,\quad N=\overline{u'v'}$.

Assuming a frictionless atmosphere, equations (13.6.1) and (13.6.2) are then expanded and substituted into equations (13.6.5) and (13.6.6), respectively; using the horizontal non-divergence (equation (13.6.8)), we can then obtain

$$\bar{\mathbf{v}}\cdot\nabla\bar{u}+(\overline{u'^2})_x+(\overline{u'v'})_y=fv_a \tag{13.6.11}$$

$$\bar{\mathbf{v}}\cdot\nabla\bar{u}+(\overline{v'^2})_y+(\overline{u'v'})_x=-fu_a\,. \tag{13.6.12}$$

Equations (13.6.11) and (13.6.12) show that, if the transient vortices change, the mean circulations and ageostrophic adjustment respond correspondingly. (13.6.11) and (13.6.12) are used to eliminate the ageostrophic wind to give the vorticity equation:

$$\bar{\mathbf{v}}\cdot\nabla\bar{\zeta}+\nabla\cdot(\overline{\mathbf{v}'\zeta'})=0\,, \tag{13.6.13}$$

where $\zeta'=v'_x-u'_y$ is the transient vorticity. The change in mean vorticity corresponds to the convergence of the transient vorticity flux.

The transient vortex flux and divergence can be written as

$$\overline{\mathbf{v}'\zeta'}=(-M_y+N_x,\ -M_x-N_y) \quad \text{and} \tag{13.6.14}$$

$$\nabla\cdot(\overline{\mathbf{v}'\zeta'})=-2M_{xy}+N_{xx}-N_{yy}\,, \text{ respectively.} \tag{13.6.15}$$

Generally, the changes in transient speed in the zonal direction are relatively small, whereas those in the meridional direction are relatively large. Assuming that $|N_{xx}|\sim|N_{yy}|$ and neglecting N_{xx} in (13.6.15),

we have

$$\nabla \cdot (\overline{\mathbf{v}' \zeta'}) \simeq -2M_{xy} - N_{yy} . \tag{13.6.16}$$

The E vector is defined as

$$E = (-2M, -N) = (\overline{v'^2 - u'^2}, -\overline{u'v'}), \tag{13.6.17}$$

and (13.6.17) can also be written as

$$\nabla \cdot (\overline{\mathbf{v}' \zeta'}) \approx \frac{\partial}{\partial y}(\nabla \cdot E) . \tag{13.6.18}$$

When the divergence of the E vector decreases with increasing latitude, i.e., $\frac{\partial}{\partial y}(\nabla \cdot E) < 0$, then $\nabla \cdot (\overline{\mathbf{v}' \zeta'}) < 0$. Substituting these into (13.6.13), we get $\overline{\mathbf{v}} \cdot \nabla \overline{\zeta} > 0$, which suggests that the mean vorticity is transported to the area where the E vector decreases with increasing latitude by the mean-flow. Thus, convergence of the transient vorticity flux occurs in this area, the vorticity increases, and the cyclone develops (see Figure 13.6.2).

As the development of a cyclone (anticyclone) is favorable (unfavorable) to the formation and development of mesoscale systems, mesoscale systems can develop when the divergence of the E vector decreases with increasing latitude and can be suppressed when the divergence of the E vector increases with increasing latitude. Thus, the E vector links the mean circulations and perturbation circulations, and also allows dynamic predictions of the background circulations in developing mesoscale systems to be made.

13.7 The Wave-action Vector

In atmospheric studies, a physical quantity can be separated into a mean state and a perturbation component: the mean state is constructed by taking the spatial or temporal average, whereas the perturbation (or disturbance) is a deviation from the mean state. Such separation is an important method of the study of atmospheric waves, and the interaction between the mean state and the perturbation can be depicted by the "wave-action vector" or "wave-action equation".

The wave-action equation can be written as

$$\frac{\partial A}{\partial t}+\nabla\cdot\mathbf{F}=S\,, \tag{13.7.1}$$

where A is the wave-action density, which is a form of energy, $\mathbf{F}$ is the wave-action vector, and S denotes the source/sink term, which incorporates a turbulence-induced friction term and diabatic heating. For a perturbation with a small amplitude, A and $\mathbf{F}$ are second-order perturbation quantities. If the source/sink term, S, is excluded, equation (13.7.1) has the form of a conservation law:

$$\frac{\partial A}{\partial t}+\nabla\cdot\mathbf{F}=0\,. \tag{13.7.2}$$

For a closed system, the wave action is conserved; i.e.,

$$\frac{d}{dt}\iiint A dxdydz=0\,. \tag{13.7.3}$$

From (13.7.2), we get

$$\frac{\partial A}{\partial t}=-\nabla\cdot\mathbf{F}\,. \tag{13.7.4}$$

Equation (13.7.4) states that the divergence or convergence of the wave-action vector can cause a local change in the wave-action density. Thus, if the spatial distribution of the wave-action vector is known, the change in wave energy can be predicted.

Previously, the wave-action vector that was used was two-dimensional,

quasi-geostrophic, and hydrostatic, which is suitable for application to large-scale systems but not ageostrophic and non-hydrostatic mesoscale systems. If a mesoscale wave-flow interaction theory could be established, then the application of the wave-action vector could be extended to the study of mesoscale systems, which would be helpful in studies of the development of such systems.

14.7.1 Control Equations

The "momentum–Casimir" and "energy–Casimir" methods that will be discussed in this subsection are important methods for studying wave-flow interactions. The "energy–Casimir" method was developed in the former Soviet Union by V. I. Arnol'd in the 1960s. This method combined the variational principle and prior estimates in the study of the nonlinear stability of two-dimensional, inviscid incompressible fluids. Two criteria were established: these are known as the first and second Arnol'd theorems. A related method known as the "energy–Casimir" method was also developed. The basic idea is to construct the Hamilton invariant from the energy and generalized potential vorticity and to construct a Hamiltonian system with governing equations. This Hamiltonian system generally has an infinite number of dimensions and is irregular. There is also a nontrivial invariant functional, C_β, the so-called Casimir function. Generally speaking, the basic state (steady state) corresponds to the stagnation point of $H_\beta + C_\beta$ (the variation of $H_\beta + C_\beta$ is zero; $\delta\left(H_\beta + C_\beta\right) = 0$; H_β is the Hamiltonian function). If the second variation of $H_\beta + C_\beta$ is positive or negative, the upper limit of the growth of the perturbation is derived. Thus, the basic state is formally

stable.

McIntyre and Shepherd (1987) and Haynes (1988) applied the "energy–Casimir" method in their investigations of the wave-action equation. When using the barotropic potential vorticity equation to derive the wave-action conservation equation for a finite-amplitude disturbance in a non- parallel basic shear flow, McIntyre and Shepherd (1987) noticed that the invariant, $H_\beta + C_\beta = \iint (\frac{1}{2}|\mathbf{v}|^2 + C_\beta(\lambda))dxdy$ (where $\mathbf{v}$ is the velocity, and $C_\beta = C_\beta(\lambda)$ is the Casimir function). The first-order variation of this is zero, which means that a local conservation relation for the disturbance can be derived and its terms expressed by the square of quantities of the disturbance. In other words, by choosing the appropriate form of the Casimir function, $C_\beta(\lambda)$, we can obtain

$$\frac{1}{2}|\mathbf{v}_0 + \mathbf{v}_e|^2 - \frac{1}{2}|\mathbf{v}_0|^2 + C_\beta(\lambda_0 + \lambda_e) - C_\beta(\lambda_0). \tag{13.7.5}$$

This can be written as the sum of the square of quantities of the disturbance and the disturbance divergence (the subscript "0" represents the fundamental state, and the subscript "e" represents the disturbed state that deviates from the fundamental state); the conservation equation for the wave action can then be derived. Based on the works of McIntyre and Shepherd (1987), Haynes (1988)[14] abandoned the constraints of the dynamic Hamiltonian system and, by considering the forced dissipation, the equations of action for the waves of a finite-amplitude disturbance in zonal symmetric and non-zonal symmetric basic flows were derived for an isentropic coordinate system.

The momentum–Casimir method is similar to the energy–Casimir method: the main difference between them is that the Hamiltonian

function (H) in the momentum–Casimir method represents momentum rather than energy.

We consider a three-dimensional, inviscid, compressible, adiabatic, rotating and nonhydrostatic flow in a β plane described in Cartesian coordinates (x, y, z, t). The system of equations Governing equations are

$$\frac{\partial u}{\partial t}+(\mathbf{v}\cdot\nabla)u-(f_0+\beta y)v=-\frac{1}{\rho}\frac{\partial p}{\partial x}, \tag{13.7.6}$$

$$\frac{\partial v}{\partial t}+(\mathbf{v}\cdot\nabla)v+(f_0+\beta y)u=-\frac{1}{\rho}\frac{\partial p}{\partial y}, \tag{13.7.7}$$

$$\frac{\partial w}{\partial t}+(\mathbf{v}\cdot\nabla)w=-\frac{1}{\rho}\frac{\partial p}{\partial z}-g, \tag{13.7.8}$$

$$\frac{\partial \theta}{\partial t}+(\mathbf{v}\cdot\nabla)\theta=0, \tag{13.7.9}$$

$$\frac{\partial \rho}{\partial t}+\nabla\cdot(\rho\mathbf{v})=0, \tag{13.7.10}$$

$$p=\rho RT, \tag{13.7.11}$$

$$\theta=T(\frac{p_0}{p})^{\frac{R}{c_p}}. \tag{13.7.12}$$

From equations (13.7.6)–(13.7.11), the equation for the conservation of the potential vorticity in dry air, which is often used in synoptic diagnosis and analysis, can be derived:

$$\frac{\partial Q}{\partial t}+(\mathbf{v}\cdot\nabla)Q=0, \tag{13.7.13}$$

where $Q=\xi_a\cdot\nabla\theta/\rho$ is the Ertel potential vorticity, and

$$\boldsymbol{\xi}_a = (\partial w/\partial y - \partial v/\partial z, \partial u/\partial z - \partial w/\partial x, \partial v/\partial x - \partial u/\partial y + f_0 + \beta y)$$

.

In order to use the momentum–Casimir and energy–Casimir methods to derive the wave-action equation, we introduce the Casimir function, C_β. C_β is defined as a primary function of the potential vorticity and potential temperature: $C_\beta = C_\beta(\mathrm{Q}, \theta)$. Its conservation can be proved by using equations (13.7.9) and (13.7.13); that is,

$$\frac{\partial C_\beta}{\partial t} + \mathbf{v} \cdot \nabla C_\beta = 0 . \tag{13.7.14}$$

The equation for the momentum in the x-direction can be written as

$$\frac{\partial U}{\partial t} + \mathbf{v} \cdot \nabla U + \frac{1}{\rho}\frac{\partial p}{\partial x} = 0 , \tag{13.7.15}$$

where $U = u - f_0 y - \beta y^2/2$ is the absolute momentum density in the x-direction. In addition, the total energy equation for dry air can be derived from equations (13.7.6)–(13.7.11):

$$\frac{\partial E}{\partial t} + \mathbf{v} \cdot \nabla E + \frac{1}{\rho}\nabla \cdot (\mathbf{v}p) = 0 , \tag{13.7.16}$$

where $E = \frac{1}{2}u^2 + \frac{1}{2}v^2 + \frac{1}{2}w^2 + gz + c_v T$ is the total energy density, which is the sum of the kinetic energy, potential energy, and internal energy of dry air.

By adding equation (13.7.14) to equation (13.7.15) and equation (13.7.16), the following pseudo-momentum and pseudo-energy equations

can be obtained by using the mass continuity equation (13.7.10):

$$\frac{\partial}{\partial t}[\rho(U+C_\beta)]+\nabla\cdot[\rho\mathbf{v}(U+C_\beta)]+\frac{\partial p}{\partial x}=0 \qquad (13.7.17)$$

$$\frac{\partial}{\partial t}[\rho(E+C_\beta)]+\nabla\cdot[\rho\mathbf{v}(E+C_\beta)]+\nabla\cdot(\mathbf{v}p)=0\,, \qquad (13.7.18)$$

where , $\rho(U+C_\beta)$ and $\rho(E+C_\beta)$ are known as the pseudo-momentum and pseudo-energy respectively. Next, we will use these two equations to derive the conservation equations for the pseudo-momentum and pseudo-energy wave action.

13.7.2 The Pseudo-momentum Wave-action Equation

In this section, we use the momentum–Casimir method (Ran et al., 2007)[15] to derive the pseudo-momentum wave-action equation from the pseudo-momentum equation. It is assumed that a physical quantity can be written as the sum of the fundamental state and the perturbed state; that is

$$u=u_0(y,z)+u_e,\ \ v=v_e,\ \ w=w_e,\ \ p=p_0^*(y,z)+p_e,$$

$$\rho=\rho_0(y,z)+\rho_e,$$

$$T=T_0(y,z)+T_e,\theta=\theta_0(y,z)+\theta_e, \text{ and } \ q=q_0(y,z)+q_e,$$

(13.7.19)

where the subscript "0" represents the fundamental state and the subscript "e" represents the perturbed state. Here, we assume that the fundamental state is steady and is a function of y and z only. In addition, the y- and z-velocities of the fundamental state are zero: that is $v_0=0$ and

$w_0 = 0$. The basic state satisfies the following relations describing the geostrophic equilibrium and static equilibrium:

$$(f_0 + \beta y)u_0 = -\frac{1}{\rho_0}\frac{\partial p_0^*}{\partial y}, \tag{13.7.20}$$

$$\frac{1}{\rho_0}\frac{\partial p_0^*}{\partial z} = -g, \tag{13.7.21}$$

$$p_0^* = \rho_0 R T_0 \quad \text{, and} \tag{13.7.22}$$

$$\theta_0 = T_0 (\frac{p_0}{p_0^*})^{\frac{R}{c_p}}. \tag{13.7.23}$$

Taking the partial derivatives of both sides of equation (13.7.20) and then using equations (13.7.21)–(13.7.23), we obtain

$$(f_0 + \beta y)\frac{\partial u_0}{\partial z} = -g\frac{\partial \ln \theta_0}{\partial y} + (f_0 + \beta y)u_0 \frac{\partial \ln \theta_0}{\partial z}. \tag{13.7.24}$$

This equation represents the relationship between the vertical shear of the basic flow and the spatial gradient of the potential temperature of the basic state. If the second term on the right-hand side of this equation is omitted, the equation represents the thermal-wind equilibrium.

For small-amplitude disturbances, the corresponding linearized perturbation equations are

$$\frac{\partial u_e}{\partial t} = (f_0 + \beta y)v_e - u_0\frac{\partial u_e}{\partial x} - v_e\frac{\partial u_0}{\partial y} - w_e\frac{\partial u_0}{\partial z} - \frac{1}{\rho_0}\frac{\partial p_e}{\partial x}, \tag{13.7.25}$$

$$\frac{\partial v_e}{\partial t} = -(f_0 + \beta y)u_e - u_0\frac{\partial v_e}{\partial x} - \frac{1}{\rho_0}\frac{\partial p_e}{\partial y} + \frac{\rho_e}{\rho_0^2}\frac{\partial p_0}{\partial y}, \tag{13.7.26}$$

$$\frac{\partial w_e}{\partial t} = -u_0 \frac{\partial w_e}{\partial x} - \frac{1}{\rho_0}\frac{\partial p_e}{\partial z} - g\frac{\rho_e}{\rho_0}, \tag{13.7.27}$$

$$\frac{\partial \theta_e}{\partial t} = -u_0 \frac{\partial \theta_e}{\partial x} - v_e \frac{\partial \theta_0}{\partial y} - w_e \frac{\partial \theta_0}{\partial z}. \tag{13.7.28}$$

Suppose that the basic state Ertel potential vorticity, Q_0, is given by

$$Q_0 = \frac{\boldsymbol{\xi}_{\alpha 0} \cdot \nabla \theta_0}{\rho_0}, \tag{13.7.29}$$

where $\boldsymbol{\xi}_{\alpha 0} = (0, \partial u_0/\partial z, f_0 + \beta y - \partial u_0/\partial y)$, then the corresponding perturbed Ertel potential vorticity, Q_e, can be expressed as

$$Q_e = \frac{1}{\rho}(\boldsymbol{\xi}_{ae} \cdot \nabla \theta_0 + \boldsymbol{\xi}_{ae} \cdot \nabla \theta_e + \boldsymbol{\xi}_{a0} \cdot \nabla \theta_e - \rho_e Q_0), \tag{13.7.30}$$

where

$$\boldsymbol{\xi}_{ae} = (\partial w_e/\partial y - \partial v_e/\partial z, \partial u_e/\partial z - \partial w_e/\partial x, \partial v_e/\partial x - \partial u_e/\partial y).$$

We expand the Casimir function, $C_\beta(Q,\theta)$, at (Q_0, θ_0) as a Taylor series and consider a small-amplitude disturbance, omitting disturbances corresponding to the third order and above. The Taylor series for $C_\beta(Q,\theta)$ can then be written as

$$C_\beta(Q,\theta) = C_{\beta 0} + \frac{\partial C_{\beta 0}}{\partial Q_0} Q_e + \frac{\partial C_{\beta 0}}{\partial \theta_0}\theta_e + \frac{1}{2}\left(\frac{\partial^2 C_{\beta 0}}{\partial Q_0^2} Q_e^2 + \frac{\partial^2 C_{\beta 0}}{\partial \theta_0^2}\theta_e^2\right) + \frac{\partial^2 C_{\beta 0}}{\partial Q_0 \partial \theta_0} Q_e \theta_e, \tag{14.7.31}$$

where $C_{\beta 0} = C_\beta(Q_0, \theta_0)$ is the Casimir function for the basic state.

By substituting (13.7.19) and (13.7.31) into the expression for the pseudo-momentum, $\rho(U + C_\beta)$, and by using (13.7.30), $\rho(U + C_\beta)$ can be written as follows:

$$\begin{aligned}
&\rho(U + C_\beta) \\
&= \frac{\partial}{\partial x}\left(\frac{\partial C_{\beta 0}}{\partial Q_0}\frac{\partial \theta_0}{\partial z} v_e - \frac{\partial C_{\beta 0}}{\partial Q_0}\frac{\partial \theta_0}{\partial y} w_e\right) + \frac{\partial}{\partial y}\left(\frac{\partial C_{\beta 0}}{\partial Q_0}\frac{\partial u_0}{\partial z}\theta_e - \frac{\partial C\beta_0}{\partial Q_0}\frac{\partial \theta_0}{\partial z} u_e\right) \\
&+ \frac{\partial}{\partial z}\left[\frac{\partial C_{\beta 0}}{\partial Q_0}\frac{\partial \theta_0}{\partial y} u_e + \frac{\partial C_{\beta 0}}{\partial Q_0}\left(f_0 + \beta y - \frac{\partial u_0}{\partial y}\right)\theta_e\right] + u_e\left[\rho_0 + \frac{\partial \theta_0}{\partial z}\frac{\partial}{\partial y}\left(\frac{\partial C_{\beta 0}}{\partial Q_0}\right) - \frac{\partial \theta_0}{\partial y}\frac{\partial}{\partial z}\left(\frac{\partial C_{\beta 0}}{\partial Q_0}\right)\right] \\
&- \theta_e\left[\frac{\partial u_0}{\partial z}\frac{\partial}{\partial y}\left(\frac{\partial C_0}{\partial Q_0}\right) + \left(f_0 + \beta y - \frac{\partial u_0}{\partial y}\right)\frac{\partial}{\partial z}\left(\frac{\partial C_0}{\partial Q_0}\right) - \rho_0\frac{\partial C_0}{\partial \theta_0}\right] \\
&+ \rho_e\left(U_0 + C_{\beta 0} - Q_0\frac{\partial C_{\beta 0}}{\partial Q_0}\right) + \rho_0\left(U_0 + C_{\beta 0}\right) + J
\end{aligned} \tag{13.7.32}$$

where $U_0 = u_0 - f_0 y - \beta y^2/2$ and

$$J = \rho_e\left(u_e + \frac{\partial C_{\beta 0}}{\partial \theta_0}\theta_e\right) + \frac{\partial C_{\beta 0}}{\partial Q_0}\boldsymbol{\xi}_{ae}\cdot\nabla\theta_e + \rho_0\left[\frac{1}{2}\left(\frac{\partial^2 C_{\beta 0}}{\partial Q_0^2}Q_e^2 + \frac{\partial^2 C_{\beta 0}}{\partial \theta_0^2}\theta_e^2\right) + \frac{\partial^2 C_{\beta 0}}{\partial Q_0 \partial \theta_0}Q_e\theta_e\right]$$

. (13.7.33)

The basic idea behind the momentum–Casimir" method is to write equation (13.7.32) as the sum of the basic state, the divergence of the first-order disturbance, and the second-order disturbance. In order to do this, we take the coefficients of the first-order disturbance, ρ_e, u_e, and θ_e, to be zero in the equation to give

$$\rho_0 + \frac{\partial \theta_0}{\partial z}\frac{\partial}{\partial y}\left(\frac{\partial C_{\beta 0}}{\partial Q_0}\right) - \frac{\partial \theta_0}{\partial y}\frac{\partial}{\partial z}\left(\frac{\partial C_{\beta 0}}{\partial Q_0}\right) = 0, \tag{13.7.34}$$

$$\frac{\partial u_0}{\partial z}\frac{\partial}{\partial y}\left(\frac{\partial C_{\beta 0}}{\partial Q_0}\right)+\left(f_0+\beta y-\frac{\partial u_0}{\partial y}\right)\frac{\partial}{\partial z}\left(\frac{\partial C_{\beta 0}}{\partial Q_0}\right)-\rho_0\frac{\partial C_{\beta 0}}{\partial \theta_0}=0,$$

and (13.7.35)

$$U_0+C_{\beta 0}-Q_0\frac{\partial C_{\beta 0}}{\partial Q_0}=0. \tag{13.7.36}$$

From the fundamental state equations ((13.7.20)–(13.7.23)), it is easy to prove that equation (13.7.36) is equivalent to equations (13.7.34) and (13.7.35); that is, the solution to equation (13.7.36) automatically satisfies equations (13.7.34) and (13.7.35). By integrating equation (13.7.36), the solution for $C_{\beta 0}$ can be found:

$$C_{\beta 0}=Q_0\int^{Q_0}s^{-2}U_0\left(s,\theta_0\right)ds+Q_0\kappa\left(\theta_0\right), \tag{13.7.37}$$

where $\kappa\left(\theta_0\right)$ is an arbitrary function of θ_0. Equation (13.7.32) then becomes

$$\begin{aligned}&\rho(U+C_\beta)\\&=\frac{\partial}{\partial x}\left(\frac{\partial C_{\beta 0}}{\partial Q_0}\frac{\partial \theta_0}{\partial z}v_e-\frac{\partial C_{\beta 0}}{\partial Q_0}\frac{\partial \theta_0}{\partial y}w_e\right)+\frac{\partial}{\partial y}\left(\frac{\partial C_{\beta 0}}{\partial Q_0}\frac{\partial u_0}{\partial z}\theta_e-\frac{\partial C_{\beta 0}}{\partial Q_0}\frac{\partial \theta_0}{\partial z}u_e\right)\\&+\frac{\partial}{\partial z}\left[\frac{\partial C_{\beta 0}}{\partial Q_0}\frac{\partial \theta_0}{\partial y}u_e+\frac{\partial C_{\beta 0}}{\partial Q_0}\left(f_0+\beta y-\frac{\partial u_0}{\partial y}\right)\theta_e\right]+\rho_0\left(U_0+C_{\beta 0}\right)+J\end{aligned} \tag{13.7.38}$$

Using equations (13.7.34)–(13.7.36), this can be further simplified to

$$\rho(U+C_\beta)=\rho_0(u_e+\frac{\partial C_{\beta 0}}{\partial \theta_0}\theta_e)+\frac{\partial C_{\beta 0}}{\partial Q_0}(\boldsymbol{\xi}_{ae}\cdot\nabla\theta_0+\boldsymbol{\xi}_{a0}\cdot\nabla\theta_e+\boldsymbol{\xi}_{a0}\cdot\nabla\theta_0)+J \quad (13.7.39)$$

By substituting expressions (13.7.38) and (13.7.39) into, respectively, the pseudo-momentum variation term and flux-divergence term on the left-hand side of equation (13.7.17) and then using equations (13.7.25)–(13.7.28) to eliminate the local variation term for the first-order disturbance and omitting disturbances of the second order and above, the pseudo-momentum wave-action equation in dry air can be obtained:

$$\frac{\partial J}{\partial t}+\nabla\cdot\mathbf{F}=0 \quad , \quad (13.7.40)$$

where $\mathbf{F}=(F_x,F_y,F_z)$ is called the pseudo-momentum wave-action flux, which has the three components

$$F_x=u_0J+u_e[\rho_0(u_e+\frac{\partial C_{\beta 0}}{\partial \theta_0}\theta_e)+\frac{\partial C_{\beta 0}}{\partial Q_0}(\boldsymbol{\xi}_{ae}\cdot\nabla\theta_0+\boldsymbol{\xi}_{a0}\cdot\nabla\theta_e)], \quad (13.7.41)$$

$$F_y=v_e[\rho_0(u_e+\frac{\partial C_{\beta 0}}{\partial \theta_0}\theta_e)+\frac{\partial C_{\beta 0}}{\partial Q_0}(\boldsymbol{\xi}_{ae}\cdot\nabla\theta_0+\boldsymbol{\xi}_{a0}\cdot\nabla\theta_e)], \text{ and} \quad (13.7.42)$$

$$F_z=w_e[\rho_0(u_e+\frac{\partial C_{\beta 0}}{\partial \theta_0}\theta_e)+\frac{\partial C_{\beta 0}}{\partial Q_0}(\boldsymbol{\xi}_{ae}\cdot\nabla\theta_0+\boldsymbol{\xi}_{a0}\cdot\nabla\theta_e)]. \quad (13.7.43)$$

Equation (13.7.40) shows that the pseudo-momentum wave-action density for adiabatic dry air without friction is locally conserved. If the

component of the wave-action flux perpendicular to the boundary is zero, then the pseudo-momentum wave action of the volume integral is conserved—that is, $\frac{d}{dt}\iiint_V JdV = 0$. Since the above equations, (13.7.40) - (13.7.43) is set up in the dynamic framework of ageostrophic equilibrium and non-hydrostatic equilibrium, it can describe the evolution and propagation of mesoscale disturbances.

When $\nabla \cdot \mathbf{F} > 0$ and $\frac{\partial J}{\partial t} < 0$, the energy of the disturbance is locally divergent and the disturbance will be locally attenuated; when $\nabla \cdot \mathbf{F} < 0$ and $\frac{\partial J}{\partial t} > 0$, the perturbed system will develop locally. It should be emphasized here that the establishment of equation (13.7.40) is based on some preconditions: it is required that the basic state of the atmosphere and $C_{\beta 0}$ satisfy the equations for the basic state (equations (13.7.20)–(13.7.23) and (13.7.36)).

13.7.3 The pseudo-energy wave-action equation

In this section, we use the energy–Casimir method to derive the pseudo-energy wave-action equation from the pseudo-energy equation (13.7.18). As before, it is assumed that the physical quantities can be decomposed into a basic state and a perturbed state:

$$u = u_0 + u_e,\ v = v_0 + v_e,\ w = w_e,\ p = p_0^* + p_e,\ T = T_0 + T_e,$$

$$\rho = \rho_0 + \rho_e,\ \theta = \theta_0 + \theta_e, \text{ and } Q = Q_0 + Q_e, \tag{13.7.44}$$

where the subscript "0" represents the basic state and the subscript "e" represents the perturbed state. Here, we assume that the basic states are steady and three-dimensional in space and that they automatically satisfy

the primary equations

$$u_0 \frac{\partial u_0}{\partial x} + v_0 \frac{\partial u_0}{\partial y} - (f_0 + \beta y) v_0 = -\frac{1}{\rho_0} \frac{\partial p_0^*}{\partial x}, \tag{13.7.45}$$

$$u_0 \frac{\partial v_0}{\partial x} + v_0 \frac{\partial v_0}{\partial y} + (f_0 + \beta y) u_0 = -\frac{1}{\rho_0} \frac{\partial p_0^*}{\partial y} \quad , \tag{13.7.46}$$

$$\frac{\partial p_0^*}{\partial z} = -\rho_0 g \, , \tag{13.7.47}$$

$$\frac{\partial \rho_0 u_0}{\partial x} + \frac{\partial \rho_0 v_0}{\partial y} = 0, \tag{13.7.48}$$

$$u_0 \frac{\partial \theta_0}{\partial x} + v_0 \frac{\partial \theta_0}{\partial y} = 0, \tag{13.7.49}$$

$$p_0^* = \rho_0 R T_0 \, , \tag{13.7.50}$$

$$\theta_0 = T_0 (\frac{p_0}{p_0^*})^{\frac{R}{c_p}} . \tag{13.7.51}$$

For a small-amplitude disturbance, the linearized disturbance equations are

$$\frac{\partial u_e}{\partial t} = -u_0 \frac{\partial u_e}{\partial x} - v_0 \frac{\partial u_e}{\partial y} + \left(f_0 + \beta y\right) v_e - \mathbf{v}_e \cdot \nabla u_0 - \frac{1}{\rho_0} \frac{\partial p_e}{\partial x} + \frac{\rho_e}{{\rho_0}^2} \frac{\partial p_0^*}{\partial x}$$

, (13.7.52)

$$\frac{\partial v_e}{\partial t} = -u_0 \frac{\partial v_e}{\partial x} - v_0 \frac{\partial v_e}{\partial y} - \left(f_0 + \beta y\right) u_e - \mathbf{v}_e \cdot \nabla v_0 - \frac{1}{\rho_0} \frac{\partial p_e}{\partial y} + \frac{\rho_e}{{\rho_0}^2} \frac{\partial p_0^*}{\partial y}$$

, (13.7.53)

$$\frac{\partial w_e}{\partial t} = -u_0 \frac{\partial w_e}{\partial x} - v_0 \frac{\partial w_e}{\partial y} - \frac{1}{\rho_0} \frac{\partial p_e}{\partial z} - g \frac{\rho_e}{\rho_0}, \tag{13.7.54}$$

$$\frac{\partial \rho_e}{\partial t} = -\nabla \cdot \left(\rho_0 \mathbf{v}_e \right) - \frac{\partial}{\partial x} \left(\rho_e u_0 \right) - \frac{\partial}{\partial y} \left(\rho_e v_0 \right), \text{ and} \tag{13.7.55}$$

$$\frac{\partial \theta_e}{\partial t} = -u_0 \frac{\partial \theta_e}{\partial x} - v_0 \frac{\partial \theta_e}{\partial y} - \mathbf{v}_e \cdot \nabla \theta_0 . \tag{13.7.56}$$

Generally, $\left| \frac{\theta_e}{\theta_0} \right| < 1$, $\left| \frac{\rho_e}{\rho_0} \right| < 1$, $\left| \frac{T_e}{T_0} \right| < 1$, and $\left| \frac{p_e}{p_0^*} \right| < 1$; therefore, by substituting equation (13.7.44) into equations (13.7.11) and (13.7.12), subtracting (13.7.50) and (13.7.51) from these two equations, respectively, and then omitting the second-order and higher-order disturbances, the linear relationships between the thermodynamic variables of the disturbance can be obtained as

$$\frac{p_e}{p_0^*} \approx \frac{\rho_e}{\rho_0} + \frac{T_e}{T_0} \tag{13.7.57}$$

$$\frac{\theta_e}{\theta_0} \approx \frac{T_e}{T_0} - \frac{R}{c_p} \frac{p_e}{p_0^*} . \tag{13.7.58}$$

By eliminating $\frac{p_e}{p_0^*}$ from (14.7.57) and (14.7.58), the following approximate expression can be obtained:

$$T_e \approx \frac{c_p}{c_v} \frac{T_0}{\theta_0} \theta_e + \frac{R}{c_v} \frac{T_0}{\rho_0} \rho_e . \tag{13.7.59}$$

Then, substituting (13.7.44) and (13.7.31) into the pseudo-energy expression, $\rho\left(E+C_\beta\right)$, and also by using (13.7.30) and (13.7.59), $\rho\left(E+C_\beta\right)$ can be written as follows:

$$
\begin{aligned}
&\rho\left(E+C_\beta\right)\\
&=\rho_0\left(E_0+C_{\beta 0}\right)\\
&\quad+\frac{\partial}{\partial x}[\frac{\partial C_{\beta 0}}{\partial Q_0}(v_e\frac{\partial\theta_0}{\partial z}-w_e\frac{\partial\theta_0}{\partial y}-\theta_e\frac{\partial v_0}{\partial z})]\\
&\quad+\frac{\partial}{\partial y}[\frac{\partial C_{\beta 0}}{\partial Q_0}(w_e\frac{\partial\theta_0}{\partial x}+\theta_e\frac{\partial u_0}{\partial z}-u_e\frac{\partial\theta_0}{\partial z})]\\
&\quad+\frac{\partial}{\partial z}[\frac{\partial C_{\beta 0}}{\partial Q_0}(u_e\frac{\partial\theta_0}{\partial y}-v_e\frac{\partial\theta_0}{\partial x}+(\frac{\partial v_0}{\partial x}-\frac{\partial u_0}{\partial y}+f_0+\beta y)\theta_e)]\\
&\quad+\rho_e(\frac{1}{2}u_0^2+\frac{1}{2}v_0^2+gz+c_pT_0+C_{\beta 0}-Q_0\frac{\partial C_{\beta 0}}{\partial Q_0})\\
&\quad+u_e[\rho_0u_0+\frac{\partial\theta_0}{\partial z}\frac{\partial}{\partial y}(\frac{\partial C_{\beta 0}}{\partial Q_0})-\frac{\partial\theta_0}{\partial y}\frac{\partial}{\partial z}(\frac{\partial C_{\beta 0}}{\partial Q_0})]\\
&\quad+v_e[\rho_0v_0+\frac{\partial\theta_0}{\partial x}\frac{\partial}{\partial z}(\frac{\partial C_{\beta 0}}{\partial Q_0})-\frac{\partial\theta_0}{\partial z}\frac{\partial}{\partial x}(\frac{\partial C_{\beta 0}}{\partial Q_0})]\\
&\quad+w_e[\frac{\partial\theta_0}{\partial y}\frac{\partial}{\partial x}(\frac{\partial C_{\beta 0}}{\partial Q_0})-\frac{\partial\theta_0}{\partial x}\frac{\partial}{\partial y}(\frac{\partial C_{\beta 0}}{\partial Q_0})]\\
&\quad+\theta_e[\rho_0(c_p\frac{T_0}{\theta_0}+\frac{\partial C_{\beta 0}}{\partial\theta_0})+\frac{\partial v_0}{\partial z}\frac{\partial}{\partial x}(\frac{\partial C_{\beta 0}}{\partial Q_0})\\
&\qquad-\frac{\partial u_0}{\partial z}\frac{\partial}{\partial y}(\frac{\partial C_{\beta 0}}{\partial Q_0})-(\frac{\partial v_0}{\partial x}-\frac{\partial u_0}{\partial y}+f_0+\beta y)\frac{\partial}{\partial z}(\frac{\partial C_{\beta 0}}{\partial Q_0})]+A
\end{aligned}
\tag{13.7.60}
$$

Here, $E_0 = u_0^2/2 + v_0^2/2 + gz + c_p T_0$ and

$$A = \rho_e(u_0 u_e + v_0 v_e + c_v T_e + \frac{\partial C_{\beta 0}}{\partial \theta_0}\theta_e) + \frac{\partial C_0}{\partial Q_0}\xi_{ae}\cdot\nabla\theta_e + \frac{1}{2}\rho_0(u_e^2 + v_e^2 + w_e^2 + \frac{\partial^2 C_{\beta 0}}{\partial Q_0^{\,2}}Q_e^{\,2} + \frac{\partial^2 C_{\beta 0}}{\partial \theta_0^{\,2}}\theta_e^{\,2}) + \rho_0\frac{\partial^2 C_{\beta 0}}{\partial Q_0 \partial \theta_0}Q_e\theta_e \quad . \tag{13.7.61}$$

Equation (13.7.61) represents the second-order disturbance and is known as the equation for the pseudo-energy wave-action density.

The basic idea of the energy–Casimir method is to write equation (13.7.60) as the sum of the basic state, the divergence of the first-order disturbance, and the second-order disturbance. In order to do this, the coefficients of the first-order perturbations, u_e, v_e, w_e, θ_e, and ρ_e, should be taken to be zero:

$$\rho_0 u_0 + \frac{\partial \theta_0}{\partial z}\frac{\partial}{\partial y}(\frac{\partial C_{\beta 0}}{\partial Q_0}) - \frac{\partial \theta_0}{\partial y}\frac{\partial}{\partial z}(\frac{\partial C_{\beta 0}}{\partial Q_0}) = 0\,, \tag{13.7.62}$$

$$\rho_0 v_0 + \frac{\partial \theta_0}{\partial x}\frac{\partial}{\partial z}(\frac{\partial C_{\beta 0}}{\partial Q_0}) - \frac{\partial \theta_0}{\partial z}\frac{\partial}{\partial x}(\frac{\partial C_{\beta 0}}{\partial Q_0}) = 0\,, \tag{13.7.63}$$

$$\frac{\partial \theta_0}{\partial y}\frac{\partial}{\partial x}(\frac{\partial C_{\beta 0}}{\partial Q_0}) - \frac{\partial \theta_0}{\partial x}\frac{\partial}{\partial y}(\frac{\partial C_{\beta 0}}{\partial Q_0}) = 0\,, \tag{13.7.64}$$

$$\rho_0(c_p\frac{T_0}{\theta_0}+\frac{\partial C_{\beta 0}}{\partial \theta_0})+\frac{\partial v_0}{\partial z}\frac{\partial}{\partial x}(\frac{\partial C_{\beta 0}}{\partial Q_0})$$
$$-\frac{\partial u_0}{\partial z}\frac{\partial}{\partial y}(\frac{\partial C_{\beta 0}}{\partial Q_0})-(\frac{\partial v_0}{\partial x}-\frac{\partial u_0}{\partial y}+f_0+\beta y)\frac{\partial}{\partial z}(\frac{\partial C_{\beta 0}}{\partial Q_0})=0 \quad , \tag{13.7.65}$$

$$\frac{1}{2}u_0^2+\frac{1}{2}v_0^2+gz+c_pT_0+C_{\beta 0}-q_0\frac{\partial C_{\beta 0}}{\partial Q_0}=0. \tag{13.7.66}$$

Similarly, it can be proved from the equations for the basic state (equations (13.7.45)–(13.7.51)) that equation (13.7.66) is equivalent to equations (13.7.62)–(13.7.65); that is, the solution ($C_{\beta 0}$) of equation (13.7.66) automatically satisfies equations (13.7.62)–(13.7.65). By integrating equation (14.7.66), $C_{\beta 0}$ can be found:

$$C_{\beta 0}=Q_0\int^{Q_0}s^{-2}E_0(s,\theta_0)ds+Q_0\kappa(\theta_0), \tag{13.7.67}$$

where, $\kappa(\theta_0)$ is an arbitrary function of θ_0. Equation (13.7.60) then becomes

$$\rho(E+C_\beta)=\rho_0(E_0+C_{\beta 0})+\frac{\partial}{\partial x}[\frac{\partial C_{\beta 0}}{\partial Q_0}(v_e\frac{\partial \theta_0}{\partial z}-w_e\frac{\partial \theta_0}{\partial y}-\theta_e\frac{\partial v_0}{\partial z})]$$
$$+\frac{\partial}{\partial y}[\frac{\partial C_{\beta 0}}{\partial Q_0}(w_e\frac{\partial \theta_0}{\partial x}+\theta_e\frac{\partial u_0}{\partial z}-u_e\frac{\partial \theta_0}{\partial z})]$$
$$+\frac{\partial}{\partial z}[\frac{\partial C_{\beta 0}}{\partial Q_0}(u_e\frac{\partial \theta_0}{\partial y}-v_e\frac{\partial \theta_0}{\partial x}+(\frac{\partial v_0}{\partial x}-\frac{\partial u_0}{\partial y}+f_0+\beta y)\theta_e)]+A \tag{13.7.68}$$

Using equations (13.7.62)–(13.7.66), (13.7.68) can be written as

$$\rho(E+C_\beta)$$
$$=-p_0^*+\rho_0[u_0u_e+v_0v_e+(c_p\frac{T_0}{\theta_0}+\frac{\partial C_{\beta 0}}{\partial\theta_0})\theta_e]+\frac{\partial C_{\beta 0}}{\partial Q_0}(\boldsymbol{\xi}_{ae}\cdot\nabla\theta_0+\boldsymbol{\xi}_{a0}\cdot\nabla\theta_e+\boldsymbol{\xi}_{a0}\cdot\nabla\theta_0)+A$$

. (14.7.69)

By substituting (13.7.68) and (13.7.69) into the local variation term for the pseudo-energy and the flux-divergence term on the left-hand side of (13.7.18), respectively, the term for the local variation in the first-order perturbation can be eliminated by using the system of equations that describe the perturbation (equations (13.7.52)–(13.7.56)). If the second-order and the higher-order disturbances are also omitted, we can then obtain the pseudo-energy wave-action equation for dry air:

$$\frac{\partial A}{\partial t}+\nabla\cdot\mathbf{F}=0\,, \tag{13.7.70}$$

where $\mathbf{F}=\left(F_x,F_y,F_z\right)$ and the three components of **F** are

$$F_x=u_0A+\rho_0u_e[u_0u_e+v_0v_e+(c_p\frac{T_0}{\theta_0}+\frac{\partial C_{\beta 0}}{\partial\theta_0})\theta_e]+u_e\frac{\partial C_{\beta 0}}{\partial Q_0}(\boldsymbol{\xi}_{ae}\cdot\nabla\theta_0+\boldsymbol{\xi}_{a0}\cdot\nabla\theta_e)+u_ep_e\,, \tag{13.7.71}$$

$$F_y=v_0A+\rho_0v_e[u_0u_e+v_0v_e+(c_p\frac{T_0}{\theta_0}+\frac{\partial C_{\beta 0}}{\partial\theta_0})\theta_e]+v_e\frac{\partial C_{\beta 0}}{\partial Q_0}(\boldsymbol{\xi}_{ae}\cdot\nabla\theta_0+\boldsymbol{\xi}_{a0}\cdot\nabla\theta_e)+v_ep_e\,, \tag{13.7.72}$$

$$F_z=\rho_0w_e[u_0u_e+v_0v_e+(c_p\frac{T_0}{\theta_0}+\frac{\partial C_{\beta 0}}{\partial\theta_0})\theta_e]+w_e\frac{\partial C_{\beta 0}}{\partial Q_0}(\boldsymbol{\xi}_{ae}\cdot\nabla\theta_0+\boldsymbol{\xi}_{a0}\cdot\nabla\theta_e)+w_ep_e\,. \tag{13.7.73}$$

Equation (13.7.70) shows that the wave-action density of the pseudo-energy in adiabatic frictionless dry air is locally conserved. In the same way as for the pseudo-momentum wave-action equation, equation (13.7.70) can also be used to diagnose and analyze the evolution and propagation of mesoscale disturbances. The local variation in the pseudo-energy wave-action density depends entirely on the divergence of the pseudo-energy wave-action flux. Convergence of this flux means that

the disturbance will develop locally; divergence of this flux means that the disturbance will decay locally.

Equation (13.7.70) is also a prerequisite for the establishment of the pseudo-energy wave-action equation shown above. This requires that the atmospheric basic state and C_0 satisfy the basic state equations (13.7.45)–(13.7.51) and (13.7.66).

13.8 Case Studies

This section focuses on two cases of heavy precipitation. One is a strong convection case that occurred in the west of China on 8 July 2009. During this event, the precipitation system moved slowly eastward along a belt stretching from 36°N to 39°N. The other case occurred between 12:00 UTC on 18 August and 06:00 UTC on 19 August 2009. In this case, the precipitation started in the north of Shanxi province and the center of Inner Mongolia and then quickly spread northeast. For these two cases, we examine the ability of the virtual pseudo-energy wave-action density to diagnose the heavy rainfall. The physical meaning of this quantity is also discussed.

13.8.1 Data

Grid-analysis data used were used to perform the case study and the related diagnosis. The data were obtained from the ARPS model. National Centers for Environmental Prediction (NECP) final analysis data and routine observational data were read into the ARPS data assimilation system (ADAS) module, and then an objective analysis was conducted. The grid used here covered northern China (27.9°N–49.6°N, 100°E–132°E) and was centered at (39.9°N, 146.7°E). There were 77 × 77 cells in the grid, and the grid spacing was 30 km in both the zonal and meridional directions. The vertical depth was divided into 34 layers with a mean

spacing of 500 m. Grid data for the different height levels were output at six-hour intervals.

13.8.2. Results

To analyze the integral characteristics of the wave-action density, A, in the troposphere, we calculated the vertical mean of A by computing the divergence of the wave-action vector, $\mathbf{F}$. The horizontal distribution characteristics of A for the two events were then examined. Figure(13.8.1) presents the horizontal distribution of A at 00:00 UTC, 06:00 UTC, 12:00 UTC, and 18:00 UTC on 8 July 2009. It can be seen that, for the whole of this heavy rainfall event, the regions with positive values of A correspond well to the observations of the six-hour precipitation. The anomaly of A changes as the precipitation system and the areas of heavy rainfall develop. It should be noted that A has a high positive value in the regions of no precipitation because of its anomalous value in the upper troposphere. The region of negative values is close to the region of positive values and, together, these areas form an alternating pattern. The precipitation is closely aligned with the region of positive values of A. Further analysis shows that the term $A_{chief} = \frac{\partial C_0}{\partial q_0} \boldsymbol{\xi}_e \cdot \nabla \theta_{ve}$ is the chief contributor to A. (The relevant figures are omitted due to space limitations.) Since the term $\frac{\partial C_0}{\partial q_0}$ is invariant with time, the term A_{chief} mainly represents the temporal variation in the second-order potential vorticity $(\boldsymbol{\xi}_e \cdot \nabla \theta_{ve})$. Analysis also shows that the term $(\boldsymbol{\xi}_e \cdot \nabla \theta_{ve})$ is mainly dominated by the barotropic component of the perturbation potential vorticity

($(\frac{\partial v_e}{\partial x}-\frac{\partial u_e}{\partial y})\frac{\partial \theta_{ve}}{\partial z}$). The perturbation, θ_{ve}, increases with height in the middle and lower troposphere in the precipitation region, meaning that $\frac{\partial \theta_{ve}}{\partial z}>0$. Moreover, there exists a strong perturbation in the cyclonic vorticity (that is, $(\frac{\partial v_e}{\partial x}-\frac{\partial u_e}{\partial y})>0$) (Again, the relevant figures are omitted.) These two factors represent important dynamic and thermodynamic characteristics of precipitation: their values are high in the precipitation region, which, in turn, results in positive anomalies of $\xi_e \cdot \nabla \theta_{ve}$, A_{chief}, and A. The anticyclonic vorticity perturbation (which means that $(\frac{\partial v_e}{\partial x}-\frac{\partial u_e}{\partial y})<0$) and the positive vertical gradient of θ_{ve} give rise to the negative anomalies of $\xi_e \cdot \nabla \theta_{ve}$, A_{chief}, and A in the region of negative values of A.

The above analysis suggests that positive anomalies in the virtual pseudo-energy wave-action density are capable of indicating regions of precipitation. To verify this, another heavy rainfall event that occurred on 18 August and 19 August 2009 was investigated (see Figure 13.8.2). In this case, the region of positive anomalies of A corresponds strongly with the precipitation areas. Both regions can be observed to spread northeastward in step with each other. This consistency can also be explained by considering that the vorticity perturbation is cyclonic and that the virtual potential temperature perturbation increases vertically over the precipitation regions.

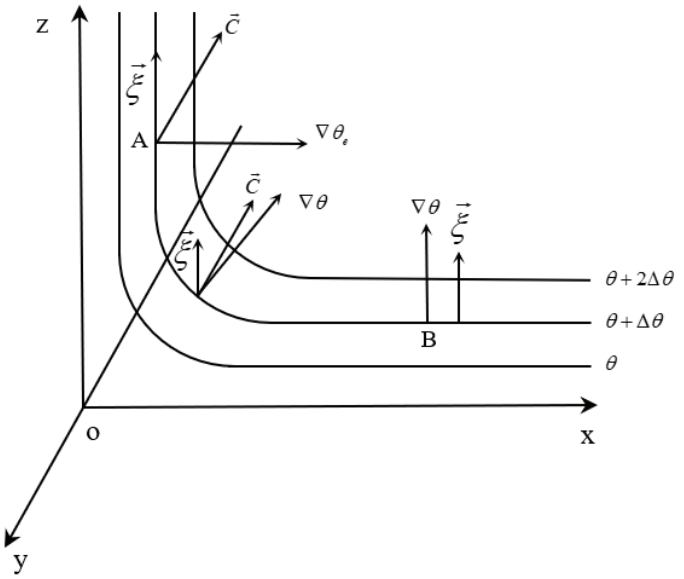

Fig. 13.1.1. The distribution of the potential temperature

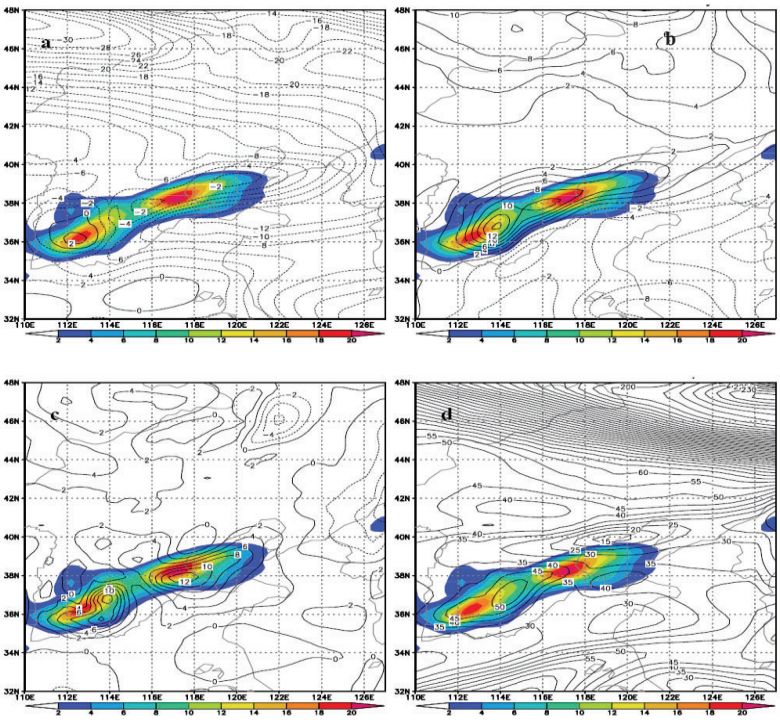

Fig. 13.1.2. Horizontal distributions of (a) $[C_x]$ (10^{-2} s^{-1} K), (b) $[C_y]$ (10^{-2} s^{-1} K), (c) $[C_z]$ (10^{-4} s^{-1} K), and (d) PV (10^{-4} s^{-1} K) at 00:00 UTC on 13 August 2004. The shaded areas denote different values of CH (10^{-1} kg m^{-2}).

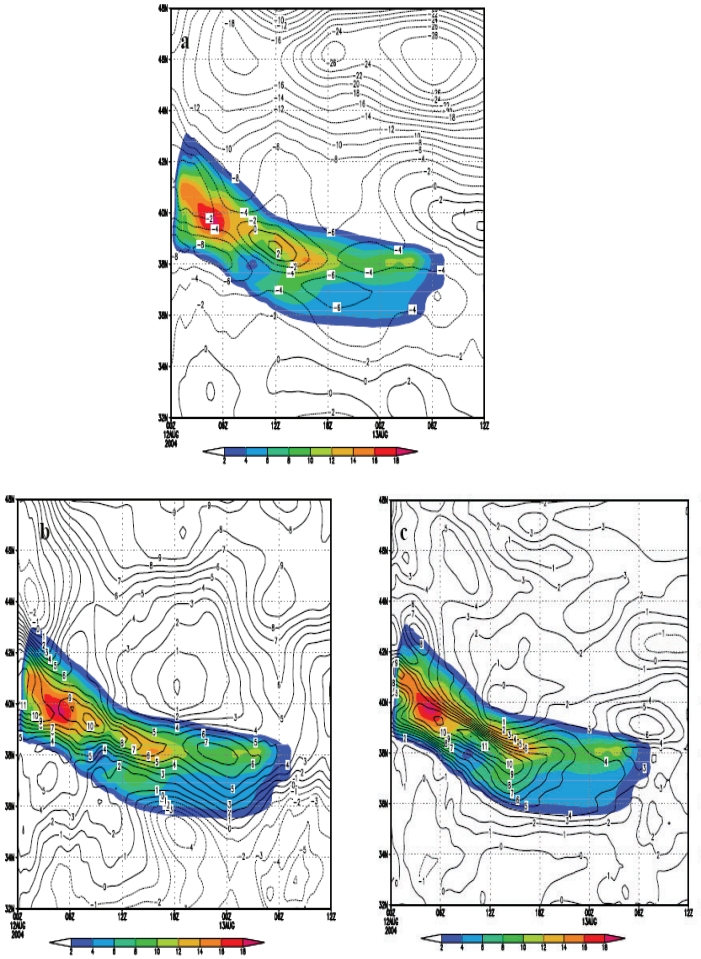

Fig. 13.1.3. The evolution of the distribution of (a) $[C_x]$ (10^{-2} s^{-1} K), (b) $[C_y]$ (10^{-2} s^{-1} K), and (c) $[C_z]$ (10^{-4} s^{-1} K) averaged over the area from 37°N to 42°N and 112°E to 119°E for the period 00:00 UTC on 12 August to 12:00 UTC on 13 August 2004. The shaded areas denote different values of CH (10^{-1} kg m^{-2})

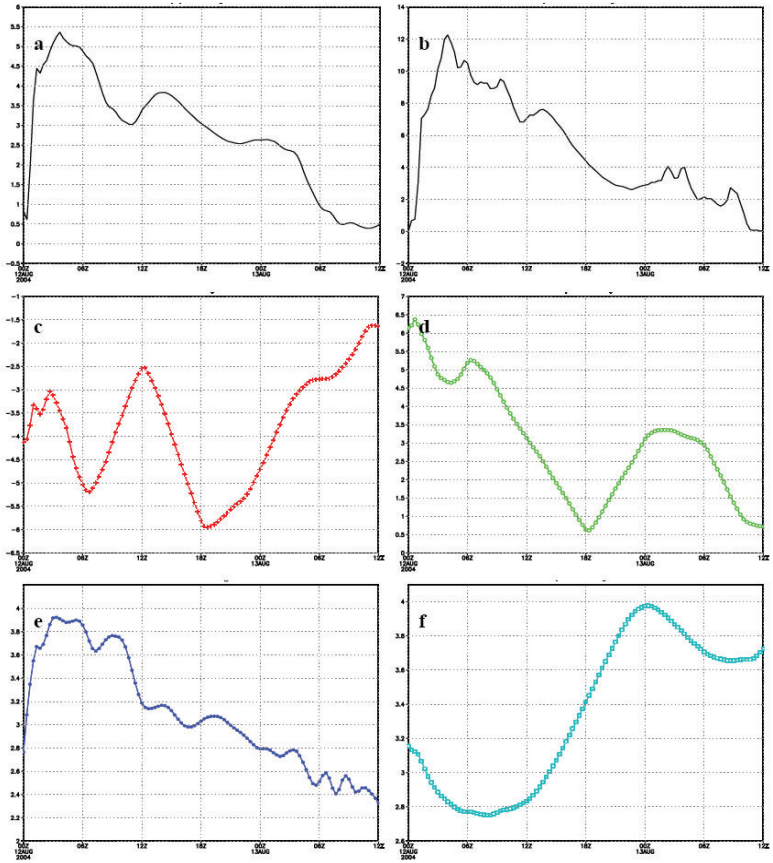

Fig. 13.1.4. The evolution of (a) CH (10^{-1} kg m^{-2}), (b) the rainfall rate (mm h^{-1}), (c) $[C_x]$ (10^{-2} s^{-1} K), (d) $[C_y]$ (10^{-2} s^{-1} K), (e) $[C_z]$ (10^{-4} s^{-1} K), and (f) PV (10^{-4} s^{-1} K) averaged over the area from 37°N to 42°N and 112°E to 119°E for the period 00:00 UTC on 12 August to 12:00 UTC on 13 August 2004

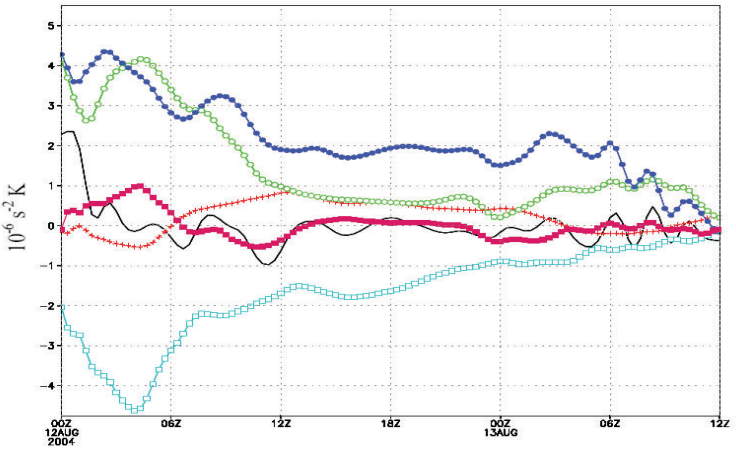

Fig. 13.2.1. The evolution of CZT (black), CZ1 (red), CZ2 (green), CZ3 (blue), CZ4 (cyan), and CZ5 (pink). The values are averaged over the area 34°N–43°N and 112°E–119°E for the period 00:00 UTC, 12 August to 12:00 UTC, 13 August 2004.

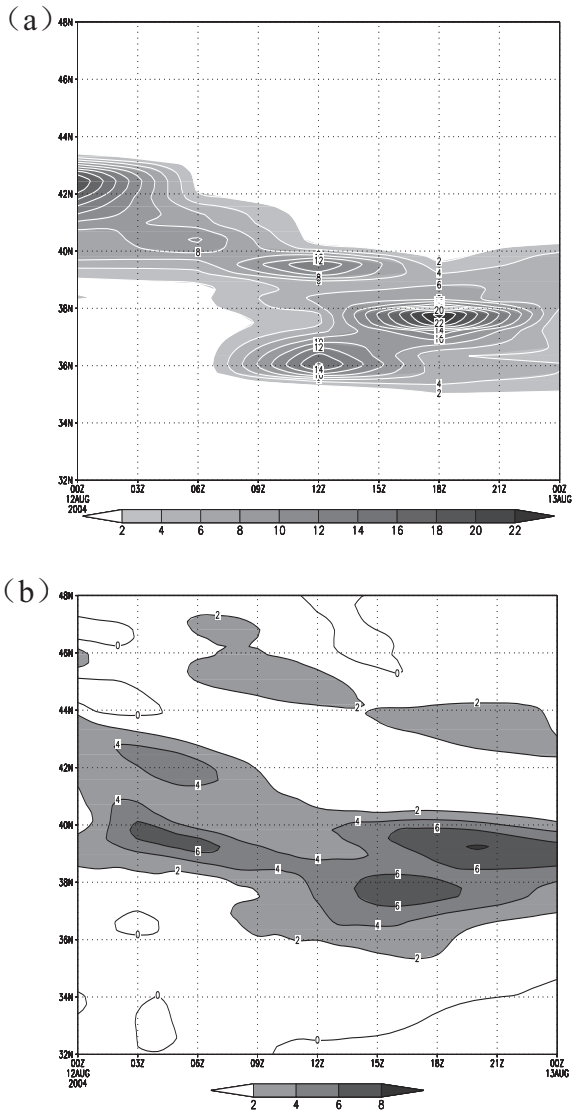

Fig. 13.2.2 (a) The evolution of the distribution of the six-hour cumulative rainfall amount (left; contour spacing: 2 mm) and (b) the vertical component of the CVV (right; units: 10^{-4} s^{-1} K) along 116°E for 00:00 UTC on 12 August to 12:00 UTC on 13 August 2004.

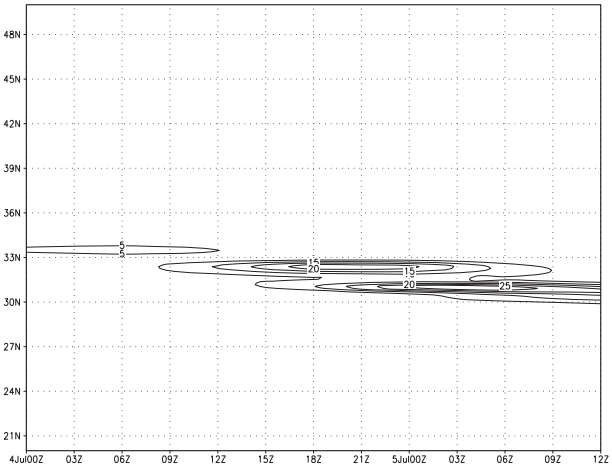

Fig. 13.5.1. Evolution of the distribution of the six-hour cumulative rainfall amount (mm) along 118°E from 00:00 UTC on 4 July to 12:00 UTC on 5 July 2003

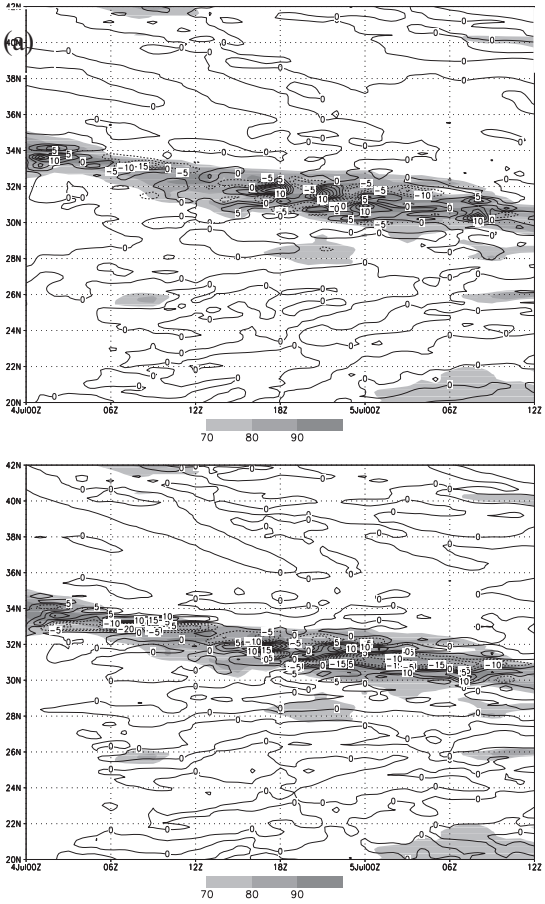

Fig. 13.5.2. Evolution of the distribution of (a) Q_{umx} (10^{-12} hPa^{-1} s^{-3} m) and the relative humidity (%) and (b) Q_{umy} (10^{-12} hPa^{-1} s^{-3} m) and the relative humidity (%) at 750 hPa along 118°E from 00:00 UTC on 4 July to 12:00 UTC on 5 July 2003

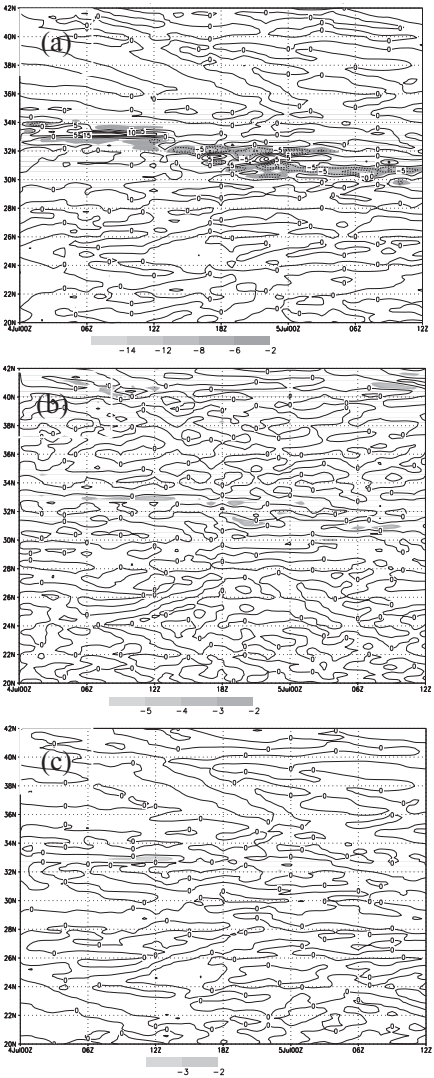

Fig. 13.5.3. Evolution of the distribution of (a) the horizontal divergence of Q_{umx} (10^{-16} hPa^{-1} s^{-3}), (b) the horizontal divergence of Q_{dry} (10^{-16} hPa^{-1} s^{-3}), and (c) the horizontal divergence of Q_m (10^{-16} hPa^{-1} s^{-3}) along 118°E at 750 hPa from 00:00 UTC, 4 July to 02:00 UTC, 5 July 2003. The shaded area denotes value of less than −2.

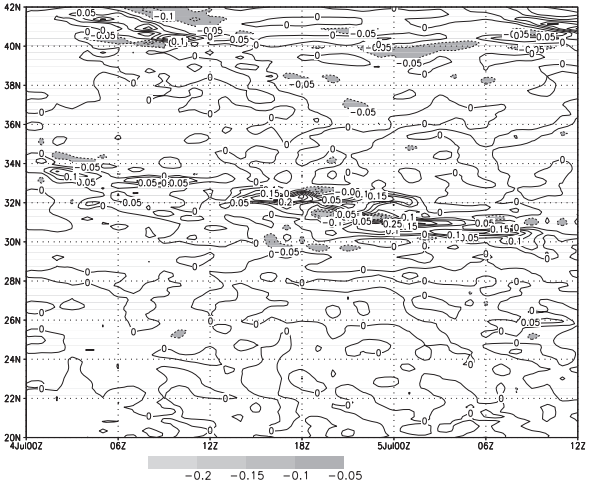

Fig. 13.5.4. The evolution of the distribution of the vertical velocity ω (hPa s^{-1}) along 118°E at 750 hPa from 00:00 UTC, 4 July to 02:00 UTC, 5 July 2003. The shaded area denotes values of less than −0.05.

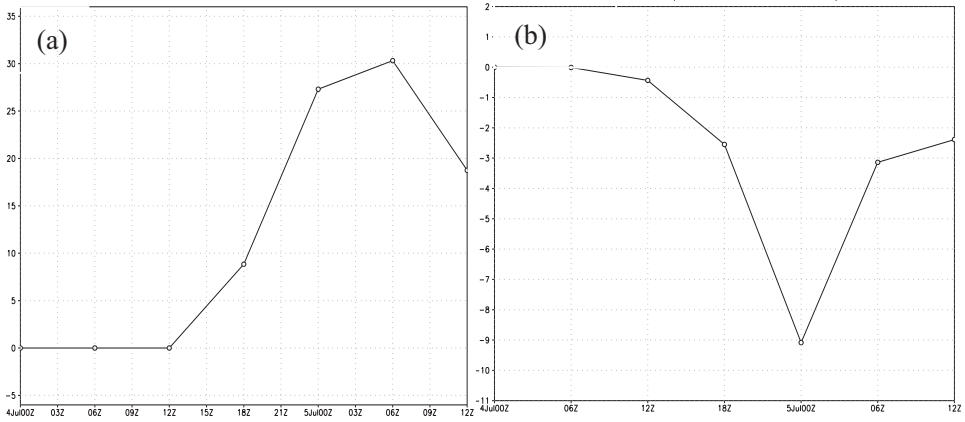

Fig. 13.5.5. Time series of (a) the six-hour cumulative rainfall amount (mm) and (b) the horizontal divergence of Q_{um} (10^{-16} hPa^{-1} s^{-3}) over the rainfall center

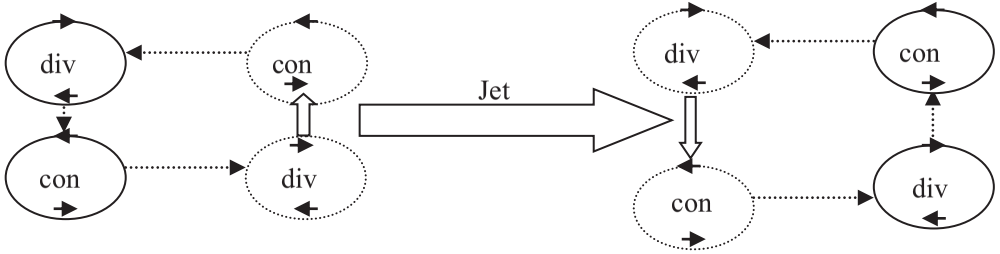

Fig. 13.6.1. Schematic diagram of the vertical circulations at the entrance and exit of high-level jets

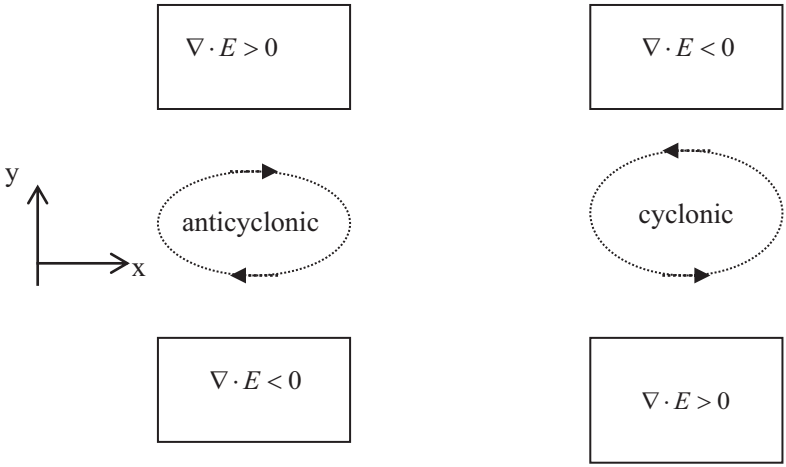

Fig. 13.6.2. Schematic diagram of the relationship between the divergence of the E vector and the development of a cyclone

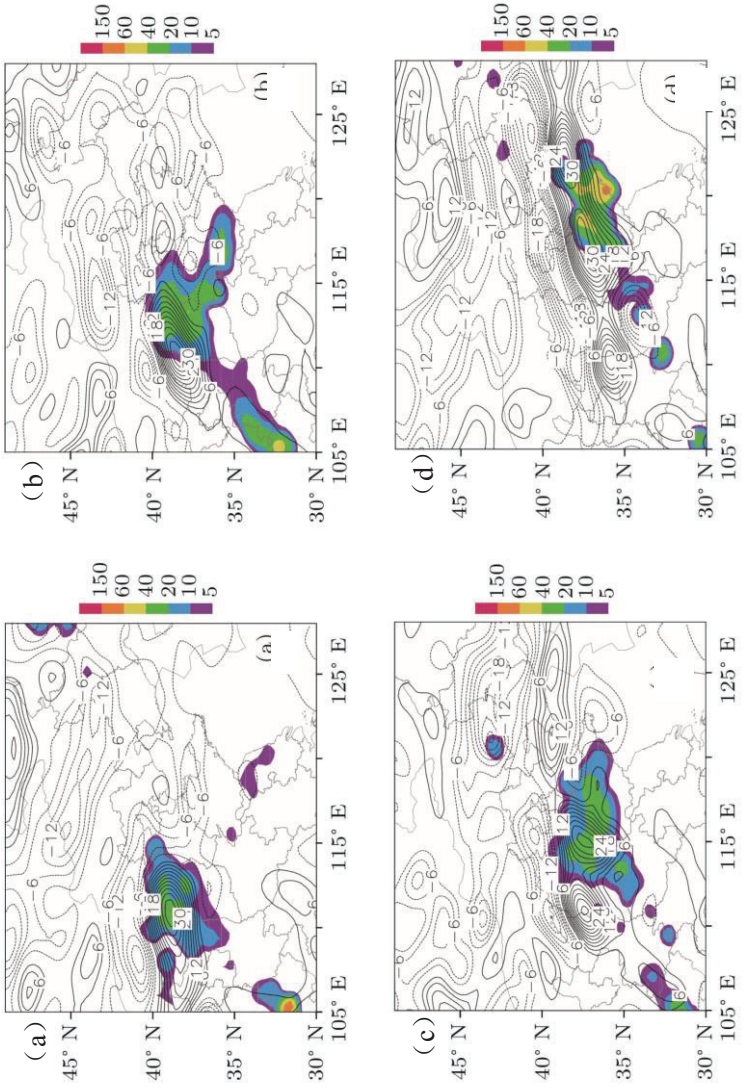

Fig. 13.8.1. The virtual pseudo-energy wave-action density (contours of 10^2 kg/(m·s^2)) and the observed six-hour rainfall (shaded; mm) at (a) 00:00 UTC, (b) 06:00 UTC, (c) 12:00 UTC, and (d) 18:00 UTC on 8 July 2009

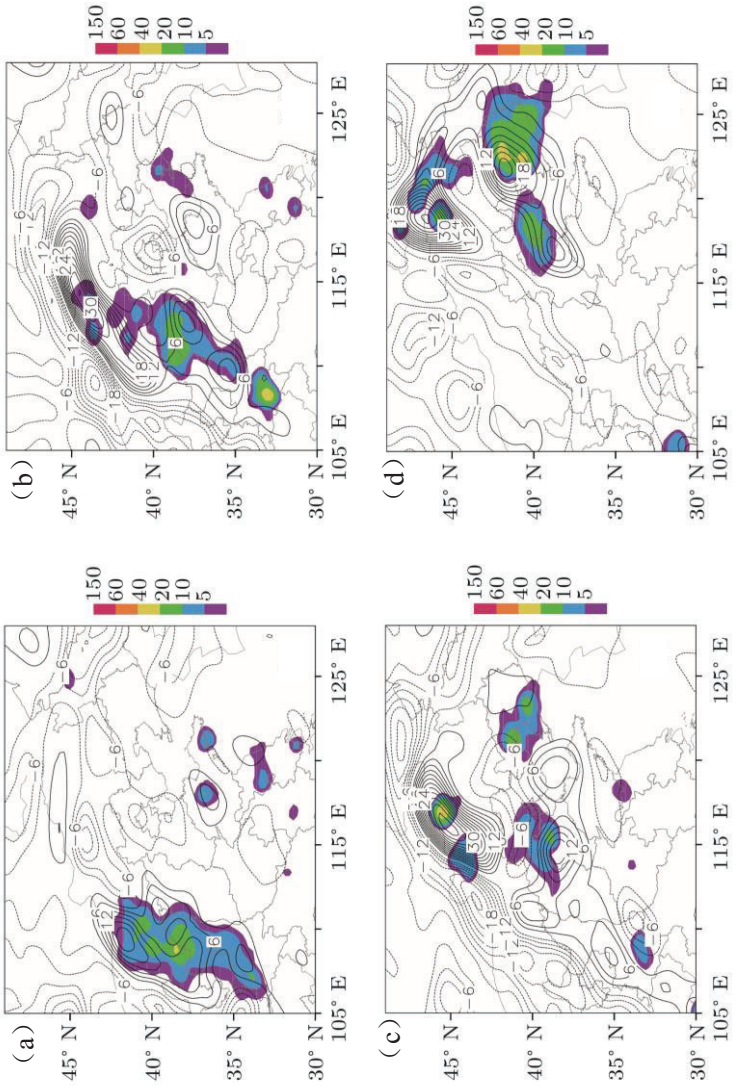

Fig. 13.8.2. The virtual pseudo-energy wave-action density (contours of 10^2 kg/(m·s^2) and the observed six-hour rainfall (shaded; mm) at (a) 12:00 UTC, 18 August, (b) 18:00 UTC, 18 August, (c) 00:00 UTC, 18 August, and (d) 06:00 UTC, 19 August 2009

Notes

[1]Hoskins, B. J., M. E. McIntyre and A. W. Robertson (1985) "On the use and significance of isentropic potential vorticity maps," *Quarterly Journal of the Royal Meteorological Society,* 111(470):877-946.

[2]McIntyre, M. E. and T. G. Shepherd (1987) "An exact local conservation theorem for finite amplitude disturbances to non-parallel shear flows, with remarks on Hamiltonian structure and on Arnol'd 's stability theorems," *Journal of Fluid Mechanics*, 181(1):527-565.

[3]McIntyre, M. E. and W. A. Norton (2000) "Potential vorticity inversion on a hemisphere," *Journal of Atmospheric Sciences*, 57(9):1214–1235.

[4]Gao, S., F. Ping, X. Li, et al. (2004) "A convective vorticity vector associated with tropical convection: A two-dimensional cloud-resolving modeling study," *Journal of Geophysical Research*, 109(D14), doi: 10.1029/2004JD004807.

[5]Gao, S., X. Li, W. K. Tao, et al. (2007) "Convective and moist vorticity vectors associated with tropical oceanic convection: A three-dimensional cloud-resolving simulation," *Journal of Geophysical Research: Atmospheres*, 112(D1), doi: 10.1029/2006JD007179.

[6] Gao, S., X. Cui, Y. Zhou, et al. (2005) "A modeling study of moist and dynamic vorticity vectors associated with tow-dimensional tropical convection," *Journal of Geophysical Research*, 110(D17), doi: 10.1029/2004JD005675.

[7]Hoskins, B. J., I. Draghici and H. C. Davies (1978) "A new look at the ω-equation," *Quarterly Journal of the Royal Meteorological Society*, 104(347):31-38.

[8]Huang, W. G., B. S. Deng and T. N. Xiong (1997) "The primary analysis on a typhoon torrential rain," *Quarterly Journal of Applied Meteorology*, 8(2):247-251. (in Chinese with English abstract)

[9]Davies-Jones, R. P. (1991) "The frontogenetical forcing of secondary circulations. Part I: The Duality and Generalization of the Q Vector," *Journal of Atmospheric Sciences*, 48(4):497-509.

[10]Yao, X. P., Y. B. Yu and S. Shou (2004) "Diagnostic analyses and application of

the moist ageostrophic vector Q," *Advances in Atmospheric Sciences*, 21(1):96-102.

[11]Xu, Q. (1992) "Ageostrophic pseudovorticity and geostrophic C-vector forcing—A new look at the Q vector in three dimensions," *Journal of Atmospheric Sciences*, 49(12):981–990.

[12]Gao, S., X. Wang and Y. Zhou (2004) "Generation of generalized moist potential vorticity in a frictionless and moist adiabatic flow," *Geophysical Research Letters*, 31(12), doi: 10.1029/2003GL019152.

[13]James, I. N. (1995) Introduction to circulating atmospheres, Météorologie. *Cambridge University Press*.

[14]Haynes, P. H. (1988) "Forced, dissipative generalizations of finite-amplitude wave activity conservation relations for zonal and nonzonal basic flows," *Journal of Atmospheric Sciences*, 45(16):2352-2362.

[15]Ran, L. and S. Gao (2007) "A three-dimensional wave-activity relation for pseudomomentum," *Journal of Atmospheric Sciences*, 64(6):2126-2134.

CHAPTER FOURTEEN

METHODS OF FORECASTING TORRENTIAL RAINFALL USING DYNAMIC FACTORS

China is located in the East Asia monsoon area. Each year, during the summer monsoon season, torrential rain is frequent, and this often leads to tremendous loss of life and property (Tao et al., 1980; Cheng and Feng., 2001; Li and Chen., 2002; Gao et al., 2003; Deng et al., 2010; Toth and Kalnay, 1997; Bright and Mullen, 2002)[1-7]. For example, the torrential rainfall that occurred in Henan Province in August 1975 caused floods in over 100 counties in the Huai River area and resulted in over 30,000 deaths. Torrential rainfall and associated floods led to economic losses of 60 billion yuan in the Jiang–Huai area in May–July 1991. The floods in the Yangtze River area that occurred in June–August 1998 affected 100 million people, causing 1800 deaths and economic losses of 150 billion yuan. The record-breaking torrential rainfall event that hit Beijing in July affected 1.9 million people, causing 78 deaths and economic losses of nearly 10 billion yuan. Thus, as part of disaster prevention and reduction in China and with the aim of avoiding these tremendous losses, efforts are focused on making accurate precipitation forecasts.

The operational forecasting of precipitation mainly relies on nowcasting extrapolated from numerical simulations and on observations made using satellite and radar measurements. These numerical simulations and observations all have their own advantages and shortcomings. For example, the numerical forecasting of precipitation includes forecasts of resolvable-scale precipitation and subgrid-scale precipitation. The resolvable-scale precipitation is calculated based on the terminal velocity

flux of hydrometeors (raindrops, snow, and graupel), which is determined by cloud microphysical processes. The subgrid-scale precipitation is calculated using cumulus parameterization schemes, which depends on the precipitation efficiency and water-vapor sources including the water-vapor convergence and surface evaporation. In fact, precipitation is a rather complex physical process, and the cloud microphysical and cumulus parameterization schemes used in numerical model predictions are subjective. These schemes are also not well suited to the presentation of precipitation-related physical processes, which involves large uncertainties in the predicted precipitation at both scales. Because the models need to be spun up, the application of model simulations to nowcasting of torrential rainfall is limited. Although forecasts extrapolated from radar observations can be used for nowcasting, they cannot provide high-quality forecasts for more than two hours ahead. To overcome these difficulties, scientists from China and other countries have developed various forecasting techniques based on numerical models as well as on satellite and radar observations, and has improved the forecasting of torrential rainfall. To reduce the errors in precipitation forecasts caused by uncertainties in numerical models and initial conditions, the ECMWF, NCEP, CMA, and JMA have constructed global medium-range and regional ensemble forecast systems (Molteni and Buizza, 1999)[8]. These systems efficiently reduce the errors in forecasts of torrential rainfall (Di et al., 2013)[9]. Since neither numerical forecasts nor forecasts extrapolated from observations are perfect, the two types of forecasts are combined, to improve the predictions of torrential rainfall. A lot of attention has been paid to the assimilation of mesoscale and microscale observational data into high-resolution numerical regional models. Zhou et al. (2002)[10] and Fang et al. (2003)[11] found that assimilations based on quality-controlled, hourly cloud-derived wind data improved the quality of the modeled wind-pressure fields and water-vapor field, which improved the predictions accuracy of location and intensity of torrential rainfall. Zhang et al. (2012)[12] studied the possibility of

improving the accuracy of local forecasts of torrential rainfall in Beijing by merging numerical rainfall products and sounding data. Cheng et al. (2013)[13] developed a merged scheme that was based on "extrapolation", nowcasting, and quantitative precipitation forecasts (QPFs) from mesoscale numerical models; this scheme was used to overcome the shortcomings of short-term convective-scale predictions of precipitation. This merged scheme produced improved 0–6 hour QPF, that were better than those based on now casting or mesoscale numerical models alone. High-resolution numerical models can be used to provide relatively accurate details of circulations, which can be used to develop methods of forecasting torrential rainfall from a dynamical point of view. For instance, Yue et al. (2007)[14] developed a moist Q vector and its dynamic interpretation and application method, in which the precipitation was derived from the relation between the divergence of the moist Q vector and the vertical velocity. The precipitation derived in this way produced better predictions than numerical models in cases where there was precipitation or more than 10 mm/24hrs of precipitation. Zhang et al. (2010)[15] traced the formation of torrential rainfall systems through the diagnosis of temporal and spatial changes in the "ingredients", including water vapor, lifting, and stability. Using the fact that torrential rainfall is often located along the convergence line of perturbation winds, Qian et al. (2013)[16] used 850-hPa convergence lines decomposed from ECMWF model forecasting products to detect torrential rainfall bands. Gao and Li (2010)[17] used surface rainfall budget equations to make quantitative precipitation forecasts based on water-vapor phase transformation processes. Other forecast methods have been constructed based on statistical relations between precipitation and forecast factors derived from the products of numerical models, to perform or improve objective forecast of precipitation (Liu and Ma 1996)[18]. Li and Zhao (2009)[19] developed a forecasting model for typhoon-type rainstorms using synthetic multilevel analogous forecasting technology, which was shown to have

some advantages. Liu and Zhao (2004)[20] used model output statistics (MOS) to predict the temperature, precipitation, relative humidity, wind, cloud amount, and visibility. The short-term forecasts of temperature and relative humidity were shown to be usable in operational forecasts. Zeng et al. (2008)[21] used a K-nearest neighbor approach to produce forecasts of clear sky or rainfall amounts of 10 mm and achieved better results than those obtained from numerical or MOS forecasts.

Various types of precipitation occur in China. Although the associated mechanisms are different, the synoptic backgrounds have certain similarities, such as a warm air mass encountering a cold air mass, low-level convergence, high-level divergence, strong vertical motion, water-vapor convergence, vertical wind shear, slantwise isentropic surface, atmospheric baroclinicity, the release of latent heat due to condensation, and potential instability. Torrential rainfall is often associated with water vapor and its phase changes. Thus, the accurate description of the dynamic and thermodynamic states of a moist atmosphere is key to improving forecasts of torrential rainfall. Therefore, we have developed a generalized potential temperature theory for accurately depicting the thermodynamic state of moist atmosphere. Mesoscale systems can produce torrential rainfall. To study the development of mesoscale systems, we also developed a mesoscale wave-flow interaction theory. Using these theories combined with the dynamic and thermodynamic characteristics of torrential rainfall, we can take advantage of the relatively accurate forecasts of temperature, water vapor, pressure, and wind to construct dynamic factors such as the moist thermodynamic advection parameter for a non-uniformly saturated atmosphere and the convective vorticity vector. These dynamic factors include dynamic, thermodynamic, and water-vapor informations and have clear physical meanings. These factors relatively accurately describe typical dynamic, thermodynamic, and water-vapor vertical profiles associated with the generation of torrential rainfall, thus demonstrating the dynamic and thermodynamic nature of precipitation

systems and the associated circulations. Thus, these dynamic factors are intimately associated with torrential rainfall processes.

Based on the correlation between these dynamic factors and observations of precipitation, in this chapter, an ensemble method of forecasting torrential rainfall based on dynamic factors is developed.

14.1 Dynamic Factors Based on the Generalized Potential Temperature

Based on the non-uniform distribution of water vapor during torrential rainfall and taking the dynamic and thermodynamic nature of torrential rainfall into consideration, Gao et al. (2009)[22] and Ran et al. (2013)[23] used the generalized potential temperature to develop various macro physical quantities associated with torrential rainfall. These dynamic factors are briefly discussed in the following.

14.1.1 Moist Thermodynamic Advection Parameter

The Meiyu front over the Jiang–Huai river basin is an important system inducing torrential rainfall in China. The Meiyu front is a dew-point front. Although there are contrasts in both temperature and moisture across the front, the moisture gradient is more significant. There are active warm and cold advections near the front, which are accompanied by the strong vertical transport of heat. The discontinuity in water vapor and temperature inside the front causes the isentropic surface to tilt significantly, and there is strong baroclinicity.

The moist thermodynamic advection parameter is defined as the dot product between the horizontal gradient of the three-dimensional potential temperature advection and the horizontal gradient of the generalized potential temperature (Wu et al., 2011)[24]:

$$M_{tp} = \nabla_h(-\mathbf{v}\cdot\nabla\theta)\cdot\nabla_h\theta^* . \tag{14.1.1}$$

Where θ^* is the general potential temperature, with $\theta^* = \theta\hat{y}$.

This parameter can be used to describe the thermodynamic advection and the strong baroclinicity that are characteristic of the front. If the atmosphere is adiabatic and frictionless, from the thermodynamic equation, i.e., $\frac{\partial\theta}{\partial t} + \mathbf{v}\cdot\nabla\theta = 0$, equation (14.1.1) becomes

$$M_{tp} = \frac{\partial(\nabla_h\theta)}{\partial t}\cdot\nabla_h\theta^*, \tag{14.1.2}$$

where $\frac{\partial(\nabla_h\theta)}{\partial t}$ is the local change in the horizontal gradient of potential temperature, which denotes frontogenesis. The horizontal gradient of the generalized potential temperature θ^* can be written as

$$\nabla_h\theta^* = \hat{\eta}\nabla_h\theta + \gamma^*\theta^*\nabla_h\alpha + \alpha\theta^*\nabla_h\gamma^*, \tag{14.1.3}$$

where $\hat{\eta} = \exp(\alpha\gamma^*)$, $\alpha = \frac{L_v q_s}{c_p T_c}$, and $\gamma^* = (\frac{q}{q_s})^k$. It can be shown that $\nabla_h\theta^*$ depends on the gradients of potential temperature ($\hat{\eta}\nabla_h\theta$), the latent heat due to condensation ($\gamma^*\theta^*\nabla_h\alpha$) and the water vapor ($\alpha\theta^*\nabla_h\gamma^*$). Thus, (14.1.2) becomes

$$M_{tp} = \frac{e^{\alpha\gamma^*}}{2}\frac{\partial(|\nabla_h\theta|^2)}{\partial t} - \theta^*\nabla_h(\mathbf{v}\cdot\nabla\theta)\cdot\nabla_h(\alpha\gamma^*), \tag{14.1.4}$$

where $\alpha\gamma^* = \frac{L_v q_s}{c_p T}(\frac{q}{q_s})^k$ denotes the effect of the latent heat

associated with condensation. For a dry atmosphere ($q = 0$ and $\gamma^* = 0$), (14.1.4) becomes $M_{tp} = \frac{1}{2}\frac{\partial(|\nabla_h \theta|^2)}{\partial t}$, which represents the local change of potential temperature gradient. Thus, the first term on the right-hand side of (14.1.4) denotes horizontal frontogenesis. The second term represents the coupling of horizontal gradients of potential temperature advection and the latent heat of condensation. Therefore, the moist thermodynamic advection parameter is related to horizontal frontogenesis and latent heat.

An analysis of torrential rainfall along the Meiyu front at 06:00 UTC on 11 July 2010 shows that the moist thermodynamic advection parameter is well able to describe the vertical dynamic and thermodynamic structures of the warm vertical advection and the horizontal gradient of the isentropic surface (Figure 14.1.1). There is good correlation between the parameter and the observed rainfall.

14.1.2 The Thermodynamic Helicity and the Vertical Flux of Thermodynamic Divergence

The helicity is an important physical quantity that represents the physical characteristics of a rotating fluid moving in the direction of its own rotation. However, the use of helicity in diagnosis of torrential rainfall is limited because the helicity is a pure dynamic quantity, and cannot describe thermodynamic and water-vapor processes. The thermodynamic helicity is defined to introduce the concept of generalized potential temperature in a non-uniformly saturated moist atmosphere into the vertical helicity, namely,

$$Helth = w[\frac{\partial}{\partial x}(v\theta^*) - \frac{\partial}{\partial y}(u\theta^*)] = w\theta^*(\frac{\partial v}{\partial x} - \frac{\partial u}{\partial y}) + w(v\frac{\partial \theta^*}{\partial x} - u\frac{\partial \theta^*}{\partial y}). \quad (14.1.5)$$

The thermodynamic helicity accounts for the coupling of vertical heat flux, vertical relative vorticity, and the atmospheric baroclinicity.

The low-level convergence, high-level divergence, and strong vertical motion are important dynamic characteristics of rainfall areas and form the basis of rainfall forecasts. The low-level convergence collects heat and water vapor into the rainfall areas. The strong vertical motion transports heat and water vapor to high levels. The vertical flux of thermodynamic divergence is defined in a way that accounts for both the collection of heat and water vapor and the strong vertical motion, namely,

$$Wptediv = w\nabla_h \cdot (\mathbf{v}_h\theta^*) = w\theta^*\nabla_h \cdot \mathbf{v}_h + w\mathbf{v}_h \cdot \nabla_h\theta^*. \quad (14.1.6)$$

This quantity combines the vertical motion, horizontal divergence, and thermodynamic advection, describing the dynamic and thermodynamic coupling. $Helth$ and $Wptediv$ can be used to study precipitation systems that involve strong vertical motion, vortex, convergence, and moist baroclinicity. As shown in Figure 14.1.2, during the torrential rainfall associated with a cold vortex that lay over northeast China at 18:00 UTC on 27 July 2010, the high values of $Helth$, $Wptediv$, and the observed rainfall amounts were well correlated. This means that these two dynamic factors played an important role in the evolution of the cold-vortex rainfall.

14.1.3 The Q Vector Involving the Generalized Potential Temperature

The Q vector has been widely used to analyze vertical motion and

frontogenesis in anomalous atmosphere. Davies-Jones (1991)[25] broke the limitation of quasi-geostrophic theory to derive the generalized ω equation and proposed the generalized Q vector. In order to include the latent heat, Yao et al. (2004)[26] and Yue et al. (2009)[27] introduced the saturation specific humidity in ω equation and proposed the ageostrophic Q vector for moist air. It is a powerful tool for the dynamic diagnosis of severe weather such as typhoons and torrential rainfall. Since the atmosphere is not saturated everywhere and the saturation is non-uniform, the Q vector involving the generalized potential temperature is derived by replacing saturation specific humidity with the specific humidity. The diabatic heating term is hard to calculate accurately, however, the generalized potential temperature includes the latent heat effects. As a result, the Q vector including the generalized potential temperature is suitable for diagnosing torrential rainfall. In the pressure coordinates, the Omega equation involving the generalized potential temperature is given by

$$\frac{\partial}{\partial x}(\sigma_\varepsilon \frac{\partial \omega}{\partial x}) + \frac{\partial}{\partial y}(\sigma_\varepsilon \frac{\partial \omega}{\partial y}) + f^2(\frac{\partial^2 \omega}{\partial p^2}) = -(\frac{\partial q_x^{\#}}{\partial x} + \frac{\partial q_y^{\#}}{\partial y}), \quad (14.1.7)$$

where σ_ε is the stability parameter related to the generalized potential temperature, which is usually positive (Gao et al. 2004)[28].

$$q_x^{\#} = f(\frac{\partial u}{\partial x}\frac{\partial v}{\partial p} - \frac{\partial u}{\partial p}\frac{\partial v}{\partial x}) - \mu_* \frac{\theta}{\theta^{\#}}\frac{\partial \mathbf{v}_h}{\partial x}\cdot\nabla_h\theta^{\#} - \mu_*\frac{\partial \theta}{\partial x}\frac{d\beta^*}{dt} - \mu_*\theta\frac{d}{dt}(\frac{\partial \beta^*}{\partial x})$$

, (14.1.8)

$$q_y^{\#} = f(\frac{\partial u}{\partial y}\frac{\partial v}{\partial p} - \frac{\partial u}{\partial p}\frac{\partial v}{\partial y}) - \mu_* \frac{\theta}{\theta^{\#}}\frac{\partial \mathbf{v}_h}{\partial y}\cdot\nabla_h\theta^{\#} - \mu_*\frac{\partial \theta}{\partial y}\frac{d\beta^*}{dt} - \mu_*\theta\frac{d}{dt}(\frac{\partial \beta^*}{\partial y}).$$

(14.1.9)

are the components of the **Q** vector ($Q^{\#} = (q_x^{\#}, q_y^{\#})$). $\theta^{\#} = \theta \exp(\beta^*)$ is the generalized potential temperature, where $\beta^* = \frac{L_v q}{c_p T}(\frac{q}{q_s})^k$. If the atmosphere is dry ($q = 0$), $\theta^{\#}$ can be reduced to θ, and the equation (14.1.7) is then the same as the traditional *Omega* equation without the latent heat of condensation. When the atmosphere is saturated, the generalized potential temperature becomes the equivalent potential temperature, and the equation presents the forcing effect of latent heating on the vertical velocity.

The Q vector with generalized potential temperature was used to diagnose the torrential rainfall event that occurred in Shanxi Province, China on 11–14 July 2013. Due to the lack of diabatic heating information in the data, the last two terms on the right-hand sides of (14.1.8) and (14.1.9) were not calculated in this case. The results show that mid- and low-level convergence of Q vector along with the low-level airflow convergence, high-level airflow divergence, and convective instability contributed to the formation and development of torrential rainfall (Figure 14.1.3). The divergence of Q vector and the observation of cumulated six-hour rainfall are closely correlated, showing that the Q vector can be used as a predictor of rainfall.

14.2 The Moist Potential Vorticity and its Derivative Physical Quantities

The potential vorticity has been widely used in synoptic analysis. The atmospheric momentum equations, thermodynamic equation, and mass continuity equation are used to derive the potential vorticity equation. Under adiabatic and frictionless conditions, the potential vorticity is a

conserved quantity. Due to the importance of the potential vorticity, it can be extended to construct physical quantities closely associated with torrential rainfall.

14.2.1 The Generalized Moist Potential Vorticity

The potential vorticity of dry air can be used to diagnose dry-air intrusion. The potential vorticity of the saturated atmosphere can be applied to invest symmetric instability. Dry air and saturated air are two extreme conditions. For non-uniformly saturated moist air, Gao et al. (2004)[28] used the generalized potential temperature to define the generalized moist potential vorticity as

$$Gmpv = \frac{\xi_a \cdot \nabla \theta^*}{\rho}, \tag{14.2.1}$$

where ξ_a is the absolute vorticity and ρ is the air density Since the generalized moist potential vorticity contains θ^* and ξ_a, it is a physical quantity presenting the dynamic and thermodynamic characteristics of non-uniform moist atmosphere. Liang et al. (2010)[29] showed that the generalized moist potential vorticity mainly describes the coupling of vertical vorticity and vertical gradient of generalized potential temperature.

14.2.2 Solenoidal Vorticity

The vorticity is a three-dimensional vector. The potential vorticity is just a projection of the vorticity on the gradient of potential temperature. So it cannot depict component of the vorticity on an isentropic surface. Thus, the potential vorticity does not contain the complete information of

vorticity. In diagnostic analysis of torrential rainfall, two diagnostic quantities are defined to efficiently describe the vorticity components on an isentropic surface:

$$Msv = \boldsymbol{\xi}^* \cdot (\nabla p \times \nabla \alpha^*) \tag{14.2.2}$$

$$Mpsv = \boldsymbol{\xi}^* \cdot [(\nabla p \times \nabla \alpha^*) \times \nabla \theta^*], \tag{14.2.3}$$

where, $a^* = 1/\rho^*$ is the specific volume of moist air, $\rho^* = \rho/\hat{\eta}$ is the density of moist air, with $\hat{\eta} = \exp(\alpha\gamma^*)$, $\boldsymbol{\xi}^* = \nabla \times \mathbf{v}^*$ is the vorticity vector in moist air, and $\boldsymbol{v}^* = (\hat{\eta}u,\ \hat{\eta}v,\ \hat{\eta}w)$ is the wind vector in moist air. Here $\nabla\theta^*$, $\nabla p \times \nabla \alpha^*$, and $(\nabla p \times \nabla \alpha^*) \times \nabla \theta^*$ are orthogonal to each other Msv is called solenoidal vorticity, including the vorticity component in the direction of $\nabla p \times \nabla \alpha^*$. $Mpsv$ is called thermodynamic solenoidal vorticity, including the vorticity component in the direction of $(\nabla p \times \nabla \alpha^*) \times \nabla \theta^*$. Thus, the generalized moist potential vorticity, solenoidal vorticity, and thermodynamic solenoidal vorticity involve the three components of vorticity, respectively. Using the scale analysis, the expressions for Msv and $Mpsv$ can be simplified to

$$Msv \approx \frac{\partial p}{\partial z}\left(\frac{\partial \boldsymbol{v}_h^*}{\partial z} \cdot \nabla_h \alpha^*\right) \tag{14.2.4}$$

$$Mpsv \approx -\frac{\partial \theta^*}{\partial z}\frac{\partial p}{\partial z}\left[\left(\frac{\partial \boldsymbol{v}_h^*}{\partial z} \times \nabla_h \alpha^*\right) \cdot \mathbf{k}\right]. \tag{14.2.5}$$

Here, Msv describes the coupling of the vertical wind shear and the horizontal gradient of moist specific volume, which is weighted by the vertical gradient of pressure, and $Mpsv$ represents the coupling of convective stability, vertical wind shear, and the horizontal gradient of moist specific volume, weighted by the vertical gradient of pressure.

Low-pressure troughs are one of main types of weather systems that generate torrential rainfall over northern China. These torrential rainfall systems have a strong vertical wind shear, large vertical vorticity, strong baroclinicity, and high geopotential instability. Diagnostic analysis of the torrential rainfall associated with a trough at 00:00 UTC on 19 July 2010 shows that the generalized moist potential vorticity, solenoidal vorticity, and thermodynamic solenoidal vorticity can be used effectively to depict the vertical wind shear, vertical vorticity, horizontal gradient of specific volume, and vertical gradient of the generalized potential temperature. Anomalous values of these quantities existed in the lower troposphere, and were highly correlated with the rainfall observation (Figure 14.2.1).

14.2.3 The Potential Divergence, Potential Shearing Deformation, and Potential Stretching Deformation

In addition to the rotation, divergence and deformation also are the essential characteristic of horizontal wind. Low-level convergence and high-level divergence are the necessary dynamic conditions for the formation of torrential rainfall. Generally, torrential rainfall also takes place in an atmospheric deformation field. The deformation is an unstable state and easily transform into vorticity and divergence. Here the potential divergence, potential shearing deformation, and potential stretching deformation are proposed in order to study the divergence and deformation of horizontal wind. Rotating the horizontal wind vector, $\mathbf{v}_h = (u, v, 0)$,

about coordinates produces three horizontal vectors $\mathbf{v}_h^{shr} = (-u, v, 0)$, $\mathbf{v}_h^{str} = (-v, -u, 0)$, and $\mathbf{v}_h^{div} = (-v, u, 0)$ (Figure 14.2.2). Taking the dot product of these vectors with the gradient of generalized potential temperature, the potential divergence, *R*, potential shearing deformation, *M*, and potential stretching deformation, *J*, are obtained:

$$R = -\frac{\partial v}{\partial z}\frac{\partial \theta^*}{\partial x} - \frac{\partial u}{\partial z}\frac{\partial \theta^*}{\partial y} + \left(\frac{\partial v}{\partial x} + \frac{\partial u}{\partial y}\right)\frac{\partial \theta^*}{\partial z}, \tag{14.2.6}$$

$$M = -\frac{\partial u}{\partial z}\frac{\partial \theta^*}{\partial x} - \frac{\partial v}{\partial z}\frac{\partial \theta^*}{\partial y} + \left(\frac{\partial u}{\partial x} + \frac{\partial v}{\partial y}\right)\frac{\partial \theta^*}{\partial z}, \tag{14.2.7}$$

$$J = -\frac{\partial u}{\partial z}\frac{\partial \theta^*}{\partial x} + \frac{\partial v}{\partial z}\frac{\partial \theta^*}{\partial y} + \left(\frac{\partial u}{\partial x} - \frac{\partial v}{\partial y}\right)\frac{\partial \theta^*}{\partial z}. \tag{14.2.8}$$

In additional to the vertical wind shear, these physical quantities also account for the horizontal divergence (14.2.6), stretching deformation (14.2.7), and shearing deformation (14.2.8). They denote the coupling of the divergence and deformation with atmospheric thermodynamic effects. These quantities produced good forecasts of torrential Meiyu rainfall in the Jiang–Huai region (Figure 14.2.3) (Chu et al., 2013; Qi et al., 2010)[30-31].

14.2.4 The Second-order Potential Vorticity and Convective Vorticity Vector

The analysis of generalized moist potential vorticity shows that the high-value centers of generalized moist potential vorticity can be correlated with the locations of typhoons. The rain bands along the typhoon eye wall are often located inside the gradient of generalized moist potential vorticity. This is consistent with the situation of torrential rainfall

due to fronts and low pressure. Thus, the second-order potential vorticity is defined as the dot product of vorticity vector and gradient of the generalized moist potential vorticity, i.e.,

$$Secpv = -\frac{\partial v}{\partial z}\frac{\partial q}{\partial x} + \frac{\partial u}{\partial z}\frac{\partial q}{\partial y} + (\frac{\partial v}{\partial x} - \frac{\partial u}{\partial y})\frac{\partial q}{\partial z}. \tag{14.2.9}$$

This quantity contains the horizontal and vertical gradients of generalized moist potential vorticity.

In two-dimensional meridional–vertical cross section, the potential vorticity approaches zero in the equator and cannot be used to describe the strong convection evolution in the tropics. Gao et al. (2004) proposed the concept of convective vorticity vector (CVV), which overcomes the shortcomings of the two-dimensional potential vorticity in the equator, namely,

$$CVV = \frac{\boldsymbol{\xi}_a \times \nabla\theta_e}{\rho}. \tag{14.2.10}$$

where is the equivalent potential temperature.

Unlike the potential vorticity (the dot product of vorticity vector and gradient of potential temperature), the convective vorticity vector denotes the cross product between vorticity and gradient of equivalent potential temperature. Ideally, the horizontal motion is dominant for large-scale systems, the isentropic surface is horizontal, and its value increases with height when no convection occurs. Thus, the direction of isentropic surface gradient is vertical. If an air parcel moves along an isentropic surface, the direction of vorticity vector is also vertical. The dot product of vorticity vector and gradient of equivalent potential temperature is $\boldsymbol{\xi}_a \cdot \nabla\theta_e$ ($= |\boldsymbol{\xi}_a||\nabla\theta_e|\cos\alpha$), where α is the angle between the two vectors. When the two vectors are parallel, this angle

is zero, $\cos\alpha = 1$, and the dot product reaches its maximum. In the case of deep convection, the vertical motion inducing mixing, together with the release of latent heat, causes the isentropic surface to be nearly vertical. In an extreme situation, if the gradient direction of equivalent potential temperature becomes horizontal, and so it is at 90° to the vorticity vector of large-scale horizontal motion, $\cos\alpha = 0$, and the potential vorticity is zero. Also, the cross product of the vorticity vector and the gradient of equivalent temperature produces a strong signal because $\xi_a \times \nabla\theta_e = |\xi_a||\nabla\theta_e|\sin\alpha\,\mathbf{k}$, and if $\alpha =$ 90°, $\sin\alpha = 1$. ($\mathbf{k}$ is the direction of the cross product of the two vectors). This ideal condition is most likely to occur inside the eye wall and spiral rain bands of typhoons.

The analysis shows that the second-order potential vorticity and the vertical component of convective vorticity vector (CVZ) can describe the vertical characteristics of generalized potential vorticity gradient and moist isentropic surface inside the eye wall and rain bands of typhoons. In the case of Typhoon Fanapi, from Figure 14.2.4, it can be seen that high values of these quantities coincided with the torrential rainfall at 06:00 UTC on 20 September 2010. Thus, $Secpv$ and CVZ are suitable to present the evolution of rainfall in the eye wall and spiral bands of a typhoon.

14.3 The Wave-activity Density

Large-scale systems provide a favorable background for torrential rainfall, whereas mesoscale convective systems can act as direct generators of torrential rainfall. Thus, how to depict the mesoscale systems is a key question. Based on the theory of large-scale wave-flow interaction, we develop the theory of mesoscale wave-flow interaction. The wave-flow

interaction is an important subject of atmospheric dynamics. The wave-activity density is an essential concept in wave-flow interactions. The wave-activity density corresponds to the square or to higher orders of the perturbation amplitude and denotes the wave energy. It also describes the dynamic and thermodynamic features of perturbation and satisfies the following equation,

$$\frac{\partial A}{\partial t} + \nabla \cdot \mathbf{F} = S \,, \tag{14.3.1}$$

where A is the wave-activity density, $\mathbf{F}$ is the wave-activity flux, and S is the source/sink. Equation (14.3.1) shows that convergence (divergence) of the wave-activity flux can lead to a local increase (decrease) in the wave-activity density, thus leading to the development (decay) of mesoscale systems. The wave-activity equation can therefore be used to analyze the evolution of mesoscale systems. In this section, the potential vorticity was used to develop the wave-activity density and wave-activity equation suitable to mesoscale systems.

The strongest ascent motion is often located over the torrential rainfall area and surrounded by the compensatory subsidence, which produces a horizontal gradient of vertical velocity. To depict the characteristics of vertical velocity and latent heat over rainfall area, the wave-activity density is defined as the Jacobian of perturbation vertical velocity and perturbation latent heat, namely,

$$Waveeta = \frac{\partial w_e}{\partial y}\frac{\partial \eta_e}{\partial x} - \frac{\partial w_e}{\partial x}\frac{\partial \eta_e}{\partial y} \,, \tag{14.3.2}$$

where the subscript "$_e$" denotes perturbation. The low-filter technique is used to conduct horizontal filtering of grid data. The filtered data are used as the basic states, and perturbation fields are then constructed by subtracting the basic state from the original data.

The above wave-activity density contains only the vertical velocity perturbation without the horizontal velocity. Furthermore, we define also

the wave-activity density as the dot product of vorticity vector perturbation and the latent-heat gradient. Based on the theory of potential vorticity, the definition is

$$Wavepveta = (\nabla \times \mathbf{v}_{he}) \cdot \nabla \eta_e = -\frac{\partial v_e}{\partial z}\frac{\partial \eta_e}{\partial x} + \frac{\partial u_e}{\partial z}\frac{\partial \eta_e}{\partial y} + (\frac{\partial v_e}{\partial x} - \frac{\partial u_e}{\partial y})\frac{\partial \eta_e}{\partial z}, \quad (14.3.3)$$

where $\mathbf{v}_{he} = (u_e, v_e, 0)$ is the perturbed horizontal wind vector. Wavepveta denotes the projection of the perturbed vorticity vector on the gradient of latent-heat function. This is a second-order perturbation for the quantity ($(\nabla \times \mathbf{v}_h) \cdot \nabla \hat{\eta}$) and describes the dynamic effects of the vertical wind shear perturbation and vertical vorticity perturbation.

In order to present the divergence and deformation of wind, we replace $\mathbf{v}_{he}$ in (14.3.3) by $\mathbf{v}_{he}^{div}$, $\mathbf{v}_{he}^{str}$, and $\mathbf{v}_{he}^{shr}$ to give, respectively, three kinds of wave-activity density. The potential divergence wave-activity density associated with latent heat is

$$Wavediveta = (\nabla \times \mathbf{v}_{he}^{div}) \cdot \nabla \eta_e = -(\frac{\partial u_e}{\partial z}\frac{\partial \eta_e}{\partial x} + \frac{\partial v_e}{\partial z}\frac{\partial \eta_e}{\partial y}) + (\frac{\partial u_e}{\partial x} + \frac{\partial v_e}{\partial y})\frac{\partial \eta_e}{\partial z}, \quad (14.3.4)$$

the potential shear deformation wave-activity density associated with latent heat is

$$Waveshearеta = (\nabla \times \mathbf{v}_{he}^{shr}) \cdot \nabla \eta_e = -\frac{\partial v_e}{\partial z}\frac{\partial \eta_e}{\partial x} - \frac{\partial u_e}{\partial z}\frac{\partial \eta_e}{\partial y} + (\frac{\partial v_e}{\partial x} + \frac{\partial u_e}{\partial y})\frac{\partial \eta_e}{\partial z}, \quad (14.3.5)$$

The potential stretching deformation wave-activity density associated with

latent heat is,

$$Wavestretcheta = (\nabla \times \mathbf{v}_{he}^{str}) \cdot \nabla \eta_e = \frac{\partial u_e}{\partial z}\frac{\partial \eta_e}{\partial x} - \frac{\partial v_e}{\partial z}\frac{\partial \eta_e}{\partial y} - (\frac{\partial u_e}{\partial x} - \frac{\partial v_e}{\partial y})\frac{\partial \eta_e}{\partial z} \quad . (14.3.6)$$

The above three kinds of wave-activity density involve the vertical shear of horizontal wind perturbation as well as the perturbations of horizontal divergence $(\frac{\partial u_e}{\partial x} + \frac{\partial v_e}{\partial y})$, shearing deformation $(\frac{\partial v_e}{\partial x} + \frac{\partial u_e}{\partial y})$, and stretching deformation $(\frac{\partial u_e}{\partial x} - \frac{\partial v_e}{\partial y})$.

Topography often triggers gravity waves and induces torrential rainfall or increases rainfall. The wave-activity densities are capable of presenting topographic gravity waves. A torrential rainfall event occurred over Sichuan and Guizhou, China at 00:00 UTC on 17 July 2010 (Figure 14.3.1). The analysis shows that the wave-activity densities can effectively trace the torrential rainfall over the complex topography region.

14.4 An Ensemble Method of Forecasting Torrential Rainfall Using Dynamic Factors

The analysis of the dynamic factors such as the second-order potential vorticity, the wave-activity density and so on has shown that the factors become strong signals in areas of torrential rainfall and weak signals in areas of light rain or no rainfall. Statistical analysis indicates that there is a strong correlation between these factors and the observation of six-hour rainfall. The correlation coefficients range from 0.2 to 0.8 and the average coefficient is over 0.4. The correlation coefficients are relatively large over the Chinese cities of Wuhan, Guangzhou, Changchun, Xi'an, and

Zhengzhou, whereas they are relatively low over Wenzhou, Xiamen, Chengdu, and Kunming in China. This demonstrates that there are regional differences. How these dynamic factors can be applied to forecasts of torrential rainfall is a question that needs to be considered. A single dynamic factor only takes into account some aspects of the dynamic, thermodynamic, and water-vapor characteristics and, thus, there are limitations to use in forecasts. In contrast, the forecast of torrential rainfall can be improved when all of these dynamic factors are used.

14.4.1 The Equation for Ensemble Rainfall Forecasts Using Dynamic Factors

Based on the dynamic factors described previously, an ensemble method of forecasting torrential rainfall using dynamic factors is developed. This method makes the forecast of torrential rainfall by detecting rainfall systems using model outputs of temperature, pressure, water vapor, and wind. The method compensates for some weaknesses of numerical rainfall forecast.

The method consists of three steps. First of all, a statistical dynamic model that connects the individual dynamic factor and the cumulative six-hour observed rainfall was developed. It can be written as

$$y \propto c_i x_i , \tag{14.4.1}$$

where y is the observation of six-hour rainfall amount, x_i is the ith dynamic factor calculated with model output data, and c_i is the coefficient of x_i . Here, x_i was calculated using six-hourly NCEP/UCAR GFS (Global Forecasting System) data for the periods 1 June 2009 to 1 October 2009 and 1 June 2010 to 1 October 2010. A linear

regression between x_i and y was constructed using (14.4.1), and the coefficients, c_i, were obtained by using the least-squares method. The following equation was used to calculate the i th dynamic factor and retrieve the rainfall amount:

$$y_i = c_i x_i . \tag{14.4.2}$$

The correlation coefficients between the rainfall amounts retrieved from the individual dynamic factors and the observed rainfall amount were then calculated. Finally, arranging the correlation coefficients from largest to smallest, the retrieved rainfall amounts from the *m* dynamic factors were also arranged in the same order. The weighting functions were constructed as

$$w_i = \mathbf{exp}(-\frac{r_i^2}{m^2}) , \tag{14.4.3}$$

where r_i represents the position in the order of y_i. For instance, $r_i = 1$ for the retrieved rainfall of the i th dynamic factor with the maximum correlation coefficient; $r_l = m$ for the retrieved rainfall of the l th dynamic factor with the smallest dynamic factor. A statistical analysis was carried out on a long time series of data to obtain c_i and w_i, and then, construct the equation for the ensemble rainfall forecast with dynamic factors, namely,

$$\bar{\tilde{y}} = \frac{\sum_{i=1}^{m} w_i \tilde{y}_i}{\sum_{i=1}^{m} w_i}, \tag{14.4.4}$$

where

$$\tilde{y}_i = c_i \tilde{x}_i. \tag{14.4.5}$$

In (14.4.5), $\tilde{x}_i$ is the i th dynamic forecast factor calculated using GFS forecast data and $\tilde{y}_i$ is the cumulative six-hour rainfall amount retrieved by $\tilde{x}_i$; i.e. the rainfall amount forecast by the i th dynamic factor. $\bar{\tilde{y}}$ is the average cumulative six-hour rainfall forecast constructed by linearly adding the m rainfall forecasts by the m dynamic factors with the weight coefficient. The observed rainfall amount is a six-hour cumulative quantity, whereas the dynamic factors are instantaneous quantities. To make (14.4.1), (14.4.2), and (14.4.5) consistent, x_i and $\tilde{x}_i$ are averaged in the rainfall observation period.

14.4.2 Forecast Validation

The ensemble rainfall forecasting equation based on dynamic factors was validated by using GFS forecast data and six-hour cumulative observed rainfall data from the summers of 2010, 2012, and 2013. Figure 14.4.1 shows the ETS score of the ensemble rainfall forecast in southern China from 00:00 UTC 2 June to 1 October 2010. The scores of ensemble forecasts are higher than those of GFS forecasts for over 10 mm and 20 mm rainfall. For the summers as a whole (489 data points), the average

scores of the ensemble forecasts are also slightly higher than those of GFS forecasts. This means that the ensemble rainfall forecasts are slightly superior to the GFS model in a degree. The biases for both the forecasts are larger than 1. The results for 2012 and 2013 are similar to those for 2010.

Since the ensemble forecast is constructed from model outputs, its skill scores largely depends on the accuracy of the original numerical forecast. The ensemble forecast is an extension of the numerical model forecast and based on the vertical dynamic and thermodynamic factors, but it is different from the numerical model forecasts (which mainly result from the cloud microphysical processes). In fact, the two forecasts may compensate each other. The ensemble method could be used for designing parameterization schemes and setting up the initial conditions for numerical modeling.

14.4.3 Conclusion

Several large-scale physical quantities including the generalized moist potential vorticity, convective vorticity vector, moist thermodynamic advection parameter, wave-activity density have been discussed in this chapter. These quantities contain dynamic and thermodynamic information and have explicit physical meanings. They can be used to depict the vertical structures of dynamic, thermodynamic, and water-vapor fields, and thus are closely related to mesoscale systems. The high values of these dynamic factors and rainfall are correlated, suggesting that these factors can be served as indicators of rainfall. A statistical analysis of long-term time series showed that the evolution of dynamic factors was similar to that of cumulative six-hour observed rainfall amounts with high correlation coefficient.

The dynamic factors were used to develop an ensemble forecasting method for torrential rainfall. A statistical forecast model was constructed with analysis data and observation of rainfall. The weight functions were

constructed based on the correlation coefficients between the retrieved rainfall and observed rainfall. The weight average of rainfall forecasts with the dynamic factors were taken to produce the final rainfall forecasts. This forecast method takes the advantages of multi dynamic factors, reflecting the general and specific characteristics of torrential rainfall. The ETS scores for the ensemble rainfall forecasts were higher than those for the GFS model forecasts.

This ensemble method of forecasting rainfall is a dynamic extension of numerical model outputs. These two kinds of rainfall forecasts compensate for each other. The ensemble forecasts can serve as a reference to the operational forecasts.

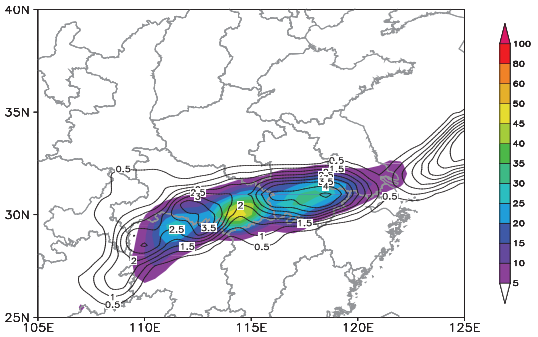

Fig. 14.1.1. Horizontal distribution of the moist thermodynamic advection parameter (10^{-8} K^2 m^{-1} s^{-13}) at 06:00 UTC, 11 July 2010. The shadow area represent the cumulative six-hour observed rainfall amount (mm).

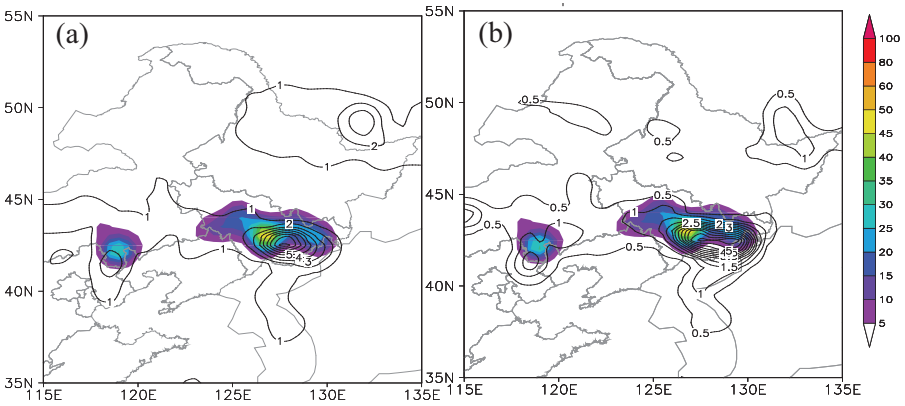

Fig. 14.1.2. (a) The thermodynamic helicity (10^3 km^2 s^{-2}) and (b) vertical flux of the thermodynamic divergence (10^3 km^2 s^{-2}) during torrential rainfall associated with a cold vortex over northeast China at 18:00 UTC, 27 July 2010. The shadow area represent the cumulative six-hour observed rainfall amount (mm).

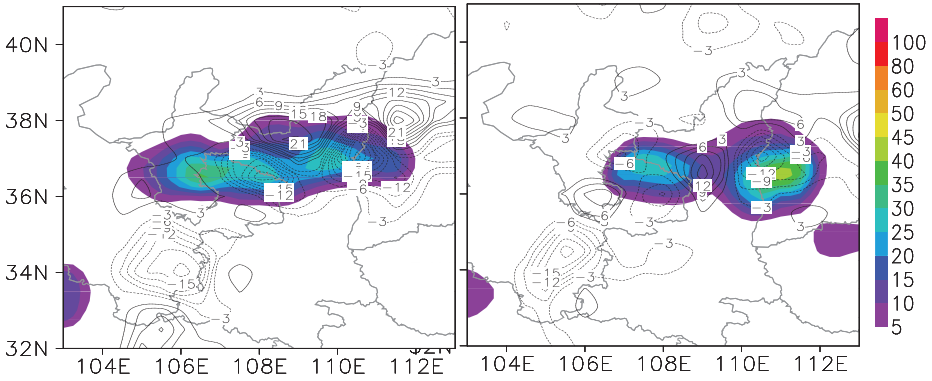

(a) (b)

Fig. 14.1.3. The horizontal distribution of the divergence of the Q vector with generalized potential temperature at 700 hPa on (a) 00:00 UTC 12 July and (b) 00:00 UTC 13 July 2013. The shadow area represent the cumulative six-hour observed rainfall amount (mm).

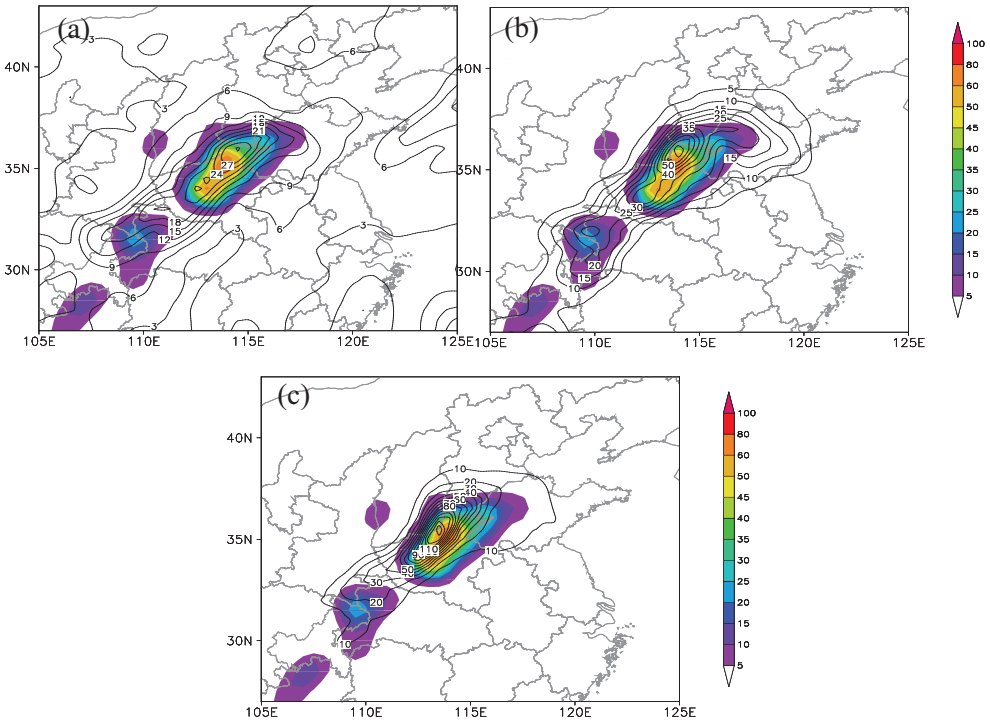

Fig. 14.2.1. (a) The generalized moist potential vorticity (10^{-2} K s^{-1}), (b) solenoidal vorticity (10^{-4} m s^{-3}), and (c) thermodynamic solenoidal vorticity associated with the torrential rainfall produced by a trough at 00:00 UTC, 19 July 2010. The shadow area represent the cumulative six-hour observed rainfall amount (mm).

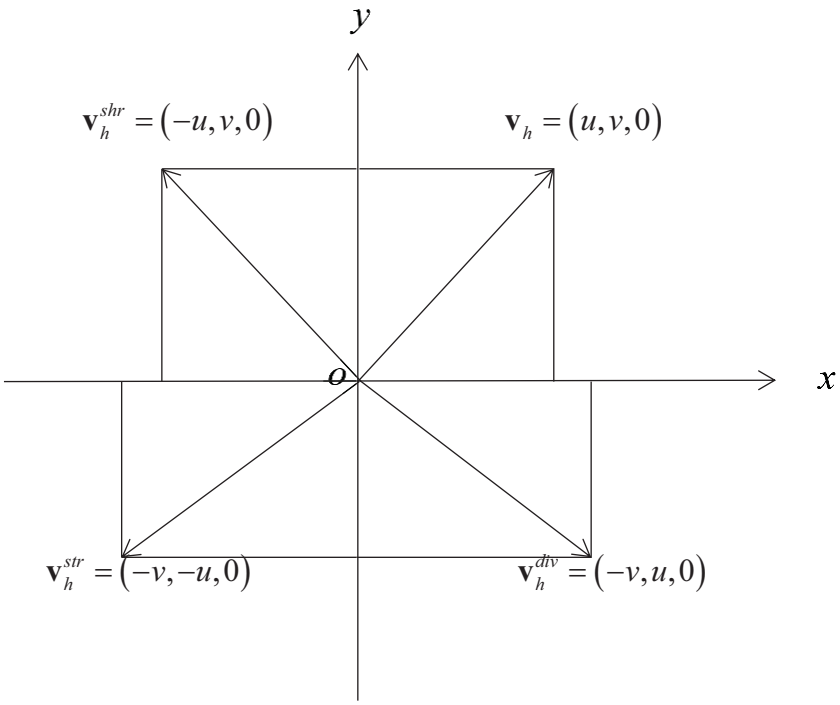

Fig. 14.2.2. Schematic diagram of horizontal wind vectors.

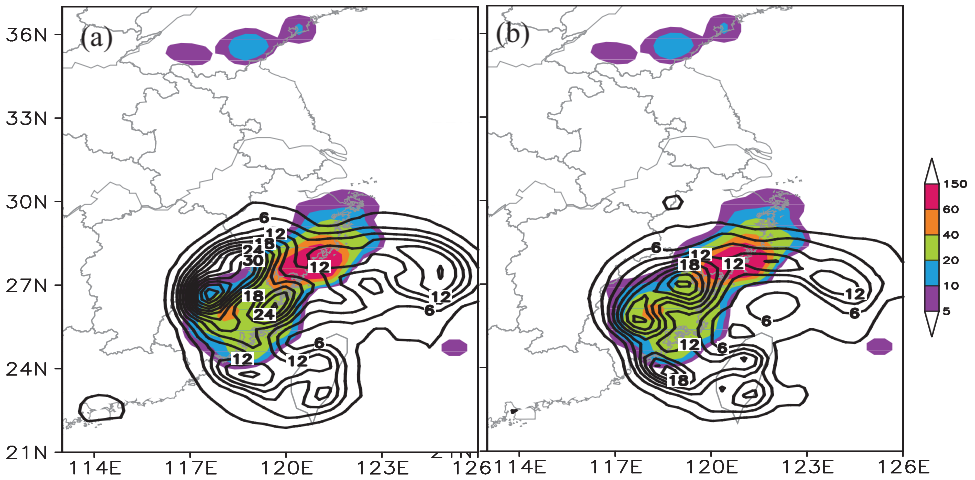

Fig. 14.2.3. Horizontal distributions of (a) potential divergence and (b) potential stretching deformation (10^{-4} K s^{-1}) for 00:00 UTC, 9 August 2009. The shadow area represent the cumulative six-hour observed rainfall amount (mm).

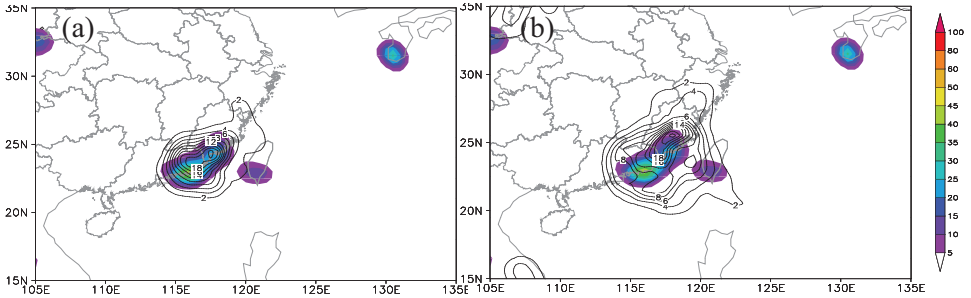

Fig. 14.2.4. (a) The second-order potential vorticity (10^{-10} km^{-1} s^{-2}) and (b) the vertical component of the convective vorticity vector (10^{-3} K s^{-1}) associated with the torrential rainfall of Typhoon Fanapi at 06:00 UTC on 20 September 2010. The shadow area represent the cumulative six-hour observed rainfall amount (mm).

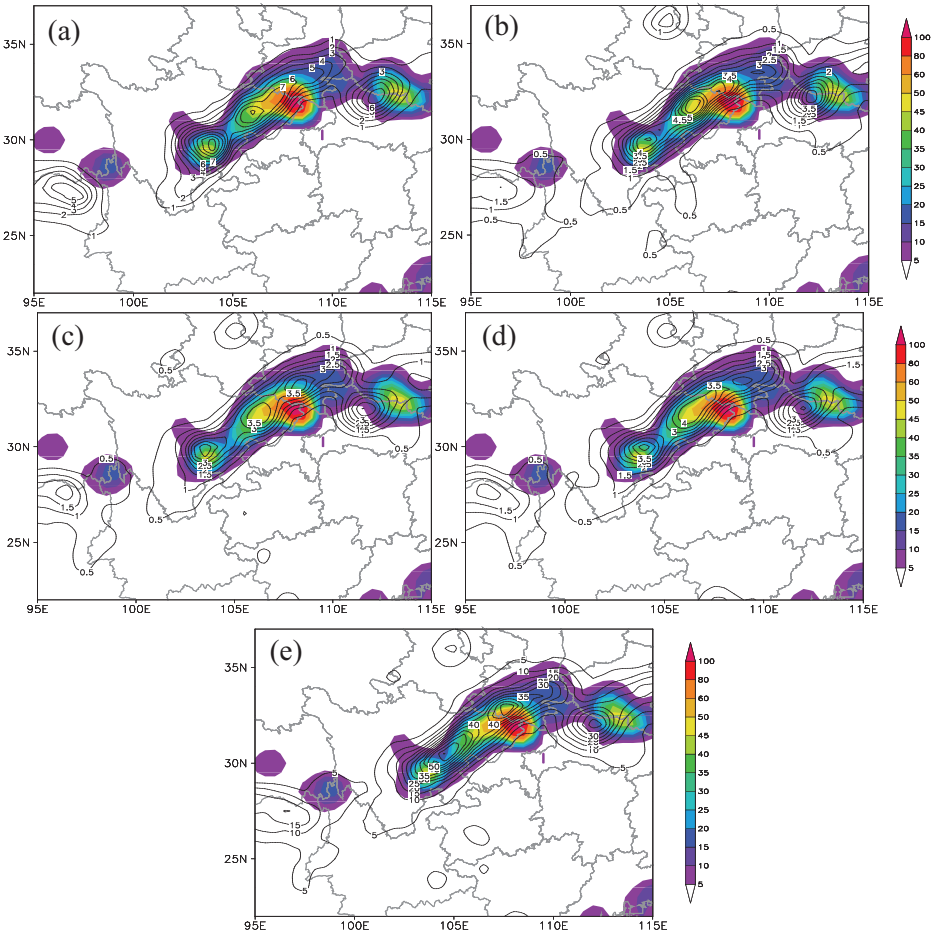

Fig. 14.3.1. The wave-activity densities of (a) the latent heat of condensation (10^{-7} s^{-1}), (b) potential vorticity of the latent heat of condensation (10^{-6} s^{-1}), (c) potential divergence of the latent heat of condensation (10^{-6} s^{-1}), (d) potential shearing deformation of the latent heat of condensation (10^{-6} s^{-1}), and (e) potential stretching deformation of the latent heat of condensation (10^{-6} s^{-1}) associated with the torrential rainfall occurred over Sichuan and Guizhou, China at 00:00 UTC on 17 July 2010. The shadow area represent the cumulative six-hour observed rainfall amount (mm).

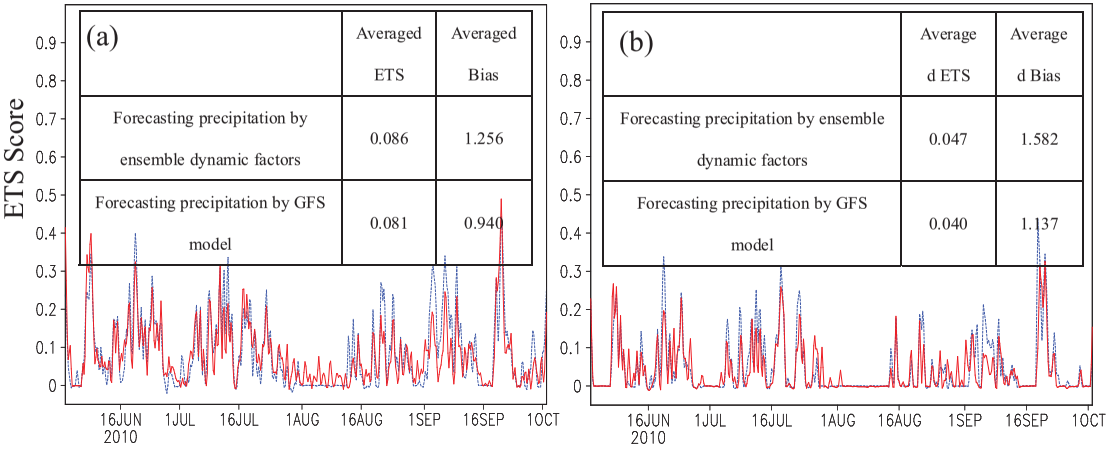

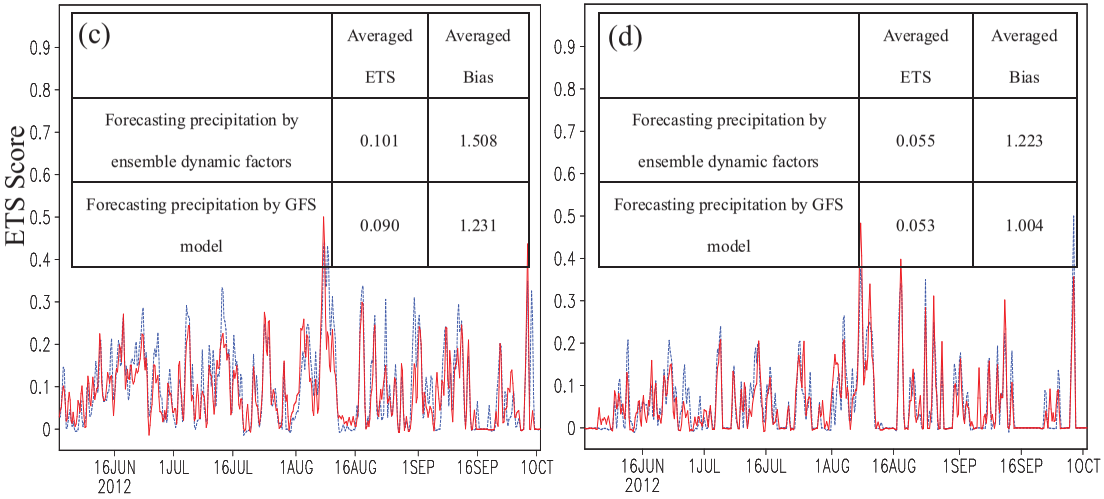

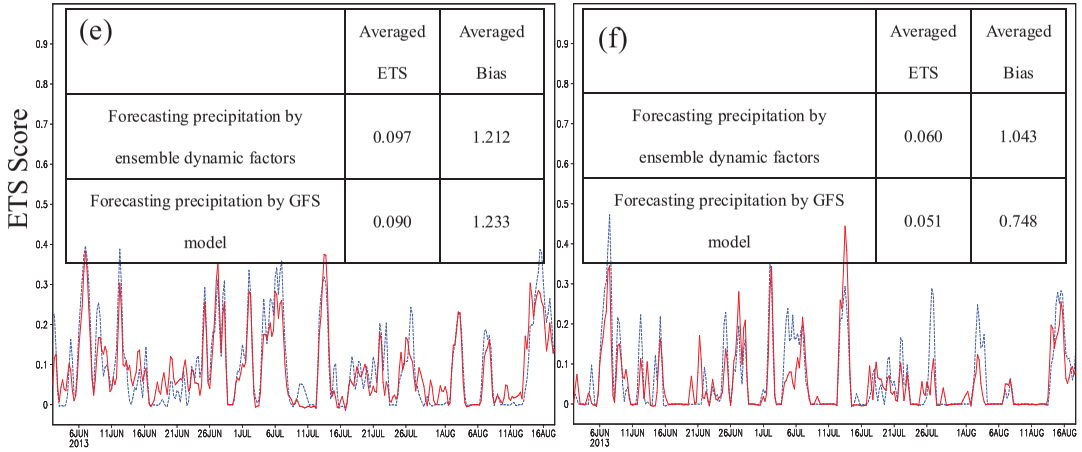

Fig. 14.4.1. Time series of the ETS scores of the six-hour cumulative rainfall amounts forecast in 24 hour using the ensemble rainfall forecast method with dynamic factors (solid red lines) and the GFS model (dashed lines). The results shown are for forecasts of (a) over 10 mm/6 hours and (b) over 20 mm/6 hours for southern China (20°N–35°N, 105°E–125°E) for 00:00 UTC, 2 June to 1 October 2010. (c) and (d) are the same as (a) and (b), respectively, but for 2012, and (e) and (f) are the same as (a) and (b), respectively, but for 2013.

Notes

[1]Tao, S. et al. (1980) *Torrential Rain in China*. Beijing Science Press.

[2]Cheng, L. and W. Feng (2001) "Analyses and numerical simulation on an abrupt heavy rainfall and structure of a mesoscale vortex during July 1998," *Chinese Journal of Atmospheric Sciences*, 25(4):465-478. (in Chinese with English abstract)

[3]Li, Z. and D. Chen (2002) "The development and application of the operational ensemble prediction system at National Meteorological Center," *Journal of Applied Meteorological Science*, 13(1):1-15.

[4]Gao, S., S. Zhao, X. Zhou, et al. (2003) "Progress of research on sub-synoptic scale and mesoscale torrential rain systems," *Chinese Journal of Atmospheric Sciences*, 27(4):618-627. (in Chinese with English abstract)

[5]Deng, G., J. Gong, L. Deng, et al. (2010) "Development of mesoscale ensemble prediction system at National Meteorological Center," *Journal of Applied Meteorological Science*, 21(005):513-523.

[6]Toth, Z. and E. Kalnay (1997) "Ensemble forecasting at NCEP and the breeding method," *Monthly Weather Review*, 125(12):3297-3319.

[7]Bright, D. R. and S. L. Mullen (2002) "Short-range ensemble forecasts of precipitation during the Southwest monsoon," *Weather & Forecasting*, 17(5):1080-1100.

[8]Molteni, F. and R. Buizza (1999) "Validation of the ECMWF ensemble prediction system using empirical orthogonal functions," *Monthly Weather Review*, 127(10):2346-2358.

[9]Di, J., L. Zhao, G. Zhao, et al. (2013) "Study on precipitation multimodel super ensemble forecast technique," *Meteorological Monthly*, 39(6):691-698.

[10]Zhou, B., H. Xu, G. Wu, et al. (2002) "Numerical simulation of CMWDA with its impacting on torrential rain forecast," *Acta Meteorologica Sinica*, 60(003):309-317. (in Chinese with English abstract)

[11]Fang, C., Q. Wan, W. Li, et al. (2003) The difference and reason of the numerical predictions of severe convective heavy rain using synoptic scale initial data in the

different practical initial situations, *Chinese Journal of Atmospheric Sciences*, 27(2):281-288. (in Chinese with English abstract)

[12]Zhang, W., S. Fan and M. Chen (2012) "Applications of mesoscale model-generated sounding in Beijing local rainstorm forecasting," *Torrential Rain Disasters*, 31(1):8-14. (in Chinese with English abstract)

[13]Cheng, C. L., M. X. Chen and J. J. Wang (2013) "Short term quantitative precipitation forecast experiment based on fusion technology of radar extrapolation and mesoscale numerical prediction," *Acta Meteorologica Sinica*, 71(003):397-415. (in Chinese with English abstract)

[14]Yue, C., Y. Shou, S. Shou, et al. (2007) "Wet Q vector interpretation technique with its application to quantitative precipitation forecast," *Journal of Applied Meteorological Science*, 18(5):666-676.

[15]Zhang, X., S. Tao and J. Sun (2010) "Ingredients-based heavy rainfall forecasting," *Chinese Journal of Atmospheric Sciences*, 34(4):754-756. (in Chinese with English abstract)

[16]Qian, W. H., J. Li and X. L. Shan (2013) "Synoptic interpretation of mesoscale model disturbance wind in 2010 Regional Rainstorm Forecast," *Science China*, 35(5):862-873.

[17]Gao, S. and X. Li (2010) "Precipitation equation and their applications to the analysis of diurnal variation of tropical oceanic rain-fall," *Journal of Geophysical Research*, 115(D8), doi: 10.1029/2009JD012452.

[18]Liu, Y. and K. Ma (1996) "A study of heavy rain prediction in typhoon over the South China Sea with statistical method," *Scientia Meteorologica Sinica*, 16(2):173-177. (in Chinese with English abstract)

[19]Li, B. and S. Zhao (2009) "Development of forecasting model of typhoon type rainstorm by using SMAT," *Meteorological Monthly*, 35(6):3-12.

[20]Liu, H., S. Zhao, Z. Lu, et al. (2004) "Objective element forecasts at NMC – a MOS system," *Journal of Applied Meteorological Science*, 15(2):181-191.

[21]Zeng, X., M. Shao, S. Wang, et al. (2008) "Forecasting precipitation experiment with KNN based on crossing verification technology," *Journal of Applied Meteorology Science*, 19(4):471-478.

[22]Gao, S. and L. Ran (2009) "Diagnosis of wave activity in a heavy-rainfall event," *Journal of Geophysical Research*, 114(D08), doi: 10.1029/2008JD010172.
[23]Ran, L., N. Li and S. Gao (2013) "PV-based diagnostic quantities of heavy precipitation: solenoidal vorticity and potential solenoidal vorticity," *Journal of Geophysical Research*, 118(11):5710-5723.
[24]Wu, X., L. Ran and Y. Chu (2011) "Diagnosis of a moist thermodynamic advection parameter in heavy-rainfall events," *Advances in Atmospheric Sciences*, 28(4):957-972.
[25]Davies-Jones, R. P. (1991) "The frontogenetical forcing of secondary circulations. Part I: The duality and generalization of the Q vector," *Journal of Atmospheric Sciences*, 48(4):497-509.
[26]Yao, X., Y. Yu and S. Shou (2004) "Diagnostic analyses and application of the moist ageostrophic Q vector," *Advances in Atmospheric Sciences*, 21(001):96-102.
[27]Yue, C. J. (2009) "The Q vector analysis of the heavy rainfall from Meiyu front cyclone: A case study," *Acta Meteorologica Sinica*, 66(1):3-7. (in Chinese with English abstract)
[28]Gao, S., X. Wang and Y. Zhou (2004) "Generation of generalized moist potential vorticity in a frictionless and moist adiabatic flow," *Geophysical Research Letters*, 31(12), doi: 10.1029/2003GL019152.
[29]Liang, Z., C. Lu and E. I. Tollerud (2010) "Diagnostic study of generalized moist potential vorticity in a non-uniformly saturated atmosphere with heavy precipitation," *Quarterly Journal of the Royal Meteorological Society*, 136(650):1275-1288.
[30]Chu, Y., Z. Wang, L. Ran, et al. (2013) "Diagnosis and application of potential shear deformation wave-activity density in the torrential rain of typhoon Morokat (2009)," *Acta Physica Sinica*, 62(9), doi: 10.7498/aps.62.099201.
[31]Qi, Y., L. Ran and Y. Hong (2010) "Diagnosis of thermodynamic shear advection parameter in heavy rainfall events," *Chinese Journal of Atmospheric Sciences*, 34(6):1201-1213. (in Chinese with English abstract)

BIBLIOGRAPHY

Books

Andrews D. G. (2000) *An Introduction to Atmospheric Physics*. Cambridge University Press.

Chen, Q. (1987) Dynamics of Synoptic and Sub-Synoptic Systems. Science Press. (in Chinese)

Cushman-Roisin B (1994). Introduction to Geophysical Fluid Dynamics, Printice-Hall, Inc.

Dodd, K. R., J. C. Elibeck, J. D. Gibbon and *et al.* (1982) *Solitons and Nonlinear Wave Equations*. London: Academic Press.

Driscoll, D. M. (1985) Handbook of Applied Meteorology, *D. D. Houghton, Ed. John Wiley and Sons*.

Durran D.R. (1999) *Numerical methods for wave equations in*, *Geophys Fluid Dyn*. Springer-Verlag New York, Inc.

Eliassen, A. and E. Kleinschmidt (1957) *Handbuch der Physik*.Berlin: Springer-Verlag.

Emanuel K. A. (1994) *Atmospheric Convection*. New York Oxford: Oxford University press.

Green, J. (1999) Atmospheric Dynamics, Cambridge University Press.

Holton, J. R. (1972) *An Introduction to Dynamical Meteorology*, Academic Press.

Holton, J. R. (1975) *The Dynamic Meteorology of the Stratosphere and Mesosphere*, American Meteorological Society.

Norbury, J. and I. Roulstone (2002). *Large-Scale Atmosphere-Ocean Dynamics Volume I: Analytical Methods and Numerical Models*.

Cambridge University Press.

James, I. N. (1995) *Introduction to circulating atmospheres*, Météorologie. Cambridge University Press.

Pedlosky, J. (1979) *Geophysical Fluid Dynamics*. Springer-Verlag New York Inc

Petterssen S. (1956) Weather analysis and forecasting, Vol.1: *Motion and Motion Systems*, 2nd edition, McGraw-Hill, 428pp.

Petterssen S. (1956) *Weather analysis and forecasting: Vol I.* Science Press.

Scorer R. S. (1997) *Dynamics of Meteorology and Climate*. Praxis Publishing Ltd.

Shou, S. W., S. S. Li and X. P. Yao (2003) *Mesoscale Meteorology*, Meteorological Press, Beijing. (in Chinese)

Tao, S. et al. (1980) *Torrential Rain in China.* Beijing Science Press.

Tritton, D. J. (1977) *Physical Fluid Dynamics*. Van Nostrand Reinhold Company.

Vallis G. K. (2006) *Atmospheric and Oceanic Fluid Dynamics: Fundamentals and Large-Scale Circulation*. Cambridge University Press.

Wiin-Nielsen A. (1973) *Compendium of meteorology*: *Vol I.,* World Meteorological Organization. *No.364.*

Wu R. S. (2002) *Atmospheric Dynamics*, High Education Press.

Wu R. S., S. T. Gao, Z. M. Tan and et al. (2004) *Frontal Processes and Mesoscale Disturbances*. Beijing: Meteorological Press

Zeng Q. C. (1979) *Mathematical and Physical Basis of the Numerical Weather Forecast*. Beijing: Science Press

Articles

Allen, J. S., J. A. Barth and P. A. Newberger (1990) “On intermediate models for barotropic continental shelf and slope flow fields. Part I: Formulation Comparison Exact Solutions,” *Journal of Physical Oceanography*, 20(7).

Andrews, D. G. (1983). "Finite-amplitude Eliassen-Palm theorem in isentropic coordinates," *Journal of Atmospheric Sciences*, 40(8).

Andrews, D. G. (1987) "On the interpretation of the Eliassen-Palm flux divergence," *Quarterly Journal of the Royal Meteorological Society*, 113(475).

Ari Sadarjoen I. and F. H. Post (2000) "Detection, quantification, and tracking of vortices using streamline geometry," *Journal of Computational and Graphical statistics,* 24(3).

Bannon P. R. (2002) "Theoretical foundations for models of moist convection," *Journal of Atmospheric Sciences*, 59(12).

Bartels, D. L and R. A. Maddox (1991) "Midlevel cyclonic vortices generated by mesoscale convective systems," *Monthly Weather Review*, 119(1).

Barth, J. A., J. S. Allen and P. A. Newberger (1990) "On intermediate models for barotropic continental shelf and slope flow fields, Part II: Comparison of Numerical Model Solutions in Doubly Periodic Domains," *Journal of Physical Oceanography*, 27(20).

Beardsley, R. C. and C. D. Winant(1979) "On the mean circulation in the Mid-Atlantic Bight," *J Phys Oceanogr,* 9(3).

Beer, T. and I. Tolstoy (1975) "Atmospheric waves," *Physics Today,* 28(11).

Bennetts D. A. and B. J. Hoskins (1979) "Conditional symmetric instability-A possible explanation for frontal rainbands," *Quarterly Journal of the Royal Meteorological Society*, 105(446).

Betts, A. K. and F. J. Dugan (1973) "Empirical formula for saturation pseudoadiabats and saturation equivalent potential temperature," *Journal of Applied Meteorology*, 12(4).

Bishop C. H. and A. J. Thorpe(1994a) "Frontal wave stability during moist deformation frontogenesis. Part I: Linear wave dynamics," *Journal of Atmospheric Sciences,* 51(6).

Bishop C. H. and A. J. Thorpe (1994b) "Frontal wave stability during moist deformation frontogenesis. Part II: The suppression of nonlinear wave development," *Journal of Atmospheric Sciences,* 51(6).

Bolton, D. (1980) "The computation of equivalent potential temperature," Monthly Weather Review, 108(7).

Brandes, E. A. (1990) "Evolution and structure of the 6-7 May 1985 mesoscale convective system and associated vortex," *Monthly Weather Review*, 118(1).

Brandes E. A., R. P. Davies-Jones and B. C. Johnson (1988) "Streamwise vorticity effects on supercell morphology and persistence," *Journal of Atmospheric Sciences*, 45(6).

Bright, D. R. and S. L. Mullen (2002) "Short-range ensemble forecasts of precipitation during the Southwest monsoon," *Weather & Forecasting*, 17(5).

Brooks H. E., C. A. Doswell III and R. P. Davies-Jones (1990) "Environmental helicity and the maintenance and evolution of low-level meso-cyclones," *the Tornado: its Structure, Dynamics, Prediction, and Hazards*, Geophysics, Monograph, American Geophysical Union, 79.

Brooks H. E. and R. B. Wilhelmson (1990) "The effect of low-level hodograph curvature on supercell structure," *Preprints 16th Conference on Severe Local Storms, Kananaskis Park, Alberta, Canada*, American Meteorological Society

Brunet, G. and P. H. Haynes (1996) "Low-latitude reflection of Rossby wave trains," *Journal of Atmospheric Sciences*, 53(3).

Buizza, R. and T. N. Palmer (1995) "The singular-vector structure of the atmospheric global circulation," *Journal of Atmospheric Sciences,* 52(9).

Cai M. (1992) "A physical interpretation of the stability property of a localized disturbance in a deformation flow," *Journal of Atmospheric Sciences,* 49(23).

Cai M. and M. Mak (1990) "On the basic dynamics of regional cyclogenesis," *Journal of Atmospheric Sciences,* 47(12).

Cao J. and Q. Xu (2011) "Computing hydrostatic potential vorticity in terrain-following coordinates," *Monthly Weather Review*, 139(9).

Cao Z. and H. Cho (1995) "Generation of moist vorticity in extratropical cyclones," *Journal of Atmospheric Sciences*, 52(18).

Cao, Z. H. and D. L. Zhang (2005) "Sensitivity of cyclone tracks to the initial moisture distribution moist potential vorticity perspective," *Advances in Atmospheric Sciences*, 22(6).

Caracena F., R. A. Maddox, L. R. Hoxit and et al. (1979) "Mesoanalysis of the big Thompson storm," *Monthly Weather Review*, 107(1).

Charney J. G. (1947) "The dynamics of long waves in a baroclinic westerly current," *Journal of Meteorology,* 4(5).

Charney, J. G. (1955) "The use of primitive equations of motion in numerical prediction," *Tellus*, 7(1).

Charney, J. G. (1962) "Integration of the primitive and the balance equations," *Proc. International Symposium of Numerical Weather Prediction, Tokyo*, Meteorological Society of Japan

Charney, J. G. and J. G. Devore (1979) "Multiple flow equilibria in the atmosphere and blocking," *Journal of Atmospheric Sciences,* 36(7).

Charney J. D. and Y. Ogura (1962) "A numerical model of thermal convection in the atmosphere," *Journal of the Meteorological Society of Japan*, 38(6).

Chen Z. M., K. Q. Yang and H. Y. Wu (2009) "Mechanism of heavy rainfall maintenance and increment in convergence excited by coupling forces between dynamic and thermodynamic fields," *Acta Physica Sinica*, 58(6).

Cheng, C. L., M. X. Chen and J. J. Wang (2013) "Short term quantitative precipitation forecast experiment based on fusion technology of radar extrapolation and mesoscale numerical prediction," *Acta Meteorologica Sinica*, 71(003). (in Chinese with English abstract)

Cheng, L. and W. Feng (2001) “Analyses and numerical simulation on an abrupt heavy rainfall and structure of a mesoscale vortex during July 1998,” *Chinese Journal of Atmospheric Sciences*, 25(4). (in Chinese with English abstract)

Cho, J. Y. N. (1995) “Inertio-gravity wave parameter estimation from cross-spectral analysis,” *Journal of Geophysical Research*, 100(D9).

Chu, Y., Z. Wang, L. Ran, et al. (2013) “Diagnosis and application of potential shear deformation wave-activity density in the torrential rain of typhoon Morokat (2009),” *Acta Physica Sinica*, 62(9).

Clark, T. L., T. Hauf, and J. P. Kuettner (1986) “Convectively forced internal gravity waves: results from twodimensional numerical experiments,” *Quarterly Journal of the Royal Meteorological Society*, 112(474).

Danielsen E. F. (1968) “Stratospheric-tropospheric exchange based on radioactivity, ozone and potential vorticity,” *Journal of Atmospheric Sciences,* 25(3).

Danielsen E. F. and R. S. Hipskind (1980) “Stratospheric-tropospheric exchange at polar latitudes in Summer,” *Journal of Geophysical Research*, 85(C1).

Davis C. A. and K. A. Emanuel (1991) “Potential vorticity Diagnostics of cyclogenesis,” *Monthly Weather Review,* 119(8).

Davis C. A. and M. L. Weisman (1994) “Balanced dynamics of mesoscale vortices in simulated convective systems,” *Journal of Atmospheric Sciences*, 51(14).

Davies-Jones R. P. (1982) *Observational and Theoretical Aspects of Tornadogenesis. Intense Atmospheric Vortices*, L. Bengtsson and J. Lighthill, Eds. Springer-Verlag

Davies-Jones R. P. (1984) “Streamwise vorticity: the origin of updraft rotation in supercell storms,” *Journal of Atmospheric Sciences*, 41(20).

Davies-Jones R. P. (1985) “Comments on “A kinematic analysis of frontogenesis associated with a nondivergent vortex,” *Journal of*

Atmospheric Sciences, 42(19).

Davies-Jones, R. P. (1991) "The frontogenetical forcing of secondary circulations. Part I: The Duality and Generalization of the Q Vector," *Journal of Atmospheric Sciences*, 48(4).

Davies-Jones, R. P. (1991) "The frontogenetical forcing of secondary circulations. Part I: The duality and generalization of the Q vector," *Journal of Atmospheric Sciences*, 48(4).

Davies-Jones R., D. W. Burgess and M. Foster (1990) "Test of helicity as a forecast parameter," *Preprints 16th Conference on Severe Local Storms, Kananaskis Park, Alberta, Canada*, American Meteorological Society

Deng, G., J. Gong, L. Deng, et al. (2010) "Development of mesoscale ensemble prediction system at National Meteorological Center," *Journal of Applied Meteorological Science*, 21(005).

Di, J., L. Zhao, G. Zhao, et al. (2013) "Study on precipitation multimodel super ensemble forecast technique," *Meteorological Monthly*, 39(6).

Doswell III C. A. (1984) "A kinematic analysis of frontogenesis associated with a nondivergent vortex," *Journal of Atmospheric Sciences*, 41(7).

Doswell, C. A. (1987) "The distinction between large-scale and mesoscale contribution to severe convection: A case study example," *Weather & Forecasting*, 2(1).

Droegemeier K. K., S. M. Lazarus and R. P. Davies-Jones (1993) "The influence of helicity on numerically simulated convective storms," *Monthly Weather Review*, 121(7).

Durran, D. R. (1995) "Pseudomomentum diagnostics for two-dimensional stratified compressible flow," *Journal of Atmospheric Sciences*, 52(22).

Durran D. R. and J. B. Klemp (1982) "On the effects of moisture on the brunt-Väisalä frequency," *Journal of Atmospheric Sciences*, 39(10).

Eady, E.T. (1949) "Long Waves and Cyclone Waves," Tellus, 1(3):33–52.

Elhmaidi D., A. Provenzale, T. Lili and *et al.* (2004) "Stability of two-dimensional vorticity Filaments," *Physical Letters A,* 333(1-2).

Emanuel K. A. (1979) "Inertial instability and mesoscale convective systems. Part I: Linear theory of inertial instability in rotating viscous fluids," *Journal of Atmospheric Sciences*, 36(12).

Ertel H. (1942) "Ein Neuer hydrodynamischer wir-belsatz," *Meteorologische Zeitschrift,* 59:271–281.

Etling D. (1985) "Some aspects of helicity in atmosphere flows," *Beiträge zur Physik Der Atmosphäre*, 58(1).

Fang, C., Q. Wan, W. Li, et al., 2003: The difference and reason of the numerical predictions of severe convective heavy rain using synoptic scale initial data in the different practical initial situations, *Chinese Journal of Atmospheric Sciences*, 27(2). (in Chinese with English abstract)

Farrell B. F. (1989) "Transient development in confluent and diffluent flow," *Journal of Atmospheric Sciences,* 46(21).

Fei S. Q. and Z. M. Tan (2001) "On the helicity dynamics of severe convective storms", *Advances in Atmospheric Science*, 18(1).

Fernandez W. and A. J. Thorpe (1979) "An evaluation of theories of storm motion using observations of tropical convective systems," *Monthly Weather Review,* 107(10).

Fetzer, E, J. and J. C. Gille (1994) "Gravity wave variance in LIMS temperatures. Part I. Variability and comparison with background winds," *Journal of Atmospheric Sciences*, 51(17).

Fovell, R., D. Durran, and J. R. Holton (1992) "Numerical simulations of convectively generated stratospheric gravity waves," *Journal of Atmospheric Sciences*, 49(16).

Fraser, A. B., R. C. Easter and P. V. Hobbs (1973) "A theoretical study of the flow of air and fallout of solid precipitation over mountainous terrain: Part I. Air flow model," Journal of Atmospheric Sciences, 30(5).

Fritsch J. M. and R. A. Maddox (1981) "Convectively driven mesoscale weather systems aloft. Part I: Observations," *Journal of Applied Meteorology*, 20(1).

Fritsch, J. M., J. D. Murphy and J. S. Kain (1994) "Warm-core vortex amplification over land," *Journal of Atmospheric Sciences*, 51(13).

Fritts, D. C. (1984) "Gravity wave saturation in the middle atmosphere: a review of theory and observations," *Reviews of Geophysics*, 22(3).

Fulton S. R., W. H. Schubert and S. A. Hausman (1995) "Dynamical adjustment of mesoscale convective anvils," *Monthly Weather Review*, 123(11).

Gao, S. and S. Sun (1986) "Determining the instability of mesoscale perturbations with Richardson number," Sci Atmospheric Sinica, 10(2). (in Chinese)

Gao S. and X. Cui (2006) "A modified potential vorticity equation for mesoscale systems," *J Graduate School of Chinese Academy of Sciences*, 118(23).

Gao S. T. and T. Lei (2000) "Streamwise vorticity equation," *Advances in Atmospheric Science*, 17(3).

Gao S. T., T. Lei, and Y. S. Zhou (2002) "Moist potential vorticity anomaly with heat and mass forcings in torrential rain system," *Chinese Physical letters*, 19(6).

Gao S. T., T. Lei, Y. S. Zhou and et al. (2002) "Diagnostic analysis of moist potential vorticity anomaly torrential rain systems," *Journal of Applied Meteorological Science*, 13(6). (in Chinese with English abstract)

Gao, S. and X. Li (2010) "Precipitation equation and their applications to the analysis of diurnal variation of tropical oceanic rain-fall," *Journal of Geophysical Research*, 115(D8).

Gao, S., X. Li, W. K. Tao, et al. (2007) "Convective and moist vorticity vectors associated with tropical oceanic convection: A three-dimensional cloud-resolving simulation," *Journal of Geophysical Research*, 112(D1).

Gao, S. T. and K. R. Liu (1998) "A study of the effect of gravitly wave breaking on middle atmospheric circulation," *Acta Meteorologica Sinica*, 12(4).

Gao, S., F. Ping, X. Li, et al. (2004) "A convective vorticity vector associated with tropical convection: A two-dimensional cloud-resolving modeling study," *Journal of Geophysical Research*, 109(D14).

Gao, S. and L. Ran (2009) "Diagnosis of wave activity in a heavy-rainfall event," *Journal of Geophysical Research*, 114(D08).

Gao S. T., S. Y. Tao and Y. H. Ding (1990) "The generalized E-P flux of wave-mean flow interactions," *Science China S B,* 33(6).

Gao S. T., X. Wang and Y. Zhou (2004) "Generation of generalized moist potential vorticity in a frictionless and moist adiabatic flow," *Geophysical Research Letters*, 31(12).

Gao, S.T., P. C. Xu, N. Li and et al. (2014) "Second-order potential vorticity and its potential applications," *Science China Earth Science*, 57(10).

Gao S.T., P. C. Xu, L. K. Ran and et al. (2012) "On the generalized Ertel–Rossby invariant," *Advances in Atmospheric Sciences*, 29(4).

Gao S. T., S. Yang, M. Xue and *et al.* (2008) "Total deformation and its role in heavy precipitation events associated with deformation-dominant flow patterns," *Advances in Atmospheric Sciences,* 25(1).

Gao, S. T. and H. D. Zhang and W. S. Lu (2004) "Ageostrophic generalized e–p flux in baroclinic atmosphere," *Chinese Physics Letters*, 21(3).

Gao, S., S. Zhao, X. Zhou, et al. (2003) "Progress of research on sub-synoptic scale and mesoscale torrential rain systems," *Chinese Journal of Atmospheric Sciences*, 27(4). (in Chinese with English abstract)

Gao, S. T. and F. Zhou (2006) "Mesocale balance equation and the diagnostic method of unbalanced flow based on helicity," *Chinese Journal of Atmospheric Sciences*, 30(5). (in Chinese with English

abstract).

Gao, S., Y. Zhou, X. Cui et al. (2004) "Impacts of cloud-induced mass forcing on the development of moist potential vorticity anomaly during torrential rains," *Advances in Atmospheric Sciences*, 21(6).

Gray M. E. B. (1999) "An investigation into convectively generated potential-vorticity anomalies using a mass-forcing model," *Quarterly Journal of the Royal Meteorological Society*, 125(557).

Gray M. E. B., G. J. Shutts and G. C. Craig (1998) "The role of mass transfer in describing the dynamics of mesoscale convective systems," *Quarterly Journal of the Royal Meteorological Society*, 124(548).

Grivet-Talocia, S., F. Einaudi, W. L. Clark et al. (1999) "A 4-yr climatology of pressure disturbances using a barometer network in central Illinois," *Monthly Weather Review*, 127(7).

Harasti P. R. and R. List (2005) "Principal component analysis of Doppler radar data. Part I: Geometric connections between eigenvectors and the core region of atmosphere vortices," *Journal of Atmospheric Sciences*, 62(11).

Haynes, P. H. (1988) "Forced, dissipative generalizations of finite-amplitude wave activity conservation relations for zonal and nonzonal basic flows," *Journal of Atmospheric Sciences*, 45(16).

Haynes P. H. and M. E. McIntyre (1987) "On the evolution of vorticity and potential vorticity in the presence of diabatic heating and frictional or other forces," *Journal of Atmospheric Sciences,* 44(5).

Haynes P. H. and M.E. McIntyre (1990) "On the conservation and impermeability theorems for potential vorticity," *Journal of Atmospheric Sciences*, 47(16).

Helmholtz, H. (1868) "On the discontinuous movement of fluids," *Philosophical Magazine,* 36(4).

Hirota, I. and T. Niki (1985) "A statistical study of inertia-gravity waves in the middle atmosphere," *Journal of the Meteorological Society of Japan*, 63(6).

Höppe, P. (1999) “The Physiological equivalent temperature – a universal index for the biometeorological assessment of the thermal environment,” *International Journal of Biometeorology*, 43(2).

Houze, R. A., B. F. Smull and P. Dodge (1990) “Mesoscale organization of springtime storms in Oklahoma,” *Monthly Weather Review*, 118(3).

Hoskins B. J. and P. Berrisford (1988) “A potential vorticity perspective of the storm of 15-16 October 1987,” *Weather,* 43(3).

Hoskins B. J. and F. P. Bretherton (1972) “Atmospheric frontogenesis models: mathematical formulation and Solution,” *Journal of Atmospheric Sciences*, 29(1).

Hoskins, B. J., I. Draghici and H. C. Davies (1978) “A new look at the ω-equation,” *Quarterly Journal of the Royal Meteorological Society*, 104(347).

Hoskins B. J., M. E. McIntyre and A. W. Robertson (1985) “On the use and significance of is entropic potential-vorticity maps,” *Quarterly Journal of the Royal Meteorological Society*, 111(470).

Hoskins B.J. and K. I. Hodges (2002) “New perspectives on the Northern Hemisphere winter storm tracks,” *Journal of Atmospheric Sciences,* 59(6).

Hoxit L.R., J. M. Fritsch and C. F. Chappell (1978) [Reply]: Reply, *Monthly Weather Review*, 106(7).

Huang, W. G., B. S. Deng and T. N. Xiong (1997) “The primary analysis on a typhoon torrential rain,” *Quarterly Journal of Applied Meteorology*, 8(2). (in Chinese with English abstract)

James, T. M. and W. A. Abeling (1988) “A diagnosis of unbalanced flow in upper levels during the AVE-SESAME 1 period,” *Monthly Weather Review*, 116(12).

Jiang, H. and D. J. Raymond (1995) “Simulation of a mature mesoscale convective system using a nonlinear balance model,” *Journal of Atmospheric Sciences*, 52(2).

Jiang Y. Q. Study on the dynamic mechanism of formation of mesoscale weather systems triggered by wind perturbations [*Ph.D dissertation of Nanjing University*], 2011.

Jiang Y. Q., Y. Wang, Z. G. Zhou and et al. (2011) "Interaction index of vortex and deformation Field," *Journal of PLA University of Science and Technology*, 12(6).

Kalkstein, L. S. and K. M. Valimont (1986) "An Evaluation of Summer Discomfort in the United State Using a Relative Climatological Index," *Bulletin of the American Meteorological Society*, 67(7).

Karl, T. R. and R. W. Knight (1997) "The 1995 Chicago heat wave: How likely is a recurrence?" *Bulletin of the American Meteorological Society*, 78(6).

Kelvin, W. (1871) "The influence of wind on waves in water supposed frictionless," *Philosophical Magazine,* 42.

Keyser D., M. J. Pecnick and M. A. Shapiro (1986) "Diagnosis of the role of vertical deformation in a two-dimensional primitive equation model of upper-level frontogenesis," *Journal of Atmospheric Sciences,* 43(8).

Keyser D., M. J. Reeder and R. J. Reed (1988) "A generalization of Pettersen's frontogenesis function and its relation to the forcing of vertical motion," *Monthly Weather Review,* 116(3).

Keyser D. and R. Rotunno (1990) "On the formation of potential vorticity anomalies of upper-level jet front systems," *Monthly Weather Review,* 118(9).

Keyser, D., B. D. Schmidt and D. G. Duffy (1989) "A technique for representing three-dimensional vertical circulations in baroclinic disturbances," *Monthly Weather Review*, 117(11).

Koch, S. E. and P. B. Dorian (1988) "A mesoscale gravity wave event observed durntain CCOPE. Part III: Wave environment and probable source mechanisms," *Monthly Weather Review*, 116(12).

Krishnamurti, T. N. (1968) "A diagnostic balance model for studies of weather systems of low and high latitudes, Rossby number less than 1,"

Monthly Weather Review, 96(4).

Kuo H. L. (1949) "Dynamics instability od two-dimensional non-divergent flow in a barotropic atmosphere," *Journal of Meteorology,* 6(2).

Lalas, D. P. and F. Einaudi (1974) "On the correct use of the wet adiabatic lapse rate in stability criteria of a saturated atmosphere," Journal of Applied Meteorology, 13(3).

Leary, C. A. and E. N. Rappaport (1987) "The lifecycle and internal structure of a mesoscale Convective complex," *Monthly Weather Review*, 115(8).

Li, B. and S. Zhao (2009) "Development of forecasting model of typhoon type rainstorm by using SMAT," *Meteorological Monthly*, 35(6).

Liang, Z., C. Lu and E. I. Tollerud (2010) "Diagnostic study of generalized moist potential vorticity in a non-uniformly saturated atmosphere with heavy precipitation," *Quarterly Journal of the Royal Meteorological Society*, 136(650).

Liu, H., S. Zhao, Z. Lu, et al. (2004) "Objective element forecasts at NMC – a MOS system," *Journal of Applied Meteorological Science*, 15(2).

Li N., L. K. Ran and S. T. Gao (2019) "On the interactions of vorticity, divergence and deformation in a meso-α scale vortex," *Meteorology and Atmospheric Physics,* 132.

Li Y. H. and S. W. Shou (1999) "Rotational wind helicity and its effects on torrential rain process," *Transactions of Atmospheric Sciences*, 22(1).

Li, Z. and D. Chen (2002) "The development and application of the operational ensemble prediction system at National Meteorological Center," *Journal of Applied Meteorological Science*, 13(1).

Lilly D. K. (1986a) "The structure, energetics and propagation of rotating convective storms, Part I: Energy exchange with the mean flow," *Journal of Atmospheric Sciences*, 43(2).

Lilly D. K. (1986b) "The structure, energetics and propagation of rotating convective storms, Part II: Helicity and storm stabilization," *Journal of*

Atmospheric Sciences, 43(2).

Lilly, D. K. and P. J. Kennedy (1973) "Observations of a stationary mountain wave and its associated momentum flux and energy dissipation," *Journal of Atmospheric Sciences*, 30(6):.

Lindzen, R. S. (1974) "Stability of a helmholtz velocity profile in a continuously stratified, Infinite Boussinesq fluid—applications to clear air turbulence," *Journal of Atmospheric Sciences*, 31(6).

Lindzen, R. S. (1981) "Turbulence and stress owing to gravity wave and tidal breakdown," *Journal of Geophysical Research*, 86(C10).

Liu, D. and S. T. Gao (2003) "The brunt-Väisälä frequency in a saturated atmosphere and the revised equivalent potential temperature," *Acta Meteorological Sinica*, 61(3). (in Chinese with English abstract)

Liu, Y. and K. Ma (1996) "A study of heavy rain prediction in typhoon over the South China Sea with statistical method," *Scientia Meteorologica Sinica*, 16(2). (in Chinese with English abstract)

Liu S. K. and S. D. Liu (1997) "Toroidal-poloidal decomposition and Beltrami flows in atmosphere motions," *Chinese Journal of Atmospheric Science*, 21(2).

Lu, C., S. E. Koch and N. Wang (2005): "Determination of temporal and spatial characteristics of gravity waves using cross-spectral analysis and wavelet transformation," *Journal of Geophysical Research*, 110(D01).

Lu H. J. and S. T. Gao (2003) "On the helicity and the helicity equation", *Acta Meteorogica Sinica*, 61(6). (in Chinese with English abstract)

Luo Z. X. and K. Dai (2008) "A climatological investigation of the activity of summer subtropical vortices", *Acta Meteorologica Sinica,* 22(1).

MacKay, M. D. (1998) "A pseudoenergy conservation law for the two-dimensional primitive equations," *Journal of Atmospheric Sciences*, 55(13).

Maddox R. A., F. Canova and L. R. Hoxit (1980a) “Meteorological characteristics of flash flood events over the western United States,” *Monthly Weather Review*, 108(11).

Maddox R. A., L. R. Hoxit and C. F. Chappell (1980b) “A study of tornadic thunderstorm interactions with thermal boundaries,” *Monthly Weather Review*, 108(3).

Maddox R. A., L. R. Hoxit, C. F. Chappell and et al. (1978) “Comparison of meteorological aspects of the big Thompson and rapid city flash floods,” *Monthly Weather Review*, 106(3).

Magnusdottir, G. and P. H. Haynes (1996) “Application of wave-activity diagnostics to baroclinic-wave life cycles,” *Journal of Atmospheric Sciences*, 53(16):.

Mak M. (1991) “Dynamics of an atmospheric blocking as deduced from its local Energetics,” *Quarterly Journal of the Royal Meteorological Society,* 117(499).

Mak M. and M. Cai (1989) “Local barotropic instability,” *Journal of Atmospheric Sciences,* 46(21).

Markowski P. M., J. M. Straka, E. N. Rasmussen and et al. (1998) “Variability of storm-relative helicity during vortex,” *Monthly Weather Review*, 126(11).

Matsuno, T. (1982) “A quasi one-dimensional model of the middle atmospheric circulation interacting with internal gravity waves,” *Journal of the Meteorological Society of Japan*, 60(1).

McFarlane, N. A. (1987) “The effect of orographically exited gravity wave drag on the general circulation of the lower stratosphere and troposphere,” *Journal of Atmospheric Sciences*, 44(14).

McIntyre, M. E. (1980) “An introduction to the generalized Lagrangian-mean description of wave, mean-flow interaction,” *Pure and Applied Geophysics*, 118.

McIntyre, M. E. and T. G. Shepherd (1987) “An exact local conservation theorem for finite amplitude disturbances to non-parallel shear flows,

with remarks on Hamiltonian structure and on Arnol'd 's stability theorems," *Journal of Fluid Mechanics*, 181(1).

McIntyre, M. E. and W. A. Norton (2000) "Potential vorticity inversion on a hemisphere," *Journal of Atmospheric Sciences*, 57(9).

McLandress, C., M. J. Alexander, and D. L. Wu (2000) "Microwave Limb Sounder observations of gravity waves in the stratosphere: A climatology and interpretation," *Journal of Geophysical Research*, 105(D9).

Miller J. E. (1948) "On the concept of frontogenesis," *Journal of Meteorology*, 5(4).

Moffatt H. K. (1969) "The degree of knottedness of tangled vortex lines," *Journal of Fluid Mechanics*, 35(1).

Moffatt H. K. (1981) "Some developments in the theory of turbulence," *Journal of Fluid Mechanics*, 106(1).

Molteni, F. and R. Buizza (1999) "Validation of the ECMWF ensemble prediction system using empirical orthogonal functions," *Monthly Weather Review*, 127(10).

Montgomery M. T. and J. Enagonio (1998) "Tropical cyclogenesis via convectively forced vortex Rossby waves in a three-dimensional quasigeostrophic model," *Journal of Atmospheric Sciences,* 55(20).

Montgomery M. T. and B. F. Farrell (1992) "Polar low dynamics," *Journal of Atmospheric Sciences*, 49(24).

Montgomery M. T. and B. F. Farrell (1993) "Tropical cyclone formation," *Journal of Atmospheric Sciences*, 50(2).

Moon Y. and D. S. Nolan (2015) "Spiral rainbands in a numerical simulation of Hurricane Bill (2009). Part II: Propagation of inner rainbands," *Journal of Atmospheric Sciences,* 72(1).

Nielsen-Gammon, J. W. and D. Keyser (2000) "Effective Stratification for Pseudo adiabatic Ascent," Monthly Weather Review, 128(8).

Ninomiya K.(1984) "Characteristics of Baiu front as a predominant subtropical front in the summer northern hemisphere," *Journal of the*

Meteorological Society of Japan, 62(6).

Ninomiya K. (2000) "Large- and meso-scale characteristics of Meiyu/Baiu front associated with intense rainfalls in 1-10 July 1991," *Journal of the Meteorological Society of Japan*, 78(2).

Oboukhov A. M. (1949) "The problem of geostrophic adaptation," Izuestiya of Academy of Science USSR, *Ser, Gograhpy and Geophysics,* 13.

Ogura Y. and N. A. Phillips (1962) "Scale analysis of deep and shallow convection in the atmosphere," *Journal of Atmospheric Sciences*, 19(2).

Okubo A. (1970) "Horizontal dispersion of floatable particles in the vicinity of velocity singularity such as convergences," *Deep Sea Research,* 17(3).

Ooyama, K. (1966) "On the stability of the baroclinic circular vortex: a sufficient criterion for instability," *Journal of Atmospheric Sciences,* 23(4).

Ogura, Y. and N. A. Phillips (1962) "Scale analysis of deep and shallow convection in the atmosphere," *Journal of Atmospheric Sciences*, 19(2).

Palmin E. and C. W. Newton (1948) "A study of the mean wind and temperature distribution in the vicinity of the polar front in winter," *Journal of Meteorology*, 5(5).

Petterssen S. (1936) "Contribution to the theory of frontogenesis," *Geofys Publ*, 11(6).

Phillips N. A. (1956) "The general circulation of the atmosphere, a numerical experiment," *Quarterly Journal of the Royal Meteorological Society*, 82(352).

Piani, C., D. Durran, M. J. Alexander, et al. (2000) "A numerical study of three- dimensional gravity waves triggered by deep tropical convection and their role in the dynamics of the QBO," *Journal of Atmospheric Sciences*, 57(22).

Preusse, P., B. Schaeler, J. T. Bacmeister et al. (1999) "Evidence for gravity waves in CRISTA temperatures," *Advances in Space Research*, 24(11).

Qi, Y., L. Ran and Y. Hong (2010) "Diagnosis of thermodynamic shear advection parameter in heavy rainfall events," *Chinese Journal of Atmospheric Sciences*, 34(6). (in Chinese with English abstract)

Qian, W. H., J. Li and X. L. Shan (2013) "Synoptic interpretation of mesoscale model disturbance wind in 2010 Regional Rainstorm Forecast," *Science China*, 35(5).

Qiu, C., J. Bao and Q. Xu (1993) "Is the mass sink due to precipitation negligible?" *Monthly Weather Review*, 121(3).

Ran, L. and S. Gao (2007) "A three-dimensional wave-activity relation for pseudomomentum," *Journal of Atmospheric Sciences*, 64(6).

Ran, L., N. Li and S. Gao (2013) "PV-based diagnostic quantities of heavy precipitation: solenoidal vorticity and potential solenoidal vorticity," *Journal of Geophysical Research*, 118(11).

Ran L. K., L. Liu, N. Li and et al. (2013) "The analysis of the potential-divergence wave activity density and its application to typhoon precipitation," *Chinese Journal of Geophysics*, 56(10).

Rayleigh, L. (1880) "On the stability, or instability, of certain fluid motions," *Proceedings of the London Mathematical Society*, s1-11(1).

Raymond, D. J. (1992) "Nonlinear balance and potential vorticity thinking at large Rossby Number," *Quarterly Journal of the Royal Meteorological Society*, 118(507).

Raymond D. J. and H. Jiang (1990) "A theory for long-lived mesoscale convective systems," *Journal of Atmospheric Sciences*, 47(24).

Ren, S. (2000) "Finite-amplitude wave-activity invariants and nonlinear stability theorems for shallow water semigeostrophic dynamics," *Journal of Atmospheric Sciences*, 57(20.

Renfrew I. A., A. J. Thorpe and C. H. Bishop (1997) "The role of the environmental flow in the development of secondary frontal cyclones,"

Quarterly Journal of the Royal Meteorological Society, 123(542).

Rivière G. and A. Joly(2006a) "Role of the low-frequency deformation field on the explosive growth of extratropical cyclones at the jet exit. Part I: Barotropic critical region," *Journal of Atmospheric Sciences,* 63(8).

Rivière G. and A. Joly (2006b) "Role of the low-frequency deformation field on the explosive growth of extratropical cyclones at the jet exit. Part II: Baroclinic critical region," *Journal of Atmospheric Sciences,* 63(8).

Robinson, P. J. (2001) "On the definition of a heat wave," *Journal of Applied Meteorology*, 40(4).

Robinson W. A. (1989) "On the structure of potential vorticity in baroclinic instability," *Tellus,* 41A.

Rossby C. G. (1937) "On the mutual adjustment of pressure and velocity distribution in certain simple current systems, I," *Journal of Marine Research*, 1(1).

Rossby C. G. (1938) "On the mutual adjustment of pressure and velocity distribution in certain simple current systems, II," *Journal of Marine Research*, 1(3).

Rossby, C. G. (1940) "Planetary flow patterns in the atmosphere," *Journal of the Royal Meteorological Society*, 66(1940).

Rozoff C. M., W. H. Schubert, B. D. McNoldy and et al. (2006) "Rapid filamentation zones in intense tropical cyclones," *Journal of Atmospheric Sciences,* 63(1).

Rutledge, S. A. (1991) "Middle latitude and tropical mesoscale convective systems," *Reviews of Geophysics*, 29(S1).

Schöch, A., G. Baumgarten, D. C. Fritts et al. (2004) "Gravity waves in the troposphere and stratosphere during the MaCWAVE/MIDAS summer rocket program," *Geophysical Research Letters*, 31(24).

Schubert W. H. and B. T. Alworth (1987) "Evolution of potential vorticity in tropical cyclones," *Quarterly Journal of the Royal Meteorological*

Society, 113(475).

Schultz D. M. and P. N. Schumacher (1999) "The use and misuse of conditional symmetric Instability," *Monthly Weather Review*, 127(12).

Scinocca, J. F. and T. G. Shepherd (1992) "Nonlinear wave-activity conservation laws and Hamiltonian structure for the two-dimensional anelastic equations," *Journal of Atmospheric Sciences*, 49(1).

Shutts G. J. (1983) "The propagation of eddies in diffluent jet-streams: eddy vorticity forcing of "blocking" flow fields," *Quarterly Journal of the Royal Meteorological Society,* 109(462).

Shutts G. J. and M. E. B. Gray (1994) "A numerical modeling study of the geostrophic adjustment process following deep convection," *Quarterly Journal of the Royal Meteorological Society*, 120(519).

Simpson, R. H. (1978) "On the computation of equivalent potential temperature," Monthly Weather Review, 106(1).

Smith, R. B. (1988) "Linear theory of hydrostatic flow over an isolated mountain in isosteric coordinates," Journal of Atmospheric Sciences, 45(24).

Spensberger C. and T. Spengler (2014) "A new look at deformation as a diagnostic for large-scale flow," *Journal of Atmospheric Sciences,* 71(11).

Stone, P. H. (1966) "On the non-geostrophic baroclinic stability," *Journal of Atmospheric Sciences,* 23(4).

Tan M. Z. and R. S. Wu (1994) "Helicity dynamics of atmospheric flow," *Advances in Atmospheric Science,* 11(2).

Tao Z. Y., X. G. Zhou and Y. G. Zheng (2012) "Vorticity, potential vorticity and stratospheric dry intrusion: origin, application and misuse of potential vorticity concept," *Meteorological Monthly*, 38(1).

Thomas L. N. (2012) "On the effects of frontogenetic strain on symmetric instability and inertia-gravity waves," *Journal of Fluid Mechanics,* 711.

Thorpe A. J. (1985) “Diagnosis of balanced vortex structure using potential vorticity,” *Journal of Atmospheric Sciences*, 42(4).

Thorpe A. J. (1990) “Frontogenesis at the boundary between air-masses of different potential vorticity,” *Quarterly Journal of the Royal Meteorological Society,* 116(493).

Toth, Z. and E. Kalnay (1997) “Ensemble forecasting at NCEP and the breeding method,” *Monthly Weather Review*, 125(12).

Tsuda, T., M. Nishida, C. Rocken, et al. (2000) “A global morphology of gravity wave activity in the stratosphere revealed by the GPS occultation data (GPS/MET),” *Journal of Geophysical Research*, 105(D6).

Vincent, R. A., S. J. Allen, and S. D. Eckermann (1997) Gravity-wave parameters in the lower stratosphere In *Gravity Wave Processes and Their Parameterization in Global Climate Models, Gravity Wave Processes*. Hamilton, K. Ed. Heidelberg, Springer-Verlag.

Vincent, R. A. and M. J. Alexander (2000) “Gravity waves in the tropical lower stratosphere: an observational study of seasonal and interannual variability,” *Journal of Geophysical Research*, 105(27).

Torrence, C. and G. P. Compo (1998) “A practical guide to wavelet analysis,” *Bulletin of the American Meteorological Society*, 79(1).

Wang L. M. and H. B. Luo (1980) “The basic dynamic equations and main properties of the saturated moist air,” *Acta Meteorologica Sinica*, 38(1). (in Chinese with English abstract)

Wang X. B. and R. S. Wu (2001) “The development of symmetric disturbance superposed on baroclinic frontal zone under the action of deformation field,” *Acta Meteorologica Sinica,* 15(4).

Wang X. R. and K. J. Wu (1999) “The introduction of condensation probability function and the dynamic equations on non-uniform saturated moist air,” *Journal of Tropical Meteorology*, 15(1). (in Chinese with English abstract).

Wang Y. Q. (2008) "Rapid filamentation zone in a numerically simulated tropical cyclone," *Journal of Atmospheric Sciences,* 65(4).

Weisman M. L. and J. B. Klemp (1982) "The dependence of numerically simulated convective storms on vertical wind shear and buoyancy," *Monthly Weather Review,* 110(6).

Weiss J. (1991) "The dynamics of enstrophy transfer in two-dimensional hydrodynamics," *Physica D,* 48(2-3).

Whitaker J. S. and R. M. Dole (1995) "Organization of storm tracks in zonally varying Flows," *Journal of Atmospheric Sciences,* 52(8).

Whitcher, B., P. Guttorp and D. B. Percival (2000) "Wavelet analysis of covariance with application to atmospheric time series," *Journal of Geophysical Research*, 105(D11).

Williams R. T. (1967) "Atmosphere frontogenesis, a numerical experiment," *Journal of Atmospheric Sciences*, 24(6).

Wu B. J., C. H. Xu, Y. Y. Liu and et al. (1996) "Applying helicity to analysis of torrential rain over the Changjiang Gorges," *Quarterly Journal of Applied Meteorology*, 7(1).

Wu G. X., Y. P. Cai and X. J. Tang (1995) "Moist potential vorticity and slantwise vorticity development," *Acta Meteorologica Sinica*, 53(4). (in Chinese with English abstract)

Wu G. X. and H. Z. Liu (1999) "Complete form of vertical vorticity tendency equation and slantwise vorticity development," *Acta Meteorogica Sinica*, 57(1). (in Chinese with English abstract)

Wu R. S. and M. Z. Tan (1989) "Generalized vorticity and potential vorticity versation law and application," *Acta Meteorologica Sinica,* 47(4). (in Chinese with English abstract)

Wu W. S., D. K. Lilly and R. M. Kerr (1992) "Helicity and thermal convection with shear," *Journal of Atmospheric Sciences*, 49(19).

Wu, X., L. Ran and Y. Chu (2011) "Diagnosis of a moist thermodynamic advection parameter in heavy-rainfall events," *Advances in Atmospheric Sciences*, 28(4).

Xie Y. B. (1978) “Synoptic Dynamic Problems of the Moist Baraclinic Atmosphere,” *Torrential Rain Corpus.* Changchun: Jilin People's Publishing House (in Chinese with English abstract)

Xu Q. (1992) “Formation and evolution of frontal rainbands and geostrophic potential vorticity anomalies,” *Journal of Atmospheric Sciences*, 49(8).

Xu, Q. (1992) “Ageostrophic pseudovorticity and geostrophic C-vector forcing—A new look at the Q vector in three dimensions,” *Journal of Atmospheric Sciences*, 49(12).

Xu, Q. (1994) “Semibalance Model-Connection between geostrophic type and balanced type intermediate models,” *Journal of Atmospheric Sciences*, 51(7).

Xu, Q. and S. Gao (1995). “An analytic model of cold air damming and its applications,” Journal of Atmospheric Sciences, 52(3).

Yang S., S. T. Gao and C. G. Lu (2014) “A generalized frontogenesis function and its Application,” *Advances in Atmospheric Sciences,* 31(5).

Yang S., S. T. Gao and C. G. Lu (2015) “Investigation of the Mei-yu front using a new deformation frontogenesis function,” *Advances in Atmospheric Sciences,* 32(5).

Yang Y. K., Y. L. Liu, Z. S. Wan and et al. (1994) “The helicity analysis of Mei-yu front storm rainfall during July 1991,” *Acta Meteorogica Sinica*, 52(3).

Yao X. P., G. X. Wu, Y. M. Liu and et al. (2007) “Case study on the impact of the vortex in the easterlies over the tropical upper troposphere on the subtropical anticyclone over the western Pacific Ocean,” *Acta Meteorogica Sinica*, 65(2). (in Chinese with English abstract)

Yao, X. P., Y. B. Yu and S. Shou (2004) “Diagnostic analyses and application of the moist ageostrophic vector Q,” *Advances in Atmospheric Sciences*, 21(1).

Yeh T. C. (1957) "On the formation of quasi-geostrohpic motion in the atmosphere," *Journal of the Meteorological Society of Japan,* 75th Anniversary Volume,35A.

Yeh T. C. and M. Li (1982) "On the characteristics of scales of the atmospheric motions," *Journal of the Meteorological Society of Japan,* 60(1).

Yue, C. J. (2009) "The Q vector analysis of the heavy rainfall from Meiyu front cyclone: A case study," *Acta Meteorologica Sinica*, 66(1). (in Chinese with English abstract)

Yue, C., Y. Shou, S. Shou, et al. (2007) "Wet Q vector interpretation technique with its application to quantitative precipitation forecast," *Journal of Applied Meteorological Science*, 18(5).

Zeng Q. C. (1963a) "The effect of original disturbance structure on adaptation and the application of observed wind field," *Acta Meteorologica Sinica,* 33(1). (in Chinese with English abstract).

Zeng Q. C. 1963b: "The adaptation and development in atmosphere," *Acta Meteorologica Sinica,* 33(2). (in Chinese with English abstract).

Zeng Q. C. 1963c: "The adaptation and development in atmosphere," *Acta Meteorologica Sinica,* 33(8). (in Chinese with English abstract)

Zeng, X., M. Shao, S. Wang, et al. (2008) "Forecasting precipitation experiment with KNN based on crossing verification technology," *Journal of Applied Meteorology Science*, 19(4).

Zhang, D.-L. and J. M. Fritsch (1988) "A numerical investigation of a convectively generated Inertially stable, extratropical warm-core mesovortex over land. Part I," *Monthly Weather Review*, 116(12).

Zhang, F., S. E. Koch, C. A. Davis, et al. (2000) "A survey of unbalanced flow diagnostics and their application," *Advances in Atmospheric Sciences*, 17(2).

Zhang, W., S. Fan and M. Chen (2012) "Applications of mesoscale model-generated sounding in Beijing local rainstorm forecasting," *Torrential Rain Disasters*, 31(1). (in Chinese with English abstract).

Zhang, X., S. Tao and J. Sun (2010) "Ingredients-based heavy rainfall forecasting," *Chinese Journal of Atmospheric Sciences*, 34(4). (in Chinese with English abstract)

Zhou, B., H. Xu, G. Wu, et al. (2002) "Numerical simulation of CMWDA with its impacting on torrential rain forecast," *Acta Meteorologica Sinica*, 60(003) 7. (in Chinese with English abstract)

Zhou Y. S., G. Deng, S. T. Gao and et al. (2002) "The study on the influence Characteristic of teleconnection caused by the underlying surface of the Tibetan Plateau I: data analysis," *Advances in Atmospheric Sciences*, 19(4).

Zhou Y. and L. Ran (2010) "Advective vorticity equation and its application to the vorticity variation of Typhoon Bilis in 2006," *Acta Physica Sinica*, 59(2).

Zink, F. and R. A. Vincent (2001) "Wavelet analysis of stratospheric gravity wave packets over Macquarie Island1. Wave parameters," *Journal of Geophysical Research*, 106(D10).

INDEX

Advection vorticity equation, 83, 84, 88, 89, 90, 113
Ageostrophic Eady mode, 30
Allen, J.S., 290, 295
Andrews, D.G., 61
Ari Sadarjoen I., 135
Bannon P.R., 56
Barotropic ideal atmosphere equations, 34
Bartels, D.L., 295
Barth, J.A., 295
Beardsley, R.C., 206
Beer, T., 198
Bennetts, D.A., 57, 64, 187, 218
Betts, A.K., 19, 56, 59
Bishop C.H., 130
Bolton, D., 19, 20, 58
Boussinesq approximation, 10, 40, 41, 42, 45, 212, 263
Brandes, E.A., 91, 295
Bright, D.R., 460
Brooks H.E., 100
Brunt–Väisälä frequency, 15, 23, 207
Buizza, R., 198, 461
Burger number, 3, 4, 5
Cai M., 129, 135
Cao J., 185, 186
Cao, Z.H., 58, 324
Caracena F., 153
Charney J.G., 42, 129, 205, 290
Chen, Q., 293, 299
Chen, Z.M., 118
Cheng, C.L., 461
Cheng, L., 462
Cho, H.R., 58
Chu, Y., 473
Clark, T.L., 239
Conditional symmetric instability, 218
Convective vorticity vector, 394, 395, 396, 397, 398, 399, 403, 463, 473, 474, 475, 482, 487
Cushman-Roisin. B., 3, 6, 23
Danielsen. E.F., 64, 135, 187
Davis. C.A., 51, 66, 135, 191, 295
Davies-Jones, R.P., 90, 100, 108, 148, 406, 407, 468
Deformation forecasting method, 339, 340

Deformation-vorticity–divergence interactions, 134, 138, 139
Deng, G., 460
Di, J., 461
Divergence equation, 35, 46, 49, 116, 117, 118, 136, 291, 295, 299, 300, 302, 304, 305, 307, 310, 311
Dodd, K.R., 204, 205, 206
Doswell, C.A., 148,
Driscoll, D.M., 317
Droegemeier K.K., 100
Durran, D.R., 16, 20, 35, 43
Dynamic factors, 118, 460, 463
Dynamic vorticity vector, 403, 405, 406
E vector, 418, 422, 455
Eady, E.T., 30, 129, 148,
Elhmaidi D., 129,
Eliassen, A., 209
Emanuel, K.A., 51, 56, 64, 135, 187
Enstrophy trend equations, 136
Ertel, H., 50, 51, 52, 63, 69, 180, 187, 194, 395, 426, 430
Etling, D., 99
Fang, C., 461
Farrell, B.F., 51, 64, 129, 187
Fei, S.Q., 100
Fernandez, W., 128
Fetzer, E, 240
Forecasting method for cyclone motion, 324
Fovell, R., 239
Fraser, A.B., 16
"Freezing-in" nature of the vorticity, 80
Fritsch, J.M., 66, 191, 295
Fritts, D.C., 271
Fulton, S.R., 67, 192
Gao, S., 25, 27, 37, 51, 57, 64, 66, 68, 70, 91, 129, 132, 162, 171, 182, 184, 187, 191, 263, 271, 294, 334, 395, 403, 460, 468
Generalized frontogenesis function, 149, 158, 161, 163, 164, 167, 170, 171, 172
Generalized moist potential vorticity, 63, 187, 195, 316, 320, 348, 403, 470, 482
Generalized potential temperature, 57, 119, 162, 171, 187, 195, 322, 463, 467
Gravity waves, 5, 135, 182, 236, 244, 255, 263, 269, 294
Gravity-wave breaking parameterization, 269
Gray, M.E.B., 66, 67, 191, 192
Green, J., 20
Harasti, P.R., 150
Haynes, P.H., 70, 135, 425
Helicity equation, 34, 98, 100, 109,

296, 308
Helmholtz, H., 198, 199, 220
Hirota, I., 240, 241,
Holton, J.R., 19, 56, 198, 271
Hoskins, B.J., 51, 56, 64, 66, 74, 135, 148, 187, 191, 218, 395, 406
Hoxit, L.R., 153
Huang, W.G., 407
Ideal baroclinic unsaturated atmosphere equations, 37
Impermeability of the moist potential vorticity substance, 70, 71, 72, 73, 74, 328, 331, 332,
Impermeability principle, 70
Inertial gravity waves, 5, 264, 303
Inertial instability, 200, 209, 217, 218, 219, 220
Internal Froude number, 1
James, I.N., 418
James, T.M., 291, 300
Jiang, H., 67, 192, 195
Jiang Y.Q., 130
Kalkstein, L.S., 317
Karl, T.R., 317
Kelvin, W., 198, 199, 220
Keyser, D.M., 51, 66, 131, 135, 161, 191, 292
Koch, S.E., 292
Krishnamurti, T.N., 198, 293
Kuo H.L., 129
Lalas, D.P., 16
Leary, C.A., 195
Li, B., 462
Li, N., 139
Li, X., 462
Li, Y.H., 107
Li, Z., 3
Liang, Z., 470
Liu, H., 463
Liu, D., 17
Liu, Y., 462
Liu, S.K., 52, 99
Lilly, D.K., 99, 100, 105, 110, 238
Lindzen, R.S., 238, 271
Lu, C., 253
Lu, H.J., 100
Luo, H.B., 56
Luo, Z.X., 135
Maddox, R.A., 66, 153, 191, 295
Mak, M., 129, 135
Markowski, P.M., 91
Matsuno, T., 271
McFarlane, N.A., 271, 274
McIntyre, M.E., 70, 135, 305, 306, 307, 395, 425
McLandress, C., 240
Mesoscale balance equation, 296, 298
Mesoscale instability, 198, 218,
Method of analyzing instability, 200

Miller, J.E., 148, 149
Moffatt, H.K., 99
Moist potential vorticity anomaly, 74, 324,
Moist thermodynamic advection parameter, 463, 464, 466, 482
Molteni, F., 461
Montgomery, M.T., 51, 64, 135, 187
Moon, Y., 129
Nielsen-Gammon, J.W., 20
Ninomiya, K., 148
Norbury, J., 5
Oboukhov, A.M., 45
Ogura Y., 272
Okubo, A., 129, 135
Ooyama, K., 198, 202
Palmin, E., 148
Pedlosky, J., 51, 198, 202, 206, 221
Petterssen, S., 45, 128, 129, 130, 131, 135, 148, 149, 154, 155
Piani, C., 239
Potential divergence, 119, 120, 123, 472, 473
Potential vorticity, 34, 50
Potential vorticity equation, 34, 50, 67, 69, 70, 74, 194, 425, 469
Potential-vorticity retrieval, 289, 293, 302, 303, 304, 307, 312
Potential vorticity substance equation, 50, 51, 53
Preusse, P., 240
Pseudo-incompressible approximation, 40, 42, 44, 45, 49
Q vector, 406, 407, 414, 416, 418, 462, 467
Qi, Y., 473
Qian, W.H., 462
Qiu, C., 334
Ran, L., 119, 428, 464
Rayleigh, L., 198, 205
Raymond, D.J., 67, 192, 294, 295
Renfrew, I.A., 130
Richardson number, 1, 3, 5, 6, 20, 22, 23, 25, 200, 207, 211, 212, 230
Rivière, G., 129
Robinson, P.J., 318
Robinson, W.A., 51
Rossby, C.G., 45, 128, 135, 180
Rossby number, 1, 3, 4, 290, 291, 294
Rozoff, C.M., 129, 135
Rutledge, S.A., 295
Scalar frontogenesis function, 149, 153, 154, 156, 159, 161, 162, 163, 170, 171
Schubert, W.H., 51
Schultz, D.M., 57
Scorer, R.S., 91, 198, 202, 220

Second-order potential vorticity, 182, 183, 185, 186, 442, 473, 474, 475, 478
Shear instability, 23, 199, 220, 221, 230, 238
Shou, S.W., 27, 57
Shutts, G. J., 67, 129, 192
Simpson, R.H., 19
Smith, R.B., 10
Solenoidal vorticity, 470, 471, 472
Spensberger, C., 135
Static instability, 200, 206
Stone, P.H., 209
Streamline vortex, 90, 92, 95, 98
Symmetric instability, 23, 129, 199, 209, 214, 217, 218, 219, 470
Tan, M.Z., 45, 99, 108
Tao, S., 460
Tao Z.Y., 120
Thermodynamic helicity, 466, 467
Thomas, L.N., 129
Thorpe, A.J., 51 64, 128, 130, 187
Total deformation, 46, 130, 136, 154, 162, 170, 340
Toth, Z., 460
Tsuda, T., 240
Tritton, D.J., 220
Vallis, G.K., 80
Vapor potential vorticity, 343, 346, 403
Vincent, R.A., 240,
Vortex-layer instability, 225
Vorticity equation, 27, 34, 46
Wang L.M., 56
Wang X.B., 129
Wang X.R., 56
Wang Y.Q., 129
Wave-action equation, 423, 425, 427, 428, 433
Wave-action vector, 423
Weisman, M.L., 66, 128, 191, 195
Weiss, J., 129, 135
Whitaker, J.S., 129
Williams, R.T., 148
Wiin-Nielsen, A., 128
Wu, B., 108
Wu, G.X., 40, 56, 83
Wu, K.J., 56
Wu, R.S., 45, 99, 130, 149
Wu, W.S., 99
Wu, X., 465
Xie, Y.B., 56
Xu, Q., 10, 64, 185, 186, 187, 295, 407
Yang, S., 129
Yang, Y.K., 107, 108
Yao, X.P., 84, 407, 416, 468
Yeh, T.C., 45, 128
Yue, C.J., 462, 468
Zeng, Q.C., 45, 128, 149, 199
Zeng, X., 463

Zhang, D.-L., 295, 324
Zhang, F., 262, 291, 293
Zhang, W., 461
Zhang, X., 462
Zhou, B., 461
Zhou, Y., 66, 88, 191
Zink, F., 240